

H 24/3836

No Restrictions.

MONASH UNIVERSITY
THESIS ACCEPTED IN SATISFACTION OF THE
REQUIREMENTS FOR THE DEGREE OF
DOCTOR OF PHILOSOPHY

ON..... 8 February 2005.....

Sec. Research Graduate School Committee

Under the Copyright Act 1968, this thesis must be used only under the normal conditions of scholarly fair dealing for the purposes of research, criticism or review. In particular no results or conclusions should be extracted from it, nor should it be copied or closely paraphrased in whole or in part without the written consent of the author. Proper written acknowledgement should be made for any assistance obtained from this thesis.

Errata

- p vi para 3, last sentence: "structure of GaN based" for "structure of a GaN based"
- p vii para 3, last sentence: "resolution in the latter" for "resolution for in the latter"
- p 1 para 2, last sentence: "velocity as a function of" for "velocity as function of"
- p 6 para 2, line 7: "magnitude of the k-vector" for "magnitude of k-vector"
- p 11 para 2, last sentence: "nitride parameters are given in Table" for "nitride parameters given in Table"
- p 12 last line: "directly on α -sapphire" for "directly on an α -sapphire"
- p 16 para 1, line 20: "contributions to the peak width" for "contributions of the peak width"
- p 17 para 2, line 4: "dislocation line direction." for "dislocation line."
- p 18 para 1, line 4: "dislocation line direction and" for "dislocation line and"
- p 18 para 1, line 6: "dislocation line direction are" for "dislocation line are"
- p 18 para 1, line 10: "magnitude of each of the partial Burgers vectors is" for "magnitude of the Burgers vector is"
- p 18 para 2, line 2: "dislocation line direction can" for "dislocation line can"
- p 20 para 1, line 1: "to determine the growth" for "for determining the growth"
- p 20 para 2, line 8: "by a mosaic block model" for "by a mosaic blocks model"
- p 20 para 3, line 2: "techniques described. The" for "techniques described The"
- p 22 para 1, line 4: "by electrons to" for "by electron to"
- p 23 para 1, line 2: "typically of the order" for "typically on the order"
- p 24 para 1, line 2: "wavelength of the order" for "wavelength on the order"
- p 26 Eqs. (2.7), (2.8), (2.9) and (2.10): insert full stop.
- p 27 para 1, line 3: "vectors s_0 and s respectively" for "vectors s and s_0 respectively"
- p 27 2nd line after Eq. (2.12): "called the electron scattering" for "called electron scattering"
- p 27 Eq. (2.13): delete full stop.
- p 28 Eq. (2.14): insert full stop.
- p 28 Eq. (2.18): delete full stop.
- p 28 Last line: delete "where F"
- p 33 para 4, line 4: "density, or more specifically" for " density. More specifically"
- p 35 Eq. (2.41): insert full stop.
- p 43 Eq. (2.69): delete full stop.
- p 46 line after Eq. (2.73): "can also be split" for "can be also be split"
- p 46 Eq. (2.75): insert full stop.
- p 47 Eq. (2.77): delete full stop.
- p 48 Eq. (2.83): delete full stop.
- p 49 Eq. (2.88): insert full stop.
- p 49 2nd line after Eq. (2.89): "neglecting any extrinsic" for "neglecting the any extrinsic"
- p 50 line after Eq. (2.95): "displayed on the right" for "displayed on right"
- p 51 Eq. (2.104): insert full stop.
- p 52 Eq. (2.107): " 0),(2.107)" for " 0),(2.107)"
- p 53 Eq. (2.108): delete full stop.
- p 55 Eq. (2.121): insert full stop.
- p 60 Figure 2.13 caption, line 4: "These scans allow" for "These scan allow"
- p 62 para 1, line 4: " α -sapphire substrates." for " α -sapphire substrate."
- p 64 Table 3.1: The thickness of the AlN layer for samples D05, D30 and D42 should read 30 nm instead of 20 nm.
- p 73 Footnote 6, line 1: "ActiveX is a software" for "ActiveX is software"
- p 78 para 3, line 4: "over the q_z coordinate" for "over q_z the coordinate"
- p 79 line 14 after Eq. (3.4): "total number of points" for "total number points"

p 89 last para, line 3:	"by partitioning the sub-layer" for "by partition the sub-layer"
p 99 para 3, line 2:	"compare the various" for "compare of the various"
p 99 para 3, line 5:	"peak of height unity" for " peak of height of unity"
p 106 para 4, line 2:	"profile shown in Fig. 4.14 have" for "profile shown 4.14 have"
p 113 para 2, line 6:	"This suggests that" for "This suggest that"
p 114 para 2, line 3:	"the AlN peak the" for "the peak AlN the"
p 114 para 5, line 2:	"The effect different" for "The affect different"
p 119 para 2, line 11:	"are not perfectly parallel." for "are not be perfectly parallel."
p 126 para 1, line 8:	"scans could be matched more" for "scans could matched more"
p 133 para 2, line 2:	"the InN composition" for "the composition of the InN composition"
p 133 para 3, line 2:	"the growth for sample" for "the growth for of sample"
p 140 para 1, line 1:	"centre of the GaN peak." for "centre of GaN peak."
p 148 para 1, line 1:	"predicted by the" for "predicted by for the"
p 151 para 1, line 5:	"peaks could arise from" for "peaks could be arise from"
p 153 para 1, line 11:	"Nistor <i>et al.</i> " for "However, Nistor <i>et al.</i> "
p 157 Table 4.29:	"Indeterminate" for "Indeterminant"
p 161 para 1, line 22:	"These observations suggest" for "These observation suggest"
p 162 para 1, line 2:	"scans in the $q_x - q_y$ plane" for "scans in $q_x - q_y$ plane"
p 163 para 3, line 13:	"and with an AlN buffer" for "and with AlN buffer"
p 164 para 4, line 5:	"the InGaN layers between" for "the InGaN layer between"
p 165 line 2:	"determination of the dislocation" for "determination for the dislocation"
p 166 para 4, line 1:	"studied a ZnSe-based" for "studied ZnSe-based"
p 167 para 2, line 13:	"reciprocal space depends" for "reciprocal space is depends"
p 182 para 1, line 8:	"investigated in both" for "investigated in the both"
p 185 para 1, line 1:	"strength being positioned" for "strength begin positioned"
p 188 Eq. (6.8):	delete one comma.
p 189 Eq. (6.17):	insert full stop.
p 190 para 3, line 5:	"that it is small" for "that it is a small"
p 192 Eq. (6.27):	delete full stop.
p 208 para 2, line 8:	"and the match" for "and that the match"
p 215 para 1, line 4:	"generated artifacts, the most" for "generated artifacts. The most"
p 215 para 2, line 14:	"gave more meaningful results." for "gave more meaning results."
p 216 para 1, line 3:	"reflections can be attributed" for "reflections can been attributed"
p 217 line 3:	"respectively; for asymmetric scans" for "respectively; for symmetric scans"
p 218 para 2, line 14:	"would require reciprocal" for "would required reciprocal"
p 219 Fig. 7.2 caption, line 2:	"diffracted from the plane which has" for "diffracted from the which has"
p 222 Eq. (A.14):	insert full stop.
p 223 3rd equation:	insert a full stop.

Characterisation of Group III Nitrides using
Hard X-ray Synchrotron Radiation

A THESIS SUBMITTED FOR THE DEGREE OF
DOCTOR OF PHILOSOPHY

By
Stephen Mudie B. Sc. (Hons.)

School of Physics and Materials Engineering,
Monash University,
Australia.

October 2004

© Copyright 2004
by
Stephen Mudie B. Sc. (Hons.)

Contents

Declaration	v
Summary	vi
Acknowledgements	x
1 Introduction	1
1.1 Optoelectronics	2
1.1.1 The Blue LED	4
1.2 Group III Nitrides	5
1.2.1 Band Structure	6
1.2.2 Crystal Structure	6
1.2.3 Bulk Group III Nitride Growth	8
1.2.4 Epitaxial Growth	9
1.2.5 Dislocations	17
1.3 Summary and Scope of the Thesis	19
2 X-ray Diffraction Theory	21
2.1 X-ray Sources	21
2.1.1 X-ray Tubes	21
2.1.2 Synchrotron Radiation	22
2.2 X-ray Scattering	24
2.2.1 Thomson Scattering	24
2.2.2 Scattering from an Atom	26
2.2.3 Geometrical Diffraction from Perfect Crystals	29
2.3 Reciprocal Space	31
2.4 Dynamical Diffraction Theory - Perfect Crystals	32
2.4.1 Two Wave Approximation	35
2.4.2 Dispersion Surface	37
2.5 Dynamical Diffraction Theory - Deformed Crystals	39
2.6 Kinematical Theory of X-ray diffraction	41
2.6.1 Derivation of the Kinematical Theory from Structure Factors	42

2.7	Mosaic Crystals	44
2.8	Statistical Diffraction Theory	45
2.8.1	Kato's Integral Formalism	46
2.8.2	Kato's Differential Formalism	49
2.8.3	Statistical Kinematical Diffraction Theory	51
2.9	Models for Crystal Defects	54
2.10	Reciprocal Space Mapping of Crystal Structures	57
3	Experimental and Modelling Techniques	62
3.1	Group III Nitride Samples	62
3.2	Synchrotron Experiments	63
3.2.1	Beamline Specifications and Equipment	64
3.2.2	Experimental Arrangement for Collection of Reciprocal Space Scans	67
3.2.3	Experimental Method	69
3.3	Simulation of Diffraction Profiles	71
3.3.1	Modelling Software	72
3.3.2	Techniques for Optimisation of Model Parameters	80
4	Results and Analysis of $\text{In}_x\text{Ga}_{1-x}\text{N}/\text{GaN}/\text{AlN}$ Samples	85
4.1	Introduction	85
4.2	Sample Series A and B: LT-AlN Buffer Layers	86
4.3	Sample Series C: GaN on a LT-AlN Buffer Layer	99
4.4	Sample Series D: InGaN Grown on GaN/AlN Buffer Layers	116
4.4.1	Sample D05: 20 nm $\text{In}_{0.05}\text{Ga}_{0.95}\text{N}$	120
4.4.2	Sample D30: 20 nm $\text{In}_{0.30}\text{Ga}_{0.70}\text{N}$	134
4.4.3	Sample D42: 200 nm $\text{In}_{0.42}\text{Ga}_{0.58}\text{N}$	146
4.5	Comparison of Statistical Diffraction Theory and Williamson-Hall Analysis	157
4.6	Periodic Noise and Spurious Peaks	158
4.7	Asymmetric Reflections	161
4.8	Summary of the Results	162
4.8.1	Comparison of Buffer Layers	162
4.8.2	Variation of InGaN Layers with Composition	164
4.8.3	Dislocation Densities	164

5	Development of an Imaging Plate Technique for Rapid RSM Collection	166
5.1	Overview of RSM Collection with Position Sensitive Detectors	166
5.2	Reciprocal Space Geometry for Collecting RSMs using Imaging Plates	168
5.2.1	RSM Collection Method	168
5.3	Experimental Results and Interpolation Methods	171
5.4	Discussion of Experimental and Interpolation Results	174
5.5	Conclusion	182
6	Chemical Ordering of Group III Nitrides	184
6.1	Introduction to Ordering of Group III Nitrides	184
6.2	Experiment	186
6.3	Williamson-Hall Analysis	187
6.4	Statistical Diffraction Theory	190
6.4.1	Composition Gradient Model	191
6.5	Results and Discussion	196
6.5.1	As Grown Samples	197
6.5.2	Annealed Samples	204
6.6	Conclusion	211
7	Conclusions and Future Work	213
7.1	Review of Major Results	213
7.2	Directions for Future Research	216
7.3	Summary	220
A	The Wave Equation in Polarisable Media	221
B	Conversion of Angular Co-ordinates to Reciprocal Space Vectors	223

Declaration

I declare that this thesis contains no material which has been accepted for the award of any other degree or diploma at any university. To the best of my knowledge and belief this thesis contains no material published or written by another person, except where due reference is made in the text.

A solid black rectangular box used to redact the author's signature.

Stephen Thomas Mudie

Summary

Group III nitrides are direct bandgap semiconductors suitable for short wavelength optoelectronic applications. By varying the composition, x , of ternary alloys, such as $\text{Al}_x\text{Ga}_{1-x}\text{N}$ and $\text{In}_x\text{Ga}_{1-x}\text{N}$, emission is achieved across the electromagnetic spectrum from red to ultraviolet. Blue light emitters are utilised for producing full colour semiconductor displays, while blue/UV emitters can excite phosphors at any visible wavelength. GaN based light emitting diodes are currently used in a wide range of applications, such as traffic signals and document scanners. Violet laser diodes, based on GaN, have also been commercialised. These devices will soon replace red laser diodes currently used for reading and writing optical (DVD) media.

Optoelectronic devices are constructed by growing multiple layers of semiconductor material on a crystal substrate. The ideal substrate for GaN epitaxial growth is bulk GaN. However, it is exceptionally difficult to grow bulk GaN, so alternative materials are used, typically sapphire and silicon carbide. The structural and thermal properties of GaN do not match those of readily available substrates. This causes the GaN epitaxial layers to be highly strained, resulting in large dislocation densities on relaxation. GaN epilayers are improved by employing an AlN buffer layer (grown at low temperatures) between the substrate and the GaN epitaxial layer. Structural characterisation of Group III nitride epitaxial layers, including buffer layers, impacts on device development by facilitating optimisation of the growth process.

Triple axis diffractometry (TAD) is one of a number of non-destructive techniques suited to studying these materials. Using TAD the distribution of the diffracted intensity about a reciprocal lattice point can be mapped (reciprocal space mapping). Epitaxial layers of Group III nitrides have high defect densities that produce broad X-ray diffraction peaks. Statistical diffraction theory can be used to describe the diffracted intensity - with the defect structure characterised by the ensemble average and spatial pair correlation function of the deformation in the crystal structure. The principal aim of this thesis is to characterise the crystal structure of a GaN based semiconductor multilayers, using TAD and statistical diffraction theory.

Chapter 1 details the Group III nitride semiconductor system, including a description of the dominant defect structures in these materials. In particular the role of low temperature deposited buffer layers in reducing the defect density of GaN is discussed. In Chapter 2 we describe X-ray diffraction theory, including Takagi's diffraction theory for deformed crystals, and Kato's statistical diffraction theory. The kinematical limit to statistical diffraction theory is also presented, along with the mosaic block model used to describe defect structures.

Triple axis diffractometry measurements on samples of Group III nitrides are described in Chapter 3. The samples were grown using metal-organic chemical vapour deposition (MOCVD), and are representative of the structure at several stages of the growth process. The first set of samples included 30 nm and 70 nm AlN buffer layers deposited at 400°C (some of the samples were also annealed at 1100°C). The second set of samples incorporated a 30 nm GaN overlayer on 30 nm and 70 nm AlN buffer layers. The final samples incorporated a 30 nm AlN buffer, a 2 μm thick GaN buffer and an InGaN top layer. Three InGaN compositions were investigated: $\text{In}_{0.05}\text{Ga}_{0.95}\text{N}$, $\text{In}_{0.30}\text{Ga}_{0.70}\text{N}$ and $\text{In}_{0.42}\text{Ga}_{0.58}\text{N}$. The InGaN layer constitutes the optically active material with the composition determining the wavelength of the emitted light.

All TAD experiments were carried out at the Australian National Beamline Facility at the Photon Factory, Tsukuba, Japan. This beamline is a bending magnet source, with the experimental end station housing a large diffractometer that can be evacuated to reduce air scatter. The first set of experiments utilised an additional monochromator (downstream from the beamline monochromator) to ensure a very small beam divergence (≈ 7 arcseconds) with an analyser crystal restricting the angular window of the detector. However, later experiments only employed the beamline monochromator and a slit. Although the angular resolution for in the latter experiment was not as high, the larger X-ray intensity significantly increased the signal to noise ratio.

The diffracted intensity from the mosaic block model was calculated using statistical diffraction theory. Chapter 3 describes the program written by the author using IDL¹ to produce simulated scans. These were compared with the experimental diffraction data collected using TAD. The model parameters include, the mosaic block size, distribution of block tilt (misorientation), whole layer tilt, strain, and layer thicknesses. Each parameter was adjusted systematically to match the simulated diffraction profiles to the experimental data.

¹The Interactive Data Language (IDL) is produced by Research Systems Inc. (see e.g., <http://www.rsinc.com>)

Chapter 4 presents the experimental X-ray diffraction profiles collected for each of the samples. Analysis of the AlN buffers showed the as deposited layer formed from two low quality sub-layers (i.e., small crystallites with random orientation). Annealing the 30 nm buffer layer significantly improved one of the sub-layers, by orienting the crystallites (perpendicular to the sample surface) and increasing their size (parallel to the sample surface). This effect was not seen for the 70 nm buffer layer. It has been reported in the literature (Tabuchi *et al.*, 2002) that an approximately 30 nm thick AlN buffer layer produces a better GaN crystal structure than a 70 nm buffer layer. We suggest this is due to the high quality sub-layer (i.e., well oriented and large lateral block size) observed for the annealed 30 nm AlN buffer. The analysis of the diffraction profiles from the InGa_xN layers showed that the mosaic block model is inadequate for matching the shape of the diffraction peaks originating from In_{0.42}Ga_{0.58}N. This suggests that another defect structure is present, which modifies the distribution of the diffracted intensity. We conjecture that clusters (of In or InN) have formed within the InGa_xN layer, because InN is only completely miscible in GaN at low concentrations (the equilibrium GaN rich concentration for InGa_xN is 6% InN). Clusters were also expected for the In_{0.30}Ga_{0.70}N layer; however, there was no evidence of these clusters.

Chapter 5 describes a novel experimental technique for collecting reciprocal space maps. This technique utilised an imaging plate, which acts as a one-dimensional detector by masking the plate with Weissenberg screens. Careful interpolation of the data is required because the one-dimensional scans collected by the plate are not parallel to the reciprocal space vectors. Additionally, the number of one-dimensional scans is limited by the imaging plate size. It was shown that this technique is simple to implement and increases the collection rate for RSMs, but because of the lower spatial resolution it is best used to investigate broad diffraction peaks.

Chapter 6 describes an investigation of an Al_{0.564}Ga_{0.436}N layer grown by molecular beam epitaxy. The as grown AlGa_xN layer showed significant chemical ordering of the Ga and Al species. This was deduced from the presence of forbidden reflections in the X-ray diffraction patterns. However, after annealing at high temperature and pressure, the ordering was destroyed, which suggests that the chemical ordering is due to growth kinetics. A mosaic block model was used to describe these samples, although some modifications to the formalism described in Chapter 2 were required. In particular two different mosaic block sizes were used to account for the shape of the 'forbidden' reflection peaks. The annealed samples showed significant inter-mixing of the layers, leading to a composition gradient through the sample. This composition gradient modified the diffraction profile, requiring that a non-statistical

strain distribution be included in the defect model.

Finally, in Chapter 7 we summarise the principal results of the thesis and point to future work. This includes the development of a more complicated mosaic block model, specific to the Group III nitrides. Such a model would include rotation of the blocks about the axis perpendicular to the sample surface (twist) and the inclusion of hexagonal blocks. These theoretical refinements can be validated by further experimental work, employing grazing incidence in-plane diffraction that is sensitive to twist.

Acknowledgements

I wish to express my deep gratitude to my supervisors, Associate Professor Michael Morgan and Dr. Konstantin Pavlov. Their guidance, patience, and expertise, have been invaluable during my PhD candidature.

I also wish to thank Dr. James Hester for his assistance with the experimental work at the ANBF. I am indebted to Professor Yoshikazu Takeda and Dr. Masao Tabuchi for their warm hospitality during my visit to their laboratory, and Professors H. Amano and I. Akasaki for providing the samples used in this thesis. I would also like to thank Dr. Lutz Kirste for his collaboration.

I want to thank my fellow PhD students Marcus Kitchen, Andrew Kingston, Tamar Greaves, and Russell Horney, for their friendship. I value you all greatly.

Financial support was provided by an Australian Postgraduate Award. The synchrotron work was supported by the Australian Synchrotron Research Program, which is funded by the Commonwealth of Australia under the Major National Research Facilities Program.

Finally I want to thank my family and friends, and particularly my Mother, for their unceasing love, support, inspiration, and prayers. I especially want to honour my wife, Kate, who has had the arduous task seeing me through my PhD. Praise be to God, without whom my life have no meaning.

This thesis is dedicated to the memory of Edna Mudie.

List of Tables

1.1	Lattice parameters for Group III nitride semiconductors.	9
1.2	Physical parameters for the substrates.	11
1.3	Physical parameters for Group III nitrides.	12
3.1	Sample designations used in the present work	64
4.1	Experimental parameters for samples of type A and B.	86
4.2	Experimental scan parameters for samples of type A.	87
4.3	Simulation parameters for sample A30 (without strain distribution). . .	91
4.4	Simulation parameters for sample A30 (with strain distribution). . . .	91
4.5	Simulation parameters for sample A70 (without strain distribution). . .	91
4.6	Simulation parameters for sample A70 (with strain distribution). . . .	91
4.7	Experimental scan parameters for samples of type B.	93
4.8	Simulation parameters for sample B30 (without strain distribution). . .	96
4.9	Simulation parameters for sample B30 (with strain distribution). . . .	96
4.10	Simulation parameters for sample B70 (without strain distribution). . .	96
4.11	Simulation parameters for sample B70 (with strain distribution). . . .	96
4.12	Experimental parameters for samples of type C.	99
4.13	Experimental scan parameters for sample C30.	100
4.14	Simulation parameters for sample C30 (without strain distribution). . .	104
4.15	Simulation parameters for sample C30 (with strain distribution). . . .	104
4.16	Experimental scan parameters for sample C70.	110
4.17	Simulation parameters for sample C70, optimised for the (0004) re- flection	113
4.18	Simulation parameters for sample C70, optimised for the (0002) re- flection	113
4.19	Experimental scan parameters used for samples of type D.	116
4.20	Experimental scan parameters for sample D05	121
4.21	Summary of the composite scans for sample D05	121
4.22	Simulation parameters for sample D05.	127
4.23	Experimental scan parameters for sample D30	134
4.24	Summary of the composite scans for sample D30	135
4.25	Simulation parameters for sample D30.	135
4.26	Experimental scan parameters for sample D42	146

4.27	Summary of the composite scans for sample D42	147
4.28	Simulation parameters for sample D42.	147
4.29	Summary of material parameters for the InGaN layer for sample type D using Williamson-Hall (WH) analysis and statistical diffraction theory	157
6.1	Parameters determined using the Williamson-Hall procedure for the as grown AlGaIn sample. The regression analysis was performed by plotting Δq versus q	200
6.2	Parameters determined using the Williamson-Hall procedure for the as grown AlGaIn sample. The regression analysis was performed by plotting Δq^2 versus q^2	200
6.3	Parameters determined from the statistical diffraction theory for the as grown AlGaIn sample.	200
6.4	Parameters determined from a Williamson-Hall analysis for the an- nealed AlGaIn sample.	204
6.5	Parameters determined from the statistical diffraction theory for the annealed AlGaIn sample.	207

List of Figures

1.1	Schematic plot of electron drift velocity at 300 K versus electric field	2
1.2	Schematic diagram of a high electron mobility transistor	2
1.3	Schematic diagram of the band structure of GaN	7
1.4	The stacking sequence for wurtzite and zincblende and a 3D ball and stick representation of wurtzite	8
1.5	Orientation of AlN/GaN epitaxial layers on an α -sapphire substrate .	13
1.6	Schematic of the growth process proposed by Hiramatsu <i>et al.</i> (1991)	15
1.7	Schematic diagram of the mosaic structure of GaN showing the tilt and twist of the mosaic blocks	17
1.8	An edge dislocation	18
1.9	Determining the Burgers vector	19
1.10	Screw dislocation.	19
2.1	Classical X-ray scattering from a single free electron	25
2.2	The projection of the acceleration perpendicular to the vector connecting the charge at the origin and the observation point P	25
2.3	Illustration showing the path length difference between two waves. . .	27
2.4	Diffraction from a grating.	29
2.5	The scatter geometry applicable to Bragg's law.	30
2.6	The Ewald sphere construction and diffraction from a plane	32
2.7	Schematic diagram illustrating dynamical diffraction	36
2.8	Correction of the Ewald sphere for the refractive index of the medium and the dispersion surface construction	38
2.9	Schematic of wavelets 'zigzagging' through a crystal	47
2.10	Schematic of mosaic blocks	56
2.11	Schematic diagram of the triple axis diffractometry experiment	58
2.12	Angle definitions in angular and reciprocal space	58
2.13	Various scan directions in reciprocal space	60
3.1	Schematic diagram of the Group III nitride sample growth regime . .	63
3.2	Photographs of the various components used for the experiments at the ANBF	65
3.3	Schematic of the triple axis diffractometry experimental arrangements	67
3.4	Diagram of the sample holder	69

3.5	The Excel simulation interface	74
3.6	Visual Basic for Applications simulation interface	75
3.7	Flowchart for the simulation program	76
3.8	Schematic of the strain gradient model	82
4.1	One-dimensional scans of sample A30	88
4.2	One-dimensional scans of sample A70	88
4.3	Strain weighting and associated depth profile used for simulating sample A30	89
4.4	Strain weighting and associated depth profile used for simulating sample A70	89
4.5	One-dimensional scans of sample B30	94
4.6	One-dimensional scans of sample B70	94
4.7	Strain weighting and associated depth profile used for simulating sample B30	97
4.8	Strain weighting and associated depth profile used for simulating sample B70	97
4.9	Experimental and simulated reciprocal space maps for sample B30	98
4.10	Experimental and simulated reciprocal space maps for sample B70	98
4.11	$\theta - 2\theta$ scans for sample C30	101
4.12	ω scans for sample C30	103
4.13	ω scan of the GaN peak for sample C30	103
4.14	Strain weighting and associated depth profile used for simulating sample C30	105
4.15	Tilt distribution profiles used for simulating sample C30	105
4.16	Misorientation, Δ_m , distribution profiles used for simulating sample C30	105
4.17	Reciprocal space map for sample C30, indicating rotation of the diffracted peak in the q_x - q_z plane	107
4.18	$\omega - 2\theta$ scan for sample C30 about AlN(0002), with $\Delta\omega = -1.08^\circ$	107
4.19	Reciprocal space maps for sample type C	108
4.20	$\theta - 2\theta$ scans for sample C70	111
4.21	Strain weighting and associated gradient profile, optimised for the (0004) reflection, used for simulating sample C70	112
4.22	Strain weighting and associated gradient profile, optimised for the (0002) reflection, used for simulating sample C70	112
4.23	$\omega - 2\theta$ scan for sample C70 about AlN(0002), with $\Delta\omega = -1.42^\circ$	112
4.24	ω scans for sample C70	115
4.25	An example of a composite scan	118

4.26	Experimental profile and simulated profile for the $\theta - 2\theta$ scans for sample D05 using a narrow (0.5 mm) slit	122
4.27	Experimental and simulated profiles for the $\theta - 2\theta$ scan about the (0002) reflection for sample D05 (using a wide (10 mm) slit)	123
4.28	RSMs for sample D05	124
4.29	$\omega - 2\theta$ scan for sample D05 near Ga(0002)	126
4.30	Experimental profiles and simulated profiles for the ω scans near the GaN(0002) reflection for sample D05	128
4.31	Experimental profiles and simulated profiles for the ω scans near the GaN(0004) reflection for sample D05	129
4.32	Experimental and simulated profiles for the $(11\bar{2}4)$ reflection	130
4.33	Reciprocal space maps of the GaN($11\bar{2}4$) reflection for sample D05	131
4.34	Reciprocal space map of the GaN($11\bar{2}4$) reflection for sample D05, collected using the imaging plate technique	131
4.35	Reciprocal space construction showing the origin of the streak due to mosaic block misorientation.	132
4.36	Experimental profile and simulated profiles for the $\theta - 2\theta$ scans for sample D30 using a narrow (0.5 mm) slit.	136
4.37	Experimental profiles and simulated profiles for sample D30 using a wide (10 mm) slit.	137
4.38	Experimental profiles and simulated profiles for the ω scans for sample D30 using a narrow (0.5 mm) slit	138
4.39	Experimental profiles and simulated profiles for ω scans for sample D30 using a narrow (0.5 mm) slit	139
4.40	$\omega - 2\theta$ scan for sample D30, with $\Delta\omega = 0.345^\circ$	140
4.41	Reciprocal space maps for sample D30	141
4.42	$\theta - 2\theta$, scan and ω scan about the $(11\bar{2}4)$ reflection for sample D30	142
4.43	Experimental and simulated RSMs about the $(11\bar{2}4)$ reflection for sample D30	143
4.44	Reciprocal space map collected about the $(11\bar{2}4)$ reflection using the imaging plate technique	144
4.45	Experimental profiles and simulated profiles for the $\theta - 2\theta$ scans for sample D42 using a narrow (0.5 mm) slit	148
4.46	Experimental profiles and simulated profiles for the $\theta - 2\theta$ scans for sample D42 using a wide (10 mm) slit	149
4.47	$\omega - 2\theta$ scan for sample D42, with a $\Delta\omega$ offset of -0.18°	150

4.48	Experimental profiles and simulated profiles for ω scans for sample D42 using a narrow (0.5 mm) slit	151
4.49	Experimental profiles and simulated profiles for ω scans for sample D42 using a narrow (0.5 mm) slit	152
4.50	$\theta - 2\theta$ and ω scans about the $(11\bar{2}4)$ reflection for sample D42	152
4.51	(a) Experimental RSM, and (b) simulated RSM, about the $(11\bar{2}4)$ reflection for sample D42.	153
4.52	Reciprocal space map about the $(11\bar{2}4)$ reflection for sample D42, collected using the imaging plate technique	153
4.53	An RSM collected using the imaging plate method described in Chapter 5. Streaks are observed, which have the appearance of powder diffraction lines.	154
4.54	Crystal truncation rod scan for sample D42, showing many diffraction peaks	154
4.55	Reciprocal space maps for sample D42	155
4.56	Periodic noise observed in RSMs and $\theta - 2\theta$ scans	158
4.57	Profiles showing that the noise does not depend on magnitude of count rate	159
5.1	Symmetric reflection with a position sensitive detector	169
5.2	Schematic diagram of the diffractometer configuration	170
5.3	Section of an unprocessed imaging plate scan.	172
5.4	Entire RSM from a single imaging plate.	172
5.5	The position of the experimental data points before and after interpolation using method I	173
5.6	The position of the experimental points and the added points for method III	173
5.7	Comparison of a triple axis diffractometry RSM with the interpolated IP data. Interpolated IP using method I	175
5.8	Comparison of a triple axis diffractometry RSM with the interpolated IP data. Interpolated IP using method II	175
5.9	Comparison of a triple axis diffractometry RSM with the interpolated IP data. Interpolated IP using method III	176
5.10	Comparison of a triple axis diffractometry RSM with the interpolated high resolution IP data	176
5.11	Comparison of a triple axis diffractometry RSM with the reduced triple axis diffractometry RSM	177
5.12	Reciprocal space maps (in angular space) for the $(11\bar{2}4)$ reflections	177

5.13	Schematic diagram explaining the origin of peak splitting when ω_{step} is large	179
5.14	Powder lines collected across the whole imaging plate, possibly due to In segregation.	180
5.15	Angle designations for the three-dimensional diffraction geometry. . .	182
6.1	Possible kinetic model leading to chemical ordering of Group III nitride ternary alloys	185
6.2	Schematic diagram of a Bartels-DuMond type monochromator.	186
6.3	A comparison of the error function calculated using IDL and Mathematica [®]	195
6.4	The model used to describe the composition of the annealed sample (which shows chemical intermixing) for the statistical diffraction analysis	196
6.5	X-ray diffraction patterns for the as grown and annealed samples. . .	197
6.6	Experimental profile and Voigt fits for the as grown AlGa _N sample .	198
6.7	Williamson-Hall plots of Δq versus q_z for the as grown AlGa _N sample.	198
6.8	Williamson-Hall plots of Δq^2 versus q_z^2 for the as grown AlGa _N sample	199
6.9	An anti-phase domain in AlGa _N	201
6.10	Experimental profiles and simulated profiles based on the statistical diffraction theory, in the q_x direction for the fundamental and superlattice reflections, for the as grown AlGa _N sample	202
6.11	Experimental profiles and SDT fits in the q_z direction for the as grown AlGa _N sample	203
6.12	(a) Strain distribution for ϵ_{xx} (○) and ϵ_{zz} (□), from the surface (0 nm) to the substrate (740 nm), for the as grown AlGa _N sample. These were determined from the q_z scans of the (00 <i>l</i>) reflections and RSMs of (11 <i>l</i>) and ($\bar{1}\bar{1}$. <i>l</i>) reflections, using statistical diffraction theory. (b) The experimental (○) and simulated profiles (—) in the q_x direction for the ($\bar{1}\bar{1}$.4) reflection from the as grown AlGa _N sample. The simulated profile is based on statistical diffraction theory.	203
6.13	Experimental RSMs for the as grown AlGa _N sample	205
6.14	Simulated RSMs, calculated using statistical diffraction theory, for the as grown AlGa _N sample	206
6.15	Experimental profile and Voigt functions fitted to the experimental data for the annealed AlGa _N sample	207
6.16	Williamson-Hall plot of Δq_x^2 versus q_z^2 for the annealed and non-annealed AlGa _N sample. Δq is equivalent to <i>B</i> in the text.	208

6.17	Experimental profiles for scans in the q_z direction, and simulated profiles based on statistical diffraction theory, for the annealed AlGaIn sample	209
6.18	Experimental profiles for scans in the q_x direction and simulated profiles based on statistical diffraction theory, for the annealed AlGaIn sample	210
7.1	Schematic diagram of a diffraction peak showing streaks due to finite mosaic block size and misorientation of the blocks.	217
7.2	A schematic diagram of the grazing incidence in-plane X-ray diffraction technique	219

CHAPTER 1

Introduction

Semiconductor technology is an integral part of modern society, with components based on semiconductor materials found in nearly every appliance or device manufactured. These components fulfill many roles, such as switching, logic control, sensing, and display. The demand for enhanced capability and better performance under more demanding conditions has motivated the investigation of a wide range of material systems.

A semiconductor system that has recently received much attention is the Group III nitrides - in particular GaN and the ternary alloys, AlGaN and InGaN. These materials have many properties that make them useful in a wide range of applications. In particular, they have a wide bandgap, a large breakdown field, high chemical stability (due to the strong bonding typical of nitrogen), and a high electron velocity (Ambacher, 1998; Burm, 1999). Figure 1.1 compares the electron drift velocity as function of electric field for GaN, Si, SiC and GaAs.

These electronic and chemical properties make Group III nitrides an important system for high power and high frequency transistors. An important example is the high electron mobility transistor (Ambacher, 1998; Burm, 1999; Xing *et al.*, 2001). Figure 1.2 shows a schematic diagram of this transistor. The high electron mobility transistor (HEMT) exploits the properties of Group III nitrides, particularly a large bandgap discontinuity that confines charge carriers to a heterointerface (e.g., the interface between the $\text{Al}_x\text{Ga}_{1-x}\text{N}$ and GaN layers), creating a 2-dimensional electron gas (2DEG) (Redwing *et al.*, 1996). The charge density in the 2DEG for GaN based materials is large, even without doping, because of strong polarisation fields in the heterostructures (Hsu and Walukiewicz, 2001). The electron mobility within the 2DEG is much greater than in the bulk crystal. The high electron mobility allows these devices to operate at high frequencies, such as found in microwave applications. The high thermal stability of GaN is also important for high power microwave applications.

The HEMT is not the only device that benefits from the physical properties of GaN. For example, high electron velocities suggest improved performance for integrated circuits, and good chemical/thermal stability leads to improved device

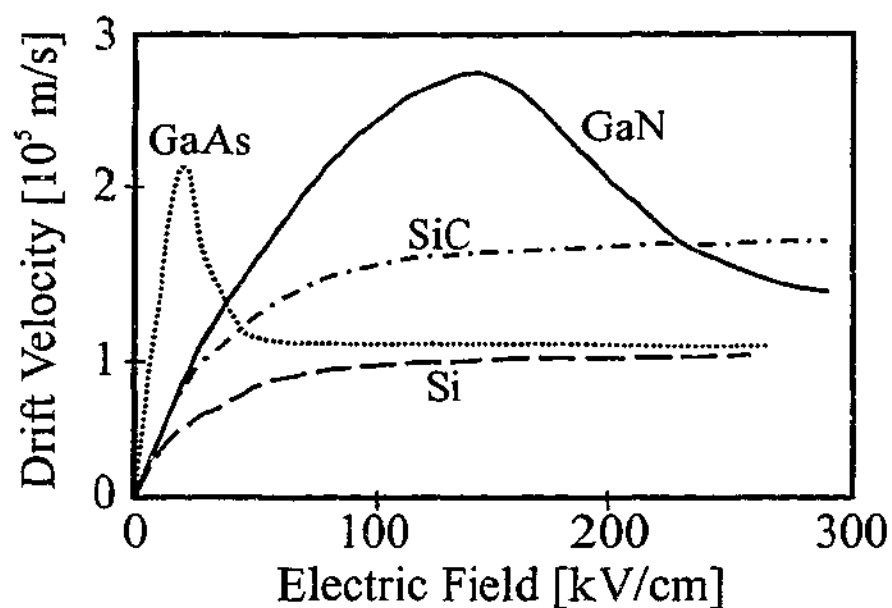


Figure 1.1: Schematic plot of electron drift velocity at 300 K versus electric field (after Ambacher, 1998).

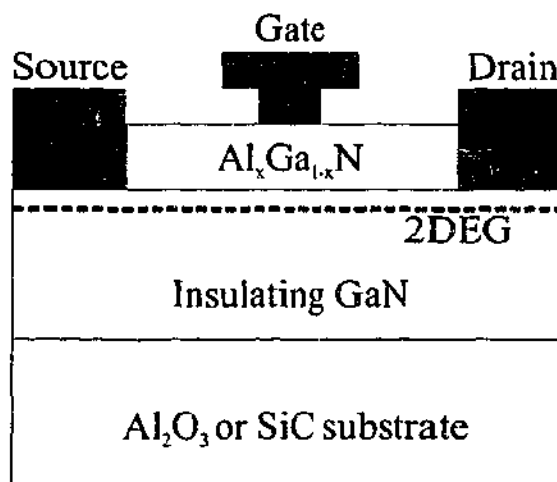


Figure 1.2: Schematic diagram of a high electron mobility transistor (after Uren *et al.*, 2002). The 2 dimensional electron gas (2DEG) is formed at the interface between the $\text{Al}_x\text{Ga}_{1-x}\text{N}$ and GaN layers.

performance at high temperatures and under radiation exposure (Xing *et al.*, 2001).

Although Group III nitrides have significant advantages in high frequency, high power applications, it is their potential as an optoelectronic material that has driven recent research efforts (Akasaki and Amano, 1997).

1.1 Optoelectronics

Optoelectronic devices emit or detect light by directly converting electricity to photons, or vice versa. The most basic optoelectronic device is the light emitting diode (LED). As its name suggests, an LED in its simplest form is just a p-n junction.

The LED emits light when it is forward biased due to radiative electron-hole recombination. The characteristic frequency of the emitted light is determined by the bandgap of the material. A more sophisticated device is the laser diode. The population inversion is achieved in this device by forward biasing the diode. By making the recombination layer small and current large the radiative process exceeds the absorption processes. The optoelectronic active region of the device is terminated by reflective cleaved or etched interfaces, forming a cavity allowing laser action to take place.

LEDs have several advantages over traditional light sources. They are robust, have a long life (lasting over 50,000 hours¹), comparatively efficient, and small. The long life and robustness is due to the device being completely solid state and undergoing little heating in comparison to incandescent light sources. Two different efficiencies are specified for LEDs, the internal and external quantum efficiency. The internal quantum efficiency of the material is related to the fraction of excited carries that recombine radiatively. The internal quantum efficiency, η_{int} , is (Nakamura *et al.*, 2000),

$$\eta_{int} = \frac{\tau_{nr}}{\tau_{nr} + \tau_r}, \quad (1.1)$$

where τ_{nr} is the non-radiative lifetime and τ_r is the radiative lifetime. As the name suggests radiative process give rise to photons. The external quantum efficiency is a measure of the total efficiency of the device, and includes absorption of the generated photons by the material itself. This is the figure of merit for comparison with other light emitters. The quantum efficiency and current density determine the brightness of the device.

Although LEDs have been touted as very efficient light emitters, they are still rivaled by other sources, particularly fluorescent lighting in those situations requiring white light. For example, a typical white LED efficiency² is 20 lumens/watt³; however devices are being manufactured that can deliver approximately 30 lumens/watt⁴, with compact fluorescent lights giving between 30 and 60 lumens/watt, and 32 watt fluorescent tubes having up to 85 to 95 lumens/watt.⁵ Hence for room

¹This number is determined as the estimated time required for the intensity to drop to 70% of its original value (see <http://www.lumileds.com/pdfs/AB17.pdf>).

²See e.g., <http://www.lumileds.com/pdfs/AB17.pdf>

³Lumens/watt is a standard measure of light efficiency.

⁴For example, Nichia Chemical Company manufacture a LED that produces a typical flux of 42 lumens for a voltage drop of 3.8 volt and forward bias current of 350 mA (see e.g., <http://www.nichia.co.jp/product/led-smd-powerled.html>).

⁵See e.g., http://www.otherpower.com/otherpower_lighting.html

lighting the fluorescent light is more efficient, although the LED has a greater potential for improvement. However, if the light must be of a particular wavelength, an LED is much more efficient, since other sources must be filtered to produce the required colour; this significantly reduces the efficiency of those light sources. Furthermore, coloured LEDs are more efficient than white LEDs because the latter use a phosphor to generate the broad spectrum light, thereby increasing power losses.

The comparatively high efficiency of LEDs stems from the direct conversion of electricity to light. The major power losses for an LED include absorption by the light emitting material itself and total internal reflection at the semiconductor/air interface (Nakamura *et al.*, 2000). The wavelength of an LED depends on the energy bandgap of the material, as well as other parameters such as strain, and spatial confinement (Alferov, 2001). Spatial confinement is an area of particular interest for LED and laser diode researchers. By confining the electrons to two-dimensions (quantum well), one-dimension (quantum wire) or zero-dimension (quantum dot), the band structure becomes atom-like, allowing it to be tailored by the degree of confinement. Traditionally the wavelength has been varied by alloying of the optoelectronic materials.

1.1.1 The Blue LED

Until the mid 1990's the utility of LEDs was severely limited because bright green and blue emitters were not available. The blue LED is technologically significant since blue light is at the upper photon energy. Consequently, they are capable of exciting phosphors at any visible wavelength, and can be used to produce white light. Although several semiconductor systems are theoretically capable of producing blue light, such as the Group II-VI materials, ZnSe and SiC, it has been the Group III nitrides that are the most successful. The first commercial (Nichia Chemical Industries) Group III nitride blue light emitting diode was released in 1993 (Nakamura *et al.*, 1994; Nakamura, 1999). These LEDs had a much higher luminescent output than the SiC-based devices available at the time.

The Group III nitride based LED has paved the way for optoelectronic devices to penetrate markets previously dominated by other technologies. Examples include display technologies (direct RGB display, and white LEDs for back lighting of LCDs⁶), traffic signalling (Akasaki, 2002), and environmental lighting. Conventional incandescent traffic lights are currently being replaced with LED technology. In this role the LEDs use between 30% and 50% of the energy required for the equivalent

⁶See e.g., <http://www.lumileds.com/solutions/solution.cfm?id=10>

incandescent light, while providing better visibility and an enhanced service life.⁷ Furthermore blue LED technology has been optimised through the variation of the bandgap, by alloying, to produce a range of colours directly. The use of phosphors, or multiple LEDs radiating at different wavelengths, has allowed white light emitters to be produced.

Laser diodes have also been manufactured from Group III nitrides (Nakamura, 1999), with the violet laser diode commercialised in 1999 (Nakamura *et al.*, 2000). These devices have had a significant impact on optical data storage. Optical storage media will soon (2005-2006) achieve increased data densities by replacing the current 650 nm red laser diode used in DVD technology with a blue (405 nm) laser diode. Due to diffraction limits the pit diameter for an optical storage disc scales as wavelength and hence the area scales as the square of the wavelength.⁸ A consortium of thirteen electronics and computer companies have developed the standard for a blue laser diode based technology (called Blu-ray⁹), with a Sony Blu-ray recorder already on the market in Japan; many other manufactures are also developing prototypes. The Blu-ray discs will hold up to 27 gigabytes per layer (with two layers per side), compared to a DVD which holds 4.7 gigabytes per layer.¹⁰

1.2 Group III Nitrides

The advantages of the Group III nitrides, and in particular GaN, has been known for a long time. Single crystal GaN was grown on a sapphire substrate in 1969 (Maruska and Tietjen, 1969), and shown to have a direct bandgap with an energy of about 3.39 eV. This bandgap is significant for two reasons. First the energy equates to a wavelength of about 500 nm (blue-green). Secondly GaN has a direct transition bandgap allowing efficient light generation. Although some laboratory emitters were constructed, commercial development was frustrated because of two major technical issues; namely, the production of high quality material seemed impossible because of poor matching of the substrate and epilayer, and it was difficult to produce p-type doped crystals because of a high residual electron concentration (Akasaki, 2002). As a consequence, much research was focussed on the Group II-V systems. However, in the mid to late 1980's Akasaki and Amano found solutions to both problems. They discovered that growing a low temperature buffer layer on the substrate (before

⁷<http://www.eurotechnology.com/bluelaser/blueslide3.html>

⁸<http://cnx.rice.edu/content/mi011/latest/>

⁹www.blu-ray.com

¹⁰Another blue laser optical disc format, called HD-DVD, is being developing by Toshiba and NEC, but this technology is less mature, (see e.g., <http://www.nec.co.jp/press/en/0208/2901.html>).

GaN growth) allows relatively high quality GaN layers to be produced (Amano *et al.*, 1986; Akasaki, 2002). Furthermore Low Energy Electron Beam Irradiation (LEEBI) of Mg doped GaN was found to produce p-type doped material (Amano *et al.*, 1989; Akasaki, 2002). These findings, as well as the work by Nakamura (see Nakamura *et al.* (2000) for a detailed description) lead to the commercialisation of the first GaN based blue LED by Nichia Chemical Industries in 1993 (Nakamura *et al.*, 1994). It is interesting to note that the as grown Group II-VI materials have a much lower (4 orders of magnitude) defect density than the Group III nitrides; however, in operation the former have a very short lifetime. The fact that Group III nitrides are superior to Group II-VI materials is not fully understood. One possibility is that the Group II-VI materials are far more fragile than structures based on GaN materials, since they lack the strong bonding afforded by nitrogen (Nakamura *et al.*, 2000).

1.2.1 Band Structure

The Group III nitrides have a direct transition bandgap as shown in Fig. 1.3. The most probable transition in an intrinsic semiconductor is from the bottom of the conduction band to the top of the valence band. In a direct transition bandgap the minimum of the conduction band and the maximum of the valence band are both at the same k -value, (usually $k=0$). For a radiative transition both the energy and momentum need to be conserved. For a direct transition the change in momentum is essentially zero. The magnitude of k -vector (momentum) of the photon is given by $2\pi/\lambda$, and for visible wavelengths this is $\approx 10^7 \text{ m}^{-1}$, which is small on the scale of the band structure ($\approx 10^{10} \text{ m}^{-1}$). Hence, most of the energy in a direct transition is coupled into photon energy. For indirect transitions the minimum of the conduction band and the maximum of the valence band are not at the same k -value. Hence momentum needs to be transferred for the transition to occur. Usually this is to the lattice in the form of phonons. In this situation less energy is released as photons. The exception is when localised states are available (e.g., electron donors near the conduction band edge, or acceptors near the valence band edge); localisation means that the k -value is smeared within reciprocal space and hence transitions can occur with little momentum change.

1.2.2 Crystal Structure

Group III nitrides can form three crystal structures: wurtzite, zincblende, and rocksalt (Morkoç, 1999). Rocksalt and zincblende can be present as a small fraction of any Group III nitride material. Both of these polytypes can be exclusively grown

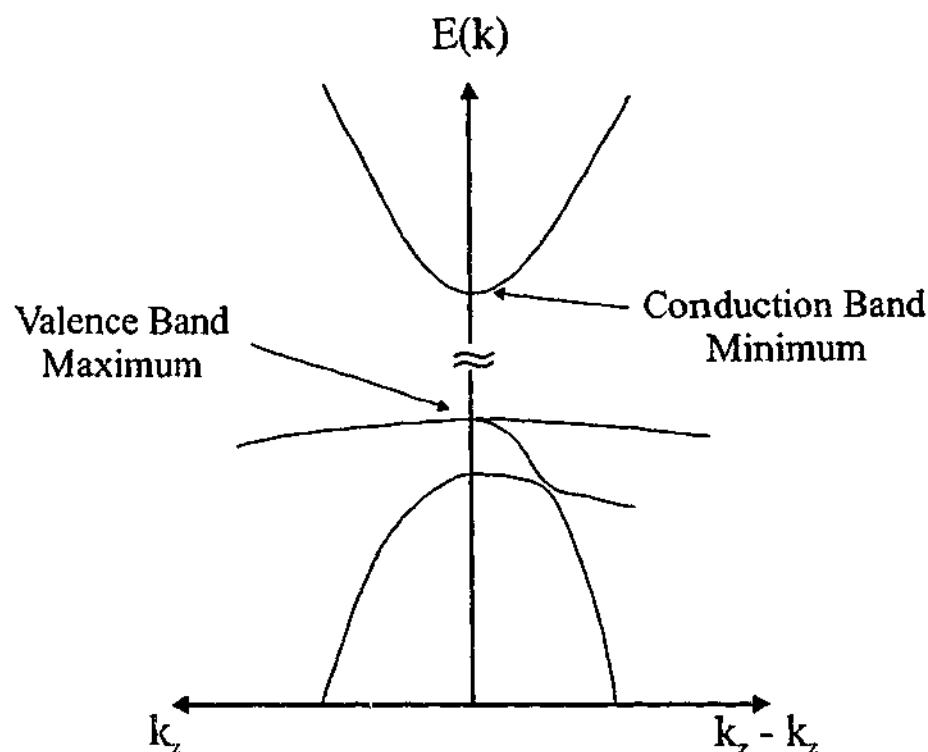


Figure 1.3: Schematic of the band structure of GaN, showing the direct transition bandgap (after Chuang and Chang, 1996a).

under specific conditions, i.e., selection of an appropriate substrate or growth pressures. However, wurtzite is the thermodynamically stable structure for bulk AlN, GaN, and InN. The work presented throughout this thesis considers the wurtzite structure unless otherwise specified.

The wurtzite structure (Fig. 1.4) is formed from two interpenetrating hexagonal close packed (hcp) lattices (each composed of a different atomic element) offset along the c -axis (Morkoç, 1999). The stacking order of wurtzite, which is important when considering defects, is the same as hcp. The stacking is shown in Fig. 1.4(a). Of the three possible sites which could be occupied for a hexagonal or cubic close packed structure only sites **A** and **B** are occupied by the Group III element/nitrogen pair. Hence the stacking sequence is ...**ABABABAB**... along the $[0001]$ direction (Northrup and Romano, 1999a; Takeda and Tabuchi, 1999; Leszczynski, 1999). The **C** site is occupied for the zincblende structure (cf. hcp and fcc). The primitive unit cell comprises 4 atoms with a pair at **A** and **B**, as indicated in Fig. 1.4(b). The equilibrium positions of the atoms are $(\frac{1}{3}, \frac{2}{3}, 0)$, $(\frac{2}{3}, \frac{1}{3}, \frac{1}{2})$ for one element and $(\frac{1}{3}, \frac{2}{3}, \frac{3}{8})$, $(\frac{2}{3}, \frac{1}{3}, \frac{7}{8})$ for the other element.

Three parameters are used to describe the (non-primitive) unit cell (as shown in Fig. 1.4(b)); namely, the two hexagonal lattice parameters a and c , and the ratio, u , of the hcp lattice separation (i.e., the ratio of the bond length in the c direction

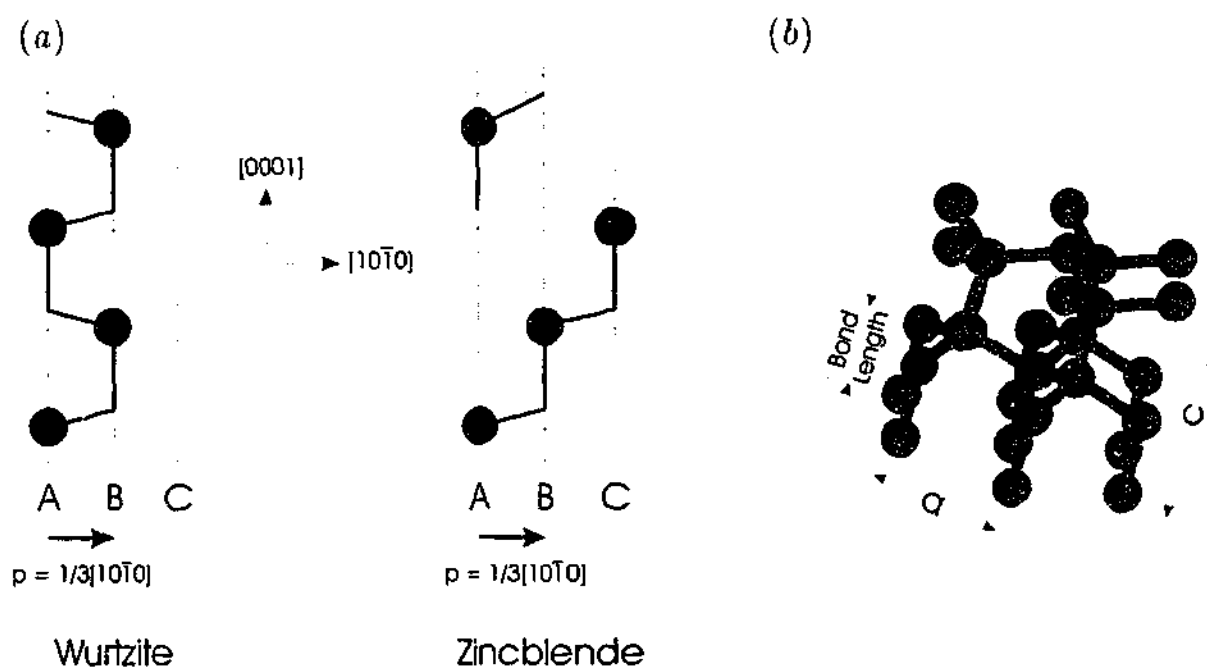


Figure 1.4: (a) The stacking sequence for wurtzite and zincblende (after Northrup and Romano, 1999a), and (b) a 3D ball and stick representation of wurtzite.

to the c lattice parameter).

Each atom is tetrahedrally coordinated to 4 other atoms of the opposite atomic element. A wurtzite structure with equal bond lengths and angles has a c/a ratio of 1.633 and an u -value of 0.375 (Leszczynski, 1999). Real materials deviate from this ideal arrangement with the c/a and u values varying, e.g., AlN has $c/a = 1.601$ and $u = 0.3821$ (Leszczynski, 1999). Distortions of the structure occur in such a way that the tetrahedral bond distances are kept approximately constant, with the bond angles distorting to accommodate the changes. A correlation is seen between the c/a ratio and the u parameter (Leszczynski, 1999).

Table 1.1 summarises some of the Group III nitride lattice parameters reported in the literature. A single set of parameters cannot be given for the bulk material, as it is exceptionally difficult to grow bulk Group III nitrides. Most of the reported results are for epitaxial layers. There are many techniques and conditions for epitaxial growth, which accounts for the wide range of parameters.

1.2.3 Bulk Group III Nitride Growth

Group III nitrides are difficult to grow as bulk materials, more so than other Group III-V semiconductors. The main difficulty is that nitrogen is highly volatile. Furthermore, as the bonding between nitrogen and Group III elements is strong, a high growth temperature is required to produce high quality materials, further increasing

Table 1.1: Lattice parameters for Group III nitride semiconductors.

Material	a (Å)	c (Å)	Comment	Reference
GaN:	3.1876	5.1846	GaN:Mg, bulk	Porowski (1998)
	3.1876	5.1846	Undoped homoepitaxial GaN on GaN:Mg bulk	Porowski (1998)
	3.1881	5.1844	Undoped homoepitaxial GaN	Porowski (1998)
	3.1881-3.1890	5.1856-5.1864	Undoped GaN bulk	Porowski (1998)
	3.189	5.185	-	Morkoç (1999)
	3.1892	5.1850	-	Pereira <i>et al.</i> (2002)
	3.1892	5.185	-	Chuang and Chang (1996b)
	3.1892	5.1850	-	Schuster <i>et al.</i> (1999) and references therein
	3.1908	5.1838	Measured from (00.2) and (10.5) reflections	O'Donnell <i>et al.</i> (2001)
	3.189	5.186	-	Zielinska-Rohozinska <i>et al.</i> (2001)
Average:	3.189	5.185		
AlN:	3.112	4.982		Morkoç (1999)
	3.1106	4.9795	Bulk Crystal	Leszczynski <i>et al.</i> (1999)
	3.1130	4.9816	Powder	Angerer <i>et al.</i> (1997)
	3.110	4.980	Layer on SiC	Leszczynski <i>et al.</i> (1999)
	3.110	4.980	-	Amano and Akasaki (1999)
Average:	3.111	4.981		
InN:	3.548	5.760	5.760 seems erroneously large	Morkoç (1999)
	3.5378	5.7033	-	Pereira <i>et al.</i> (2002)
	3.544	5.718	-	Park and Chuang (1999)
	3.540	5.700	-	Schuster <i>et al.</i> (1999)
	3.536	5.709	-	O'Donnell <i>et al.</i> (2001)
	3.538	5.703	-	Zielinska-Rohozinska <i>et al.</i> (2001)
Average:	3.541	5.716		

the nitrogen partial pressure (Stringfellow, 1999). This combination of high temperature and high pressure results in a high nitrogen vacancy concentration in the material. The nitrogen vacancies possibly act as electron donors, producing the high n-type carrier concentrations observed; however, there is still some conjecture in the literature concerning the source of the carriers (Van de Walle *et al.*, 1999; Morkoç, 1999). Although bulk GaN has been grown (see e.g., Porowski, 1998), to date there are no commercially available bulk Group III nitride crystals.

1.2.4 Epitaxial Growth

Many optoelectronic and electronic devices utilise layers of semiconductor material. These epitaxial layers are grown using a variety of techniques. The most important epitaxial growth techniques for Group III nitrides are metal-organic chemical vapour deposition (MOCVD) and molecular beam epitaxy (MBE).

1.2.4.1 Epitaxial Growth Techniques

MOCVD, also known as organo-metallic vapour phase epitaxy (OMVPE)¹¹, is well suited to the chemistry of nitrogen and aluminium, and can be readily scaled up to grow commercially viable batches (see e.g., Stringfellow, 1999). This technique is also used to grow Group II-VI semiconductors (e.g., ZnS or ZnSe), as well as Group III-V semiconductors (e.g., GaAs, InP, and the Group III nitrides). The science of growth by MOCVD is complex, incorporating thermodynamics, hydrodynamics, kinetics, chemistry, and surface science. However, from a broad viewpoint the technique is simple. Precursors of the constituent atomic species of the desired compound semiconductor are carried to a heated substrate in a vapour stream where they decompose under the action of heat. The liberated metallic cations (Group II or III) react with the anions (Group IV or V) to form the epitaxial layer on the substrate.

The common Group III precursors are metal complexes (the metal-organics). The ligands generally bonded with the Group III metal are short hydrocarbon chains. For a methyl ligand the precursors are trimethylgallium (TMGa), trimethylaluminium (TMAI), and trimethylindium (TMIn). TMGa and TMAI are liquids at room temperature (TMIn is a solid). These metal-organics are admitted to the growth chamber in a carrier gas (H_2) by passing the gas through the liquid precursor. NH_3 is normally used as the precursor for nitrogen, which is admitted to the growth chamber directly as a gas. There are a number of parameters that can be adjusted to alter the growth. These include the substrate temperature and the relative pressures of the gases. The relative gas pressures will impact on the stoichiometry of the layers. Typically for GaN growth the reaction chamber is near atmospheric pressure and the substrate is at a temperature of approximately $1,000^\circ C$.

Another important growth technique is molecular beam epitaxy. It differs from MOCVD in several ways. First the growth chamber is under ultra high vacuum, and generally the constituent atoms are delivered to the substrate as atomic or molecular fluxes. Conventionally the sources for MBE are Knudsen effusion cells (Farrow, 1995). The source elements or compounds (solid or liquid) are radiatively heated in a crucible, which increases the vapour pressure inside the cell. The pressure difference between the cell and the growth chamber leads to effusion, producing a beam of molecules or atoms. The cell is designed so that the beam uniformly covers the substrate. The pressure in the cell, and thus the beam flux, is varied by changing

¹¹MOCVD and OMVPE are also known as MOVPE and OMCVD. Although these acronyms refer to essentially the same technique, the term epitaxy is usually reserved specifically for thin crystal growth, where the layer replicates the crystal structure of the substrate (Thompson, 1997).

Table 1.2: Physical parameters for the substrates.

Substrate	Lattice Parameter Å	Thermal Expansion Coef. 10^{-6} K^{-1}	Thermal Conductivity $\text{W m}^{-1} \text{ K}^{-1}$
$\alpha\text{-Al}_2\text{O}_3$	a	4.758 ^a	46 ^a (near room temp.)
	c	12.99 ^a	
6H-SiC	a	3.0806 ^d	490 ^a (near room temp.)
	c	15.1173 ^d	

^aTakeda and Tabuchi (1999).

^bBulk crystal, 300-350 K, Krukowski *et al.* (1999).

^cBulk crystal, 700-750 K, Krukowski *et al.* (1999).

^dHanser and Davis (1999).

the temperature. Therefore the stoichiometry of the grown layers is determined, in part, by the temperature of the Knudsen cells. N_2 cannot be used directly for nitride growth, as it is too strongly bonded. Thus it must be dissociated before reaching the substrate. This is achieved using a plasma, although attempts have been made to dissociate N_2 or NH_3 at the substrate, using high temperature (see e.g., Yoshida *et al.*, 1983; Morkoç, 2001).

1.2.4.2 Epitaxy of Group III Nitrides using OMVPE

Growth of epitaxial layers requires a substrate material on which the layer is deposited. Usually the layers are grown on a native substrate, i.e., a substrate with the same, or similar, chemical composition and structure as the layers. However, as no viable native substrates are available for Group III nitrides, alternatives have been sought. To date the most important substrates are sapphire (Al_2O_3), particularly the (0001) face (α -sapphire), and silicon carbide (SiC), particularly the hexagonal polytype 6H-SiC. A summary of the physical parameters for these substrates is given in Table 1.2; the appropriate nitride parameters given in Table 1.3 for comparison.

For high quality epitaxial layers the lattice parameters and coefficient of thermal expansion of the substrate must be closely matched to the overlayer. Hence an initial measure of substrate suitability is the mismatch of these two parameters along the interface (i.e., perpendicular to the growth direction). The coefficient of thermal expansion is important as the layers are always grown at elevated substrate temperatures, hence any differences in this parameter will produce strain (or damage) in the layer upon cooling.

Consideration of thermal expansion and thermal conductivity is also important in high power applications, since matching the thermal expansion of the substrate

Table 1.3: Physical parameters for Group III nitrides.

Nitride	Lattice Parameter ^a Å	Thermal Expansion Coef. ^b 10 ⁻⁶ K ⁻¹	Thermal Conductivity ^c W m ⁻¹ K ⁻¹
GaN	a 3.189	a 3.1 ^d , 6.2 ^e	1.3 ^f
	c 5.185	c 2.8 ^d , 6.1 ^e	1.7 ^g
AlN	a 3.111	a 2.9 ^g , 1.3 ^h	2.85 (300 K)
	c 4.981	c 3.4 ^g , 1.0 ^h	0.96 (600 K) 0.48 (1000 K)

^aAverages from Table 1.1.

^bKrukowski *et al.* (1999).

^cKrukowski *et al.* (1999).

^dBulk crystal, 300-350 K.

^eBulk crystal, 700-750 K.

^fMeasured from layers grown on sapphire substrate.

^gPowdered crystal, 300 K.

^h600 K (Morkoç, 1999).

and epilayers impacts on the stability of the system, particularly in situations involving thermal cycling. In many applications a SiC substrate is more suitable than sapphire.

To correctly determine the lattice mismatch it is critical to know the orientation of the layer with respect to the substrate. Figure 1.5 shows the orientation of GaN (or AlN) with respect to α -sapphire. Sapphire exhibits hexagonal symmetry, but it is not a wurtzite structure. The nitride overlayer rotates 30° with respect to the substrate in the manner shown in Fig. 1.5, thus reducing the lattice mismatch. The mismatch in the lattice parameter can be determined from the data in Tables 1.2 and 1.3. Simple geometry shows that the oxygen spacing for the sapphire layer is $a_{\text{Al}_2\text{O}_3}/\sqrt{3}$. Comparing the oxygen separation with the atomic separation in the layer along the $[2\bar{1}\bar{1}0]$ direction for GaN, which is parallel to the $[1\bar{1}00]$ direction for Al_2O_3 , we have (at room temperature) (Morkoç, 1999),

$$\frac{a_{\text{GaN}} - \frac{1}{\sqrt{3}}a_{\text{Al}_2\text{O}_3}}{\frac{1}{\sqrt{3}}a_{\text{Al}_2\text{O}_3}} = \frac{3.189 - 2.747}{2.747} = 0.16 \text{ or } 16\%.$$

In a similar manner upon substituting for AlN gives a mismatch of 13%.

This significant mismatch in lattice parameter between sapphire and Group III nitrides, as well as poor matching of thermal expansion coefficients, induces a large density of defects in epitaxial layers. The driving force creating the defects is strain relaxation. Consequently, GaN layers grown directly on an α -sapphire substrates

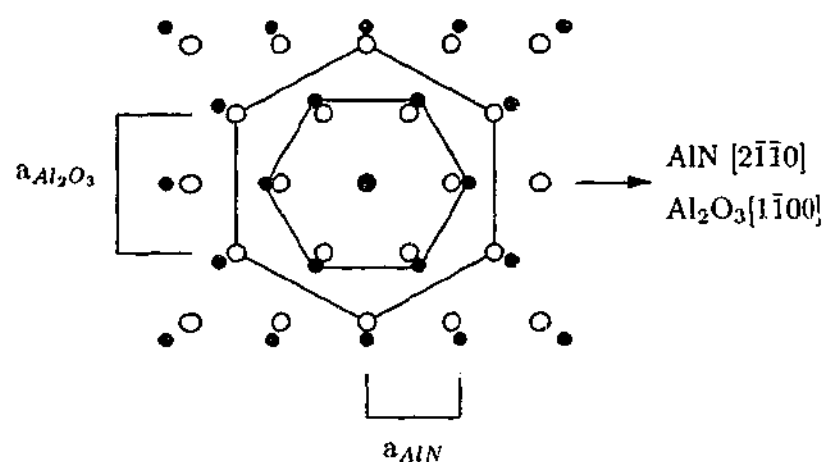


Figure 1.5: Orientation of AlN/GaN epitaxial layers on an α -sapphire substrate. The closed circles (\bullet) represent the Group III or nitrogen sites at the interface and the open circles (\circ) the oxygen positions for sapphire (Takeda and Tabuchi, 1999).

are usually highly deformed. They exhibit rough surfaces, dominated by hexagonal hillocks (Ambacher, 1998; Akasaki *et al.*, 1989; Akasaki, 2002), significant cracking (Amano *et al.*, 1986; Itoh and Rhee, 1985), and a dislocation density greater than 10^{11} cm^{-2} (Akasaki, 2002). Amano *et al.* (1986) demonstrated that higher quality GaN could be grown, using OMVPE, by first depositing a 50 nm AlN buffer layer on the sapphire substrate. (Yoshida *et al.*, 1983 showed similar effects using MBE). Initially they deposited the AlN at between 800-1000°C, however, for subsequent experiments this temperature was reduced to 600°C, with the GaN layer deposited at 1000°C (Akasaki *et al.*, 1989). GaN layers grown on the buffer layers had a smooth appearance that was free of cracks or pits, and a dislocation density of between 10^9 cm^{-2} to 10^{10} cm^{-2} . (Buffer layers have been used with other substrates, see e.g., Einfeldt *et al.*, 2003 for 6H-SiC substrates, and growth techniques, see e.g., Ebel *et al.*, 1999 for Molecular Beam Epitaxy).

The growth of semiconductor materials is complicated, with a number of parameters requiring optimisation. Low-temperature (LT) buffer layers (both AlN and GaN) grown by OMVPE continue to be the subject of research (see e.g., Zhang *et al.*, 2004; Sumiya *et al.*, 2003; Gonsalves *et al.*, 2002; Cho *et al.*, 2001; Figge *et al.*, 2000; Kobayashi *et al.*, 1998; Hersee *et al.*, 1997). The buffer layer parameters investigated in the literature include: layer thickness, growth temperature and pressure, and Group V-III ratio during growth (i.e., the ratio of nitrogen to the Group III species in the chamber). Other conditions pertinent to growth are annealing of the substrate (including nitriding) before buffer layer growth, and annealing of the buffer layer under various atmospheres. Buffer layer annealing is unavoidable because the substrate must be heated for growth of the GaN layer. Kobayashi *et al.* (1998) have

shown that LT-GaN buffer layers are unstable at elevated temperatures, because the vapour pressure of N_2 is several orders of magnitude larger for GaN than for AlN. Hence, a N_2 atmosphere is required when annealing GaN buffer layers. The quality of the buffer layer can be studied by techniques such as X-ray photoelectron spectroscopy, X-ray diffraction, transmission electron microscopy, atomic force microscopy, and luminescence. *In situ* techniques, such as reflection high-energy electron diffraction and shallow angle reflectance are used to characterise the buffer and overlayers. It has been found that there is an optimum thickness for the LT-AlN layer in order to produce the highest quality GaN (see e.g., Ito *et al.*, 1999; Tabuchi *et al.*, 2002; Zhang *et al.*, 2004). The actual thickness depends on the preparation of the substrate before deposition. Tabuchi *et al.* (2002) investigated buffer layers grown at 400°C with and without a nitridation process. The layers investigated were 10 nm, 30 nm, and 70 nm thick. Using crystal truncation rod scattering and X-ray reflectivity experiments, it was shown that samples produced without nitridation of the substrate had a poorer GaN overlayer structure on a 70 nm buffer than on a 30 nm buffer layer. However, the opposite was found when the substrates were nitrided. In this thesis we extend the work by Tabuchi *et al.* (2002), by carrying out a more thorough analysis of samples that do not have a nitrided substrate.

A number of authors have discussed the mechanism by which the buffer layer improves epilayer growth in OMVPE. Akasaki *et al.* (1989) gave a simple description of the growth mode, while Hiramatsu *et al.* (1991) provided a more complete description. The latter investigated GaN/AlN/ α -sapphire structures using transmission electron microscopy (TEM) and scanning electron microscopy (SEM). In this work the 50 nm thick AlN layers were deposited at 600°C and the GaN layer at 1030°C. Cross-sectional TEM showed three regions in the GaN layer. The region closest to the AlN shows a fine contrast indicative of a high density of defects. This region is approximately 50 nm thick, and is termed the 'faulted zone'. The next region, the 'semi-sound zone', exhibits trapezoidal crystals (confirmed by SEM to be pyramidal mesas). This region is approximately 150 nm thick and has a much lower defect density. The remaining region has a much lower defect density, particularly for layers thicker than 300 nm. This is the 'sound zone'. It was also shown that the AlN layer consisted of columnar fine crystals, with a diameter on the order of 10 nm. Hiramatsu *et al.* (1991) suggested that the AlN layer is amorphous-like at the deposition temperature (600°C), but that it is crystallised into the columnar structure upon heating to 1030°C for GaN growth.

The growth mechanism suggested by Hiramatsu *et al.* (1991) is summarised in Fig. 1.6. After annealing, the AlN layer has a columnar structure (Fig. 1.6(a)) that

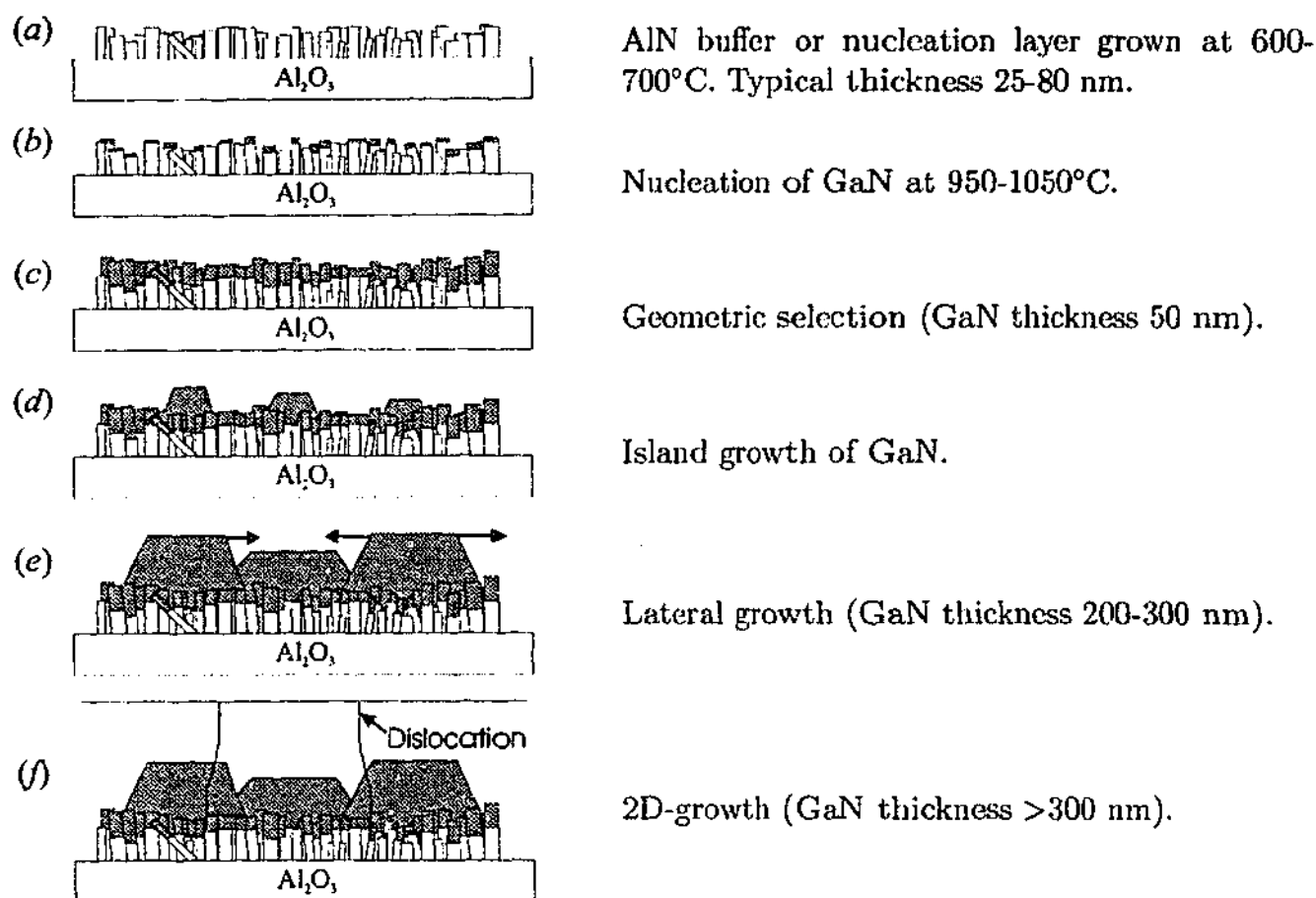


Figure 1.6: Schematic of the growth process proposed by Hiramatsu *et al.* (1991). After Ambacher (1998) and Hiramatsu *et al.* (1991).

provides a high density of nucleation sites for the GaN layer (Fig. 1.6(b)). The GaN columnar crystals will be randomly oriented; however, the fastest growth direction is perpendicular to the substrate. Those crystals that have their *c*-axis directed perpendicular to the substrate will grow fastest; this is geometrical selection (Fig. 1.6(c)). Eventually trapezoidal crystals, with *c*-faces, are formed on the columnar crystals (Fig. 1.6(d)). These islands grow preferentially, covering smaller islands. The trapezoidal crystals grow at a higher rate in the lateral direction (Fig. 1.6(e)) and hence begin to coalesce. Continued growth produces a smooth face because each of the islands grow with a similar orientation. Subsequent growth is in a uniform layer by layer manner, producing the 'sound zone' (Fig. 1.6(f)). In summary the low-temperature buffer layer works by supplying nucleation centres with the same orientation as the substrate, and by promoting lateral growth of the GaN film by decreasing the interfacial free energy between the film and the substrate (Ambacher, 1998).

Although a GaN layer grown with a LT-AlN buffer layer has a much lower defect density (and a higher quality surface), than GaN grown directly on sapphire, it still

has a high defect density compared to other semiconductor systems, such as GaAs. It appears that although the crystallites coalesce, the film is still a polycrystal, not a single crystal (Hersee *et al.*, 1997). This structure is also referred to as a mosaic, with each crystallite known as a mosaic block. Figure 1.7 shows the variation of the orientation within the GaN mosaic. The misorientation of the mosaic blocks can be described by their 'tilt' (rotation of the *c*-axis from the vertical) and 'twist' (rotation of the block about the *c*-axis) (Chierchia *et al.*, 2001). For thick films the GaN (sound zone) crystal quality within each block is high, suggesting that the dislocations are concentrated at the boundaries between the two blocks. For the threading dislocations normal to the surface, tilt is associated with screw type dislocations, and twist with edge type dislocations (Lafford *et al.*, 2003a; Heinke *et al.*, 1999). Characterisation of mosaic structure (and dislocation density and types), is usually achieved using TEM, or X-ray diffraction. TEM allows the dislocations to be imaged; however, the field of view is small and the technique requires significant sample preparation, which causes damage. X-ray diffraction is less direct, and has the advantage of averaging over a larger sample volume; this technique requires minimal sample preparation and it is non-destructive. For a mosaic crystal the width of a Bragg reflection, measured using high resolution X-ray diffractometry (HRXRD), depends on the crystal size, twist, tilt, and heterogeneous strain (Heinke *et al.*, 1999; Metzger *et al.*, 1998). In order to disentangle these different contributions of the peak width a number of techniques have been employed. The most common technique is Williamson-Hall analysis (Williamson and Hall, 1953; Metzger *et al.*, 1998). This was originally formulated for cold worked metals, but later extended to semiconductor systems (Ayers, 1994). This method relies on the relative contributions to the peak width changing for different reflections. Other methods use complicated diffraction theories (based on dynamical diffraction), such as that presented by Brandt *et al.* (2002) specifically for Group III nitrides. In this thesis the full diffraction profiles are modelled using the statistical diffraction theory originally formulated by Kato (see e.g., Kato, 1976a, 1980a,b). Variants of this theory have been used to successfully study other semiconductor systems, but this approach has been rarely applied to Group III nitrides. (Although Fewster, 1999, 2003; Fewster *et al.*, 2001 has used a similar theoretical frame work to study Group III multilayers). The statistical diffraction theory is discussed in Chapter 2.

The optoelectronic active layer for Group III nitrides is normally based on the ternary alloys $\text{Al}_x\text{Ga}_{1-x}\text{N}$ or $\text{In}_x\text{Ga}_{1-x}\text{N}$. By varying the composition of the material, x , the bandgap, and hence the emission wavelength, can be adjusted. The bandgap is also affected by strain within the material. Determination of the strain

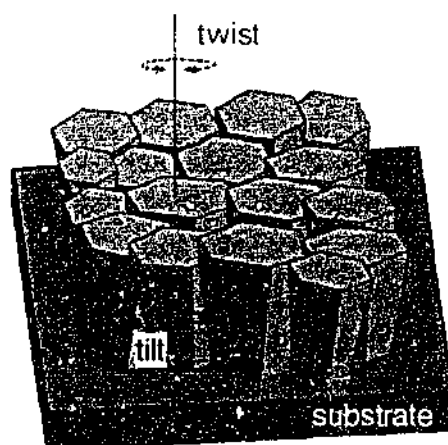


Figure 1.7: Schematic diagram of the mosaic structure of GaN showing the tilt and twist of the mosaic blocks. Rotation of the c -axis from the vertical is called 'tilt'; rotation of the block about the c -axis is called 'twist' (figure provided by Dr L. Kirste, Fraunhofer Institut für Angewandte Festkörperphysik).

and composition of Group III nitride ternary alloys is commonly achieved using X-ray diffraction techniques (see e.g., Vickers *et al.* 2003; Schuster *et al.*, 1999; Pereira *et al.*, 2002; Herres *et al.*, 2002; O'Donnell *et al.*, 2001). Changes in strain and composition modify the spacing of the atomic planes, and hence change the Bragg peak positions. The simplest way of determining the strain and compositional components is to measure the position of symmetric (i.e., $(00.l)$ ¹² type reflections) and asymmetric Bragg reflections (combined with a knowledge of the elastic stiffness constants of the material).

1.2.5 Dislocations

As has been highlighted above, Group III nitrides exhibit high dislocation densities. There are three types of dislocation: edge, screw and mixed (Northrup and Romano, 1999a). They can be discriminated from each other by their Burgers vector, \mathbf{b} , and dislocation line. An edge dislocation is easiest to visualise, and helps clarify the notion that a dislocation is a 1-dimensional defect. Figure 1.8 shows a schematic of an edge dislocation. The end-on view (Fig. 1.8(a)) shows that the dislocation can be considered as an extra half plane of atoms above the slip plane. The termination of this extra half plane of atoms defines the dislocation line, which runs perpendicular to the plane of the paper. The oblique view (Fig. 1.8(b)) shows the full line. If the crystal is subjected to a shear stress the dislocation will move perpendicular to the dislocation line. The movement of the dislocation is associated with an atomic displacement below the slip plane. This displacement is the Burgers vector, \mathbf{b} . The

¹²The '.' signifies the redundant Miller index

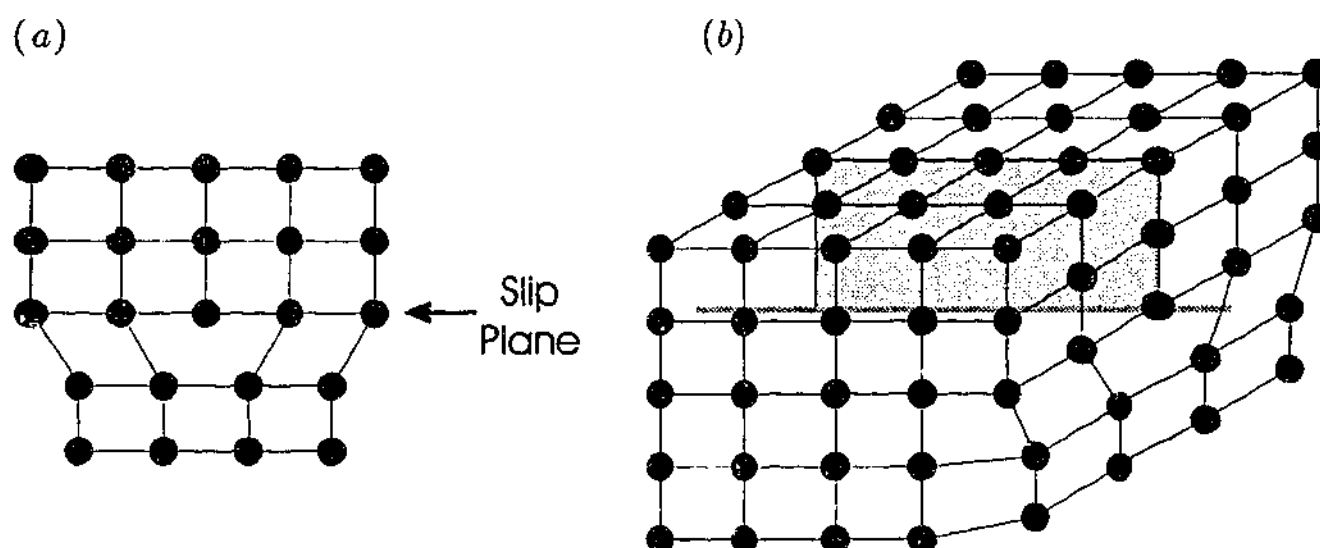


Figure 1.8: An edge dislocation. (a) End on view, and (b) oblique view. The shaded area in (b) indicates the extra half plane associated with the edge dislocation.

Burgers vector can also be determined by taking a closed path in the crystal (without a dislocation), and then placing a single dislocation within the region bounded by the path. The path will no longer be closed - the difference is the Burgers vector. This is shown in Fig. 1.9. Hence an edge dislocation is one where the dislocation line and Burgers vector are perpendicular. For a screw dislocation the Burgers vector and dislocation line are parallel, and for a mixed dislocation the angle between them is intermediate (i.e., a mixture of an edge and screw dislocation). Visualising a mixed dislocation is difficult, so a diagram is not given; however the screw dislocation is shown in Fig. 1.10. These examples are all perfect dislocations. It is also possible to have partial dislocations where the magnitude of the Burgers vector is less than a lattice vector.

Group III nitrides can exhibit all three types of perfect dislocation, with $b = 1/3 \langle 11\bar{2}0 \rangle$, $\langle 0001 \rangle$, or $1/3 \langle 11\bar{2}3 \rangle$,¹³ where the dislocation line can be along any direction. The most common dislocation observed in a sample depends on the growth process. However, for high defect density material ($\geq 10^{10} \text{ cm}^{-2}$) grown on α -sapphire, the most common dislocation is an edge dislocation, with its line directed perpendicular to the $\langle 0001 \rangle$ growth plane (Romano, 1999). Such dislocations are termed threading dislocations. As was discussed in Sec. 1.2.4 Group III nitrides have a very high dislocation density when compared to many other semiconductor materials.

¹³The notation $\langle \rangle$ indicates a family of directions, i.e., all directions indistinguishable from the one given.

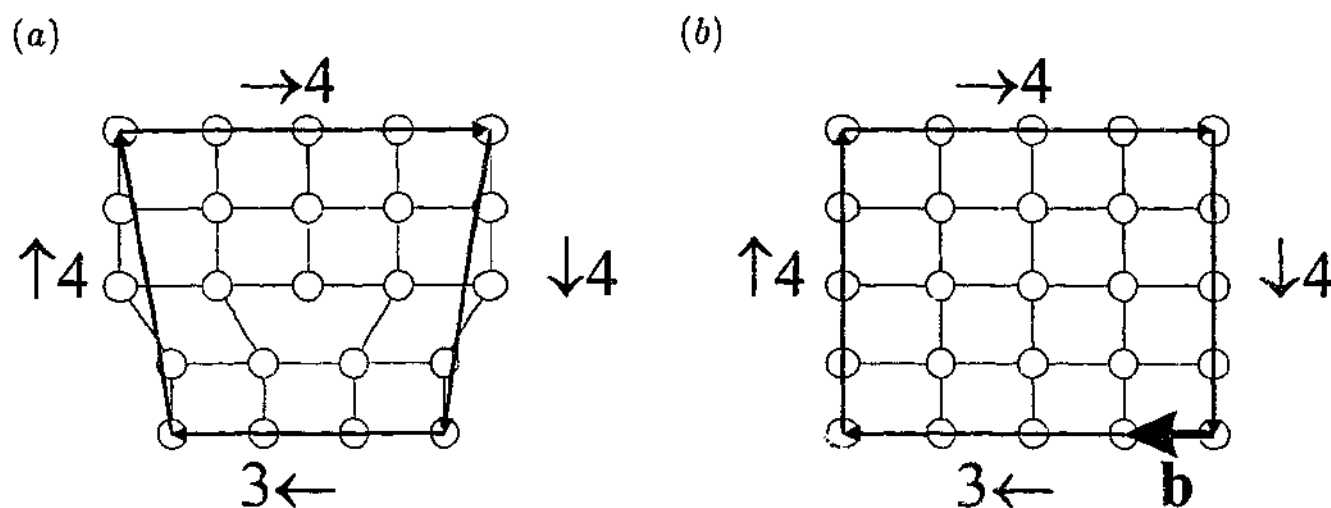


Figure 1.9: Determining the Burgers vector. (a) A closed path about an edge dislocation, and (b) a closed path in a perfect crystal. The arrows indicate the number of unit cells traversed in that direction. The difference between the two paths is the Burgers vector, \mathbf{b} .

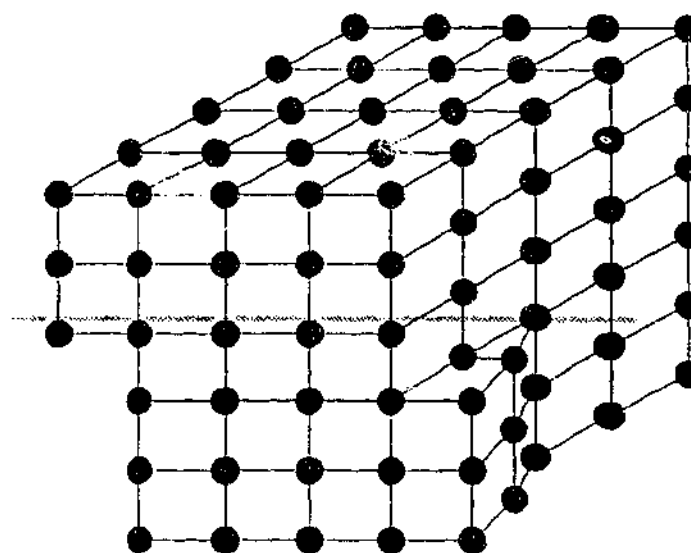


Figure 1.10: Screw dislocation.

1.3 Summary and Scope of the Thesis

Group III nitride semiconductors have been introduced as exhibiting key characteristics that make them useful for a wide range of applications, particularly in optoelectronics. Unfortunately there are significant difficulties in producing these materials, because there are no commercially available substrates that are matched (thermally and structurally) to the Group III nitrides. This leads to significant defect densities within the as grown layers. Methods for growing quality layers on mismatched substrates include the use of low temperature deposited buffer layers. Although these buffer layers have been in use for nearly two decades, work continues

for determining the growth conditions that produce optimum structural and optical characteristics.

The aim of this thesis is to characterise the defect structure of a series of Group III nitride samples. These samples encompass the structure of buffer layers of various thickness, and InGaN layers of various compositions. The materials are characterised using X-ray diffraction, specifically triple axis diffractometry (TAD) for collection of reciprocal space maps (RSM). The X-ray diffraction profiles are analysed using statistical diffraction theory. Chapter 2 presents a summary of X-ray diffraction theory, with the statistical diffraction theory presented in Sec. 2.8. The defect structure of the Group III nitrides are described by a mosaic blocks model, which is introduced in Sec. 2.9. The mosaic block model is characterised by the size of the blocks and their misorientation. The mosaic block size is an indication of the extent of the short range order, and gives a measure of the dislocation density.

In Chapter 3 synchrotron X-ray diffraction experiments are reported, and the modelling techniques described. The results and analyses are presented in Chapter 4. The significance of the results are discussed, as well as discrepancies between the experimental data and the theoretical formalism.

In Chapter 5 a data collection method, based on imaging plates, to reduce collection time, is described. Scans collected using this technique are compared to scans collected using conventional triple axis diffractometry. The relative merits of this data collection technique are discussed.

Group III nitrides can exhibit chemical ordering of the metal cations within the structure. This has implications in terms of the optical and electrical properties of material. Ordering is explored in Chapter 6, by examining an AlGaIn layer before and after annealing. Statistical diffraction theory and Williamson-Hall analysis are used to characterise the mosaic structure of the layer. A comparison of the Williamson-Hall and statistical diffraction theory is also made. The final Chapter summarises the key results and discusses possible extensions to the research programme.

CHAPTER 2

X-ray Diffraction Theory

X-ray diffraction from crystalline materials was discovered in 1912 by von Laue *et al.* (1912, 1913). The interaction of X-rays with crystalline materials is strong because the X-ray wavelength is comparable to the spacing between atomic planes within the crystalline lattice. Analysis of diffraction patterns can reveal information about the internal structural ordering of a sample with minimal or no damage to the material. Furthermore, as the beam can have a large extent, X-ray diffraction reveals structural information over a much larger characteristic length than is capable with other techniques, such as transmission electron microscopy. Additionally the large beam size can be used to determine parameters averaged over a large sample volume.

2.1 X-ray Sources

X-rays may be produced by the Bremsstrahlung mechanism from an X-ray tube, or via synchrotron radiation from a bending magnet (or insertion device).

2.1.1 X-ray Tubes

Radiation is generated in X-ray tubes by accelerating electrons at a metal anode (e.g., Cu). The electrons are decelerated when they hit the anode, producing a continuous spectrum of X-ray photons, known as Bremsstrahlung (braking radiation). Bremsstrahlung has a definite minimum (cut off) wavelength due to complete conversion of the electron energy into X-ray photons. Superposed on this spectrum are a number of sharp peaks - the characteristic radiation. These peaks are due to electron transitions from higher energy states to lower energy states that have been vacated through collisions with incident electrons. Characteristic radiation is far more intense than Bremsstrahlung. By filtering the output from an X-ray tube the characteristic radiation can be isolated and used for experiments requiring monochromatic radiation. X-ray tubes are very inefficient ($< 0.3\%$) (Holý *et al.*, 1999). The intensity can be increased through improved cooling, beam focusing, and utilising a rotating anode system. The latter can accommodate a higher current because the electron beam is spread over a larger area of the anode.

2.1.2 Synchrotron Radiation

Synchrotron radiation is generated when relativistic charged particles (e.g., electrons or positrons) are accelerated by a magnetic field. The relativistic charged particles (usually electrons) circulate within an evacuated 'storage' ring; resonant cavities replenish the kinetic energy lost by electron to synchrotron radiation on each orbit.

The storage ring of a synchrotron is not circular, but rather it is formed from a lattice consisting of straight and curved sections (the number and length of these sections depend on the facility). Bending (dipole) magnets positioned at the curved sections produce a radiation spectrum that is continuous over a large energy range, with a brightness far exceeding an X-ray tube (Wiedemann, 2003). Insertion devices are used to increase the brightness of the X-rays in a particular direction by several orders of magnitude; these are placed in the straight sections of the storage ring. There are two types of insertion device; wiggler and undulator (Wiedemann, 2003). Both undulators and wigglers subject the electrons to a periodic transverse magnetic field (rather than just the simple dipole field), causing the electrons to oscillate back and forth perpendicular to their direction of travel. Each magnetic pole acts as a bending magnet, producing a beam of radiation; however, the photon flux is determined from the sum of the amplitude or intensity of the radiation from each of the poles. Furthermore, the magnetic field is not restricted by the geometry of the storage ring, as there is no net deflection of the electron beam by the insertion device.

The principal difference between wigglers and undulators is the maximum angular deviation of the electron's direction of motion from the undulator axis (Als-Nielsen and McMorrow, 2001). This depends on the amplitude of the oscillations, which in turn depends on the strength of the magnetic field and the magnetic period (spatial period of the magnetic poles) of the undulator or wiggler. The maximum deflection angle, θ_{max} , is given by (Duke, 2000)

$$\theta_{max} = \frac{K}{\gamma} \quad (2.1)$$

where

$$K = 93.4 B_0 \lambda_0 \quad (\text{units of Tm})$$

and

$$\gamma = \frac{1}{\sqrt{1 - \frac{v^2}{c^2}}}$$

B_0 is the maximum magnetic field in the undulator or wiggler, λ_0 is the magnetic

period, v is the electron velocity, and c is the speed of light. For undulators K is typically on the order of unity, and $\gg 1$ for wigglers. Hence undulators employ a weaker magnetic field, or shorter magnetic period, than wigglers. For small values of K the transverse motion of the electrons is approximately non-relativistic and sinusoidal. As such the electron behaves as a dipole oscillator and the radiation emitted for one oscillation is coherent with the radiation from the next oscillation. Hence the amplitudes of emitted waves add (with the intensity the square of the sum of the amplitudes). As the magnetic field strength is increased the transverse motion becomes relativistic and hence non-sinusoidal. The emission spectrum then exhibits a number of harmonics. The number of harmonics depends on the field strength. Wigglers operate at high field strength and longer pole separation (large K), such that the harmonics overlap creating a smooth, broad energy spectrum. Additionally for wigglers the waves from each oscillation are not in phase, hence the intensities add (not the amplitudes). Therefore the radiation delivered by a wiggler is incoherent and broad spectrum, while the radiation from an undulator is coherent and quasi-monochromatic (Als-Nielsen and McMorrow, 2001).

The electrons travel around the ring in bunches at relativistic speeds (several picoseconds long, and several nanoseconds apart). Relativistic effects (i.e., Lorentz contraction) ensures that the radiation emitted by the particles is confined to a narrow cone parallel to the direction of motion. The particle beam will decay over time continuously reducing the radiation intensity. The lifetime of the particles depends upon the quality of the vacuum system. The problem of finite beam lifetime can be ameliorated using 'top-up', in which electrons are injected into the accelerator in a quasi-continuous manner (Emery and Borland, 1999).

Synchrotron beams are classified by their brilliance or brightness (Als-Nielsen and McMorrow, 2001), defined by

$$\text{Brilliance} = \frac{\text{Number of photons per second}}{\text{mrad}^2 \times \text{mm}^2 \times 0.1\% \text{bandwidth}} \quad (2.2)$$

The brilliance is the number of photons emitted in 1 second from a source area of 1 mm^2 into a cone defined by 1 mrad^2 and normalised to a spectral bandwidth of 0.1%. Brightness is defined by replacing the source area with the beam current (Holý *et al.*, 1999),

$$\text{Brightness} = \frac{\text{Number of photons per second}}{\text{mrad}^2 \times \text{mA}^2 \times 0.1\% \text{bandwidth}} \quad (2.3)$$

Some authors interchange the above designations (see e.g., Duke, 2000). As undulators have a smaller spectral bandwidth than wigglers, they have the highest brilliance (or brightness) of the sources described.

2.2 X-ray Scattering

A major focus of this thesis is the interaction of X-rays with crystalline materials. X-rays are a form of electromagnetic radiation with a wavelength on the order of angstroms. The interaction of X-rays with matter is mediated by the electric and magnetic fields. However, as the interaction of the magnetic field with matter is neglected compared to the electric field, except in specific circumstances not encountered in our work, it is neglected throughout this treatment. Furthermore, since the amplitude of a scattered electromagnetic wave is inversely proportional to the mass of the scattering particle, scattering from atomic nuclei can be negligible compared to scattering from electrons. In order to present the theory in a systematic manner, we begin by considering the interaction of X-rays with a single electron.

A free electron exposed to an X-ray beam will oscillate due to the force exerted by the sinusoidally varying electric field. Classically the oscillating electron will radiate an electromagnetic field with the same frequency as the incident X-ray. This is an elastic process (Thomson scattering). However, a treatment of this process using quantum electrodynamics (QED) shows that scattering from a free electron is in fact inelastic (Compton scattering) (Guinier, 1994). Therefore the scattered wave has a reduced energy, and hence lower frequency, than the incident wave. The change in energy for the wave is due to the acceleration (recoil) of the electron. In X-ray diffraction the measured intensity is due to interference, which can only occur if there is a definite phase relationship between scattered waves. However, since there is a change in frequency between the incident and scattered waves, the phase relationship is destroyed, the scattering is incoherent, and interference cannot occur, i.e., interference can only occur if the X-rays are scattered elastically. Elastic scattering is observed for bound electrons (i.e., atomic electrons) because the electrons have discrete energy levels.

Although elastic (Thomson) and inelastic (Compton) scattering are properly treated within the framework of quantum electrodynamics (see e.g., Greiner and Reinhardt, 1994), the classical treatment provides several important results.

2.2.1 Thomson Scattering

The following treatment is based on that presented by Warren (1969). Consider a linearly polarised X-ray beam incident upon a single electron located at the origin, O (see Fig. 2.1). The incident electric field, $\mathbf{E} = \mathbf{E}_0 e^{i(\omega t - kz)}$ is perpendicular to the beam propagation direction (z), and can be resolved into two components, $\mathbf{E}_y = \mathbf{E}_{0y} e^{i(\omega t - kz)}$ and $\mathbf{E}_x = \mathbf{E}_{0x} e^{i(\omega t - kz)}$. The co-ordinate axes are chosen such that the observation point P is in the xz plane and the line \overline{OP} is of length R and makes

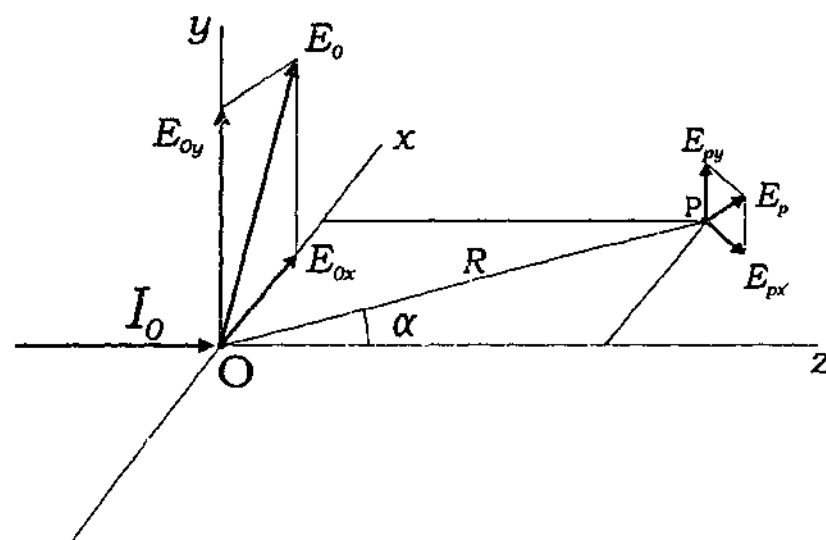


Figure 2.1: Classical X-ray scattering from a single free electron (after Warren, 1969). The electron is located at the origin, O , with the incident X-rays, with intensity I_0 , directed along the z axis. The scattered radiation is observed at point P , which is in the xz plane. The line \overline{OP} has a length R , and makes an angle α to the z -axis. The incident, E_0 , and observed, E_p , electric field amplitudes are resolved into two components, E_{0x} , E_{0y} , and E_{px} , E_{py} , respectively.

an angle α with the z -axis, as depicted in Fig. 2.1. The acceleration of the electron due to the x -component of the electric field is:

$$a_x = \frac{f_x}{m} = -\frac{|e|E_{0x}}{m} e^{i(\omega t - kz)}, \quad (2.4)$$

where e and m are charge and rest mass of an electron, respectively. Then the magnitude of the field at P , due to the acceleration of the electron, a_x , is given by (Warren, 1969)

$$E_{Px'} = -\frac{|e|a_x \cos \alpha}{Rc^2} \quad (\text{cgs units}), \quad (2.5)$$

where $a_x \cos \alpha$ is the projection of the acceleration perpendicular to the vector connecting the charge and P , as shown in Fig. 2.2. As is common in theoretical treatments of X-ray diffraction we adopt cgs (Gaussian) units (see e.g., Pinsker (1978)).

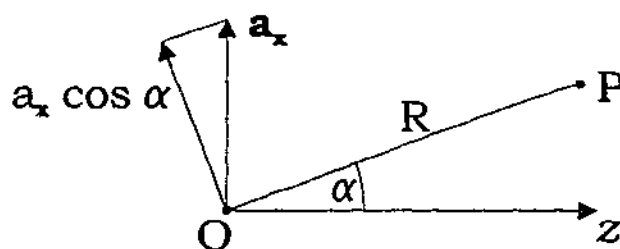


Figure 2.2: The projection of the acceleration perpendicular to the vector connecting the charge at the origin, O , and the observation point P .

Substituting Eq. (2.4) we find:

$$E_{Px'} = \frac{e^2 E_{0x} \cos \alpha}{m R c^2} e^{i(\omega t - k z)} = E_{P0x'} e^{i(\omega t - k z)}, E_{P0x'} = \frac{e^2 E_{0x} \cos \alpha}{m R c^2} \quad (2.6)$$

where the direction of $\mathbf{E}_{Px'}$ is shown in Fig. 2.1. The \mathbf{E}_{0y} -component of the field at the origin leads to the following amplitude at P:

$$E_{Py} = \frac{e^2 E_{0y}}{m R c^2} e^{i(\omega t - k z)} \quad (2.7)$$

Finally the total field at P is given by:

$$(E_P)^2 = (E_{Px'})^2 + (E_{Py})^2 = \left[\frac{e^2}{m R c^2} \right]^2 [E_{0x}^2 \cos^2 \alpha + E_{0y}^2] \quad (2.8)$$

If the initial beam was unpolarised, an average over the possible orientations would be required, i.e.,

$$\begin{aligned} \langle E_{0y}^2 \rangle + \langle E_{0x}^2 \rangle &= \langle E_0^2 \rangle = I_0 \\ \langle E_{0y}^2 \rangle &= \langle E_{0x}^2 \rangle = \frac{1}{2} \langle E_0^2 \rangle = \frac{1}{2} I_0 \\ \langle I^2 \rangle &= \langle I_0^2 \rangle \left[\frac{e^2}{m R c^2} \right]^2 \left[\frac{1 + \cos^2 \alpha}{2} \right] \end{aligned} \quad (2.9)$$

Equation (2.9) represents Thomson scattering for a free electron. As previously discussed, scattering from a free electron is inelastic, however the Thomson scattering equation describes an elastic process. From QED the inelastically scattered intensity (Compton scattering) from a free electron is given by the Thomson equation multiplied by a factor of $(\frac{\nu'}{\nu})^3$ where ν and ν' are incident and scattered photon frequencies respectively (Guinier, 1994). For bound electrons the total scattered intensity, $I_{coh} + I_{incoh}$, is given by the Thomson equation (2.9).

2.2.2 Scattering from an Atom

From quantum theory the squared modulus of the wave function, Ψ , gives the probability density for locating a particle in a particular volume element dv . For an electron the charge density may be written as

$$\rho(\mathbf{r}) = -|e| |\Psi(\mathbf{r})|^2 \quad (2.10)$$

A charge element at any \mathbf{r} is given by $dQ = \rho(\mathbf{r}) dv$. Hence, an X-ray scattered by a charge element has an amplitude $\rho(\mathbf{r}) dv$ times that scattered by a single electron (Guinier, 1994).

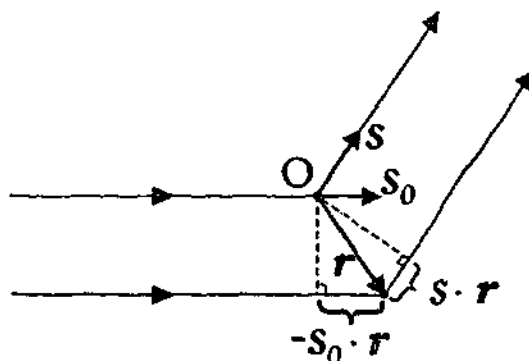


Figure 2.3: Illustration showing the phase difference between two waves scattered from the origin, O, and the charge element at r . The unit vectors s_0 and s point in incident and scattered directions respectively.

Figure 2.3 illustrates the path difference between waves scattered from the origin and a charge element at r . The incident and scattered directions are specified by the unit vectors s and s_0 respectively. The phase difference between the two waves, ϕ , given by

$$\phi = \frac{2\pi \mathbf{r} \cdot (\mathbf{s}_0 - \mathbf{s})}{\lambda} \quad (2.11)$$

Consider an atom with a single electron. This electron is not localised, rather it is described by the charge density $\rho(\mathbf{r})$. Therefore the wave amplitude scattered from a single atomic electron, E_{elec} , is given by

$$\begin{aligned} E_{\text{elec}} &= f_e E_{\text{loc}} \\ f_e &= \int \rho(\mathbf{r}) e^{i\phi} d\mathbf{v} \end{aligned} \quad (2.12)$$

where E_{loc} is the amplitude of the wave scattered by a single localised electron, and f is called electron scattering factor. The integral in Eq. (2.12) is over the volume of the atom where ρ is not zero. The coherent scattering intensity from a single atomic electron is

$$I_{\text{coh}} = I_{\text{Thom}} |f_e|^2 \quad (2.13)$$

where I_{Thom} is the intensity scattered from a single localised electron, as given by the Thompson equation (2.9). The modulus, $|f_e|^2$ arises because the electron scattering factor is generally complex.

The intensity scattered from an atom is then calculated by summing over all atomic electrons (Guinier, 1994), whence we obtain,

$$I_{\text{coh}} = \left| \sum_{j=1}^Z f_{ej} \right|^2 I_e = |f|^2 I_e$$

where

$$f_{ej} = \int \rho_j(\mathbf{r}) e^{i\phi} dv \quad (2.14)$$

Here ρ_j is the charge distribution for the j^{th} electron, and f is the atomic scattering factor (or form factor). In general the atomic scattering factor is complex. The imaginary components are introduced via the electron distribution (unless it has spherical symmetry), and the dispersion corrections. The determination of the atomic scattering factor above assumes that the electrons are not bound. However, the atomic electrons are bound to atoms, with the most tightly bound electrons having binding energies of a similar order as X-ray photon energies. Hence the oscillatory response of these tightly bound electrons to the electric field is damped, thus modifying the atomic scattering factor. The change in atomic scattering factor is denoted f' . At energies corresponding to the absorption edge of the atomic element, a resonance in the value of f' is observed. Associated with the resonance is a phase lag, which is incorporated as an imaginary component, f'' , of the atomic scattering factor. The values f' and f'' are called the dispersion corrections. Incorporating these terms, the atomic scattering factor becomes

$$f = f_0 + f' + if'' , \quad (2.15)$$

where f_0 is the atomic scattering factor for unbound electrons, and f' and f'' are tabulated for several X-ray energies in the International Tables of Crystallography C (Prince, 1999).

A collection of atoms (e.g., a molecule or crystal lattice) is treated in a similar fashion as electrons in an atom; the amplitude is determined by summing the contributions from each atom, with the phase factor accounting for interference effects. Here we find the scattered intensity,

$$I_{\text{coh}} = |F|^2 I_e \quad (2.16)$$

$$(2.17)$$

where

$$F = \sum_i^N f_i e^{i\phi} . \quad (2.18)$$

where F is called the structure factor.

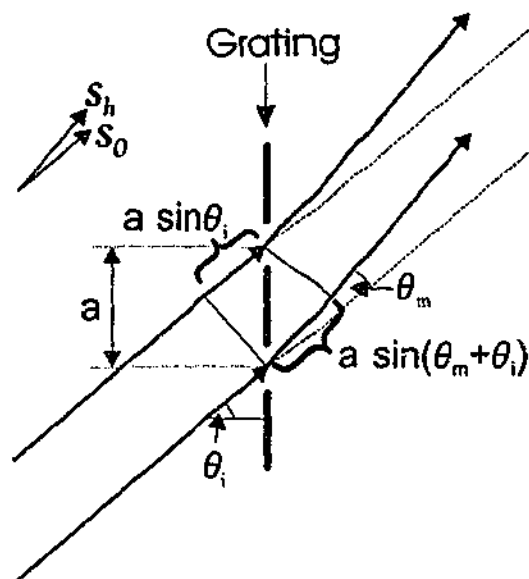


Figure 2.4: Diffraction from a grating: s_0 and s_h are unit vectors in the incident and diffracted wave directions respectively. The propagation direction of the incident wave make an angle θ_i to a line normal to the grating, and the diffracted wave make an angle θ_m to the incident wave direction.

2.2.3 Geometrical Diffraction from Perfect Crystals

We will now consider diffraction from a periodic array of scattering centres, e.g., atoms in a crystal. Figure 2.4 shows a one dimensional row of scatters (i.e., a diffraction grating) illuminated by a plane coherent electromagnetic wave. If \mathbf{a} is the vector connecting nearest equivalent points on the diffraction grating (the period of the diffraction grating is $|\mathbf{a}|$), then the scattering power can be written $P(\mathbf{x}) = P(\mathbf{x} + m\mathbf{a})$ where \mathbf{x} is the position along the grating, and m is an integer.

Constructive interference will occur when the path length difference between the two rays shown in Fig. 2.4 is equal to an integer multiple of the wavelength, (Zachariasen, 1967),

$$\mathbf{a} \cdot (\mathbf{s}_h - \mathbf{s}_0) = m\lambda \quad (m = \pm 1, \pm 2, \pm 3, \dots) \quad (2.19)$$

$$\mathbf{a} \cdot (\mathbf{k}_h - \mathbf{k}_0) = 2\pi m, \quad (2.20)$$

where \mathbf{k}_0 and \mathbf{k}_h are the wavevectors, defined by

$$\mathbf{k}_0 \equiv \frac{2\pi \mathbf{s}_0}{\lambda} \quad (2.21a)$$

$$\mathbf{k}_h \equiv \frac{2\pi \mathbf{s}_h}{\lambda}, \quad (2.21b)$$

where \mathbf{s}_0 and \mathbf{s}_h are the directions of the incident and diffracted wavefields respectively.

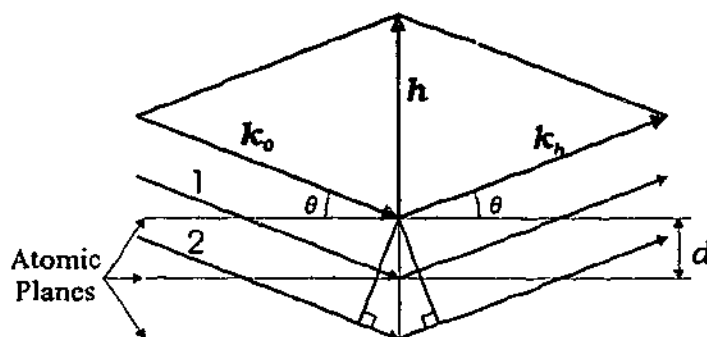


Figure 2.5: The scatter geometry applicable to Bragg's law (after Zachariasen (1967)). The incident, \mathbf{k}_0 , and diffracted, \mathbf{k}_h , wavevectors make an angle θ to the atomic planes. The diffraction vector, \mathbf{h} , is the change in the wavevector between the incident and diffracted waves and d is the plane spacing. The diffraction condition is determined from the path length difference for the two rays labelled 1 and 2).

A more general case, applicable to crystals, is a three-dimensional grating. The scattering power is written as $P(\mathbf{r}) = P(\mathbf{r} + m_1\mathbf{a}_1 + m_2\mathbf{a}_2 + m_3\mathbf{a}_3)$, where \mathbf{a}_1 , \mathbf{a}_2 , and \mathbf{a}_3 are the repeat vectors (analogous to \mathbf{a} for the one dimensional grating) in three non-coplanar directions, m_1 , m_2 , and m_3 are integers, and $\mathbf{r} = x\mathbf{a}_1 + y\mathbf{a}_2 + z\mathbf{a}_3$ is the position in the grating. Setting any two of m_1 , m_2 , and m_3 constant will give the one-dimensional grating equation. Hence:

$$\mathbf{a}_1 \cdot (\mathbf{k}_h - \mathbf{k}_0) = 2\pi m_1 \quad (2.22)$$

$$\mathbf{a}_2 \cdot (\mathbf{k}_h - \mathbf{k}_0) = 2\pi m_2 \quad m_i = \pm 1, \pm 2, \pm 3, \dots (i = 1, 2, 3) \quad (2.23)$$

$$\mathbf{a}_3 \cdot (\mathbf{k}_h - \mathbf{k}_0) = 2\pi m_3, \quad (2.24)$$

which are the Laue equations (von Laue *et al.*, 1912, 1913). These can be written in a more compact form as:

$$\mathbf{k}_h - \mathbf{k}_0 = \mathbf{G}_h, \quad (2.25)$$

where $\mathbf{G}_h = m_1\mathbf{g}_1 + m_2\mathbf{g}_2 + m_3\mathbf{g}_3$; $\mathbf{g}_1, \mathbf{g}_2, \mathbf{g}_3$ are reciprocal to $\mathbf{a}_1, \mathbf{a}_2$, and \mathbf{a}_3 , satisfying

$$\mathbf{a}_i \cdot \mathbf{g}_j = 2\pi\delta_{ij}, \quad (2.26)$$

where δ_{ij} is the Kronecker delta symbol. This will be discussed further in the Sec. 2.3.

An alternative way of describing diffraction is Bragg's law (Bragg and Bragg, 1913a; Bragg, 1913b). Consider Fig. 2.5, which shows diffraction from parallel planes within a crystal. Here we assume that the incident and diffracted rays both make an angle θ to the diffracting planes. Assuming that the planes are separated

by a distance d (the d -spacing) the difference in path length, Δ , for rays 1 and 2 (see Fig. 2.5) is given by:

$$\Delta = 2d \sin \theta . \quad (2.27)$$

By varying θ we can determine the diffraction angle corresponding to a particular d -spacing, i.e., the angle which will make the path length an integer multiple of the wavelength, λ . This is called the Bragg angle, θ_B , and is determined from Bragg's law (Bragg, 1912; Bragg and Bragg, 1913a; Bragg, 1913,b):

$$m\lambda = 2d \sin \theta_B \quad m = 1, 2, 3, \dots \quad (2.28)$$

The d -spacing for the Bragg reflection associated with the (hkl) plane (where hkl are the Miller indices) is

$$d = \sqrt{\frac{a^2}{h^2 + k^2 + l^2}} \quad \text{for a cubic crystal} \quad (2.29)$$

and

$$d = \frac{1}{\sqrt{\frac{4}{3} \left(\frac{h^2 + hk + k^2}{a^2} \right) + \frac{l^2}{c^2}}} \quad \text{for a hexagonal crystal,} \quad (2.31)$$

where a and c are the lattice parameters.

2.3 Reciprocal Space

X-ray diffraction is strongly determined by the geometry of the crystal lattice, and hence constructions that simplify or clarify the geometry are essential. The reciprocal space representation is a particularly useful tool for describing X-ray diffraction.

A crystal is a periodic structure that is constructed from a repeating basic unit (the unit cell) in three dimensions. The periodicity is utilised to describe the crystal in reciprocal space. Within a crystal any two-dimensional plane of atoms will repeat with a particular spatial period (lattice periodicity). The planes can be described by normal vectors to the plane, with spatial frequency $2\pi/d$, where d is the spacing between the planes in the normal direction. These vectors lie in reciprocal space. For a particular crystal structure the complete set of these vectors defines the reciprocal lattice. The utility of this construction is apparent when one considers the wavevector \mathbf{k} (c.f. Eq. 2.21a). The wavevector describes the X-ray plane wave in the same way that the reciprocal lattice vectors describe crystal planes, i.e., directed normal to the planar wavefronts (in this case the direction of propagation) with $|\mathbf{k}| = 2\pi/\lambda$. Hence the wave can be described in the same space as the crystal lattice. An important construction in reciprocal space is the Ewald sphere (Ewald, 1913, 1916a).

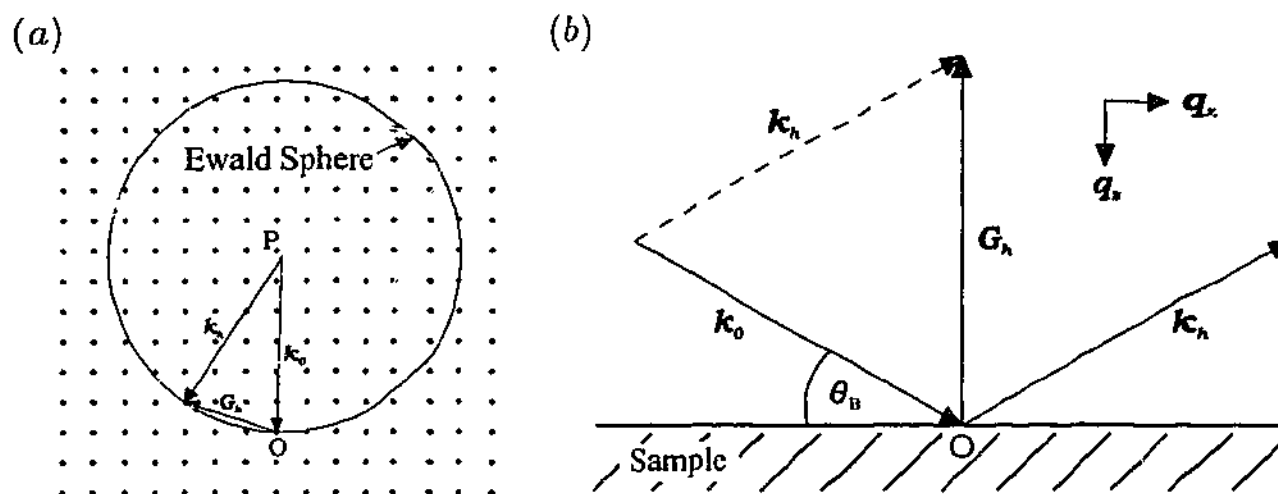


Figure 2.6: (a) The Ewald sphere construction and (b) diffraction from a plane. The symbols k_0 and k_h are the incident and diffracted wavevectors respectively, G_h is the diffraction vector, O is the origin of reciprocal space, θ_B is the Bragg angle, and q_z and q_x are the reciprocal space vectors perpendicular and parallel to the sample surface.

Figure 2.6(a) shows a two-dimensional reciprocal space lattice. O is defined as the origin of the reciprocal lattice, with k_0 denoting the wavevector of an incident plane wave. The Ewald sphere (circle in 2-dimensions) has a radius of $k_0 = |k_0|$, and is centred on the origin of the incident wavevector. From Eq. (2.25) diffraction occurs when the triangle of vectors k_0 , k_h and G_h is closed, i.e., when $k_0 + G_h = k_h$. Assuming that the wavelength of the X-ray is not changed during diffraction, k_h has the same length as k_0 and hence $k_0 + G_h$ must lie on the circle of radius $k_0 = k_h$. This does not imply that there is diffracted intensity in every direction as G_h is restricted. Specifically it must describe the family of diffracting planes, i.e., it is a vector from the origin to a reciprocal space lattice point. Therefore diffraction will only occur if there is two or more reciprocal lattice points lying on the Ewald sphere, with one being the origin, and the other describing the diffracting planes.

An alternative description of the diffraction condition is shown in Fig. 2.6(b), where q_z is perpendicular to the sample surface (defined positive pointing into the crystal). This diagram readily shows the Bragg angle and diffraction vector, and is important when discussing reciprocal space maps (see Sec. 2.10).

2.4 Dynamical Diffraction Theory - Perfect Crystals

In Sec. 2.3 we introduced the kinematical theory of diffraction, which provides an understanding of diffraction maxima in reciprocal space. However, to determine the

relative diffraction peak intensities, or indeed peak shape, requires a more sophisticated treatment of diffraction. In what follows we describe the dynamical diffraction theory for perfect and deformed crystals. This theory provides an accurate framework for calculating the diffracted intensity.

The different variants of the dynamical diffraction theory were originally introduced by Darwin (1914a,b), Ewald (1913, 1916a,b, 1917), and von Laue (1931). Our treatment will follow that by Authier (1996a, 2001), Pinsker (1978), Holý *et al.* (1999), and the review paper by Batterman and Cole (1964).

Although the kinematical theory determines the X-ray diffraction peak positions quite well, the calculation of peak intensities using a kinematical model is simplistic, with only the scattering power of the scattering centres and their relative positions being taken into account.

A full treatment of the diffraction process - the so called dynamical diffraction theory, requires that Maxwell's equations be solved inside the crystal. The properties of the medium are incorporated into Maxwell's equations via the electric current density. More specifically using the equation

$$\mathbf{j} = \frac{\partial \mathbf{P}}{\partial t}, \quad (2.32)$$

where \mathbf{P} is the polarisation and \mathbf{j} is the current density. In a vacuum the polarisation, and hence the current density will be zero; however, in a medium the action of the incident radiation causes the charges to oscillate, polarising the material. The polarisation is determined by the dielectric susceptibility (also referred to as the polarisability), χ , and the electric field vector, \mathbf{E} . For an isotropic homogeneous medium we write (Pinsker, 1978)

$$\chi = \frac{4\pi P}{E} = \epsilon - 1 \quad (\text{cgs units}), \quad (2.33)$$

where ϵ is the relative permittivity of the material. It is assumed that the dielectric susceptibility is a continuous function of position and is proportional to the charge density (von Laue, 1931). The response of the crystal to the external electromagnetic field is entirely described by the susceptibility. An alternative approach due to Ewald (1916a) is to model the crystal as many dipoles that are excited by the electric field of the incident X-ray beam. Each oscillating dipole emits a spherical wave ('wavelets') that affects the oscillation of the other dipoles. The wave that interacts with each dipole is the superposition of the wave incident on the crystal and the spherical waves from each of the other dipoles.

Maxwell's equations within the crystal can be reduced to a single wave (propagation) equation. The derivation of the wave equation is presented in Appendix A,

with the following result (see Eq. (A.14)):

$$\nabla \times (\nabla \times \mathbf{E}) - k^2(1 + \chi(\mathbf{r}))\mathbf{E} = 0. \quad (2.34)$$

Using a vector identity¹ the wave equation can be rewritten as

$$\nabla(\nabla \cdot \mathbf{E}) - \nabla^2 \mathbf{E} - k^2(1 + \chi(\mathbf{r}))\mathbf{E} = 0. \quad (2.35)$$

In the present formalism we assume that the divergence of \mathbf{E} is approximately zero. This is equivalent to the transversality condition² in which \mathbf{E} is perpendicular to the wavevector, \mathbf{k} ; we implicitly assume a harmonic time dependence $\mathbf{E} = \mathbf{E}_0 e^{i\omega t}$, where ω is the spatial frequency.

The dielectric susceptibility is a three-dimensional periodic function, with the same period as the crystal lattice, and can be expressed as a Fourier series:

$$\chi = \sum_{\mathbf{h}} \chi_{\mathbf{h}} \exp(-i\mathbf{h} \cdot \mathbf{r}), \quad (2.36)$$

where \mathbf{h} is a reciprocal lattice vector. The Fourier coefficients, $\chi_{\mathbf{h}}$ are proportional to the structure factor, i.e.,

$$\chi_{\mathbf{h}} = -\frac{r_0 \lambda^2 F_{\mathbf{h}}}{\pi V}, \quad (2.37)$$

where V is the volume of the unit cell, r_0 is the classical radius (Thomson scattering length) of the electron, λ is the wavelength of the incident radiation, and $F_{\mathbf{h}}$ is the structure factor defined in Eq. (2.18). In an absorbing crystal the susceptibility has real and imaginary components, which have the same periodicity as the full complex susceptibility.

A solution to the wave equation is sought in the form of a Bloch wavefunction (also known as an Ewald wave):

$$\mathbf{E}(\mathbf{r}) = \exp(-i\mathbf{K}_0 \cdot \mathbf{r}) \sum_{\mathbf{h}} \mathbf{E}_{\mathbf{h}} \exp(-i\mathbf{h} \cdot \mathbf{r}). \quad (2.38)$$

Defining $\mathbf{K}_{\mathbf{h}} = \mathbf{K}_0 + \mathbf{h}$, we can write Eq. (2.38) as

$$\mathbf{E}(\mathbf{r}) = \sum_{\mathbf{h}} \mathbf{E}_{\mathbf{h}} \exp(-i\mathbf{K}_{\mathbf{h}} \cdot \mathbf{r}), \quad (2.39)$$

¹ $\nabla \times (\nabla \times \mathbf{a}) = \nabla(\nabla \cdot \mathbf{a}) - \nabla^2 \mathbf{a}$

²Using the ansatz $\mathbf{E} = \mathbf{E}_0 e^{i\mathbf{k} \cdot \mathbf{r}}$ for the electric field, we have

$$\nabla \cdot \mathbf{E} = (\nabla \cdot \mathbf{E}_0) e^{i\mathbf{k} \cdot \mathbf{r}} + i\mathbf{k} \cdot \mathbf{E}.$$

Since \mathbf{E}_0 is independent of position, $\nabla \cdot \mathbf{E}_0 = 0$, which implies $\mathbf{k} \cdot \mathbf{E} = 0$ for $\nabla \cdot \mathbf{E} = 0$ and therefore \mathbf{E} is transverse to \mathbf{k} .

where \mathbf{K}_0 and \mathbf{K}_h are the wavevectors corresponding to the incident and diffracted wavefields inside the crystal.

The wavefield is a sum of an infinite number of plane waves, with amplitudes \mathbf{E}_h and wavevectors \mathbf{K}_h . Each of the wavevectors, \mathbf{K}_h , are defined by a reciprocal lattice point in reciprocal space (see Sec. 2.3). To determine the amplitudes of the waves corresponding to each of the wavevectors, Eq. (2.36) and Eq. (2.39) are substituted into the wave equation (2.35) (with $\nabla \cdot \mathbf{E} = 0$) to obtain (Authier, 2001):

$$\frac{K_h^2 \mathbf{E}_{h[h]} - k^2 \mathbf{E}_h}{k^2} = \sum_{h'} \chi_{h-h'} \mathbf{E}_{h'} \quad (2.40)$$

where $\mathbf{E}_{h[h]}$ is the component of electric field vector \mathbf{E}_h perpendicular to the wave vector \mathbf{K}_h . However, invoking the transversality assumption, $\nabla \cdot \mathbf{E} \approx 0$, \mathbf{E}_h is perpendicular to \mathbf{K}_h and hence $\mathbf{E}_{h[h]} = \mathbf{E}_h$. Therefore Eq. (2.40) can be written as:

$$\mathbf{E}_h = \frac{k^2}{K_h^2 - k^2} \sum_{h'} \chi_{h-h'} \mathbf{E}_{h'} \quad (2.41)$$

These are called the fundamental equations of the dynamical theory. Equation (2.41) relates the amplitude of one of the waves in the wavefield to all other amplitudes. In principle this equation cannot be solved because it incorporates an infinite number of terms (describing an infinite set of wavevectors). However, the factor $\frac{k^2}{K_h^2 - k^2}$, called the resonance factor, is very large for a small subset of wavevectors, i.e., those approximately equal to k (the vacuum wavevector). Geometrically the resonance factor is large for terms associated with reciprocal lattice points close to the Ewald sphere. Only the wavevectors (or equations) for which the resonance factor is large need to be included when finding the solution of Eq. (2.41). This allows Eq. (2.41) to be solved for specific situations.

2.4.1 Two Wave Approximation

Equation (2.41) can be written as $3p$ scalar equations, where p denotes the number of terms for which the resonant factor is large (number of points near the Ewald sphere). However, as we have assumed that $\nabla \cdot \mathbf{E} = 0$ there is no component of \mathbf{E} parallel to the wave vector, hence we can reduce it to $2p$ scalar equations. To solve Eq. (2.41), we must restrict the number of terms, p , considered. Assuming that there is only one non-zero term (i.e., one large resonance factor) then we have the one-wave (one-beam) approximation. This applies far from the Bragg conditions, i.e., no diffracted wave is present. Hence, there is only one reciprocal lattice point near the Ewald sphere; that associated with the incident wavevector. In the two-wave (two-beam) approximation there are two equations for each polarisation. The

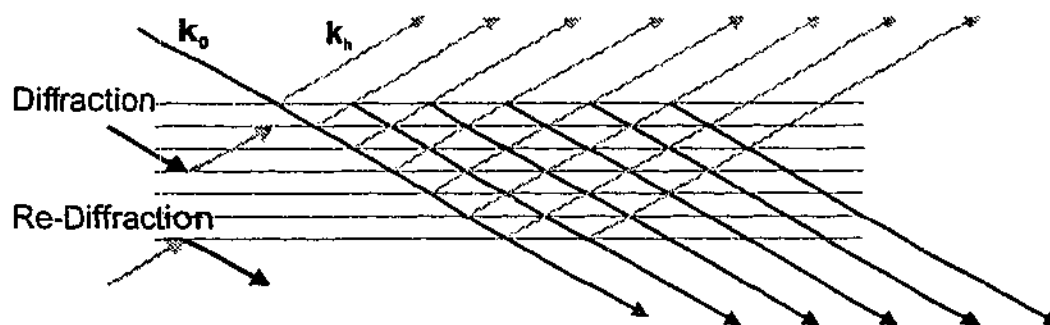


Figure 2.7: Schematic diagram illustrating dynamical diffraction. The incident X-ray beam, with wavevector k_0 is diffracted into the direction of the diffracted wavevector k_h . The beam travelling in the k_h direction can be diffracted a second time (re-diffraction) so that the beam is travelling in the k_0 direction.

two-wave approximation describes the usual diffraction conditions, i.e., it includes the incident and diffracted waves, labelled with subscripts 0 and h , respectively.

Decomposing Eq. (2.41) into two parts gives (for one polarisation state),

$$\frac{K_0^2 - k^2}{k^2} E_0 = \chi_0 E_0 + \chi_h E_h \quad (2.42)$$

$$\frac{K_h^2 - k^2}{k^2} E_h = \chi_0 E_h + \chi_h E_0. \quad (2.43)$$

Equations (2.42) and (2.43) are coupled, because the field amplitudes for a beam travelling in either direction depends on the amplitude of both beams. The coupling terms are the Fourier components of the susceptibilities. Specifically χ_0 describes the photoelectric absorption, χ_h corresponds to the strength of the diffraction of the incident beam into the diffracted beam direction, and χ_h can be associated with the strength of the diffraction of the diffracted beam back into the incident beam direction (see Fig. 2.7). Therefore the energy is transferred from the incident beam to the diffracted beam and back, all the while being absorbed by the crystal. This leads to the phenomenon of extinction (Darwin, 1914a,b, 1922); as the incident beam traverses the crystal its power is reduced as energy is transferred into the diffracted beam direction.

Non-trivial solution to the homogeneous Eqs. (2.42) and (2.43) requires that the secular determinant vanishes, i.e.,

$$\begin{vmatrix} K_0^2 - k^2 - k^2 \chi_0 & -k^2 \chi_h \\ -k^2 \chi_h & K_h^2 - k^2 - k^2 \chi_0 \end{vmatrix} = 0. \quad (2.44)$$

This determinant can be simplified via the following identifications:

$$2k\xi_0 \equiv K_0^2 - k^2 - k^2 \chi_0 \quad (2.45)$$

$$2k\xi_h \equiv K_h^2 - k^2 - k^2 \chi_0. \quad (2.46)$$

The first of these equations can be written as

$$2k\xi_0 = [(K_0^2)^{\frac{1}{2}} - k(1 + \chi_0)^{\frac{1}{2}}][(K_0^2)^{\frac{1}{2}} + k(1 + \chi_0)^{\frac{1}{2}}]. \quad (2.47)$$

Assuming that $k \approx K_0$ (a good approximation since the refractive index of a crystal is very close to unity for X-rays) gives

$$2k\xi_0 \approx 2k \left[(K_0^2)^{\frac{1}{2}} - k \left(1 + \frac{1}{2}\chi_0 \right) \right], \quad (2.48)$$

and likewise for Eq. (2.46)

$$2k\xi_h \approx 2k \left[(K_h^2)^{\frac{1}{2}} - k \left(1 + \frac{1}{2}\chi_0 \right) \right]. \quad (2.49)$$

Hence we have:

$$\xi_0 \approx (K_0^2)^{\frac{1}{2}} - k \left(1 + \frac{1}{2}\chi_0 \right) \quad (2.50)$$

$$\xi_h \approx (K_h^2)^{\frac{1}{2}} - k \left(1 + \frac{1}{2}\chi_0 \right). \quad (2.51)$$

Therefore the scalar determinant in Eq. (2.44) reduces to

$$2k\xi_0 2k\xi_h - k^4 \chi_h \chi_0 = 0 \quad (2.52)$$

$$\xi_0 \xi_h = \frac{1}{4} k^2 \chi_h \chi_0. \quad (2.53)$$

All of the terms on the right hand side of Eq. (2.53) are constants, thus $\xi_0 \xi_h$ is a constant. Therefore this equation is in the form $xy = c$ and describes a hyperbola. The transformation of the fundamental equation into the form given in Eq. (2.53) allows a geometric interpretation to be developed - the dispersion surface, from which solutions can be found (see e.g., Batterman and Cole, 1964).

2.4.2 Dispersion Surface

The Ewald sphere is shown in Fig. 2.6. Usually this sphere is constructed such that the radius of the sphere is the vacuum wavevector k . However, the average refractive index of X-rays within materials is slightly less than unity. If this is taken into account, the wavelength of the radiation within the material will be slightly longer, and the wavevector shorter than in the vacuum, since $K_{inside} = k(1 + \frac{1}{2}\chi_0)$. Hence the radius of the Ewald sphere will be smaller. Figure 2.8(a) shows an Ewald sphere, of radius $k(1 + \frac{1}{2}\chi_0)$, with its centre labelled Q. If the Ewald sphere had a radius of k its centre would have been situated at L (the Laue point). The distance between Q and L has been exaggerated in Fig. 2.8(a). A geometrical construction equivalent to the Ewald sphere, also shown in Fig. 2.8(a), is to draw two spheres,

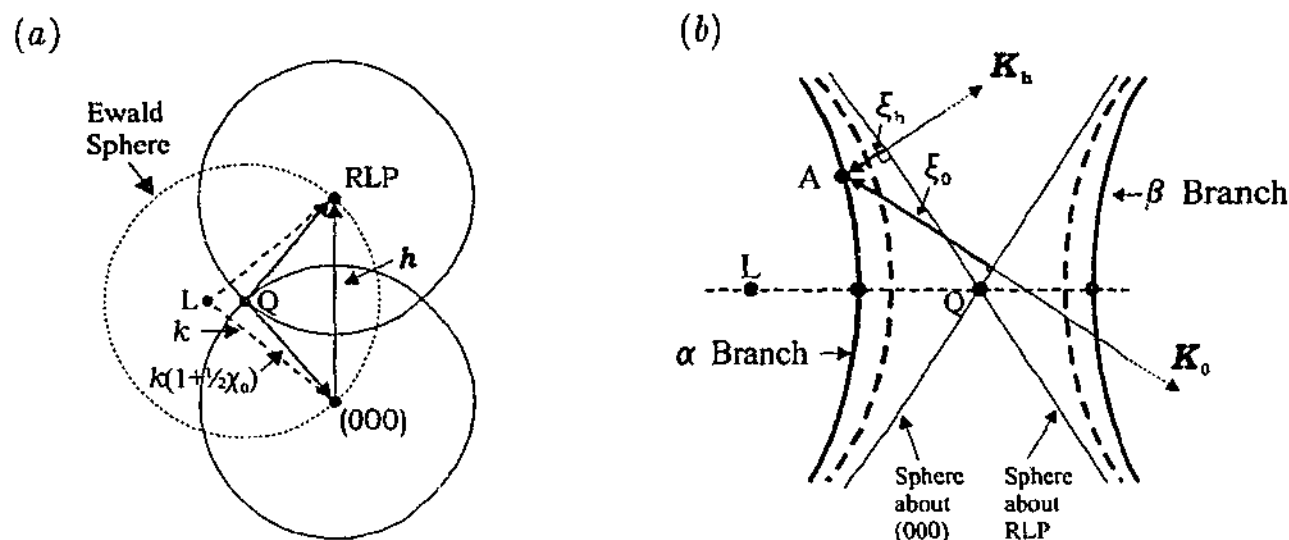


Figure 2.8: (a) Correction of the Ewald sphere for the refractive index of the medium and (b) the dispersion surface construction (after Batterman and Cole (1964)). Q is the centre of the Ewald sphere in the medium (and equivalently Q is the point of intersection for spheres centred on the origin of reciprocal space (000) and the reciprocal lattice point (RLP)). In a vacuum the centre of the Ewald sphere would be at L (the Laue point). The hyperbolae in (b) are the dispersion surfaces (solid lines represent σ -polarisation and dotted lines π -polarisation). The point A is distance ξ_0 from the sphere about (000) and distance ξ_h from the sphere about the reciprocal lattice point. Any point on the dispersion surface, such as A, is called a tie-point.

about the origin and the diffraction reciprocal lattice point, using K_{inside} as the radius. These two spheres intersect at the origin of the Ewald sphere, as shown. The region of intersection is shown in Fig. 2.8(b).

A point in the vicinity of the centre of the sphere, say A, can be chosen such that the wavevectors K_0 and K_h satisfy Eq. (2.53). By definition (i.e., Eqs. (2.50) and (2.51)), ξ_0 and ξ_h are the perpendicular distances from the spheres (about the origin and reciprocal lattice point) to point A. This point will be close to the spheres allowing them to be approximated as straight lines, as shown in Fig. 2.8(b). The loci of all points that satisfy the Eq. (2.53) form the hyperbolae shown - the dispersion surface. The asymptotes to the hyperbolae are the spheres about the origin and reciprocal lattice point. Note that in Fig. 2.8 the solid hyperbolae are for the σ -polarisation state, and the dotted hyperbolae are for the π -polarisation state.

Since ξ is dependent upon the structure factor, it may be complex, with the imaginary part related to absorption. The real part of ξ_0 and ξ_h has been plotted in Fig. 2.8. ξ_0 and ξ_h are used to determine the ratio of the electric field amplitudes appearing in Eqs. (2.42) and (2.43). From the secular determinant (2.44) and the

approximations (2.50) and (2.51) the following ratio can be obtained:

$$\frac{E_h}{E_0} = \frac{2\xi_0}{kC\chi_h} = \frac{kC\chi_h}{2\xi_h}, \quad (2.54)$$

where C is the polarisation state, defined by

$$C = \begin{cases} 1 & : \text{for } \sigma \text{ polarisation} \\ \cos 2\theta & : \text{for } \pi \text{ polarisation.} \end{cases} \quad (2.55)$$

This is by no means a complete treatment of the dynamical diffraction theory for a perfect crystal, however, it does provide a good starting point for developing the specific theories that are required. The samples investigated in this thesis are far from perfect crystal structures, so it is necessary to consider the dynamical theory for deformed crystals.

2.5 Dynamical Diffraction Theory - Deformed Crystals

Henceforth any local structural or chemical change to an ideal crystal will be referred to as a defect. A defect present within a crystal destroys the strict three-dimensional periodicity of a perfect crystal, whence the dielectric susceptibility is not strictly periodic.

Although several authors have considered dynamical diffraction from deformed crystals (e.g., Penning and Polder (1961); Kato (1963, 1964a,b); Afanas'ev and Kohn (1971)), the most successful and widely used dynamical diffraction theory applicable to deformed crystals is due to Takagi (1962, 1969) and Taupin (1964). The resulting 'Takagi-Taupin' equations have been used as the starting point for discussing diffraction from imperfect crystals (including the statistical diffraction theory presented below). More recent theories, based on quantum electrodynamics, have been developed that require fewer assumptions than the Takagi approach, however, they suffer from being complicated and less useful in practice (Härtwig, 2001).

The treatment in this section draws from Takagi (1969), Authier (1996b), and Authier (2001). We begin by considering defects that modify the position of the atomic species, (i.e., a deformation). The deformation generated by the defect is quantified by the vector, $\mathbf{u}(\mathbf{r})$, defined as:

$$\mathbf{r}' = \mathbf{r} + \mathbf{u}(\mathbf{r}), \quad (2.56)$$

where \mathbf{r} is a vector to an atom in the perfect crystal, and \mathbf{r}' is the vector to the same atom after deformation. Assuming the deformation is small, that is

$$\frac{\partial u_i}{\partial x_j} \ll 1 \quad (2.57)$$

where $i, j = 1, 2$, and 3 , and $\mathbf{r} = (x_1, x_2, x_3)$, then we can make the approximation

$$\mathbf{r} = \mathbf{r}' - \mathbf{u}(\mathbf{r}) \simeq \mathbf{r}' - \mathbf{u}(\mathbf{r}') . \quad (2.58)$$

Substituting Eq. (2.58) into Eq. (2.36) gives

$$\begin{aligned} \chi &= \sum_{\mathbf{h}} \chi_{\mathbf{h}} \exp\{-i\mathbf{h} \cdot (\mathbf{r} - \mathbf{u}(\mathbf{r}))\} \\ &= \sum_{\mathbf{h}} \chi'_{\mathbf{h}} \exp\{-i\mathbf{h} \cdot \mathbf{r}\} \end{aligned} \quad (2.59)$$

where

$$\chi'_{\mathbf{h}} = \chi_{\mathbf{h}} \exp\{i\mathbf{h} \cdot \mathbf{u}(\mathbf{r})\} .$$

In this case we seek a solution to the wave equation of the form

$$\mathbf{E} = \sum_{\mathbf{h}} \mathbf{E}_{\mathbf{h}}(\mathbf{r}) \exp(-i\mathbf{K}_{\mathbf{h}} \cdot \mathbf{r}) . \quad (2.60)$$

This equation differs from the solution (2.39), used for the perfect crystal, as the amplitudes vary with position. (In fact there is another formulation where the wavevector is also position dependent (Härtwig, 2001)). However, it is assumed that $\mathbf{E}_{\mathbf{h}}(\mathbf{r})$ and its first derivative are slowly varying functions of position such that the second derivatives ($\nabla^2 \mathbf{E}_{\mathbf{h}}(\mathbf{r})$) can be neglected. Therefore the solution is a sum of 'gently' modified plane waves. In the Takagi formalism (Takagi, 1969), there are two field variations in the crystal; the microscopic variation of the wavefield itself, and a macroscopic variation on the order of the extinction length. An example of the later is the Pendellösung effect (Batterman and Cole, 1964). The restriction that the deformation of the crystal is small ensures that the typical length of the macroscopic variation is much larger than the wavelength.

Inserting Eqs. (2.59) and (2.60) into the wave equation (2.35) produces a set of partial differential equations. In the two beam case we have (Pinsker, 1978)

$$-i \frac{\lambda}{\pi} \frac{\partial E_0(\mathbf{r})}{\partial s} = \chi_0 E_0(\mathbf{r}) + C \chi'_{\mathbf{h}}(\mathbf{r}) E_{\mathbf{h}}(\mathbf{r}) \quad (2.61)$$

$$-i \frac{\lambda}{\pi} \frac{\partial E_{\mathbf{h}}(\mathbf{r})}{\partial s_{\mathbf{h}}} = (\chi_0(\mathbf{r}) - \alpha_{\mathbf{h}}) E_{\mathbf{h}}(\mathbf{r}) + C \chi'_{\mathbf{h}}(\mathbf{r}) E_0(\mathbf{r}) \quad (2.62)$$

where s_0 and $s_{\mathbf{h}}$ are coordinates in the direction of the incident and diffracted waves, respectively, and $\alpha_{\mathbf{h}}$ is a measure of the deviation from the Bragg condition. These are the 'Takagi-Taupin' equations, written in a similar form to Eqs. (2.42) and (2.43) for the perfect crystal. In the two beam approximation, the differential equations describe the co-dependence of the amplitudes for the incident and diffracted beams.

Specifically Eq. (2.61) describes the change in the beam amplitude in the incident direction and Eq. (2.62) describes the amplitude in the diffracted beam direction. The susceptibility terms have the same interpretation as for Eqs. (2.42) and (2.43). The first term on the right hand side of Eq. (2.61) determines the change in the amplitude of the incident beam, because of absorption and refraction, the second term describes the change in the incident beam by the diffraction of the beam travelling in the s_h direction into the s_0 direction. The first term on the right hand side of Eq. (2.62) describes the change in the diffracted beam amplitude by absorption, refraction, and the crystal angular position, and the final term determines the change due to the diffraction of the incident beam.

The deviation term, α_h , arises from the restriction that the vector triangle must be closed within the crystal, i.e., $\mathbf{k}_h - \mathbf{k}_0 = \mathbf{h}$; as the incident vector, \mathbf{k}_0 , is rotated the diffraction vector, \mathbf{k}_h is also modified at fixed \mathbf{h} .

The Takagi equations can be solved analytically for particular cases, such as for a perfect crystal (with $\mathbf{u}(\mathbf{r}) = 0$). In this case we reproduce the results given in Sec. 2.4. Analytical solutions can also be obtained for constant strain gradients (as well as other more 'exotic' strain functions). However, numerical methods are required to solve more complicated systems.

2.6 Kinematical Theory of X-ray diffraction

The kinematical theory of diffraction can be derived in two ways; directly from the structure factor, or as a specific case of the dynamical theory, under certain restrictions concerning the crystal.

A straightforward way to reproduce kinematical theory is to use the Takagi equations (2.61) and (2.62) in the two-beam approximation. The key approximation of the kinematical theory is that the re-scattering (re-diffraction) term (see Eq. (2.61)) is zero. That is the diffracted beam is not re-scattered into the incident direction, and the incident and diffracted beams no longer form a coupled system. This is a strong approximation; however, it makes the solution easy to determine. It is generally valid when the diffracted beam is far less intense than the incident beam; such an approximation is valid when the crystal is thin, or highly deformed. For deformed crystals re-scattering is less likely because a diffracted X-ray must encounter a region of the crystal with the same orientation and d -spacing as the region from which it was diffracted. Although the kinematical theory requires a strong approximation it is applicable to many crystal systems studied using X-ray diffraction. However, it needs to be emphasised that this approximation violates energy conservation, since

the diffracted beam intensity increases without any reduction in the incident beam, i.e., extinction is not treated.

2.6.1 Derivation of the Kinematical Theory from Structure Factors

The kinematical theory can be derived without recourse to the dynamical theory. This derivation begins with Eq. (2.18) and assumes that the total amplitude, diffracted from the entire crystal, is the summation of the contributions from each unit cell (accounting for the phase differences).

We take the distance from a crystal to the observation point, R , to be large compared to the crystal size. The vector that describes the position of any other unit cell is:

$$\mathbf{r}_m = m_1 \mathbf{a}_1 + m_2 \mathbf{a}_2 + m_3 \mathbf{a}_3 \quad (2.63)$$

where $\{m_1, m_2, m_3\} = 0, \pm 1, \pm 2, \pm 3, \dots$ and $\{\mathbf{a}_1, \mathbf{a}_2, \mathbf{a}_3\}$ are the basis vectors for the unit cell of the crystal. Therefore the scattered electric field amplitude for a crystal, E_{xt} , is (Zachariassen, 1967):

$$E_{xt} = E_{elec} F \sum_m e^{i\mathbf{h} \cdot \mathbf{r}_m} \quad (2.64)$$

$$\sum_m e^{i\mathbf{h} \cdot \mathbf{r}_m} = \sum_{m_1=0}^{N_1-1} e^{im_1 \mathbf{h} \cdot \mathbf{a}_1} \sum_{m_2=0}^{N_2-1} e^{im_2 \mathbf{h} \cdot \mathbf{a}_2} \sum_{m_3=0}^{N_3-1} e^{im_3 \mathbf{h} \cdot \mathbf{a}_3}, \quad (2.65)$$

where E_{elec} is the scattered field amplitude due to a single electron, N_1 , N_2 , and N_3 are the number of unit cells in the crystal in \mathbf{a}_1 , \mathbf{a}_2 , and \mathbf{a}_3 directions, respectively. The total number of unit cells in the crystal is $N = N_1 N_2 N_3$. Utilising the observation that each of the lattice sums in Eq. (2.65) is a geometric series, we have

$$\sum_{m_1=0}^{N_1-1} e^{im_1 \mathbf{h} \cdot \mathbf{a}_1} = (e^{(i\mathbf{h} \cdot \mathbf{a}_1)N_1} - 1) / (e^{i\mathbf{h} \cdot \mathbf{a}_1} - 1) \quad (2.66)$$

with a similar expression for the other two lattice sums. Hence Eq. (2.65) can be written as

$$\begin{aligned} \sum_m e^{i\mathbf{h} \cdot \mathbf{r}_m} &= (e^{(i\mathbf{h} \cdot \mathbf{a}_1)N_1} - 1) / (e^{i\mathbf{h} \cdot \mathbf{a}_1} - 1) \\ &\quad \times (e^{(i\mathbf{h} \cdot \mathbf{a}_2)N_2} - 1) / (e^{i\mathbf{h} \cdot \mathbf{a}_2} - 1) \\ &\quad \times (e^{(i\mathbf{h} \cdot \mathbf{a}_3)N_3} - 1) / (e^{i\mathbf{h} \cdot \mathbf{a}_3} - 1). \end{aligned}$$

Finally, from Eq. (2.64) we write the diffracted amplitude as

$$\frac{E_{xt}}{E_{elec}} = F \prod_{j=1}^3 \frac{(e^{(i\mathbf{h} \cdot \mathbf{a}_j)N_j} - 1)}{(e^{i\mathbf{h} \cdot \mathbf{a}_j} - 1)}. \quad (2.67)$$

Multiplying Eq. (2.67) by its complex conjugate, we obtain the equation for intensity³, for the case of a polarised incident beam:

$$\frac{I_{xl}}{I_{\text{Thom}}} = C^2 |F|^2 \prod_{j=1}^3 \frac{\sin^2 \frac{1}{2} N_j \mathbf{h} \cdot \mathbf{a}_j}{\sin^2 \frac{1}{2} \mathbf{h} \cdot \mathbf{a}_j} \quad (2.69)$$

where I_{Thom} is the intensity scattered from a single localised electron, as given by the Thompson equation (2.9). This equation has a maximum when $\mathbf{h} \cdot \mathbf{a}_j = 2\pi m_j$ (for all j), where m_j are zero or integers. The maximum intensity is determined using L'Hopital's rule, i.e.,

$$\lim_{x \rightarrow 2m\pi} \frac{\sin^2(\frac{1}{2}Nx)}{\sin^2(\frac{1}{2}x)} = N^2 \quad (2.70)$$

Hence the maximum diffracted intensity is $I_{xl}^{\text{max}} = I_e C^2 |F_h|^2 N^2$, where N is the number of unit cells and F_h is the structure factor for the reflection.

The intensity determined by Eq. (2.69) does not consider attenuation (absorption) of the incident or diffracted X-ray beams by the crystal. Clearly X-rays will be attenuated as they propagate through a crystal medium. The processes for attenuation are photoelectric absorption, Compton scattering, and extinction. For photoelectric absorption the X-ray photons are absorbed by atoms with the energy converted into the kinetic energy of an ejected electron, leaving the atom in an excited state. For Compton scattering, as introduced in Sec. 2.2, the scattered X-ray photons have a reduced energy (frequency) compared to the incident photons, because the scattering electrons recoil. These photons cannot contribute to the diffracted intensity because they do not have a fixed phase relationship with other photons (because the frequency has changed). Extinction, as noted in Sec. 2.4.1, is the reduction of the incident beam intensity by diffraction (elastic scattering). In other words part of the incident beam is transferred to the diffracted beam. Clearly this will be most evident when the diffraction condition (see e.g., Eq. (2.27)) is satisfied. The photoelectric absorption and Compton scattering can be incorporated into the kinematical theory using (Zachariasen, 1967)

$$I(x) = I_0 e^{-\mu x} \quad (2.71)$$

³Using the following identity:

$$(e^{ix} - 1)(e^{-ix} - 1) = e^{ix}e^{-ix} - (e^{ix} + e^{-ix}) + 1 = 2 - 2\cos(x) = 4\sin^2\left(\frac{x}{2}\right) \quad (2.68)$$

where I_0 is the incident intensity and μ is the linear absorption coefficient and x is the path length through the crystal.⁴ However, the dynamical diffraction theory is required to describe extinction.

For an ideal crystal the assumption that attenuation processes are negligible will depend upon the size of the crystal. From Eq. (2.71) if μx is much less than one, then $I \approx I_0$, and hence attenuation of the incident beam via photoelectric absorption and Compton scattering is small. Crystal imperfection does not impact significantly on these two processes, since they depend on the electron density and the thickness of the crystal. The degree of attenuation via extinction is determined by the strength of diffraction, which is specified by Eq. (2.69). From this equation it is evident that a small crystal (i.e., small N) will exhibit a smaller diffracted intensity, hence less attenuation of the incident beam by extinction. Crystal imperfections will also reduce the diffracted intensity. Thus for highly disordered samples attenuation due to the photoelectric effect and Compton scattering may be considered, however extinction can be safely ignored. Finally, the measured intensity can differ from the theoretical prediction, due to a non ideal incident beam (e.g., non-monochromatic and non-planar), and a finite detector aperture size.

2.7 Mosaic Crystals

Darwin (1914a,b) categorised two forms of extinction: primary and secondary. For perfect crystals primary extinction describes the attenuation of the incident beam by diffraction, as described in Sec. 2.4.1 and 2.6.1. Secondary extinction was introduced with the mosaic crystal model. The mosaic crystal model was introduced by Darwin (1914a,b) to address the discrepancies between experimental data and results of (kinematical) theory for X-ray diffraction. A mosaic crystal is formed from many small crystallites, called mosaic blocks. Each of the blocks is a perfect crystal, however the crystals are misaligned with one another. Usually the displacement between the blocks is large compared to X-ray wavelengths so that there is no definite phase relationship between the beam diffracted from each block. Therefore, the intensity scattered from each block is added to find the total diffracted intensity. The X-ray intensity incident on a block within a mosaic crystal will be reduced by diffraction from blocks closer to the surface of the crystal. This is secondary extinction. Since there is a degree of misalignment of the blocks, not all blocks will be in the Bragg condition at the same time, hence not all blocks that are traversed by the X-ray beam will contribute to the secondary extinction. Primary extinction

⁴This is commonly called the Lambert-Beers or Beers-Lambert Law (Hsieh, 2003).

can be considered to occur within the mosaic blocks.

2.8 Statistical Diffraction Theory

Although the Takagi equations can be used to determine the intensity from deformed crystals (assuming the differential equations can be solved), they are only applicable when the deformation can be specified as a function of position, (e.g., a bent crystal). However, many structural defects are statistically distributed throughout a crystal. Furthermore, the size or orientation of the defects may also be statistical in nature. This requires a 'statistical' theory of X-ray diffraction. The original work in this area was performed by Kato in a series of papers (see e.g., Kato, 1976*a,b*, 1980*a,b*). The original formalism focussed on linking primary and secondary extinction, within one theoretical framework. Before this work, primary extinction was addressed using wave equations, and secondary extinction was treated using energy transfer equations. Guigay and Chukhovskii (1992, 1995), Chukhovskii and Guigay (1993), Davis (1991, 1992, 1993, 1994), Kulda (1987, 1988*a,b*), Becker and Al Haddad (1990, 1992), Holý *et al.* (1993*a,b*, 1994), Punegov (1991*b*, 1993, 1994), Bushuev (1989*a,b*), and Pavlov *et al.* (1995) among others, have also addressed X-ray diffraction from crystals containing statistical defects. Work in this area has included re-formalisation of Kato's original theory to improve its accuracy and range of application (see e.g., Becker and Al Haddad, 1990, 1992; Guigay and Chukhovskii, 1995) typically by relaxing some of his strong approximations. However, some authors have explored alternative theoretical approaches, (see e.g., Kulda, 1987; Davis, 1991; Holý *et al.*, 1993*a*). Kulda (1987) treats the crystal as consisting of elastically deformed domains (rather than the usual Darwin (1922) model of mosaic blocks). A further example is due to Davis (1991), who describes the 'motion' of a point on complex reflectance plane as determining the propagation of the X-ray in the crystal, with the diffraction from imperfect crystals described by a Fokker-Planck equation. Holý *et al.* (1993*a*) uses the notion of a mutual coherence function, which is related to the spatial correlation function. In the kinematical approximation the integral of the mutual coherence function over volume is the Fourier transform of the dielectric susceptibility (Holý *et al.*, 1999).

The following treatment of statistical diffraction theory is based on Kato's original papers (Kato, 1976*a,b*, 1980*a,b*), Kato (1996) and Authier (2001). The exact formalism used for analysis of our samples is given in Sec. 2.8.3.

The statistical dynamical diffraction theory can be derived from the Takagi equations; it is assumed that the deformation vector, defined in Eq. (2.56), can be split

into two components, i.e., the average deformation and a statistical fluctuation:

$$\mathbf{u}(\mathbf{r}) = \langle \mathbf{u}(\mathbf{r}) \rangle + \delta \mathbf{u}(\mathbf{r}), \quad (2.72)$$

where the $\langle \cdot \rangle$ denotes an ensemble average and $\delta \mathbf{u}$ is the fluctuation about $\langle \mathbf{u} \rangle$. The ensemble average is the average value of \mathbf{u} at \mathbf{r} over all defect arrangements. Incorporating this deformation into the phase factor,

$$\Phi = \exp(i\mathbf{h} \cdot \mathbf{u}), \quad (2.73)$$

means the phase factor can be also be split into two factors

$$\Phi = \langle \Phi \rangle + \delta \Phi. \quad (2.74)$$

It is also postulated that the total intensity is given by

$$I = \langle E^* E \rangle = \langle E^* \rangle \langle E \rangle + \langle \delta E^* \delta E \rangle = I^c + I^i \quad (2.75)$$

The term $\langle E^* \rangle \langle E \rangle$ is called the coherent intensity, I^c , and the term $\langle \delta E^* \delta E \rangle$ is called the incoherent intensity, I^i .

There are two approaches to developing the appropriate equations - an integral approach and a differential approach. The integral formalism is more descriptive, although it was developed for a point-source. The differential formalism is mathematically more simple for a plane-wave approach.

2.8.1 Kato's Integral Formalism

The integral approach is formulated for a point source on the crystal surface. We are interested in determining the wavefield at some observation point. The wavefield is considered to be formed from a sum of 'wavelets', each of which can take a particular route through the crystal. Each wavelet will follow a zigzag path (see Fig. 2.9) through the crystal by changing from the incident beam direction to the diffracted direction (labelled as the θ and h directions) and vice versa, from the entrance to the observation point. Each change in direction is an \mathbf{h} or $\bar{\mathbf{h}}$ reflection. The point where the propagation direction changes is called a kink (see Fig. 2.9). If there are an even number of kinks from the entrance point to the observation point the wavelet adds to the wave intensity in the θ direction, an odd number of kinks adds to the wave intensity in the h direction. The wavelet is modified in two ways: at each kink, the amplitude is changed by the coupling constant (i.e., the Fourier component of the susceptibility, as described by Eqs. (2.61) and (2.62)), and the phase is modified by the phase factor. The phase factor will depend on the local

the phase factors are only known in a statistical sense. The advantage of this theory is that a statistical description of the deformation is all that is required. The ensemble average on the right of Eqs. (2.78) and (2.79) contains many correlations between the phase factors. In this framework only the first and second order statistical parameters are considered. These are the ensemble average,

$$f = \langle \Phi(\mathbf{r}) \rangle, \quad (2.80)$$

which is real if spatial homogeneity and isotropy are assumed, and the spatial pair correlation function (Kato, 1996),

$$G(\mathbf{z}) = \langle \Phi^*(\mathbf{r})\Phi(\mathbf{r} + \mathbf{z}) \rangle = \langle \Phi^*(\mathbf{r}) \rangle \langle \Phi(\mathbf{r} + \mathbf{z}) \rangle + \langle \delta\Phi^*(\mathbf{r})\delta\Phi(\mathbf{r} + \mathbf{z}) \rangle. \quad (2.81)$$

The statistical ensemble average, f , is the value of Φ at \mathbf{r} averaged over all defect configurations, and \mathbf{z} is a vector between neighbouring kink points. Here, f is called the static Debye-Waller factor, which is analogous to the usual temperature Debye-Waller factor that describes the effect of temperature on the diffracted intensity. The static Debye-Waller factor indicates how the 'average' atoms is displaced from its ideal position. It is a measure of the deviation from long range ordering within the crystal. The pair correlation function measures the correlation between the deformation field at \mathbf{r} and $\mathbf{r} + \mathbf{z}$. If they are in the same deformation state then coherency is maintained and they are perfectly correlated. It is usual to define the intrinsic correlation function, $g(\mathbf{z})$, such that

$$G(\mathbf{z}) = f^2 + (1 - f^2)g(\mathbf{z}), \quad (2.82)$$

where we have assumed f is real. This allows the correlation length to be defined (Kato, 1996):

$$\tau_n = \int_0^\infty [g(z)]^n dz. \quad (2.83)$$

where spatial homogeneity and isotropy has been assumed, thus g is real and depends only on the separation z of the kink points. The correlation length characterises the short range perfection of the crystal.

Figure 2.9 shows two types of kinks; namely, 'isolated kinks' and kink pairs (enclosed by an 'ellipse'). If an isolated kink occurs at a point in the lattice that is statistically deformed (i.e., has a $\delta\Phi$ component), then the wavelet does not add to the coherent wavefield because there is no fixed phase relationship between this wavelet and those in the coherent wavefield. The two kinks involved in a kink pair both have the same deformation component in their phase factor; the second kink effectively undoing the phase shift of the first kink. The characteristic distance between two kinks in a kink pair is determined by the correlation length.

2.8.2 Kato's Differential Formalism

The differential approach, first reported by Kato (1980a), starts by rewriting the Takagi equations (2.61) and (2.61) in the following form (Kato, 1980a):

$$\frac{\partial E_0}{\partial s_0} = i\frac{\pi}{\lambda}\Phi\chi_h E_h \quad (2.84)$$

$$\frac{\partial E_h}{\partial s_h} = i\frac{\pi}{\lambda}\Phi^*\chi_h E_0. \quad (2.85)$$

Taking the statistical average of these equations gives

$$\frac{\partial \langle E_0 \rangle}{\partial s_0} = i\frac{\pi}{\lambda}\chi_h \langle \Phi E_h \rangle, \quad (2.86)$$

$$\frac{\partial \langle E_h \rangle}{\partial s_h} = i\frac{\pi}{\lambda}\chi_h \langle \Phi^* E_0 \rangle. \quad (2.87)$$

The average wave amplitudes are associated with the coherent part of the intensity.

It is necessary to determine the form of $\langle \Phi E_h \rangle$ in Eq. (2.86):

$$\begin{aligned} \langle \Phi E_h \rangle &= \langle \Phi \rangle \langle E_h \rangle + \langle \delta \Phi E_h \rangle \\ &= \langle \Phi \rangle \langle E_h \rangle + i\frac{\pi}{\lambda}\chi_h \int_0^{s_h} \langle \delta \Phi \langle \Phi^* \rangle E_0(s_0, s_h - \eta) \rangle d\eta \\ &\quad + i\frac{\pi}{\lambda}\chi_h \int_0^{s_h} \langle \delta \Phi(s_0, s_h) \delta \Phi^*(s_0, s_h - \eta) E_0(s_0, s_h - \eta) \rangle d\eta \end{aligned} \quad (2.88)$$

A similar derivation can be done for $\langle \Phi^* E_0 \rangle$. In writing Eq. (2.88) we utilise the integral solution to the Takagi's equation, i.e.,

$$E_h(s_0, s_h) = i\frac{\pi}{\lambda}\chi_h \int_0^{s_h} \Phi^*(s_0, s_h - \eta) E_0(s_0, s_h - \eta) d\eta. \quad (2.89)$$

Since $\langle \delta \Phi \rangle = 0$ we only retain the second order correlation, $\langle \delta \Phi \delta \Phi^* \rangle$, at neighbouring kinks; neglecting the any extrinsic correlation, such as between $\delta \Phi$ and E_0 , we obtain

$$\langle \Phi E_h \rangle = \langle \Phi \rangle \langle E_h \rangle + i\frac{\pi}{\lambda}\chi_h \int_0^{s_h} \langle \delta \Phi(s_0, s_h) \delta \Phi^*(s_0, s_h - \eta) \rangle \langle E_0(s_0, s_h - \eta) \rangle d\eta. \quad (2.90)$$

The first term on the right hand side of Eq. (2.90) is associated with an isolated kink, and the correlation within the integral is a paired kink. The definition of the spatial pair correlation function (2.81) and the intrinsic correlation function (2.82), allow us to replace $\langle \delta \Phi(s_0, s_h) \delta \Phi^*(s_0, s_h - \eta) \rangle$ in Eq. (2.90) with $(1 - f^2)g(z)$. If we assume that the variation of $\langle E \rangle$ is small over the correlation length, τ , then $\langle E \rangle$ can be removed from the integral giving

$$\langle \Phi E_h \rangle = \langle \Phi \rangle \langle E_h \rangle + i\frac{\pi}{\lambda}\chi_h (1 - f^2) \langle E_0 \rangle \int_0^{s_h} g(\eta) d\eta. \quad (2.91)$$

Finally recognising that the remaining integral is the correlation length (2.83) we obtain for the coherent amplitude (Kato, 1996)

$$\frac{\partial \langle E_h \rangle}{\partial s_h} = i \frac{\pi}{\lambda} \chi_h f \langle E_0 \rangle - \left(\frac{\pi}{\lambda} \right)^2 (1 - f^2) \chi_h \chi_{\bar{h}} \tau \langle E_h \rangle, \quad (2.92)$$

where $f = \langle \Phi \rangle$ is the static Debye-Waller factor (2.80), and τ is the correlation area (see Eq. 2.83). A similar expression is found for E_0

$$\frac{\partial \langle E_0 \rangle}{\partial s_0} = i \frac{\pi}{\lambda} \chi_{\bar{h}} f \langle E_h \rangle - \left(\frac{\pi}{\lambda} \right)^2 (1 - f^2) \chi_h \chi_{\bar{h}} \tau \langle E_0 \rangle. \quad (2.93)$$

Since $I_0^c = \langle E_0^* \rangle \langle E_0 \rangle$ then $\frac{\partial I_0^c}{\partial s_0} = \langle E_0^* \rangle \frac{\partial \langle E_0 \rangle}{\partial s_0} + \langle E_0 \rangle \frac{\partial \langle E_0^* \rangle}{\partial s_0}$ (and likewise for I_h). Hence the partial differential equations for I_0^c and I_h^c can be found from Eqs. (2.93) and (2.92), E_0 and E_h , and the appropriate complex conjugates, as follows ((Kato, 1996)):

$$\frac{\partial I_0^c}{\partial s_0} = i \frac{\pi}{\lambda} \chi_{\bar{h}} f \langle E_0^* \rangle \langle E_h \rangle - \left(\frac{\pi}{\lambda} \right)^2 (1 - f^2) \chi_h \chi_{\bar{h}} \tau I_0^c + cc \quad (2.94)$$

$$\frac{\partial I_h^c}{\partial s_h} = i \frac{\pi}{\lambda} \chi_h f \langle E_h^* \rangle \langle E_0 \rangle - \left(\frac{\pi}{\lambda} \right)^2 (1 - f^2) \chi_h \chi_{\bar{h}} \tau I_h^c + cc \quad (2.95)$$

where cc denotes the complex conjugate of all the terms displayed on right hand side of the equations. The cc designation is used in a number of the following equations.

As was introduced in Eq. (2.75) the total intensity can be given by the sum of the coherent and incoherent intensities. Written for the diffracted intensity, I_h , this is given by:

$$I_h = I_h^c + I_h^i \quad (2.96)$$

where I_h^c is the coherent diffracted intensity and I_h^i the incoherent (or diffuse) diffracted intensity. The coherent part,

$$I_h^c = |\langle E_h \rangle|^2, \quad (2.97)$$

is related to the primary extinction, and the incoherent part

$$I_h^i = |\delta E_h|^2 \quad (2.98)$$

is related to the secondary extinction (see e.g., Authier, 2001).

Beginning with the Takagi equations (2.84) and (2.85) the differential equations for the total intensity can be found using similar approaches as used for the coherent intensities (see e.g., Kato, 1980a). Under the assumption that the variation of E_0 and E_h is negligible within a correlation length and that the correlation length for

the incident and diffracted waves are identical, the partial differential equations are (Kato, 1996)

$$\begin{aligned} \frac{\partial I_0}{\partial s_0} &= i\frac{\pi}{\lambda}\chi_{\bar{h}}f\langle E_0^*E_h\rangle - \left(\frac{\pi}{\lambda}\right)^2\chi_h\chi_{\bar{h}}(1-f^2)\tau\langle I_0\rangle \\ &\quad + \left(\frac{\pi}{\lambda}\right)^2|\chi_{\bar{h}}|^2(1-f^2)\tau\langle I_h\rangle + cc, \end{aligned} \quad (2.99)$$

$$\begin{aligned} \frac{\partial I_h}{\partial s_h} &= i\frac{\pi}{\lambda}\chi_hf\langle E_h^*E_0\rangle - \left(\frac{\pi}{\lambda}\right)^2\chi_h\chi_{\bar{h}}(1-f^2)\tau\langle I_h\rangle \\ &\quad + \left(\frac{\pi}{\lambda}\right)^2|\chi_h|^2(1-f^2)\tau\langle I_0\rangle + cc. \end{aligned} \quad (2.100)$$

The differential equations for the incoherent intensity can be determined by subtracting the coherent terms from the total intensity terms (see e.g., Kato, 1980a):

$$\begin{aligned} \frac{\partial I_0^i}{\partial s_0} &= i\frac{\pi}{\lambda}\chi_{\bar{h}}f\langle\delta E_0^*\delta E_h\rangle + \left(\frac{\pi}{\lambda}\right)^2|\chi_{\bar{h}}|^2(1-f^2)\tau I_h^c \\ &\quad - \left(\frac{\pi}{\lambda}\right)^2\chi_h\chi_{\bar{h}}(1-f^2)\tau I_0^i + \left(\frac{\pi}{\lambda}\right)^2|\chi_{\bar{h}}|^2(1-f^2)\tau I_h^i + cc, \end{aligned} \quad (2.101)$$

$$\begin{aligned} \frac{\partial I_h^i}{\partial s_h} &= i\frac{\pi}{\lambda}\chi_hf\langle\delta E_h^*\delta E_0\rangle + \left(\frac{\pi}{\lambda}\right)^2|\chi_h|^2(1-f^2)\tau I_0^c \\ &\quad - \left(\frac{\pi}{\lambda}\right)^2\chi_h\chi_{\bar{h}}(1-f^2)\tau I_h^i + \left(\frac{\pi}{\lambda}\right)^2|\chi_h|^2(1-f^2)\tau I_0^i + cc. \end{aligned} \quad (2.102)$$

2.8.3 Statistical Kinematical Diffraction Theory

The samples used in this thesis were composed of very thin, deformed layers. Hence, the kinematical theory is valid (see Sec. 2.6), and a statistical kinematical diffraction was utilised. The theoretical formalism is found in Nesterets and Punegov (2000) and is based on the more general dynamical treatment by Pavlov and Punegov (2000). A significant feature of this theory (Nesterets and Punegov, 2000) is that it is directly applicable to triple crystal diffractometry, which is the experimental technique used to study our samples.

The derivation begins with the two-beam Takagi equations (2.61) and (2.62); however, the re-scattering term is neglected:

$$-i\frac{\lambda}{\pi}\frac{\partial E_0(\mathbf{r})}{\partial s_0} = \chi_0 E_0(\mathbf{r}) \quad (2.103)$$

$$-i\frac{\lambda}{\pi}\frac{\partial E_h(\mathbf{r})}{\partial s_h} = (\chi_0(\mathbf{r}) - \alpha_h)E_h(\mathbf{r}) + C\chi_h(\mathbf{r})\exp[i\mathbf{h}\cdot\mathbf{u}(\mathbf{r})]E_0(\mathbf{r}) \quad (2.104)$$

This allows the partial differential equation (2.103)(with respect to the 0 direction) to be solved directly, as it is independent of the second equation (2.104). The solution to Eq. (2.103) is of the form

$$E_0(\mathbf{r}) = E_0(x - \cot\theta_1 z, y, 0)\Psi_0(\mathbf{r}), \quad (2.105)$$

where

$$\Phi_0(\mathbf{r}) = \exp \left\{ i \int_0^z \sigma_0[x + \cot\theta_1(s - z), y, s] ds \right\},$$

where $\sigma_0(\mathbf{r}) = \pi\chi_0(\mathbf{r})/(\lambda\gamma_0)$ with $\gamma_0 = \sin(\theta_B - \varphi)$ (φ is the asymmetry angle, i.e., the angle between the crystal surface and the diffracting planes). The solution to the second equation (2.104) can also be found analytically. For example, using Bragg geometry the amplitude at the top surface ($z = 0$) of the crystal (Nesterets and Punegov, 2000) is:

$$E_h(q_x, q_y, z = 0) = \hat{E}_h(q_x, q_y, z = l) + (i/2\pi) \int_0^l dz \int_{-\infty}^{\infty} dx \int_{-\infty}^{\infty} dy \\ \times \sigma_h(\mathbf{r}) \exp\{-i[\mathbf{q}\mathbf{r} + \mathbf{h}\mathbf{u}(\mathbf{r})]\} \Phi_0(\mathbf{r})\Phi_h(\mathbf{r})E_0(x - \cot\theta_1 z, y, 0). \quad (2.106)$$

where $\mathbf{q} = (q_x, q_y, q_z)$ is the reciprocal space vector, $\sigma_h(\mathbf{r}) = \pi\chi_h(\mathbf{r})C/\lambda\gamma_h$ (with $\gamma_h = \sin(\theta_B + \varphi)$), and $\Phi_h(\mathbf{r}) = \exp\{ib \int_0^z \sigma_0[x - \cot\theta_2(s - z), y, s] ds\}$. The reciprocal space vector \mathbf{q} defines any point in reciprocal space, whereas the diffraction vector \mathbf{h} defines the reciprocal space point corresponding to the Bragg reflection. The first term on the right hand side of Eq. (2.106), $\hat{E}_h(q_x, q_y, z = l)$, is the amplitude coming from the bottom of the crystal ($z = l$). \hat{E} indicates that the amplitude has a specific normalisation. In practice this term describes the amplitude diffracted from the substrate material for a layered sample; it can be calculated by dynamical diffraction theory, or simply neglected if the Bragg angle for the layer significantly differs from that for the substrate.

The coherent amplitude is given by

$$E_h^c(\mathbf{q}) = \langle E_h(\mathbf{q}) \rangle = \langle \hat{E}_h(q_x, q_y, z = l) \rangle + (i/2\pi) \int_0^l dz \int_{-\infty}^{+\infty} dx \int_{-\infty}^{+\infty} dy \sigma_h(\mathbf{r}) \\ \times f(\mathbf{r})\Phi_0(\mathbf{r})\Phi_h(\mathbf{r}) \exp\{-i[\mathbf{q}\mathbf{r} + \mathbf{h}\langle\mathbf{u}(\mathbf{r})\rangle]\} E_0(x - \cot\theta_1 z, y, 0) \quad (2.107)$$

where $f(\mathbf{r}) = \langle \exp[-i\mathbf{h}\delta\mathbf{u}(\mathbf{r})] \rangle$ is the static Debye-Waller factor introduced in Sec. 2.8.1. The coherent intensity is defined as $I_h^c(\mathbf{q}) = |E_h^c(\mathbf{q})|^2$. The incoherent intensity (also known as the diffuse intensity) is the difference between the total intensity and the coherent intensity, i.e., $I_h^d(\mathbf{q}) = \langle E_h(\mathbf{q})E_h^*(\mathbf{q}) \rangle - \langle E_h(\mathbf{q}) \rangle \langle E_h^*(\mathbf{q}) \rangle$.

Substituting Eq. (2.106) into the definition of $I_h^d(\mathbf{q})$ gives (Nesterets and Pune-gov, 2000),

$$I_h^d(\mathbf{q}) = \int_0^l dz \int_{-\infty}^{+\infty} dx \int_{-\infty}^{+\infty} dy |\sigma_h(\mathbf{r})|^2 [1 - f^2(\mathbf{r})] \tau(\mathbf{r}, \mathbf{q}) \\ \times \exp \left\{ - \int_0^z (\mu[x + \cot \theta_1(s - z), y, s] + b\mu[x - \cot \theta_2(s - z), y, z]) ds \right\} \\ \times I_0(x - \cot \theta_1 z, y, 0). \quad (2.108)$$

where $\mu = 2\text{Im}(\sigma_0)$ is the photoelectric absorption coefficient (with $\text{Im}(\sigma_0)$ denoting the imaginary part of σ_0), and τ is the correlation volume defined by

$$\tau(\mathbf{r}, \mathbf{q}) = (2\pi)^{-2} \int_{-\infty}^{\infty} d\rho g(\mathbf{r}, \rho) \exp(-i\{\mathbf{q}\rho + \mathbf{h}[\langle \mathbf{u}(\mathbf{r} + \rho) \rangle - \langle \mathbf{u}(\mathbf{r}) \rangle]) \\ \times \exp[i(1 + b)\sigma_0(\mathbf{r})\rho_z], \quad (2.109)$$

where $\rho = \mathbf{r} - \mathbf{r}'$ and $g(\mathbf{r}, \rho)$ is the intrinsic correlation function (2.83) given by

$$g(\mathbf{r}, \rho) = \frac{\langle \exp\{-i\mathbf{h}[\delta\mathbf{u}(\mathbf{r} + \rho) - \delta\mathbf{u}(\mathbf{r})]\} \rangle - f^2(\mathbf{r})}{1 - f^2(\mathbf{r})}. \quad (2.110)$$

Here the correlation volume corresponds to three-dimensional resolution in reciprocal space. The triple-axis diffractometry setup (described in Sec. 2.10) has a two-dimensional resolution in reciprocal space. In this setup the correlation volume is transformed to a correlation area. This is obtained by integrating over the \mathbf{q}_y -axis, because the analyser crystal usually does not have high resolution in the \mathbf{q}_y direction, i.e.,

$$\tau(\mathbf{r}; q_x, q_z) = \int_{-\infty}^{+\infty} dq_y \tau(\mathbf{r}, \mathbf{q}) \\ = (1/2\pi) \int_{-\infty}^{+\infty} d\rho_z \int_{-\infty}^{+\infty} d\rho_x (\exp[-i(q_z\rho_z + q_x\rho_x)]) \\ \times \exp[i(1 + b)\sigma_0(\mathbf{r})\rho_z] \\ \times \exp\{-\mathbf{h}[\langle \mathbf{u}(x + \rho_x, y, z + \rho_z) \rangle - \langle \mathbf{u}(\mathbf{r}) \rangle]\} \\ \times g(\mathbf{r}; \rho_x, 0, \rho_z). \quad (2.111)$$

Equations 2.110 and 2.111 provide the theoretical framework for calculating the diffracted intensity, however, a model for the correlation function is required. The model defines the deformation vector $\mathbf{u}(\mathbf{r})$, which depends on the form of the crystal defect. In this way the theory can be used to describe various different defect structure, by including the appropriate correlation function.

2.9 Models for Crystal Defects

There are a number of defect models described in the literature that are amenable to analysis using the statistical diffraction theory. For example Holý *et al.* (1993a) uses spherical mosaic blocks and Nesterets and Punegov (2000) describes models for spherical amorphous clusters with various strain distributions in the surrounding crystal matrix. Pavlov and Punegov describe several models for spherically symmetrical defects (Punegov and Pavlov, 1996; Pavlov and Punegov, 1996, 1997). The correlation function for a mosaic block was determined by Kato (1982); Bushuev (1989a,b); Holý *et al.* (1993b). The model used in the present work assumes parallelepiped mosaic blocks (see Fig. 2.10), characterised by their lateral extent, l_x , height, l_z , their misorientation, Δ_m , and average strain parallel and perpendicular to the sample surface (Nesterets and Punegov, 2000; Pavlov *et al.*, 2004). The misorientation is a measure of the width of the Gaussian distribution of the rotation of the mosaic blocks, α . These parameters are shown in Fig. 2.10(a). The mosaic block is otherwise assumed perfect. Referring to Eq. (2.110), the first step in determining the correlation function is specifying the fluctuation $\delta\mathbf{u}$. For this deformation model the blocks can only be rotated; a lattice position in the perfect crystal is rotated by an angle α about the centre of the block to its position in the deformed crystal. This is shown in Fig. 2.10(b). Further we assume that the average block orientation is the same as for the perfect crystal. Referring to Fig. 2.10(b), the deformation vector is given by:

$$\begin{aligned} x &= r \cos \beta, z = r \sin \beta \\ \delta u_x &= r[\cos(\beta - \alpha) - \cos \beta] = r[\cos \beta \cos \alpha + \sin \beta \sin \alpha - \cos \beta] \\ &= x[\cos \alpha - 1] + z \sin \alpha \end{aligned} \quad (2.112)$$

$$\begin{aligned} \delta u_z &= r[\sin(\beta - \alpha) - \sin \beta] = r[-\cos \beta \sin \alpha + \cos \alpha \sin \beta - \sin \beta] \\ &= z[\cos \alpha - 1] - x \sin \alpha \end{aligned} \quad (2.113)$$

$$\delta \mathbf{u} = (\delta u_x, \delta u_z) \quad (2.114)$$

$$\approx (\alpha z, -\alpha x). \quad (2.115)$$

Equation (2.115) is only valid for $\alpha \ll 1$. Taking φ as the angle between the sample surface and the diffracting planes, the diffraction vector, \mathbf{h} , can be written as $\mathbf{h} = -h(\sin \varphi, \cos \varphi)$. Hence, $\mathbf{h} \cdot \delta \mathbf{u}$ is

$$\mathbf{h} \delta \mathbf{u} = h(-\alpha z \sin \varphi, \alpha x \cos \varphi). \quad (2.116)$$

If we assume that $f = 0$, which is equivalent to saying that there is not a long range ordering between the different blocks (there is no phase correlation between

the waves diffracted from each block), then the correlation function can be written as (Nesterets and Punegov, 2000):

$$g(\rho) = p(\rho) \int_{-\infty}^{+\infty} d\alpha W(\alpha) \exp[ih\alpha(\rho_z \sin \varphi - \rho_x \cos \varphi)] \quad (2.117)$$

where $p(\rho)$ is the probability that two points separated by the vector ρ are within the same mosaic block, and $W(\alpha)$ is the misorientation distribution. The probability, $p(\rho)$, is given by $p(\rho) = p_x(\rho_x)p_y(\rho_y)p_z(\rho_z)$, where

$$p_i(\rho_i) = \begin{cases} 1 - |\rho_i|/l_i, & |\rho_i| \leq l_i \\ 0, & \text{otherwise.} \end{cases} \quad i = x, y, z \quad (2.118)$$

The misorientation distribution is assumed to be Gaussian, and is normalised to have an area of unity, so that the integral Eq. (2.117) gives the average value from the ensemble. Different forms for $W(\alpha)$ may be adopted. For example Nesterets and Punegov (2000) use

$$W(\alpha) = \sqrt{\log_e 2/\pi} (1/\Delta_m) \exp[-\log_e 2(\alpha^2/\Delta_m^2)], \quad (2.119)$$

while Pavlov *et al.* (2004) use

$$W(\alpha) = (1/\Delta_m) \exp[-\pi(\alpha^2/\Delta_m^2)]. \quad (2.120)$$

Both forms of $W(\alpha)$ have a normalised area; however, $W(\alpha)$ defined in Eq. (2.119) has a half-width-at-half-maximum equal to Δ_m , whereas the normalisation in Eq. (2.120) does not. Nesterets and Punegov (2000) integrate Eq. (2.117) analytically with respect to α to obtain

$$g(\rho) = p(\rho) \exp\{[-h^2\Delta_m^2(\rho_z \sin \varphi - \rho_x \cos \varphi)^2]/4\log_e 2\} \quad (2.121)$$

Upon substitution into Eq. (2.111), one can numerically integrate over ρ_x and ρ_z to determine the correlation area and subsequently the diffuse intensity.

In contrast Pavlov *et al.* (2004) substitute Eq. (2.117) directly into Eq. (2.111), integrate analytically over ρ_x and ρ_z to obtain

$$\hat{\tau}_1^c = [1/(1 - f^2)] \int d\alpha \frac{e^{-\pi(\alpha/\Delta_m)^2}}{\Delta_m} \frac{2}{l_z l_x \beta^2 \psi^2} (1 + i\psi l_z - e^{i\psi l_z}) (1 - \cos(i\beta l_x)), \quad (2.122)$$

where

$$\psi = q_z - h\alpha \sin \varphi \quad (2.123)$$

$$\beta = q_x - h\alpha \cos \varphi. \quad (2.124)$$

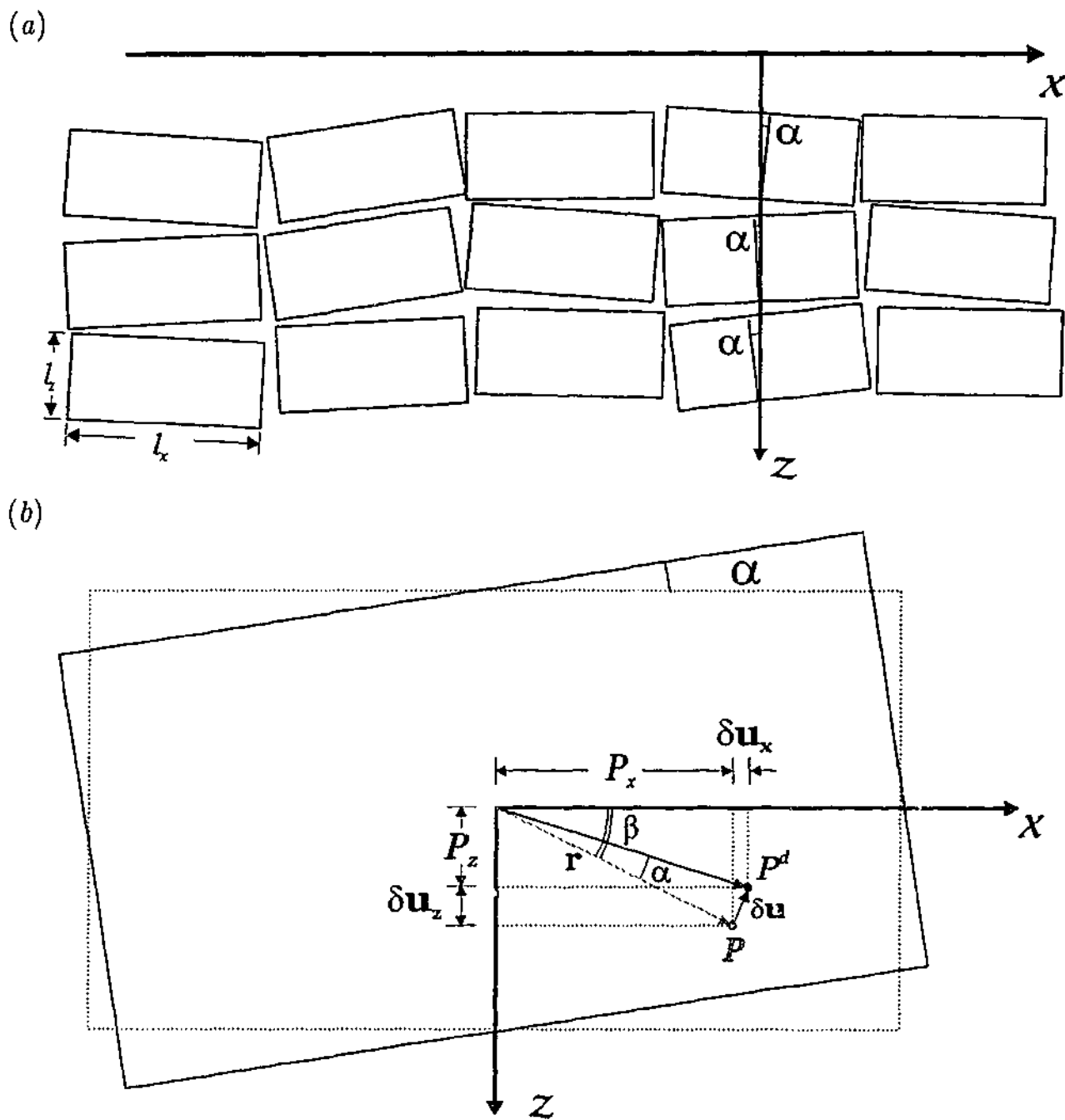


Figure 2.10: (a) Schematic of mosaic blocks, indicating the block orientation, α , and the size perpendicular, l_z , and parallel, l_x , to the sample surface, and (b) the construction of the deformation vector. An atom at position P (specified by a vector r , which makes an angle β with the x -axis) in a non-deformed crystal is rotated through an angle α to point P^d in the deformed crystal. The deformation translates the atom by δu .

The correlation area, and hence the diffuse intensity, is found using numerical integration of Eq. (2.122). The advantage of this second method is that the numerical integration is over a single coordinate, which should reduce the computation time compared to a numerical integral over two coordinates. Equation (2.122) is the basis of the analysis of our data.

2.10 Reciprocal Space Mapping of Crystal Structures

Section 2.3 described a perfect, infinite, crystal in terms of its reciprocal lattice. The reciprocal lattice consists of a three-dimensional array of points. However, deviations from the perfect lattice cause the diffraction peaks at the reciprocal lattice points to be shifted and broadened. The specific shape of the broadening is indicative of the departure from a perfect lattice. Although we can determine the gross structural type of the sample from low resolution diffraction experiments, by determining which reciprocal lattice points are observable, in order to determine defect structure we must collect information from a small region of reciprocal space about a number of lattice points. Data collected in two or three dimensions in reciprocal space is called a reciprocal space map (RSM) (Iida and Kohra, 1979; Fewster, 1993, 1997). Typically triple axis diffractometry (TAD) (Iida and Kohra, 1979) is employed to gather RSMs, as it provides good resolution in reciprocal space. The TAD arrangement is shown in Fig. 2.11, where ω is the angular deviation from the sample Bragg condition and ε is the deviation from the Bragg condition of the analyser crystal. We have the following the equivalence between the Bragg angle θ_B and the asymmetry angle φ (see Fig. 2.12):

$$\theta_1 \cong \theta_B - \varphi \quad (2.125)$$

$$\theta_2 \cong \theta_B + \varphi \quad (2.126)$$

where θ_1 is the angle between the sample surface and the incident ray, and θ_2 is the angle between the sample surface and the diffracted ray.

The size of the region in reciprocal space that is both viewed by the detector and illuminated by the source is called the instrumental function. The detector will integrate the intensity over this region, and hence it needs to be kept small. The purpose of the analyser crystal is to restrict the angular range of the intensity collected by the detector, which in turn improves the resolution in reciprocal space compared to just the detector with a narrow aperture. The monochromator reduces the region of reciprocal space illuminated by the source. This is why TAD has such good resolution. (If no analyser crystal is used ε is the angular deviation of the detector from the Bragg condition for the diffracted beam from the sample).

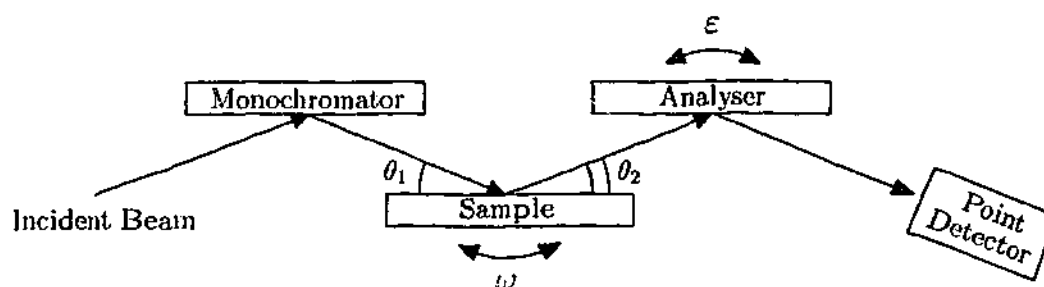


Figure 2.11: Schematic diagram of the triple axis diffractometry experiment, where ω is the angular deviation of sample from its Bragg position and ϵ is angular deviation of the analyser crystal from its Bragg position. The monochromators reduce the angular divergence and wavelength dispersion of the incident X-ray beam and the analyser crystal reduces the angular window viewed by the detector.

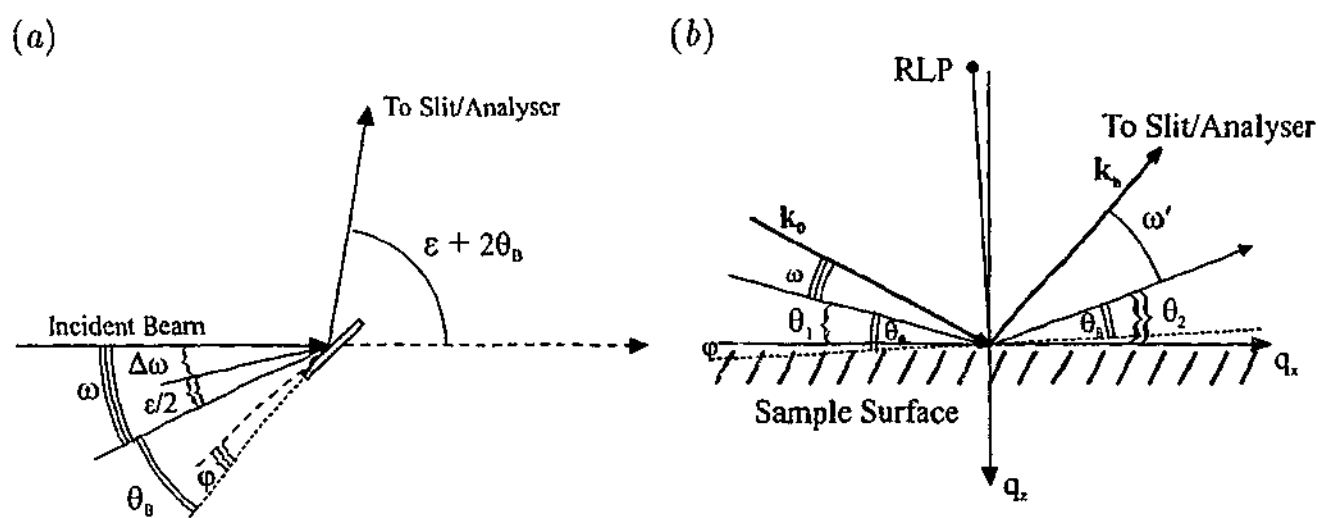


Figure 2.12: Angle definitions in (a) angular space, and (b) reciprocal space.

Figure 2.12 shows the experimental arrangement in more detail. Here θ_B is the Bragg angle for the particular reflection under investigation, ω' is the angular deviation from the Bragg condition of the diffracted beam striking the analyser crystal at $\theta_{B_{analyser}}$, and φ is the asymmetry angle for the sample. The introduction of $\Delta\omega$ (shown in the real space construction in Fig. 2.12(a)) allows us to write

$$\omega = \Delta\omega + \frac{\epsilon}{2}. \quad (2.127)$$

This is a convenient relation, as $\Delta\omega$ describes the angular deviation of the sample from the $\theta - 2\theta$ scan. The importance of $\Delta\omega$ will be revealed below.

Rotating the whole sample until it is horizontal, and replacing the incident and diffracted rays with their appropriate wavevectors results in the arrangement shown in Fig. 2.12(b). The required rotation is $\omega + \theta_B - \varphi$. Hence the angle between the q_x -axis and the direction to the middle of the angular window of the analyser

crystal is given by

$$\begin{aligned}\omega' + \theta_2 &= 2\theta_B + \varepsilon - (\omega + \theta_B - \varphi) \\ &= \theta_2 + \varepsilon - \omega,\end{aligned}\quad (2.128)$$

whence

$$\omega' = \varepsilon - \omega. \quad (2.129)$$

To calculate the magnitude of the reciprocal space vectors, (relative to the reciprocal lattice point being investigated) from the angle of the sample and analyser, we utilise (Nesterets and Punegov, 2000)

$$q_x = 2k\omega \sin \theta_B \cos \varphi - k\varepsilon \sin \theta_2, \quad (2.130)$$

$$q_z = -2k\omega \sin \theta_B \sin \varphi - k\varepsilon \cos \theta_2. \quad (2.131)$$

This means the origin of the $q_x - q_z$ coordinate system is taken as the reciprocal lattice point (RLP) being studied. However, the origin of reciprocal space is taken as the RLP (000). The shift of the $q_x - q_z$ coordinate system relative to reciprocal space origin is

$$\mathbf{q}_{\text{shift}} = k(\cos(\theta_B + \varphi) - \cos(\theta_B - \varphi))\hat{\mathbf{q}}_x - k(\sin(\theta_B + \varphi) + \sin(\theta_B - \varphi))\hat{\mathbf{q}}_z, \quad (2.132)$$

where $\hat{\mathbf{q}}_x$ and $\hat{\mathbf{q}}_z$ are the unit vectors:

$$\hat{\mathbf{q}}_x = \frac{\mathbf{q}_x}{|\mathbf{q}_x|}, \quad (2.133)$$

$$\hat{\mathbf{q}}_z = \frac{\mathbf{q}_z}{|\mathbf{q}_z|}. \quad (2.134)$$

The derivation of Eqs. (2.130) and (2.131) is achieved using simple geometric considerations, and assumes that ω and ε are small. The full derivation is given in Appendix B. Substituting Eq. (2.127) for ω in Eqs. (2.130) and (2.131) gives

$$q_x = 2k\Delta\omega \sin \theta_B \cos \varphi - k\varepsilon \cos \theta_B \sin \varphi, \quad (2.135)$$

$$q_z = -2k\Delta\omega \sin \theta_B \sin \varphi - k\varepsilon \cos \theta_B \cos \varphi. \quad (2.136)$$

For symmetric reflections, $\varphi = 0$, q_x and q_z reduce to

$$q_x = 2k\Delta\omega \sin \theta_B, \quad (2.137)$$

$$q_z = -k\varepsilon \cos \theta_B. \quad (2.138)$$

Equation (2.137) indicates that for symmetric reflections, q_x is proportional to $\Delta\omega$, and q_z is proportional to ε . Note that this is only true for small angles.

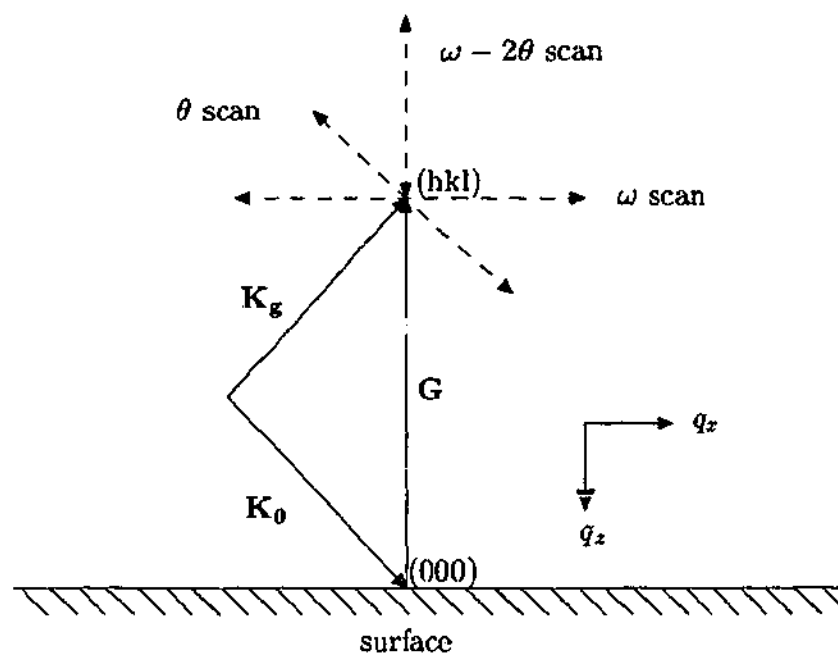


Figure 2.13: Various scan directions in reciprocal space. The $\omega - 2\theta$ scan is collected by rotating the detector at twice the rate of the sample. The ω scan is collected by rotating the sample while keeping the detector position fixed, and the θ scan by keeping the sample position fixed and rotating the detector. These scan allow different profiles of the (hkl) reflection can be collected.

Several different one-dimensional scans are used to measure intensity profiles through reciprocal space with the three most common depicted schematically in Fig. 2.13. The $\omega - 2\theta$ scan is achieved by rotating the analyser at twice the angular rate of the sample. If ω is equal to $\varepsilon/2$ (i.e., $\Delta\omega = 0$) then this scan (specifically referred to as a $\theta - 2\theta$ scan) points from the origin of reciprocal space to the centre of the reciprocal lattice point. For symmetric reflections this is along the q_z -axis. When ω and ε are small the $\omega - 2\theta$ scans are approximately parallel (to the $\theta - 2\theta$ -scan).

The ω scan is collected by rotating the sample without changing the analyser setting (or detector position if there is no analyser crystal), i.e., $\Delta\omega$ is varied but ε is kept constant. For symmetric reflections (and small angles) this scan is parallel to the q_x -axis. Relaxing the assumption of small angles, the scan is a circular arc of radius $2k \sin(\theta_B + \varepsilon/2)$, centred on the origin of reciprocal space. The θ scan is performed by holding the sample position fixed and rotating the analyser. For symmetric reflections (and small angles) the scan is approximately a straight line that makes an angle θ_B to the q_z -axis. Relaxing the small angle assumption the scan is a circular arc with radius k . The tangent to the curve at the q_z -intercept is still θ_B .

Collection of two-dimensional RSM data is usually accomplished by making a series of $\omega - 2\theta$ scans for a range of $\Delta\omega$ values. In this way a two-dimensional patch of reciprocal space can be covered. If the same set of ϵ positions are used for each scan, and the $\Delta\omega$ step size is kept constant, then for small angles the scan lies on a regular cartesian grid within reciprocal space. However, for large angles the scans are not parallel, and the RSM covers a region of reciprocal space roughly trapezoidal in shape.

Another scan regime commonly used is the crystal truncation rod (CTR) scan (see e.g., Tabuchi *et al.*, 2002). In this mode a position sensitive detector (usually an imaging plate) is used to measure the diffracted intensity. The detector integrates the intensity at each angle while the sample (angular) position is oscillated (i.e., rocked back and forth). This causes the intensity to be integrated in the q_x direction. A CTR scan is parallel to a $\theta - 2\theta$ scan.

In Chapter 3 we describe the samples investigated in this thesis and the experimental techniques utilised. The modelling procedure, based on the theory presented in this chapter, is also explained.

CHAPTER 3

Experimental and Modelling Techniques

This thesis utilises high resolution X-ray diffractometry to investigate the structural characteristics of Group III nitride semiconductor multilayers. In the present chapter we detail the experimental and analysis techniques used to characterise a series of $\text{In}_x\text{Ga}_{1-x}\text{N}/\text{GaN}/\text{AlN}$ layers grown on α -sapphire substrate. These samples are from various stages of the growth process. Other ancillary experiments are presented in later chapters. Specifically Chapter 5 details an experiment to determine the suitability of imaging plates for the rapid collection of RSMs, and Chapter 6 an investigation of chemical ordering in AlGaN layers.

3.1 Group III Nitride Samples

The InGaN/GaN/AlN multilayer samples were grown on α -sapphire using metal-organic chemical vapour deposition (MOCVD) (see Sec. 1.2.4) by the group headed by Professors H. Amano and I. Akasaki in the Department of Materials Science and Engineering, Meijo University, Japan. The growth regime is shown in Fig. 3.1. Initially the sapphire substrate was annealed at 1150°C in a hydrogen atmosphere. After annealing the substrate was cooled, with ammonia (NH_3) flow initiated once the substrate temperature was below 800°C.¹ Low-temperature (LT) deposited AlN buffer layers were grown on the sapphire substrates at 400°C. Three different thicknesses were investigated for the LT-AlN layer: 10 nm, 30 nm, and 70 nm. The first set of samples (labelled 'A##') were removed from the growth chamber at this stage. The substrate temperature was then increased to 1100°C in preparation for GaN growth. This procedure effectively annealed the AlN layers. The second set of samples (labelled 'B##') were removed just prior to GaN growth. The GaN buffer was then grown on top of the annealed LT-AlN layer, with the third set of samples (labelled 'C##') removed after deposition of 30 nm of GaN. The remainder of the GaN layer was deposited (total thickness 2 μm) before reducing the substrate temperature to 800°C for InGaN deposition. Three different InGaN layers were produced; a 20 nm thick $\text{In}_{0.05}\text{Ga}_{0.95}\text{N}$ layer, a 20 nm thick $\text{In}_{0.30}\text{Ga}_{0.70}\text{N}$ layer, and

¹This is not the nitridation process discussed in Chapter 1, in that case the ammonia flow is initiated at 1150°C during annealing.

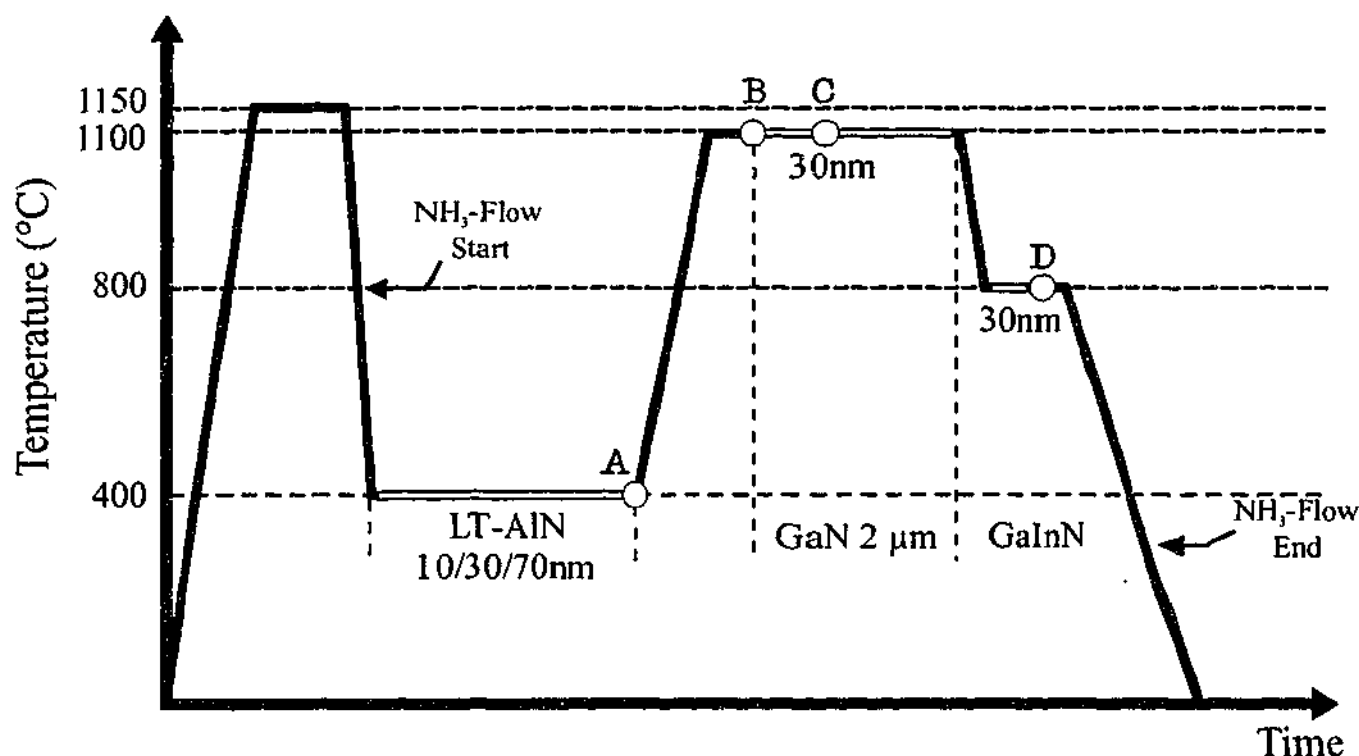


Figure 3.1: Schematic diagram of the Group III nitride sample growth regime. Samples were removed from the chamber at various stages denoted by A, B, C, and D. Table 3.1 provides details of the sample at each of these stages..

a 200 nm thick $\text{In}_{0.42}\text{Ga}_{0.58}\text{N}$ layer. These compositions are only a rough estimate provided with the samples. The InGaN layers were only grown on samples with 30 nm LT-AlN and 2 μm GaN buffer layers. These were our final set of samples (labelled 'D##'). The sample designations and parameters are summarised in Table 3.1. All thicknesses presented in Table 3.1 were determined by the growth times, using growth rates previously determined for the MOCVD system utilised. These values were deemed accurate enough for our purposes.

Each of the samples was approximately square, with an edge of about 1cm, and approximately 2mm thick. All samples were transparent, with a mark scored on the bottom of the substrate so that the top and bottom surfaces could be distinguished.

3.2 Synchrotron Experiments

Triple axis diffractometry was introduced briefly in Sec. 2.10; this technique was used to characterise the samples. A synchrotron facility was required to collect data with good counting statistics because some of the sample layers were very thin (nanometre scale) and highly deformed and hence exhibited low diffracted intensity. All experiments were performed at the Australian National Beamline Facility (ANBF). This facility is located on beamline 20B at the Photon Factory, Tsukuba,

Table 3.1: Sample designations used in the present work.

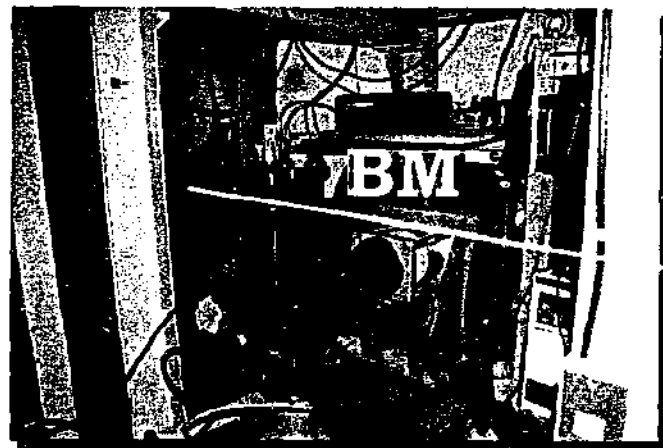
Sample	Layer Parameters				
	AlN		GaN	InGaN	
	Thickness (nm)	Annealed	Thickness (nm)	Composition (%InN)	Thickness (nm)
A10	10	×	—	—	—
A30	30	×	—	—	—
A70	70	×	—	—	—
B10	10	✓	—	—	—
B30	30	✓	—	—	—
B70	70	✓	—	—	—
C10	10	✓	30	—	—
C30	30	✓	30	—	—
C70	70	✓	30	—	—
D05	20	✓	2000	5	20
D30	20	✓	2000	30	20
D42	20	✓	2000	42	200

Japan.

3.2.1 Beamline Specifications and Equipment

Beamline 20B is a bending magnet source producing radiation from 4 keV to 25 keV, corresponding to a wavelength range of $\approx 3 \text{ \AA} - 0.5 \text{ \AA}$. The pertinent beamline equipment is shown in Fig. 3.2. The beamline monochromators are situated 10.85 metres down stream from the storage ring, with the centre of the diffractometer 3.08 metres further. Two monochromators are available, a water cooled channel cut Si(111) monochromator, which can be de-tuned to reject higher harmonics, and a sagittally focusing Si(111) monochromator (Foran *et al.*, 1998; Creagh *et al.*, 1998). The X-ray flight tube terminates in the experimental hutch wall with a Kapton[®] window. Immediately inside the hutch is a goniometer head mounted on vertical and horizontal translation stages. The goniometer head is mounted vertically with its axis of rotation oriented horizontally; it accepts standard 10 mm posts. Following this is a set of aluminium attenuators, a large (0.6 m radius) diffractometer, and finally an optical bench. The optical bench is primarily used for X-ray absorption spectroscopy experiments, but can be used for a variety of purposes. A laser is also mounted on this stage to help locate the X-ray beam path through the apparatus.

BM: Beamline Monochromator
A : Attenuators
V : Vacuum Pump
E : Entrance to the Diffractometer
R : Optical Rail
IC : Ion Chamber
IP : Image Plate Cassette
 θ : θ Rotation Stage
 2θ : 2θ Rotation Arm



B : Optical Bench
AC : Analyser Crystal
D : Scintillation Detector
S : Sample Holder/Goniometer
W : X-ray Flight Tube Kapton Window
HM: Hutch Monochromator Stage

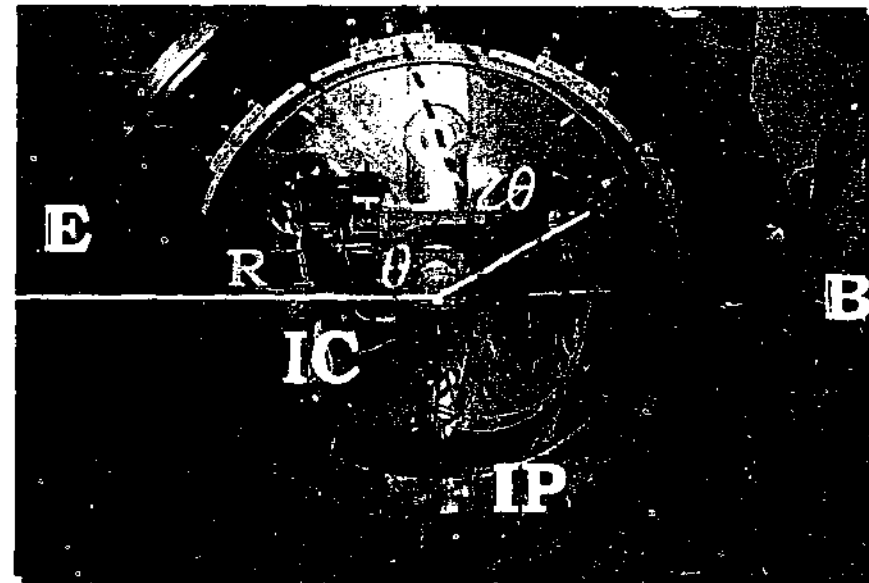
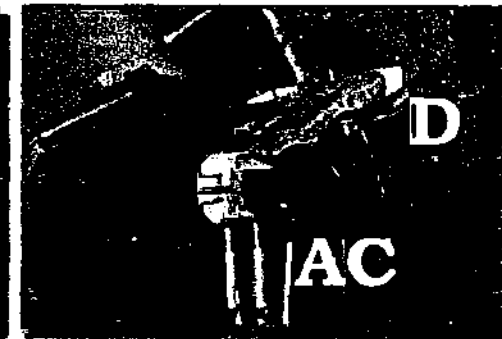
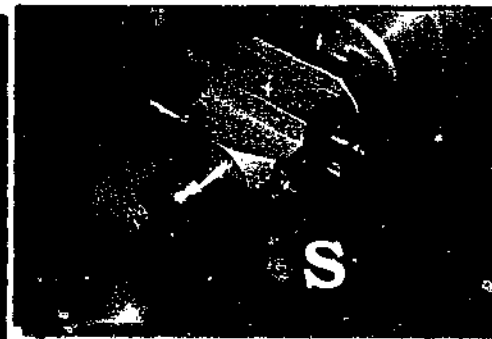
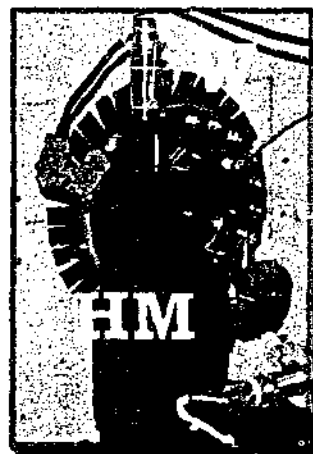


Figure 3.2: Photographs of the various components used for the experiments at the ANBF. The approximate beam path is shown as the white line. The X-rays enter from the left hand side. The photograph shows the vertical plane of the diffractometer chamber.

The diffractometer (Barnea *et al.*, 1992; Garrett *et al.*, 1995), used for all our synchrotron experiments, is also shown in Fig. 3.2. It has a vertical plane of diffraction and is housed in a large stainless steel enclosure, allowing the diffractometer to be sealed and evacuated. The chamber pressure can be reduced to 0.01 torr in about 20 minutes. The whole chamber is mounted on jacks so that its height can be adjusted with a pin dial used to measure height changes. The entrance and exit ports of the chamber, shown in Fig. 3.2, have Kapton[®] windows to transmit the X-ray beam. The entrance has motorised slits to restrict the physical size of the beam. Three aluminium foils, of increasing thickness, are also available for attenuating the X-ray beam. Each attenuator could be used independently, or in combination, to reduce the count rate. The attenuators were moved using vacuum actuators. The diffractometer can be configured for a number of different experiments, such as powder diffraction and high resolution diffractometry. It houses a Huber 410 goniometer and a Huber 420 rotation arm, which are coaxially mounted at the centre of the diffractometer, with the axis of rotation oriented horizontally. The goniometer head incorporates an $x - y$ translation stage with a 10 mm circular mount. The rotation arm is a standard optical rail, allowing a range of equipment to be installed and rotated about the centre of the diffractometer. An optical rail also runs horizontally across the back of the diffractometer to allow other components to be installed, e.g., an ion chamber (as shown in Fig. 3.2). An imaging plate cassette is installed around the circumference of the chamber. The cassette has a radius of 0.573 m and covers $\pm 160^\circ$ in 2θ ; it can be translated perpendicular to the plane of diffraction. The imaging plate system is discussed in more detail in Chapter 5, where we describe the collection of reciprocal space maps using the imaging plate system.

Most of the diffractometer functions and ancillary equipment are controlled from a Linux based computer running *spec*². This includes tuning the beamline monochromator to a particular energy, rotating the Huber goniometer and rotation arm, setting slit widths and positions, inserting and removing attenuators, opening and closing shutters, setting detector voltage parameters, and reading count rates from detectors. The *spec* software has a macro language that includes looping and conditional statements, thereby allowing experimental scans to be automated. The scans were performed in a stepwise manner by driving the appropriate stages to their starting positions, counting for a specified dwell period, and then moving to the next position. This process can be repeated, with the stage positions and photon counts recorded to a log file on the computer.

²*spec* is an instrument control and data acquisition software package by Certified Scientific Software. See e.g., <http://www.certif.com/>

3.2.2 Experimental Arrangement for Collection of Reciprocal Space Scans

The diffractometer at the ANBF has the necessary rotation axes for triple axis diffractometry, and it can be evacuated to reduce air scatter and hence background noise. The high X-ray flux on BL20B is necessary for Group III nitrides, which have large defect densities thereby reducing the diffracted intensity. This situation is exacerbated when thin layers are studied.

Triple axis diffractometry (TAD) utilises three diffraction elements; the monochromator, the sample, and an analyser crystal. However, the specific experimental arrangement can have many forms. In the present work two different experimental arrangements were used for the characterisation of the samples. These are shown schematically in Fig. 3.3.

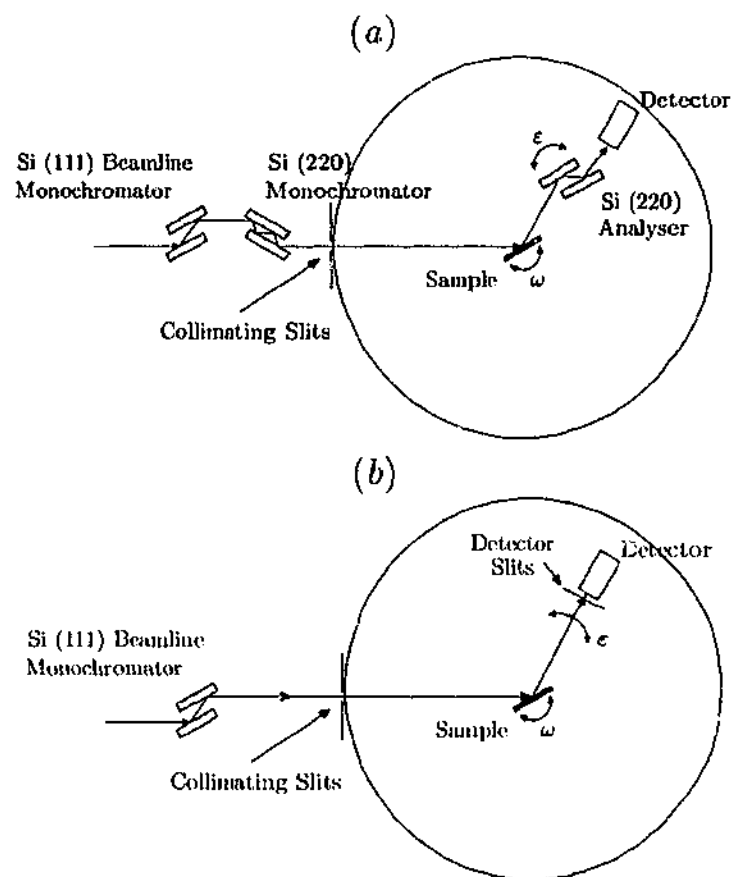


Figure 3.3: Schematic of the triple axis diffractometry experimental arrangements. (a) Configuration used in the first and second set of experiments, and (b) configuration used in the final experiments.

The arrangement shown in Fig. 3.3(a) was adopted in the first two experimental visits to the Photon Factory. On these visits sample types A, B, and C were investigated. In this arrangement a four bounce Si(220) channel cut crystal was mounted on the goniometer at the exit of the flight tube. This served as an

additional monochromator, reducing the incident divergence to approximately 7 arc-seconds and the wavelength dispersion, $\Delta\lambda/\lambda$, to 7×10^{-5} (Mudie *et al.*, 2002). A silicon(220) two bounce channel cut crystal was used as an analyser to reduce the angular range registered by the Radicon[®] high count rate scintillation detector. The analyser crystal was mounted on a high precision rotation stage so that it could be brought to its Bragg position. The detector and analyser system (crystal/rotation stage) was mounted on the 2θ rotation arm of the diffractometer, with the spacing between them as small as possible to minimise background radiation reaching the detector. Lead shielding was also positioned about the detector aperture to reduce the background count rate. A feature of this setup was that the experimental broadening was exceptionally low, and hence very high resolution scans were able to be collected. However, this was at the expense of intensity, because the X-ray beam underwent nine reflections en route to the detector. It was also difficult to set up, because many crystals had to be aligned; it was also necessary to lower the diffractometer because the secondary monochromator reduced the beam height. Since each of the crystals were symmetrically cut the laser could be used in this case to check alignment (because the specular and Bragg reflections were identical).

The first two experiments were only two months apart, and the experimental design was not modified in that time. However, after analysing the experimental data it was decided that the signal to noise ratio needed to be improved for a more accurate analysis. Since the resolution of the system far exceeded that required to measure the broad diffraction peaks produced by our samples the secondary monochromator was not installed, and the analyser crystal was replaced with slits for the final experiment. This significantly improved the counting statistics. Since no analyser crystal was used, this was not a triple axis arrangement; however, the angular acceptance of the slit could be made very small and hence it was a good approximation to a TAD experiment.

The sample holder used in the experiments is shown in Fig. 3.4. The cutout and stub were made from aluminium. The 10 mm diameter stub is standard for matching to goniometer heads. A glass microscope slide was attached to the aluminium cutout with epoxy glue. The slide was the only component of the holder to be illuminated by the beam, keeping spurious X-ray scattering low. The cutout was designed so that when the sample was attached to the slide, its surface was at the centre of rotation. If this was not the case, different regions of the sample would be illuminated as it was rotated. A bead of glue was run along the edge of the sample to attach it to the slide. A glue was chosen that dried quickly, but remained rubbery so that it could be removed easily.

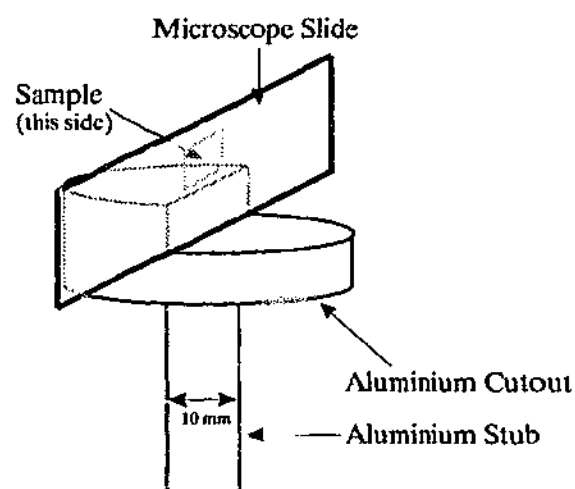


Figure 3.4: Diagram of the sample holder. The sample was attached to the microscope slide using a bead of glue. The cutout was designed so that the sample surface was positioned at the centre of rotation. The stub was cylindrical with a diameter of 10 mm to match the goniometer mounts.

3.2.3 Experimental Method

Apart from the different beamline configurations all experiments were performed in a similar manner. The beamline monochromator was adjusted to give a wavelength corresponding to copper K_{α_1} radiation, (i.e., 1.5406 Å), without higher order harmonics being present. This wavelength was chosen because previous X-ray work on these samples was done using a copper anode laboratory source. Furthermore, the secondary monochromator and analyser crystals were designed to work at this wavelength. The absorption edges of the sample materials were not in the vicinity of this X-ray energy.

Before installing the sample holder the θ goniometer (see Fig. 3.2) was rotated to its zero angle position. A spirit level was used for an initial horizontal alignment. A sample was then glued to the microscope slide so that the X-ray beam would strike near its centre. The first sample examined on each visit to the Photon Factory was used to align the centre of rotation of the sample stage with the centre of the X-ray beam. The sample holder geometry ensure this was equivalent to bringing the sample surface, when horizontal, to the centre of the X-ray beam. In order to do this the sample holder was translated completely out of the beam and the 2θ -arm rotated to be horizontal. The X-ray intensity was then measured using the detector (aluminium attenuators were used to prevent saturation of the detector in the direct beam). The sample holder was then translated into the beam until the count rate dropped to approximately half. It was then rotated approximately $\pm 1^\circ$ to find the maximum intensity. Rotating the holder to the maximum intensity

angle brought the sample surface parallel to the beam, i.e., exactly horizontal. The holder was then translated further into the beam to once again reduce the count rate to half the unobscured beam intensity. At this point the sample surface was at the centre of rotation. The alignment was confirmed by rotating the sample holder 180° and checking the count rate, which should not have changed. For convenience the `spec` command `chg_dial` was used to change the reported angular position of the θ goniometer to 0° . The `chg_dial` command only replaces the motor position stored within `spec` (without moving the motor), regardless of the encoder position. This procedure was required only once during each visit to the Photon Factor, as the goniometer was not translated during the experiments (only rotated) and the sample holder remained in the goniometer at all times.

Next a strong substrate Bragg peak was sought, in this case the sapphire (0006) reflection. The sample and detector were rotated to the appropriate angles. The exact peak position was determined by making ω , θ , and $\theta - 2\theta$ scans to find the maximum count rate. Once the detector and sample were positioned at the peak position, the `chg_dial` command was invoked to set the reported θ goniometer and 2θ -arm positions to those expected for sapphire (0006). In this way the diffractometer was calibrated to a standard within the sample, namely the sapphire. This assumed that the substrate was essentially perfect, i.e., it had not been strained or damaged during the growth of the epitaxial layers. In general this is a good assumption because the substrate is much thicker than the epitaxial Group III nitride layers.

At this point the diffractometer was evacuated for approximately 20 minutes to produce a vacuum pressure of 0.01 Torr. After evacuation the substrate peak position was re-checked, as vibration from the vacuum pump can affect the position of the rotation stage. If there had been movement the rotation axes were re-calibrated by locating the peak and using `chg_dial`.

As many different scan parameters were used only a general overview of the procedures and methodology can be given here (see Chapter 4 for details of the scan parameters). Several reflections were scanned for each sample, usually (0002)³, (0004), and (11 $\bar{2}$ 4). To scan a particular peak, the sample and detector were rotated to the expected peak position, with the precise peak position determined using the same technique as used to find the substrate peak. Once located, several scans were made (see Sec. 2.10 for a description of the different types of scans). High resolution $\theta - 2\theta$ scans were collected for each reflection. The three epitaxial layers (see Table

³The Group III nitrides studied here have a hexagonal (wurtzite) structure, hence there are four Miller indices.

3.1) used have very similar lattice parameters, thus their peak positions are similar. Hence for sample types C (two different epitaxial layers) and D (three different epitaxial layers) the range of the $\theta - 2\theta$ scan, for a single reflection, was chosen to include the peaks from all of the layers. In several cases the range of the $\theta - 2\theta$ scan for the symmetric reflections was chosen to incorporate the sapphire (0006) peak. This peak was then used to check the calibration of the scans during the analysis of the data. The angular position of the sapphire (0006) peak is intermediate to the (0002) and (0004) peaks from the epitaxial layers. ω scans were also collected for most of the observed peaks, including any satellites. The ω scans were collected by rotating the sample and detector to the maximum peak position, and then rotating only the sample while recording the intensity. θ scans were only used to calibrate the detector position, and not for data collection.

Reciprocal space maps (RSMs) were also collected for each reflection by performing a number of $\omega - 2\theta$ scans, with the $\Delta\omega$ offset changed for each scan. A spec macro was used to automate the collection of the RSMs. The RSMs collected were of a lower resolution than the $\theta - 2\theta$ or ω scans, because even at low resolution each of the RSMs required 3-4 hours to collect.

Measurement of the asymmetric reflections proved problematic, especially for the RSMs. This is because strain parallel and perpendicular to the sample surface modifies the peak position, and hence can be outside the range chosen for the RSM. (For symmetric reflections the strain parallel to the sample surface does not affect the peak position). Hence, the optimum range and position of an experimental scan was hard to determine accurately, and some features in reciprocal space were missed.

3.3 Simulation of Diffraction Profiles

This section details the computer program and analysis techniques used to generate the simulated scans. In Chapter 4 we will analyse the experimental results by comparison with the simulated scans. The simulations were based on the kinematical statistical diffraction theory introduced in 2.8.3 using the mosaic block model introduced in 2.9. There were two types of parameters required for generating the simulated scans: material specific values that are model independent (susceptibility, Bragg angle etc), and model parameters (such as block size and orientation). The goal is to find the optimum model parameters so that the simulated scans match the experimental data. Specific approaches and strategies for determining the optimum model parameters are explained in Sec. 3.3.2.

3.3.1 Modelling Software

All simulations were performed using software written by the author using IDL (Interactive Data Language⁴) and Microsoft® Excel. IDL was chosen as the main programming language because it has a fully featured programming environment with debugging and program flow control; it also provides access to many routines in Numerical Recipes.⁵ The user interface was an Excel workbook, which allowed the output from a set of simulations to be saved in one file, compete with the simulation parameters. This file also included plots for comparison of the experimental data with the simulation results. The following sections describe the Excel interface and IDL code.

3.3.1.1 Excel Interface Code

Figure 3.5 shows the input Excel worksheet for the simulation software. The scan parameters are inserted at the top left hand corner. The parameters include the X-ray wavelength, beam polarisation (C), the number of layers used in the simulation, the scan ranges and the number of data points in the $\Delta\omega$ and ω directions, the epsilon change for minimisation, and a switch for indicating if the weighting between layers was used. To the right of the scan parameters is a cell that indicates the reflection being simulated. In the case shown two reflections are available, (0002) and (0004). If (0002) is entered into the cell the simulation parameters from the 'Simulation parameters 0002' worksheet (as displayed) are used, however, if (0004) is entered the parameters from the 'Simulation Parameters 0004' worksheet are used.

The material parameters used for the simulation appear in the table at the bottom of the interface. The case shown in Fig. 3.5 utilised a large number of layers, however, in many cases there were only 2-3 layers (2-3 rows of data). The left section of this table contains the parameters which were not modified in fitting the data. This includes the 000, hkl , and $\bar{h}\bar{k}\bar{l}$ Fourier components of the susceptibilities, the Bragg angle, θ_B , and the asymmetry angle, φ . The right hand section, which extends far beyond the edge of Fig. 3.5, contains the model fitting parameters that are varied to fit the scan to the experiment. This includes the layer thickness, layer tilt, lateral and perpendicular mosaic block dimensions, mosaic block misorientation width, strain perpendicular and parallel to the sample surface, and a weighting value for each layer. For each of these parameters there are three input values - an upper and lower bound and an initial value. The bounds were required by the minimisation

⁴IDL is a product of Research Systems Inc. See <http://www.rsinc.com>

⁵The Numerical Recipes are a set of standard mathematical programming routines appearing in Press (1992). See also <http://www.nr.com/>

procedure explained in Sec. 3.3.1.2.

In order to populate the cells, values were entered directly (or as a formula). A formula was used if a particular trend was required from one layer to the next, or calculated from some other piece of data. The rest of the worksheet was used for making calculations, plotting charts, inserting notes, e.g., see cells E6 to H7 (partially obscured by a label) in Fig. 3.5.

Besides the 'Simulation Parameter' sheets, three other worksheets were used by the software for each reflection; namely the 'Experimental Data', 'Simulated Data', 'Minimised Parameter' sheets. The experimental data for the appropriate scan was entered on the 'Experimental Data' sheet. When the simulation was complete the final minimised parameters (or simply the initial values if the minimisation routine was not used) appear in the 'Minimised Parameter' sheet, while the simulated scan appears in the 'Simulated Data' sheet.

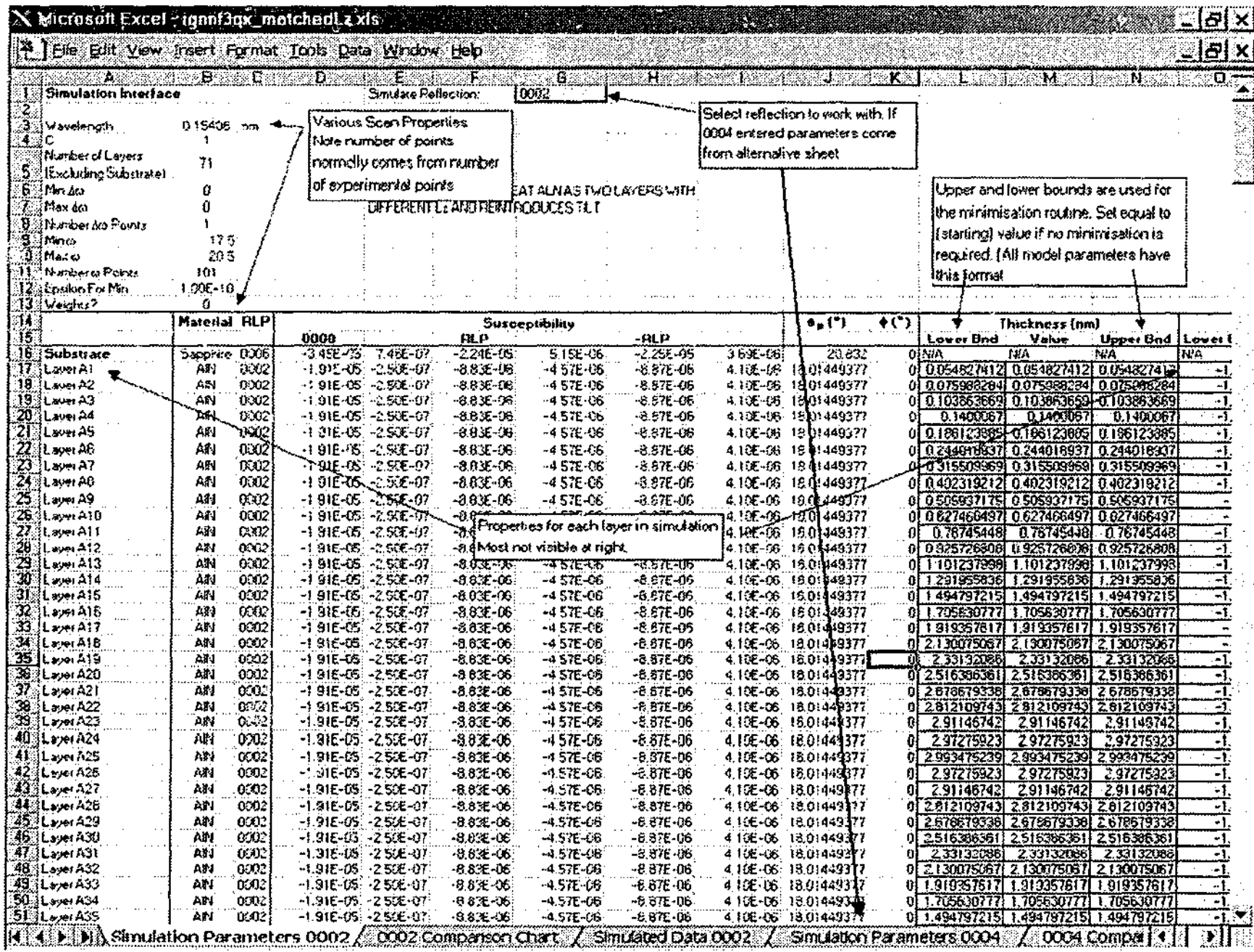
The automation of Excel and interfacing to IDL were achieved using Visual Basic for Applications (VBA). VBA is a programming language built into all Microsoft® Office Applications. A VBA program was written to allow Excel to communicate with IDL via ActiveX.⁶ The ActiveX control provided by IDL is called IDLDrawWidget. The IDLDrawWidget allows data to be transferred between the host code and IDL, as well as the execution of IDL functions and display of IDL graphical output. The VBA program copied all of the simulation parameters from the Excel spreadsheets, as well as the experimental data, and passed it to IDL via ActiveX and IDLDrawWidget. The data was stored within a 'structure'.⁷ The VBA program, ActiveX, and IDLDrawWidget were also used to return the simulated data back into Excel, along with the minimised simulation parameters.

The VBA program was built into a form as shown in Fig. 3.6. This form has two main options and the IDLDrawWidget container. The two options were for starting the simulation or exporting parameters to an external file. The external file can be read into IDL using another procedure, so that the simulation can be executed without Excel. The IDLDrawWidget displays graphics generated by any IDL routine. This allowed us to indicate the progress of the simulation by plotting the squared difference between the simulated scan and the experimental scan (this is described in more detail in Sec. 3.3.1.2).

⁶ ActiveX is software protocol for allowing software components written in different programming languages to interact. It uses an object-oriented approach. The ActiveX object (or control) allows information to be passed between the host code and the external program.

⁷ A 'structure' is a group of variables stored under one name. A structure can contain variables of different data types (e.g., integers, floating point, strings) simultaneously.

Figure 3.5: The Excel simulation interface. The parameters contained in cells B3 through B13 are general parameters, and includes the angular range and number of points to be simulated. The parameters from row 17 and below are the layer specific parameters (which extend far to the right of the displayed area. Note that the model parameters have an initial value and upper and lower bounds. If cell G1 is changed to read '0004' the parameters from the simulation parameters 0004 worksheet are used instead.



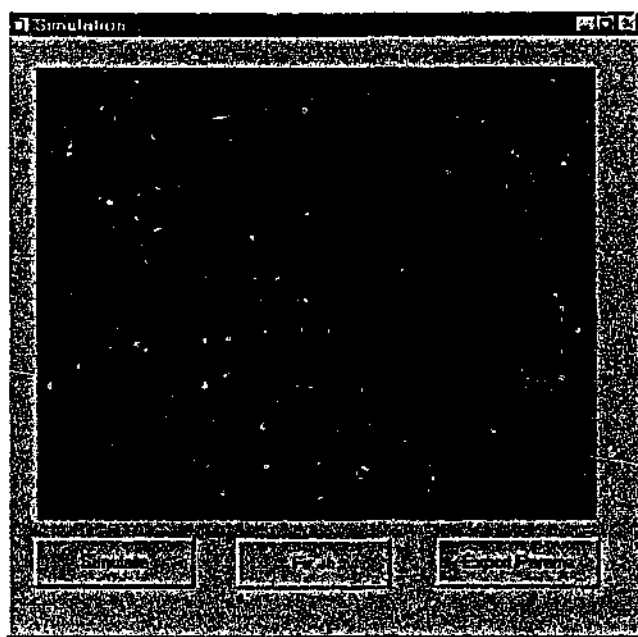


Figure 3.6: Visual Basic for Applications simulation interface; the black square is the IDLDrawWidget container, which displays graphical output from the IDL routine called via the IDLDrawWidget. In this case the container shows the progression of the sum of the squared differences between the simulated and experimental profiles (the simulation has looped 200 times).

3.3.1.2 Simulation Code

Here we describe the IDL code used to calculate the diffracted intensity, according to the statistical kinematical statistical theory (using a mosaic block model), for the supplied scan and model parameters. Figure 3.7 shows a simplified flowchart of the program. The input parameters for the simulation program were stored in an IDL 'structure' by the interface program. All non-model parameters, such as the wavelength and Bragg angle, are available to all parts of the code. The model parameters, however, are mediated by a minimisation routine. The minimisation routine was used to optimise the model parameters automatically (i.e., determine the closest fit possible between the simulated and experimental data) for a single scan, by minimising the sum of the squared differences between the experimental and simulated scans. The minimisation routine made use of the IDL `Constrained_Min` procedure. This procedure solves optimisation problems of the form⁸: Minimise or maximise $g_p(X)$, subject to

$$\begin{aligned}
 glb_i \leq g_i(X) \leq gub_i \quad \text{for } i = 0, \dots, n\text{funs}-1, i \neq p \\
 xlb_j \leq x_j \leq xub_j \quad \text{for } j = 0, \dots, n\text{funs}-1,
 \end{aligned}
 \tag{3.1}$$

⁸From page 217 of the IDL Reference Guide for IDL Version 5.4 .

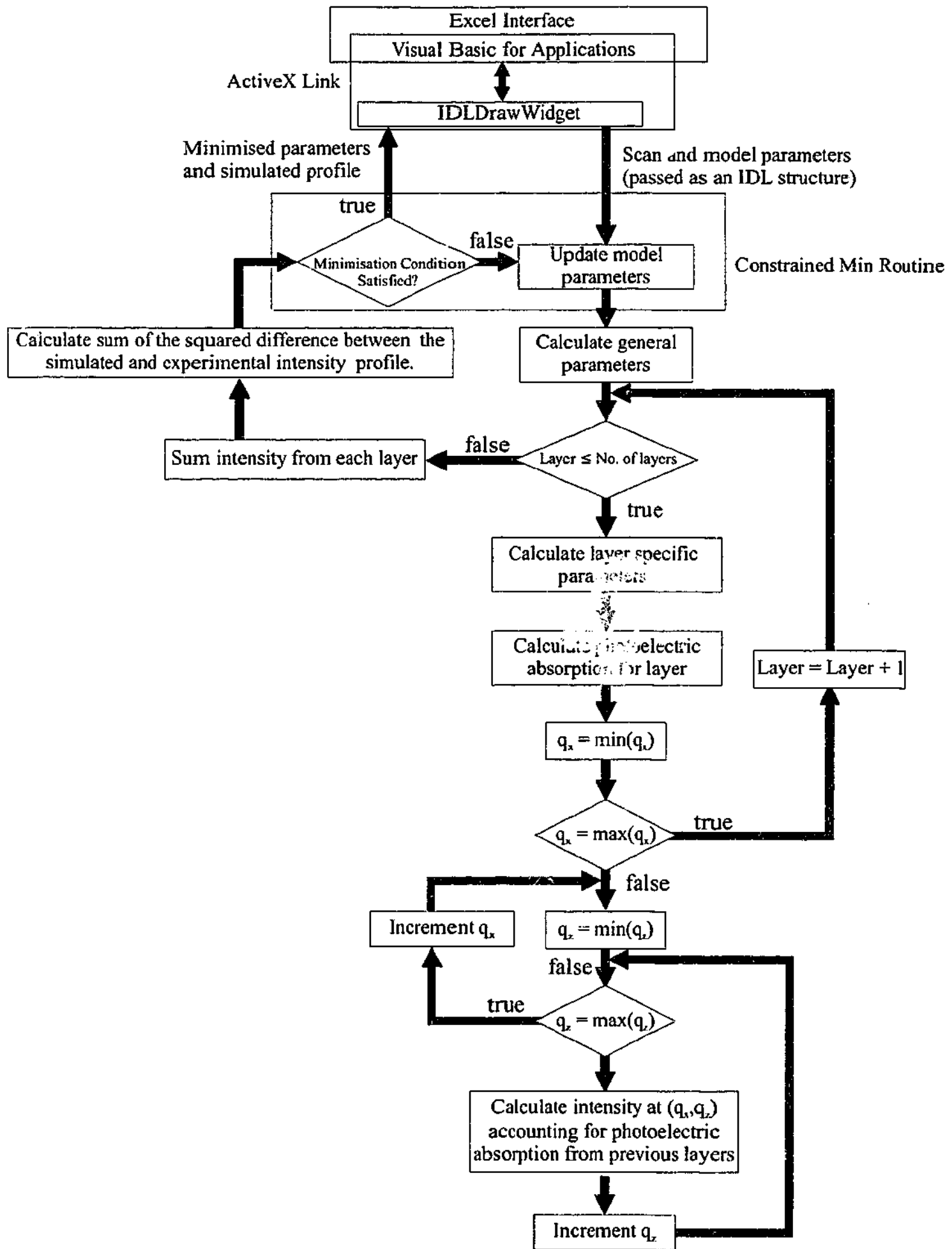


Figure 3.7: Flowchart for the simulation program. The diamonds indicate a decision.

where X is a vector of $nvars$ variables, $x_0, \dots, x_{nvars} - 1$, gub_i and glb_i are the upper and lower bounds for the function g_i , xub_j and xlj_j are the upper and the lower bounds for parameter x_j , and g_p is the function out of g_i that is being minimised or maximised. Additionally the vector of $nfuncs$ functions $g_0, \dots, g_{nfuncs} - 1$, which all depend on X , is labelled G . In other words this procedure finds the minimum (or maximum) of a function by systematically adjusting certain variables upon which the function depends. The variables are bounded, as are any number of ancillary functions that also depend on these variables. The routine uses the generalised reduced gradient method to approach the minimum (or maximum) (Lasdon *et al.*, 1978). This method uses the first partial derivatives of the each function g_i with respect to each variable x_j . These are calculated by the routine using a finite difference approximation.

The `Constrained_Min` procedure takes as input an $nvars$ -element array containing the initial values for each of the variables, x_j , a $2 \times nvars$ array containing the lower, xlj_j , and upper, xub_j , bounds of the variables, and a $2 \times nfuncs$ array with the lower, glb_i , and upper, gub_i , bounds of the ancillary functions, G . The functions, G (which includes the function to be minimised), are all calculated by a user supplied/written IDL routine. This routine accepts an $nvars$ -element array as input (i.e., the values of x_j for the current minimisation step), and returns an $nfuncs$ -element array with the values of each of the functions for the x_j input. The name of this function is supplied to the `Constrain_Min` procedure as well as the subscript, $i = p$, of the function from within G , that is to be minimised.

For the simulations described here there are no ancillary functions, only the target function, and seven variables (layer thickness, layer tilt, mosaic block size parallel and perpendicular to the sample surface, mosaic block misorientation, and strain parallel and perpendicular to the sample surface). Hence, the model parameters (the initial value and bounds) are passed directly from the input structure to the `Constrained_Min` procedure. The function being minimised is the sum of the squared differences between the simulation and experimental scans. The variation of this value with changes in the model parameters is tracked by the minimisation routine. The minimisation is determined to converge when the fractional change in the function is less than a specified value, ϵ , for a particular number of iterations (usually 3). Hence, to find the best fit the simulation is automatically run a number of times, by `Constrained_Min`, for a variety of different parameter settings. The first set of variables is the initial values recorded in the Excel interface. If no minimisation is required, then the upper and lower bounds are both set equal to the initial value, forcing the simulation to run only once.

The first part of the IDL function called by the minimisation procedure (i.e., `Constrained_Min`) for generating the simulated profile initialises the variables and arrays, and calculates the reciprocal space coordinates for the scan. The reciprocal space coordinates are calculated from the angular range of the scan, the number of data points required, and the Bragg angle of the reflection being investigated. The Bragg angle will depend on the material being studied, hence the reciprocal space coordinates are calculated with respect to the expected peak position for a reference layer (generally chosen to be the thickest epitaxial layer). I.e., the expected Bragg peak position for the reference layer is at $(q_z, q_x) = (0,0)$.

The diffracted intensity is calculated for each layer in turn and then summed to give the full diffraction profile. As shown in Fig. 3.7 the code used to calculate the simulated intensity is executed once for each layer using a loop statement. The first task within the loop is to calculate the layer dependent parameters from the input parameters. The calculations made inside the loop are independent for each of the layers except for the reciprocal lattice offset and beam attenuation. The reciprocal lattice offset is the \mathbf{q} -vector translation between the reciprocal lattice point of the current layer and that of the reference layer. If only one material type is used then there will be no offset for any layer. However, if more than one material is used these values are used to offset the results from each layer so that they are in the correct relative positions in reciprocal space. The beam attenuation accounts for photoelectric absorption by reducing the diffracted intensity by a factor related to the imaginary part of the zeroth order Fourier component of the susceptibility and the thicknesses of the layers above the current layer. The code is written to calculate from the top layer of the sample to the bottom, accumulating the beam attenuation. Dynamical effects, such as extinction, were not included.

The correlation area (Sec. 2.9) and hence the diffuse intensity, are functions of the \mathbf{q} -vector. To calculate the simulated profile two, nested, loops were used; the outside loop over q_x and the inside loop over q_z . When simulating an $\omega - 2\theta$ scan there is only a loop over q_z the coordinate and for an ω scan only a loop over the q_x coordinate (small angles were assumed, meaning the $\Delta\omega$ -axis is parallel to the \mathbf{q}_x -axis as discussed in Sec. 2.10). For RSMs the code loops more than once for both q_x and q_z . Inside the loops the \mathbf{q} -vector is determined from the loop numbers (subscripting the arrays containing the reciprocal space coordinates of the scan) and the offset between the expected Bragg peak position for the current layer compared to the reference layer. The correlation area can be found using Eq. (2.122), repeated

here:

$$\hat{\tau}_1^c = [1/(1 - f^2)] \int_{-5\Delta_m}^{+5\Delta_m} d\alpha \frac{e^{-\pi(\alpha/\Delta_m)^2}}{\Delta_m} \frac{2}{l_x l_x \beta^2 \psi^2} (1 + i\psi l_z - e^{i\psi l_z}) (1 - \cos(i\beta l_x)), \quad (3.2)$$

where

$$\psi = q_z + h\alpha \sin \varphi \quad (3.3)$$

$$\beta = q_x - h\alpha \cos \varphi, \quad (3.4)$$

where l_x and l_z are the mosaic block sizes parallel and perpendicular to the sample surface, f is the static Debye-Waller factor, Δ_m is the FWHM of the Gaussian distribution of block orientation, and φ is the asymmetry angle. In order to determine the correlation area from Eq. (3.2) a numerical integration over the mosaic block orientation, α , is required. This is achieved using the IDL `qsimp` routine. This routine, from the Numerical Recipes (Press, 1992), performs a numerical integration of a user defined IDL function using Simpson's rule. The user function must accept a single value as input (the variable of integration) and return a single value (the ordinate result for the input variable). The `qsimp` routine begins by calculating the integral using three, evenly spaced, points from the function. Using this result, and the values of two more points (spaced between those already used) the integral is recalculated. The routine continues by refining the integration by adding additional points in between those already calculated. Each iteration calculates $n - 1$ more points, spaced between those already computed, where n is the total number points calculated across the function at the previous iteration. When the fractional change in the integral from one iteration to the next is smaller than a specified value (usually 1×10^{-6}), the `qsimp` routine terminates, returning the final calculated integral as the result. The integration is performed in this way to improve efficiency.

An IDL function calculating the integrand of Eq. (3.2) was written, which takes the block orientation, α , as input. All other variables were passed to the function using 'Common Blocks'.⁹ The range of the integration is set when the `qsimp` routine is called. In this case it is plus or minus five times the width of the Gaussian profile describing the misorientation (i.e., $\pm 5\Delta_m$), because $W(|\alpha| > 5\Delta_m)$ is essentially zero. If ψ or β is zero then the denominator in Eq. (3.2) becomes zero hence conditional statements are required to check for this possibility to avoid an overflow

⁹Common Blocks, once defined, allow variables to be accessed by any procedure or function that references the block. The specific variables that need to be accessed must be specified in the Common Block definition.

error. After the correlation area was determined the diffuse intensity was calculated, again using the `qsimp` routine, via the integral of Eq. (2.108).

IDL is designed to work efficiently with arrays. Therefore the `qsimp` routine was modified by the author to use arrays to reduce the number of loops within the code. In order to do this the user supplied function (for calculating the integrand) is required to accept and return arrays.

Having determined the intensity for all scan coordinates, the q_x and q_z loops terminate and the calculations for the next layer are commenced. The total diffracted intensity is the sum of the intensity from each of the layers. In order to determine how close the simulated scan matches the experimental data, the sum of the squared differences is computed. For this to be done without interpolation, the simulated profile is calculated for the same \mathbf{q} -vectors as the experimental scan. The code allowed the sum of the squared differences to be determined using the raw experimental and simulated intensities, or the logarithm of the intensities. The former places more emphasis on fitting the peak, while the latter increases the importance of the wings (or thickness oscillations, see Sec. 4.4.1), which can be several orders of magnitude smaller than the peak. If the fractional change of the sum of the squares is less than the 'epsilon change for minimisation' specified in the Excel interface worksheet for three consecutive iterations, the minimisation routine terminates, and returns the parameters and simulated profile to the Excel spreadsheet.

Two important options in our code are the ability to weight the various contributions to the intensity from different layers, and to simulate the effects of instrumental broadening. In the former case the intensity from each layer is multiplied by a weighting factor before the total is computed. This allows distributions of strain to be simulated (see Sec. 3.3.2). In the latter case the code allows the intensity to be calculated for a large slit size in front of the detector with no analyser crystal. A detector with a wide slit will integrate over a line in reciprocal space that makes an angle θ_B to the q_z -axis (it is in fact the same line as the θ scan described in Sec. 2.10). The program integrates the intensity along this line. Again the `qsimp` routine was used to carry out the numerical integration; however now there is a double integral, over the \mathbf{q} -vector and α . The integral over α , and the calculation of the diffracted intensity were described above.

3.3.2 Techniques for Optimisation of Model Parameters

This section provides an overview of the techniques and extensions to the model that were used to fit the data. The experimental and simulation results are described in the next chapter.

It was important to understand how the parameters of the defect model impact on the diffracted intensity, so that the fitting procedure can be approached intelligently. For the model presented here there are three parameters for the mosaic blocks: the mosaic block size parallel and perpendicular to the surface, and the mosaic block misorientation. Reducing the mosaic block size perpendicular to the sample surface caused the peak to be broadened in the q_z direction; likewise reducing the block size parallel to the surface caused the peak to be broadened in the q_x direction. Finally, increasing the misorientation increased the width of the peak in the direction perpendicular to the diffraction vector. For symmetric reflections the misorientation and parallel block size caused broadening in the same direction. However, varying the misorientation had a greater effect at the centre of the peak, while the block size has a greater effect at the wings of the peak.

There were four other parameters available for fitting the data; namely, the layer thickness, the homogenous strain parallel and perpendicular to the surface, and rotation (tilt) of the whole layer. However, these parameters are non-statistical. The thickness of the layer determines the overall intensity diffracted from the layer and impacts on peak shape; in a perfect layer this parameter would affect the period of thickness fringes, however, in this treatment it is the perpendicular block size that does this. Strain moves the peak position by changing the layer d -spacing homogeneously, and the rotation (tilt) causes the peak to move in the q_x direction.

Although the three mosaic block parameters allowed a large degree of control over the peak shape and size, this model was not capable of reproducing the peak shape for every case. In particular the mosaic block model does not address heterogeneous strain (which causes broadening in the q_z direction), even though it is evident in high defect concentration materials. An attempt to include it in the analysis was made by varying the strain from the top to the bottom of a layer, giving a strain gradient. This is achieved by dividing each of the layers (which describe the physical epilayers of the structure) into several partitions and varying the strain for each of the layers. We introduce the term partition instead of layer or sub-layer to prevent confusion, however these partitions can be considered as thin layers. The total thickness of these partitions should sum to the total thickness of the epitaxial layer they are describing. This model is shown in Fig. 3.8, where the strain in this example changes from maximum positive at the top of the layer to maximum negative at the bottom of the layer. However, in order for a correct profile to be produced the mosaic block height generally needed to be larger than the thickness of each partition (it was usually chosen to be the full thickness of the epitaxial layer). Physically this means that the strain within the block varies from the top to the

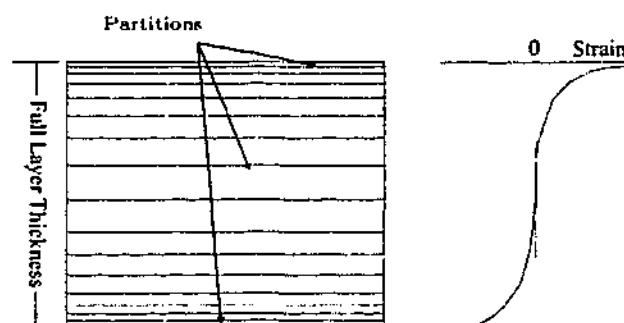


Figure 3.8: Schematic of the strain gradient model. The strain gradient model considers the epitaxial layer to be formed from multiple layers (partitions), each with a different strain. Thus the strain varies from the top to the bottom of the layer, as shown in the schematic plot. This implies the strain varies within a mosaic block.

bottom. In terms of the simulation, the parameters for each partition are included by increasing the number of layers simulated. An alternative interpretation is to consider the layer to be formed from a mixture of mosaic blocks with a range of homogeneous strain states. The strain distribution is determined by weighting the influence from each block type, which in effect specifies the volume fraction of each strain state. The parameters for each set of blocks are entered as separate layers as before (and again termed partitions), however each of these layers is set to the thickness of the epitaxial layer. The volume fraction of each type of block was set by the weighting parameter, and the intensities summed, as described in Sec. 3.3.1.2. Note that for both models, other block parameters (except the perpendicular block size) can be varied along with the strain. These two models (i.e., strain gradient and weighted volumes) result in the same intensity distribution. These models are discussed in more detail in Chapter 4.

It was not a trivial matter to find the best model parameters. For simple one-dimensional scans with a small number of parameters (i.e., when a strain distribution was not required, or when only one peak was evident) the minimisation routine could be used to determine the fitting parameters quickly and accurately. However, it was not appropriate for more complex analyses (including RSMs), since the time required to fit the data was excessively long and the results were not always physically meaningful. It is also necessary to ensure that the one set of parameters fitted all reflections for a single sample. This requirement also reduced the utility of the minimisation routine, because an optimised set of parameters for one reflection may not be appropriate for the other reflections. Further development of the minimisation routine to allow it to handle multiple reflections, and other more complex analyses, would be advantageous, as it would allow the analysis to be completed

much quicker. In our case most of the parameter fitting was done by varying the parameters by hand, and judging the effect by comparing the experimental and simulated data graphically.

To ensure efficiency when fitting the data it was important to follow a standard procedure, otherwise it was very easy to spend much time fitting a particular feature, only to find the parameters were not appropriate for a different scan type or reflection. In all cases the fitting was initially done using the high resolution one-dimensional scans (not the RSMs), because it is difficult to compare two-dimensional scans graphically, and the lower resolution RSMs can miss some features, such as very narrow peaks. However, after the fitting was finished (and during the fitting process to confirm that the results were converging) the simulation and RSM were compared. One-dimensional scans were extracted from the RSM, and fitted, to elucidate certain diffraction features not covered by the dedicated $\theta - 2\theta$ and ω scans.

Initially the simplest model was assumed correct (one layer per peak) to keep the number of fitting parameters to a minimum. The strain required for each layer to give correct peak positions was determined. If thickness oscillations were evident (see Sec. 4.4.1) they were used to find the perpendicular block size; however, if no oscillations were observed the peak width in q_z direction was used because the perpendicular block size has a strong impact on the peak width in the q_z direction. The peak width and shape in the q_x direction (or more correctly the ω scan direction), were used to find the parallel block size, the misorientation width, and the tilt of the whole layer. Although each parameter affects the shape of the scan in a different way, they are not completely independent, particularly when using a wide slit. For example, many of the parameters also affect the overall intensity of the peak. If there is more than one peak then this is an important consideration. Hence, each of the parameters had to be varied many times before the parameters that produced the simulated profile closest to the experimental data were determined. If more than one reflection was recorded for a particular sample, all reflections were checked at each stage of the fitting procedure. In order to achieve the best overall fit for all reflections (as determined by comparing the experimental and simulated scans graphically, using linear and logarithmic intensity scales), the quality of any individual fit may not be as high as could be achieved in isolation (i.e., some compromises were required to ensure reasonable matching of the simulations to all experimental data).

If a diffraction peak could not be fitted by assuming a single layer, then the inhomogeneous strain model was implemented, adding more and more partitions until a suitable fit could be achieved. In this situation the strain and weighting

parameters were chosen so that a graph of strain versus weighting was similar to the experimental intensity profile. This served as a starting point for the fitting procedure. It was also found that some peaks had a slight rotation in the q_x - q_z plane. This could be simulated using the strain-weight model by introducing a tilt distribution, where each partition had a different tilt. To help keep track of the fitting process, the results from each simulation were recorded within the Excel spreadsheet, hence the variation of the simulation with respect to different parameters could be charted. However, this approach became somewhat unwieldy once many simulations had been completed thus slowing progress.

Further discussion of the modelling process is made in the next chapter where the results and analysis for the structural characterisation of the $\text{In}_x\text{Ga}_{1-x}\text{N}/\text{GaN}/\text{AlN}$ semiconductor samples is presented.

CHAPTER 4

Results and Analysis of $\text{In}_x\text{Ga}_{1-x}\text{N}/\text{GaN}/\text{AlN}$
Samples

4.1 Introduction

Tabuchi *et al.* (2002) used crystal truncation rod (CTR) measurements to show that without substrate nitridation, better quality GaN layers are grown on a 30 nm buffer layer than on a 70 nm buffer layer. This is consistent with Ito *et al.* (1999), where a buffer thickness of 20 nm was determined to be optimal for GaN growth on the AlN buffer layer. Furthermore Zhang *et al.* (2004) investigated the effect of AlN buffer thickness on the structural and luminescence properties of the GaN epitaxial layer. It was shown that 20 nm - 30 nm thick buffer layers produced the best properties. In order to investigate the effect of buffer thickness we completed TAD experiments for samples with 10 nm, 30 nm, and 70 nm thick LT-AlN buffer layers. These samples were grown by the same research group as those studied by Tabuchi *et al.* (2002), and were similar in composition. This investigation encompasses sample types A, B, and C.

We investigated three $\text{In}_x\text{Ga}_{1-x}\text{N}$ layers of different compositions, x , grown on a 2 μm GaN layer with a 30 nm LT-AlN buffer. The $\text{In}_x\text{Ga}_{1-x}\text{N}$ layer is the active layer for optoelectronics, with the composition (among other factors) determining the bandgap and hence the emission wavelength. The composition $\text{In}_x\text{Ga}_{1-x}\text{N}$ ($0 \leq x \leq 1$) almost covers the entire visible spectrum (plus a segment of the ultraviolet region). However, the InN/GaN alloy has a large miscibility gap¹ preventing growth of all compositions (Ho and Stringfellow, 1996). Two of the $\text{In}_x\text{Ga}_{1-x}\text{N}$ alloys used here have an InN composition below the value at which segregation becomes dominant, and one above. These samples were labelled type D in Chapter 3.

Throughout this discussion four mosaic block parameters are referred to extensively; the perpendicular, l_z , and lateral, l_x , block sizes, the misorientation, Δ_m , and the tilt. In this thesis the misorientation value is the width of the Gaussian profile describing the orientation distribution of the mosaic blocks (it was defined in Sec.

¹A miscibility gap refers to the range of compositions for which an alloy is unstable, decomposing into two or more alloys with stable compositions.

2.9). The tilt is the rotation of the entire layer (or sub-layer).

4.2 Sample Series A and B: LT-AlN Buffer Layers

This section presents the results for samples of type A and B. These samples consist of only a low temperature deposited AlN buffer layer on an α -sapphire substrate. After AlN growth the type A samples were cooled (from the growth temperature of 400°C) and removed from the growth chamber; however, the type B samples were heated to 1100°C before cooling. Table 4.1 summarises the experimental parameters used in conducting the TAD experiments for both the type A and type B samples. The results presented in this section were published in Mudie *et al.* (2002, 2003).

The TAD arrangement used for these samples incorporated two monochromators (the beamline monochromator and a monochromator mounted inside the experimental hutch) and a double bounce analyser. This ensured very high angular resolution. However, the monochromator and analyser crystal significantly reduced the X-ray intensity, leading to a poor signal to noise ratio. Useful results could only be collected for the AlN(0002) reflection for samples A30, B30, A70 and B70, and even for this reflection the scans were noisy. Higher order reflections were too weak to be detected, as were all reflections from the 10 nm layer of samples A10 and B10. Only three scans were collected for each sample: a $\theta - 2\theta$ scan, an ω scan, and an RSM. The scan and angle labels used throughout this chapter were described in Sec. 2.10.

The experimental scan parameters are summarised in Table 4.2 for samples A30 and A70. There are several parameters for each scan: the type of scan, the step size or resolution of the scan, and the background count. The experimental profiles are shown in Figs. 4.1 and 4.2 for A30 and A70, respectively. The RSMs are not

Table 4.1: Experimental parameters for samples of type A and B.

Parameter	Value
Wavelength	1.5406 nm
Entrance slit vertical size	0.5 mm
Entrance slit horizontal size	2.0 mm
Vertical divergence at sample	≈ 7 arcseconds ^a
X-ray count rate at sample	Unknown ^b
Count time per point	7 seconds

^aThe divergence was not measured. The value quoted here was calculated (see Mudie *et al.*, 2003).

^bIntensity was too large to measure with a photon counting detector.

Table 4.2: Experimental scan parameters for samples of type A.

Sample	Scan Type	Parameter	Value	
AlN 30 nm	$\theta - 2\theta$	Step size (in θ)	50 arcseconds for $16.0^\circ - 17.2^\circ$ 20 arcseconds for $17.2^\circ - 21.0^\circ$	
		Background count	76 counts/second ^a	
		ω	2θ position	$2\theta = 36.5^\circ$
	ω	Step size (in θ)	120 arcseconds	
		Background count	76 counts/second ^b	
		RSM	ϵ step size	1°
	AlN 70 nm	$\theta - 2\theta$	$\Delta\omega$ step size	120 arcseconds
			Background count	76 counts/sec ^b
			ω	2θ position
ω		Step size (in θ)	100 arcseconds	
		Background count	66 counts/second ^b	
		RSM	ϵ step size	0.7°
ω		$\Delta\omega$ step size	151 arcseconds	
		Background count	66 counts/sec ^b	

^aAs approximated from the $\theta - 2\theta$ scan.

^bAssumed value since the experimental conditions were the same as for the $\theta - 2\theta$ scan.

presented for this sample as they are of a very poor quality and do not assist with the analysis.

The shape of the $\theta - 2\theta$ scans, shown in Figs. 4.1(a) and 4.2(a), arises from a broad peak superposed on a narrower peak (although both peaks extend over several degrees, indicating poor sample quality). The broad peak extends past the low angle extreme of the scan, with the narrower peak centred at approximately 18.3° for both samples. This scan shape is indicative of the sample having two distinct vertical correlation lengths (or a strain distribution). If the layer is assumed to be laterally homogeneous then the sample can be considered to have two sub-layers, with the narrow peak associated with a smaller defect density, or narrower heterogeneous strain distribution, compared to the broader peak. Alternatively, the material could have one layer, with a more complicated strain distribution. However, for our purposes we describe the system as having two sub-layers with one sub-layer

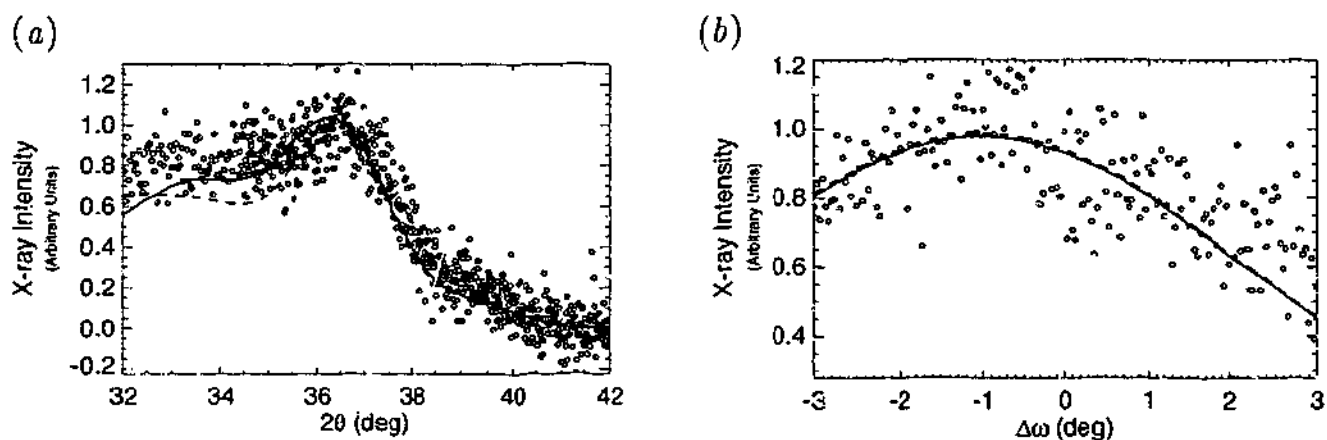


Figure 4.1: One-dimensional scans of sample A30. (a) $\theta - 2\theta$ scan, and (b) ω scan at $2\theta = 36.5^\circ$. The circles (\circ) are the experimental data points. The solid (—) and dashed (---) lines are the simulated profiles using the homogeneous model and strain distribution model, respectively. The experimental parameters are given in Table 4.2 and the simulation parameters are shown in Tables 4.3 and 4.4. The strain profile and weighting are shown in Fig. 4.3.

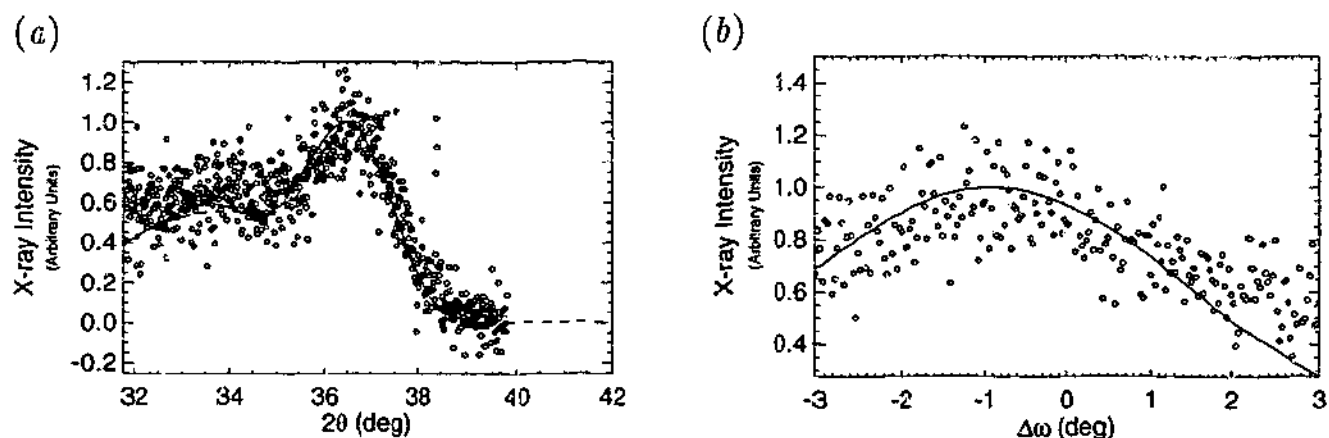


Figure 4.2: One-dimensional scans of sample A70. (a) $\theta - 2\theta$ scan, and (b) ω scan at $2\theta = 36.74^\circ$. The circles (\circ) are the experimental data points. The solid (—) and dashed (---) lines are the simulated profiles using the homogeneous model and strain distribution model, respectively. The experimental parameters are given in Table 4.2 and the simulation parameters are shown in Tables 4.5 and 4.6. The strain profile and weighting are shown in Fig. 4.4.

associated with the narrow peak and the second sub-layer with the wider peak. These designations are used in the tables and the text. The narrower peak is more prominent for A70.

The ω scans (Figs. 4.1(b) and 4.2(b)) were collected at the position of the narrower peak. Although both scans are noisy, a broad peak centred about $\Delta\omega \approx -1^\circ$ can be identified. The $\Delta\omega$ offset suggests the entire layer is tilted with respect to the substrate. It cannot be determined whether the two individual sub-layers identified above make different contributions to the ω scan. Hence, a definitive

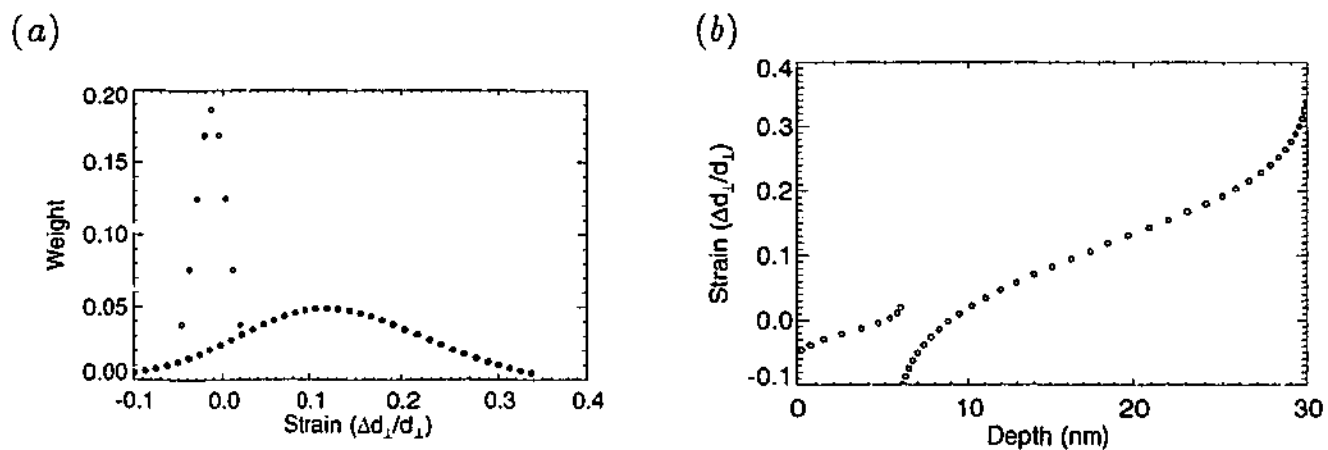


Figure 4.3: (a) Strain weighting, and (b) associated depth profile used for simulating sample A30.

conclusion cannot be drawn about the nature of the individual sub-layers from this scan, other than that at least one of the sub-layers has a high defect density and mosaicity.

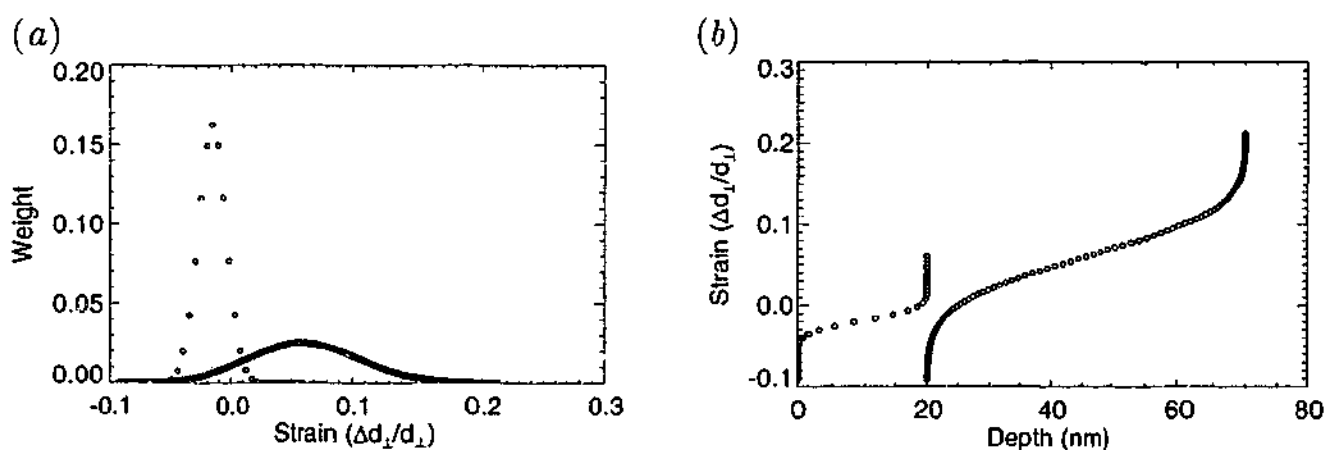


Figure 4.4: (a) Strain weighting, and (b) associated depth profile used for simulating sample A70.

Two approaches were used to fit the experimental data. The first approach only considered the two sub-layers to be homogeneous; the second approach allowed for a strain distribution by partition the sub-layer as described in Sec. 3.3.2. In the second approach all parameters were assumed constant for each partition, apart from the strain. This kept the number of fitting parameters to a minimum. The AlN layer was modelled as two sub-layers in order to generate the two peaks seen in the $\theta - 2\theta$ scans (Figs. 4.1(a) and 4.2(a)). The fitting parameters for samples A30 and A70 are given in Tables 4.3 - 4.6 for both the homogeneous and strain models. The strain quoted in approach two (strain distribution) was an average over the sub-layer. The strain distributions are shown in Figs. 4.3 and 4.4. The simulated

scans are plotted together with the experimental results in Figs. 4.1 and 4.2; the dashed line indicates the results of the simulation based on a strain distribution, while the solid line is based on homogeneous sub-layers (i.e., no strain distribution).

The variation of the strain is shown in Figs. 4.3 and 4.4. Figures 4.3(a) and 4.4(a) plot a histogram of strain versus weighting in which each data point represents a separate partition of the layer used in the simulation. Figures 4.3(b) and 4.4(b) consider the strain as varying through the sub-layer. The thickness of each partition is determined by multiplying the full layer thickness by the partitions weighting. The plot is shown for a cumulative depth (i.e., adding the thickness associated with each partition). The simulation was insensitive to the depth of the sub-layer. Therefore the depth profile is based on the assumption that the strain would be a continuous function. Even with this assumption the profile (for either sub-layer) could be reversed.

The strain distribution broadens the scan in the q_z direction, as does a smaller perpendicular block size. The main difference between the fitting parameters for the two approaches was a smaller perpendicular block size for the homogeneous model. There was little to distinguish between the two simulated $\theta - 2\theta$ scans (see Figs. 4.1(a) and 4.2(a)). The average strain was similar to the single homogeneous strain, which is expected since this determines the peak position in the $\rho - 2\theta$ scan. The layer thicknesses were also similar between the two models; given that the scans are noisy, and thus the fitting is subjective, they are in reasonable agreement. The total thickness of the AlN layer (bi-layer) was assumed to be the nominal value determined by the growth procedure, and has not been measured. The simulation does not give an indication of the layer thickness in this case. The simulated average (homogeneous) strains are very similar for the two samples, confirming that the peaks are at the same positions. For the thinner sample (A30) the ratio of the sub-layer thicknesses is approximately 1:4 (higher quality sub-layer: lower quality sub-layer), and for the thicker sample (A70) the ratio is 1.6:4 (higher quality sub-layer: lower quality sub-layer). This suggests that relative rate of growth for the higher quality sub-layer with respect to the lower quality sub-layer increases with thickness. Although the simulations cannot determine which sub-layer is on top (they are too thin for any appreciable photoelectric absorption), it is reasonable to assume that the lower quality sub-layer has grown directly on the substrate, and hence must accommodate a large strain. It appears the thinner sub-layer has relaxed (minimal strain) and has grown on top of the lower quality sub-layer. This suggests that the low temperature deposited AlN might accommodate the strain due to the mismatch with the substrate in a region close to the substrate surface,

Table 4.3: Simulation parameters for sample A30 (without strain distribution).

Sub-Layer No.	Layer Parameters				Block Parameters		
	Material	Thickness (nm)	Tilt (deg)	Perp. Strain	Lat. Size (nm)	Perp. Size (nm)	Misorientation (deg)
1	AlN	5	-1	-0.013	30	4	8
2	AlN	25	-1	0.05	30	1.2	8

Table 4.4: Simulation parameters for sample A30 (with strain distribution).

Sub-Layer No.	Layer Parameters				Block Parameters		
	Material	Thickness (nm)	Tilt (deg)	Perp. Strain	Lat. Size (nm)	Perp. Size (nm)	Misorientation (deg)
1	AlN	6	-1	-0.013	30	6	8
2	AlN	24	-1	0.12	30	20	8

Table 4.5: Simulation parameters for sample A70 (without strain distribution).

Sub-Layer No.	Layer Parameters				Block Parameters		
	Material	Thickness (nm)	Tilt (deg)	Perp. Strain	Lat. Size (nm)	Perp. Size (nm)	Misorientation (deg)
1	AlN	22	-0.9	-0.016	30	4.2	6
2	AlN	48	-0.9	0.06	30	1.5	6

Table 4.6: Simulation parameters for sample A70 (with strain distribution).

Sub-Layer No.	Layer Parameters				Block Parameters		
	Material	Thickness (nm)	Tilt (deg)	Perp. Strain	Lat. Size (nm)	Perp. Size (nm)	Misorientation (deg)
1	AlN	20	-0.9	-0.016	30	20	6
2	AlN	50	-0.9	0.06	30	50	6

thereby allowing higher quality GaN overlayers to be grown. This conjecture will be discussed in more detail after the results for sample series B and C have been presented.

The broadening of the peak in the q_x direction, shown in the ω scans (Figs. 4.1(b) and 4.2(b)), is specified by the misorientation and lateral block size. The misorientation and lateral block size can both be extracted from an ω scan because they affect the peak shape in different ways. However, to a large extent these effects were masked by the excessive noise in the ω scan; hence there is a large uncertainty in the parameters quoted for this sample. Nevertheless the ω scans for the two samples were broad, implying a large misorientation and small lateral block size. The misorientation width is smaller for sample A70, suggesting that it is of slightly higher quality than A30.

A parameter commonly reported as a measure of epitaxial layer quality is the threading dislocation density. As discussed in Chapter 1, Group III nitride materials have a typical threading dislocation density between 10^8 cm^{-2} to 10^{10} cm^{-2} depending on growth conditions. Assuming there is one threading dislocation per vertical wall of the mosaic block, and that the mosaic block has a square base, the threading dislocation density is twice the inverse of the block area in the plane. The lateral block size was determined to be 30 nm for both samples. This equates to a dislocation density of $2 \times 10^{11} \text{ cm}^{-2}$. However, only one ω scan was collected at the narrower peak position, and hence separate parameters for the two layers could not be determined for the q_x direction. Finally, as only one reflection was available for analysis, the accuracy of the simulations could not be definitively tested. Sections 4.3 and 4.4 discuss the importance of using multiple reflections.

The experimental parameters for samples of type B are shown in Table 4.7. Again only three scans were collected for each sample. Samples B30 and B70 were identical to A30 and A70, except that their temperature was raised to 1100°C before they were removed from the growth chamber. As the samples were similar, it is not surprising that the $\theta - 2\theta$ scans for samples B30 and B70 (see Figs. 4.5(a) and 4.6(a)) were similar to the scans for the type A samples. The experimental data was less noisy for the B samples, which is difficult to explain since the maximum count rate did not increase. The narrow peaks are more prominent for both type B samples than for the type A samples. This suggests that the sub-layer producing this peak is of a higher quality or thicker than for the type A samples. The peak positions have not changed by a significant amount in either the $\theta - 2\theta$ or ω scans. However, the annealing process seems to have produced a third layer (labelled sub-layer 3 in Tables 4.8 and 4.9) for the 30 nm sample. Evidence of the third sub-layer is the

very sharp peak seen in the ω scan (Fig. 4.5(b)) and the RSM (Fig. 4.9). This peak is not obvious in the $\theta - 2\theta$ scan, possibly because the scan, or experimental peak, had a slight $\Delta\omega$ offset, and hence the peak was missed because it is very narrow in the q_x direction. The shape of the third peak suggests that the sample has a thin sub-layer with a very low mosaicity and low defect density. This scan shape has been reported previously for low temperature deposited AlN and GaN buffer layers (Hersee *et al.*, 1997); it has been attributed to an increase in preferred orientation within the layer (i.e., reduced misorientation).

The simulations were carried out in the same manner as for samples A30 and A70. However, the model for sample B30 required a third sub-layer. The peak associated

Table 4.7: Experimental scan parameters for samples of type B.

Sample	Scan Type	Parameter	Value
AlN 30 nm	$\theta - 2\theta$	Step size (in θ)	15 arcseconds for 17.225°–17.725° and 18.725°–20.8°
		Background count	5 arcseconds for 17.725°–18.725° 66 counts/second ^a
		ω	2 θ position
	ω	Step size (in θ)	100 arcseconds
		Background count	66 counts/second ^b
		ω	2 θ position
	ω	Step size (in θ)	100 arcseconds
		Background count	66 counts/second ^b
		RSM	ϵ step size
	AlN 70 nm	$\theta - 2\theta$	$\Delta\omega$ step size
Background count			66 counts/sec ^b
ω (From RSM)			2 θ position
ω (From RSM)		Step size (in θ)	50 arcseconds
		Background count	50 counts/second ^a
		ω (From RSM)	2 θ position
RSM		Step size (in θ)	120 arcseconds
		Background count	50 counts/second ^b
		RSM	ϵ step size
RSM		$\Delta\omega$ step size	120 arcseconds
	Background count	50 counts/sec ^b	

^aAs approximated from the plot of the $\theta - 2\theta$ scan.

^bAssumed value since the conditions were the same as for the $\theta - 2\theta$ scan.

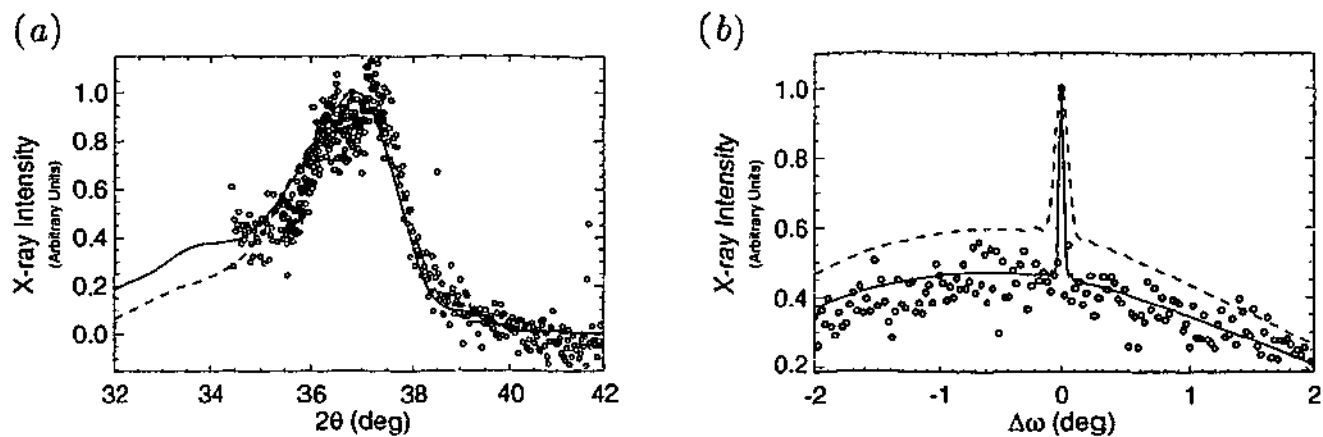


Figure 4.5: One-dimensional scans of sample B30. (a) $\theta - 2\theta$ scan, and (b) ω scan at $2\theta = 36.54^\circ$. The circles (o) are the experimental data points. The solid (—) and dashed (---) lines are the simulated profiles using the homogeneous model and strain distribution model, respectively. Experimental parameters are given in Table 4.7 and the simulation parameters are shown in Tables 4.8 and 4.9. The strain profile and weighting are shown in Fig. 4.7.

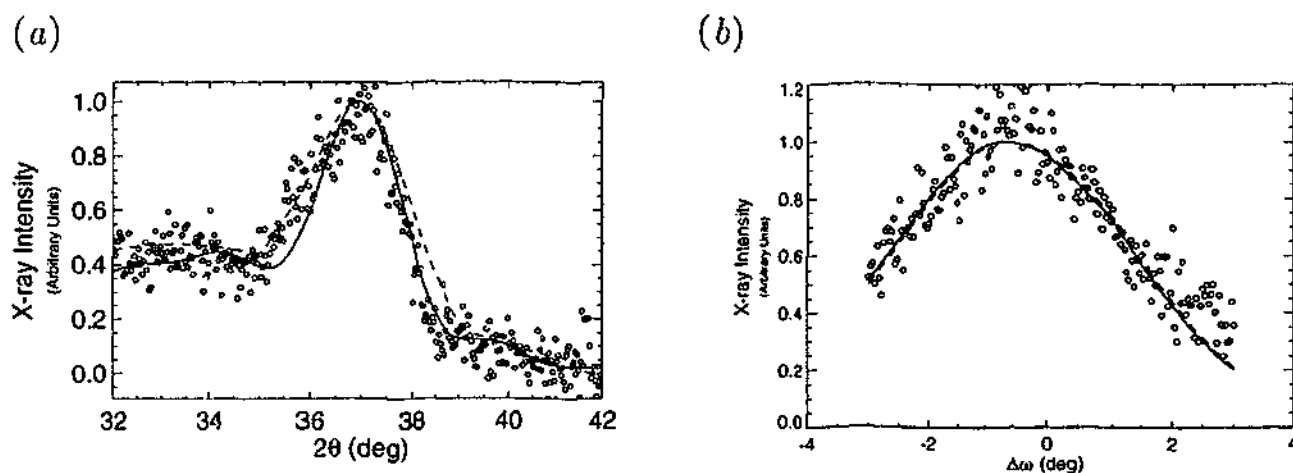


Figure 4.6: One-dimensional scans of sample B70. (a) $\theta - 2\theta$ scan and (b) ω scan at $2\theta = 37.0^\circ$. The circles (o) are the experimental data points. The solid (—) and dashed (---) lines are the simulated profiles using the homogeneous model and strain distribution model, respectively. Experimental parameters are given in Table 4.7 and the simulation parameters are shown in Tables 4.10 and 4.11. The strain profile and weighting are shown in Fig. 4.8.

with the third sub-layer was narrow, and hence the sub-layer was considered to be homogeneous (no strain distribution). The simulation parameters for samples B30 and B70 are shown in Tables 4.8 - 4.10. The simulated profiles and RSMs are shown together with the experimental data in Figs. 4.5 and 4.9, respectively.

For sample B30 the homogeneous simulations show layers 1 and 3 to be of a similar thickness, with sub-layer 2 being significantly thicker, but of worse quality. The peak positions in the $\theta - 2\theta$ scan are determined by the Bragg angle and the strain parallel to the surface of the sample. The strain determined for sub-layer 3 is approximately the same as sub-layer 1 for sample A30, and hence are at the same peak position. Furthermore these sub-layers have the same thickness. It is possible that on annealing, an as grown thin higher quality layer (sub-layer 1 for sample A30) is significantly improved. The improvement includes a drastic reduction in mosaicity and a large increase in lateral block size. Consequently the sub-layer is almost perfect in the lateral direction. The perpendicular block size is restricted by the thickness of the sub-layer. The annealing seems to cause part of the low quality interface layer to improve (possibly through some interaction with the high quality top layer). It is assumed that sub-layer 3 is at the surface of the structure, and sub-layer 2 is located on the substrate. The quality of sub-layer 2 has also improved through annealing, with a reduction in mosaicity and whole layer tilt.

Similar conclusions can be drawn from the simulations using a strain distribution. However, the evidence is not as strong, with the simulation suggesting the thicknesses for sub-layer 1 for sample A30, and sub-layer 3 for sample B30 are different from one another (6 nm and 4 nm, respectively). The parameters suggest the lower quality region of the sample consists of two equally thick sub-layers.

The simulations for sample B70 provide very similar results to sample A70, apart from a reduction in misorientation and tilt, and a slight change in the strain for each of the layers. The only conclusion that can be drawn from this sample is that the quality has increased by a small amount. The B70 sample does not exhibit the sharp peak in the ω scan, seen in sample B30; hence it does not have preferential alignment of crystallites after annealing. This is probably the reason why Tabuchi *et al.* (2002) and Zhang *et al.* (2004) found that GaN epilayers grown on 70 nm LT-AlN buffer layers are of a lower quality than those grown on 30 nm buffer layers. It is unclear why the 70 nm layer does not show the same preferred orientation as the 30 nm layer.

Table 4.8: Simulation parameters for sample B30 (without strain distribution).

Layer No.	Layer Parameters				Block Parameters		
	Material	Thickness (nm)	Tilt (deg)	Perp. Strain	Lat. Size (nm)	Perp. Size (nm)	Misorientation (deg)
1	AlN	6	-0.6	-0.032	30	6.0	5
2	AlN	19	-0.6	0.03	30	1.5	5
3	AlN	5	0	-0.008	280	5	0.01

Table 4.9: Simulation parameters for sample B30 (with strain distribution).

Layer No.	Layer Parameters				Block Parameters		
	Material	Thickness (nm)	Tilt (deg)	Perp. Strain	Lat. Size (nm)	Perp. Size (nm)	Misorientation (deg)
1	AlN	13	-0.6	-0.032	30	13	5
2	AlN	13	-0.6	0.03	30	13	5
3	AlN	4	0	-0.008	280	4	0.01

Table 4.10: Simulation parameters for sample B70 (without strain distribution).

Layer No.	Layer Parameters				Block Parameters		
	Material	Thickness (nm)	Tilt (deg)	Perp. Strain	Lat. Size (nm)	Perp. Size (nm)	Misorientation (deg)
1	AlN	18.7	-0.65	-0.027	30	4.8	5
2	AlN	51.3	-0.65	0.06	30	1	5

Table 4.11: Simulation parameters for sample B70 (with strain distribution).

Layer No.	Layer Parameters				Block Parameters		
	Material	Thickness (nm)	Tilt (deg)	Perp. Strain	Lat. Size (nm)	Perp. Size (nm)	Misorientation (deg)
1	AlN	18.7	-0.6	-0.028	30	18.7	5
2	AlN	51.3	-0.6	0.078	30	51.3	5

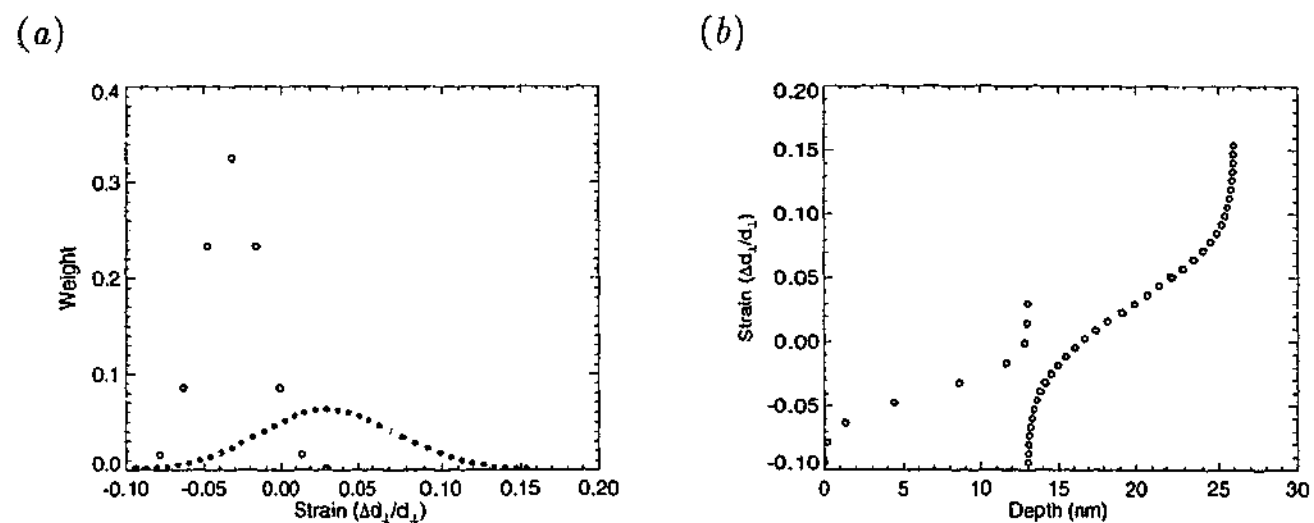


Figure 4.7: (a) Strain weighting, and (b) associated depth profile used for simulating sample B30.

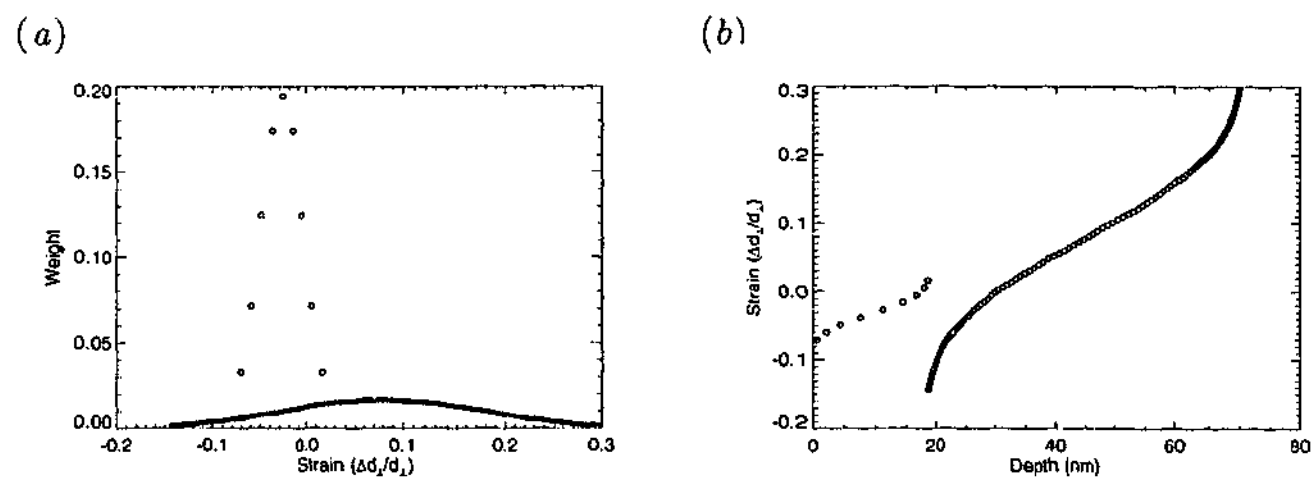


Figure 4.8: (a) Strain weighting, and (b) associated strain depth profile used for simulating sample B70.

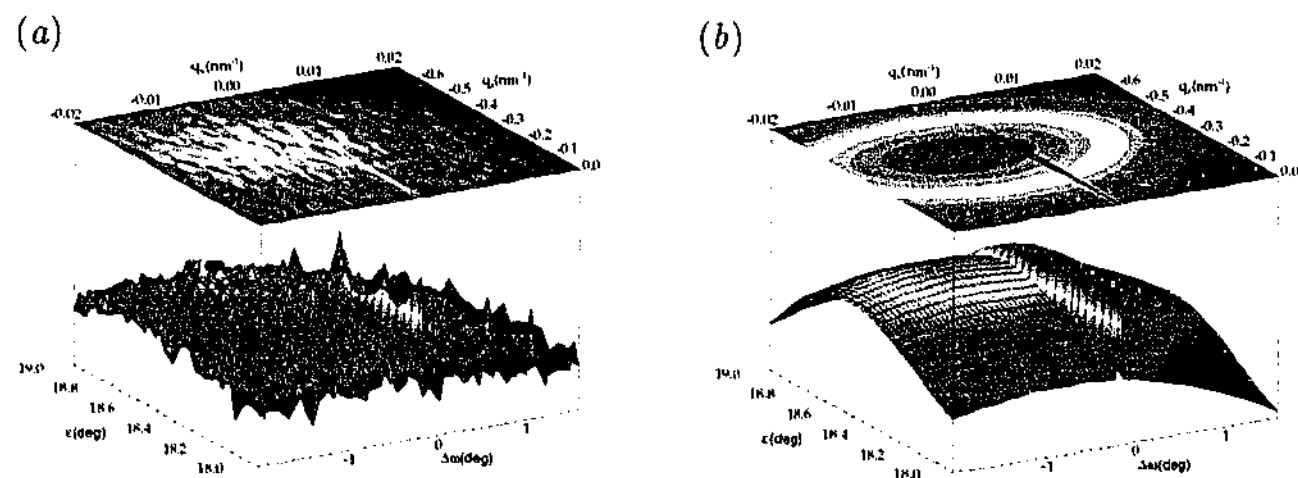


Figure 4.9: (a) Experimental reciprocal space map for sample B30, and (b) simulated reciprocal space map for sample B30.

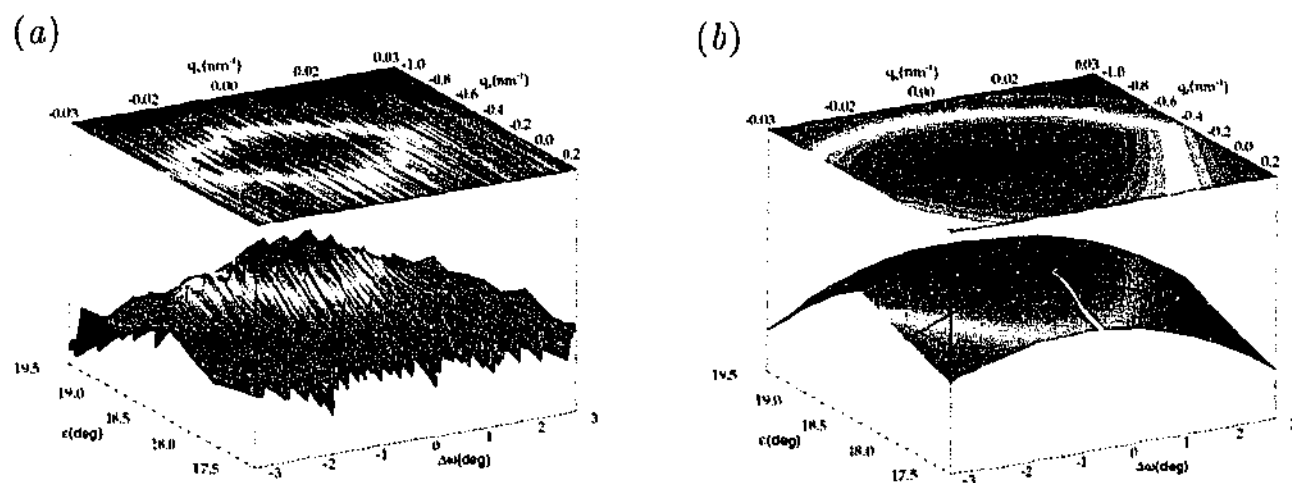


Figure 4.10: (a) Experimental reciprocal space map for sample B70, and (b) simulated reciprocal space map for sample B70.

4.3 Sample Series C: GaN on a LT-AlN Buffer Layer

The type C samples include a 30 nm layer of GaN on top of the AlN buffer. These samples allow us to investigate the nature of the initial GaN growth and its effect on the crystal structure of the AlN buffer. There were two samples: C30, a multilayer with a 30 nm LT-AlN buffer capped by a 30 nm GaN layer, and C70, a multilayer with a 70 nm LT-AlN capped by a 30 nm GaN layer. The experimental parameters used for scanning the samples are given in Table 4.12.

The only experimental change from the measurements made on sample types A and B was an increase in the size of the entrance slits from 0.5mm(V)×2.0mm(H) to 1mm(V)×2.5mm(H). This improved the signal to noise ratio, and hence the experimental data was of higher quality. The intensity registered by the detector comes from a region of reciprocal space. The size of this region is determined by the divergence of the incident beam and the size of the angular window of the analyser crystal. The larger the region the poorer the resolution of the apparatus. For this experiment the divergence of the incident beam was very low because two monochromators were used. Increasing the slit size would not have significantly increased the divergence, and hence does not degrade the resolution. Widening the slit does increase the area of the sample illuminated by the X-ray beam. Therefore the resulting diffracted intensity is from a larger volume of the sample.

The specific scan parameters for C30 are summarised in Table 4.13. In order to compare of the various scans, each scan was normalised to the maximum count rate of the (0002) reflection in the $\theta - 2\theta$ scan. The incident beam intensity was not known for the experiment; hence the simulation of the (0002) reflection in the $\theta - 2\theta$ scan was normalised to a peak of height of unity (thereby the simulated and experimental peak heights are both unity for this scan). All other simulations

Table 4.12: Experimental parameters for samples of type C.

Parameter	Value
Wavelength	1.5406 nm
Entrance slit vertical size	1.0 mm
Entrance slit horizontal size	2.5 mm
Vertical divergence at sample	≈ 7 arcseconds ^a
Count rate at sample	Unknown ^b
Count time per point	7 seconds (unless otherwise specified)

^aThe divergence was not measured. The value quoted here was calculated (see Mudie *et al.*, 2003).

^bIntensity was too large to measure with a photon counting detector.

Table 4.13: Experimental scan parameters for sample C30.

Sample	Scan Type	Parameter	Value	
AlN 30 nm	$\theta - 2\theta$ (0002)	Step size (in θ)	50 arcseconds	
		Background count	20 counts/second ^a	
		ω	2θ position	36.11°
		Step size (in θ)	50 arcseconds	
		Background count	20 counts/second ^b	
		ω	2θ position	38.25°
		Step size (in θ)	50 arcseconds	
		Background count	20 counts/second ^b	
	RSM (0002)	ϵ step size	432 arcseconds	
		$\Delta\omega$ step size	288 arcseconds	
		Background count	20 counts/sec ^b	
	$\theta - 2\theta$ (0004)	Step size (in θ)	50 arcseconds	
		Background count	91 counts/second ^a	
	ω	2θ position	78.4356°	
		Step size (in θ)	288 arcseconds	
		Background count	91 counts/second ^b	

^aAs approximated from the $\theta - 2\theta$ scan.

^bAssumed value since the experimental conditions were the same as for the $\theta - 2\theta$ scan.

adopted the same normalising factor.

For sample C30, a large peak was observed at $2\theta \approx 38.25^\circ$ and a small peak at $2\theta \approx 36.1^\circ$; the $\theta - 2\theta$ scan about AlN(0002) is shown in Fig. 4.11. On cursory inspection one might assume that one of the peaks originates from the GaN layer and one from the AlN layer. However, since the unstrained peak position is at $2\theta \approx 36.03^\circ$ for AlN and at $2\theta \approx 34.57^\circ$ for GaN, it is possible that the small peak at $2\theta \approx 36.1^\circ$ originates from an unstrained AlN layer. If this was the case the larger peak would also arise from the AlN layer because GaN has a smaller 2θ peak position (larger d -spacing) than AlN. In this model the AlN layer consists of two sub-layers with different strain states, defect densities, and mosaicities. The difficulty with this model is that if both peaks are due to AlN there would be no evidence of the GaN layer in any of the (0002) scans. This is not likely since the GaN layer is the same thickness as the AlN layer and should diffract at least as strongly. This demands a closer examination of the experimental data.

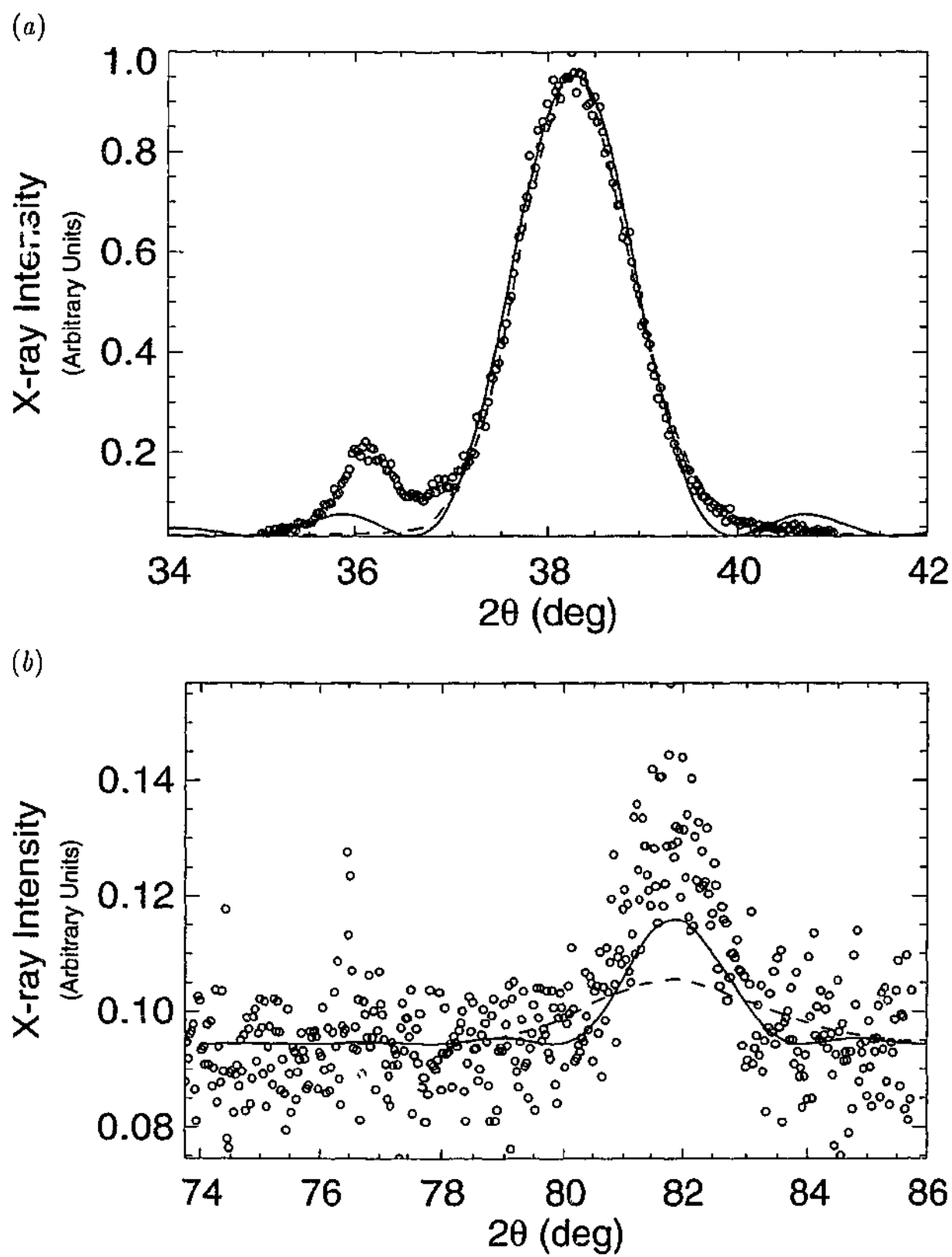


Figure 4.11: $\theta - 2\theta$ scans for Sample C30. (a) (0002) reflection, and (b) (0004) reflection. The experimental data is denoted by circles (\circ). The solid line (—) is a fit based on the homogeneous model and the dashed line (---) represents the results for the strain distribution model. Experimental scan parameters are given in Table 4.13, with the simulation parameters reproduced in Tables 4.14 and 4.15. The strain profile and weighting are shown in Fig. 4.14.

Assuming that the large peak is due to the AlN layer, we can determine the a and c lattice parameters (a_{strained} and c_{strained}) from the peak position, according to

$$\frac{\Delta c_0}{c_0} = -2 \frac{c_{13}}{c_{33}} \frac{\Delta a_0}{a_0}, \quad (4.1)$$

where $\Delta c_0 = c_{\text{strained}} - c_0$, $\Delta a_0 = a_{\text{strained}} - a_0$, c_{13} and c_{33} are elastic stiffness constants, and c_0 and a_0 are the relaxed lattice parameters. The c lattice parameter is determined to be 0.4702 nm (nominally the AlN(0002) d -spacing is 0.4982 nm) and the a lattice parameter is 0.3400 nm (nominally 0.3112 nm). The c_{13} and c_{33} parameters used were 120 GPa and 395 GPa, respectively (Amano and Akasaki, 1999).

The c lattice parameter for coherently grown GaN (the same a lattice parameter as the underlayer) can be determined using Eq. (4.1), and the elastic stiffness constants for GaN ($c_{13} = 103$ GPa and $c_{33} = 405$ GPa). The result is $a = 0.4980$ nm, which gives a (0002) peak position of $2\theta = 36.04^\circ$. This agrees with the small peak position, and suggests strongly that the two peaks are indeed strained GaN and AlN.

As discussed in Sec. 1.2.4 the a lattice parameter for AlN is smaller than that for sapphire; however, the orientation and specific coordination of the atoms at the interface results in a compressive strain parallel to the surface. Furthermore the coefficient of thermal expansion for sapphire is larger than AlN (Sec. 1.2.4), hence it will shrink more than the epitaxial overlayer, again creating a compressive strain parallel to the surface. This compressive strain will expand the layer perpendicular to the surface (i.e., enlarge the c lattice parameter), displacing the AlN peak to lower 2θ angles. This is contrary to the experimental results where the AlN peak has clearly shifted to a larger 2θ angle, suggesting a tensile strain parallel to the surface. In order to validate that the AlN layer is under a tensile strain in the plane, it is important to check the peak positions for the $\theta - 2\theta$ scan about the AlN(0004) reflection. The $\theta - 2\theta$ scan about the AlN(0004) reciprocal lattice point has a lower intensity, and hence a worse signal to noise ratio than the AlN(0002) scan. Nevertheless, it also exhibits two peaks at $2\theta = 78.4356^\circ$ and $2\theta = 73.1022^\circ$. However, the d -spacings associated with these peak positions do not agree with those in the scan about AlN(0002). In fact the position of the smaller peak seems to agree with the relaxed position for GaN ($2\theta \approx 73^\circ$). Although the peak positions do not agree with the (0002) peak positions, the angular separation of the peaks do match. Possible explanations for the positions of these peaks are some form of calibration error, drift of a rotation stage from its nominal position, or a different part of the

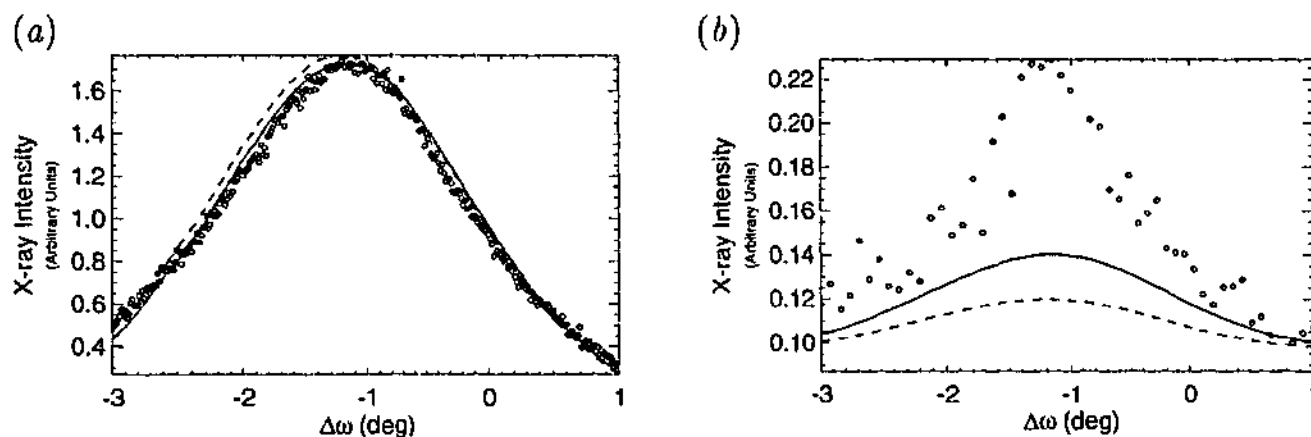


Figure 4.12: ω scans for sample C30. (a) $2\theta = 38.25^\circ$, and (b) $2\theta = 78.4356^\circ$. The $2\theta = 78.4356^\circ$ scan was simulated at 81.86° to match the simulated peak position (see text for details). The experimental data is denoted by circles (\circ). The solid line (—) is a fit based on the homogeneous model and the dashed line (---) represents the results for the strain distribution model.

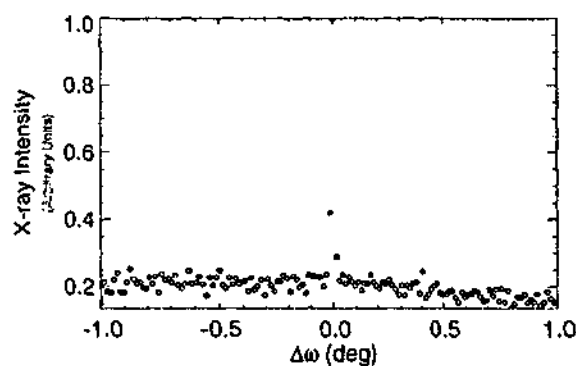


Figure 4.13: ω scan of the GaN peak for sample C30.

sample being illuminated for the (0002) and (0004) reflections (although this final suggestion is unlikely to cause such a large change in peak position). The (0002) reflection data was collected before the (0004) scan, with an RSM requiring over three and half hours of data collection. Therefore the (0002) scan is more likely to be calibrated correctly. More importantly the (0002) scan included a substrate peak (i.e., Al_2O_3 (0006)) at the correct position, confirming that the scan was calibrated correctly. Despite a compressive strain parallel to the surface being the usual strain state for AlN epilayers on α -sapphire, the c lattice parameter of the AlN layer has been reduced relative to the fully relaxed material. The origin of the tensile stress (in the plane) is unknown, but has been seen before for GaN on α -sapphire grown using MBE (Leszczynski *et al.*, 1999). It might have its origin in some form of defect structure, or possibly the GaN top layer, which has a larger lattice parameter than AlN.

Table 4.14: Simulation parameters for sample C30 (without strain distribution).

Material	Layer Parameters				Block Parameters		
	Thickness (nm)	Tilt (deg)	Lat. Strain	Perp. Strain	Lat. Size (nm)	Perp. Size (nm)	Misorientation (deg)
AlN	30	-1.16	—	-0.0605	10	5.5	2.3
GaN	—	0.0	—	-0.044	400	15	0.01

Table 4.15: Simulation parameters for sample C30 (with strain distribution).

Material	Layer Parameters				Block Parameters		
	Thickness (nm)	Tilt (deg)	Lat. Strain	Perp. Strain	Lat. Size (nm)	Perp. Size (nm)	Misorientation (deg)
AlN	30	-1.26	—	-0.064	10	30	2.3

The peak positions for the (0004) scan can be corrected against the positions in the (0002) scan. The corrected profile is plotted in Fig. 4.11(b). Having recalibrated the (0004) experimental scan, the 2θ position of the ω scans (near the (0004) peak) also had to be corrected.

The ω scans of the two peaks (Figs. 4.12 and 4.13) show the smaller peak to have a very narrow width in the q_x direction, and the larger peak to be very broad. This is confirmed by the RSM in Fig. 4.19(c), where the smaller peak is unobservable because the step size in the q_x direction is too large.

The simulations were undertaken using homogenous layers and inhomogeneous layers, in a similar manner to sample types A and B. For the inhomogeneous layer model the strain and tilt was varied across (or within) the layer. It proved impossible to fit both peaks simultaneously. The small (GaN) peak is very narrow in the q_x direction (Fig. 4.13), and hence the misorientation is small and the lateral block size large. With these parameters the simulation produces a very intense peak because the layer is diffracting almost like a perfect crystal. The simulated peak intensity can be reduced by decreasing the layer thickness; however, if the layer is made too thin the peak becomes too wide in the q_z direction. Therefore the small peak was not included in the simulated profiles shown in Fig. 4.11. The simulation parameters that give the correct peak shape and position for GaN (determined by ignoring the AlN peak) are given in Table 4.14.

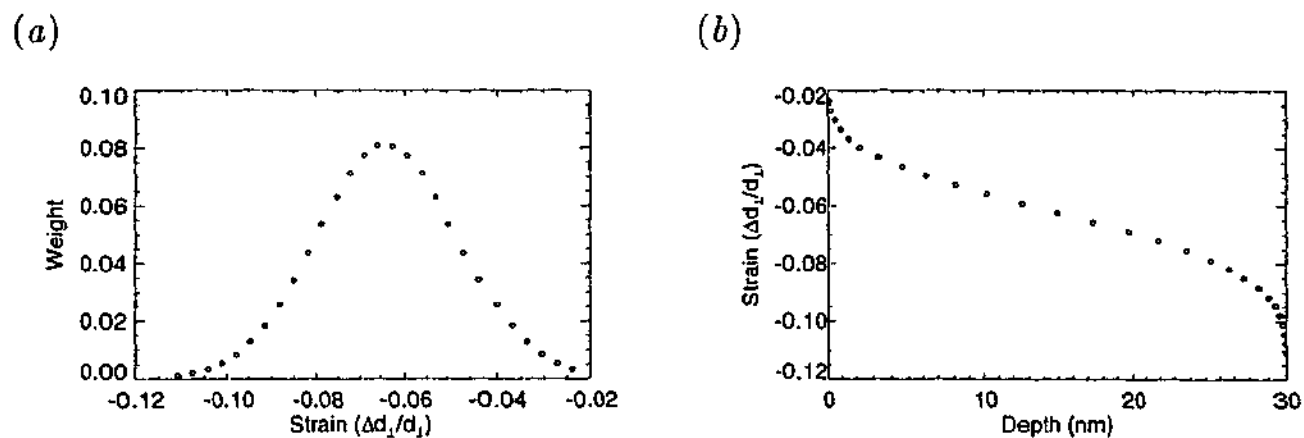


Figure 4.14: (a) Strain weighting, and (b) associated depth profile used for simulating sample C30.

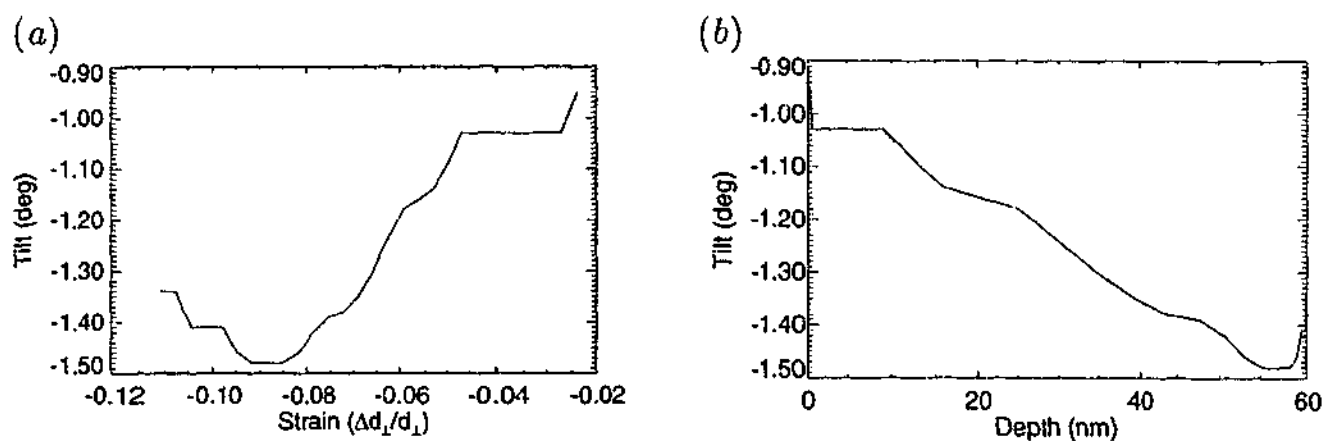


Figure 4.15: Tilt distribution profiles used for simulating sample C30. (a) Tilt versus strain, and (b) tilt versus depth.

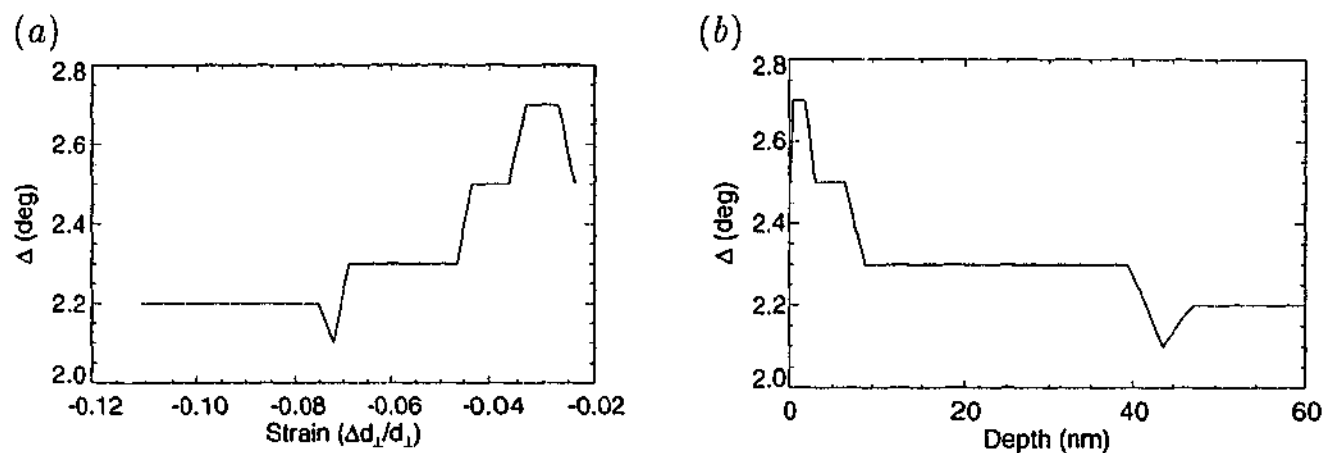


Figure 4.16: Misorientation, Δ_m , distribution profiles used for simulating sample C30. (a) Δ versus strain, and (b) Δ versus depth.

The RSM shown in Fig. 4.19(a) appears to be slightly rotated in the q_z - q_x plane (this is shown more clearly in Fig. 4.17). In order to simulate this, a distribution of layer tilt angles and strains was incorporated within the simulation (as well as a distribution of the misorientation Δ_m). Plots of the strain, tilt, and misorientation distributions are shown in Figs. 4.14, 4.15, and 4.15. Although a tilt and strain distribution can rotate the peak in the q_z - q_x space, it is also possible that the rotation could be due to one of the experimental components drifting out of alignment, since the RSMs were collected as a series of $\omega - 2\theta$ scans each covering the same 2θ range. Peak rotation is indicative of the peak appearing at a different 2θ value for each scan, which is what would be seen if the reported position of the detector was changing slightly for each scan. As the RSM was collected the AlN peak shifted toward smaller 2θ values, again agreeing with the shift in the 2θ peak positions from the (0002) to (0004). The peak shifts 0.5° from the start to the end of the RSM. However, the $\theta - 2\theta$ scan collected before the RSM more closely matches the $\omega - 2\theta$ scan at $\Delta\omega = 0^\circ$, not the scan collected first ($\Delta\omega = -3^\circ$) as would be expected if the peak shift was caused by drift. We therefore 'conclude' that a mechanism, such as tilt distribution, caused the peak rotation.

In general both simulations (with and without a strain distribution) fitted the experimental data well for the AlN peak, particularly about the (0002) reflection as shown for the $\theta - 2\theta$ scan and ω scans in Figs. 4.11 and 4.12. The RSM contour map in Fig. 4.17 shows the peak rotation for the experimental RSM. It also shows that the rotation is quite small, suggesting that it could be neglected, allowing the data to be fitted with a single layer. The RSMs and profiles in this section were plotted on a linear intensity scale. On a logarithmic scale the strained version appears to fit the peak shape far better because the homogeneous layer simulation produces large side lobes. These are thickness oscillations, (see Sec. 4.4). If the roughness of the interface was included in the model then these oscillations would not appear in the simulation of a homogeneous layer, and the data would be better matched on a logarithmic scale.

Figure 4.18 shows an $\omega - 2\theta$ scan extracted from the RSM. As expected the peak position was better matched by the simulation using a tilt distribution. The fit between the experimental and simulated $\theta - 2\theta$ profiles for the (0004) reflection is good, especially using the single layer model (no strain distribution). The ω scan of the GaN reflection produced a narrow intense peak, which was not reproduced in the simulated profile.

The physical interpretation of the strain distribution was discussed in Sec. 3.3.2. The strain weighting and associated depth profile shown 4.14 have been used to

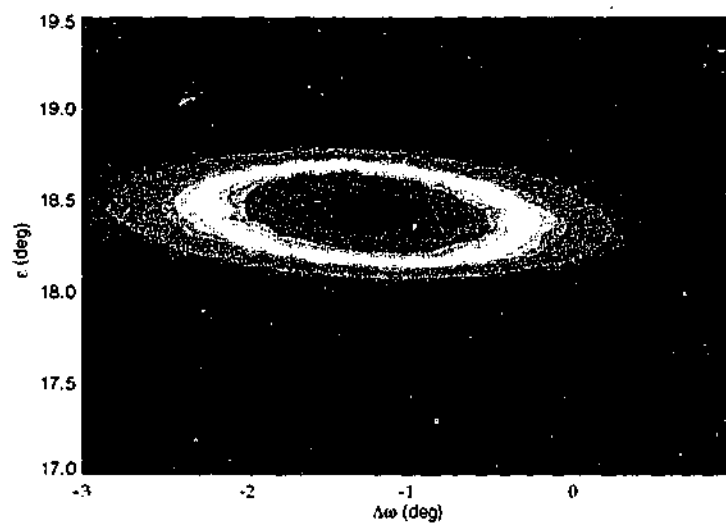


Figure 4.17: Reciprocal space map for sample C30, indicating rotation of the diffracted peak in the q_x - q_z plane. The rotation is seen by treating the peak shape as an ellipse, and observing that the major axis of the ellipse is not aligned with the $\Delta\omega$ -axis.

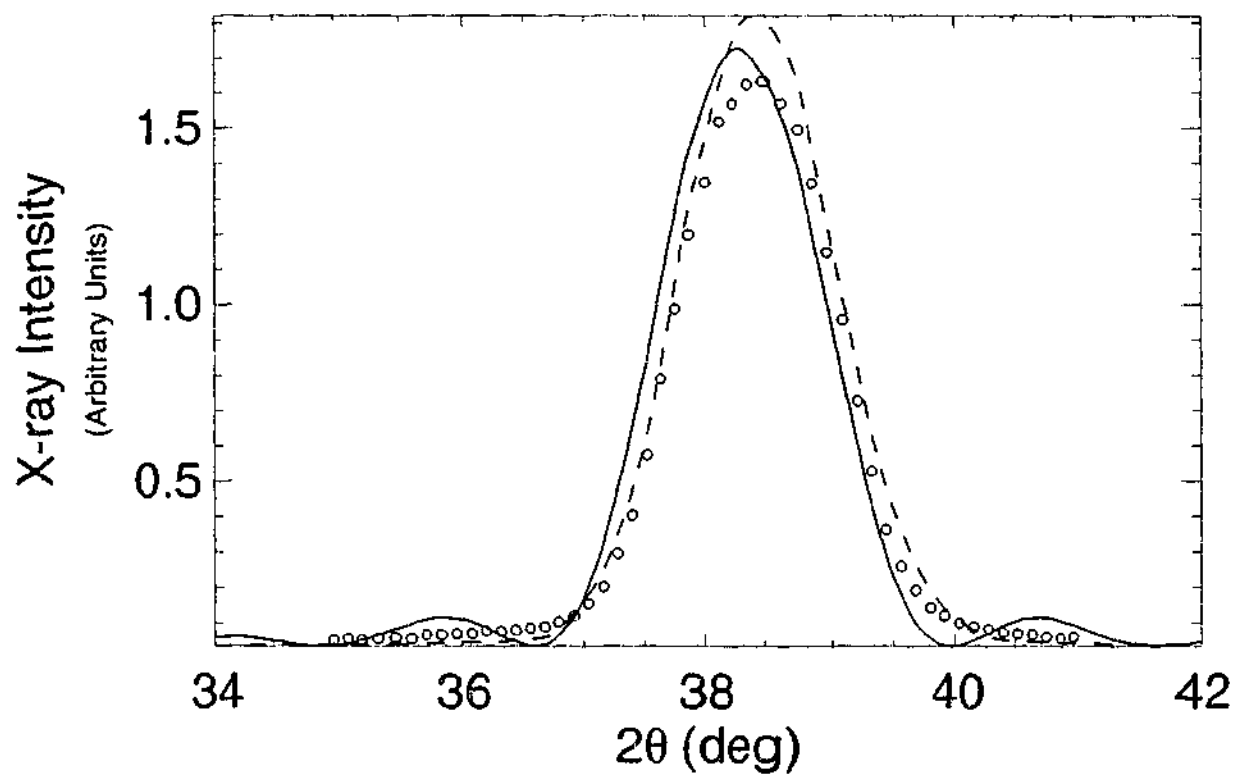


Figure 4.18: $\omega - 2\theta$ scan for sample C30 about AlN(0002), with $\Delta\omega = -1.08^\circ$. The experimental scan, denoted by circles (\circ), was extracted from the RSM shown in Fig. 4.19(a). The solid line (—) is a fit based on the homogeneous model and the dashed line (--) represents the results for the strain distribution model.

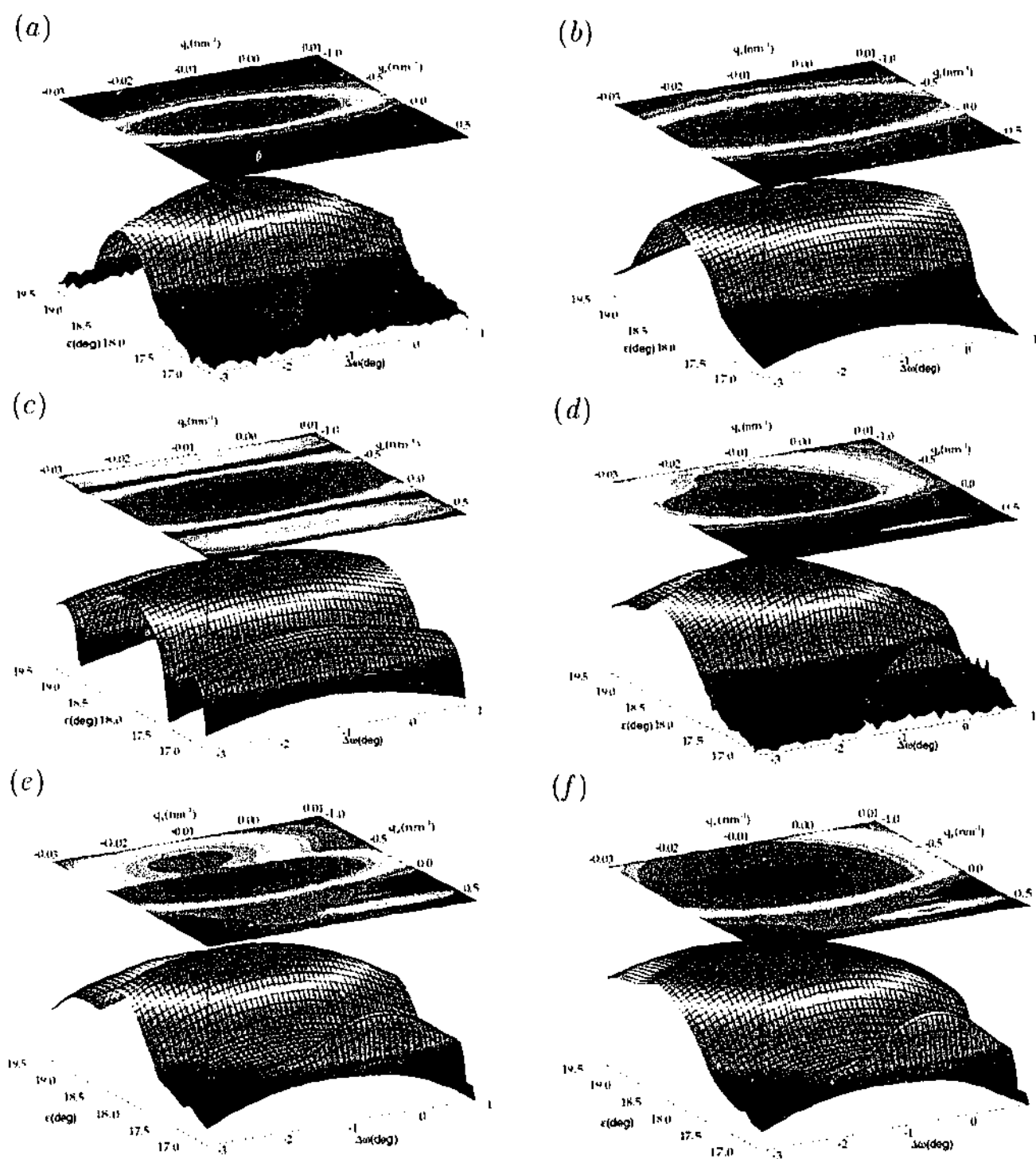


Figure 4.19: Reciprocal space maps for sample type C. (a) Experimental RSM about $\text{AlN}(0002)$ for sample C30, (b) simulated RSM about $\text{AlN}(0002)$ for C30 using a strain model, (c) simulated RSM about $\text{AlN}(0002)$ for C30 using a single layer, (d) experimental RSM about $\text{AlN}(0002)$ for C70, (e) simulated RSM about $\text{AlN}(0002)$ for C70 using the model parameters optimised for matching the (0004) reflection, (f) simulated RSM about $\text{AlN}(0002)$ for C70 using the model parameters optimised for matching the (0002) reflection.

describe the variation of strain (as explained in Sec. 4.2). For sample C30 the weighting profile was modelled as a Gaussian, which matched the experimental peak shape reasonably well. The tilt distribution (Fig. 4.15), is plotted as a function of the strain and depth. The misorientation was also varied for this sample, as shown in Fig. 4.16. The average strain, tilt and misorientation is given in Table 4.15. As is expected these average values agree with those used for the single layer model. The lateral block size for the two models is also the same. On the other hand the perpendicular block size is quite different. This is a consequence of the nature of the two models. The perpendicular block size for the strain distribution model was set to the thickness of the layer, with the peak width determined by the strain. The perpendicular block size for the single layer model was necessarily small in order to match the width of the peak in the q_z direction. The lateral block size suggests a large dislocation density of $2 \times 10^{12} \text{ cm}^{-2}$. The ω scan for the smaller peak can be fitted using a lateral block size of 400 nm. This gives a dislocation density of $1 \times 10^9 \text{ cm}^{-2}$.

The experimental scan parameters for sample C70 are summarised in Table 4.16. The (0002) reflection for sample C70 has a complex profile. The $\theta - 2\theta$ scans, shown in Fig. 4.20 exhibit a small, narrow peak centred at $2\theta \approx 34.6^\circ$ and a large, very broad peak extending from $2\theta \approx 36^\circ$ to $\approx 39.4^\circ$. Inspection of the broad peak suggests that it is composed of two overlapping peaks. Other scans confirm this conjecture. In particular the $\theta - 2\theta$ scan of the (0004) reflection (see Fig. 4.20(b)) shows two individual peaks; two peaks should be evident in the scan of the (0002) reflection. The two overlapping peaks in the $\theta - 2\theta$ scan of the (0002) reflection are centred at $\approx 36.6^\circ$ and $\approx 38.2^\circ$. The former peak is more intense. The peak positions suggest that the broad double peak is from the AlN layer, and the narrow peak at $2\theta \approx 34.6^\circ$ is from the GaN layer.

The broadening in the q_z direction was simulated by using a strain distribution (and also including a distribution of tilt and misorientation), thereby increasing the number of fitting parameters. Even allowing for this additional flexibility it was not possible to fit the experimental data very well. Two sets of simulated profiles are shown, together with the experimental results (see Fig. 4.20) in order to demonstrate the variation with the mosaic block model parameters. One set of parameters fits the (0002) scan closely, the other fits the (0004) scan. These fitting parameters are reproduced in Tables 4.17 and 4.18, and the strain distributions in Figs. 4.21 and 4.22.

The AlN peak position for the $\omega - 2\theta$ scan with a $\Delta\omega$ offset of -1.42° (Fig. 4.23) is different to the $\theta - 2\theta$ scan. This suggests that the peak is rotated in the q_x - q_z plane

Table 4.16: Experimental scan parameters for sample C70.

Sample	Scan Type	Parameter	Value	
AlN 70 nm	$\theta - 2\theta(0002)$	Step size (in θ)	50 arcseconds	
		Background count	29 counts/second ^a	
		ω	2θ position	36.6386°
	ω	$\theta - 2\theta(0002)$	Step size (in θ)	144 arcseconds
			Background count	29 counts/second ^b
			ω	2θ position
	ω	$\theta - 2\theta(0002)$	Step size (in θ)	144 arcseconds
			Background count	29 counts/second ^b
			ω	2θ position
	ω	$\theta - 2\theta(0002)$	Step size (in θ)	144 arcseconds
			Background count	29 counts/second ^b
			ω	2θ position
	ω	$\theta - 2\theta(0002)$	Step size (in θ)	48 arcseconds
			Background count	29 counts/second ^b
			ω	2θ position
RSM (0002)	ϵ	step size	300 arcseconds	
		$\Delta\omega$ step size	288 arcseconds	
		Background count	29 counts/sec ^b	
AlN 70 nm	$\theta - 2\theta(0004)$	Step size (in θ)	50 arcseconds	
		Background count	70 counts/second ^a	
		ω	2θ position	74.8244°
	ω	$\theta - 2\theta(0004)$	Step size (in θ)	144 arcseconds
			Background count	70 counts/second ^b
			ω	2θ position
	ω	$\theta - 2\theta(0004)$	Step size (in θ)	144 arcseconds
			Background count	70 counts/second ^b
			ω	2θ position
	ω	$\theta - 2\theta(0004)$	Step size (in θ)	144 arcseconds
			Background count	70 counts/second ^b
			ω	2θ position

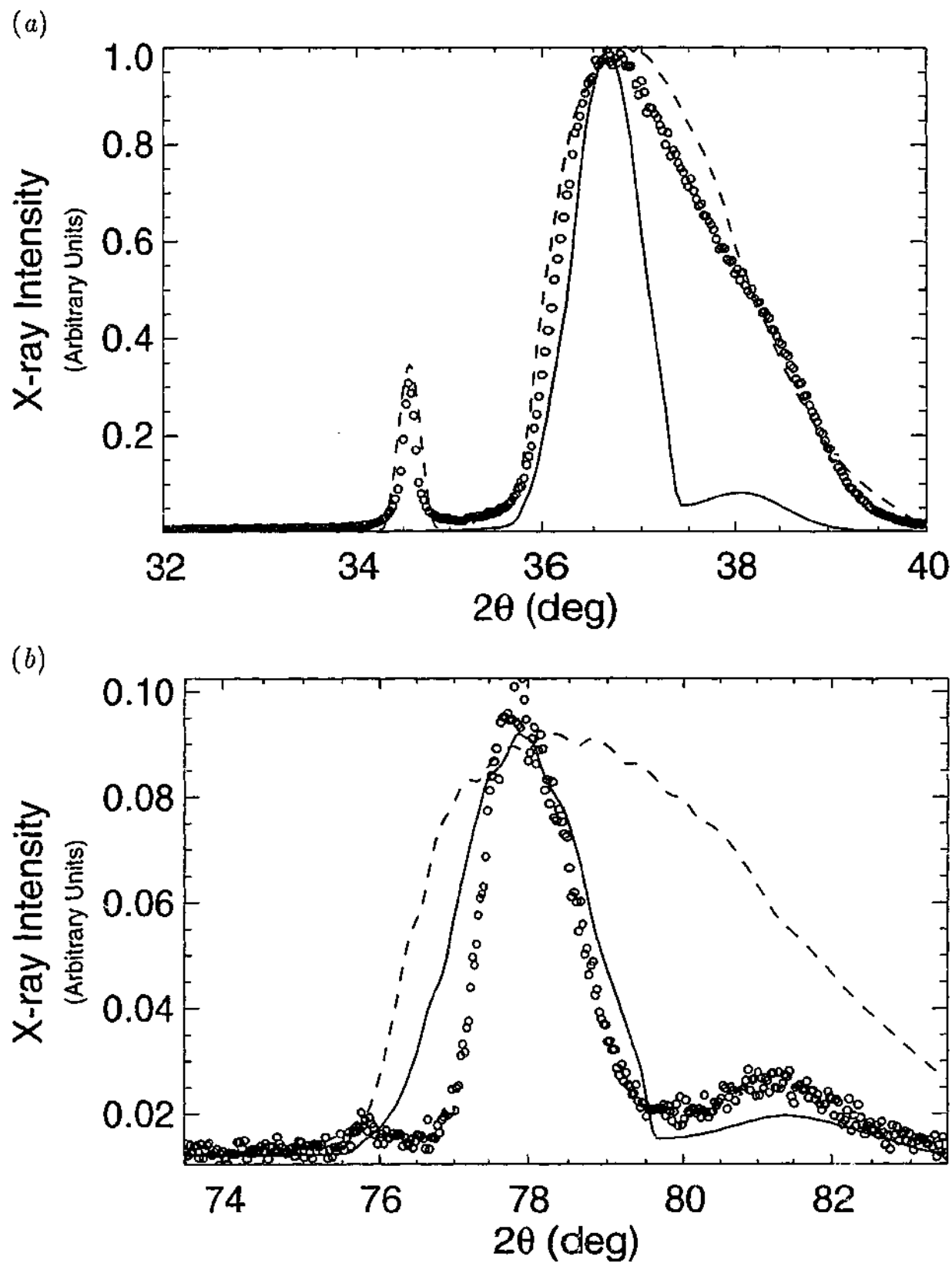


Figure 4.20: $\theta - 2\theta$ scans for sample C70. (a) (0002) reflection, and (b) (0004) reflection. This experimental data is denoted by circles (\circ). The solid line (—) is the simulated profile optimised to fit the (0004) reflection, and the dashed line (---) is the simulated profile optimised to fit the (0002) reflection. Experimental and simulation parameters are given in Tables 4.16 and 4.17, respectively. The strain profile and weighting are shown in Fig. 4.21.

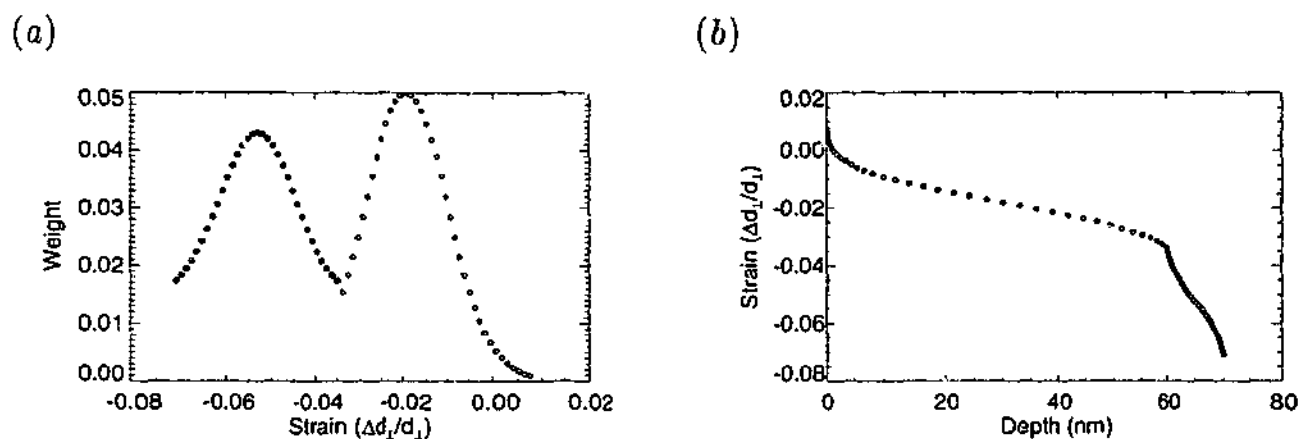


Figure 4.21: (a) Strain weighting, and (b) associated strain depth profile, optimised for the (0004) reflection. These were used for simulating sample type C70.

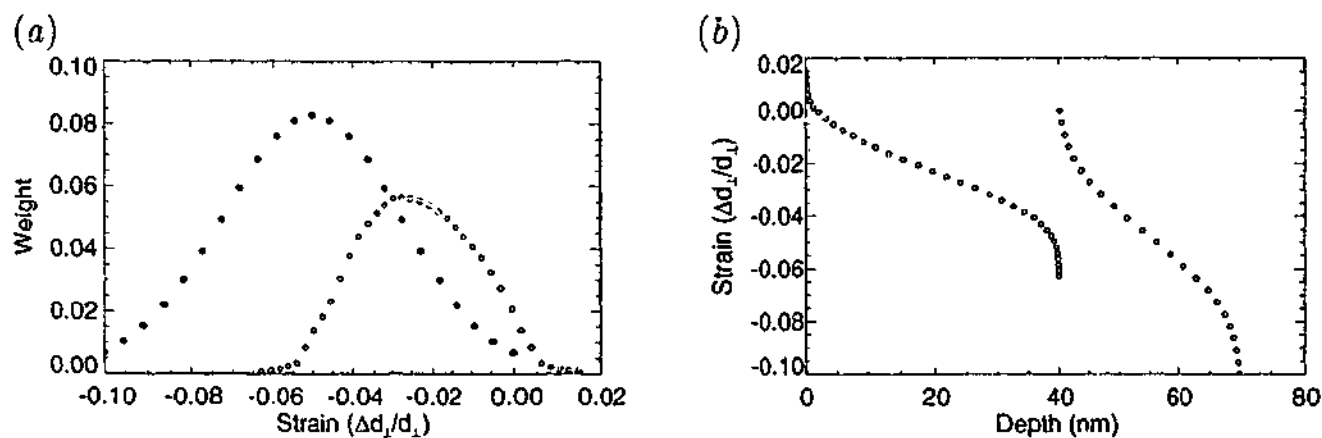


Figure 4.22: (a) Strain weighting, and (b) associated strain depth profile, optimised for the (0002) reflection. These were used for simulating sample type C70.

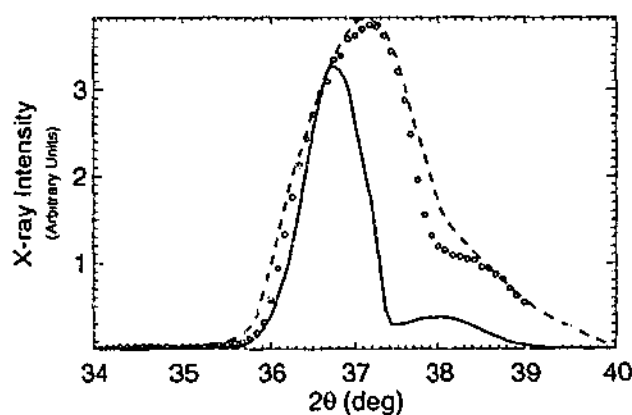


Figure 4.23: $\omega - 2\theta$ scan for sample C70 about AlN(0002), with $\Delta\omega = -1.42^\circ$. This experimental scan, denoted by circles (o) was extracted from the RSM shown in Fig. 4.19(d). The solid line (—) is the simulated profile optimised to fit the (0004) reflection, and the dashed line (---) is the simulated profile optimised to fit the (0002) reflection.

Table 4.17: Simulation parameters for sample C70, optimised for the (0004) reflection in the $\theta - 2\theta$ scan (with strain distribution).

Material	Layer Parameters				Block Parameters		
	Thickness (nm)	Tilt (deg)	Lat. Strain	Perp. Strain	Lat. Size (nm)	Perp. Size (nm)	Misorientation (deg)
AlN	60	-1.28	—	-0.018	100	60	2
AlN	10	-1.45	—	-0.053	100	10	2
GaN	—	-0.18	—	0	30	30	1

Table 4.18: Simulation parameters for sample C70, optimised for the (0002) reflection in the $\theta - 2\theta$ scan (with strain distribution).

Material	Layer Parameters				Block Parameters		
	Thickness (nm)	Tilt (deg)	Lat. Strain	Perp. Strain	Lat. Size (nm)	Perp. Size (nm)	Misorientation (deg)
AlN	40	-1.39	—	-0.024	100	40	2
AlN	30	-1.37	—	-0.050	100	30	2

(as was observed for sample C30). The RSM for sample C70 (Fig. 4.19(d)) confirms that the peak is rotated. The peak rotation is probably due to the structure of the sample, not an instrumental effect. The $\theta - 2\theta$ scan collected before the RSM, and the $\theta - 2\theta$ scan extracted from the RSM, match one another. Furthermore the GaN peak was not rotated in the q_z - q_z plane. These observations rule out experimental drift as the cause of the peak rotation (the same conclusion was reached for sample C30).

The (0002) simulation (dashed line) matches the $\theta - 2\theta$ (Fig. 4.20(a)) and $\omega - 2\theta$ (Fig. 4.23) scans closely, as do each of the ω scans near the (0002) reflection (Fig. 4.24(a),(b), and (c)). The RSM has also been reproduced (Fig. 4.19(c) and (d)). However, this simulation produced a peak too wide for the (0004) scan (see Fig. 4.20(b)). A similar effect was seen for sample C30, where the simulation used a strain distribution that was too wide for the (0004) scan. This suggests that reconstructing peak widths in the q_z direction, using only the strain distribution described in Sec. 3.3.2, cannot fit two different reflections simultaneously.

A $\theta - 2\theta$ scan of the (0004) reflection shows that the two AlN peaks are clearly resolved (see Fig. 4.20(b)). The simulation, optimised to fit the (0004) reflection,

shows two separate peaks for both the (0002) and (0004) reflections. The ω scans for the (0004) reflection are not fitted well, particularly the large AlN peak (see 4.24(e)). However, the small AlN peak is matched well by the simulated scan (see 4.24(f)). A poor fit to the ω scan for the (0004) reflection was also seen for sample C30. The reason for this is unclear.

The GaN peak has been fitted well for both the ω and $\theta - 2\theta$ scans as shown in Figs. 4.24(d) and 4.20(a), respectively. However, in order to fit this peak relative to the peak AlN the GaN layer needs to be made exceptionally thin in the simulation, thinner than the perpendicular block size required to generate the correct peak width in the $\theta - 2\theta$ scan. This effect was also seen for sample C30, and is not understood. The simulation parameters for GaN are given in Table 4.17.

The peak position for both the (0002) and (0004) reflections is determined by the atomic plane spacing perpendicular to the sample surface. Hence there is a fixed relationship between the peak position for the (0002) and (0004) reflections, namely

$$\theta_{0004} = \sin^{-1}(2 \sin(\theta_{0002})) , \quad (4.2)$$

where $2\theta_{0002}$ and $2\theta_{0004}$ are the 2θ positions of the Bragg peaks for the (0002) and (0004) reflections, respectively. However, the peak positions observed for the $\theta - 2\theta$ scan of the (0004) reflection did not match the positions from (0002) scan (a similar effect was seen for sample C30). The shift was approximately 3.1° in 2θ (for C30 it was about 3.5°). The origin of this shift is unknown, and is possibly due to some calibration error.

Two sub-layers were utilised in modelling the AlN layer for C70 (whereas C30 used only one). The strain-weight distributions (Figs. 4.21 and 4.22) show two separate peaks; the discontinuity in the strain-depth profile indicates the interface between the two layers. The average strains and tilts are reported in Tables 4.17 and 4.18. As is expected these are the same for the two simulations. The major difference between the model optimised for the (0002) and (0004) reflections is the relative thicknesses of the two sub-layers. The model optimised for the (0002) reflection uses similar thicknesses for the two sub-layers, which leads to two peaks with similar intensities. This produces the broad double peak observed for this reflection in the $\theta - 2\theta$ scan (see Fig. 4.20). The model optimised for the (0004) reflection used very different layer thicknesses, in order to produce two peaks with different intensities. Interestingly, the dislocation density is $2 \times 10^{10} \text{cm}^{-2}$, which is two orders of magnitude smaller than for the C30 sample.

This sample highlighted the importance of measuring multiple reflections for one sample. The affect different mosaic block parameters have on the peak shape varies

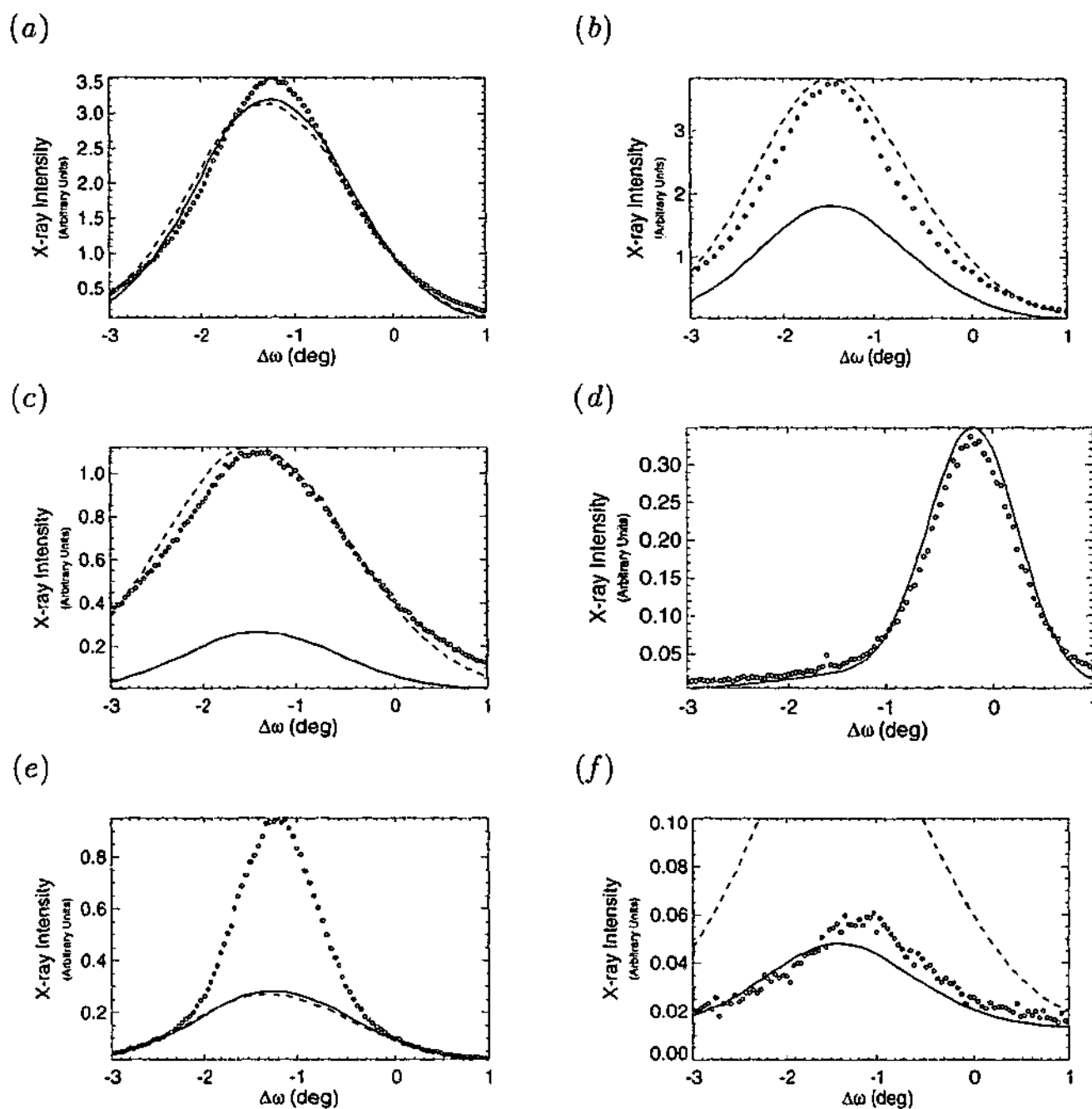


Figure 4.24: ω scans for sample type C70. (a) $2\theta = 36.6368^\circ$, (b) $2\theta = 37.167^\circ$, (c) $2\theta = 38.4167^\circ$, (d) $2\theta = 34.5556^\circ$ (the GaN peak), (e) $2\theta = 74.8244^\circ$, and (f) $2\theta = 78.13^\circ$. The circles (o) represent the experimental data. The solid line (—) is the simulated profile optimised to fit the (0004) reflection, and the dashed line (---) is the simulated profile optimised to fit the (0002) reflection.

depending on the reflection being investigated. By simultaneously fitting multiple reflections there is a tighter constraint on the fitting parameters.

4.4 Sample Series D: InGaN Grown on GaN/AlN Buffer Layers

X-ray diffraction measurements on InGaN allow the layer composition and strain to be determined (see e.g., Fewster, 1996; Schuster *et al.*, 1999). These important parameters directly impact on the bandgap and hence affect the emission wavelength of the semiconductor (O'Donnell *et al.*, 2001). Various methods for extracting the strain and composition using the peak positions of symmetric and/or asymmetric reflections have been reported in the literature (see e.g., Krost *et al.*, 1999; Schuster *et al.*, 1999; O'Donnell *et al.*, 2001; Vickers *et al.*, 2003).

Here we describe the analysis for the type D samples. Each of these samples had a 30 nm LT-AlN buffer layer and a 2 μm GaN buffer layer. Three different InGaN top layers were investigated: 20 nm $\text{In}_{0.05}\text{Ga}_{0.95}\text{N}$, 20 nm $\text{In}_{0.30}\text{Ga}_{0.70}\text{N}$ and 200 nm $\text{In}_{0.42}\text{Ga}_{0.58}\text{N}$. Table 4.19 summarises the scan parameters for the type D samples.

The statistical diffraction theory is used in conjunction with a mosaic block model to probe the defect structure of the material. The statistical diffraction theory, developed in Sec. 2.8.3, can also be used to model the strain and composition. However, it is simpler to calculate the strain and composition directly from the peak positions using the elastic stiffness constants, and use statistical diffraction theory to calculate the statistical parameters (i.e., mosaic block size and misorientation). The strain quoted in the statistical diffraction analysis assumes the composition of the layer is equal to its nominal value, and hence it incorporates the peak shift due to strain and composition.

The experimental scans collected for the type D samples have much improved signal to noise ratio compared to the other sample types. This can be directly attributed to the increased X-ray intensity due to the absence of the analyser crystal

Table 4.19: Experimental scan parameters used for samples of type D.

Parameter	Value
Wavelength	1.5406 nm
Entrance slit horizontal size	2.0 mm
Entrance slit vertical size	0.2 mm
Detector slit horizontal size	10 mm
Vertical divergence at sample	20 arcsecond
Raw count rate at sample	Unknown ^a
Count time per point	1 second

^aIntensity was too large to measure with a photon counting detector.

and secondary monochromator. A slit system was used in front of the detector to restrict the angular range. The horizontal size of the slit was 10 mm. Three different vertical slit sizes were used during the experiment: 0.5 mm, 1 mm, and 10 mm. This equates to an angular window of approximately 0.08° , 0.15° , and 1.5° , respectively (for a sample-to-detector distance of 0.37 m). The angular window of the analyser crystal used with the previous samples was ≈ 9 arcseconds; hence the increased signal to noise ratio comes at the expense of angular resolution. However, as the reflections are very broad it was decided that an increased count rate was more important than high angular resolution.

Throughout the following sections 'narrow slit' refers to the 0.5 mm slit, and 'wide slit' refers to the 10 mm slit. The 1 mm slit was only used for selected scans about the (11.4) reflection and is referred to explicitly when used.

The maximum intensity of the diffraction peaks was several orders of magnitude larger than the features of interest in the wings of the diffraction profile (such as the thickness fringes). However, the dynamic range of the detector system was not adequate to collect all of the data in one scan. In a number of cases several scans were collected for a single reflection and scan type, using various beam attenuators. Beam attenuation was achieved using different combinations of three aluminium filters of various thicknesses. The thicknesses of the aluminium filters were unknown, and could not be measured directly because they were installed in a sealed unit. The scans collected using different filters were matched empirically when they overlapped. This process involved plotting multiple sets of data on the same axes and applying a multiplying factor to the 'attenuated scan' until it matched the base scan in the region where the two scans overlapped. If the overlapping region was near the background level of one of the scans, an approximate background count was subtracted (in most cases this was not critical), so that the scans fitted together correctly. Care was needed when matching scans in regions where the intensity was close to saturating the detector because the count rate was not linear. Typically filter #1 reduced the incident intensity by a factor of 3.5, filter #2 by a factor of 40, and filter #3 by a factor 900. These values were determined by comparing scans with various combinations of filters.

An example of a composite scan is given in Fig. 4.25. The different colours represent separate scans. The peak region (red and black) was collected using two different filter combinations to prevent saturation. There is an abrupt change in peak shape where the green and red scans meet, which suggests an error in the matching of the scans. However, as the inset in Fig. 4.25 shows, the red scan matches the green scan throughout this region, hence the discontinuity at $2\theta = 35^\circ$

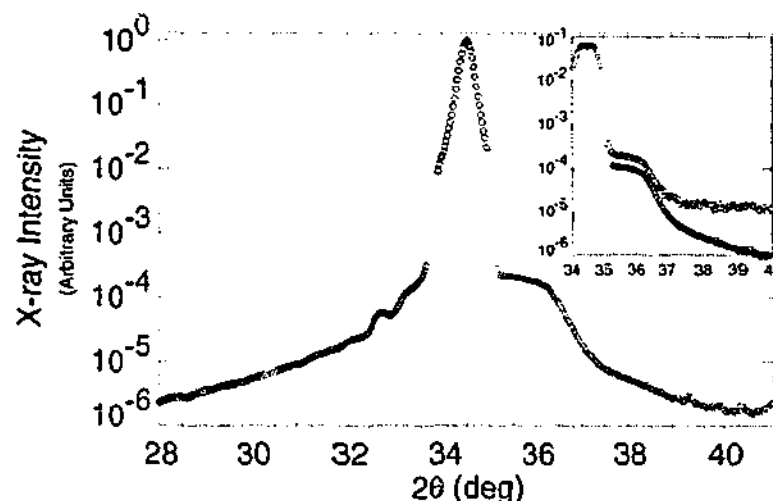


Figure 4.25: An example of a composite scan. The blue and green scans were collected using a non-attenuated X-ray beam; the red and black scans used different combinations of filters, and hence had to be normalised to the other scans. The inset shows the overlap region for the green and red scans, with the green scan deliberately offset so as to clearly see the shape of both scans.

is due to the sample and instrumental effects.² The green scan in the inset was offset vertically for clarity. Note that the red scan becomes constant at about $2\theta = 37.7^\circ$, unlike the green scan. This is because the background noise generated in the detector electronics (i.e., background not due X-rays) is a larger fraction of the count rate for the red scan, than for the green scan.

The experimental scans collected using a filter had to be scaled by the attenuation factor for the appropriate filter, or combination of filters. (The values quoted above were used if the experimental evidence did not suggest otherwise). Most composite scans were already based on a non-attenuated beam intensity, and hence were not modified. After the attenuation was taken into account the experimental and simulated scans were normalised in two different ways. For the first normalisation method an experimental peak was chosen and normalised to a height of unity. All other experimental scans were then normalised using the same factor (thus ensuring the relative peak heights were preserved). Then a simulated profile was chosen and normalised to an experimental peak, with all other simulated scans normalised with the same factor. Hence the relative peak heights are also preserved for the simulated profiles thereby allowing the scans to be assessed relative to each other.

²The scan in Fig. 4.25 was collected using a wide (10 mm) detector slit. The discontinuity is due to the very intense Bragg peak from the $2\ \mu\text{m}$ GaN layer. This causes the rapid increase in intensity. The shoulder to the right of the discontinuity is the AlN peak.

This was done separately for each sample and slit width. For the second normalisation method the simulated profiles were normalised for each scan separately - thus allowing the peak shapes to be assessed.

An important feature seen in the diffraction profiles is the so called thickness fringes. For perfect layers these fringes originate from interference of the beams diffracting from the top and bottom surfaces of a layer of crystal. Oscillations of this kind indicate high quality parallel interfaces. Since our samples have high defect densities it is not likely that the interference is between the beams diffracting from the top and bottom of the layer, but rather from an object thinner than the layer. For the mosaic block structure assumed for our samples (see Sec. 2.9), the simulated oscillations are determined by the mosaic block size perpendicular to the sample surface. The oscillations generated by the simulation have a greater amplitude than is evident in the experimental scans because for real samples the blocks are not all the same size and the top and bottom of the blocks are not perfectly parallel. Including these imperfections would dampen the oscillation. It is possible to incorporate a distribution of block sizes into the simulation, however, this significantly increases the execution time for the simulation, and is of limited utility because a distribution of block sizes is not solely responsible for dampening the oscillations. Including additional parameters to improve the fit without a well founded empirical reason does not benefit the analysis. The oscillations were dampened for the scans collected using a wide detector slit because of the inherent averaging over a large region of reciprocal space. In fact the presence of thickness fringes can be exploited to allow the mosaic block size perpendicular to the sample surface to be determined quickly and accurately.

For thick layers (or mosaic blocks) the thickness fringes will have a very small angular period. This imposes limits on the minimum angular resolution required of the detector system. It is possible that thickness fringes from the GaN layer may have been present, but not observed. The 2 μm layer thickness equates to a fringe period (in q - space), of approximately $q = 2\pi/2000 = 0.003 \text{ nm}^{-1}$, whence the angular spacing (for $\lambda = 1.5405 \text{ \AA}$) is 8 arcseconds (if the height of the mosaic blocks was the full thickness of the layer). This is at the limit of our high resolution apparatus (which is ≈ 7 arcseconds), which was used for sample types A and B. If the mosaic block height was smaller, then the fringes may have been observable with the high resolution system, and would have assisted in determining the mosaic block size perpendicular to the sample surface.

The background count was a function of the slit size, filters, and the angular position of the detector. For each scan this was either determined by observing the

peak shape and noting if a constant value was reached at the extremities (for wide scans), or by fitting the peak wings with a Lorentzian profile. In many cases the features of interest were of sufficient intensity that the background could be neglected. Where the background count was significant a constant value was added to the simulated scan, rather than subtracted from the experimental profile. Subtracting the background from an experimental scan accentuates noise when plotting on a logarithmic scale. The background will mask any oscillations that would otherwise have been apparent, and on a logarithmic scale adding a background to the simulation scan does likewise.

The $\theta - 2\theta$ scans, ω scans, and RSMs, displayed throughout this chapter use a logarithmic scale for the ordinate axis (i.e., X-ray intensity). This accentuates the peak shapes and allows low intensity features to be displayed simultaneously.

4.4.1 Sample D05: 20 nm $\text{In}_{0.05}\text{Ga}_{0.95}\text{N}$

Sample D05 was the same as sample C30 except that the GaN layer was 2 μm thick and a 20 nm top layer consisting of $\text{In}_{0.05}\text{Ga}_{0.95}\text{N}$ was present. The low InN content ensured that the InGaN layer would be of a relatively high quality, and its peak is expected to be close to the GaN peak. In fact, as shown in Fig. 4.26 the GaN and InGaN peaks overlapped, although their different peak shapes ensured they could be distinguished from one another.

The experimental scan parameters are given in Table 4.20. In addition to the earlier specifications, the vertical size of the slit in front of the detector, and the combination of filters used to attenuate the incident beam are included in the table. Table 4.21 summarises the composite scans constructed from those in Table 4.20.

A large amount of data was collected for sample D05, encompassing three reflections: (0002), (0004), and (11 $\bar{2}$ 4). The $\theta - 2\theta$ scans were collected with a 10 mm and 0.5 mm wide vertical slit in front of the detector; the ω scans and RSMs used a 0.5 mm slit only. The scans collected with the 10 mm slit were normalised to the GaN(0002) peak in the $\theta - 2\theta$ scan. The scans collected with the 0.5 mm wide slit were normalised to the InGaN(0002) peak in the $\theta - 2\theta$ scan. For this sample only homogeneous layers were considered in the simulation, i.e., no strain, tilt, or misorientation distributions were required to fit the data.

Figures 4.26 and 4.27 show the $\theta - 2\theta$ scans for the (00. l) reflections.³ A reliable composite profile for the (0002) reflection was impossible to produce using the $\theta - 2\theta$

³The notation (00. l) means the scans of type (000 l) where l is any integer. For the Group III nitrides the reflections for l =odd are forbidden (not present). The (00. l) reflections are also known as symmetric reflections.

Table 4.20: Experimental scan parameters for sample D05. This sample includes a 20 nm thick $\text{In}_{0.05}\text{Ga}_{0.95}\text{N}$ layer.

Sample No.	Reflection	Scan Type	Detector. slit (vert.) (mm)	Filter	Step size (arcsecond)	Range (deg)
D05:1	(0002)	$\theta - 2\theta$	10	#1,#2	2θ : 108	2θ : 31.0-41.5
D05:2		$\theta - 2\theta$	10	#1,#3	2θ : 108	2θ : 32.4-36.0
D05:3		$\theta - 2\theta$	10	#1,#3	2θ : 108	2θ : 41.5-42.0
D05:4		$\theta - 2\theta$	10	#1,#3	2θ : 36	2θ : 41.5-42.0
D05:5		$\theta - 2\theta$	10	None	2θ : 108	2θ : 28.0-33.9
D05:6		$\theta - 2\theta$	10	None	2θ : 108	2θ : 35.3-41.0
D05:7		$\theta - 2\theta$	0.5	#3	2θ : 108	2θ : 26.0-37.4
D05:8		$\theta - 2\theta$	0.5	None	2θ : 108	2θ : 26.0-28.0
D05:9		$\theta - 2\theta$	0.5	None	2θ : 108	2θ : 37.4-40.0
D05:10		ω ($2\theta = 32.3058^\circ$)	0.5	None	ω : 36	$\Delta\omega$: ± 1
D05:11		ω ($2\theta = 32.8212^\circ$)	0.5	None	ω : 36	$\Delta\omega$: ± 1
D05:12		ω ($2\theta = 33.1852^\circ$)	0.5	None	ω : 36	$\Delta\omega$: ± 1
D05:13		RSM	0.5	None	ϵ : 109 $\Delta\omega$: 113	$\epsilon + 2\theta_B$: 28.0-37.4 $\Delta\omega$: ± 0.345
D05:14	(0004)	$\theta - 2\theta$	10	#1,#3	108	2θ : 34.0-81.0
D05:15		$\theta - 2\theta$	10	#1,#3	108	2θ : 66.0-78.0
D05:16		ω ($2\theta = 68.986^\circ$)	0.5	None	ω : 36	$\Delta\omega$: ± 1
D05:17		ω ($2\theta = 68.257^\circ$)	0.5	None	ω : 36	$\Delta\omega$: ± 1
D05:18		ω ($2\theta = 67.771^\circ$)	0.5	None	ω : 36	$\Delta\omega$: ± 1
D05:19		RSM	0.5	None	ϵ : 219 ω : 113	$\epsilon + 2\theta_B$: 62.0-75.0 $\Delta\omega$: ± 0.345
D05:20	(11 $\bar{2}$ 4)	$\theta - 2\theta$	10	#1	2θ : 216	2θ : 94.9548 -100.9548
D05:21		$\theta - 2\theta$	10	#3	2θ : 208	2θ : 99.3548 -101.9548
D05:22		ω ($2\theta = 99.9548^\circ$)	10	#3	$\Delta\omega$: 72	$\Delta\omega$: ± 1
D05:23		RSM	1	#3	ϵ : 216 ω : 144	$\epsilon + 2\theta_B$: 89.9548 -101.9548 $\Delta\omega$: -1.5 - 0.5

Table 4.21: Summary of the composite scans for sample D05. The supplementary scans are multiplied by the attenuation factor to match them to the base scans.

No.	Base Scan		Supplementary Scan		
	Scan No.	Filter	Scan No.	Filter	Atten. Factor
D05:C1	D05:5,D05:6	None	D05:1	#1,#2	75
			D05:2,D05:4	#1,#3	3150
D05:C2	D05:13	None	D05:7	#3	900
D05:C3	D05:20	#1	D05:21	#3	800

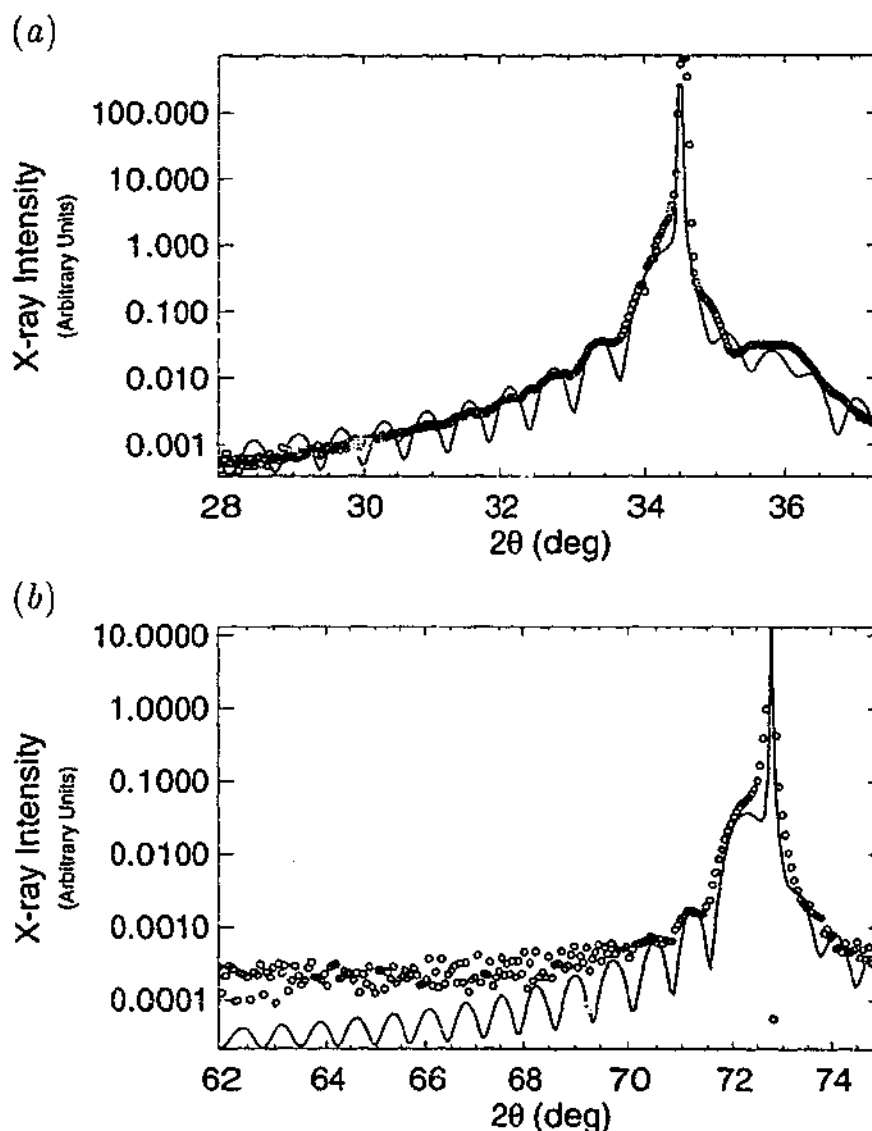


Figure 4.26: Experimental profile (\circ) and simulated profile ($—$) for the $\theta - 2\theta$ scans for sample D05 using a narrow (0.5 mm) slit. (a) (0002) reflection, and (b) (0004) reflection. The (0002) profile is a composite scan (D05:C2) from Table 4.21. The gap in the (0002) experimental profile at approximately $2\theta = 34^\circ$ is due to the detector saturation. The (0004) profile is scan D05:19 from Table 4.20.

scans collected using the narrow slit because the region immediately either side of the GaN peak was not covered adequately. Specifically the non-attenuated scans (D05:8 and D05:9) did not extend close enough to the GaN peak, and the central scan (D05:7) was too severely attenuated in that region. The attenuated scan shows the periodic noise described in Sec. 4.6. A composite profile was constructed (see Fig. 4.26(a)), using the central line from the RSM collected for the (0002) reflection (see Fig. 4.28(a)) and the attenuated scan. However, there is a small angular range (at about $2\theta = 34^\circ$) for which the detector was non-linear (due to saturation), and the attenuated scan was at the background level. This is observed as a gap

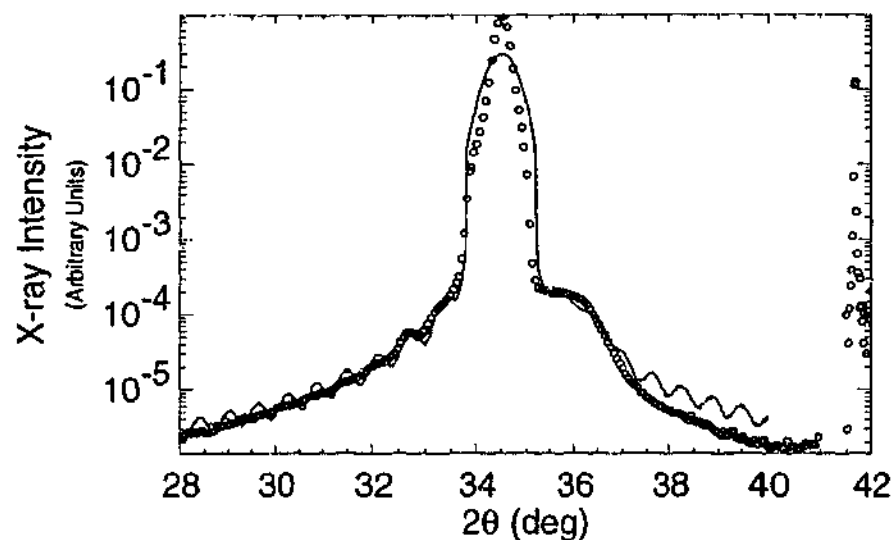


Figure 4.27: Experimental (o) and simulated (—) profiles for $\theta - 2\theta$ scans about the (0002) reflections for sample D05 using a 10 mm slit. The experimental profile is the composite scan D05:C1 in Table 4.21. The narrow peak at approximately $2\theta = 41.5^\circ$ is the sapphire (0006) reflection.

in the experimental scan in Fig. 4.26(a). The (0004) scan in Fig. 4.26(b) was extracted from the RSM collected about the (0004) reflection (Fig. 4.28(c)) because no dedicated $\theta - 2\theta$ scan was collected with a narrow slit about the (0004) reflection. The $\theta - 2\theta$ scans, collected about the (0002) reflection using a wide slit in front of the detector are a composite of several scans (see Fig. 4.27).

A closer examination of the two $\theta - 2\theta$ scans, collected using the narrow slit (Fig. 4.26), shows four features of interest: an intense narrow peak at $2\theta \approx 34.6^\circ$ for the (0002) reflection and 72.8° for the (0004) reflection, a wider peak at $2\theta \approx 34.2^\circ$ for the (0002) reflection or 72° for the (0004) reflection (overlapping with the narrow peak), a shoulder to the right of the narrow peak (only seen in the (0002) scan at about $2\theta = 36^\circ$), and small oscillations to the left of the wider peak. The narrow peak is undoubtedly due to the GaN layer, which is comparatively thick. The peak immediately to the left of the GaN peak is the InGaN peak. This is confirmed by its position in the $\theta - 2\theta$ scan. The InGaN layer is two orders of magnitude thinner than the GaN layer, hence the peak is far wider. The shoulder to the right of the GaN peak is the AlN peak, which is also confirmed by its peak position. Finally, the oscillations seen to the left of the InGaN peak are thickness fringes arising from the InGaN layer (they would also appear to the right of the InGaN peak, however they are obscured by the GaN peak).

Each of the four features has been fitted approximately by the simulations (see Fig. 4.26). The peak positions, as well as the period and maximum intensity of

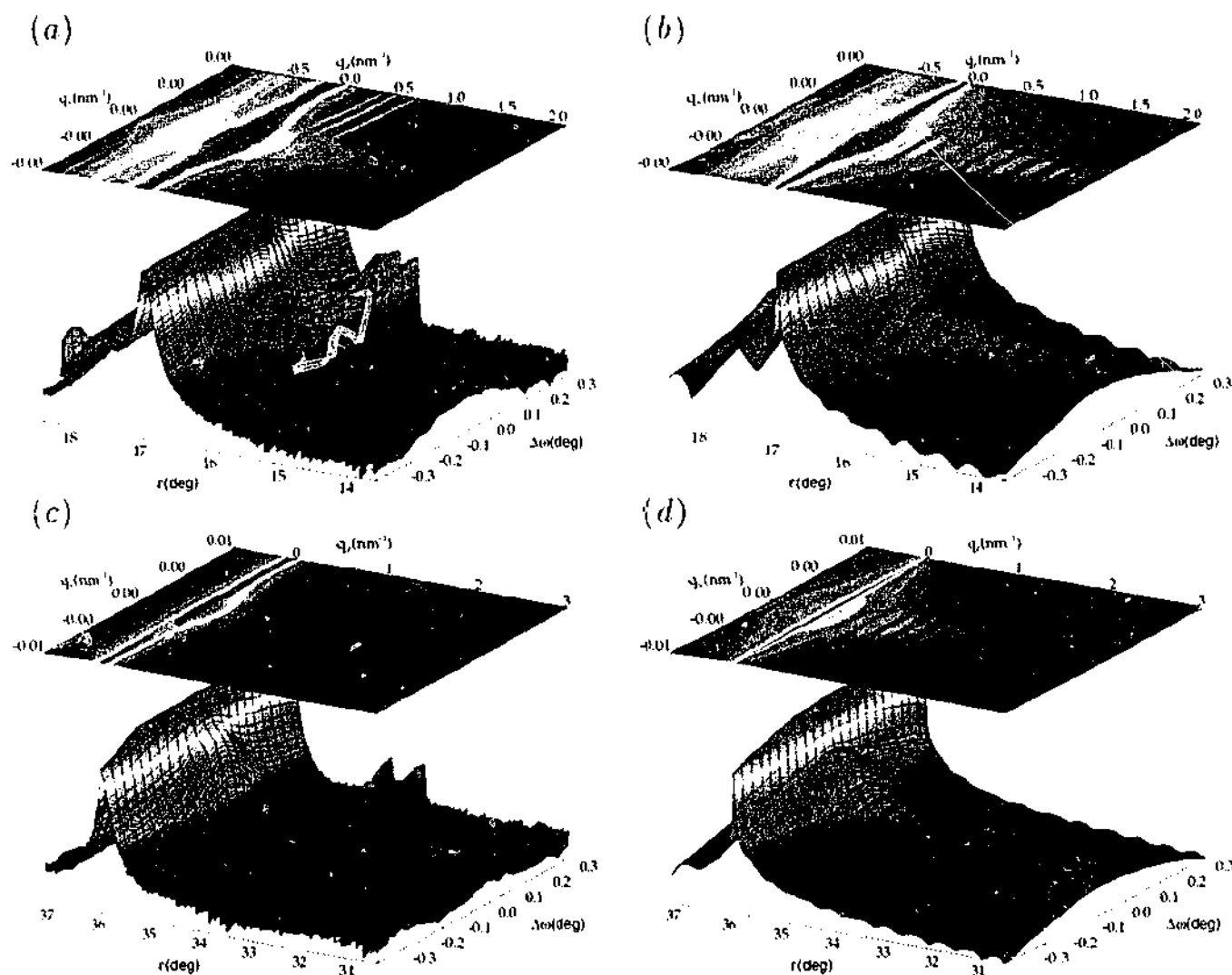


Figure 4.28: Reciprocal space maps for sample D05. (a) Experimental RSM, and (b) simulated RSM about the GaN(0002) reflection; (c) experimental RSM and (d) simulated RSM about the GaN(0004) reflection. The simulated RSMs have been scaled so that the InGaN peak heights match the experimental data.

the thickness fringes, agree well with the simulated data. It is encouraging that the simulated InGaN peak height agrees with the experimental data for the (0004) reflection, because it suggests that the simulation correctly determines the change in diffracted intensity between the different reflections. However, there are some notable discrepancies between the experimental and simulated data, e.g., the 'bulge' on the right hand side of the GaN(0002) peak (at about $2\theta = 34.8^\circ$), the height of the GaN peak, the amplitude of the thickness oscillations, and the shape of the AlN peak. The 'bulge' in the peak shape at 34.8° is discussed below. The GaN peak is narrow and very intense, thus detector saturation and/or a large step size (compared to peak width) may have prevented the true peak height from being measured. The origin of the large amplitude thickness fringes was discussed in the previous section. Apart from not matching the thickness fringes correctly, the large

oscillations strongly distort the appearance of the AlN layer peak.

The $\theta - 2\theta$ scan for the (0002) reflection collected using the wide (10 mm) slit has a different shape to the data obtained with the narrow slit (Fig. 4.27). In particular the GaN peak is much wider, and the InGaN peak cannot be resolved. However, the AlN peak and the thickness oscillations originating from the InGaN layer are apparent. An interesting feature of Fig. 4.27(a) is the very sudden drop in intensity on either side of the GaN peak. These abrupt changes (also seen in the simulated scans) are due to the very sharp (in reciprocal space) GaN peak entering and leaving the view of the detector. This allows the angular window of the slit system to be accurately determined from the experimental scan (this point is elucidated in Sec. 4.4.2). The $\theta - 2\theta$ scan for the (0004) reflection provided very little information because the filter attenuated the beam too severely; a plot has not been included.

The simulated $\theta - 2\theta$ scan matches the low intensity features of the $\theta - 2\theta$ scan for the (0002) reflection well. In particular the thickness oscillations agree with both the amplitude (at least near the peak) and period of the experimental data. Also the AlN peak shape is matched closely, unlike the narrow slit scan, because the simulated thickness oscillations have been damped by integration over reciprocal space. However, the full GaN peak shape has not been properly matched; the width at the base is correct, but the peak height as well as the width near the top of the peak are incorrect. For $\theta - 2\theta$ scans collected using an X-ray source with a small divergence and a detector with a small angular window (e.g., when an analyser crystal is employed) the peak width depends on the mosaic block size perpendicular to the sample surface and a distribution of strain or composition. However, when a detector with a wide angular window is employed, the detector integrates along a line in reciprocal space that is obtuse to the q_x -axis. Therefore the peak width also depends on features that affect the width of the peaks in the $\Delta\omega$ (q_x) direction (misorientation and lateral block size), and also the size of the detector slit (refer to Sec. 4.4.2 for a discussion of the effects of the detector slit width). The simulated $\theta - 2\theta$ scan may match the experimental data more closely by narrowing the simulated GaN peak in the $\Delta\omega$ direction by reducing the misorientation, or increasing the mosaic block size parallel to the sample surface. Usually the misorientation or lateral block size is determined by simulating the ω scans and comparing with experimental profiles. However, a suitable dedicated ω scan was not available, and the GaN peak was saturated for the RSM (see Fig. 4.28(a)). Another scan that is influenced by the width of the GaN peak is the $\omega - 2\theta$ scan (for $\Delta\omega = -0.345^\circ$) shown in Fig. 4.29. This scan was extracted from the RSM shown in Fig. 4.28(a). The relative intensity of the GaN and AlN peaks in this scan is determined, in part, by their

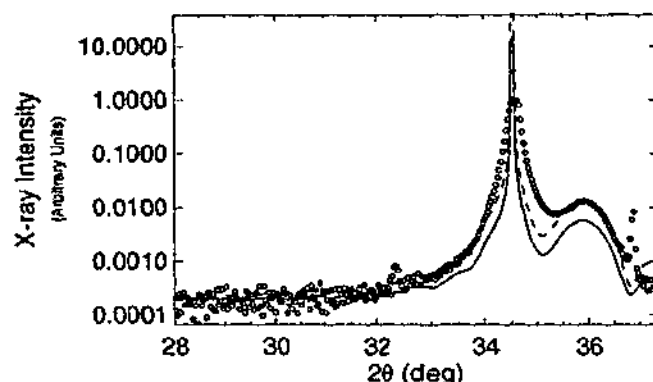


Figure 4.29: $\omega - 2\theta$ scan for sample D05 near Ga(0002). The experimental data (\circ) was extracted from the RSM for the (0002) reflection (see Fig. 4.28(a)). The solid line (—) is the simulation profile normalised using the same factor as for Fig. 4.26(a), and the dashed line (---) is the simulation profile normalised such that the experimental and simulated AlN peaks heights are the same.

width in the $\Delta\omega$ scan. By decreasing the misorientation, or increasing the lateral block size (for the GaN layer) the relative intensity of the AlN peak in the $\omega - 2\theta$ scan increases. A compromise was required for the misorientation and block size so that the simulations of the $\omega - 2\theta$ scan (Fig. 4.29) and the $\theta - 2\theta$ scan collected using the wide slit (Fig. 4.27) were in reasonable agreement with the experimental scans. If we were to ignore the $\omega - 2\theta$ scan the model parameters could be adjusted so that the simulated $\theta - 2\theta$ scan (with the wide detector slit) is in better agreement with the experimental data. In fact all experimental scans could be matched more accurately by the simulated profiles if the parameters are optimised for each scan individually. Matching all scans simultaneously allows a more correct set of parameters to be determined for the sample.

The $\theta - 2\theta$ scans show a very sharp GaN peak, which suggests a high quality layer. The presence of thickness oscillations suggests that the InGaN layer is of reasonable quality because flat parallel interfaces are required for these oscillations to be produced. The AlN layer has the poorest quality since it produces a broad peak without thickness fringes. All three peaks are close to their relaxed positions, implying that only small strain is involved. The simulated scans for the (00*l*) reflections are strongly dependent on the mosaic block size perpendicular to the sample surface, the relative layer thicknesses, and the strain perpendicular to the surface. (For the wide detector scans the other fitting parameters have some effect as well, because the results are averaged over a large region of reciprocal space). The fit to the data suggests that the specific parameters used are reasonably accurate. These parameters are summarised in Table 4.22. The perpendicular mosaic block

Table 4.22: Simulation parameters for sample D05.

Material	Layer Parameters				Block Parameters		
	Thickness (nm)	Tilt (deg)	Lat. Strain	Perp. Strain	Lat. Size (nm)	Perp. Size (nm)	Misorientation (deg)
InGaN	20	-0.02	0.0	0.0025	400	15	0.1
GaN	2000	0	0.005	0.015	600	1500	0.35
AlN	30	-0.03	—	0.035	40	10	0.7

size for the InGaN layer is particularly accurate because it is determined from the period of the thickness oscillations.

Several ω scans were collected near the Ga(0002) and Ga(0004) reflections. These scans were used to investigate the three spurious peaks seen in the RSMs for this sample (see e.g., Figs. 4.28(a) and (c)). The origin of these peaks is unknown and they have not been simulated. The ω scans for the (0002) reflection also give information about the layers of interest and are shown in Figs. 4.30(a)-(c). Only the peak about $\Delta\omega = 0$ has been simulated. The dedicated ω scans for the (0004) reflection only show the spurious peaks and have not been reproduced here. Several ω scans were extracted from the RSM, for both the (0002) and (0004) reflections, in order to compare against the simulations. These are shown in Figs. 4.30 (d) - (f) and in Fig. 4.31. The ω scans at $2\theta = 32.3058^\circ$, 32.8212° , 33.1852° , and 33.8826° , provide a measure of the width of the InGaN peak in the q_x direction. These scans confirm that the InGaN layer is of a reasonable quality, with the peak width much narrower than those seen for the AlN layers investigated earlier. The ω scan at $2\theta = 36.0052^\circ$ has two superposed peaks. The narrower peak is from the InGaN layer and the broad peak from the AlN layer. This demonstrates that the AlN layer has a high mosaicity.

In general the ω scans collected about the (0002) reflection have been fitted well (ignoring the spurious peaks, which have not been simulated). The exception is the scan collected with $2\theta = 34.853^\circ$ (see Fig. 4.30(e)). This scan corresponds to the 'bulge' to the right of the GaN peak in the experimental $\theta - 2\theta$ scan for the (0002) reflection (Fig. 4.26(a)). This 'bulge' was not seen in the simulated $\theta - 2\theta$ profile. There are two components to the peak shape in Fig. 4.30(e); a narrow peak centred at approximately $\Delta\omega = 0.02^\circ$ and a broad low intensity profile. The narrow peak is likely due to the InGaN layer, since the layer tilt and peak width (in the $\Delta\omega$ direction) are the same as for the other peaks that are attributed to InGaN. However, the position (in the $\theta - 2\theta$ scan) and intensity of the 'bulge' rule

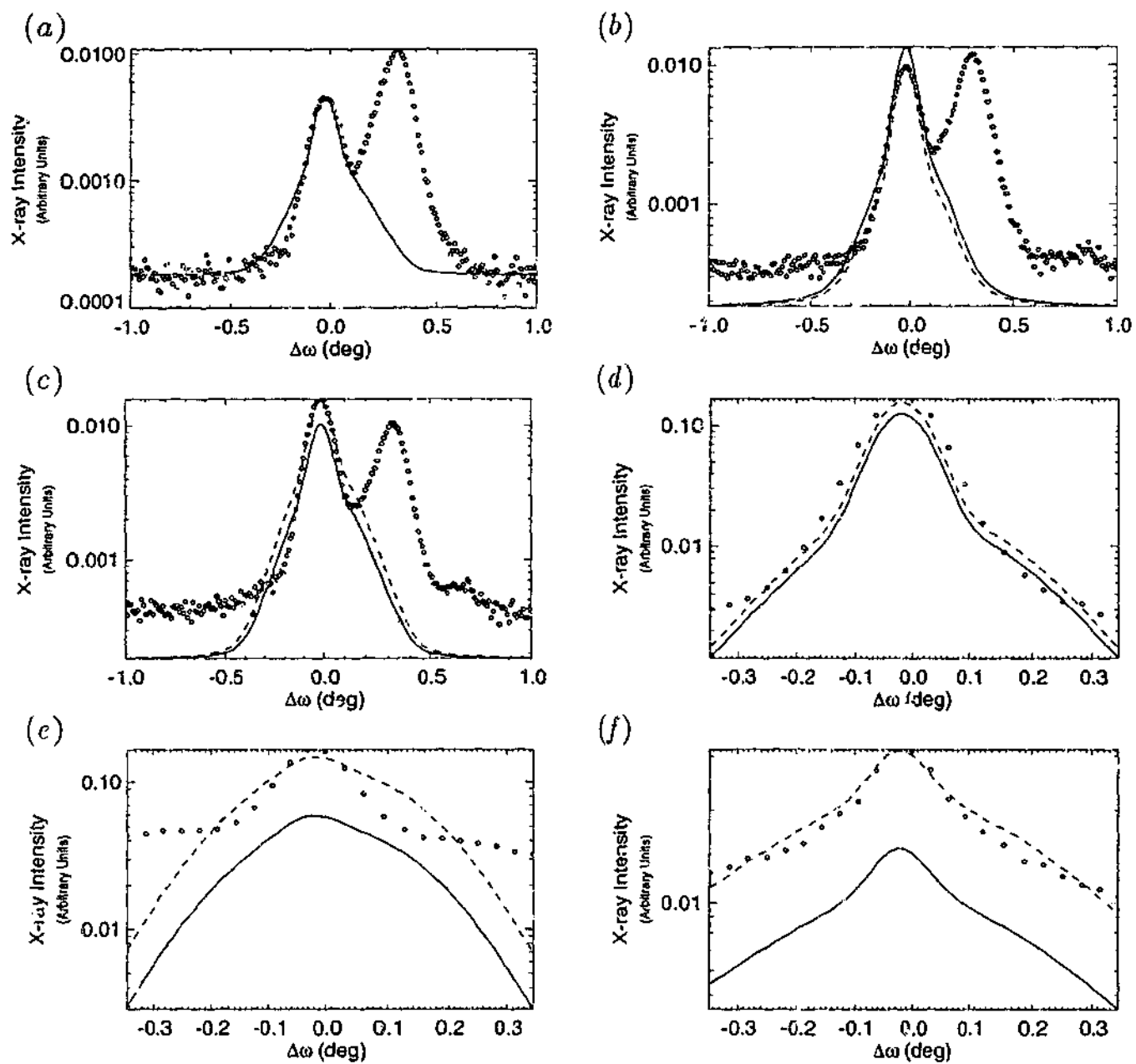


Figure 4.30: Experimental profiles (\circ) and simulated profiles (— and ---) for the ω scans near the GaN(0002) reflection for sample D05 (using a narrow slit). The solid line (—) uses the same normalisation factor as Fig. 4.26(a); the dashed line (---) is normalised to the experimental peak height. The 2θ positions for the scans are: (a) 32.3058° , (b) 32.8212° , (c) 33.1852° , (d) 33.8826° , (e) 34.853° , and (f) 36.0052° . Scans (a)-(c) were collected as dedicated ω scans using a narrow (0.5 mm) slit, and scans (d)-(f) were extracted from the RSM shown in Fig. 4.28(a).

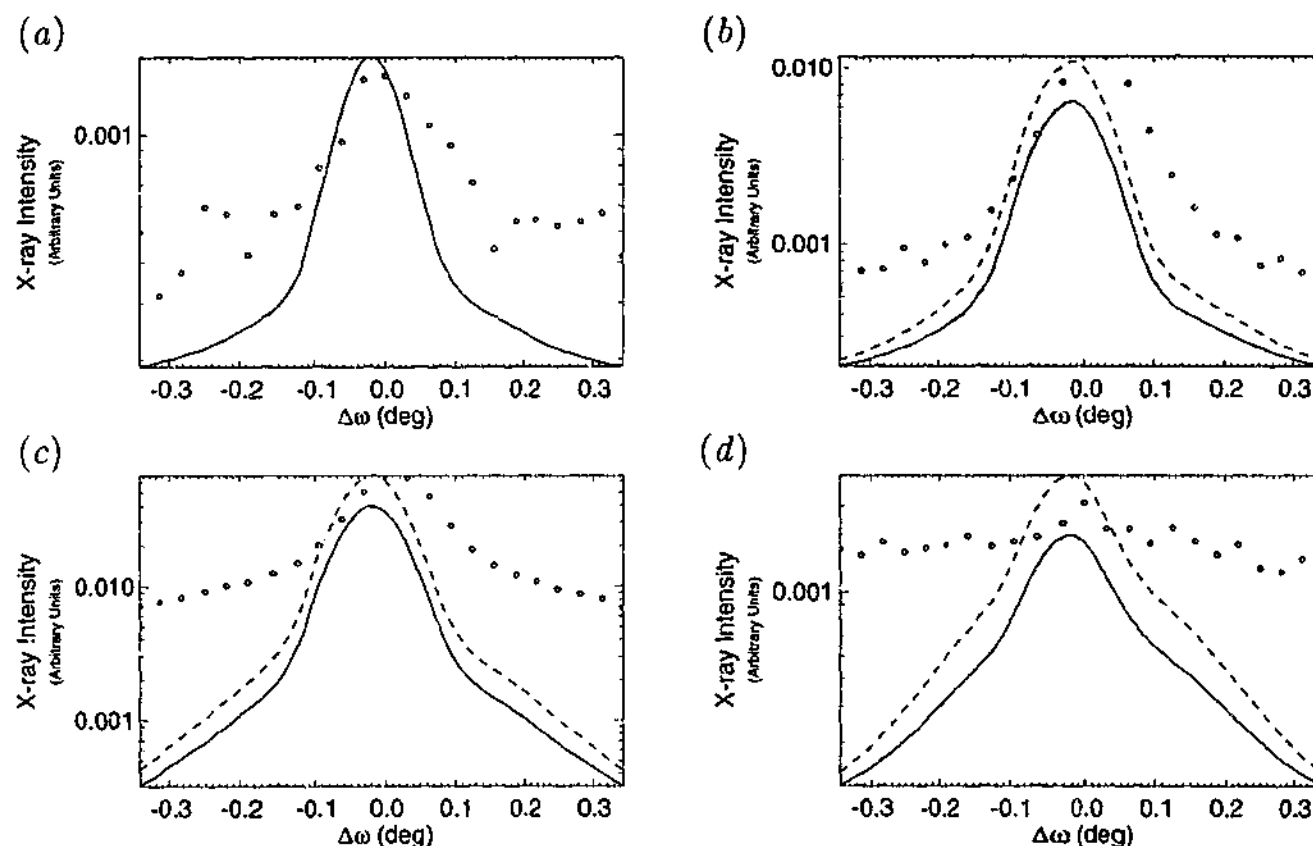


Figure 4.31: Experimental profiles (o) and simulated profiles (— and --) for the ω scans near the GaN(0004) reflection for the sample D05 (using a narrow slit). The solid line (—) uses the same normalisation factor as Fig. 4.26(a); the dashed line (--) is normalised to the experimental peak height. The 2θ positions for the scans are: (a) 71.355° , (b) 71.7802° , (c) 72.3878° , and (d) 73.542° . These scans were extracted from the RSM shown in Fig. 4.28(c).

it out as being a part of the main InGaN layer peak or a thickness oscillation. The discrepancy may be due to detector saturation, or some feature of the sample that has not been taken into account.

The two simulated ω scans near the GaN(0004) reciprocal lattice point have the correct shape and relative intensity; however they are slightly offset in the $\Delta\omega$ direction. This is a minor effect that has not been explored. It is possibly a slight calibration problem resulting from drift during the experiment, or perhaps it arises from a change in the average tilt. The latter can result when the size of the illuminated region decreases as we change from the (0002) to (0004) reflection.

The RSMs for the (00*l*) reflections are shown in Fig. 4.28. The most obvious difference between the simulation and experiment is the increased range and amplitude of the thickness fringes. A constant intensity has been added to each of the simulated RSMs to match the background intensity of the experimental data, and the simulations have been truncated to emulate the effect of detector saturation. This

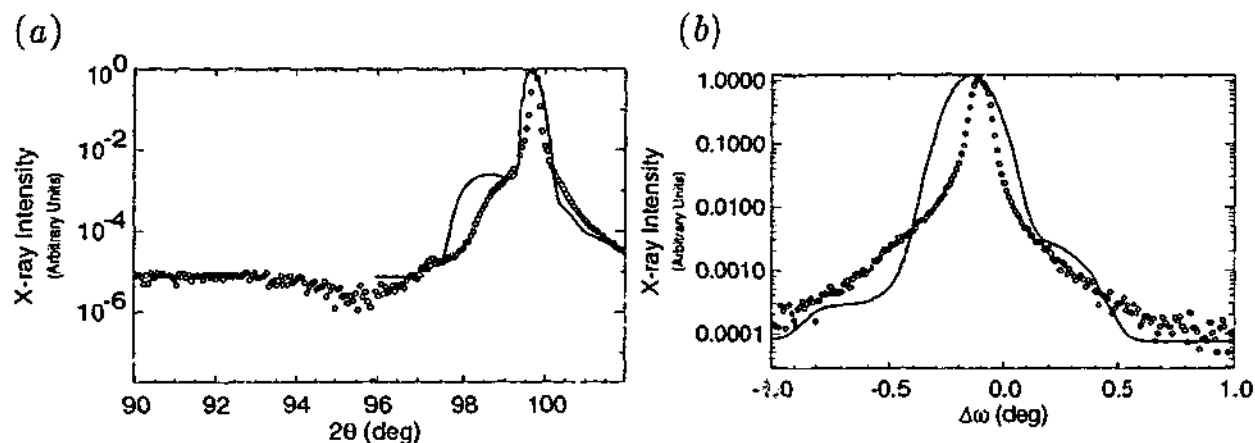


Figure 4.32: Experimental (\circ) and simulated (—) profiles for the $(11\bar{2}4)$ reflection. (a) $\theta - 2\theta$ scan and (b) ω scan.

ensures the simulated RSMs have the same 'dynamic range' as the experimental RSMs, allowing the relative peak heights to be compared.

Figures 4.32(a) and 4.32(b) show the $\theta - 2\theta$ scan and ω scan for the $(11\bar{2}4)$ reflection, respectively; the RSMs shown are shown in Figs. 4.33 and 4.34. The RSM in Fig. 4.33(a) was collected using the technique described in Sec. 2.10. Figure 4.34 was collected using a different technique as described in Chapter 5. There is only one peak visible near the GaN($11\bar{2}4$) position. This suggests that the InGaN and the GaN peaks are completely superposed. (The AlN peak is too weak to be seen in these contour plots). In order for these peaks to be superposed there must be stress parallel to the surface of the sample for at least one of these layers.

The fit to the data for the asymmetric $(11\bar{2}4)$ reflections was very poor. The simulated scans were too wide and the InGaN peak too prominent in the $\theta - 2\theta$ scan. Although the fit could be improved somewhat if these scans were considered in isolation, the correct peak shape could not be reproduced for any combination of fitting parameters. This suggests that there is a discrepancy between our model and the actual defect structure. This point is discussed in more detail in Sec. 4.7.

Despite the differences between the simulated and the experimental data the $(11\bar{2}4)$ scans allowed the lateral strain to be determined. Strain in the crystal will change the ratio c/a from its relaxed value and move the diffraction peak in reciprocal space. For relaxed crystals with the same c/a ratio, the asymmetric reflections with the same asymmetry angle lie along a line at an angle φ with respect to the \mathbf{q}_z -axis. Increasing the c/a ratio shifts the peak above the line and vice versa. The strain perpendicular to the sample surface was determined using the $(00.l)$ reflection data. The strain parallel to the surface was determined from the position of the $(11\bar{2}4)$ reflection. Figure 4.33 shows that the simulated peak positions are correct for both

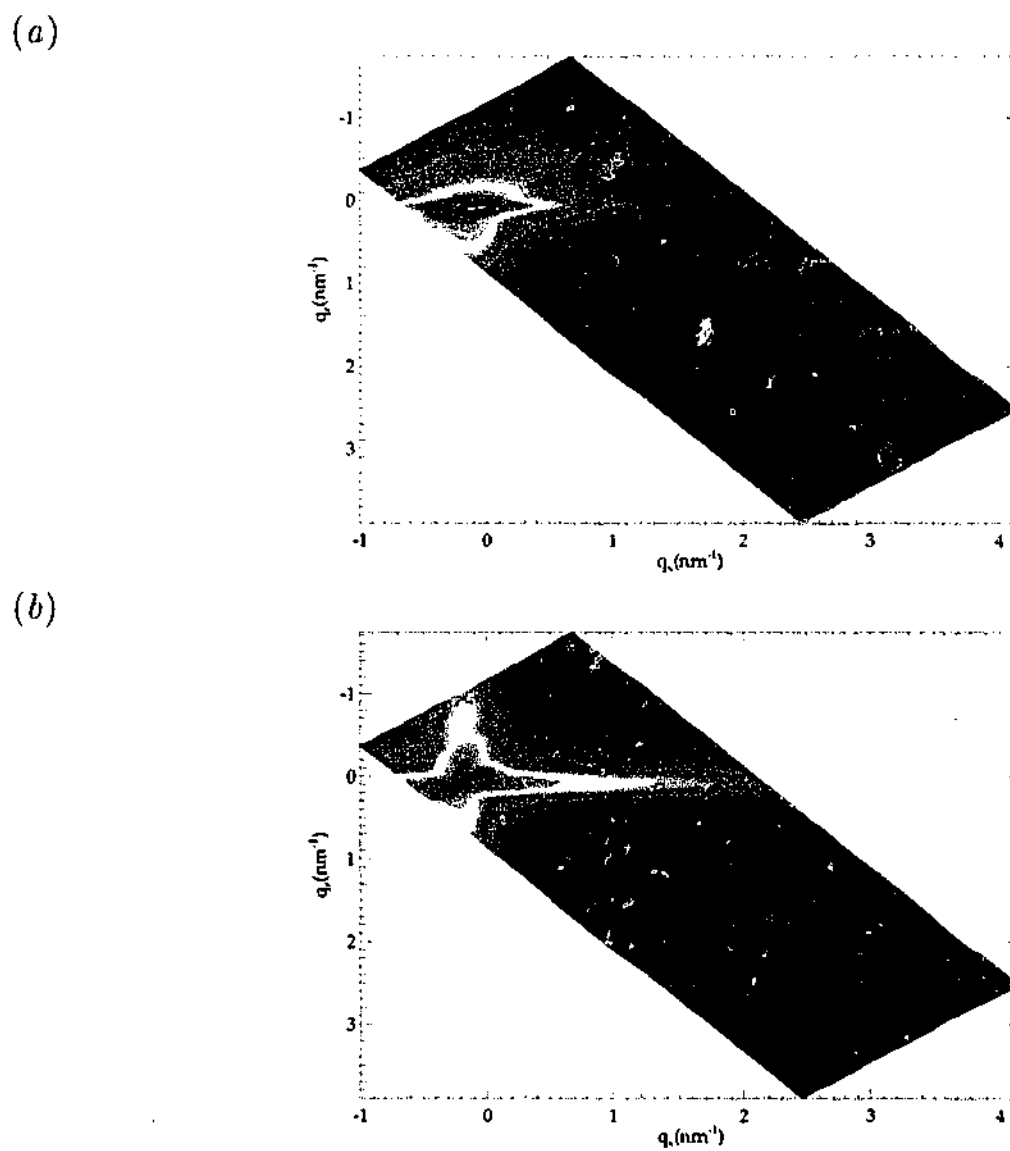


Figure 4.33: Reciprocal space maps of the GaN(11 $\bar{2}$ 4) reflection for sample D05. (a) Experimental RSM, and (b) simulated RSM.

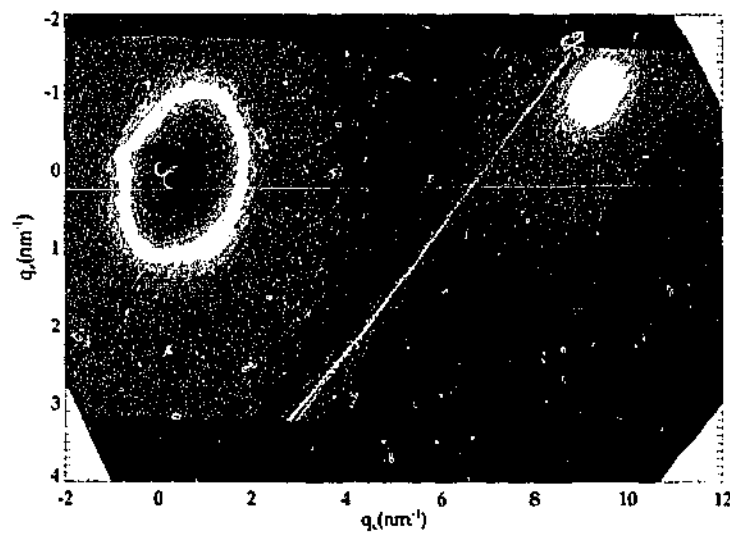


Figure 4.34: Reciprocal space map of the GaN(11 $\bar{2}$ 4) reflection for sample D05, collected using the imaging plate technique described in Chapter 5.

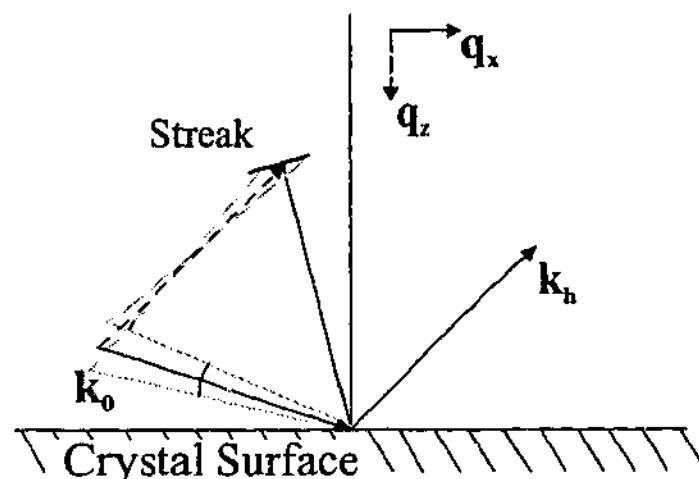


Figure 4.35: Reciprocal space construction showing the origin of the streak due to mosaic block misorientation.

scans. This is demonstrated more clearly in the RSMs shown in Fig. 4.28, where both peaks are at the same position; the InGaN peak is superposed on the GaN peak.

Although the simulated and experimental RSMs, for the $(11\bar{2}4)$ reflections, are not identical they have several features in common. In particular both RSMs exhibit peaks with streaks parallel to the q_x direction; also both show streaks running approximately 40° to the q_x -axis (although in the simulation the streak is concentrated at the centre of the peak, while for the experimental data it occurs at the extremities of the peak). The simulated scan also displays a streak parallel to the q_z direction. The streaks perpendicular and parallel to the q_z and q_x directions are due to the geometry and extent of the mosaic blocks. In effect they represent a diffraction pattern (or power spectrum) of a rectangular aperture. The streak at 40° to the q_x -axis is due to the misorientation of the mosaic blocks. For a crystal consisting of an infinite array of mosaic blocks illuminated by monochromatic plane waves, and a detector with a δ -function response in reciprocal space, broadening of the diffraction peak will be due solely to the rotation of the blocks. This is the same as a perfect crystal illuminated by a divergent source. Figure 4.35 illustrates this situation in reciprocal space. Rotating the crystal surface by a small angle (corresponding to having many crystallites with different orientations), or rotating the incident wavevector causes the diffraction vector to sweep out a path that is perpendicular to the line from the origin to the reciprocal lattice point. For larger angles the path is an arc in reciprocal space. For symmetric reflections the streaks due to the lateral block size and the misorientation are superposed and cannot be easily distinguished from one another.

There is a second peak in Fig. 4.34 at about $q_x = 9 \text{ nm}^{-1}$. The origin of this peak has not been identified; however, the peak appears to be at the correct q_x position for AlN. A very large strain parallel to the crystal surface would be required for the peak to be at that position. Further analysis of this peak has not been completed.

Assuming that the InGaN layer has grown pseudomorphically on the GaN layer, the composition of the InN composition is found to be $5\% \pm 1\%$. This agrees with the expected value of 5%, which is estimated from the growth parameters. The strain components are $(2.8 \pm 0.4) \times 10^{-3}$ and $(-5.4 \pm 0.8) \times 10^{-3}$ perpendicular and parallel to the (0001) plane, respectively. The perpendicular strain agrees with the value determined from statistical theory (see Table 4.22). The strain parallel to the (0001) plane was not determined from statistical diffraction theory because the InGaN peak is broad and close to the GaN peak position (no high resolution ω scan was collected).

The growth procedure used for sample C30 was identical to the initial stages of the growth for of sample D05. Sample C30 was removed from the growth chamber after the LT-AlN buffer layer and only 30 nm of GaN had been deposited. Comparing the results for samples C30 (see Sec. 4.3) and D05 allows us to identify the changes in the LT-AlN buffer layer during the growth of the GaN and InGaN layers. The mosaic block parameters determined for the AlN and GaN layers for sample C30 are reported in Table 4.14, with the mosaic block parameters for sample D05 given in Table 4.22. The AlN layer in sample D05 was improved over that seen for sample C30, displaying a much smaller misorientation and tilt. The block size, however, is close to that seen for sample C30, indicating a similar dislocation density of $1.2 \times 10^{11} \text{ cm}^{-2}$. The GaN layer is 70 times thicker than that used for C30, and hence its parameters are expected to be very different.

The InGaN layer is of a good quality considering that it is very thin. This is because it is grown on a thick good quality GaN layer. The InGaN layer has a very low InN content so it has similar lattice parameters and coefficients of thermal expansion as the GaN layer on which it is grown. The dislocation densities of the GaN and InGaN layers are $5.6 \times 10^8 \text{ cm}^{-2}$ and $1.3 \times 10^9 \text{ cm}^{-2}$, respectively. These dislocation densities are two orders of magnitude smaller than for the AlN layer. Hence, the AlN layer appears to be accommodating the lattice and thermal mismatch. However, these dislocation densities are still orders of magnitude larger than many other optoelectronic systems ⁴.

⁴GaAs is typically grown with a dislocation density of 10^4 cm^{-2} to 10^5 cm^{-2} (see e.g., <http://parts.jpl.nasa.gov/mmhc/3-I.PDF>)

4.4.2 Sample D30: 20 nm $\text{In}_{0.3}\text{Ga}_{0.7}\text{N}$

The 'active' layer for sample D30 was nominally $\text{In}_{0.3}\text{Ga}_{0.7}\text{N}$. The InN content is much larger than for sample D05. The experimental parameters are summarised in Table 4.23 and the scans are shown in Figs. 4.36 - 4.41. For this sample the experimental scans were normalised to the GaN peak in the $\theta - 2\theta$ scan (about the (0004) reflection). The simulations were performed in a similar fashion as for D05, with no distribution of the strain or any other block parameter included. The normalisation for the simulated scans was based on the InGaN peak in the $\theta - 2\theta$ scan of the (0004) reflection. The experimental and simulated scans for a wide detector slit were normalised against the InGaN(0002) peak.

The $\theta - 2\theta$ (0002) scan for the (0002) reflection (Fig. 4.36(a)), has a very low intensity since it was collected using the most attenuating filter. (The central RSM scan, shown in Fig. 4.41(a), gave the same result because it was also collected with the same filter). Since the InGaN layer has a much greater InN content than was

Table 4.23: Experimental scan parameters for sample D30. This sample includes a 20 nm thick $\text{In}_{30}\text{Ga}_{70}\text{N}$ layer.

Sample No.	Reflection	Scan Type	Detector slit (vert.) (mm)	Filter	Step size (arcsecond)	Range (deg)
D30:1	(0002)	$\theta - 2\theta$	10	#1,#2	2 θ : 108	2 θ : 28.0-41.5
D30:2		$\theta - 2\theta$	10	None	2 θ : 108	2 θ : 28.0-41.0
D30:3		$\theta - 2\theta$	0.5	#3	2 θ : 108	2 θ : 26.0-37.4
D30:4		ω ($2\theta=34.56^\circ$)	0.5	#1,#3	ω : 55	$\Delta\omega$: ± 1
D30:5		ω ($2\theta=34.56^\circ$)	0.5	#3	ω : 108	$\Delta\omega$: ± 3
D30:6		ω ($2\theta=33.592^\circ$)	0.5	#1,#2	ω : 48	$\Delta\omega$: ± 1
D30:7		ω ($2\theta=33.592^\circ$)	0.5	None	ω : 108	$\Delta\omega$: ± 3
D30:8		ω ($2\theta=32.632^\circ$)	0.5	#1,#2	ω : 48	$\Delta\omega$: ± 1
D30:9		ω ($2\theta=32.632^\circ$)	0.5	None	ω : 108	$\Delta\omega$: ± 3
D30:10		ω ($2\theta=31.968^\circ$)	0.5	#1,#2	ω : 48	$\Delta\omega$: ± 1
D30:11		ω ($2\theta=31.968^\circ$)	0.5	None	ω : 108	$\Delta\omega$: ± 3
D30:12		RSM	0.5	#3	ϵ : 54.6 $\Delta\omega$: 113	$\epsilon + 2\theta_B$: 28.0-37.4 $\Delta\omega$: ± 0.345
D30:13	(0004)	$\theta - 2\theta$	10	#1,#3	2 θ : 108	2 θ : 66.0-78.0
D30:14		$\theta - 2\theta$	10	#1	2 θ : 108	2 θ : 33.0-81.0
D30:15		ω ($2\theta=72.814^\circ$)	0.5	#3	ω : 108	$\Delta\omega$: ± 3
D30:16		ω ($2\theta=70.372^\circ$)	0.5	None	ω : 108	$\Delta\omega$: ± 3
D30:17		ω ($2\theta=69.288^\circ$)	0.5	None	ω : 108	$\Delta\omega$: ± 3
D30:18		RSM	0.5	None	ϵ : 109 $\Delta\omega$: 113	$\epsilon + 2\theta_B$: 62.0-75.0 $\Delta\omega$: ± 0.345
D30:19	(11 $\bar{2}$ 4)	$\theta - 2\theta$	10	#1	2 θ : 216	2 θ : 89.9548-101.9548
D30:20		$\theta - 2\theta$	10	#3	2 θ : 216	2 θ : 89.9548-101.9548
D30:21		$\theta - 2\theta$	1	None	2 θ : 216	2 θ : 89.9548-101.9548
D30:22		ω	10	#3	ω : 36	$\Delta\omega$: ± 1
D30:23		RSM	1	None	ϵ : 216 $\Delta\omega$: 109	$\epsilon + 2\theta_B$: 89.9548 -101.9548 $\Delta\omega$: -1.5 - 0.5

Table 4.24: Summary of the composite scans for sample D30. The supplementary scans are multiplied by the attenuation factor to match them to the base scans.

Sample No.	Base Scan		Supplementary Scan		
	Scan No.	Filter	Scan No.	Filter	Atten. Factor
D30:C1	D30:2	None	D30:1	#1,#2	85
D30:C2	D30:5	#3	D30:4	#1,#3	10
D30:C3	D30:7	None	D30:6	#1,#2	85
D30:C4	D30:14	#1	D30:13	#1,#3	900
D30:C5	D30:19	#1	D30:20	#3	200

Table 4.25: Simulation parameters for sample D30.

Material	Layer Parameters				Block Parameters		
	Thickness (nm)	Tilt (deg)	Lat. Strain	Perp. Strain	Lat. Size (nm)	Perp. Size (nm)	Misorientation (deg)
InGaN	20	0	-0.025	0.001	170	14.8	0.1
GaN	2000	0	—	0.0025	500	2000	0.12
AlN	30	0	—	0.008	15	6	0.7

present in the D05 sample, the InGaN and GaN peaks do not overlap to the same extent; they are clearly resolvable in all $\theta - 2\theta$ scans. The thickness oscillations are very well defined, particularly when using the narrow slit (see Fig. 4.36(b)). This indicates smooth parallel interfaces. The AlN peak is only seen in the two scans collected with a wide detector slit (see Fig. 4.37). For the (0002) scan (which was collected with a $\Delta\omega$ offset of 0.16°) the left hand side of the AlN peak is obscured by the GaN peak, in a similar fashion as for the wide slit $\theta - 2\theta$ scan collected from sample D05. The AlN peak is also evident as a slight 'bowing' of the profile centred at $2\theta \approx 76^\circ$ in the $\theta - 2\theta$ scan shown in Fig. 4.37(b).

The $\omega - 2\theta$ scan shown in Fig. 4.37(a) was intended to be a $\theta - 2\theta$ scan; however, an error was made using the `chg_dial` command that resulted in the reported angle for ω -axis being incorrect by a constant factor (0.16°). Figure 4.37(b) is a standard $\theta - 2\theta$ scan.

It should be pointed out that the peak positions observed for the $\theta - 2\theta$ scans collected using the narrow slit about (0002) do not exactly agree with the (0004) peak positions. This is evident in the slight translation of the simulated profile with

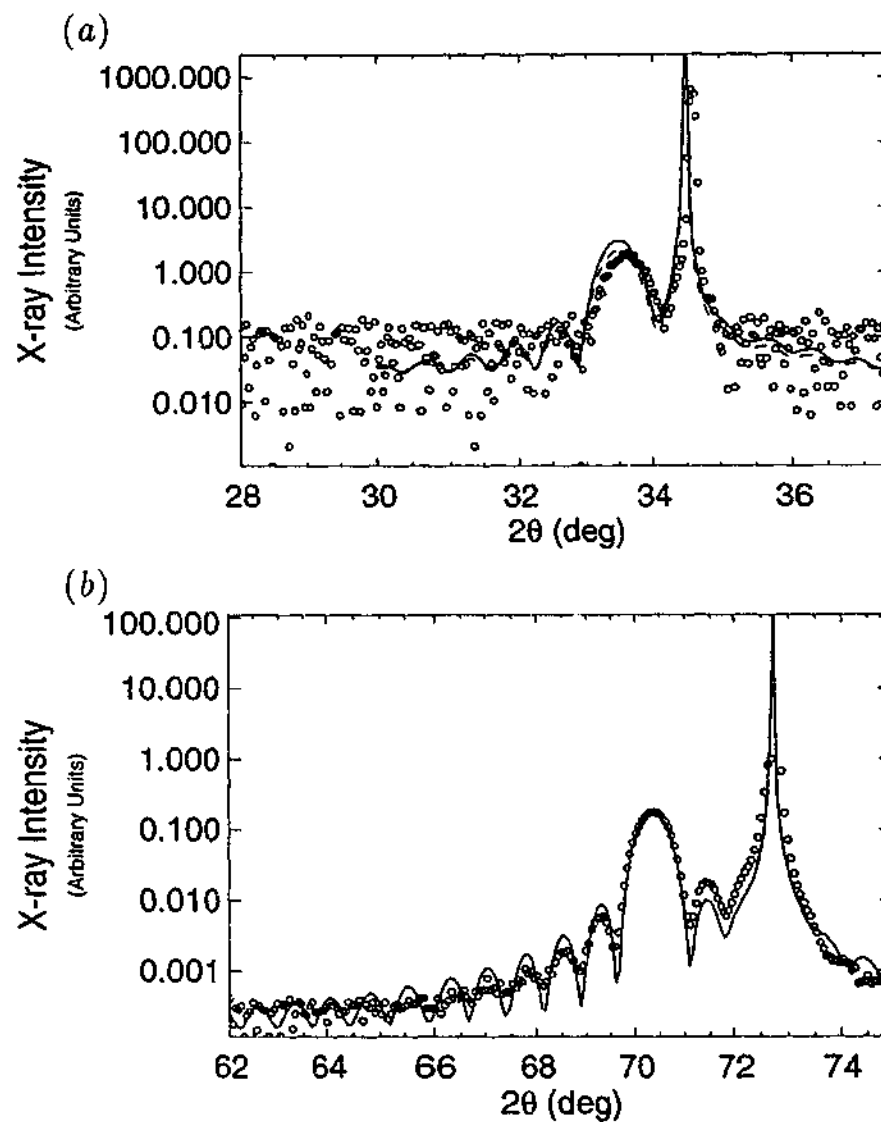


Figure 4.36: Experimental profile (\circ) and simulated profiles (— and —) for the $\theta - 2\theta$ scans for sample D30 using a narrow (0.5 mm) slit. (a) (0002), and (b) (0004) reflections. The solid line (—) is normalised to the InGaN(0004) peak for (a) and (b); the dashed line (—) in (a) is normalised to the InGaN(0002) peak.

respect to the experimental data in Fig. 4.36(a). The origin of this shift is likely due to a slight calibration problem. Although this was not an important consideration, a small modification to the strain values for the layers was required for the simulation; hence the peak positions for both the (0002) and (0004) simulations did not agree exactly with the experimental profiles. As a consequence of this calibration error the simulation of the ω scan for the GaN(0002) peak was based on the simulated peak position, rather than on the experimental data (i.e., at a 2θ value of 34.477° rather than 34.56°).

The simulation parameters are shown in Table 4.25. The simulated $\omega - 2\theta$ and $\theta - 2\theta$ scans are in excellent agreement with the experimental data. The simulated

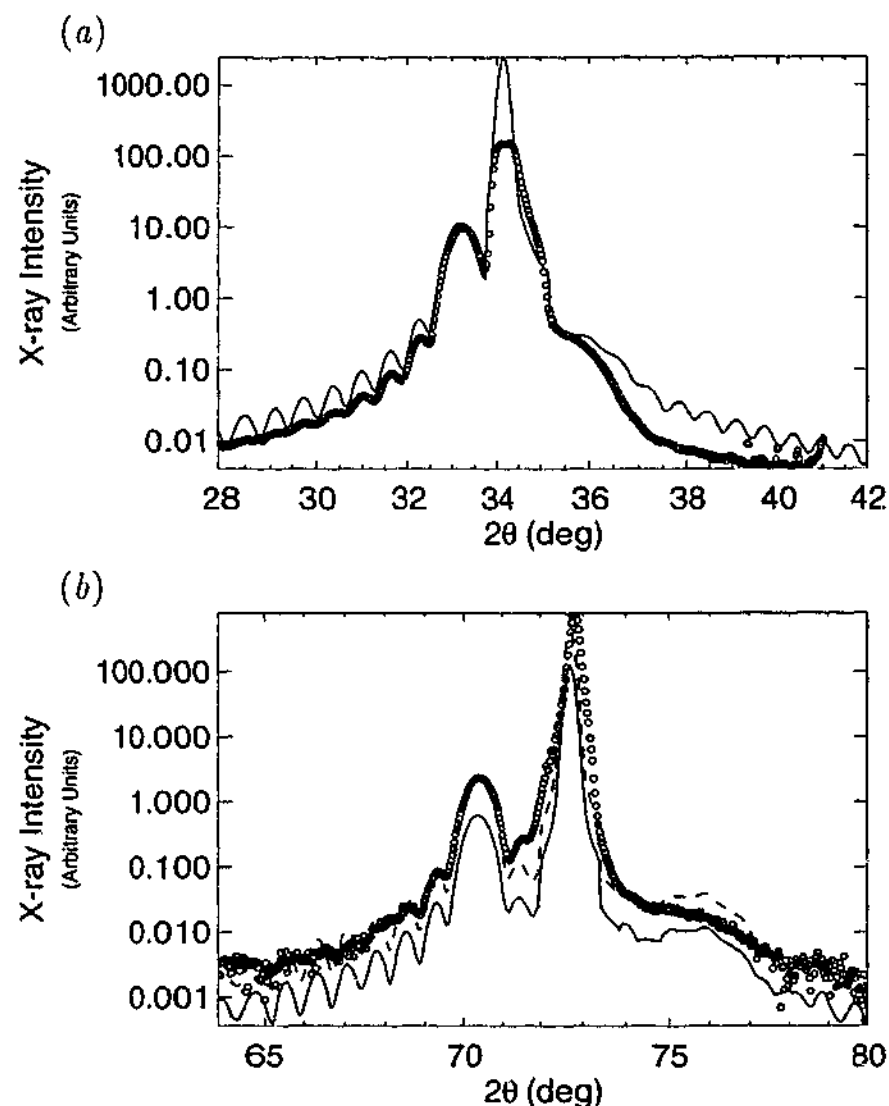


Figure 4.37: Experimental profiles (\circ) and simulated profiles (— and —) for sample D30 using a wide (10 mm) slit. Figure (a) is an $\omega-2\theta$ scan about the (0002) reflection with $\Delta\omega = 0.16^\circ$, and (b) is a $\theta-2\theta$ scan about the (0004) reflection. The solid line (—) is normalised to the InGaN(0004) peak for (a) and (b); the dashed line (—) in (b) is normalised to the InGaN(0004) peak.

scans in Figs. 4.36 and 4.37 reproduce all the features in the experimental data. After accounting for the calibration error the simulated profiles were found to be in good agreement with the experimental profiles; this highlights the sensitivity of the analysis routine. Furthermore the quality of the fit for the wide slit data shows that the instrumental function (i.e., the area of reciprocal space that is simultaneously illuminated by the incident beam and accepted by the detector - also known as a resolution element (Holý *et al.*, 1999)) can be easily accounted for in the simulation. This is a distinct advantage of the present analysis technique.

The peak shape and oscillations for the InGaN layer have been matched extremely well by the simulation, especially for the (0004) scan collected using the

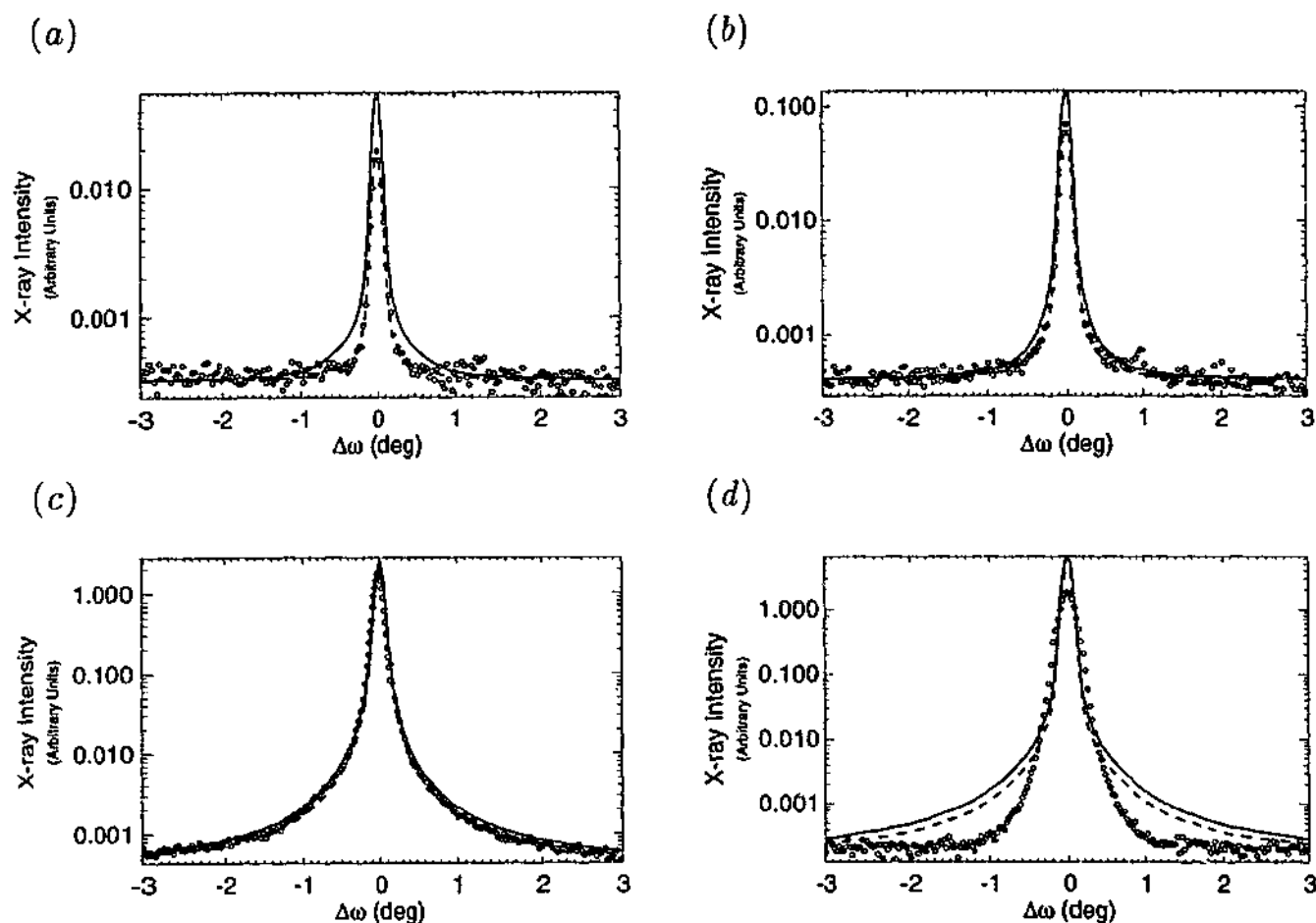


Figure 4.38: Experimental profiles (\circ) and simulated profiles ($—$ and $- -$) for the ω scans for sample D30 using a narrow (0.5 mm) slit. The solid line ($—$) uses the same normalisation factor as Fig. 4.36(b), with the dashed line ($- -$) normalised to the experimental the peak height. The 2θ positions for the scans are: (a) 31.968° , (b) 32.632° , (c) 33.592° , and (d) 34.56° .

narrow slit (see Fig. 4.36(b)). The GaN peak has also been matched very well. A compromise was required for the AlN layer parameters since the simulated AlN peak is pronounced in the (0004) scan, but these parameters provide a reasonable fit to the peak in the (0002) scan (Fig. 4.37). A better fit might be possible if the thickness of the AlN layer is reduced; however, varying the layer thicknesses was avoided to minimise the number of fitting parameters.

The ω scans about the (0002) reflection are shown in Fig. 4.38. Each of the scans are reasonably narrow, indicating low mosaicity, with no evidence of the whole layer tilting. Figures 4.38 (a) and (b) show the two lower order thickness fringes from the InGaN layer; Figs. 4.38 (c) and (d) show scans across the InGaN and GaN peaks, respectively. A small amount of detector saturation was observed at the peak of the ω scan for GaN. Several of the ω scans presented are composite scans (see Table 4.24). An experimental peculiarity was evident in the composite scan at $2\theta =$

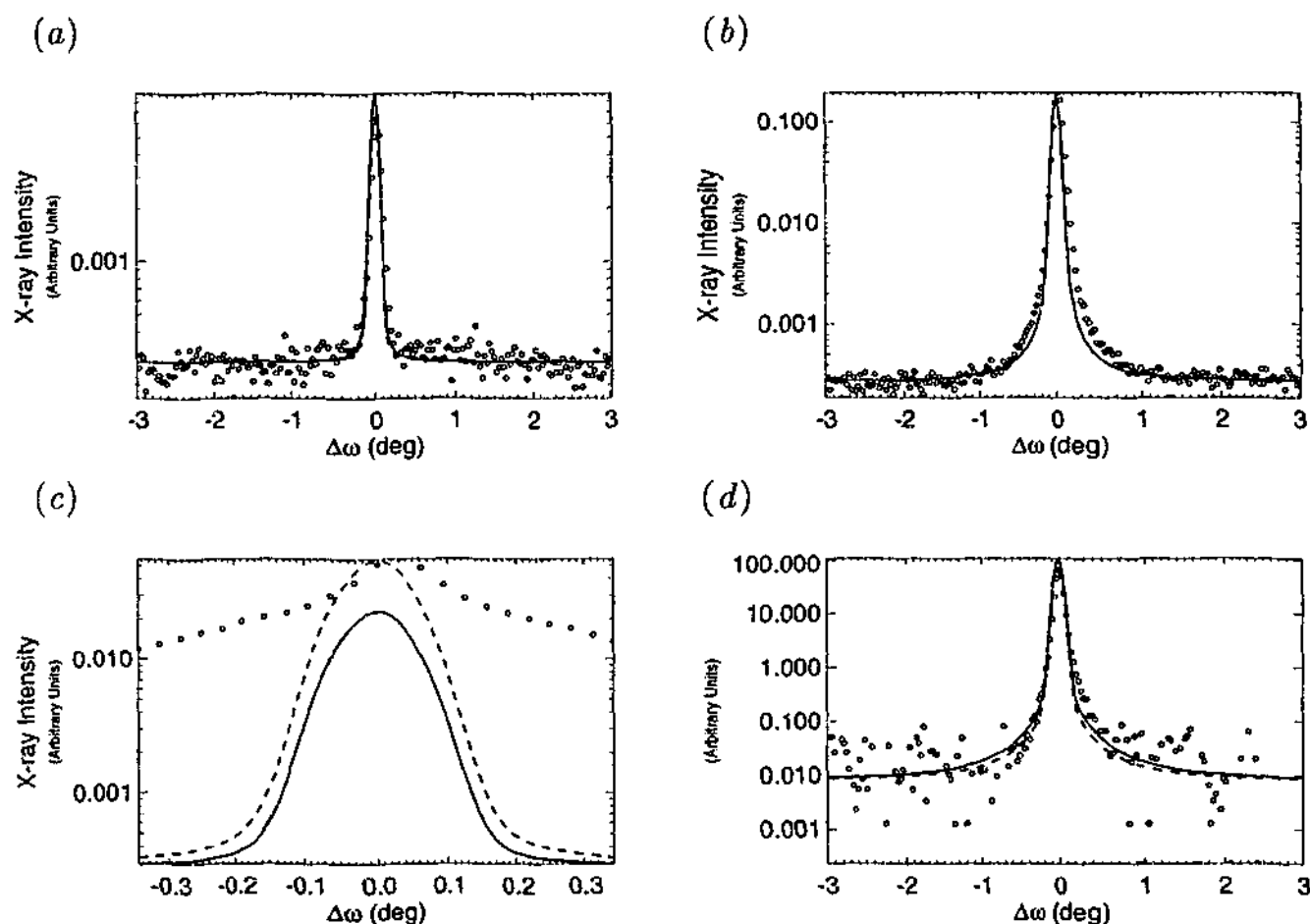


Figure 4.39: Experimental profiles (\circ) and simulated profiles ($—$ and $- -$) for ω scans for sample D30 using a narrow (0.5 mm) slit. The solid line ($—$) uses the same normalisation factor as Fig. 4.36(b), with the dashed line ($- -$) normalised to the experimental peak height. The 2θ position for the scans are: (a) 69.288° , (b) 70.372° , (c) 72.3878° , and (d) 72.814° .

34.56° (see Fig. 4.38(d)). Three sets of data were available to produce the peak: a scan extracted from the RSM with filter #3 inserted, and two dedicated scans one with both filters #1 and #3 inserted, and one with filter #3 only. Comparing the two dedicated scans suggests that filter #1 reduces the intensity by a factor of 10. However, a comparison of count rates of the scan collected using filters #1 and #3 and the RSM (which was collected with only filter #3 insert) suggest that filter #1 reduced the intensity by a factor of at most 5. The plot given in Fig. 4.38(d) used the two dedicated scans (not the scan extracted from the RSM) and an attenuation factor of 10, as these scans covered a far wider range of angles.

The ω scans collected near the (0004) reflection are displayed in Fig. 4.39. Figure 4.39 (a) shows the lowest order thickness oscillation from the InGa_{0.2}N layer, while Fig. 4.39(b) shows the main InGa_{0.2}N layer peak. Figure 4.39(c) was extracted from the RSM on the low angle side of the GaN peak (the significance of this scan is

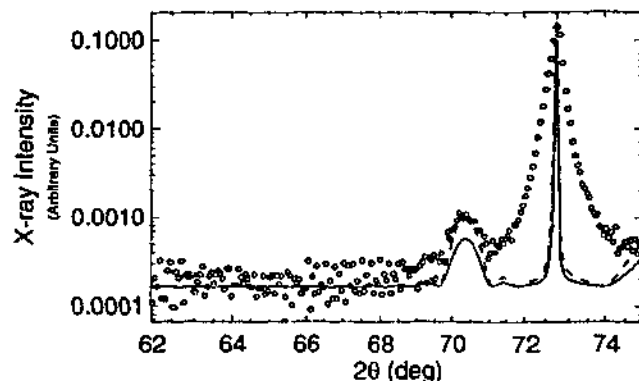


Figure 4.40: $\omega - 2\theta$ scan for sample D30, with $\Delta\omega = 0.345^\circ$. The scan was extracted from the RSM for the (0004) reflection (see Fig. 4.41(c)).

discussed below), and Fig. 4.39(d) was collected across the centre of GaN peak. The scan in Fig. 4.39(c) was extracted from the RSM and it has a much smaller range than the other scans; consequently, an accurate comparison with the other scans is precluded. The profile shown in Fig. 4.39(d) has a higher noise level because it was collected using a filter to reduce the intensity. As with the (0002) reflection these scans are indicative of reasonably low mosaicity and no tilt.

The ω scans in Figs. 4.38 and 4.39, have been reconstructed accurately by the simulation (particularly the peak shapes), although some of the amplitudes relative to the narrow slit scan of the (0004) reflection are incorrect. The fact that the shape of the simulated ω scans agrees with the experimental data suggests that the misorientation and lateral block size have been accurately determined.

Comparison of the simulated scans with the experimental data shows that the diffraction features due to the InGa_N layer agree particularly well with the simulated profiles. This includes the ω scans in Figs. 4.38(a), (b), and (c) and 4.39(a) and (b), as well as the InGa_N peak and oscillation fringes in Figs. 4.36 and 4.37. This suggests that the mosaic block model is well suited to describing the crystal structure within the InGa_N layer.

Figure 4.40 shows an $\omega - 2\theta$ scan with a $\Delta\omega$ offset of 0.345° . This was extracted from the RSM in Fig. 4.41(c). This scan shows the base of the GaN peak to be quite wide compared to the other peaks. In fact the simulated GaN peak is far too narrow. Increasing the misorientation distribution width for the GaN layer improved this fit; however, the fit to the ω scan across the GaN peak (see Fig. 4.39(d)) was worse. The GaN peak shape can also be seen clearly in the RSM in Fig. 4.41(c). Decreasing the mosaic block size perpendicular to the sample surface would increase the width of the peak in the q_z direction, thereby improving the accuracy of the simulation of the $\omega - 2\theta$ scan; however, the $\theta - 2\theta$ simulation would be incorrect.

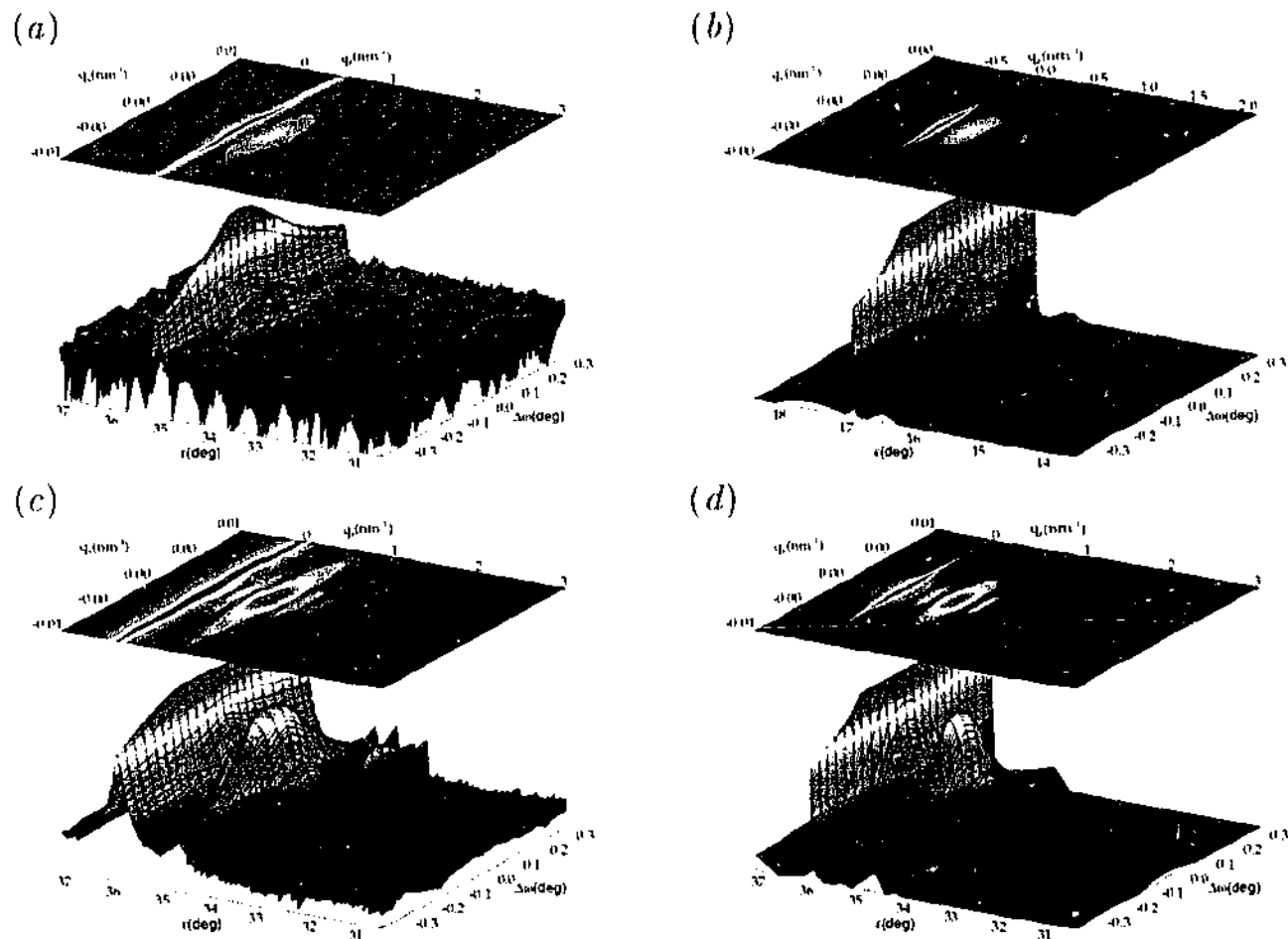


Figure 4.41: Reciprocal space maps for sample D30. (a) Experimental RSM, and (b) simulated RSM about the GaN(0002) reflection; (c) experimental RSM and (d) simulated RSM about the GaN(0004) reflection. The simulated RSMs have been scaled so that the InGaN peak heights match the experimental data.

Figure 4.41 shows the RSMs for the $(00.l)$ reflections. Apart from the base of the GaN peak, the simulated scans are well matched to the experimental data (ignoring the spurious peaks seen at approximately $q_z = 1 \text{ nm}^{-1}$, $q_x = 0.0075 \text{ nm}^{-1}$).

Figure 4.42 shows the one-dimensional profiles for the $(11\bar{2}4)$ reflection. The RSMs for this sample (see Figs. 4.43 and 4.44) highlight an interesting feature of these samples. In particular Fig. 4.44 shows the InGaN and GaN layers to be at the same q_x position. This means that the InGaN layer has grown 'coherently' on the GaN layer (see e.g., Amano and Akasaki, 1999; O'Donnell *et al.*, 2001). In this situation the a lattice parameter is identical for the two layers. Therefore the InGaN has been compressively strained parallel to the surface, and hence there is a tensile strain in the perpendicular direction. The peak position for the ternary alloy layer can be used to determine the composition of the layer. We use the following relationship (Amano and Akasaki, 1999):

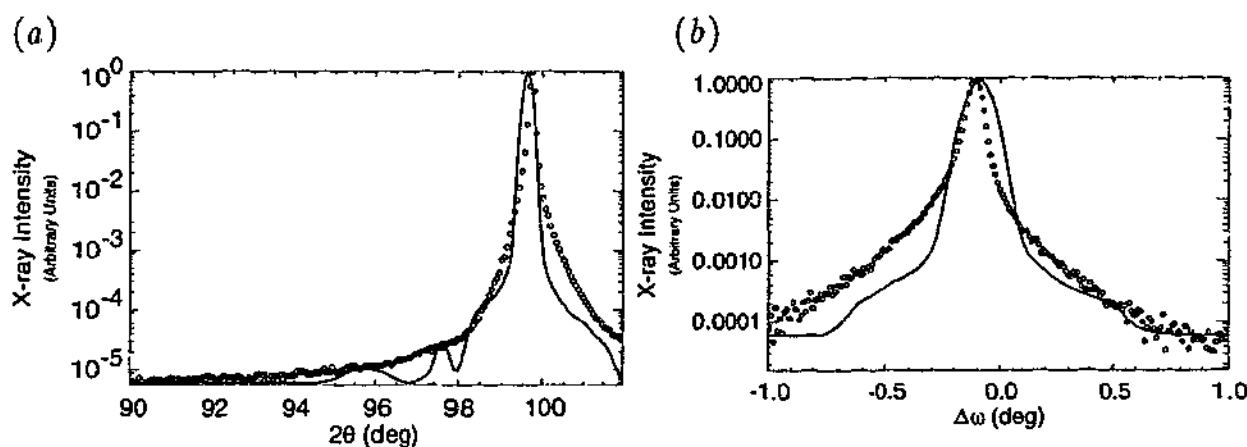


Figure 4.42: (a) $\theta - 2\theta$ scan, and (b) ω scan about the $(11\bar{2}4)$ reflection for sample D30. The circles (\circ) denote the experimental data, and the solid lines ($—$) represent the simulation.

$$\frac{\Delta c_0}{c_0} = -2 \frac{c_{13}}{c_{33}} \frac{\Delta a_0}{a_0}, \quad (4.3)$$

where $\Delta c_0 = c_{meas} - c_0$, $\Delta a_0 = a_{GaN} - a_0$, c_{meas} is the lattice constant inferred from the peak position, and a_0 and c_0 are the relaxed lattice constants for the ternary layer, determined using the relaxed lattice parameters for GaN and InN. Assuming Vegard's law (Vegard, 1921), and knowing the elastic stiffness constants, c_{13} and c_{33} for the ternary layer, which are also determined from the InN and GaN values using Vegard's law, we can solve for the layer composition. The elastic stiffness constants are $c_{13} = 103$ GPa and $c_{33} = 405$ GPa for GaN and $c_{13} = 92$ GPa and $c_{33} = 224$ GPa for InN (Pereira *et al.*, 2002). Substituting the appropriate lattice parameters into Eq. (4.3), we obtain a layer composition of $17\% \pm 1\%$ InN. Although this differs significantly from the nominal value of 30% InN, our collaborators noted⁵ that the nominal value is an estimate and is very imprecise. We are confident that 17% is accurate. The strain determined using this composition was $(1.02 \pm 0.04) \times 10^{-2}$ perpendicular to the surface, and $(-1.88 \pm 0.08) \times 10^{-2}$ laterally. These strains are much larger than those quoted in Table 4.25 where a composition of 30% was assumed. In terms of the simulation the composition of the InGa_N layer only impacts on the reported strain - it has no bearing on the peak shape.

The dislocation densities determined from the lateral block size were 8.9×10^{11} cm^{-2} for the AlN layer, 6.9×10^9 cm^{-2} for the InGa_N layer and 8.0×10^8 cm^{-2} for the GaN layer. The InGa_N and GaN layers were of a much higher quality than the AlN layer. This is because the AlN layer has been grown directly on the sapphire substrate, and hence was highly strained during growth. The dislocation densities

⁵Private communication, Tabuchi 2004.

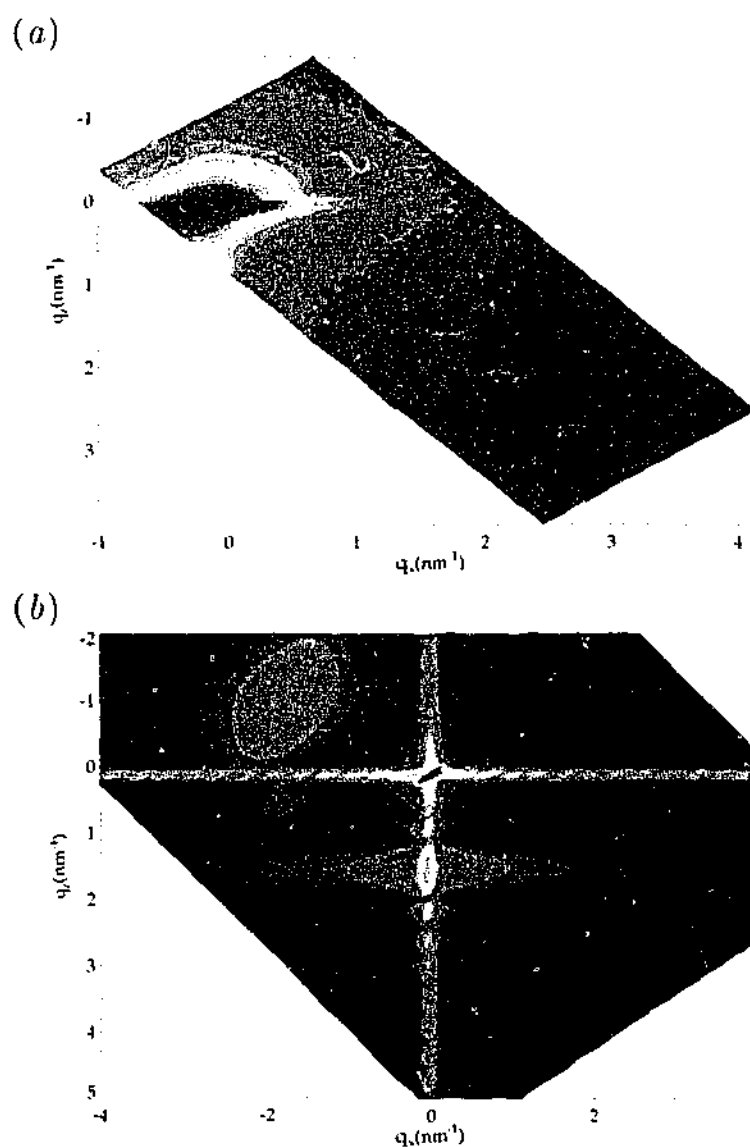


Figure 4.43: (a) Experimental and (b) simulated RSMs about the $(11\bar{2}4)$ reflection for sample D30. The simulated scan in (b) has a different scale to the experimental data shown in (a) so that it can be compared with the scan in Fig. 4.44.

agree with those quoted in the literature for Group III nitrides e.g., Akasaki (2002) quotes a dislocation density of $> 10^{11} \text{ cm}^{-2}$ for GaN grown directly on sapphire and $10^9 \text{ cm}^{-2} - 10^{10} \text{ cm}^{-2}$ on a LT-AlN buffer layer.

The width of the detector slit impacts on the broadness of the GaN peak for the $\theta - 2\theta$ scans collected with the wide (10 mm) slit. This is because the intensity registered by the detector changes abruptly as the centre of the GaN peak enters and leaves the 'field of view' of the slit system. It is these rapid changes in intensity that confirm the GaN peak width for the wide slit scans. The detector window makes an angle of 45° to the $\theta - 2\theta$ scan. The extent of the detector in the ε direction (ε was defined in Sec. 2.10 as the angular deviation of analyser crystal from its Bragg condition) is 0.7 times the detector angular extent. Treating the GaN reflection as

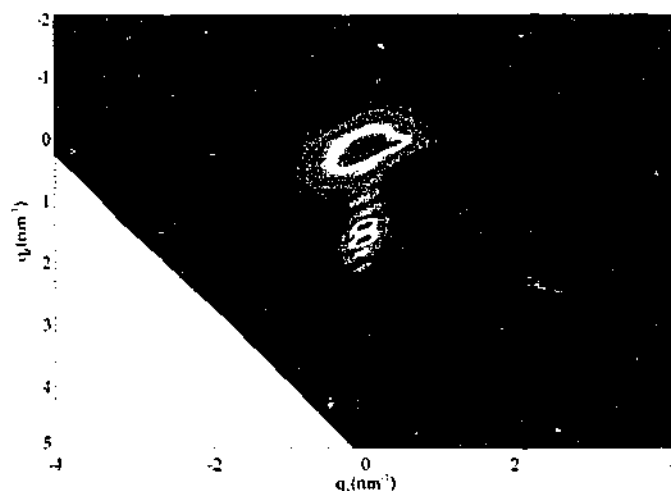


Figure 4.44: Reciprocal space map collected about the $(11\bar{2}4)$ reflection using the imaging plate technique described in Chapter 5.

a δ -function (i.e., no instrumental effects), and the slit aperture as a rectangular function, the detector width is given by:

$$\frac{\text{width (in } 2\theta) \text{ of the base of the GaN}}{2 \times 0.7} \quad (4.4)$$

A better model would consider the true shape of the GaN reflection and the aperture function. In the present case the width of the slit was determined by fitting the simulated scan. This accounts for the actual peak shape, but still assumes a rectangular slit. A trapezoidal aperture function was also used to describe the slit, but this made negligible difference to the scan profile. The slit size used during the simulation (for all three type D samples) was 1° , whereas the nominal slit size was approximately 1.5° . This value was determined from the D30 wide slit scans, which could not be fitted correctly until the assumed slit size was reduced.

The detector slit width was set by the computer system by using encoder pulses from the motors to measure the movement of the slits. The slit width was not physically measured (apart from indirectly in these experiments), and hence it is possible it was not the same as reported by the software. Additionally the sample-detector distance was not measured, but was estimated by checking photographs of the experiment and taking approximate measurements on a subsequent visit to the facility. The difference in slit width between the nominal value and the value based on simulations is greater than the uncertainty in the sample-to-detector distance; however, it may be accommodated by combining the uncertainty in the actual slit width, the sample-to-detector distance, and the uncertainty obtained from the simulations. If we assume the slit width is correct (i.e., 10 mm) we find a sample-to-detector

distance of 0.573 m (the approximate distance was 0.37 m). A sample-to-detector distance of 0.573 m gives an angular window for the narrow slit of 0.05° (the nominal value was 0.08°). For consistency 0.05° was used for the simulations, although changing this to 0.08° had a negligible effect on the simulated diffraction profile.

The simulations for the $(11\bar{2}4)$ reflection do not fit as closely as the $(00.l)$ data (this observation was also made for sample D05). The RSMs in Figs. 4.43 and 4.44 show the peak positions to be correctly determined; however their shape, and in particular the width of the GaN peak has not been reproduced correctly. The simulated GaN peak once again shows streaks due to the misorientation and finite size of the mosaic blocks, as described for sample D05. However, for sample D30 the experimental data only displays a streak in the q_x direction; this indicates lateral size broadening. (The apparent striping directed approximately 45° to the q_x -axis in Fig. 4.44 is an artifact of the experimental technique, as is the splitting of the InGaN peak. These are discussed in Chapter 5. The absence of a misorientation streak does not imply that there is no crystallite tilting within the sample, since the peak is quite broad.

4.4.3 Sample D42: 200 nm $\text{In}_{0.42}\text{Ga}_{0.58}\text{N}$

The thickness of the InGaN layer for sample D42 was 200 nm, which is ten times the thickness of the InGaN layer in samples D05 and D30. The InGaN layer consisted of 42%InN, which is higher than that normally used because segregation can become an issue (see e.g., El-Masry *et al.*, 1998). The experimental scan parameters are shown in Table 4.26, with the composite scans summarised in Table 4.27. Figures 4.45 - 4.55 show the scans collected using the narrow slit, normalised to the InGaN(0002) peak in the $\omega - 2\theta$ scan, with offset $\Delta\omega = 0.181^\circ$ (see Fig. 4.47). The scans with the wide slit were normalised to the GaN(0002) peak. Again the simulations assumed homogeneous layers, although two InGaN layers were used (see below).

The $\theta - 2\theta$ scans are shown in Figs. 4.45 and 4.46. It is apparent that the thickness fringes are absent, suggesting that the layer is of considerably lower quality than the previous samples. As the InGaN layer is ten times thicker than the previous two samples (D30 and D70), it is possible that the thickness fringes have a much shorter period (since the period is inversely proportional to the perpendicular mosaic block size), but certainly not beyond the resolution of the detector system. The

Table 4.26: Experimental scan parameters for sample D42. This sample includes a 200 nm thick $\text{In}_{0.42}\text{Ga}_{0.58}\text{N}$ layer.

No.	Reflection	Scan Type	Det. slit (vert.) (mm)	Filter	Step size (arcsecond)	Range (deg)
D42:1	(0002)	$\theta - 2\theta$	10	#1,#3	2 θ : 108	2 θ : 31.0-42.0
D42:2		$\theta - 2\theta$	10	#1,#2	2 θ : 108	2 θ : 31.0-41.5
D42:3		$\theta - 2\theta$	10	None	2 θ : 108	2 θ : 28.0-32.0
D42:4		$\theta - 2\theta$	10	None	2 θ : 108	2 θ : 35.3-41.0
D42:5		$\theta - 2\theta$	0.5	#1,#3	2 θ : 29	2 θ : 34.025-34.825
D42:6		$\omega - 2\theta$ ($\Delta\omega = -0.18^\circ$)	0.5	#1,#3	2 θ : 107	2 θ : 28.0-37.4
D42:7		ω ($2\theta = 33.1029^\circ$)	0.5	None	ω : 108	$\Delta\omega$: ± 3
D42:8		ω ($2\theta = 34.53^\circ$)	0.5	#3	ω : 108	$\Delta\omega$: ± 3
D42:9		RSM	0.5	#1	ϵ : 109 $\Delta\omega$: 113	$\epsilon + 2\theta_B$: 28.0-37.4 $\Delta\omega$: ± 0.345
D42:10	(0004)	$\theta - 2\theta$	10	#1,#3	108	2 θ : 34.0-81.0
D42:11		$\theta - 2\theta$	10	#1,#3	108	2 θ : 66.0-78.0
D42:12		ω ($2\theta = 72.8^\circ$)	0.5	#3	ω : 108	$\Delta\omega$: ± 3
D42:13		ω ($2\theta = 69.4^\circ$)	0.5	None	ω : 108	$\Delta\omega$: ± 3
D42:14		RSM	0.5	None	ϵ : 219 $\Delta\omega$: 113	$\epsilon + 2\theta_B$: 62.0-75.0 $\Delta\omega$: ± 0.345
D42:15	(11 $\bar{2}$ 4)	$\theta - 2\theta$	10	None	2 θ : 216	2 θ : 89.9548-101.9548
D42:16		$\theta - 2\theta$	10	#3	2 θ : 216	2 θ : 98.9548-101.9548
D42:17		ω	10	#3	ω : 36	$\Delta\omega$: ± 1
D42:18		RSM	1	None	ϵ : 216 ω : 144	$\epsilon + 2\theta_B$: 89.9548 -101.9548 $\Delta\omega$: -1.5 \rightarrow -0.5

Table 4.27: Summary of the composite scans for sample D42. The supplementary scans are multiplied by the attenuation factor to match them to the base scans.

No.	Base Scan		Supplementary Scan		
	Scan No.	Filter	Scan No.	Filter	Atten. Factor
D42:C1	D42:3,D42:4	None	D42:1	#1,#3	3190
			D42:2	#1,#2	85
D42:C2	D42:9	#1	D42:5	#1,#3	1550
D42:C3	D42:9	#1	D42:6	#1,#3	600

Table 4.28: Simulation parameters for sample D42.

Material	Layer Parameters				Block Parameters		
	Thickness (nm)	Tilt (deg)	Lat. Strain	Perp. Strain	Lat. Size (nm)	Perp. Size (nm)	Misorientation (deg)
InGaN:1	100	-0.27	-0.02	0	12	20	1.3
InGaN:2	80	-0.27	-0.02	0.005	12	20	1.3
GaN	2000	-0.2	-0.005	0	500	2000	0.12
AlN	30	-0.1	—	0.001	10	15	1

InGaN peak also has a different shape than seen in the previous samples.

The simulation parameters are summarised in Table 4.28. Two InGaN sub-layers, with slightly different thicknesses and d -spacings (but otherwise identical), were used to produce the simulation profile for the InGaN peak. The inclusion of two sub-layers reduced the amplitude of the thickness oscillations and the overall intensity of the InGaN peak. However, this is only an *ad hoc* attempt at fitting the peak shape. It is more likely that the peak shape is due to a different defect structure (probably InN clusters as discussed below); hence it is not appropriate to use a more refined fitting procedure based only on a mosaic model. An attempt to reproduce the peak shape using a strain gradient (as for sample C70) was made, and although initial simulations suggested that a better fit could be achieved for the $\theta - 2\theta$ scan, a strain gradient could not produce the peak shape observed in the ω scan.

The InGaN layer was not fitted as accurately as the other two type D samples because the shape of the InGaN peak does not match the peak shape generated by the mosaic block model. This is most obvious in Fig. 4.45, where on a logarithmic

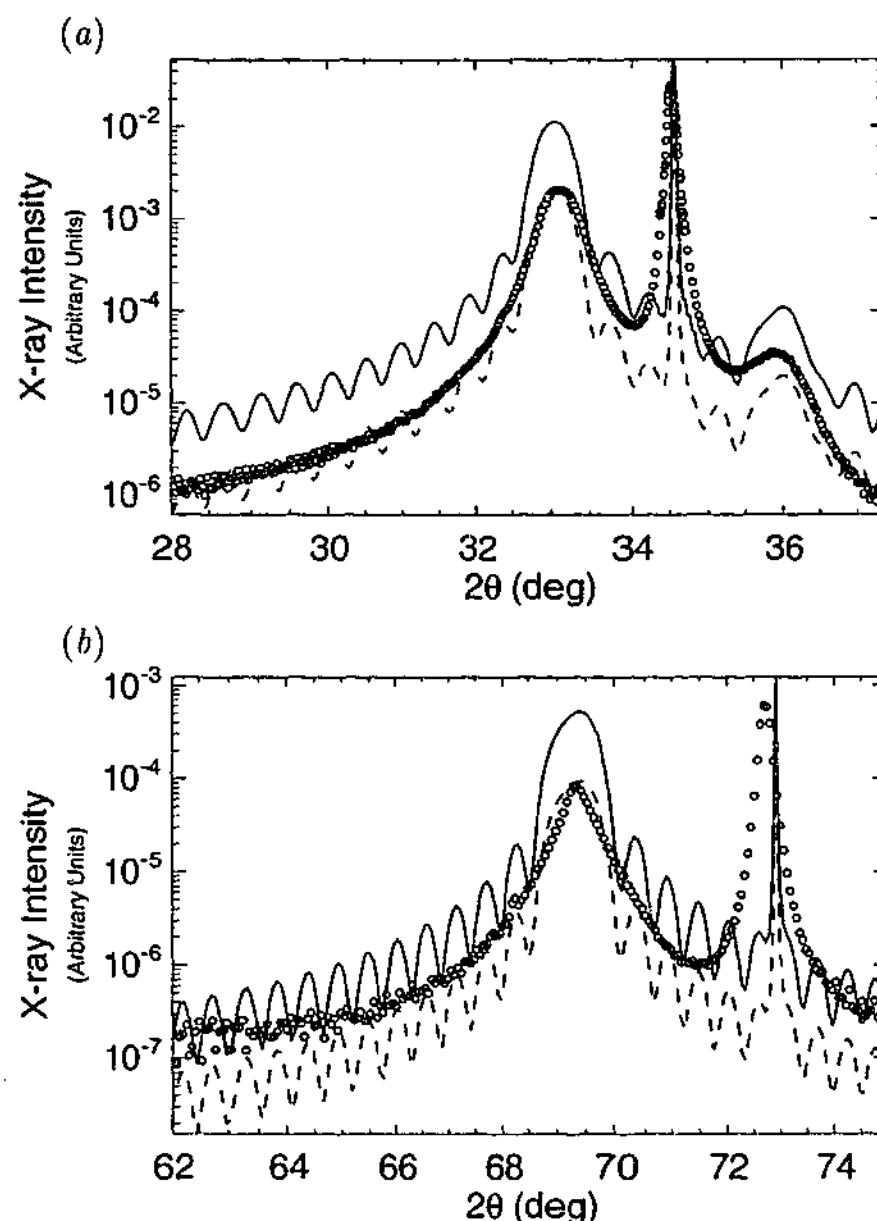


Figure 4.45: Experimental profiles (\circ) and simulated profiles ($—$) for the $\theta - 2\theta$ scans for sample D42 using a narrow (0.5 mm) slit. (a) (0002) reflection, and (b) (0004) reflection. The (0002) experimental profile is the composite scan D42:C2 and the (0004) experimental profile is the composite scan D42:14 (see Table 4.27).

intensity scale the experimental peak is more 'triangular' than predicted by for the mosaic block model; at the top of the peak the simulation is too wide, but at the base it is too narrow.

An $\omega - 2\theta$ scan about the (0002) reflection is reproduced in Fig. 4.47, (with a $\Delta\omega$ offset of -0.18°). This scan is very similar to the $\theta - 2\theta$ scan for the (0002) reflection, apart from a reduction in overall intensity.

The ω scans are shown in Figs. 4.48 and 4.49. The ω scan at $2\theta = 33.1029^\circ$ (Fig. 4.48(a)) exhibited detector saturation; however, the peak height could be

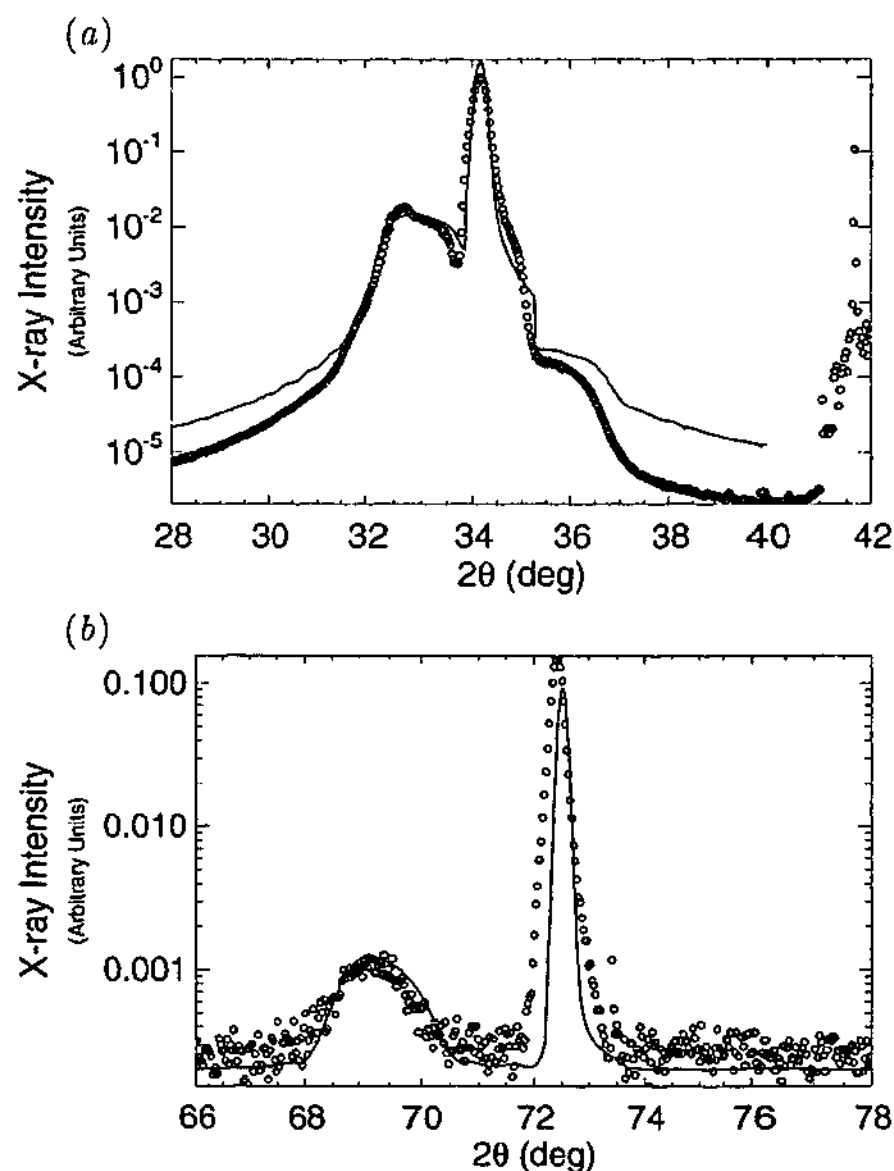


Figure 4.46: Experimental profiles (\circ) and simulated profiles ($—$) for the $\theta - 2\theta$ scans for sample D42 using a wide (10 mm) slit. (a) (0002) reflection, and (b) (0004) reflection. The (0002) experimental profile is the composite scan D42:C1 and the (0004) experimental profile is composite scan D42:11 (see Table 4.27). The narrow experimental peak at $2\theta \approx 41.5^\circ$ is the sapphire (0006) reflection (from the substrate).

approximated from a $\theta - 2\theta$ scan where a filter was employed. Comparing the peak shape of the ω scan with the equivalent scan for the (0004) reflection Fig. 4.49(a)), and matching the peak shape of the non-saturated part of the scan suggests a peak profile of the form

$$I = A \exp(-\sigma_w |\Delta\omega - \Delta\omega_c|), \quad (4.5)$$

where A is the height of the peak, σ_w is a width parameter, and $\Delta\omega_c$ is the centre of the peak. Equation (4.5) is used to generate the 'experimental' profile shown in Fig. 4.48(a). On a logarithmic scale this profile exhibits a 'triangular' shape,

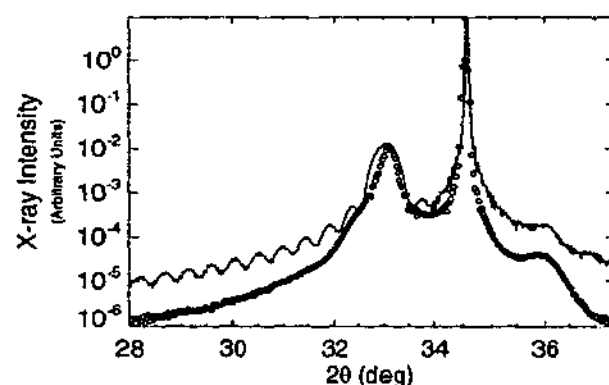


Figure 4.47: $\omega - 2\theta$ scan for sample D42, with a $\Delta\omega$ offset of -0.18° . This scan was collected near the Ga(0002) reflection. This experimental profile is the composite scan D42:C6 (see Table 4.27).

which agrees with the InGaN(0004) peak shape. The peak height does not match the value determined from the $\omega - 2\theta$ scan, although it was within about 25%. The peak profile given by Eq. (4.47) is not differentiable at $\Delta\omega = \Delta\omega_c$, and hence should be smoothed to reproduce the empirical line shape. This peak shape is very different to that obtained for samples D05 and D30.

The one-dimensional profiles about the $(11\bar{2}4)$ reflection are shown in Fig. 4.50. Reciprocal space maps (Figs. 4.51 and 4.52) indicate that the InGaN layer did not grow coherently on the GaN layer, as the InGaN and GaN peaks have different q_x coordinates. The InGaN peak lies approximately on the line connecting the origin of reciprocal space to the GaN peak position, and hence it is almost completely relaxed. In this case relaxation occurs because the InGaN layer is much thicker (200 nm compared to 20 nm), which drives the relaxation process. Further, the higher InN concentration produces a greater lattice parameter mismatch between the two layers, also driving relaxation. The InGaN peak is very broad indicating a large degree of mosaicity and high defect density. This is typical of relaxed layers because dislocations are generated to accommodate the strain. If we assume that the material has no strain then the composition can be easily determined directly from the measured lattice parameter c . The composition is then found to be $42\% \pm 2\%$, which agrees with the value estimated from the growth process.

Again the $(11\bar{2}4)$ simulations do not match the experimental data very closely (see Figs. 4.50, 4.51 and 4.51), although the peak positions have been reproduced reasonably accurately. Figure 4.53 shows an RSM for sample D42 that covers a large angular range; this data was collected using the imaging plate technique described in Chapter 5. A series of horizontal lines are clearly visible in the RSM. These lines suggest a polycrystalline structure. A crystal truncation rod (CTR) scan, covering

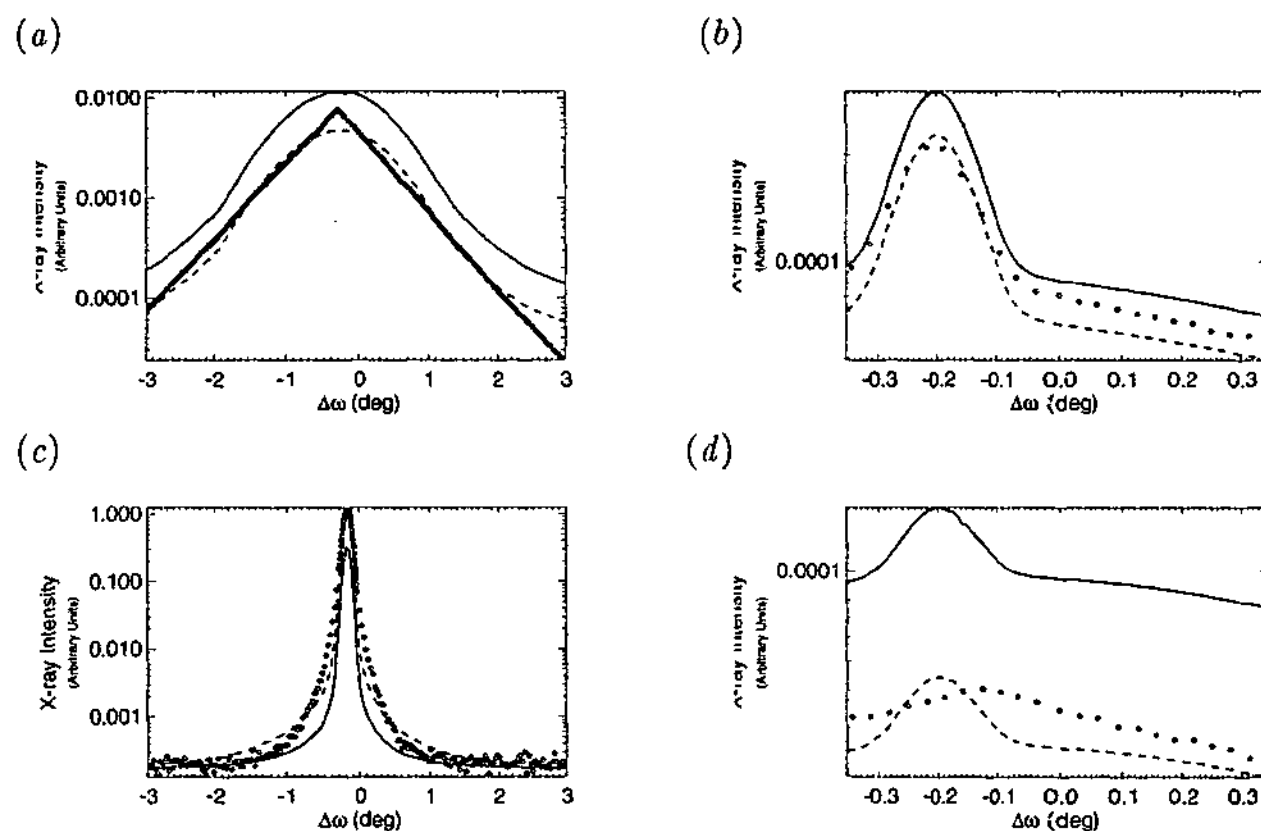


Figure 4.48: Experimental profiles (\circ) and simulated profiles (— and - -) for ω scans for sample D42 using a narrow (0.5 mm) slit. The solid line (—) uses the same normalisation factor as Fig. 4.45(b), while the dashed line (- -) is normalised against the experimental peak height. The 2θ positions are: (a) 33.1029° , (b) 34.0038° , (c) 34.53° , and (d) 35.9142° .

the region $2\theta \approx 2.7^\circ$ to 124° , was collected for this sample (see Fig. 4.54). The CTR also shows the peaks from the polycrystalline structure. The lowest angle peak is associated with a d -spacing of 10.5 \AA , which is much larger than the Group III nitride planar spacings. Sapphire does have plane spacings of this order, but it is very unlikely that these peaks could be arise from the substrate.

A defect structure capable of producing different line shapes (and possibly the powder diffraction pattern) is InN segregation. InN segregation was first reported by Osamura *et al.* (1975) at annealing temperatures of $600\text{--}700^\circ\text{C}$; these temperatures are common during the growth of Group III nitride semiconductors. Segregation occurs because of the large difference ($\approx 11\%$) in interatomic spacing between GaN and InN (El-Masry *et al.*, 1998) leading to a miscibility gap. The equilibrium solubility of InN in GaN at 800°C is approximately 6% for a GaN rich alloy (Ho and Stringfellow, 1996). El-Masry *et al.* (1998) investigated InGaN layers using XRD and TEM, with concentrations up to 50% InN and grown by MOCVD. They found that all samples with $\leq 40\%$ InN demonstrated single InGaN peaks. However, those

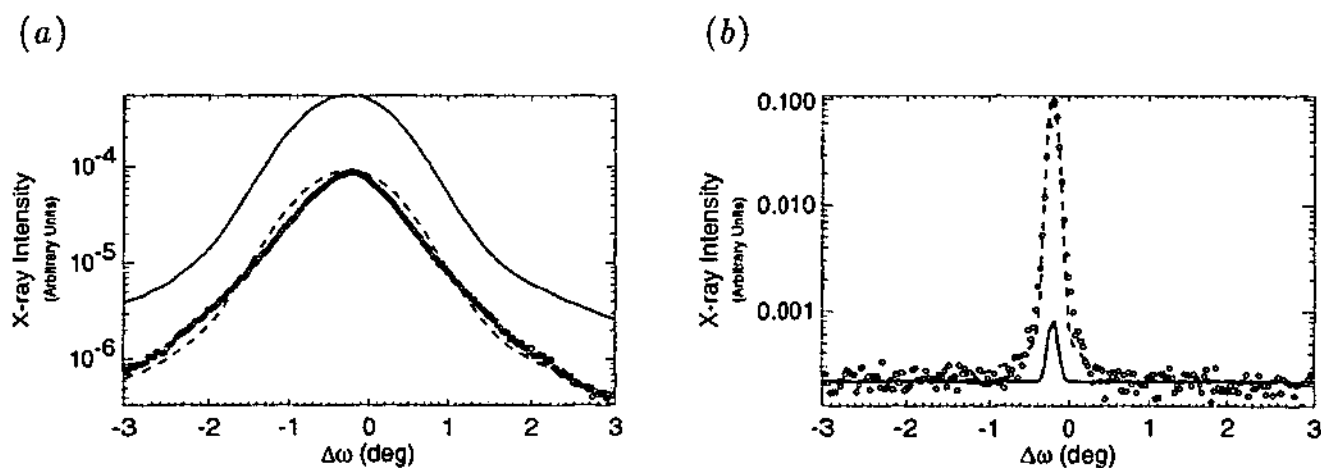


Figure 4.49: Experimental profiles (o) and simulated profiles (— and --) for ω scans for sample D42 using a narrow (0.5 mm) slit. The solid line (—) uses the same normalisation factor as Fig. 4.45(b), while the dashed line (--) is normalised against the experimental peak height. The 2θ positions of the scans are: (a) 69.4° , and (b) 72.8° .

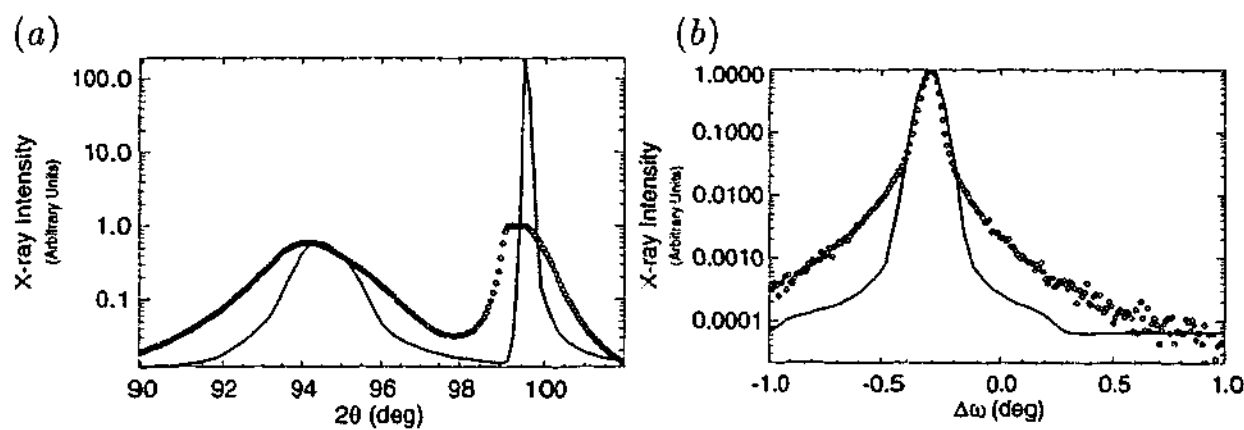


Figure 4.50: (a) $\theta - 2\theta$ and (b) ω scans about the $(11\bar{2}4)$ reflection for sample D42. The circles (o) represent the experimental data and the lines (—) the simulated profiles.

greater than 40% InN showed several InGaN peaks due to regions of different compositions. TEM confirmed that a layer with 49% InN had spinodally decomposed. Selected area electron diffraction showed peak splitting (indicative of phase separation) for InN compositions $\geq 28\%$. It was suggested that the phase separated volume was too small to be detected by XRD for InN compositions between 28% and 40%. XRD on samples grown using MBE also showed phase separation above 30% InN (Singh *et al.*, 1997). Compositional fluctuations have been observed for even lower compositions ($\approx 10\%$ InN) using Raman scattering (Behr *et al.*, 1998). Silveira *et al.* (1999) reported that the InN rich phase had an InN content of $\approx 80\%$, regardless of the composition of the original material. Ho and Stringfellow (1996) calculated the

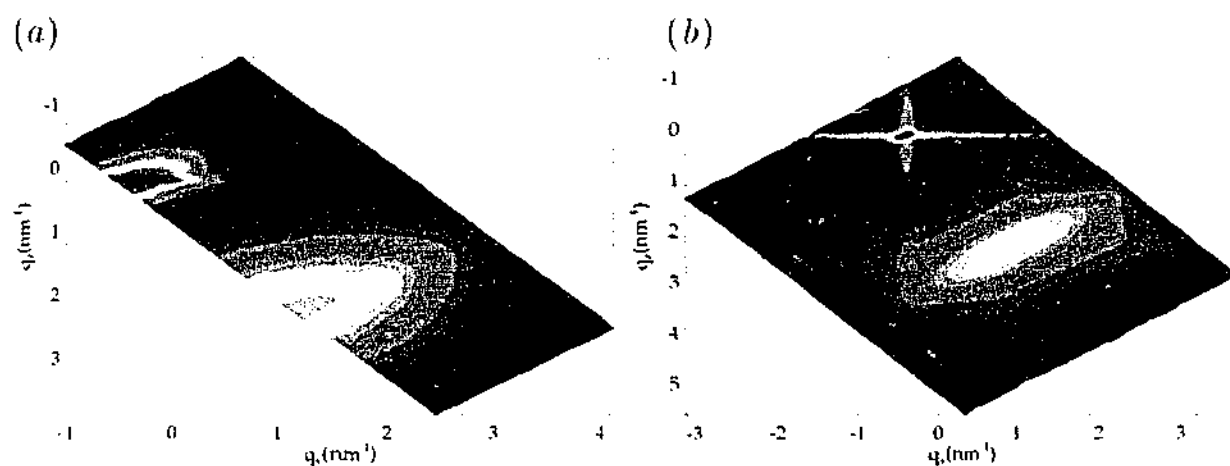


Figure 4.51: (a) Experimental RSM, and (b) simulated RSM, about the $(11\bar{2}4)$ reflection for sample D42.

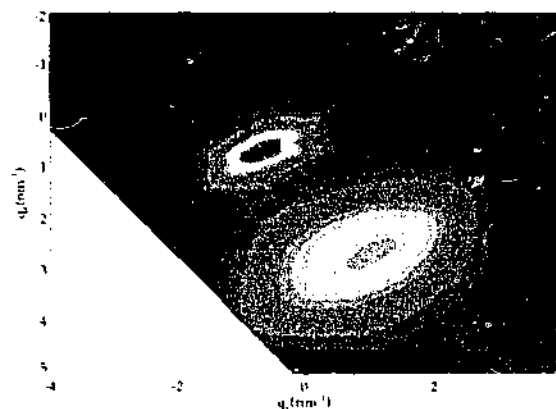


Figure 4.52: Reciprocal space map about the $(11\bar{2}4)$ reflection for sample D42, collected using the imaging plate technique described in Chapter 5. This scan indicates that the $\text{In}_{0.42}\text{Ga}_{0.58}\text{N}$ has not grown coherently on the GaN buffer (the peaks are not at the same q_x value). Furthermore the $\text{In}_{0.42}\text{Ga}_{0.58}$ peak is very broad indicating strain relaxation.

thermodynamically stable InN rich layer to be 95% InN. Phase separation normally proceeds via a spinodal decomposition, which leads to non-random fluctuations in composition (although no long-range order). However, many authors have reported that the phase separation can also produce almost pure InN clusters (quantum dots) in the InGaN active layer of quantum well structures (Martin *et al.*, 1999; O'Donnell *et al.*, 1999; Yang *et al.*, 2002). Some authors also suggest that the excellent performance of devices based on InGaN is due to quantum confinement of excitons by the InN dots (O'Donnell *et al.*, 1999). Sample D42 is very different to the samples described in these papers; the latter has a thick InGaN layer (200 nm), while the former quantum well structures typically have an InGaN thickness of only several nanometres. However, Nistor *et al.* (2000), however, report observations whereby a

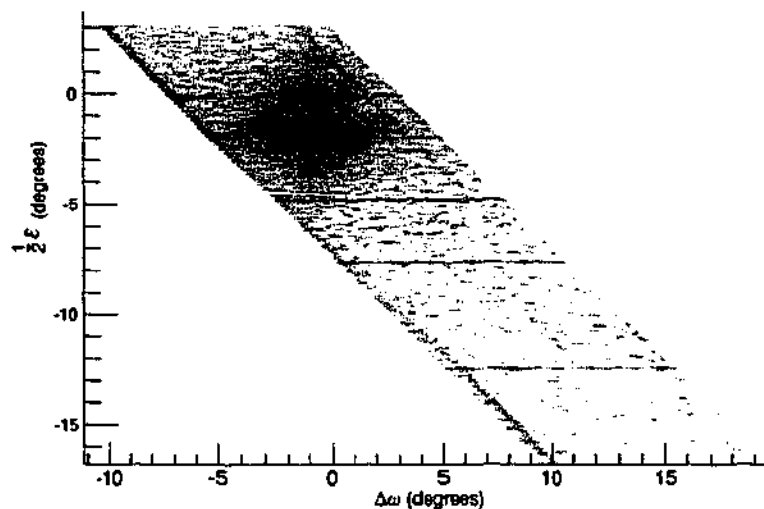


Figure 4.53: An RSM collected using the imaging plate method described in Chapter 5. Streaks are observed, which have the appearance of powder diffraction lines. These streaks suggest that a random polycrystalline material is present in the sample. Note that this RSM is plotted on angular axes (not reciprocal space).

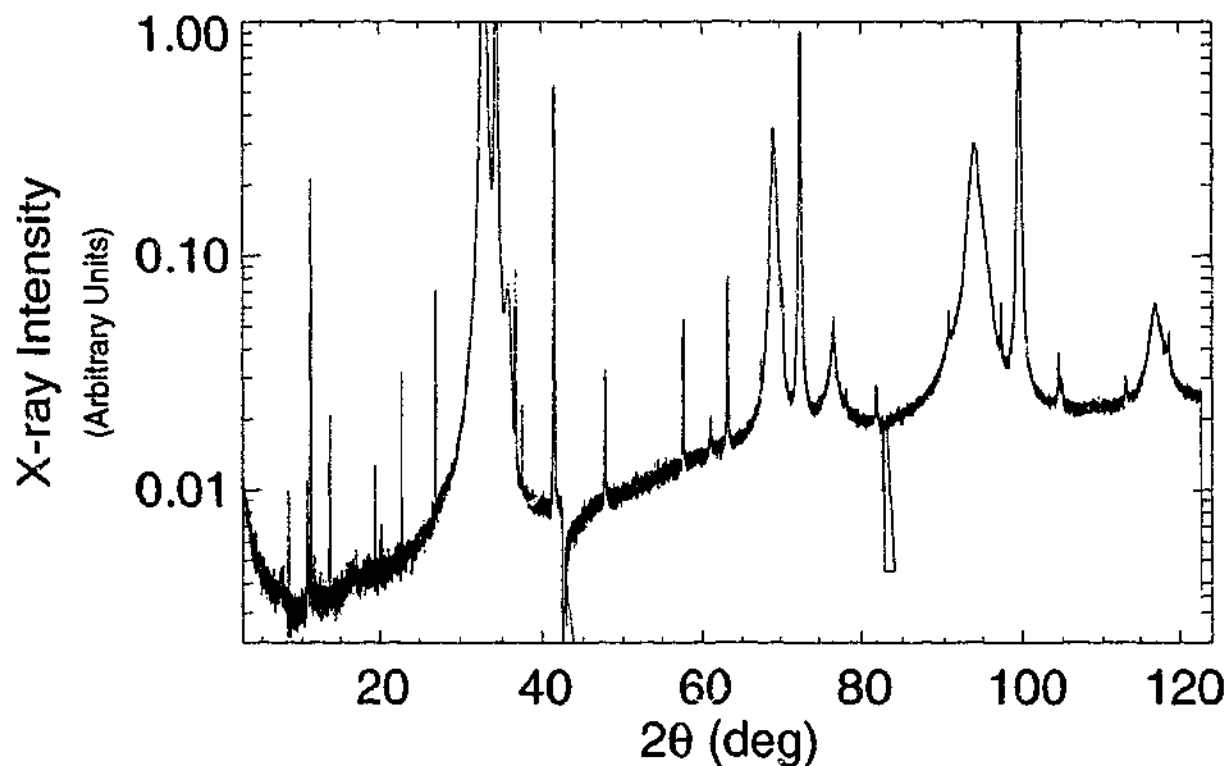


Figure 4.54: Crystal truncation rod scan for sample D42, showing many diffraction peaks. These peaks suggest that a random polycrystalline material is present in the sample.

280 nm thick InGa_N layer exhibits InN quantum dots 1.5 nm–3 nm in size, with the luminescence from the material attributed to these dots.

Our results tentatively support the conclusion that InGa_N segregates for compositions greater than 40%. However, our scans do not show the InGa_N peaks,

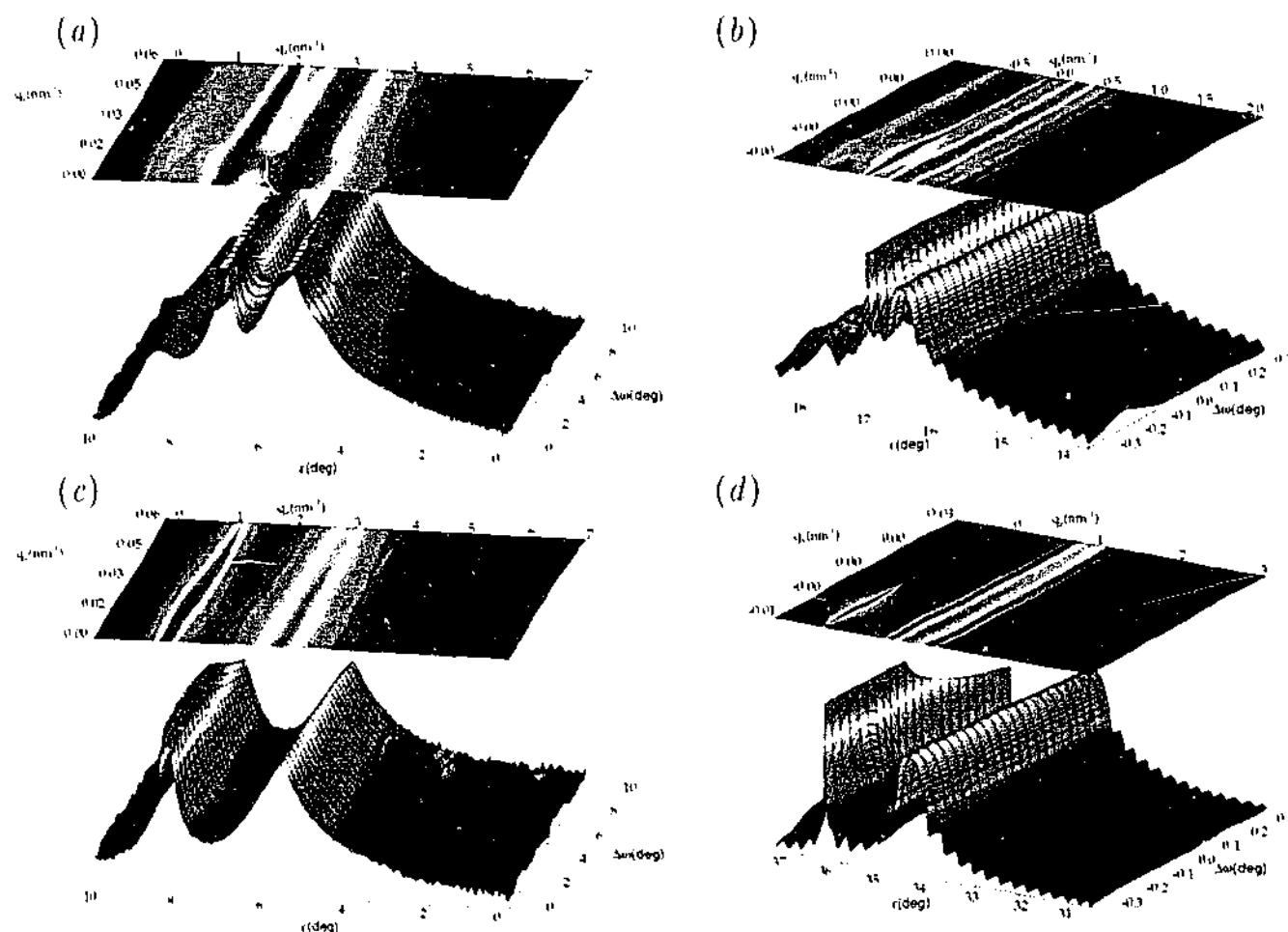


Figure 4.55: Reciprocal space maps for sample D42. (a) Experimental RSM, and (b) simulated RSM about the GaN(0002) reflection; (c) experimental RSM, and (d) simulated RSM about the GaN(0004) reflection. The simulated RSMs have been scaled so that the InGaN peak heights match the experimental data.

observed by El-Masry *et al.* (1998), which are indicative of spinodal decomposition. Instead we observe InGaN peaks whose shapes suggest the defect structure within the InGaN has been modified, and many peaks in the CTR that suggest another crystal structure (or multiple structures) is present. The InGaN peak shapes in Figs. 4.45, 4.48(a), and 4.49(a), point to the formation of InN clusters or quantum dots, which broaden and modify the shape of the InGaN peak. Nistor *et al.* (2000) showed that the InN quantum dots had a lattice parameter similar to, but slightly larger, than the surrounding InGaN matrix; this is expected if the material precipitated in its bulk (wurtzite) structure. Such clusters/quantum dots could not produce the many peaks seen in the CTR (Fig. 4.54). Kandalam *et al.* (2002) have presented calculations for Al_nN_n , Ga_nN_n , and In_nN_n ($n = 4, 5, 6$) clusters. The lowest energy configurations of the clusters are not the same as the bulk. Hence, formation of non-bulk type clusters may produce the CTR scan in Fig. 4.54, particularly if there is some form of ordering.

Incorporating a cluster defect structure into the simulation, in addition to the mosaic block model (we assume that both defect structures would coexist), would assist in clarifying whether clusters are present. Nesterets and Punegov (2000) calculated the correlation function for several types of amorphous clusters. Although incorporating a cluster defect into the mosaic block model may allow the InGaN peak shape to be reproduced, it will not account for the many peaks seen in the CTR scan, as the simulation will only generate Bragg reflections for the wurtzite crystal structure. TEM may be required to elucidate the origin of the peaks in the CTR scan.

The composition of the InGaN layer was the same as expected by the growth parameters. However, one would expect the composition to be smaller if InN segregated from the alloy. If the layer was not fully relaxed then the composition of the InGaN layer would be smaller than that quoted. Therefore, either the fraction of InN segregation is small, or the layer has not completely relaxed.

It is interesting to note that the scans collected using the wide open slit, (Fig. 4.46) match the experimental data. Even the InGaN peak, which has a broad flat top, has been correctly fitted by the model (apart from the small secondary peak). The simulation correctly reproduces the peak shape because using a wide slit means the detector integrates over a region of reciprocal space. This integration causes the InGaN peak to be flat at the top because the peak is very broad in both the q_x and q_z directions; this is correctly modelled by the simulation. Although the correct peak shape was not produced by this model, the correlation lengths based on the mosaic block dimensions are likely to be reasonably accurate. This assertion is supported by the accurate fitting of the $\theta - 2\theta$ scans collected using the wide slit. Since the defect structure probably includes clusters, in addition to the mosaic block arrangement, these will also broaden the peaks and thus the mosaic block sizes reported would be a lower limit. The dislocation densities derived from the lateral mosaic block sizes was $1.4 \times 10^{12} \text{ cm}^{-2}$ for the InGaN layer, $8.0 \times 10^8 \text{ cm}^{-2}$ for the GaN layer, and $2.0 \times 10^{12} \text{ cm}^{-2}$ for the AlN layer. The defect densities for GaN and AlN agree with those from samples D05 and D30.

4.5 Comparison of Statistical Diffraction Theory and Williamson-Hall Analysis

The Williamson-Hall technique is described in Chapter 6. This technique is commonly used to determine parameters similar to those specified by the mosaic block model. Although the experimental data was collected for analysis using the statistical diffraction theory, a brief analysis of the InGaN peaks for the D type samples was completed. The results are summarised in Table 4.29.

The mosaic block size, misorientation, and heterogeneous strain are determined from the graph of peak width (in the q_x and q_z directions) squared against peak position squared (in reciprocal space). However, since data was only collected for two different symmetric reflections, the Williamson-Hall analysis should only be treated as an indicator of the correctness of the mosaic block model. The block size for sample D05 and the lateral block size for sample D30 are minimum values. An upper bound could not be obtained because the intercept was negative. Similarly the lateral block size for sample D42 could not be determined because its intercept was also negative. Heterogeneous strain was not included because the appropriate gradients were negative. (The gradients were very small and it is assumed that the heterogeneous strain was essentially zero).

Considering that only two reflections were considered, there is a reasonable agreement between the statistical diffraction theory (using a mosaic block model) and the Williamson-Hall analysis. The misorientation matches particularly well, as does the perpendicular block size for samples D30 and D42.

Table 4.29: Summary of material parameters for the InGaN layer for sample type D using Williamson-Hall (WH) analysis and statistical diffraction theory (SDT) using a mosaic block model.

Sample	Analysis Type	Perp. block Size (nm^{-1})	Lat. Block Size (nm^{-1})	Misorientation (deg)	Heterogeneous Strain
D05	WH	≥ 46	≥ 196	0.13 ± 0.02	0.0105 ± 0.0005
	SDT	15	400	0.1	
D30	WH	16 ± 2	≥ 826	0.12 ± 0.02	≤ 0.005
	SDT	14.8	170	0.1	
D42	WH	19.3 ± 0.5	Indeterminant	2.19 ± 0.07	Indeterminant
	SDT	20	12	1.3	

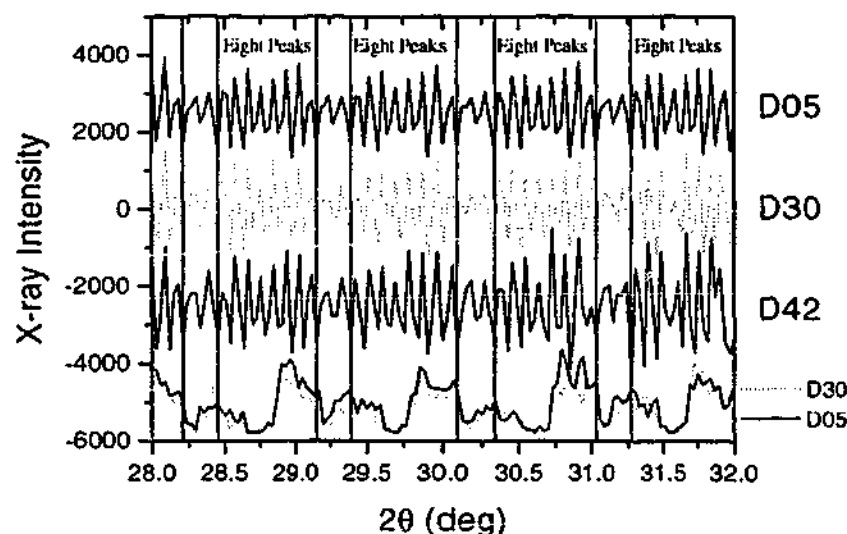


Figure 4.56: Periodic noise observed in the background intensity for the RSMs and $\theta - 2\theta$ scans for the three samples of type D. The upper three curves were generated by summing together each of the $\omega - 2\theta$ scans making up the RSMs about the (0002) reflection. The bottom scans are portions of the $\theta - 2\theta$ scans, collected using a narrow slit from samples D05 and D30 (as indicated).

4.6 Periodic Noise and Spurious Peaks

A periodic profile was observed in the background of those experimental scans acquired at a low count rate (i.e., with filter #3 inserted, or with a narrow slit in front of the detector). By integrating across a RSM in the $\Delta\omega$ direction (i.e., by adding together the $\omega - 2\theta$ -scans that form the RSM) the periodic profile was clearly revealed. Integrating in this way reduced any statistical noise. The integrated scans about the (0002) reflection are shown in Fig. 4.56 for all three type D samples. The background fluctuations were extracted from the experimental scan by subtracting the average profile. The average profile was generated by smoothing the scan using an eleven-point Savitzky-Golay method.⁶ For clarity the scans have been separated vertically in Fig. 4.56. No other processing (normalisation or horizontal translation) has been performed. The bottom two scans are portions of the $\theta - 2\theta$ scans collected using a narrow slit.

The vertical bars in Fig. 4.56 highlight the periodicity evident in the scans. A periodic profile was also seen for the (0004) reflection. The periodic pattern has a form similar to thickness fringes, or more specifically interference from a multilayer structure. Initially this was thought to be the origin of the periodicity observed here. However, each of the scans shown in Fig. 4.56 displays the same pattern despite the

⁶To determine the smoothed value at each point the Savitzky-Golay method performs a regression of a specified number of data points (eleven in this case) centred on the data point in question.

fact that a range of samples was used. If the periodicity is due to the sample then it must arise from the GaN layer, because the InGaN layers are very different for the three samples. In this case the fringe spacing must be due to a layer much thinner than the GaN layer, whence the GaN would be composed of sub-layers. The chance of a sub-layer structure being identical across three samples is unlikely, particularly as sample D42 had a much thicker InGaN layer deposited on the surface, and hence was at an elevated temperature longer. Figure 4.57 shows scans for each sample that suggest the fringe amplitude doesn't change with count rate. If the fringes were due to the sample then it is expected that the fringe amplitude would be directly related to the count rate. Figure 4.57(a) shows two scans for sample D05 near the (0002) reflection. Filter #3 was used to reduce the intensity for the left hand scan ($< 37.5^\circ$), but not for the right hand scan ($> 37.5^\circ$). The greater intensity for the latter scan results in the GaN peak still being apparent between 37.5° and 40° . However, fringes are not present, or at least they have not increased in amplitude. Figure 4.57(b) shows two scans for sample D30 about the (0004) reflection. The blue scan was collected using filters #1 and #3, and the red scan with filter #3 only. In this

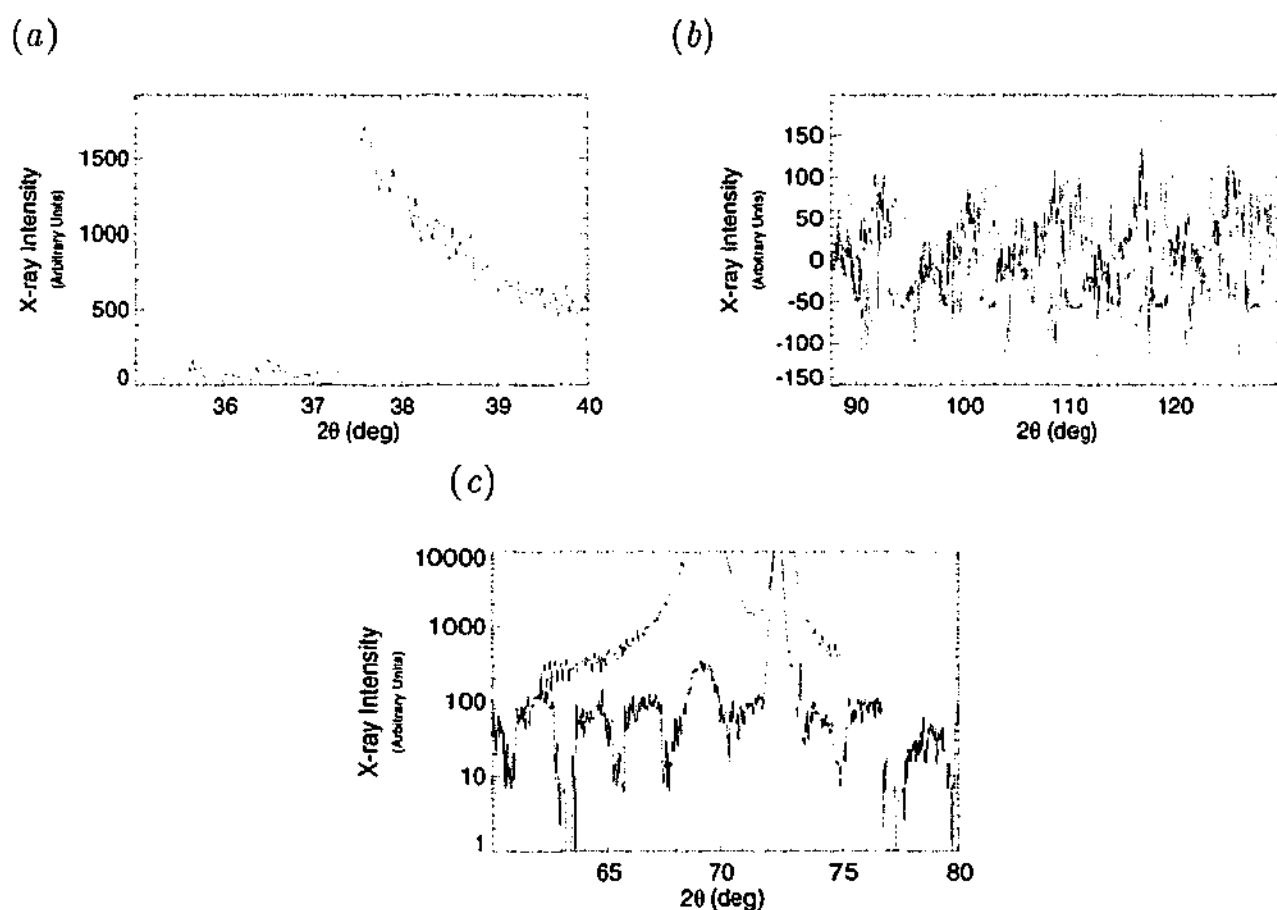


Figure 4.57: Profiles demonstrating the independence of the noise amplitude with count rate. (a) Sample D05, (b) sample D30, and (c) sample D42. See text for details.

case the average intensity has been subtracted so that both scans are superposed. Again the increase in intensity has not significantly changed the amplitude of the fringes. The scans collected at low intensity are truncated at zero intensity, and there is also a translation of the profile between the two scans. The flattening at zero intensity suggests that the mechanism causing the 'noise' can also reduce the detected intensity. The reason for the translation is unclear. The position of the GaN peaks in both scans agree, and hence the shift is not due to a calibration error. Figure 4.57(c) shows the (0004) reflection for sample D42. The bottom scan in Fig. 4.57(c) was collected with filters #1 and #3 and a 10mm detector slit. The top scan in Fig. 4.57(c) had a 0.5mm slit and no filters. Again the larger intensity scan does not show fringes (on a logarithmic intensity scale). Hence all of the evidence suggests that the fringes are due to some noise introduced by the apparatus that is correlated with sample or detector position. The actual cause has not been determined.

Another feature common to samples D05 and D30 was three spurious peaks, to the right of the $\Delta\omega = 0$ axis, as seen in the RSMs shown in Figs. 4.44, 4.41(c), 4.28(a,c) for samples D05 and D30. As these peaks appear in exactly the same position for two different samples it is very difficult to suggest a possible origin. Possible sources for the peaks are impurities introduced during growth, some form of experimental electrical noise (and hence not seen for sample D42 because the thicker InGaN layer masks the peaks), substrate damage particularly if the two samples came from the same part of the sapphire wafer, or possibly a defect in the GaN layer. Particularly perplexing is that not only can the peaks be attributed to the same d -spacing for each sample and scan, but they are also offset in the $\Delta\omega$ direction by similar amounts. The former point effectively rules out the possibility it is some form of noise spike, because the peaks are correlated with d -spacing not angle. If the peaks are due to an impurity, it must have some preferred orientation with respect to the substrate (or overlayers) so as to ensure the same $\Delta\omega$ offset was obtained for both samples. It is likely that the peaks are due to damage to the substrate as this would ensure the orientation is the same for each sample, if they are from similar parts of the sapphire wafer. However, the d -spacing does not agree with any sapphire reflections, and as the peaks are very narrow in the q_z direction it is unlikely the crystal material they originate from is strained. An impurity compound may be formed during growth; however, as the peaks are very narrow the region they originate from must be thick, which is unlikely for an impurity compound.

4.7 Asymmetric Reflections

The $(11\bar{2}4)$ reflection was not fitted as accurately as the $(00.l)$ reflections for each of the samples. The simulated peaks did not have the same shape as the experimental profiles, and generally were too narrow at the base. The reciprocal space maps indicate that the simulated intensity did not have the correct distribution in reciprocal space. Specifically the simulated intensity was concentrated in two strong streaks in the q_x and q_z directions; however, the experimental scans showed the intensity to be more uniformly distributed about the peak. As discussed briefly in Sec. 4.4.1 the two perpendicular streaks are due to the geometry of the mosaic block. A streak in the q_z direction is observed even for high quality crystalline samples because real samples always have a surface; since the diffraction volume is not infinite the streak is associated with the crystal truncation rod. The streak in the q_x direction is due to the finite size of the coherent region perpendicular to the surface. The $\theta - 2\theta$ and ω scans collected for the $(00.l)$ reflections are essentially parallel to the q_z and q_x directions, respectively, and measure the intensity distribution along the streaks in those directions. However, for the asymmetric reflections the $\theta - 2\theta$ and ω scans are not parallel to the q_x and q_z directions, and do not measure the intensity along the streaks. The peak shape in the simulated RSMs show that the scans crossing the peak, (but not directly along the q_x or q_z direction) will be narrower at the base than those in the q_x and q_z directions. If a background count had not been added to the simulated asymmetric scans, they would have covered more orders of magnitude (in intensity) than any of the experimental scans (or the simulated symmetric scans). These observations suggest there is a deficiency in the model for this class of material. Wurtzite has a hexagonal symmetry, and real mosaic blocks are likely to have a hexagonal base. This will modify the intensity distribution in q_y - q_x space. However, in q_z - q_x space, the mosaic blocks still have rectangular symmetry, and hence the diffraction peak will still have the same general shape. The theoretical model described in Sec. 2.9 includes the size and shape of the mosaic block in the probability function. Modification of the probability function to accommodate a hexagonal block has negligible effect on the simulated intensity pattern. Another possibility is twisting of the mosaic block about the z-axis. This has no effect on the diffraction vector for $(00.l)$ type reflections. For asymmetric reflections with $l \neq 0$, twisting the block will cause the diffraction vector to rotate about the q_z -axis. For small rotation angles this will have a negligible effect on the component of the diffraction vector in q_z - q_x space. For larger angles the diffraction vector will have a significant component directed out of the q_z - q_x plane, and hence the

diffracted intensity will not reach the detector. Hence twist does not affect the peak shape for these reflections. However, for scans in q_x - q_y plane (ϕ scans), and grazing incidence in-plane X-ray diffraction (GIIXD), twisting is the predominant cause for peak broadening of $l = 0$ type reflections. Additions to the model which may improve the fitting of the asymmetric scans would include distribution of block size, interfacial roughness and point defects.

4.8 Summary of the Results

4.8.1 Comparison of Buffer Layers

Diffraction peaks were observed for the as grown 30 nm and 70 nm LT-AlN buffer layers, showing that they have crystallised. The peaks were broad, indicating that the layers were of very poor quality (i.e., small crystallites/grains randomly orientated). These observations agree with the results reported by Takeda *et al.* (2003) and Tabuchi *et al.* (2002), for samples identical to ours. However, contrary to these authors our results suggest that there are two distinct correlation lengths (two different grain/mosaic block sizes) perpendicular to the surface. We conjecture that these regions are sub-layers within the material. In this model the lower quality sub-layer (smaller block size) has grown immediately on top of the sapphire substrate, with the higher quality layer (larger block size) on top. The lower quality layer has a tensile strain perpendicular to the substrate, with an in-plane compressive strain, as expected for AlN on sapphire. The higher quality layer is essentially relaxed (it has very small tensile strain in the plane). This suggests that the layer has reached a critical thickness for relaxation (about 25 nm). The misfit between the substrate and the AlN is accommodated in the bottom sub-layer.

For the 30 nm LT-AlN buffer, the annealing process drastically improved the higher quality sub-layer. Annealing increased the lateral block size and induced a very small misorientation, with no full layer tilt. The lower quality layer was almost identical to the material before annealing. The annealing process only slightly affected the 70 nm buffer layer. Tabuchi *et al.* (2002) reported that a 30 nm LT-AlN buffer layer produced better quality GaN/InGaN overlayers than a 70 nm buffer. We suggest that it is the high quality sub-layer incorporated in the 30 nm buffer layer that leads to the higher quality overlayers, compared to those grown on the 70 nm buffer layer. In general, deposition of GaN on a high quality AlN will result in a low quality GaN layer because of the lattice mismatch. However, since the high quality AlN sub-layer observed for the 30 nm LT-AlN buffer layer is very thin, it should be easily deformed to accommodate the GaN layer. The improvement in the

GaN overlayer is due to the high quality AlN sub-layer providing a regular, correctly orientated, nucleation layer. For the 70 nm buffer layer the GaN layer will nucleate on a highly misorientated layer, which is tilted with respect to the substrate. The reason annealing produces the high quality sub-layer for the 30 nm AlN buffer and not for the 70 nm buffer is unknown.

After deposition of a 30 nm GaN layer the high quality AlN sub-layer component of the 30 nm LT-AlN buffer was no longer observable. However, the lower quality material was very similar to that observed before GaN deposition (in fact any differences are smaller than the uncertainty due to the noise present in the scans for sample B30). This implies that the deposition of the GaN layer disrupted the high quality layer (as described above). It also suggests that any modification of the AlN due to annealing occurred before the GaN layer was grown. The peak positions indicated that the GaN layer grew coherently on the (lower quality) AlN layer.

Significant changes to the experimental X-ray diffraction profiles for the 70 nm AlN buffer layer occurred during deposition of the GaN layer. Before annealing there was a broad peak, superposed on a narrower peak (in the $\theta - 2\theta$ scan). After annealing there were also two peaks, however, they were of similar widths and completely separated in the (0004) scan. This could have been due to the longer time spent at high temperature (during the deposition of GaN) and/or some strain transfer from the GaN layer. The AlN layer appeared to be under tensile strain in the plane. Kim *et al.* (1999) investigated the effects of strain transfer between an AlN buffer and a GaN layer, and showed that the GaN and AlN layers have the same in-plane lattice parameter up to a critical thickness (about 5 nm). Even if this was the case, the amount of strain would not be enough to cause the observed peak shift. Furthermore, the samples investigated by Kim *et al.* (1999) were grown using molecular beam epitaxy, and with AlN buffer layer approximately ten times thinner than those we have studied here (see Kim *et al.*, 1996).

The thin GaN layer deposited on the 30 nm buffer layer had a large lateral block size, very small misorientation, and was orientated perfectly with the substrate. This would be due to the high quality AlN surface on which it was nucleated. The layer was strained, having grown coherently on the lower quality AlN sub-layer. The GaN layer grown on the 70 nm buffer layer was relaxed. Hence, the diffraction peak was much broader than for the GaN layer grown on the 30 nm buffer layer. Furthermore, the mosaic block were not exactly orientated with the substrate.

4.8.2 Variation of InGaN Layers with Composition

The 20 nm thick $\text{In}_x\text{Ga}_{1-x}\text{N}$ layers ($x \leq 0.3$) were accurately fitted using the mosaic block model. These layer grew coherently on the AlN buffer layer, as shown by the position of the (11 $\bar{2}$ 4) diffraction peak. The composition of the nominally $\text{In}_{0.3}\text{Ga}_{0.7}\text{N}$ layer was found to be $\text{In}_{0.17}\text{Ga}_{0.83}\text{N}$. However, the nominal composition was determined by the growth conditions and was very inaccurate. The 30% InN composition was actually an upper limit, which gives us confidence in our value of 17% InN.

The 200 nm thick $\text{In}_{0.42}\text{Ga}_{0.58}\text{N}$ showed significant InN segregation, as is evident in the change in the shape of the diffraction peaks. The layer was relaxed, with the peak positions indicating that the layer composition is in agreement with the expected value based on the growth conditions. This suggests that only a small fraction of the InN had segregated.

Pereira *et al.* (2002) demonstrated that multiple peaks can originate from a single InGaN layer. The position of these peaks in reciprocal space indicates variation in strain or composition. In particular when the InGaN layer reaches a critical thickness, the strain begins to relax. This relaxation may occur for just part of the layer, broadening or splitting the Bragg peak. Our samples only exhibited one InGaN peak. The 20 nm thick InGaN layer for samples D05 and D30 was completely strained, having the same lattice parameter, a , as the GaN buffer layer. The 200 nm InGaN layer for sample D30 was also completely relaxed. This suggests that the critical thickness for relaxation is greater than 20 nm but less than 200 nm. The typical critical thickness from the literature is about 75 nm (O'Donnell *et al.*, 2001). The larger InN composition would also have increased the strain (by increasing the lattice constant), thus increasing the driving force for relaxation.

4.8.3 Dislocation Densities

The dislocation densities for these samples were calculated in a simple manner (i.e., assuming one dislocation per mosaic block wall). Despite this the values determined for the samples are of the correct order i.e., the AlN layers were found to have a typical dislocation density of 10^{11} cm^{-2} , the GaN layers a typical dislocation density of approximately 10^9 cm^{-2} , and the InGaN layer between 10^9 cm^{-2} and 10^{10} cm^{-2} (except for sample D42 which had a considerably higher dislocation density for the InGaN layer, 10^{12} cm^{-2} , because of strain relaxation). Akasaki (2002) quotes dislocation densities of $> 10^{11} \text{ cm}^{-2}$ for GaN grown directly on sapphire (this agrees with our value for AlN), and 10^9 cm^{-2} to 10^{10} cm^{-2} for GaN grown on an AlN buffer layer. Lester *et al.* (1995) reports a dislocation density of $2 - 10 \times 10^{10} \text{ cm}^{-2}$ for

InGaN layers.

The determination for the dislocation densities could be improved by considering the specific types of dislocation present and the effects they would have on the diffraction profile (see e.g., Metzger *et al.*, 1998).

CHAPTER 5

Development of an Imaging Plate Technique for Rapid RSM Collection

5.1 Overview of RSM Collection with Position Sensitive Detectors

The experimental procedure described in Chapter 3 utilised a scintillation detector with an analyser crystal (or slit) to improve the angular resolution. This arrangement is capable of very high resolution scans (the smallest angular window used was 7 arcseconds). However, collection of reciprocal space maps is time consuming, because each datum point is collected individually, with sample/detector movement required for each datum. The reciprocal space maps collected using the technique detailed in Chapter 3 (and presented in Chapter 4) typically required 3-4 hours to collect. In general several maps are required for every sample and if numerous samples are to be investigated, the total scan time can become prohibitively large. This is especially true for synchrotron experiments, where experiment time is limited.

Collection time can be reduced by using a position sensitive detector (PSD). PSDs sample extended areas of reciprocal space simultaneously. Unfortunately these detectors have poorer spatial resolution, dynamic range, and signal to noise ratio than scintillation detectors. Further, the analyser crystal discriminates intensity based on angle, whereas a PSD cannot distinguish between beams striking the detector at the same position but from different angles (and hence from different parts of the sample).

PSDs are used routinely for collecting reciprocal space maps; however, not all techniques are suitable for investigating semiconductor heterostructures. It is important that the detector is able to handle the high intensities diffracted from substrates (or thick high quality layers) without being damaged. They must also have a large dynamic range so that the peaks and any oscillations in the wings of the main peaks can be detected simultaneously.

Gerhard *et al.* (2000) studied ZnSe-based laser diode structure by illuminating the sample with a highly divergent X-ray beam (from a synchrotron microfocus beamline). The diffracted intensity pattern was recorded directly in two dimensions

on an imaging plate (IP). The divergence of the incident beam is equivalent to rocking the sample during exposure to plane wave irradiation. This method is very fast and simple, although the spot size must be small ($10\ \mu\text{m}$) in order to achieve a large range of incident wavevectors. Using this method information is collected from a very small region of the sample, which can be advantageous depending upon the sample and the information required. A disadvantage of collecting a range of incident wavevector angles simultaneously is that the intensity is integrated over reciprocal space. The range of the integration depends directly on the range of the incident wavevectors. Gerhard *et al.* (2000) used a small wavevector distribution range, and so avoided excessive integration. If wide scans are required then a point or one-dimensional detector can be used to avoid integration.

A number of authors (see e.g., Kinne *et al.*, 1998; Butler *et al.*, 2000; Welberry *et al.*, 2003) used IPs as one-dimensional detectors. Weissenberg slits are employed to mask the IP, which is translated perpendicular to the plane of diffraction. Kinne *et al.* (1998) and Butler *et al.* (2000) collected RSMs by translating the IP and rotating the sample simultaneously to fill the entire plate area. Welberry *et al.* (2003) used a similar procedure except that the IP was stationary while being exposed. They collected up to three hundred strips, each 0.5 mm wide, on one imaging plate. Of these authors only Kinne *et al.* (1998) studied epitaxial layers on substrates, the sample type in which we are interested. Butler *et al.* (2000) and Welberry *et al.* (2003) studied small single crystals. These systems are simple to set up compared to triple axis diffractometry (TAD), use a widely available PSD (IPs), and have a reasonable spatial resolution and dynamic range. The amount of integration over reciprocal space is depends upon the slit width. Each of the above methods require angular calibration of the imaging plates (Kinne *et al.*, 1998; Butler *et al.*, 2000; Welberry *et al.*, 2003). This was achieved using high intensity reflections from the sample. Welberry *et al.* (2003) also required a calibration to account for the decay of the intensity recorded on the IP with time over the duration of the scan.

Osborn and Welberry (1990) and Boulle *et al.* (2002) both describe curved one dimensional position-sensitive wire (or blade) detectors, which allow many scans to be collected without the need to change the film or imaging plate. Although these detector systems allow high spatial resolution to be achieved, they are expensive and can be damaged by synchrotron beam intensities. This is particularly true for samples that exhibit strong substrate reflections. Hence, despite their advantages, these detectors are not suited to our experimental work.

This chapter describes a set of experiments exploring the capabilities of the

imaging plate system at the Australian National Beamline Facility for collecting reciprocal space maps for Group III nitrides. Our approach differs from other authors. For example, unlike Kinne *et al.* (1998) the work was carried out at a synchrotron facility, and in contrast to Kinne *et al.* (1998); Butler *et al.* (2000); Welberry *et al.* (2003) the RSMs were compared directly with our TAD results. The results of this chapter have been published in Mudie *et al.* (2004).

5.2 Reciprocal Space Geometry for Collecting RSMs using Imaging Plates

The angular representation for reciprocal space and reciprocal space scans were described in Sec. 2.10. However, if we replace the analyser crystal and the point detector from the TAD technique with a one-dimensional PSD, (keeping ω constant), the intensity is now recorded along a circular arc in reciprocal space (see Fig. 5.1(a)). A curved two-dimensional map in reciprocal space is produced by collecting data from the PSD for several ω positions. If the small angle approximation is valid then the map is not curved.

Equation (2.127), repeated here for convenience,

$$\omega = \Delta\omega + \frac{\varepsilon}{2}, \quad (2.111)$$

can be rearranged to give

$$\Delta\omega = \omega - \frac{\varepsilon}{2}. \quad (5.22)$$

For constant ω the coordinate along the PSD is linear in ε ; in $\varepsilon/2 - \Delta\omega$ space the PSD produces scans at 45° to the $\varepsilon/2$ -axis, with intercept ω (see Fig. 5.3(b)). No assumptions have been made about the size of ω or ε , hence the $\varepsilon/2 - \Delta\omega$ representation is useful for avoiding otherwise curved scans in $q_x - q_z$ space when the ω and ε ranges are large. It is particularly important for the interpolation scheme described in Sec. 5.3.

5.2.1 RSM Collection Method

As mentioned in Sec. 3.2.1 the diffractometer has a radius of 0.573 m and incorporates an imaging plate cassette that covers $\pm 160^\circ$ in 2θ . The cassette can accommodate up to eight 400×200 mm IPs, with the long side oriented along the circumference. Radioactive fiducial markers are installed in the cassette to provide an angular reference on the IP. Weissenberg screens can be installed so that only 4 mm of the plate is exposed at one time. The IP cassette can be translated perpendicular to the plane of diffraction on linear bearings, so that up to 30 exposures can be collected on one plate, with 1.5 mm between each 4 mm strip.

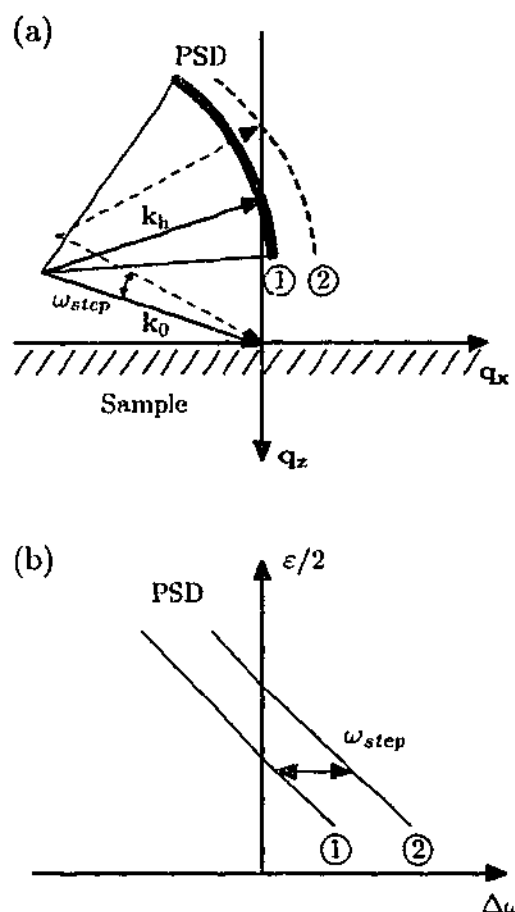


Figure 5.1: Symmetric reflection with a position sensitive detector. (a) Reciprocal space representation, and (b) angular space representation. ① and ② indicate two different ω -positions of the sample, and show how the position sensitive detector covers reciprocal space to produce an RSM.

The IPs are scanned using a Fuji Film BAS2000 system, which provides a dynamic range of 10^4 and a spatial resolution of $100 \mu\text{m}$, which equates to an angular resolution of 0.01° in 2θ . Software written in-house at the ANBF is available for angular calibration of the imaging plates using the fiducial marks, and for extracting individual strips from the scan. The D type samples described in Chapters 3 and 4 were used to test the experimental technique.

An incident wavelength of 1.54 \AA was selected, and the monochromator de-tuned to reject higher-order harmonics. The diffractometer entrance slits were adjusted to $4 \text{ mm} \times 0.1 \text{ mm}$ (width \times height). This matched the beam to the width of the IP strips, and to the spatial resolution of the IP. The sample stage was mounted on the ω goniometer, with the scintillation detector and slits mounted on the 2θ -arm. This configuration is shown schematically in Fig. 5.2.

The scintillation detector (with a 0.5 mm slit) was used to align the sample and to collect an RSM using the TAD scheme. This RSM was subsequently compared

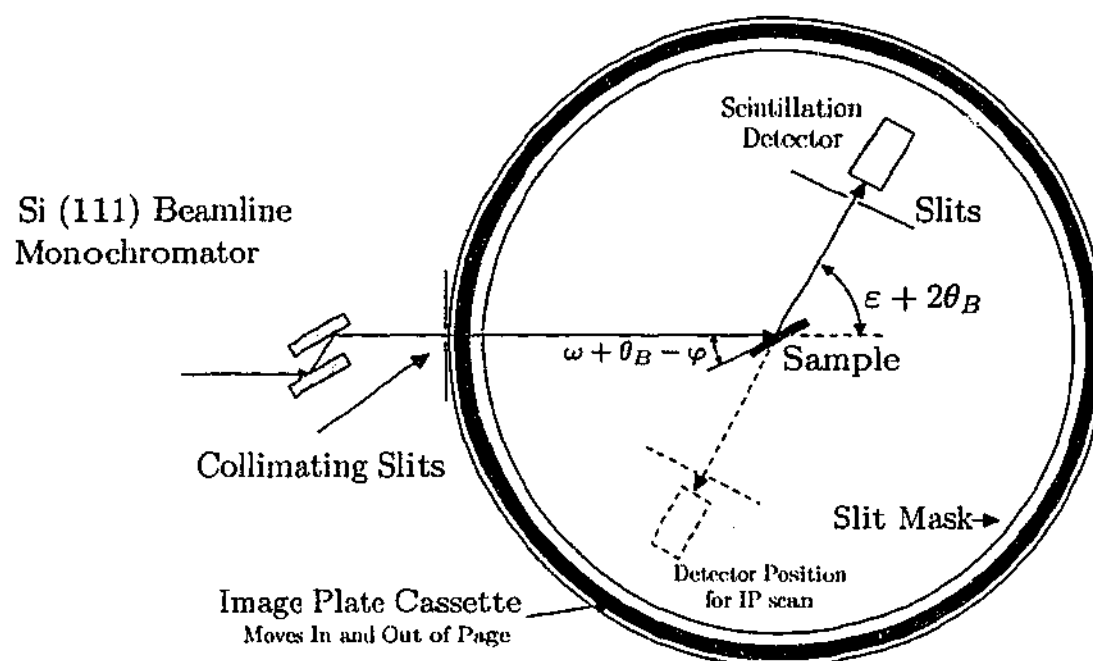


Figure 5.2: Schematic diagram of the diffractometer configuration (side view). ω is angular deviation of the sample from the Bragg condition, and ϵ is the angular deviation of the detector from the Bragg condition.

with RSMs collected using the IPs. The detector was rotated to the bottom of the diffractometer during IP collection, as indicated in Fig. 5.2, so as not to interfere with the beam. The diffractometer was evacuated for the collection of all RSMs to reduce air scatter.

The first strip on each IP was reserved for a Crystal Truncation Rod (CTR) scan (see e.g., Takeda and Tabuchi (2002) and references therein). The CTR scan was collected by rotating the sample over the angular region of interest, including the nearest substrate peak, pausing for 1 second at each ω position to expose the IP strip. The CTR was used to confirm the correct angular calibration of the plate. As only one IP was used to collect an RSM, the number of ω positions was restricted to 29, and the 2θ angular range to 40° . The 2θ angular range is superfluous, but was set by the IP size. To increase the number of ω positions the IP would need to have been changed every 29 scans. Although this is possible, it would require the diffractometer to be evacuated each time, significantly increasing the time required to collect the RSM.

A program script was written to control the ω stage, the IP cassette and the shutter during collection of the RSMs. Initially the exposure time was varied to determine a suitable value for our samples. Using the highest sensitivity on the scanner, a time of 45 seconds per strip avoided over exposing the peak due to the $2\ \mu\text{m}$ thick GaN layer, while being long enough to collect peaks originating from the

thin 20 nm – 200 nm InGaN layer.

5.3 Experimental Results and Interpolation Methods

Figure 5.3 shows a section of an ‘as collected’ imaging plate for sample D30 about the GaN(0004) reflection. The strips are clearly identifiable near the peaks; however, within each strip the peak intensity is not centred. This was corrected for later scans by varying the off-plane angle of the sample. The strip on the far left is the CTR and the bright spot on the extreme right is a fiducial mark. The IP scans were converted into 30 one-dimensional scans using in-house software. The software calibrated the ε -axis using the fiducial marks, then integrated in the ω direction across each scan to obtain the intensity.

The unprocessed data in Fig. 5.3 lies on a regular two-dimensional cartesian grid in $\omega - \varepsilon/2$ space. We can transform to $\Delta\omega - \varepsilon/2$ space (see Fig. 5.4) using Eq. (5.22), (and then to $q_x - q_z$ space using Eqs. (2.130) and (2.131)); however, the set of $\Delta\omega$ -axis coordinates for each ε value are not the same. In order to plot the RSMs and extract profiles along various directions, the data must be interpolated onto a regular (cartesian) grid. A number of interpolation schemes were implemented; however, the simplest is to interpolate in the $\Delta\omega$ direction. A cubic spline interpolation was used, as it was easy to implement and interpolates the data smoothly.

Figure 5.4 shows an entire scan after the unprocessed data (in Fig. 5.3) was transformed into angular coordinates, $\Delta\omega - (\varepsilon/2)$. Within reciprocal space the scan would be an arc, (see Fig. 5.1(a)), because the small angle approximation breaks down over such a large angular range (i.e., 20° in $\varepsilon/2$).

Each individual scan from a single IP has the same set of $\varepsilon/2$ coordinates (i.e., the IP covered the same range in 2θ), however the overlapping $\Delta\omega$ positions do not coincide. Hence in order to analyse the RSMs the data must be interpolated onto a single regular (cartesian) grid. Furthermore the grid spacing is highly anisotropic, with the step size up to 40 times larger in the ω direction compared to the $\varepsilon/2$ direction, depending on the range being investigated. Therefore although the map may contain a large number of data points, they are concentrated along particular paths in reciprocal space. Ideally the interpolation method should consider the geometry of the data and attempt to generate a higher resolution in the ω direction. Three methods of interpolation were explored:

Method I: The data was cubic spline interpolated in the $\Delta\omega$ direction, as indicated in Fig. 5.5. Note that in this case the number of $\Delta\omega$ positions was

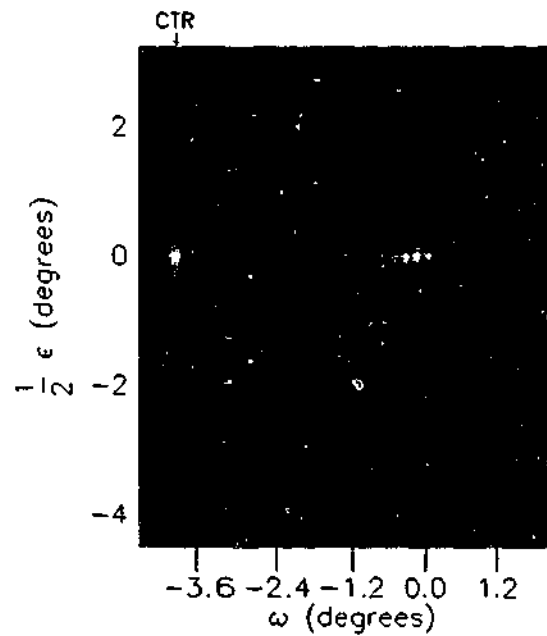


Figure 5.3: Section of an unprocessed imaging plate scan. The individual strips are clearly observable near the peak. The bright spot on the right is a fiducial mark. The single strip on the left is a crystal truncation rod (CTR) scan.

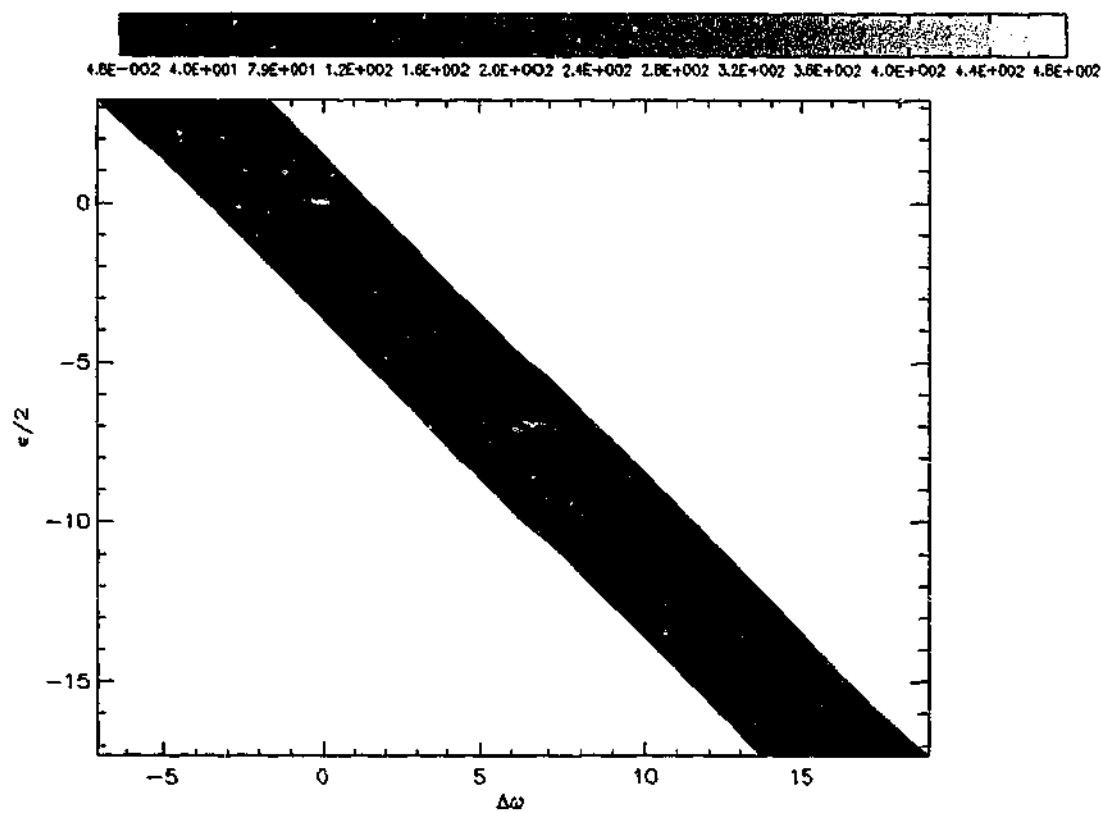


Figure 5.4: Entire RSM from a single imaging plate.

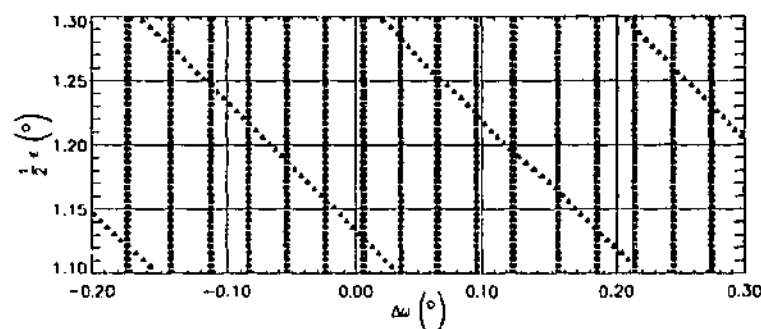


Figure 5.5: The position of the experimental data points before (\blacktriangle) and after (\blacksquare) interpolation using method I.

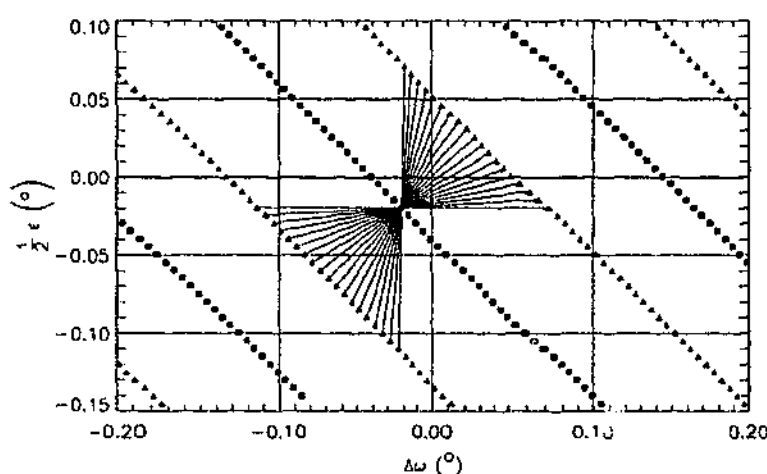


Figure 5.6: The position of the experimental points (\blacktriangle) and the added points (\blacksquare) (forming pseudo-scans) for method III. The lines indicate the 38 points used to generate one new point.

selected to be the same as used for the standard technique.

Method II: The data was linear interpolated in the scan direction so that the data was on a regular grid in the $\Delta\omega$ direction (but no longer in the $\epsilon/2$ direction) and then cubic spline interpolated in the ϵ direction to create the regular grid.

Method III: The data set was expanded by generating pseudo-scans parallel to the IP strips using an inverse distance interpolation of the 38 nearest points. The experimental and generated points are shown in Fig. 5.6. This data was then interpolated as in method I to create a regular grid.

Figures 5.7 – 5.9 show the results for the three different interpolation methods. The interpolated RSMs are based on a map collected using the IP method about the (0004)GaN peak for sample D30, and incorporates the InGaN peak. Each of the interpolated RSMs are compared to a map collected using the TAD method. The data was shifted so that the average background was zero, and then normalised to the InGaN peak height, since the GaN peak was saturated in both the IP and TAD

techniques. For the same reason the ω scans were taken across the main InGaN peak. The error is given by:

$$RSM_{Error} = \log_{10} \left(\frac{RSM_{IP}}{RSM_{TAD}} \right) \quad (5.23)$$

An IP scan was also collected with half the step size in the ω direction as shown in Fig. 5.10. Only one IP was used, which covered half the area of the RSM presented in Fig. 5.7. This results in the truncation seen in Fig. 5.10(a). The data collection time (approximately 45 mins including diffractometer chamber evacuation and IP readout) was identical to the lower resolution scan shown in Fig. 5.7.

The IP scans were collected in approximately one quarter of the time that was required for the standard technique (the standard technique typically required 3-4 hours for the scans shown in Chapter 4). Subtracting every second row and column reduces the standard RSM to one that would have been collected in approximately the same time as the IP scans. Figure 5.11 compares the original and reduced RSMs, with the smaller RSM linearly interpolated onto the same grid size as the original RSM.

Further data is shown in Fig. 5.12, where two plots around the $(11\bar{2}4)$ reflection from different samples are reproduced. To avoid further interpolation the axes are in angular space not reciprocal space. All interpolation and analysis was performed using software written in IDL by the author.

5.4 Discussion of Experimental and Interpolation Results

The aim of this experiment was to utilise IPs for collecting RSMs rapidly. Superficially the IP method appears attractive, since a scan can be acquired in about 45 min, which includes evacuation of the diffractometer chamber and readout of the IPs. A TAD scan, covering the same peak features, requires 3-4 hours depending upon the region of interest and spatial resolution. However, before IPs are adopted for routine reciprocal space mapping, it is imperative to establish the suitability of the method for various scan types and to validate the accuracy of the RSM data obtained in the present experiments. These issues are addressed in the remainder of this chapter.

Figures 5.7 – 5.9 show significant differences between the RSM collected using the TAD method, and the IP with interpolation. In particular the peaks are widened in the ω direction, and do not have the correct shape. However, the $\omega - 2\theta$ scans are more accurate, showing all features of the standard RSM. This means that the IP method can be successfully used to produce $\omega - 2\theta$ scans for Group III nitride

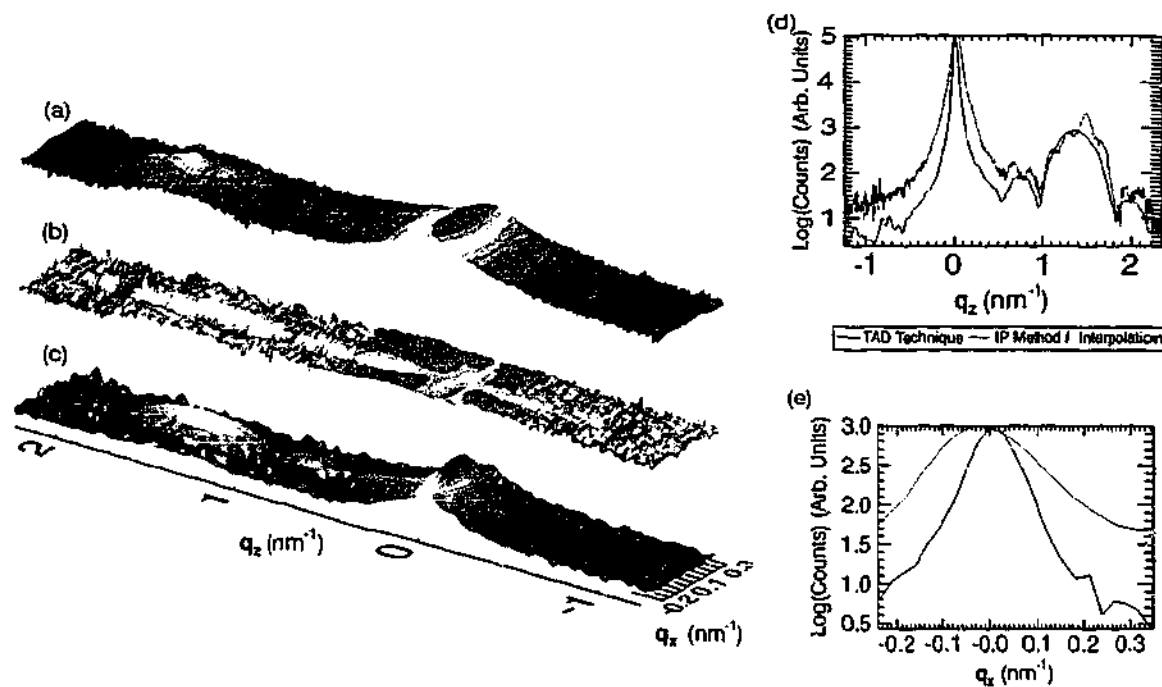


Figure 5.7: Comparison of a triple axis diffractometry RSM with the interpolated IP data. (a) Interpolated IP using method I, (b) error plot, (c) triple axis diffractometry RSM, (d) $\omega - 2\theta$ scan and (e) ω scan.

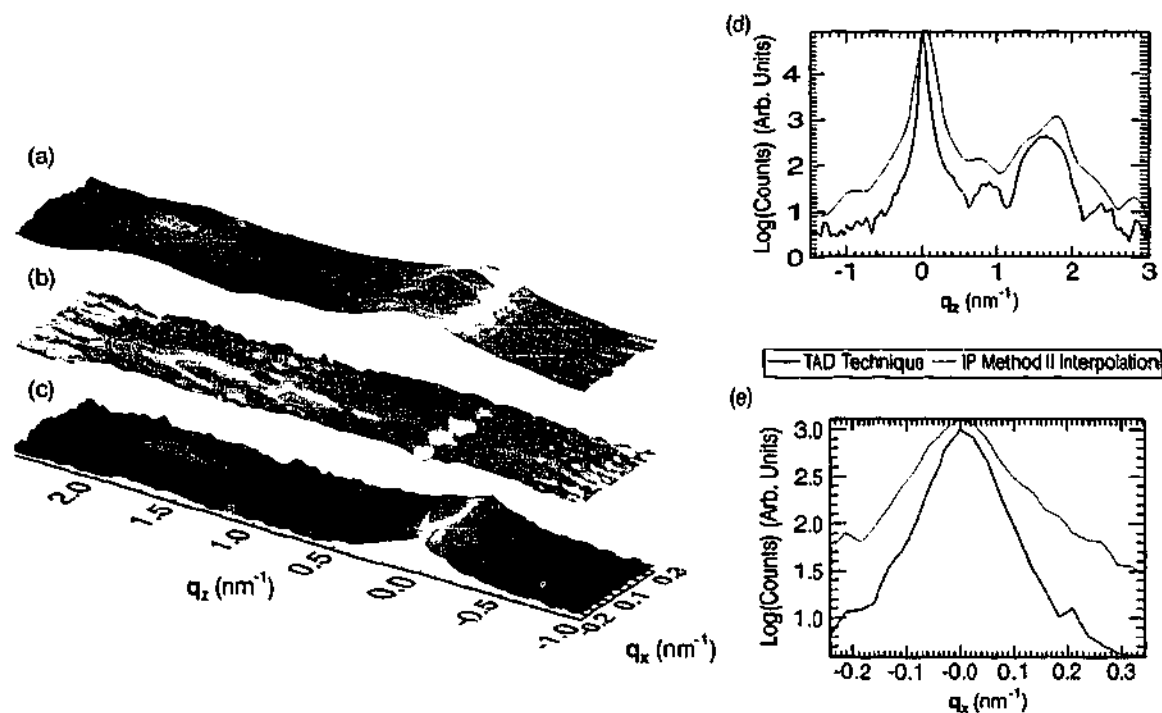


Figure 5.8: Comparison of a triple axis diffractometry RSM with the interpolated IP data. (a) Interpolated IP using method II, (b) error plot, (c) triple axis diffractometry RSM, (d) $\omega - 2\theta$ scan and (e) ω scan.

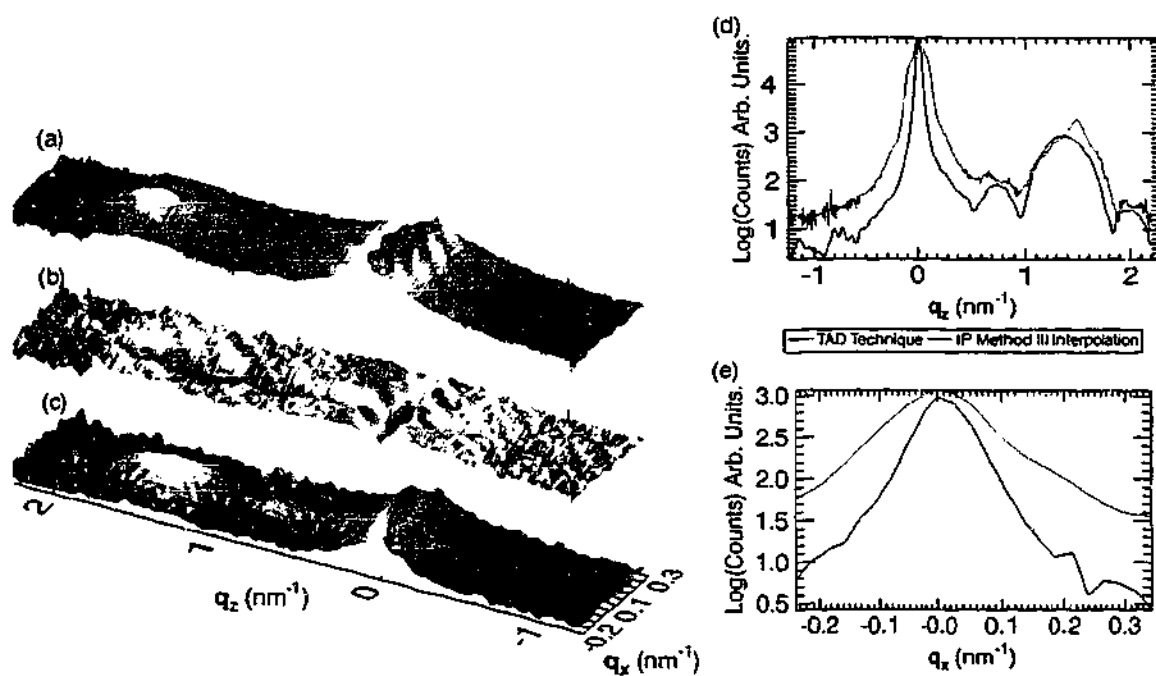


Figure 5.9: Comparison of a triple axis diffractometry RSM with the interpolated IP data. (a) Interpolated IP using method III, (b) error plot, (c) triple axis diffractometry RSM, (d) $\omega - 2\theta$ scan and (e) ω scan.

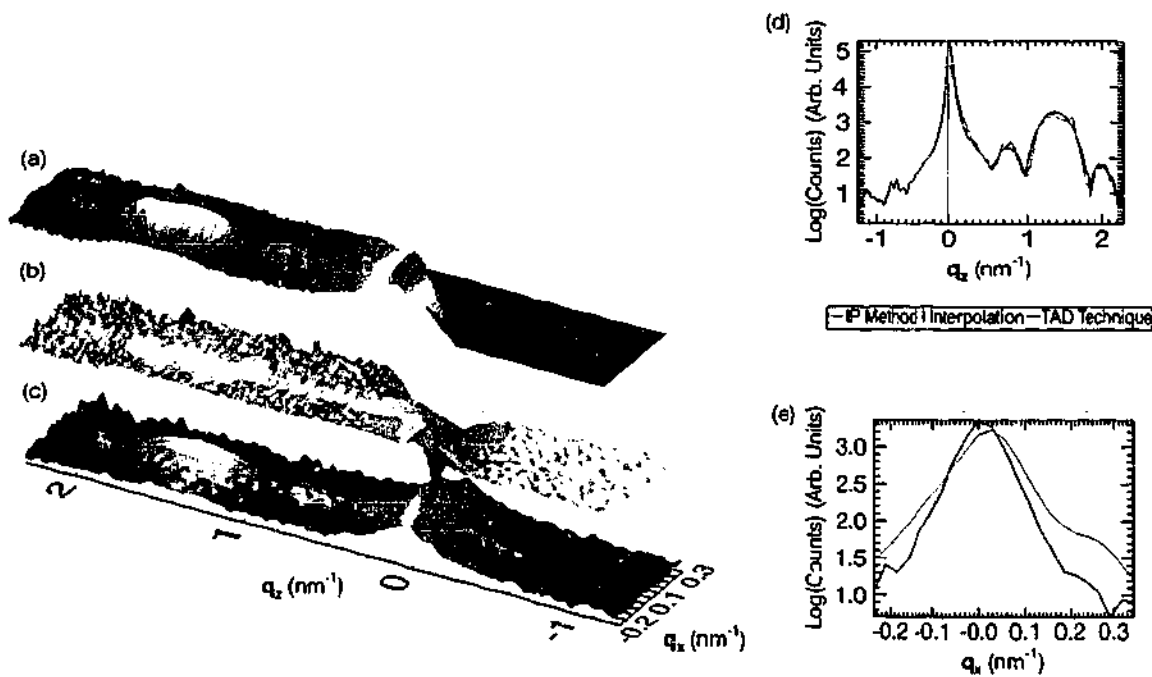


Figure 5.10: Comparison of a triple axis diffractometry RSM with the interpolated high resolution IP data using method I. (a) Interpolated IP using method I, (b) error plot, (c) triple axis diffractometry RSM, (d) $\omega - 2\theta$ scan and (e) ω scan.

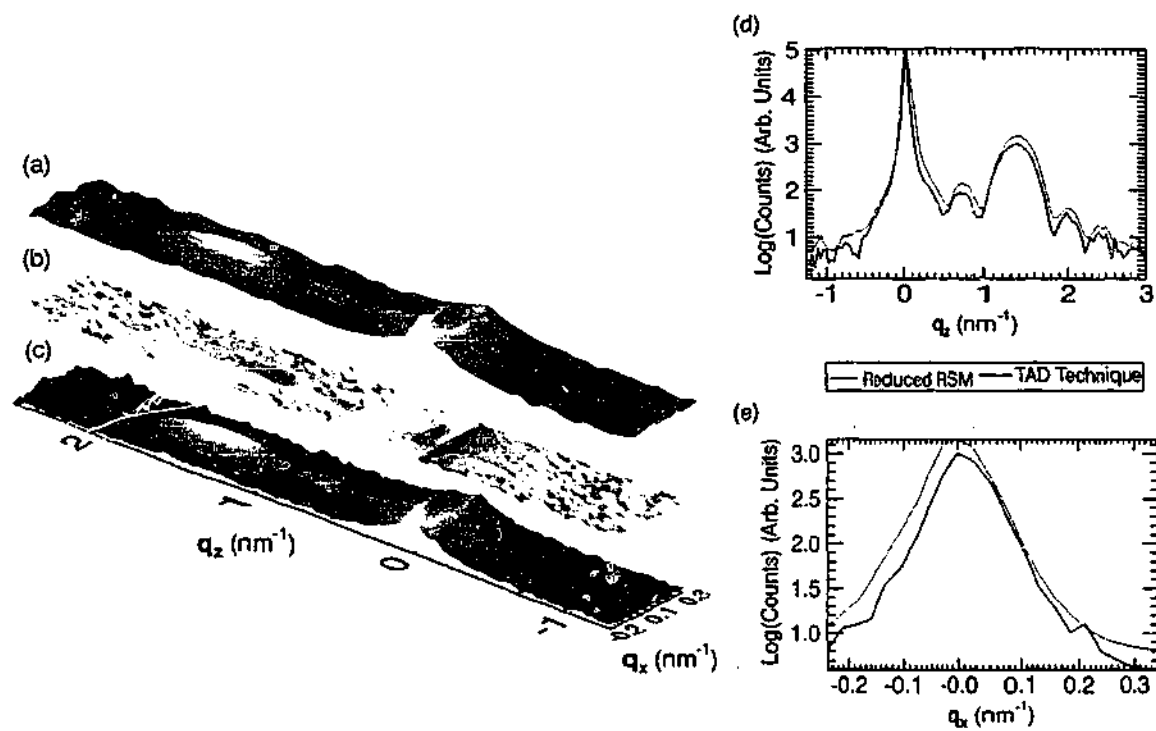


Figure 5.11: Comparison of a triple axis diffractometry RSM with the reduced triple axis diffractometry RSM. (a) Reduced triple axis diffractometry RSM, (b) error plot, (c) standard triple axis diffractometry RSM, (d) $\omega - 2\theta$ scan and (e) ω scan.

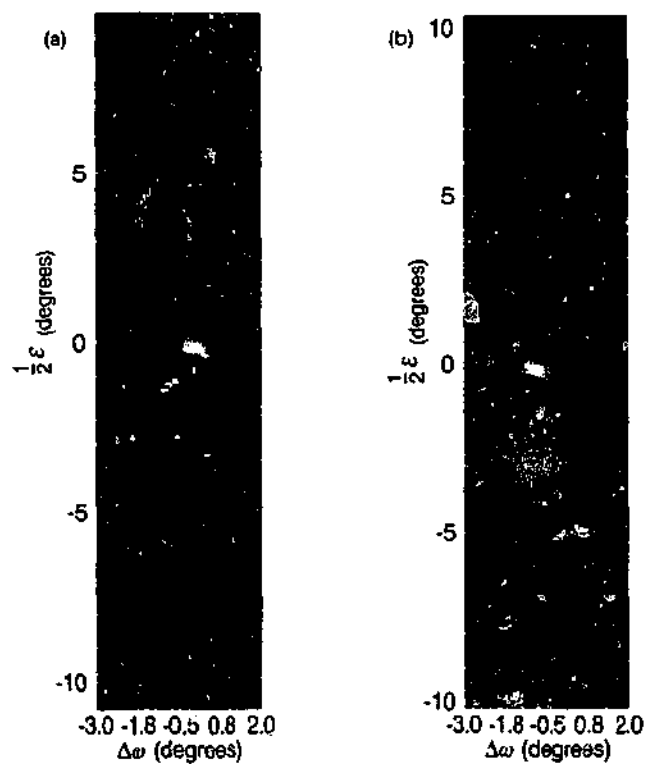


Figure 5.12: Reciprocal space maps (in angular space) for the $(11\bar{2}4)$ reflections. (a) Sample D30, and (b) sample D42.

samples. It is difficult to specify a spatial resolution for the IP scans because the data is highly asymmetric. The spacing, ω_{step} , between collected lines in the $\Delta\omega$ direction (before interpolation), is 0.18° for Fig. 5.7 and 0.09° for Fig. 5.10. However, along a single strip from the IP (see Fig. 5.1(b)) the step size is up to 20 times smaller, (i.e., 0.01°). Limiting ourselves to one IP results in a low spatial resolution compared to the data of Kinne *et al.* (1998)). The resolution could be increased using only one IP, if the Weissenberg screens were made narrower and the IP cassette step size reduced.

Figure 5.10 shows that reducing the step size, ω_{step} by a factor of two significantly improves match between the IP and TAD data, in both the q_x - and q_z directions. This suggests that for our sample type, 58 scans is sufficient to cover the range of interest. This should be easy to obtain with some minor modification to the slit and step sizes of the IP system. The majority of the collection time for a scan is spent evacuating the system and handling/scanning the IPs. Hence an increase in the number of strips on one plate will not significantly change the collection time. Information on the IP also degrades with time, and can require a correction (see Welberry *et al.* (2003)). However, we collected a small number of scans, and hence avoided this problem.

In attempting to use a large ω_{step} to cover an extended range in reciprocal space (see Fig. 5.1(b)), the interpolation procedure introduces false peaks. This can be seen in the InGaN peak, and its satellite in the $\omega - 2\theta$ scan (see Fig. 5.7(d)). Figure 5.13 shows a schematic illustration of this phenomenon for a peak elongated along the q_z direction (e.g., the GaN peak). In Fig. 5.13(a) the data points lying on the peak are generated, via interpolation in the q_x direction (Method I), from widely spaced experimental data. In general the experimental data points straddle the peak position and hence give an intensity less than the true peak intensity. This situation is evident in region ii in Fig. 5.13(a). A profile of this region is displayed in Fig. 5.13(b), which clearly indicates that the interpolated scan has a lower intensity than the true peak. Figure 5.13(a) shows that the experimental points are arranged in lines that run at an oblique angle to the axis that peak intensity is distributed along. Some experimental points lie closer to, or on, the peak leading to a more accurate peak intensity. This is the case for region i where an experimental point lies exactly on the peak. The resulting profile is shown in Fig. 5.13(b). A translation in the q_z direction produces a series of maxima as shown for region iii. A similar problem arises for the InGaN peak, which is elongated in the q_x direction, if interpolation is performed in the q_z direction (Method II). Therefore the result of interpolation depends on the geometry, and in particular the width of the peak being interpolated,

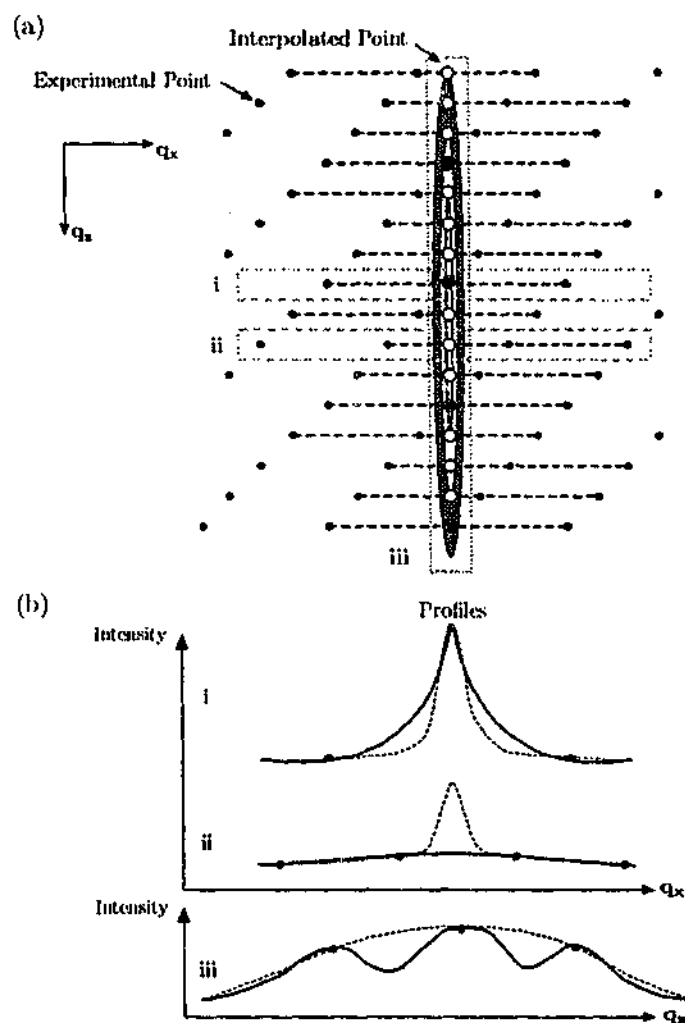


Figure 5.13: Schematic diagram explaining the origin of peak splitting when ω_{step} is large. (a) Sketch of the RSM showing the position of the experimental (filled circles) and interpolated (open circles) points compared with the 'true' peak, and (b) profiles across the 'true' (dotted line) and interpolated (solid line) peaks, from regions i, ii and iii indicated in (a).

compared to the resolution (if a large ω_{step} is used).

Method III utilised a much larger data set to interpolate each datum point, and was devised to remove the false peaks evident in the other two methods. However, Fig. 5.9 shows that although the false peaks have been reduced in intensity they are still discernible. Moreover striping is seen throughout the whole RSM; this is due to the inherent smoothness in the pseudo-scans because the number of points used to calculate the average is large.

Since no explicit smoothing has been applied (only that inherent in the interpolation scheme), further improvement may be possible through the application of suitable filtering; however, such a procedure would require careful justification.

The IP scans were collected in approximately one quarter of the time required

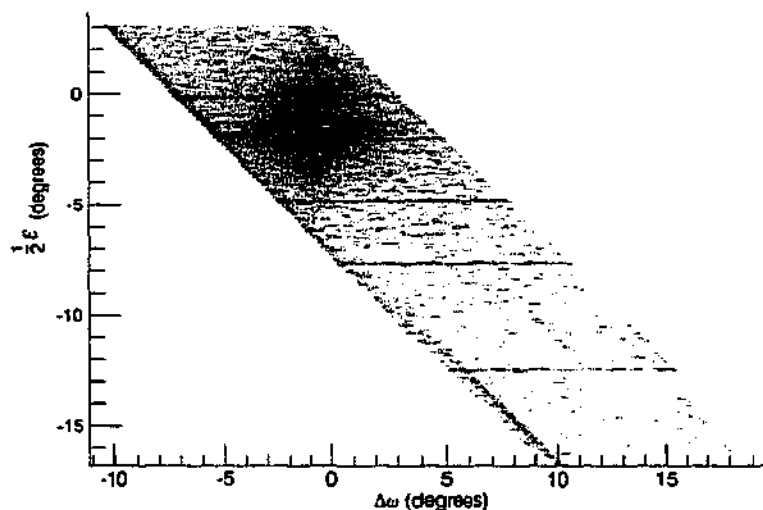


Figure 5.14: Powder lines collected across the whole imaging plate, possibly due to In segregation.

for the TAD technique. Subtracting every second row and column reduces the TAD RSM to one that would have been collected in approximately the same time as the IP scans. Figure 5.11 compares the high and low resolution TAD RSMs with the interpolated IP scans. The low resolution TAD RSM was linearly interpolated onto the same grid size as the high resolution RSM. Comparing the sparse TAD scan to the IP scan suggests that for the region of interest, similar (or better) quality data can be collected in a comparable time using the TAD method. The sparse TAD RSM has a higher spatial resolution than the IP RSM because the sample spacing is less asymmetric. However, the TAD method requires:

- i Greater time for set-up;
- ii A priori knowledge of the peak positions in reciprocal space. This is problematic for unknown samples, especially for asymmetric reflections and requires long alignment times;
- iii More complicated instrumentation, such as a second axis of rotation for the detector/analyser.

Caution should be used when analysing Fig. 5.11, because the two RSMs are not independent, originating from exactly the same experimental data. However, it does indicate that for the samples investigated a lower resolution is sufficient. The RSMs collected by the IP cover a much wider range than the specific region of interest shown in Figs. 5.7 – 5.9, although much of this extended region is featureless. There are specific cases where the large region can be useful. For example, Fig. 5.14 shows a scan where powder lines, possibly due to segregated In (or InN) clusters (see

Sec. 4.4.3), were observed across the entire RSM, simultaneously with the Bragg and diffuse peaks.

Figure 5.12 shows two RSMs about the $(11\bar{2}4)$ reflection. RSMs of asymmetric reflections must cover wide regions of reciprocal space, because the peaks do not necessarily align with the q_x - or q_z -axes. Hence the ability of the IP scans to cover a large region of reciprocal space in a short period of time is very useful in scanning asymmetric reflections (even at low spatial resolution). The range along the $\Delta\omega$ -axis as shown in Fig. 5.12 is more than seven times larger than shown for the symmetric reflections.

In comparison to Kinne *et al.* (1998) our RSMs have a lower spatial resolution because we used the IP to collect discrete strips, instead of continuously filling the IP while rocking the sample. In addition, we have introduced integration in the q_y direction by summing across the strips. Summing in the q_y direction over a small range can also introduce errors if the peaks in that direction have different widths. It may be more valid to use the central line of pixels from the strip, and hence obviate the need for integration; however this would require that the scan be perfectly centred on the strip. The TAD method also integrates in the q_y direction (see e.g., Holý *et al.*, 1999). Kinne *et al.* (1998) fill an entire IP by scanning it past a narrow slit, avoiding the need to integrate in the $\Delta\omega$ direction. However, we observed that very bright features caused streaking on the IP in the $\Delta\omega$ direction (presumably because of saturation). The separation between strips ensures the intensity of the streaks at the adjacent strip position on the IP is small. There was no separation between the strips for the procedure adopted by Kinne *et al.* (1998), although the lower count rate in the laboratory may have meant the problem was less severe.

The optimum detector for this collection regime would have on-line readout, such as that used by Boulle *et al.* (2002); furthermore, it should be capable of handling synchrotron intensities, be vacuum stable, and have an appropriate dynamic range. Such detectors are not readily available.

Experimentally we integrate over a small range of reciprocal space, because of a number of instrumental effects (e.g., the slits are not infinitely narrow). If the Weissenberg slits were removed, the lateral direction would be available for detecting intensity. This direction corresponds to q_y , which for an incident plane wave is given by

$$q_y = k \cos \theta_2 \sin \theta_3, \quad (5.24)$$

where θ_2 and θ_3 are defined in Fig. 5.15. (Note that Eqs. (2.130) and (2.131) are not valid in the three-dimensional case). Gerhard *et al.* (2000) use this fact to collect

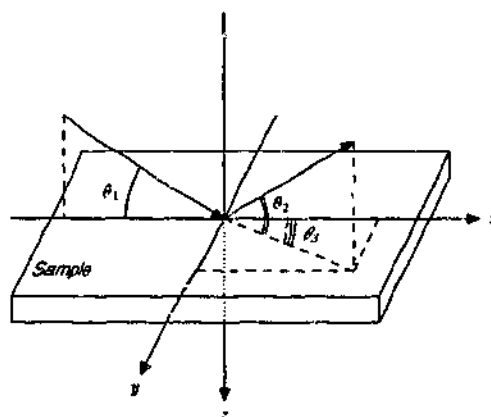


Figure 5.15: Angle designations for the three-dimensional diffraction geometry.

their RSMs. In fact their results are similar to a CTR scan (see e.g., Takeda and Tabuchi (2002)) with no Weissenberg slits installed. Such a CTR still integrates over the q_x range (determined by the ω limit selected), but provides information from a two-dimensional region of reciprocal space. The CTR covers a region in the $q_x = 0$ plane, i.e., perpendicular to the RSM. By collecting RSMs and two-dimensional CTRs, two perpendicular planes (from within reciprocal space) can be acquired without the need to rotate the sample about the q_z -axis between scans. This ensures that the same region of the sample is investigated in the both the $q_x = 0$ and $q_y = 0$ planes.

If only a small q_y range is required, and the incident beam has low angular divergence in both the q_x - and q_y directions, then our technique can be used to produce a three-dimensional RSM. The intensity distribution in the q_y direction is obtained from the profile across the strips. This cannot be easily achieved using other techniques, except for Welberry *et al.* (2003), although in this latter case it would be of a very limited range.

5.5 Conclusion

We have implemented a method for collecting reciprocal space maps using imaging plates at the Australian National Beamline Facility. The results indicate that for sparse data care must be taken when interpolating onto a regular grid. More specifically, peaks that are narrow in the q_z direction should be interpolated in the q_x direction, and vice versa, to avoid producing false peaks. For our sample type, and the range required, we found that as few as 58 strips can produce acceptable results. The IP method is very useful for rapidly scanning large areas of reciprocal space when the peak position and shape are not known exactly, which occurs for asymmetric peaks; further it does not require more sophisticated equipment, such as

analyser crystals and 2θ -arms. This method can be extended to three dimensions.

CHAPTER 6

Chemical Ordering of Group III Nitrides

This chapter describes work done in collaboration with Dr. Lutz Kirste and Dr. Nikolaus Herres of the Fraunhofer Institut für Angewandte Festkörperphysik (Fraunhofer Institute for Applied Solid-State Physics, Germany).

6.1 Introduction to Ordering of Group III Nitrides

Ternary Group III nitride materials, specifically $\text{Al}_x\text{Ga}_{1-x}\text{N}$ and $\text{In}_x\text{Ga}_{1-x}\text{N}$, can exhibit self-induced long range ordering of the Group III elements. This chemical ordering was initially identified in the wurtzite structure by Korakakis *et al.* (1997), and since then has been reported by numerous authors (see e.g., Iliopoulos *et al.*, 2001; Benamara *et al.*, 2003; Läugt *et al.*, 2003). The nature of the ordering is dependent upon the growth conditions, substrate, layer components and composition. Group III nitrides are usually grown in the [0001] direction, as detailed in Sec. 1.2.4. In this growth mode the ordering is along the [0001] growth direction, with the atoms arranged randomly in the (0001) basal plane. The simplest ordering modality has the Group III atoms alternating in the [0001] direction (Korakakis *et al.*, 1997; Iliopoulos *et al.*, 2001; Northrup *et al.*, 1999b). Other more complex arrangements (Iliopoulos *et al.*, 2001) have longer repeat units, up to 14 monolayers, and coexistence of different ordering types.

Ordering of the structure may impact on the electrical and optical properties of the material (Wright *et al.*, 2001). Hence an understanding of the formation and stability of the ordered structure is important for device manufacture. Several authors have suggested models for the formation of the ordered structure (see e.g., Northrup *et al.*, 1999b; Benamara *et al.*, 2003). The ordering is thought to be a result of the growth kinetics (i.e., it is not a thermodynamic process), and the large difference in bond strength between the nitride and each of the Group III atoms. (Specifically the In-N and Al-N bonds are stronger than Ga-N bonds). Figure 6.1 shows a conceptually simple mechanism for ordering. Growth occurs via a step process, with three different sites available for Group III bonding: B1, T1 and B2. The nitrogen coordination of these three sites (at the time the Group III adatom arrives) are different; B1 has three nitrogen atoms, B2 has two and T1 has one.

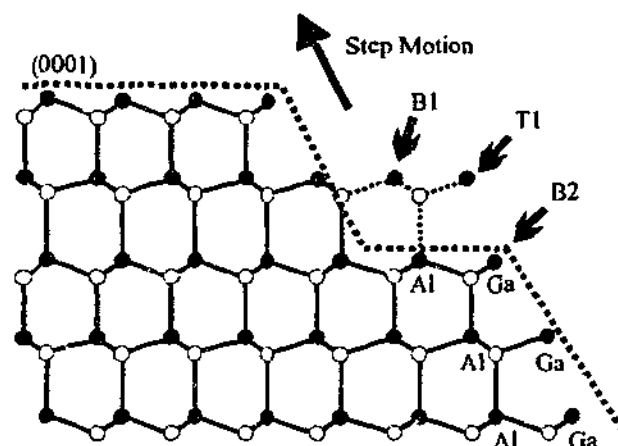


Figure 6.1: Possible kinetic model leading to chemical ordering of Group III nitride ternary alloys. In and Al have a higher bond strength with N than Ga. The free energy is minimised if In or Al is located at B1 (and Ga at T1 and B2) because there are two nitrogen bonds at B1 and only one at T1 and B2 (after Benamara *et al.* (2003)).

Energy is minimised by an atom with higher bond strength being positioned at B1 (i.e., In or Al), and an atom with lower bond strength (Ga) at B2 and T1. The geometry of the layer, and the motion of the growth front will produce ordering, which is then frozen into the bulk material. Although this simple model is specific to a particular growth mechanism, it demonstrates how different bonding strengths can lead to ordering.

Structural ordering of this kind can be easily detected by diffraction techniques, since the structure factor of the material is modified. For a ternary alloy with a wurtzite crystal structure the structure factor is

$$F_{hkl} = f_A + f_B e^{2\pi i(\frac{h+2k}{3} + \frac{l}{2})} + f_N e^{i\pi\frac{3l}{4}} \left[1 + e^{2\pi i(\frac{h+2k}{3} + \frac{l}{2})} \right], \quad (6.1)$$

where f_A and f_B are the atomic scattering factors for atoms sitting at the two Group III sites in the unit cell, and f_N is the atomic scattering factor for nitrogen. For (00. l) type reflections Eq. (6.1) reduces to

$$F_{00,l} = f_A + f_B e^{\pi i l} + f_N e^{i\pi\frac{3l}{4}} \left[1 + e^{\pi i l} \right] \quad (6.2)$$

$$F_{00,l} = \begin{cases} f_A - f_B + 0 & \text{if } l = \text{odd} \\ f_A + f_B + f_N i^{(-\frac{l}{2})} & \text{if } l = \text{even.} \end{cases} \quad (6.3)$$

For a random alloy, f_A and f_B are taken as the weighted average of the two species. It follows that for (00. l) reflections, where l is odd, the structure factor is zero. However, if ordering is present, the symmetry is broken and $F_{00,l}$ is non-zero for all l . Thus an XRD scan can determine if there is ordering in the material.

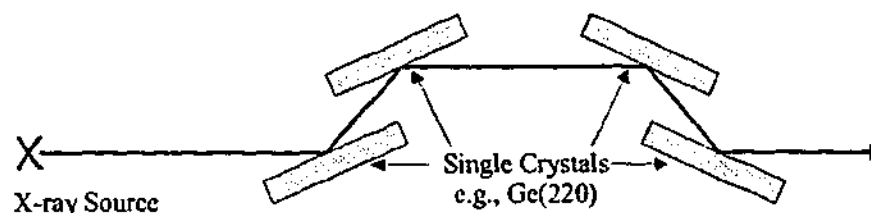


Figure 6.2: Schematic diagram of a Bartels-DuMond type monochromator. The X-ray beam height is not modified by this arrangement. Selection of a desired wavelength is achieved by rotating the crystals.

Additional peaks may also be present if some form of superstructure is involved, e.g., if the repeat length is greater than c , i.e., the lattice parameter in the $[0001]$ direction.

6.2 Experiment

A series of experiments designed to explore the chemical ordering of the Group III nitrides were completed by Drs. N Herres and L. Kirste of the Fraunhofer Institut für Angewandte Festkörperphysik (Fraunhofer Institute for Applied Solid-State Physics, Germany). The sample was grown using plasma assisted molecular beam epitaxy. The substrates were nitridated, and a 130 nm AlN buffer layer was deposited at 1050°C. A 720 nm AlGaIn layer was then grown at 820°C. After characterisation (see below) the sample was annealed for 5 hours at a temperature of 1000°C and a pressure of 9.5 kBar. A Ga overpressure was achieved by packing Ga powder into the crucible with the sample. After annealing, the sample was again characterised.

The samples were initially scanned using a double crystal diffractometer to determine lattice parameters and composition, using the extended bond technique (see e.g., Herres *et al.*, 2002). Reciprocal space maps were then collected using a triple axis diffractometer for a more detailed study of the structural imperfection of the samples. The triple axis diffractometer incorporated a parabolic mirror to increase the incident flux, with a Bartels-DuMond Ge-220 monochromator to condition the beam. A schematic of a Bartels-DuMond monochromator (DuMond, 1937; Bartels, 1983) is shown in Fig. 6.2. This monochromator has a small beam divergence. Furthermore it does not modify the beam direction, and can be tuned for a particular radiation wavelength. A Ge-220 Bartels-DuMond arrangement was also used for the analyser. This arrangement ensured minimum instrumental broadening, obviating the need to deconvolve instrumental broadening from the diffraction pattern.

Two different analysis methods were employed and compared: a Williamson-Hall analysis and statistical diffraction theory.

6.3 Williamson-Hall Analysis

A number of techniques have been described in the literature that attempt to determine microstructural information from X-ray diffraction peaks. One such approach is integral width¹ analysis (Gay *et al.*, 1953; Williamson and Hall, 1953; Hordon and Averbach, 1961; Chatterjee and Sen Gupta, 1972). This approach is popular because of its simplicity and generality, although there are questions concerning its accuracy (despite the fact that the method has been used in some form for more than 40 years). The Williamson-Hall analysis (Williamson and Hall, 1953) is one such analytical method for extracting physical parameters from the integral widths.

The integral width of an X-ray diffraction peak is defined as the area under the peak divided by the maximum peak intensity. It is used over alternative measures of peak profiles (such as Full-Width-at-Half-Maximum) because it is applicable to both symmetric and asymmetric peak shapes. The experimentally measured diffraction peak is a convolution of the diffraction profile and the instrumental function. Instrumental line broadening is caused by the divergence of the primary beam (and the acceptance angle of the detector), which is determined by the angular dependence of the reflectivity of the monochromator (and analyser). Aside from the natural (Darwin) width of the reflection there will be other contributions to the line width depending on the sample type. For example, cold-worked metals, for which these analysis methods were originally formulated (see e.g., Williamson and Hall, 1953; Hordon and Averbach, 1961), have a high dislocation density, and hence small grain size. The size of the grains, both parallel and perpendicular to the sample surface, and their misorientation will broaden the diffraction peak in specific directions in reciprocal space (see Sec. 4.4.3). Furthermore, dislocations will cause inhomogeneous strain of the lattice, which will also cause the peaks to be broadened. Although our samples are not cold-worked metals, they have similar microstructural features, i.e., high dislocation density leading to inhomogeneous strain and the formation of small grains (mosaic blocks), which show significant misorientation. In order to quantify these structural features using the line width, the different contributions must be disentangled from each other.

The instrumental function can be characterised by measuring the rocking curve of the analyser and monochromator crystals. It is then straightforward to account for the instrumental function in the analysis. According to Williamson and Hall (1953) the integral line widths due to heterogeneous strain, B_s , and particle size in

¹Here the term 'integral width' has the same meaning as 'integral breadth', which is often used in the literature.

the \mathbf{q}_z direction, B_p , are given by

$$B_s = 2\xi \tan \theta_B \quad (6.4)$$

$$B_p = \frac{\lambda}{l_z \cos \theta_B}, \quad (6.5)$$

where ξ is the integral width of the strain distribution, and l_z is the average linear dimension of the particle (mosaic block or crystallite) perpendicular to the sample surface. If both of these broadening mechanisms operate simultaneously, the integral widths need to be combined to give the total width, B (after removing instrumental effects). Assuming a Lorentzian profile the integral widths are added; for a Gaussian profile the squares of the widths are added (Williamson and Hall, 1953; Chatterjee and Sen Gupta, 1972). Assuming a Lorentzian profile we have:

$$B = 2\xi \tan \theta + \lambda / (l_z \cos \theta). \quad (6.6)$$

It is advantageous to perform this calculation in reciprocal space. For a symmetric reflection ($\varphi = 0$), and assuming the incident and diffracted angles are equal ($\theta_i = \theta_D = \theta$) the \mathbf{q}_z vector is given by

$$\mathbf{q}_z = 2k \sin \theta. \quad (6.7)$$

From this we can derive the following expression:

$$\Delta \mathbf{q}_z = 2k \Delta \theta \cos \theta, \quad (6.8)$$

where $\Delta \mathbf{q}_z$ is the change in reciprocal space, corresponding to a small change, $\Delta \theta$, in angular space. In keeping with the convention used by Williamson and Hall (1953) we define k as $k = 1/\lambda$ for this section (compared to the usual definition of the wavevector, $k = 2\pi/\lambda$). Multiplying both sides of Eq. (6.6) by $\cos \theta/\lambda$ gives

$$B_z^* = B \cos \theta / \lambda = 2\xi \sin \theta / \lambda + 1/l_z, \quad (6.9)$$

where B_z^* is the integral width in reciprocal space (in the \mathbf{q}_z direction).

Finally, upon utilising Bragg's law we obtain

$$B_z^* = \xi/d + 1/l_z, \quad (6.10)$$

where d is the lattice spacing ($\mathbf{q}_z = 1/d$). Hence plotting B^* versus \mathbf{q}_z should result in a straight line of gradient ξ and intercept $1/l_z$. Determining the structural parameters using such a plot is the basis of the Williamson-Hall technique. This

technique can be extended to extract the peak width in the q_x direction in order to determine the linear dimension of the particles parallel to the sample surface, and the integral width of the misorientation.

Assuming a symmetric reflection, the incident angle, θ_i , and the diffracted angle, θ_d , are given by

$$\theta_i = \theta + \omega \quad (6.11)$$

$$\theta_d = \theta - \omega. \quad (6.12)$$

The q_x vector is specified by

$$q_x = k(\cos(\theta + \omega) - \cos(\theta - \omega)) \quad (6.13)$$

$$= 2k\omega \cos \theta. \quad (6.14)$$

From this we can derive the following expression

$$\Delta q_x = 2k\Delta\omega \sin \theta, \quad (6.15)$$

where Δq_x is the change in reciprocal space, corresponding to a small change, $\Delta\omega$, in angular space.

The component of the peak broadening in the q_x direction, due to the particle size perpendicular to the surface of the sample in reciprocal space, is equal to $1/l_x$. It follows that the component of the peak broadening in the q_x direction, due to the particle size parallel to the surface of the sample in reciprocal space, is equal to $1/l_x$. (Using Eq. (6.15) the broadening in angular space is $\lambda/(2l_x \sin \theta_B)$).

The peak profile (in an ω scan) generated by misorientation is a direct measure of the distribution of angles of the mosaic blocks. Therefore in angular space the integral width due to misorientation is the integral width of the misorientation, which we label Δ_m . The misorientation integral width in reciprocal space is

$$B_x^* = 2\alpha k \sin \theta_B + 1/l_x \quad (6.16)$$

$$= \Delta_m/d + 1/l_x \quad (6.17)$$

The particle size parallel to the sample surface and the integral width of the misorientation can be determined from the intercept and gradient, respectively, of the graph of B^* versus q_x .

The analysis based on Eqs. (6.10) and (6.17) assumes a Lorentzian profile. If the profiles are Gaussian then Eqs. (6.10) and (6.17) are modified according to

$$(B_z^*)^2 = (\xi/d)^2 + (1/l_z)^2 \quad (6.18)$$

$$(B_x^*)^2 = (\Delta_m/d)^2 + (1/l_x)^2. \quad (6.19)$$

In this case a plot of $(B^*)^2$ versus q_z^2 will allow the appropriate parameters to be determined from the square root of the gradient and intercept. Another important functional form used in integral width analysis is the Voigt function. This function is a convolution of a Lorentzian profile with a Gaussian profile (see e.g., Balzar and Popović, 1996). The integral width of the Voigt function, B_{voigt} , can be determined from the widths of the constituent Lorentzian and Gaussian components (Schoening, 1965); however, the resulting equation is complicated. A simple, reasonably accurate approximation was given by Halder and Wagner (1966):

$$B_{\text{Voigt}}^2 = B_{\text{Lorentz}} B_{\text{Voigt}} + B_{\text{Gauss}}^2. \quad (6.20)$$

The rationale for using a Voigt function is that effects due to particle size produce a Lorentzian-type broadening, whereas the strain induces Gaussian-type line broadening (see e.g., Halder and Wagner, 1966). However, fitting the peaks using a Voigt function complicates the graphical analysis, since a plot of B^* versus q or $(B^*)^2$ versus q^2 is not linear. This will be discussed in Sec. 6.5.1. The Voigt function can be used to calculate the different contributions to line broadening by decomposing the Voigt width into its Lorentzian and Gaussian components. This may be done using Eq. (6.20), or some other appropriate approximation (see e.g., Schoening, 1965).

Group III nitrides have a high defect concentration leading to broad diffraction peaks. We can neglect the intrinsic (Darwin) width since it is narrow; instrumental broadening is also small since the Bartels-DuMond monochromator and analyser ensure very low beam divergence. We also neglect broadening due to sample curvature on the assumption that it is a small (see e.g., Hordon and Averbach, 1961).

6.4 Statistical Diffraction Theory

Modifications to the mosaic block model used in Sec. 3.3 were required in order to fit the data. Odd reflections in the q_x direction required a weighted mixture of two different lateral block sizes in order to correctly fit the line shape. However, even reflections in the q_x direction only need one block size. Simulation of the profiles in the q_z direction necessitated a strain distribution. This was simulated by dividing the layer into a large number of partitions (e.g., 60), each in a different

strain state. Fitting the annealed samples required only one lateral block size, since only even order reflections were observed. The process of annealing caused chemical intermixing of the individual layers of the sample, and the formation of a Ga rich layer on the sample surface. Intermixing is observed in the q_z profiles as the large background extending from the AlN rich peak to the GaN rich peak. The intermixed regions of the sample were modelled by assuming that the composition varied linearly from one layer to the next.

6.4.1 Composition Gradient Model

The deformation vector, $\mathbf{u}(\mathbf{r})$, for an atom originally located at \mathbf{r} , can be divided into two components: the average deformation $\langle \mathbf{u}(\mathbf{r}) \rangle$, and the statistical deviation, $\delta \mathbf{u}(\mathbf{r})$. Until now we have assumed that the average deformation vector is zero, i.e., that $\langle \mathbf{u}(\mathbf{r}) \rangle = 0$. However, if we introduce a compositional gradient, which in turn produces a non-statistical variation in the lattice constant with position, then $\langle \mathbf{u}(\mathbf{r}) \rangle$ will no longer be zero for all \mathbf{r} .

Diffraction from samples exhibiting a compositional gradient, or strain gradient, has been discussed in the literature (see e.g., Halliwell and Lyons, 1984; Punegov, 1990, 1991; Punegov and Vishnjakov, 1995). The following treatment highlights how random and non-random sample defects can be considered simultaneously within the formalism presented in Sec. 2.9. The treatment is restricted to a linear strain gradient in the z direction (i.e., normal to the surface).

The first step is to determine the average (non-statistical) deformation vector, $\langle \mathbf{u}(\mathbf{r}) \rangle$, for the atom that would be positioned at \mathbf{r} in a perfect crystal. We assume that atoms are only displaced parallel to z , hence this treatment will only be applicable to symmetric reflections. Given a strain of ε , an atom will be displaced from z to $z(1 + \varepsilon(z))$. The displacement, u , of the atom at z is $u(z) = z(1 + \varepsilon(z)) - z$. Assuming a linear strain gradient ($\varepsilon(z) = sz$) where we define $\varepsilon(z = 0) = 0$, gives

$$\begin{aligned} \langle u(z) \rangle &= z(1 + \varepsilon(z)) - z \\ &= z(1 + sz) - z \\ &= sz^2. \end{aligned} \tag{6.21}$$

Here u depends only on the z coordinate. The value of s can be approximated if two values of the lattice parameter, c , are known. For example, if we know the lattice parameters at the bottom, c_b , and top, c_t , of the layer then:

$$s = \frac{c_l - c_b}{2tc_b - c_b^2} \quad (6.22)$$

$$\langle u(z) \rangle = \left[\frac{c_l - c_b}{2tc_b - c_b^2} \right] z^2, \quad (6.23)$$

where t is the thickness of the layer.

The diffuse intensity is calculated using Eq. (2.108), i.e.,

$$\begin{aligned} I_h^d(\mathbf{q}) &= \int_0^t dz \int_{-\infty}^{+\infty} dx \int_{-\infty}^{+\infty} dy |\sigma_h(\mathbf{r})|^2 [1 - f^2(\mathbf{r})] \tau(\mathbf{r}, \mathbf{q}) \\ &\times \exp \left\{ - \int_0^z \mu[x + \cot \theta_1(s - z), y, s] + b\mu[x - \cot \theta_2(s - z), y, z] ds \right\} \\ &\times I_0(x - \cot \theta_1 z, y, 0). \end{aligned} \quad (6.24)$$

where $\tau(\mathbf{r}, \mathbf{q})$ is the correlation area, calculated using Eq. (2.111), i.e.,

$$\begin{aligned} \tau(\mathbf{r}; q_x, q_z) &= \int_{-\infty}^{+\infty} dq_y \tau(\mathbf{r}, \mathbf{q}) \quad (6.25) \\ &= (1/2\pi) \int_{-\infty}^{+\infty} d\rho_z \int_{-\infty}^{+\infty} d\rho_x \left(e^{-i(q_z \rho_z + q_x \rho_x)} e^{i(1+b)\sigma_0(\mathbf{r})\rho_z} \right. \\ &\quad \left. \times e^{-ih[(\mathbf{u}(x+\rho_x, y, z+\rho_z)) - (\mathbf{u}(\mathbf{r}))]} G(\mathbf{r}; \rho_x, 0, \rho_z) \right), \end{aligned} \quad (6.26)$$

and all other variables have been defined in Sec. 2.8.3. The term

$$e^{-ih[(\mathbf{u}(x+\rho_x, y, z+\rho_z)) - (\mathbf{u}(\mathbf{r}))]}$$

was set to unity in our treatment in Sec. 2.8.3, because the average value of the displacement vector was zero for the mosaic block model. However, with the introduction of a non-statistical variation in \mathbf{u} , this is no longer the case. Substituting Eq. (6.23) and the correlation function, $g(\mathbf{r}, \rho)$ (defined in Eq. (2.110)), into Eq. (6.25) we obtain

$$\begin{aligned} \tau(\mathbf{r}; q_x, q_z) &= (1/2\pi) \int_{-\infty}^{+\infty} d\rho_z \int_{-\infty}^{+\infty} d\rho_x \left(e^{-i(q_z \rho_z + q_x \rho_x)} e^{i(1+b)\sigma_0(\mathbf{r})\rho_z} e^{-ih[s(2z\rho_z + \rho_z^2)]} \right. \\ &\quad \left. \times p(\rho) \int_{-\infty}^{+\infty} d\alpha W(\alpha) e^{[ih\alpha(\rho_z \sin \varphi - \rho_x \cos \varphi)]} \right). \end{aligned} \quad (6.27)$$

where all terms have been defined in Secs. 2.8.3 and 2.9.

In Sec. 2.9 the correlation area was calculated by analytical integration over ρ (the separation between two points considered in the spatial correlation function),

and numerical integration over α (the rotation of a mosaic block). A similar approach was used to evaluate the integral in Eq. (6.27). We make the following substitutions:

$$p(\rho) = \left[1 - \frac{|\rho_x|}{l_x}\right] \left[1 - \frac{|\rho_z|}{l_z}\right] \text{ for } |\rho_i| \leq l_i \quad (i = x, z) \quad (6.28)$$

$$\beta = -(q_x + h\alpha \cos \varphi) \quad (6.29)$$

$$\psi = -(q_z + h(2sz - \alpha \sin \varphi) - (1 + b)\sigma_0(\mathbf{r})), \quad (6.30)$$

where all these parameters have been defined in Secs. 2.8.3 and 2.9. In terms of these new parameters

$$\begin{aligned} \tau(\mathbf{r}; q_x, q_z) &= (1/2\pi) \int_{-\infty}^{+\infty} d\alpha W(\alpha) \int_{-\infty}^{+\infty} d\rho_x \left[1 - \frac{|\rho_x|}{l_x}\right] e^{i\beta\rho_x} \\ &\times \int_{-\infty}^{+\infty} d\rho_z \left[1 - \frac{|\rho_z|}{l_z}\right] e^{i\psi\rho_z} e^{-ihs\rho_z^2}. \end{aligned} \quad (6.31)$$

Equation (6.31) is analogous to Eq. (2.111); however a compositional gradient has now been included. The appearance of ρ_z^2 in Eq. (6.31) makes the integral difficult to evaluate. The computer package Mathematica^{®2} was used to analytically evaluate the integrals over the spatial coordinates (i.e., ρ_x and ρ_z) in Eq. 6.31. The diffuse intensity is given by substitution into Eq. (6.24):

$$\begin{aligned} I_h^d(\mathbf{q}) &= I_0 |\sigma_h^2 [1 - f^2]| (1/2\pi) \int_{-\infty}^{+\infty} W(\alpha) \frac{2}{l_x \beta^2} (1 - \cos(\beta l_x)) d\alpha \\ &\times \int_0^{l_z} \left[\frac{2}{l_z} \frac{i}{2hs} - \frac{1}{l_z} \frac{i e^{i(\psi l_z - hsl_z^2)}}{2hs} - \frac{1}{l_z} \frac{i e^{i(-\psi l_z - hsl_z^2)}}{2hs} \right. \\ &+ \left(\frac{2}{l_z} \right) \frac{i^{\frac{3}{2}} \psi e^{\frac{i\psi^2}{4(hs)}} \sqrt{\pi} \operatorname{erf} \left[\frac{i^{\frac{1}{2}}(\psi)}{2\sqrt{hs}} \right]}{4(hs)^{\frac{3}{2}}} \\ &+ \left(\frac{\psi}{2hsl_z} - 1 \right) \frac{i^{\frac{3}{2}} e^{\frac{i\psi^2}{4(hs)}} \sqrt{\pi} \operatorname{erf} \left[\frac{i^{\frac{1}{2}}(-\psi + 2hsl_z)}{2\sqrt{hs}} \right]}{2\sqrt{hs}} \\ &\left. - \left(1 + \frac{\psi}{2hsl_z} \right) \frac{i^{\frac{3}{2}} e^{\frac{i\psi^2}{4(hs)}} \sqrt{\pi} \operatorname{erf} \left[\frac{i^{\frac{1}{2}}(\psi + 2hsl_z)}{2\sqrt{hs}} \right]}{2\sqrt{hs}} \right] e^{-4\mu z} dz, \end{aligned} \quad (6.32)$$

²Mathematica[®] is a symbolic computing package developed by Wolfram Research (see e.g., <http://www.wolfram.com>).

where $\text{erf}(w)$ denotes the error function³ in terms of the complex argument $w = \sqrt{i(\pm\psi + 2hsl_z)}/2\sqrt{hs}$ (or $w = \sqrt{i\psi}/2\sqrt{hs}$). All symbols have been defined in Secs. 2.8.3 and 2.9. We have assumed a (00*l*) type reflection, i.e., the sample is laterally homogenous, so that we can neglect the integrals over x and y ; the static Debye-Waller factor is zero since we have not modified the statistical part of the deformation vector. The Fourier components of the susceptibility vary in the z direction only.

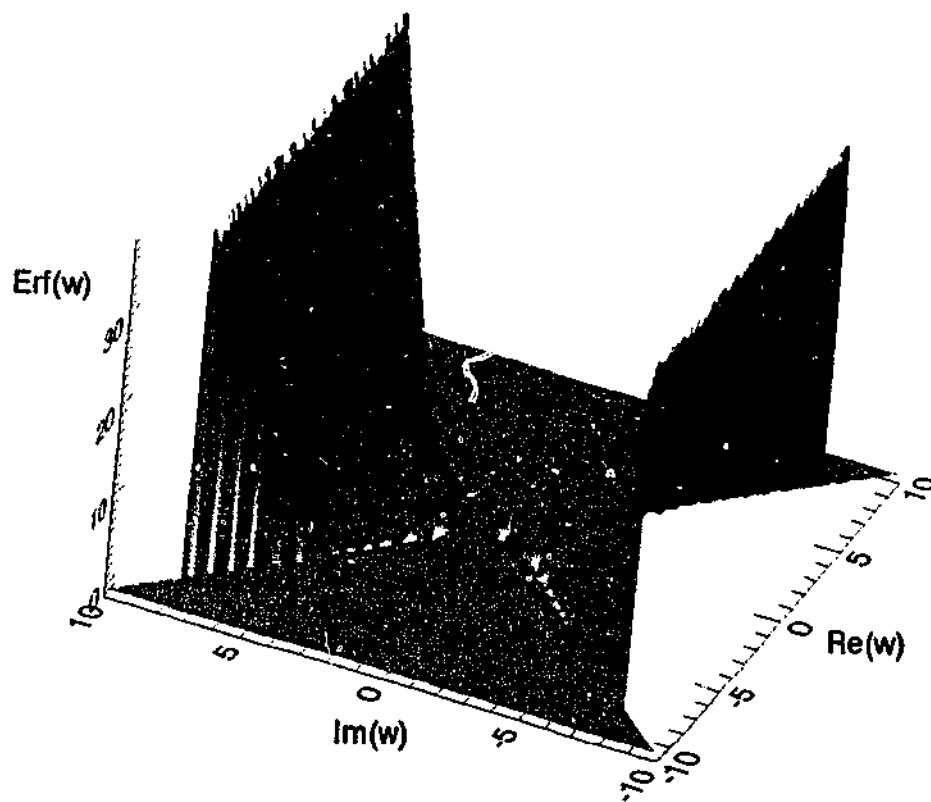
In order to simulate the diffuse intensity diffracted from these samples two different types of layer were modelled: layers with a composition gradient and homogenous layers. The homogenous layers were modelled exactly as described in Secs. 2.9 and 3.3. Modelling a composition gradient used a modified version of the code adopted for the homogenous layers. The integration over z was accomplished using Mathematica[®]. This computing package was used instead of a conventional numerical program written in the Interactive Data Language (IDL), because it handled the error function with complex arguments more robustly. This is demonstrated in Fig. 6.3, where the error function calculated by IDL and Mathematica[®] are compared. Near the origin ($w = 0$) the two outputs agree; however, for $|w| \gtrsim 5$ IDL fails to reproduce the error function correctly. IDL was still used to numerically evaluate the integral over α . Mathematica[®] was called from within IDL, with the parameters passed between the programs via an `ascii` file.

Figure 6.4 shows the model structure for the samples. To reduce the number of free parameters when simulating the intermixed layers, it was assumed that the composition at the top and bottom of these layers matched the homogenous layers at those boundaries. The sample parameters passed to Mathematica[®] for each intermixed layer were the Fourier components of the susceptibility at the top and bottom of the layer, the layer thickness, the mosaic block dimensions, the width of the tilt distribution, and the composition induced strain gradient. The susceptibility throughout the layer was determined using Vegard's law. The mosaic block dimensions and tilt were constant throughout each intermixed layer (but were not necessarily identical to the homogenous layers). The procedure for finding the best fitting parameters was essentially the same as described in Sec. 3.3.2.

³The error function is given by

$$\text{erf}(w) = \frac{2}{\sqrt{\pi}} \int_0^w e^{-t^2} dt. \quad (6.33)$$

(a)



(b)

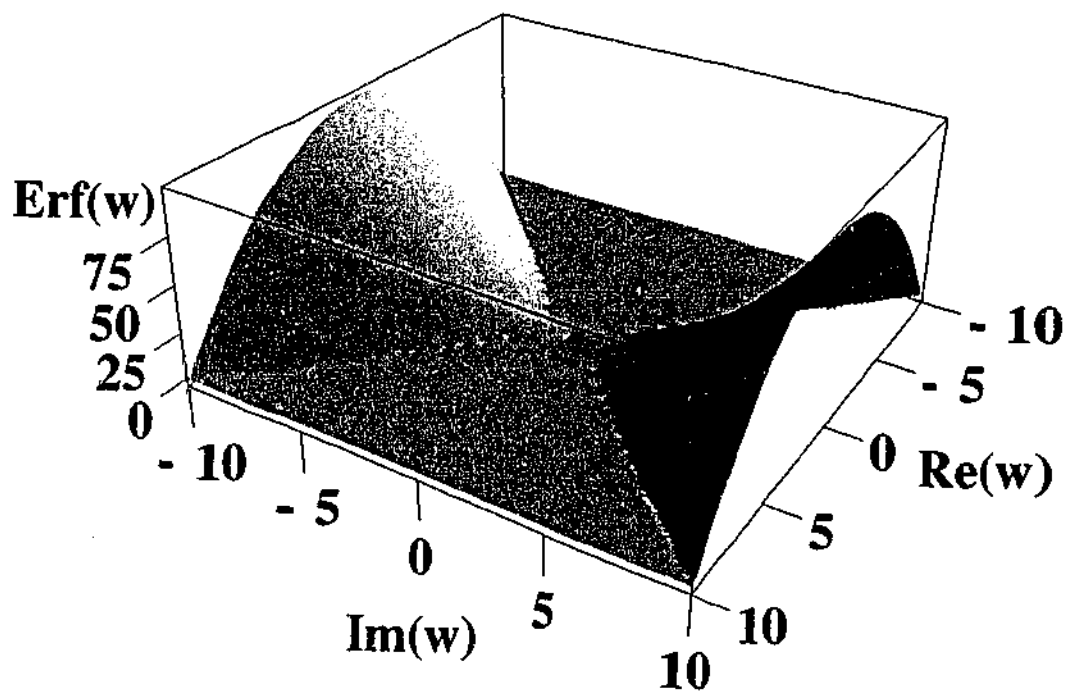


Figure 6.3: A comparison of the error function calculated using (a) IDL and (b) Mathematica[®].

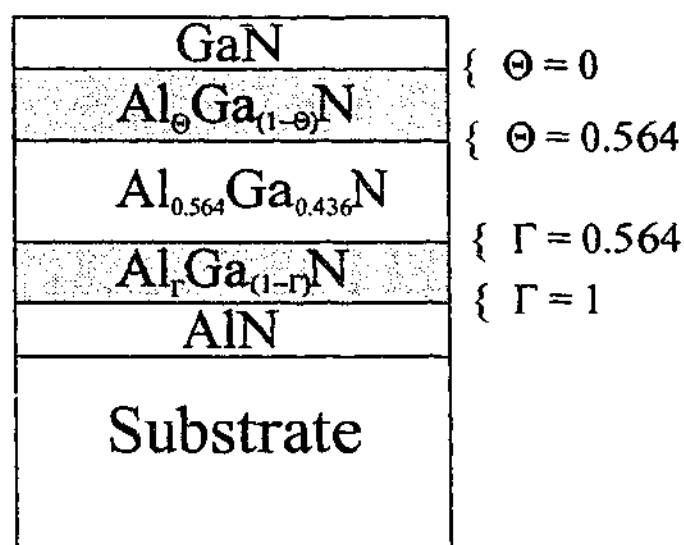


Figure 6.4: The model used to describe the composition of the annealed sample (which shows chemical intermixing) for the statistical diffraction analysis. The grey regions are intermixed layers, which have a composition varying linearly from top to bottom. The composition of the layers at the interfaces are shown on the right.

6.5 Results and Discussion

The experimental work (including sample preparation and X-ray diffraction measurements) and Williamson-Hall analysis were completed by Drs. N Herres and L. Kirste and coworkers. The statistical diffraction modelling was carried out by the author.

The lattice parameters of the as grown AlGa_N layer were $a = 3.1301 \text{ \AA}$ and $c = 5.0839 \text{ \AA}$. Based on Vegard's law the composition was determined to be Al_{0.564}Ga_{0.436}N. After annealing, the AlGa_N layer retained the same composition, however the strain state had changed.

Figure 6.5 shows a low resolution double crystal $\theta - 2\theta$ scan of the samples before and after annealing. The as grown sample clearly shows a super structure as the forbidden ((0001), (0003), and (0005)) reflections are present. However, after annealing, the superstructure reflections disappear. This provides tentative evidence that the ordering observed in the as grown samples is related to growth kinetics. The as grown samples, which may not have reached equilibrium, show superstructure reflections; however, the annealing process allows the samples to approach a state of thermodynamic equilibrium, thereby extinguishing the superstructure reflections. The thermodynamically stable state has a random distribution of Group III atoms.

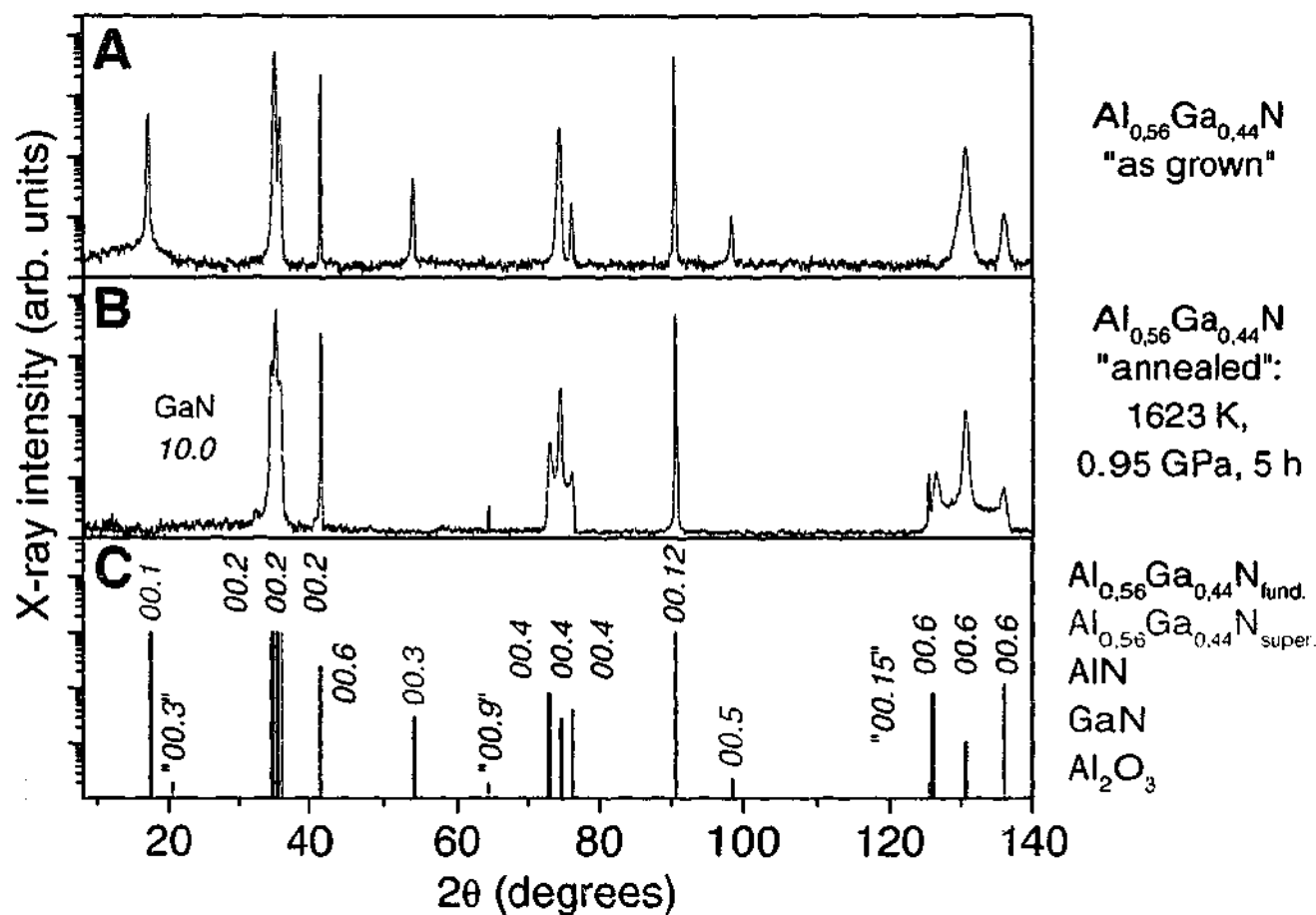


Figure 6.5: X-ray diffraction patterns for the as grown and annealed samples.

6.5.1 As Grown Samples

Diffraction profiles were collected from the as grown sample in the q_z and q_x directions for the $l = \{1, 2, 3, 4, 5, 6\}$ symmetric $(00.l)$ reflections. The diffraction peaks are shown in Fig. 6.6 together with the fitted Voigt functions. The Voigt functions accurately match the peak shapes in the both the q_z and q_x directions. As discussed in Sec. 6.3, if a Lorentzian profile had been used to fit the peaks then the Williamson-Hall analysis would be performed by plotting the integral width, B , of the Lorentzian function versus the q_z position of the reflection. If a Gaussian function is used the required plot is B^2 versus q_z^2 . However, since the Voigt function is a convolution of these two profiles, it is not strictly correct to perform the regression analysis using a plot of B versus q_z or a plot of B^2 versus q_z^2 . Therefore the Williamson-Hall analysis has been carried out for both plots, with the experimental data and regression lines shown in Figs. 6.7 and 6.8. Surprisingly all plots are linear, although a number consist of only three points. The plots of the peak width in the q_x direction versus the q_z position of the peak (see Figs. 6.7(b) and 6.8(b)) indicate that the fundamental reflections (i.e., the $(00.l)$ reflections, where l is even), and superstructure reflections (i.e., the $(00.l)$ reflections where l is odd) lie on different

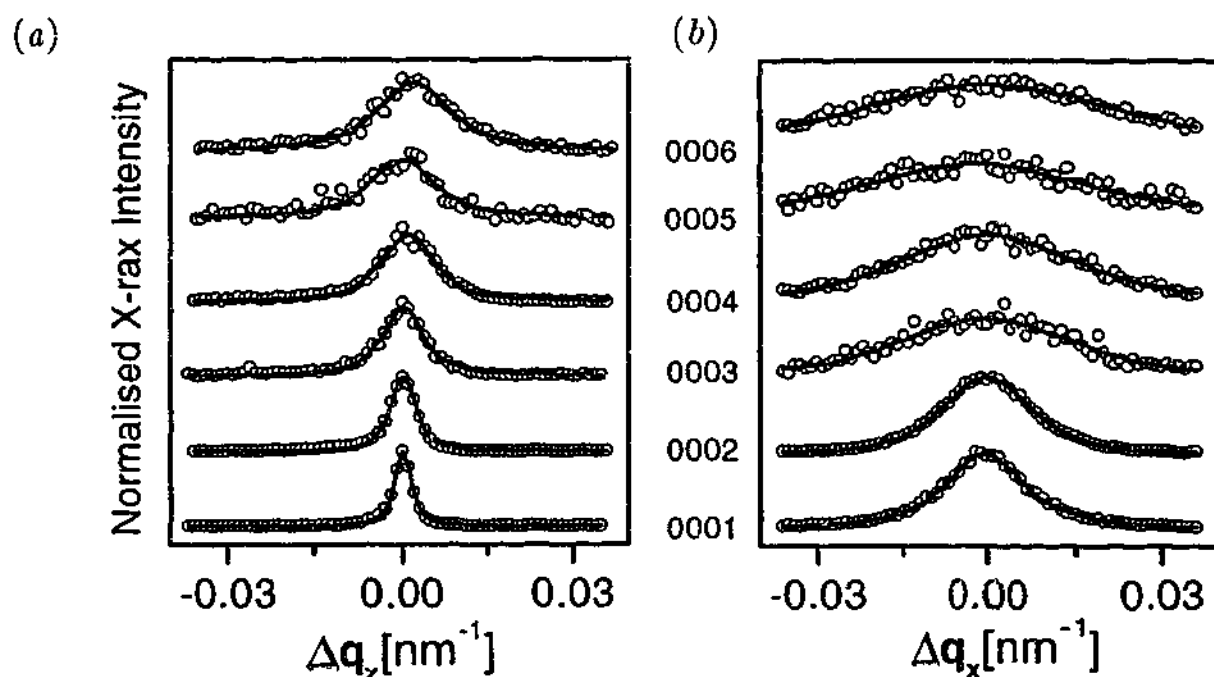


Figure 6.6: Experimental profile (o) and Voigt fits (—) for the as grown AlGaIn sample. (a) q_z direction, and (b) q_x direction.

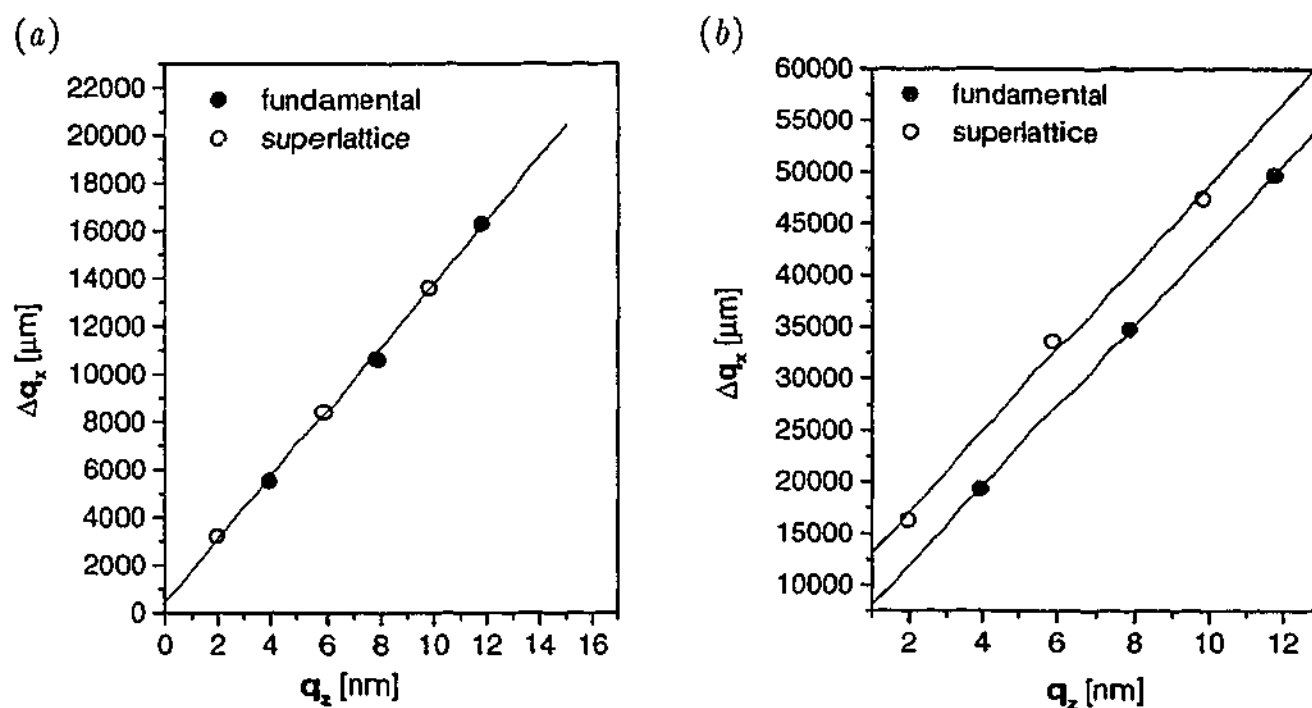


Figure 6.7: Williamson-Hall plots of Δq versus q_z for the as grown AlGaIn sample. (a) Based on peak widths in the q_z direction, and (b) based on peak widths in the q_x direction. Δq is equivalent to B in the text.

regression lines.

The mosaic block parameters determined from the Williamson-Hall analysis are given in Tables 6.1 and 6.2. The parameters determined from the gradient of the Williamson-Hall plot (misorientation and strain) agree for both the B versus q and

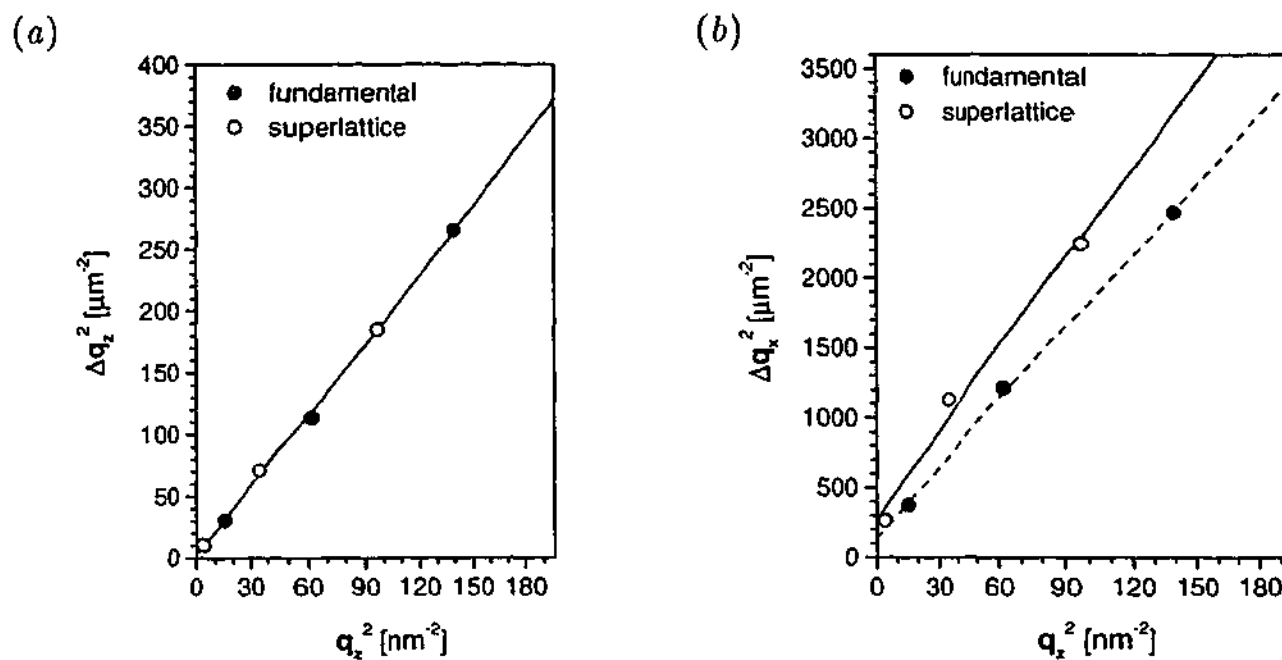


Figure 6.8: Williamson-Hall plots of Δq^2 versus q_z^2 for the as grown AlGaN sample. (a) Based on peak widths in the q_z direction, and (b) based on peak widths in the q_x direction. Δq is equivalent to B in the text.

B^2 versus q^2 plots; however, the parameters calculated from the intercepts are very different. It would seem that the analysis using a $B - q$ plot is incorrect because the size of the blocks perpendicular to the surface is larger than the layer thickness. The block size determined using a $B^2 - q^2$ plot seems reasonable. An analysis based on the fundamental and superstructure reflections for the integral widths in the q_x direction show that the misorientation agrees for both reflection types, but the block size is different. The different block sizes are possibly the result of anti-phase domain boundaries in the material. This is shown schematically in Fig. 6.9, where the phase of the structure changes on passing through an anti-phase domain boundary (i.e., the Ga and Al exchange lattice positions). For the Group III nitrides investigated here, this means that part of lattice is translated along the $[0001]$ direction. If the lattice is translated by half a unit cell in the z direction then $F'_{hkl} = F_{hkl}e^{-2\pi\frac{1}{2}l}$, where F'_{hkl} is the structure factor in the shifted region and F_{hkl} is the structure factor in the unshifted region. If the Miller index l is odd then $F'_{hkl} = -F_{hkl}$, otherwise $F'_{hkl} = F_{hkl}$. In this case the domain boundary (wall) will be apparent only for the superstructure reflections, and additional broadening (smaller apparent particle size) will be seen for these reflections. It was found that a regression analysis based on both the fundamental and superstructure reflections gave the same misorientation width. This is expected because the anti-phase domains are inside the mosaic blocks, and hence must have the same orientation.

Table 6.1: Parameters determined using the Williamson-Hall procedure for the as grown AlGa_N sample. The regression analysis was performed by plotting Δq versus q .

	l_x (nm)	Δ_m	l_z (nm)	$\langle \epsilon_{zz} \rangle (\times 10^{-3})$
Using fundamental ('even') reflections	237 ± 23	$0.22^\circ \pm 0.01^\circ$	2315 ± 692	2.66 ± 0.05
Using superlattice ('odd') reflections	102 ± 13	$0.22^\circ \pm 0.01^\circ$		

Table 6.2: Parameters determined using the Williamson-Hall procedure for the as grown AlGa_N sample. The regression analysis was performed by plotting Δq^2 versus q^2 .

	l_x (nm)	Δ_m	l_z (nm)	$\langle \epsilon_{zz} \rangle (\times 10^{-3})$
Using fundamental ('even') reflections	88 ± 31	$0.24^\circ \pm 0.04^\circ$	709 ± 36	2.75 ± 0.34
Using superlattice ('odd') reflections	61 ± 26	$0.26^\circ \pm 0.09^\circ$		

Table 6.3: Parameters determined from the statistical diffraction theory for the as grown AlGa_N sample.

	l_{x_1} (nm)	l_{x_2} (nm)	Δ_m	l_z (nm)	$\langle \epsilon_{xx} \rangle$	$\langle \epsilon_{zz} \rangle$
Using fundamental ('even') reflections	90 ± 10	n.a.	$0.29^\circ \pm 0.03^\circ$	740	11×10^{-3}	2.7×10^{-3}
Using superlattice ('odd') reflections	65 ± 7	24 ± 3	$0.30^\circ \pm 0.03^\circ$			

The simulated profiles based on the statistical kinematical diffraction theory are shown in Figs. 6.10 and 6.11 together with the experimental data. Fitting the fundamental reflections in the q_x direction was straightforward. The fitting parameters (see Table 6.3) agree well with the Williamson-Hall analysis performed in $B^2 - q^2$ space confirming that $B^2 - q^2$ plots produce more accurate results for these samples. The superstructure reflections were more difficult to fit. In Sec. 6.4 we

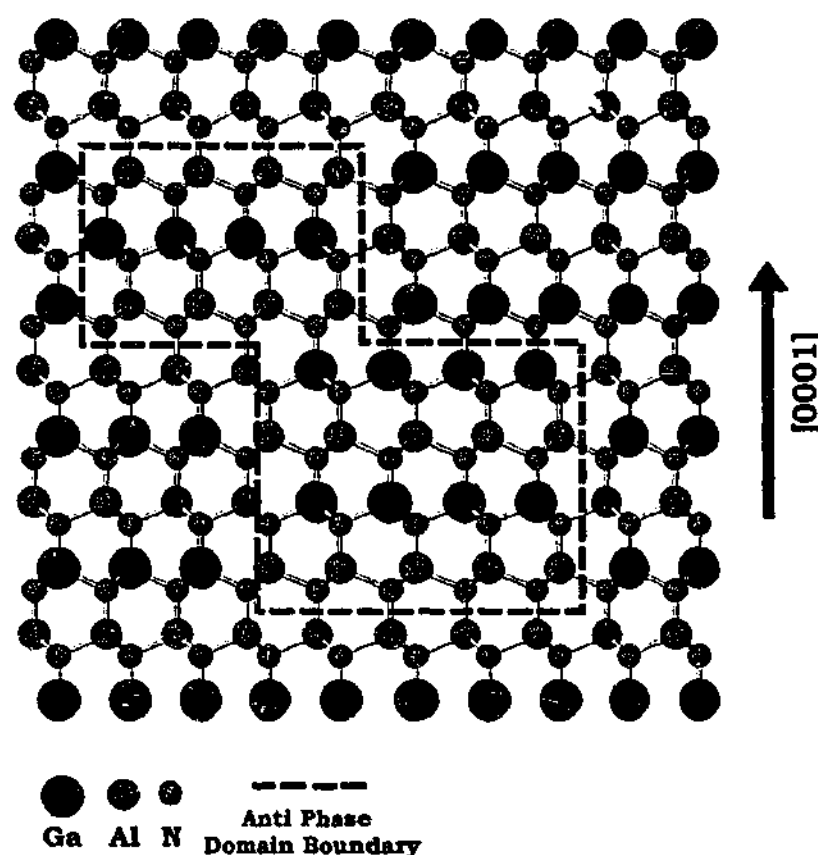


Figure 6.9: An anti-phase domain in AlGaN. At the anti-phase domain boundary the Al and Ga atoms interchange their positions in the lattice (figure provided by Dr L. Kirste).

noted that two mosaic block sizes were required to adequately fit the experimental data. The block sizes are of the same order as predicted by the Williamson-Hall analysis (with the regression based on a $B^2 - q^2$ plot). The weight given to the contribution from the two different block sizes was kept constant during the analysis, to reduce the number of free parameters. The origin of the two block sizes is unclear, although it may be related to the anti-phase domains described above. Interestingly the two block sizes add to give the block size reported for the fundamental reflections. Further, the misorientation determined using statistical diffraction theory (SDT) agrees with that given by the Williamson-Hall analysis.

The modelling in the q_z direction was more problematic, requiring a strain profile to achieve an approximate fit. As such the match is poor (see Fig. 6.11). The strain profile, ϵ_{zz} , is shown in Fig. 6.12(a). The average strain given in Table 6.3 agrees well with the Williamson-Hall analysis. Matching of asymmetric reflections by SDT simulations (see Fig. 6.12(b)) allowed the strain profile, ϵ_{xx} , parallel to the surface to be determined (see 6.12(a)). Finally, utilising all parameters full reciprocal space maps were produced and compared to the experiments (see Figs. 6.13 and 6.14). In

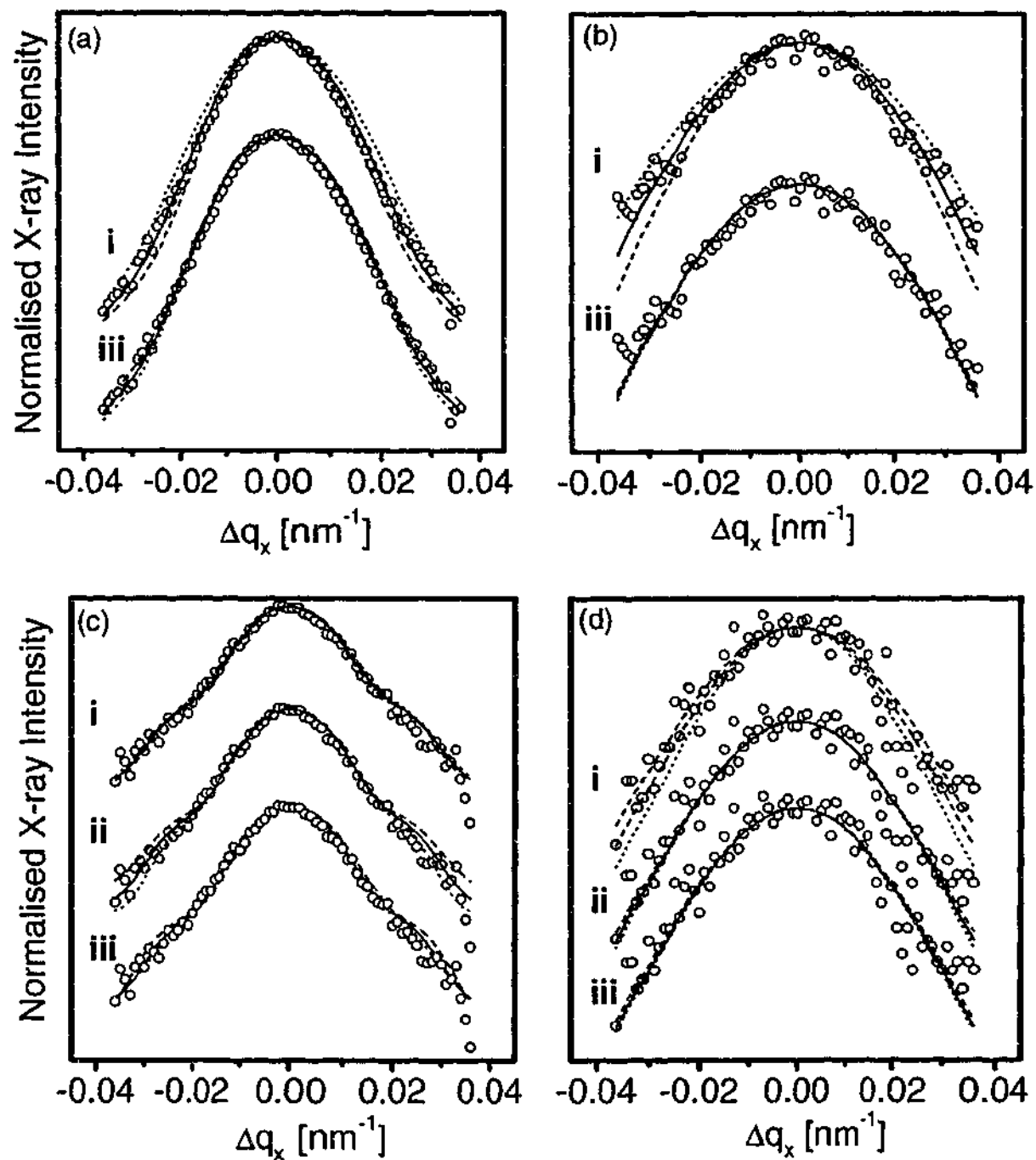


Figure 6.10: Experimental profiles (o) and simulated profiles based on the statistical diffraction theory (dotted, dashed and full lines), in the q_x direction for the fundamental and superlattice reflections, for the as grown AlGaIn sample. (a) (0002) reflection, (b) (0004) reflection, (c) (0001) reflection, and (d) (0003) reflection. Profile i indicates the effect of changing Δ_m ; profile ii shows the effect of changing l_{x2} ; and profile iii shows the effect of changing l_{x1} . The solid line is the line of best fit; the dotted and dashed lines represent +10% and -10%, of Δ_m , l_{x2} , and l_{x1} .

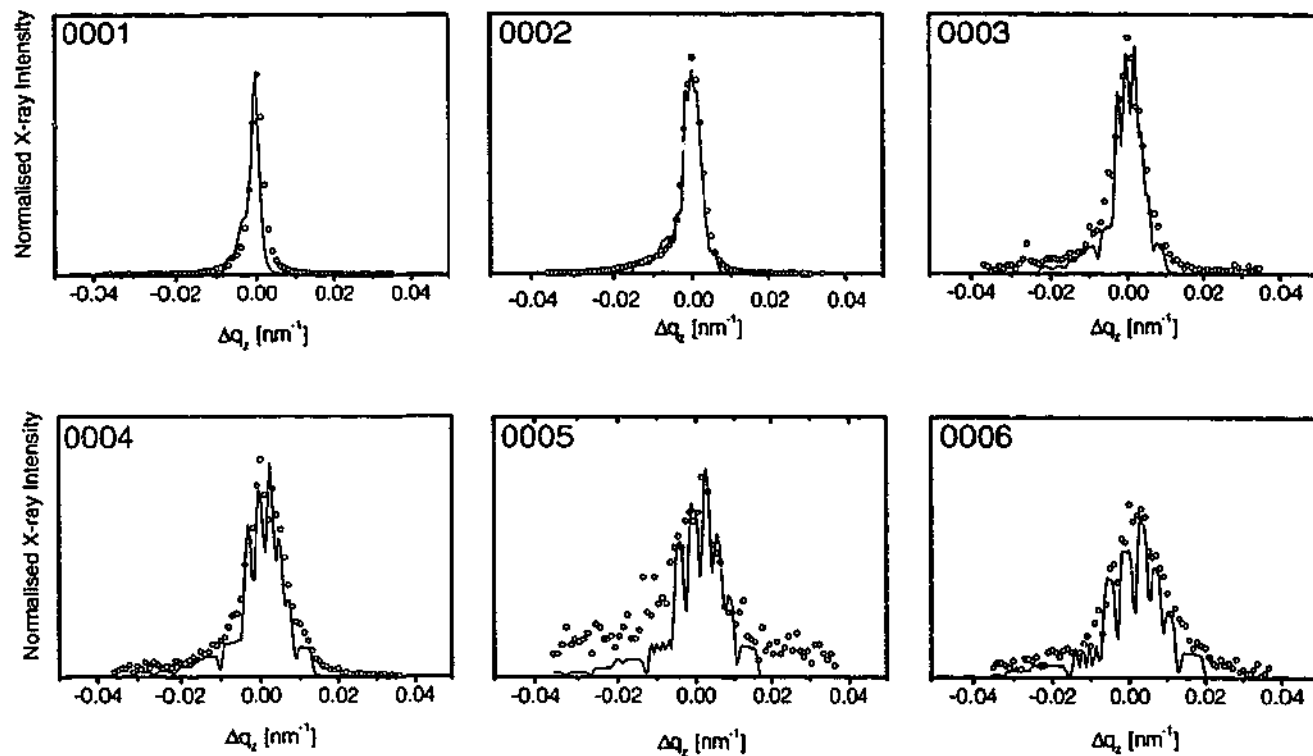


Figure 6.11: Experimental profiles (\circ) and SDT fits ($—$) in the q_z direction for the as grown AlGaIn sample.

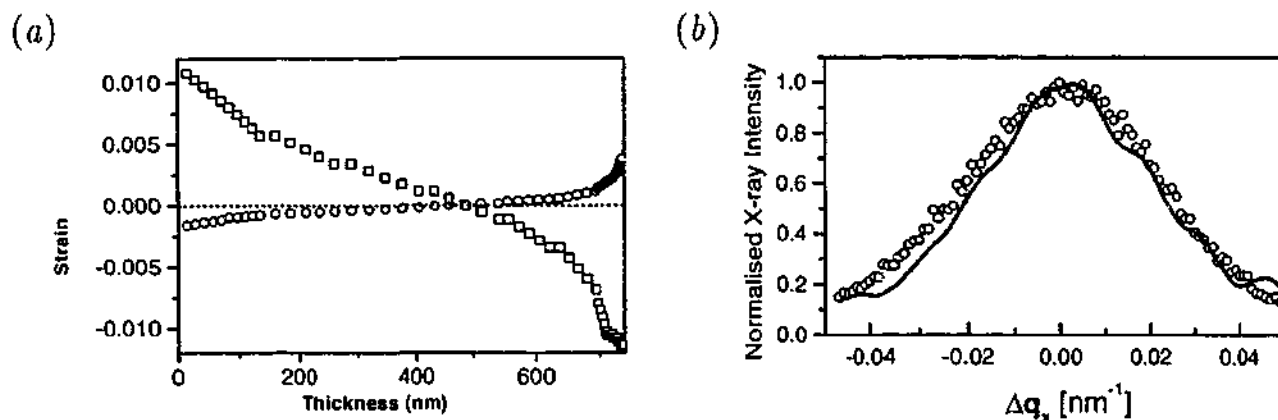


Figure 6.12: (a) Strain distribution for ϵ_{xx} (\circ) and ϵ_{zz} (\square), from the surface (0 nm) to the substrate (740 nm), for the as grown AlGaIn sample. These were determined from the q_z scans of the $(00.l)$ reflections and RSMs of $(11.l)$ and $(\bar{1}\bar{1}.l)$ reflections, using statistical diffraction theory. (b) The experimental (\circ) and simulated profiles ($—$) in the q_x direction for the $(\bar{1}\bar{1}.4)$ reflection from the as grown AlGaIn sample. The simulated profile is based on statistical diffraction theory.

general the simulated RSMs reproduce all of the features seen in the experimental RSMs, including the correct shape and size. This gives us confidence that the parameters determined by the SDT analysis are accurate.

6.5.2 Annealed Samples

Annealing the sample randomised the Al and Ga atoms within the structure, and hence the superlattice reflections ($(00.l)$ where l is odd) were no longer observable. Therefore fewer experimental diffraction profiles were collected. These profiles are shown in Fig. 6.15 together with the Voigt fits in both the q_z and q_x directions. The insets show the fitting on a logarithmic scale, highlighting that the Voigt function fails to match the experimental data in the low intensity region. In particular the fit in the q_z direction is not reliable because of the chemical intermixing (compositional gradient) driven by the annealing process. Therefore only the peaks in the q_x direction were analysed using the Williamson-Hall method. The Williamson-Hall plot (q_x direction only) is shown in Fig. 6.16 along with the Williamson-Hall plot for the as grown sample. The Williamson-Hall analysis was restricted to a $B^2 - q^2$ plot because the original results show this to be more accurate than a $B - q$ plot. The mosaic block parameters determined by the Williamson-Hall analysis are given in Table 6.4. According to this analysis the particle size in the q_x direction has increased approximately threefold compared to the as grown sample. This is expected, since annealing should decrease the dislocation density of the sample. The Williamson-Hall analysis suggested that there was only a small change in the misorientation.

The SDT analysis was performed for both the q_z and q_x scans as shown in Figs. 6.17 and 6.18. The simulation parameters are summarised in Table 6.5. The structure was randomised, precluding anti-phase domains; only one lateral block size was required to fit the data. In this case the block size in the q_x direction does not agree with the Williamson-Hall analysis, although there is agreement for the misorientation.

The chemical intermixing of the layers was quite significant, and hence fitting

Table 6.4: Parameters determined from a Williamson-Hall analysis for the annealed AlGaIn sample.

l_x (nm)	Δ_m
333 ± 51	$0.23^\circ \pm 0.01^\circ$

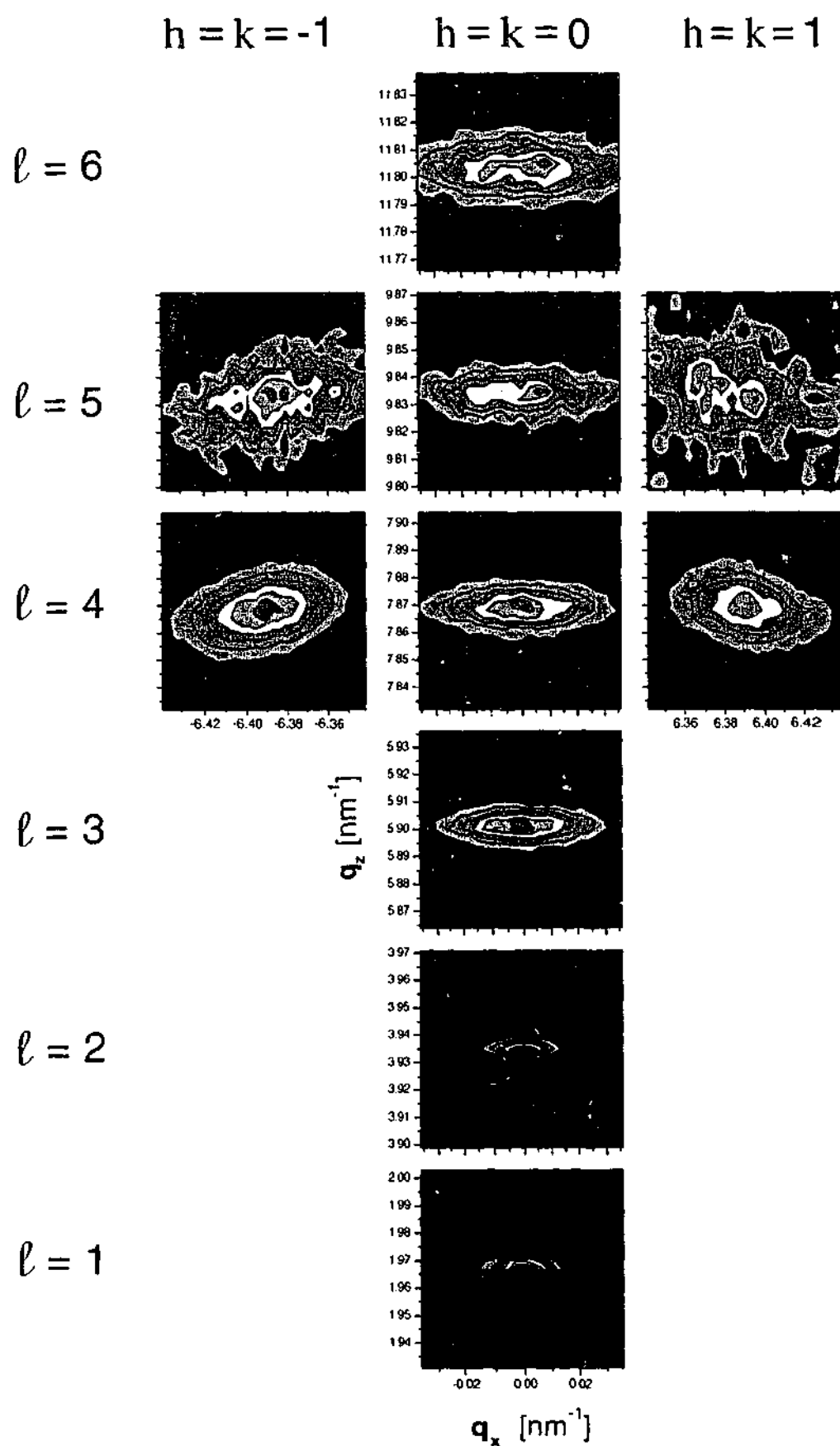


Figure 6.13: Experimental RSMs for the as grown AlGaN sample. The Miller indices (hkl) of the reflections are indicated above and to the left of each of the maps.

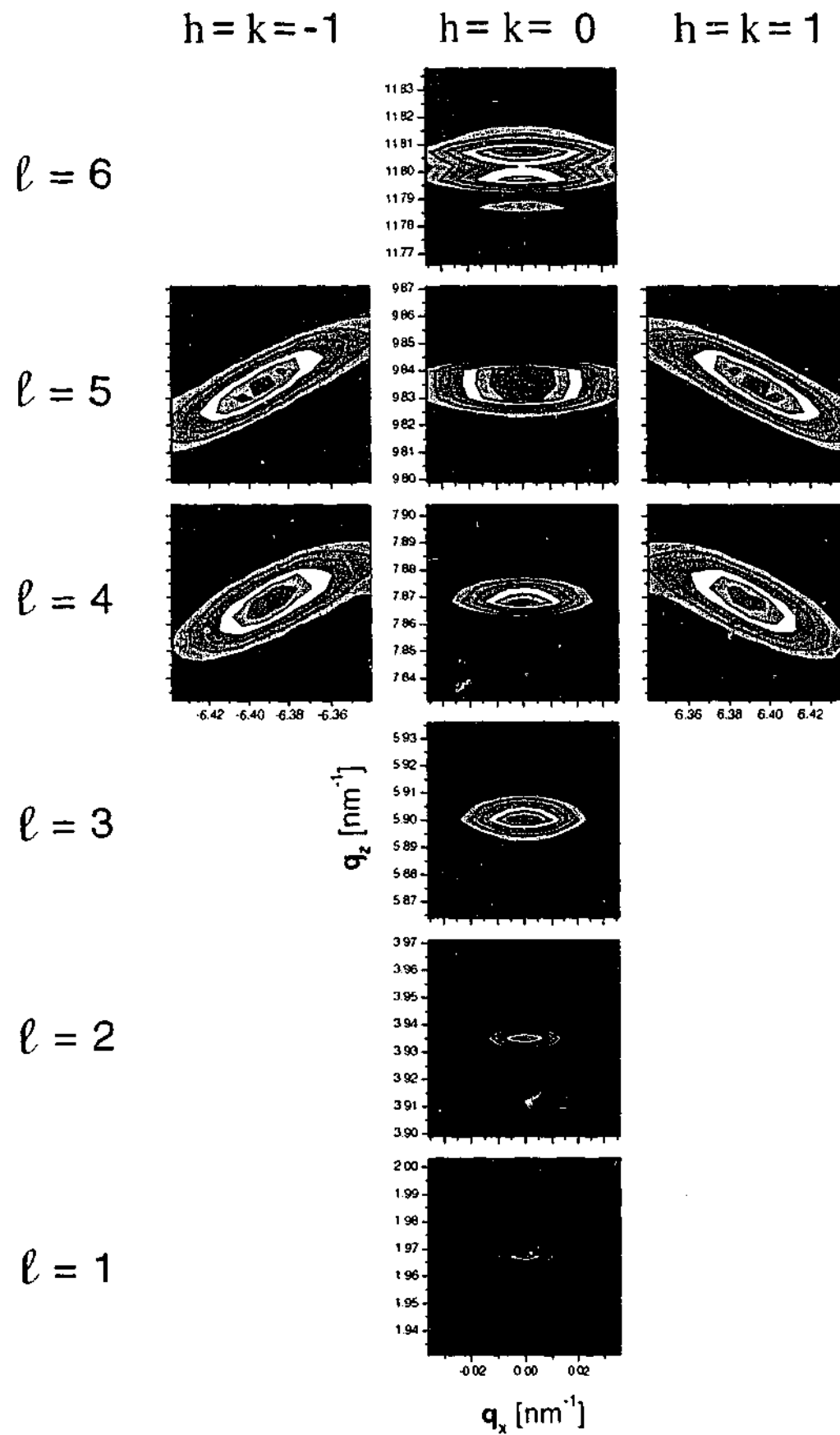


Figure 6.14: Simulated RSMs, calculated using statistical diffraction theory, for the as grown AlGa_N sample. The Miller indices ($hk.l$) of the reflections are indicated above and to the left of each of the maps.

Table 6.5: Parameters determined from the statistical diffraction theory for the annealed AlGa_N sample.

Layer	Thickness (nm)	l_x (nm)	Δ_m	l_z (nm)	$\langle \epsilon_{zz} \rangle$
GaN	60	50	0.35°	70	2.5×10^{-3}
AlGa _N	600	150 ± 15	$0.23^\circ \pm 0.02^\circ$	100	3.0×10^{-3}
AlN	110	100 ± 10	0.2°	60	1.5×10^{-3}

in the q_z direction was difficult. However, considering the complexity of the structure there is reasonable agreement between the empirical and simulated profiles (see Fig. 6.17). The linear strain model allows the intermixed region to be fitted. Significant oscillations are observed in the simulated profile for the intermixed region. These oscillations are also observed experimentally for layers having strain or composition gradients (see e.g., Halliwell and Lyons, 1984; Punegov, 1991), and hence are not simply an artefact of the simulation. Since oscillations are not evident throughout the intermixed region of the experimental diffraction profile it is likely that the strain/composition is not linear or that the oscillations have been masked by background noise. (There are some small oscillations in the experimental data near the AlN peak; however, these may be due to the AlN layer itself, not the strain/composition gradient). The simulated scans also show a decrease in

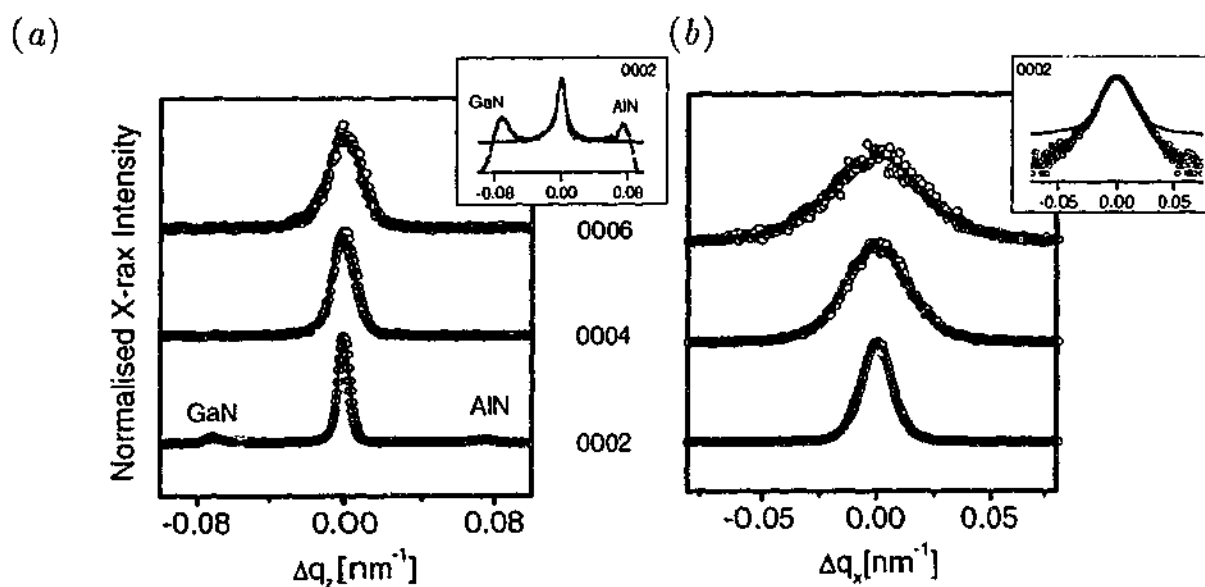


Figure 6.15: Experimental profile (\circ) and Voigt functions ($—$) fitted to the experimental data for the annealed AlGa_N sample. (a) Scan in the q_z direction, and (b) scan collected in the q_x direction. The insets show the same data on a logarithmic scale to highlight the mismatch at low peak intensities.

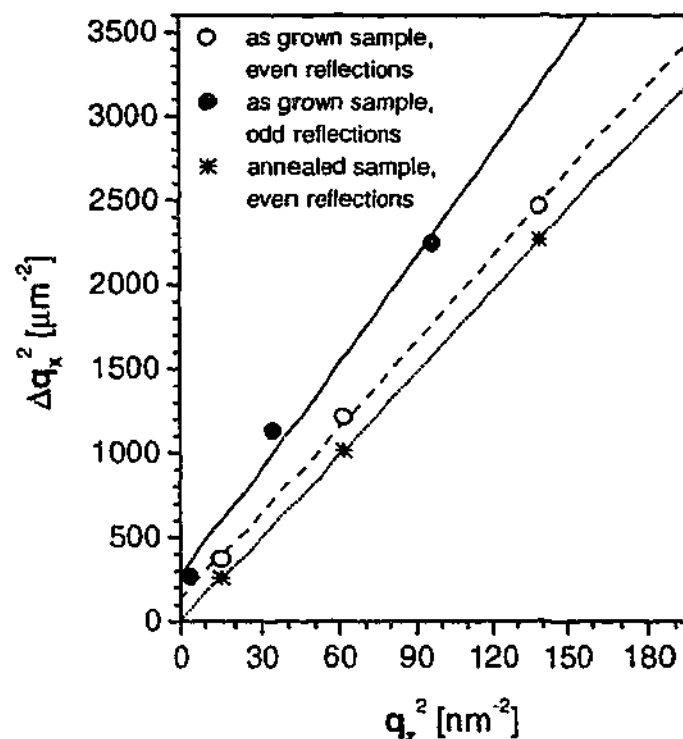


Figure 6.16: Williamson-Hall plot of Δq_x^2 versus q_z^2 for the annealed and non-annealed AlGaIn sample. Δq is equivalent to B in the text.

intensity near the AlN peak. The origin of this effect is not clear, and has not been investigated at this stage.

The perpendicular block size reported for the as grown and annealed samples (determined by SDT) are very different. The annealed sample has a smaller block size, which seems counterintuitive. The reason is that the q_z scans for the as grown samples were fitted using a strain gradient, with the block size set to the full thickness of the layer. Modelling the layer in this way means the peak width is determined by the strain gradient, not the block size. However, on annealing the strain was reduced within the AlGaIn layer, and hence the block size becomes the dominant broadening mechanism. This is consistent with the peak shape, and that the match between the simulated scan and the experimental data. The actual perpendicular block size for the as grown material would be much smaller than the block size used in the simulation.

The Williamson-Hall analysis was not capable of accommodating the constant strain gradient and hence reliable results for the perpendicular block size could not be determined. However, the entire sample structure could be handled by the SDT model, which provided a more complete 'picture' of the material. The compromise is that the SDT fitting procedure is quite involved. Furthermore the solution may not be unique, because of the large number of fitting parameters. This is especially

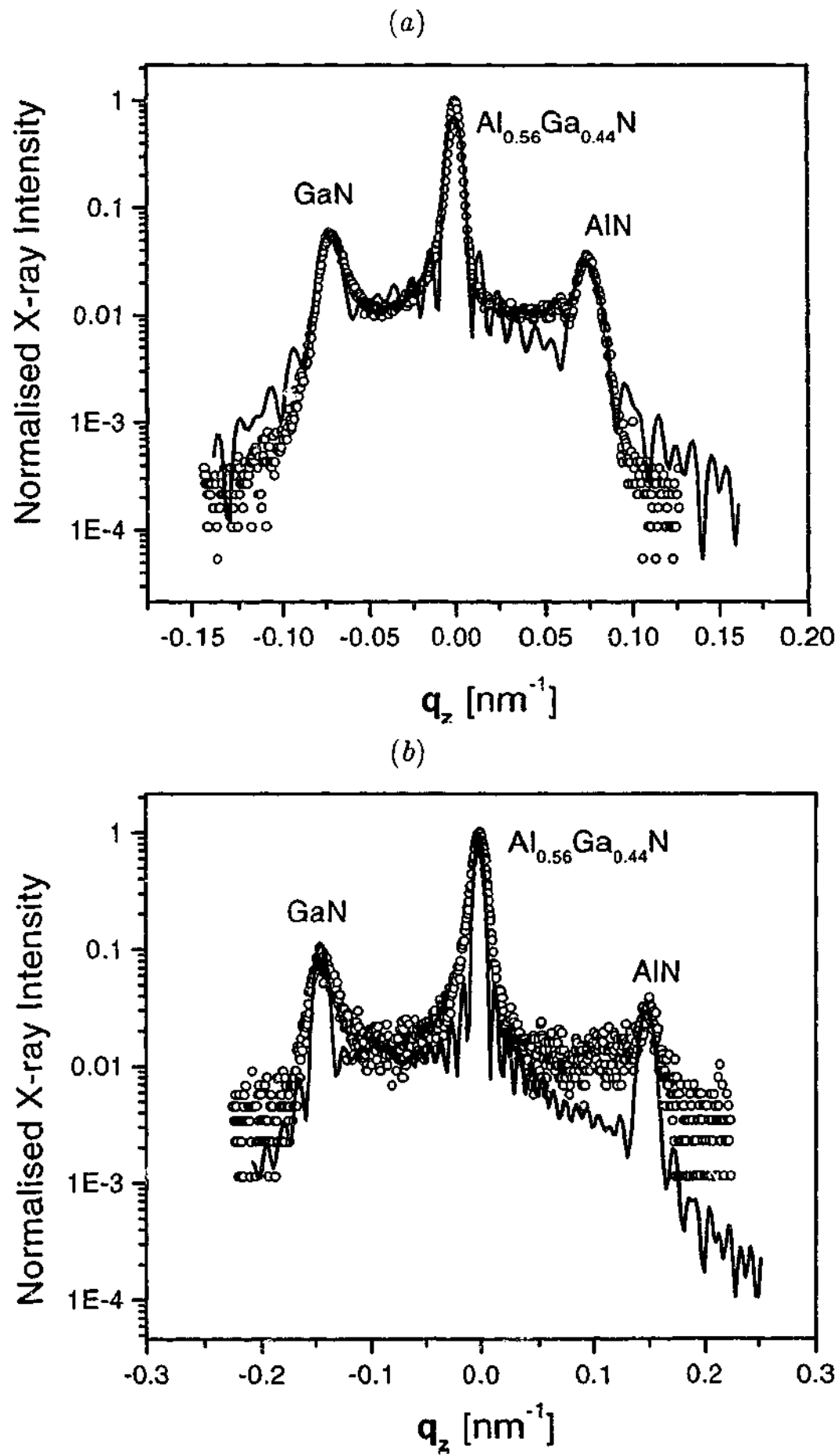


Figure 6.17: Experimental profiles (o) for scans in the q_z direction, and simulated profiles based on statistical diffraction theory (—), for the annealed AlGaIn sample. (a) (0002) reflection, and (b) (0004) reflection.

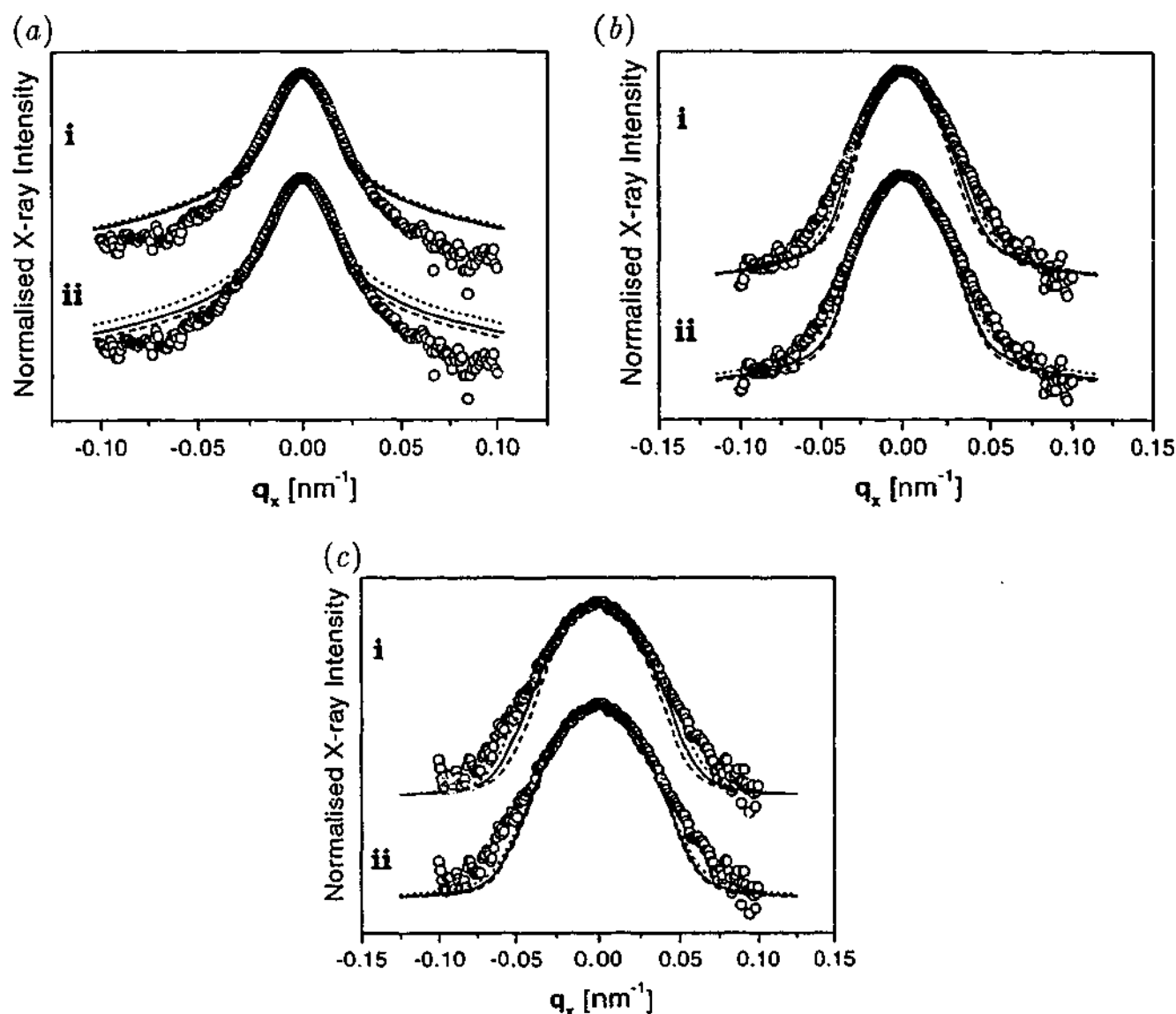


Figure 6.18: Experimental profiles (o) for scans in the q_x direction and simulated profiles (dotted, dashed, and full lines) based on statistical diffraction theory (SDT), for the annealed AlGaIn sample. (a) (0002) reflection, (b) (0004) reflection, and (c) (0006) reflection. Profile i indicates the effect of changing Δ_m (misorientation) and profile ii the effect of changing l_x (lateral block size). The solid line is the line of best fit; the dotted and dashed lines represent -10% and +10% variation to Δ_m and l_x .

true if only a limited number of experimental scans were collected, and hence the accuracy of the results cannot always be guaranteed.

6.6 Conclusion

The as grown $\text{Al}_{0.564}\text{Ga}_{0.436}\text{N}$ layer exhibited chemical ordering of the Al and Ga atomic species. The ordering was identified by the presence of forbidden $((00.l)$ where l is odd) reflections in X-ray diffraction studies. Annealing of the sample at high temperature and pressure randomised the Al and Ga atoms within the sample, demonstrating that the ordering is generated by kinetics during growth. The analysis of high resolution X-ray diffraction profiles was achieved using two different techniques: the Williamson-Hall analysis and statistical diffraction theory. For the Williamson-Hall analysis the peak profiles were fitted with Voigt functions. This meant that neither a plot of B versus q_z or B^2 versus q_z^2 were strictly correct for determining the structural parameters (i.e., mosaic block (particle) size, misorientation, heterogeneous strain). It was found that for this sample a plot of B^2 versus q_z^2 provided the most reliable results.

For the as grown sample it found that the superstructure (forbidden) and fundamental reflections suggested different lateral block sizes. This was attributed to anti-phase domains within the sample, as only the superstructure reflections were sensitive to their presence. The statistical diffraction theory results confirmed the Williamson-Hall analysis of the as grown sample, with the block sizes, misorientation, and strain all agreeing within the uncertainty of the simulation. However, a correct match between the simulated and experimental profiles in the q_x direction required two lateral block sizes. This was also attributed to the anti-phase domains.

The Williamson-Hall analysis for the annealed sample could only be completed for the q_x profiles (and hence only the lateral block size and misorientation could be determined). The Voigt function was inadequate for fitting the profile shape in the q_z direction because of chemical intermixing generating large intensity in the tails of the AlGa_N peak. A composition gradient model was introduced into the simulations based on the statistical diffraction theory, to allow the profiles to be fitted in both the q_x and q_z directions. The misorientation, for the annealed sample was determined to be 0.23° by both analysis techniques. However, the lateral block sizes were different by a factor of two.

These experiments showed that simulations based on the statistical diffraction

theory have a wider range of applicability than simple integral width analysis techniques. The statistical diffraction theory can be used to model complex sample features, such as strain or composition gradients, and is sensitive to the whole diffraction peak shape, not just the width. However, the integral width methods, such as the Williamson-Hall analysis, are simple to implement and can be completed quickly.

CHAPTER 7

Conclusions and Future Work

7.1 Review of Major Results

The aim of this thesis was to characterise the defect structure of Group III nitrides. Although these materials are routinely characterised using X-ray diffraction, statistical diffraction theory has not been widely used as a technique for simulating their X-ray diffraction patterns. In Chapters 2 and 3 we formulated the theory of statistical diffraction; this formalism is well suited to describing Group III nitrides because the epitaxially grown layers exhibit high defect densities leading to a polycrystalline-like structure. In the present formalism the deformation of the crystal is described by statistical parameters, such as the ensemble average and spatial pair correlation function. These parameters are determined by the deformation model. In the present work a mosaic block structure was assumed, in which the blocks were modelled as parallelepipeds with adjustable height, width, and orientation, with respect to the sample surface.

In Chapter 4 we investigated a series of Group III nitride multilayers at various stages of the growth process. The X-ray diffraction profiles and concomitant analysis presented in Sec. 4.2 indicate that the as grown low temperature (LT) deposited AlN buffer layers were formed from mosaic blocks (crystallites) with a small (30 nm) lateral extent. The blocks have a very broad misorientation; 8° for the 30 nm thick buffer layer and 6° for the 70 nm thick buffer layer. The analysis also suggests that the buffer layer has two distinct block sizes perpendicular to the sample surface (approximately 4 nm and 1.5 nm), possibly located in different sub-layers.

The annealed 70 nm LT-AlN buffer layer was similar to the non-annealed sample, and also exhibited two perpendicular block sizes. The mosaic block sizes were essentially unchanged by the annealing process; the mosaic block misorientation and the tilt of the sub-layers were slightly reduced (the sub-layer tilt changed from 0.9° to 0.65° and the misorientation from 6° to 5°). The annealed 30 nm LT-AlN buffer layer also displayed two sub-layers – similar to those observed for the non-annealed sample, with a reduction in misorientation and tilt. Significantly the annealed 30 nm LT-AlN buffer showed evidence of a third sub-layer, in which the mosaic blocks

have a large lateral extent (280 nm) and very small misorientation (0.01°). Furthermore the average orientation of the blocks (i.e., layer tilt) was perpendicular to the sample surface. It has been reported in the literature that a 30 nm AlN buffer allows GaN layers with a higher quality crystal structure (i.e., smaller misorientation, whole layer tilt, and increased block size) to be grown compared to a 70 nm buffer layer (Tabuchi *et al.*, 2002). Ito *et al.* (1999) reported that the optimum AlN buffer layer thickness for GaN crystallinity is 20 nm. We conjecture that this is due to the sub-layer with small misorientation and large lateral mosaic block size providing a regular, correctly orientated, nucleation layer for GaN growth.

The initial stages of GaN growth on 30 nm and 70 nm LT-AlN buffer layers was investigated in Sec. 4.3. A 30 nm thick GaN layer grown on a 30 nm LT-AlN buffer layer produced very small misorientation, and a large lateral mosaic block size that was 'perfectly' oriented with the substrate. However, a 30 nm thick GaN layer grown on a 70 nm LT-AlN buffer layer had a larger misorientation and smaller lateral block size compared to the 30 nm LT-AlN buffer layer. This difference is due to the higher quality (low mosaicity) sub-layer observed for the 30 nm LT-AlN buffer layer.

The investigation of three $\text{In}_x\text{Ga}_{1-x}\text{N}$ layers with different compositions (nominally $x = (0.05, 0.30, 0.42)$), was reported in Sec. 4.4. The nominal composition for the $x = 0.3$ was found to be incorrect, X-ray diffraction revealing the true composition to be $x = 0.17$. The diffracted intensity predicted by the mosaic block model accurately matched the experimental X-ray diffraction profiles for the samples with $x \leq 0.3$, suggesting that the mosaic block model is suitable for describing the defect structure within those layers. However, the simulated profiles did not match the experimental data for the $\text{In}_{0.42}\text{Ga}_{0.58}\text{N}$ layer. It appears that the defect structure has been significantly modified by segregation of InGaN, possibly forming clusters (the composition or structure of the cluster is unknown), hence changing the shape of the diffuse intensity. The two 20 nm thick InGaN layers grew coherently (fully strained) on the LT-AlN buffer; however, a 200 nm thick layer was completely relaxed. This suggests that the critical thickness for relaxation is less than 200 nm, but greater than 20 nm.

In Chapter 5 we described a novel technique for rapidly collecting reciprocal space maps (RSMs) using imaging plates (IPs) at the Australian National Beamline Facility. The imaging plates were used in a one-dimensional mode, employing Weissenberg screens to mask the plate. The method requires minimal time for setup, and allows an RSM to be collected (around a single reciprocal lattice point) in approximately 45 minutes; this includes evacuation of the diffractometer chamber

and readout of the IP. Mapping of the IP data onto a cartesian grid, for producing $\theta - 2\theta$ and ω scans, requires interpolation. Several interpolation methods were investigated; however, since only a small number of one-dimensional scans were collected (29) all interpolation schemes generated artifacts. The most deleterious of which are false peaks. The false peaks can be avoided if the experimental diffraction peaks, which are narrow in the q_z direction, are interpolated in the q_x direction, and vice versa. For our samples we found that as few as 58 IP strips were required to produce scans with enough spatial resolution to match the experimental scans collected using TAD. The IP method is very useful for scanning large regions of reciprocal space, where the peak position and shape are not precisely known; this situation arises for asymmetric peaks. Furthermore it does not require an analyser crystal or 2θ -arm, which reduces setup time by obviating the need to align components. Sample features that can only be observed using a large angular range, such as powder diffraction peaks (arising from cluster segregation or polycrystalline regions), can also be detected using the IP method.

In Chapter 6 we investigated chemical ordering within AlGa_N layers. Samples of Al_{0.564}Ga_{0.436}N were studied using X-ray diffraction before and after annealing at a temperature of 1350°C and a pressure of 9.5 kBar. The diffraction data were analysed using the Williamson-Hall method and statistical diffraction theory.¹ The as grown samples (see Sec. 6.5.1) exhibited forbidden reflections, indicative of ordering of Al and Ga atoms within the sample. This ordering was destroyed by the annealing process, suggesting that it is due to growth kinetics (the random alloy is the equilibrium structure). For the Williamson-Hall analysis the diffraction peaks were fitted using Voigt functions. The regression analysis was completed for both $B - q$ plots (applicable for Lorentzian peak shapes) and $B^2 - q^2$ plots (applicable for Gaussian peak shapes), where B is the integral width of the peaks. The results show that a regression analysis based on a $B - q$ plot is unreliable because it determined the block size perpendicular to the sample surface to be larger than the layer thickness. The parameters determined from a $B^2 - q^2$ plot gave more meaning results. This was confirmed by an analysis using statistical diffraction theory, which returned similar values for the misorientation and mosaic block size to those obtained from the Williamson-Hall analysis using the $B^2 - q^2$ plot. The lateral mosaic block size determined from the fundamental reflections was larger than that found

¹Drs. N. Kirste and L. Herres and co-workers from the Fraunhofer Institut für Angewandte Festkörperphysik (Fraunhofer Institute for Applied Solid-State Physics, Germany) completed the experimental work (including sample preparation) and performed the Williamson-Hall analysis. The author performed the analysis of the samples based on statistical diffraction theory.

from the forbidden reflections (this was true for both the Williamson-Hall analysis and statistical diffraction theory). The smaller lateral block size for the forbidden reflections can be attributed to the presence of anti-phase domains. The structure factor changes at an anti-phase domain wall for the forbidden reflections (but not the fundamental reflections), hence reducing the average lateral correlation length. Fitting the forbidden reflections using statistical diffraction theory required two lateral block sizes to be present - this was also attributed to the anti-phase domain structure.

The annealed samples (see Sec. 6.5.2) showed a significant compositional gradient through the sample. Hence the diffraction profile in the q_z direction could not be characterised using Williamson-Hall analysis. However, the statistical diffraction theory can be used to fit the q_z scans by extending the defect model. To model the compositional gradient and mosaic blocks simultaneously, the deformation vector, $\mathbf{u}(\mathbf{r})$, was split into two components - an average and a random (statistical) fluctuation. The average deformation for the mosaic blocks is zero, and the blocks are described by the fluctuations of the deformation vector. However, the compositional gradient is non-random, and it is described by the average component of the deformation vector. Extending the model in this way allows us to fit the experimental data in the q_z direction, although more work is required to improve the accuracy of the fit. The misorientation, determined by the Williamson-Hall analysis and statistical diffraction theory, was in agreement, with the value unchanged from the as grown sample. However, the lateral block sizes differ by a factor of two. Nevertheless, the lateral block size increased from the as grown sample (by a factor of four using Williamson-Hall analysis, or a factor of two based on statistical diffraction theory). This suggests that annealing reduces the dislocation density in the sample. In summary the flexibility of statistical diffraction theory has been demonstrated - the theory can accommodate multifarious diffraction features (such as strain gradient or mixed mosaic block sizes); however, several reflections are required to ensure that a unique set of mosaic block model parameters are determined.

7.2 Directions for Future Research

The experimental profiles collected from the Group III nitrides were, in most cases, well matched by the simulations based on statistical diffraction theory (using a mosaic block model). However, there are two significant discrepancies that need to be addressed in further work: the incorrectly simulated profile shape for the asymmetric reflections, and the inability of the defect model to describe the $\text{In}_{0.42}\text{Ga}_{0.58}\text{N}$

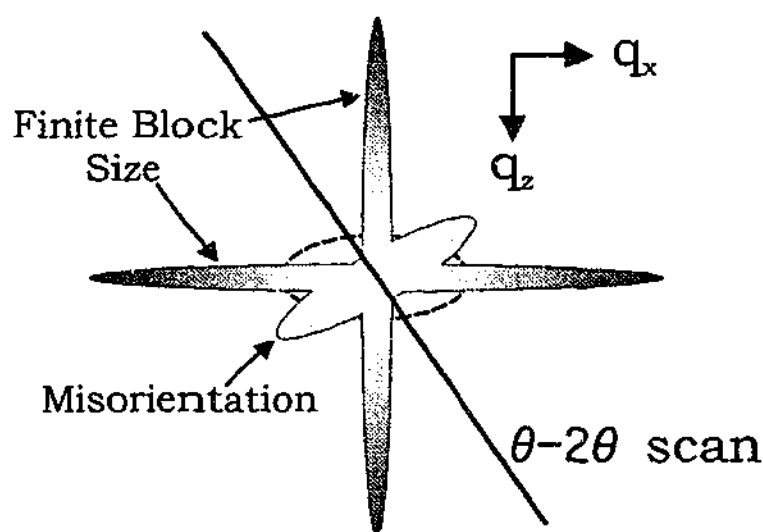


Figure 7.1: Schematic diagram of a diffraction peak showing streaks due to finite mosaic block size and misorientation of the blocks. The path of a $\theta - 2\theta$ scan (line) is shown passing through the peak. The dashed line indicates those regions in $q_x - q_z$ space that produces lower intensity in the simulated scans compared to the experimental data.

sample.

The one-dimensional profiles reported in Chapter 4 were based on $\theta - 2\theta$ and ω scans. For the symmetric reflections these scans are acquired in the q_z and q_x directions, respectively; for asymmetric scans this is not the case. The line in reciprocal space along which the $\theta - 2\theta$ scan records intensity is shown in Fig. 7.1 for an asymmetric reflection. The q_z and q_x directions are special because the streaks (truncation rods) due to the finite size of the mosaic blocks are along those directions (see Fig. 7.1 and Secs. 4.4.1 and 4.7). The simulated intensity is increased along these streaks, more so than for the experimental scans. Therefore the simulated intensity for a $\theta - 2\theta$ scan (for an asymmetric reflection) has a larger 'dynamic range' than the experimental intensity profile. A constant background intensity was used in the simulations to compensate for this large dynamic range on a logarithmic scale. The exact position of the $\theta - 2\theta$ scan, with respect to the Bragg peak, will also change the profile significantly. This is important because the peak position is modified by strain perpendicular and parallel to the sample surface.

It is anticipated that the simulated scans should be able to produce the correct intensity profile for the asymmetric reflection in the q_z and q_x directions (along the streaks in Fig. 7.1). Further work will involve collecting scans in the q_z and q_x directions, by ensuring that:

$$\frac{\Delta\omega}{\Delta\epsilon} = \frac{1}{1 + \frac{\sin(\theta_B - \varphi)}{\sin(\theta_B + \varphi)}} \quad \text{for a } \mathbf{q}_z \text{ scan,} \quad (7.1)$$

and

$$\frac{\Delta\omega}{\Delta\epsilon} = \frac{1}{1 + \frac{\cos(\theta_B - \varphi)}{\cos(\theta_B + \varphi)}} \quad \text{for a } \mathbf{q}_x \text{ scan,} \quad (7.2)$$

where θ_B is the Bragg angle for the sample, $\Delta\omega$ and $\Delta\epsilon$ are small rotations of the sample and detector from the Bragg position, and φ is the asymmetry angle of the reflection. Comparing these (q_x , q_z) scans with the simulations will confirm if the latter produces the correct intensity profiles. The RSMs collected using TAD were poorly positioned for the asymmetric scans. Repeating these measurements will also determine the true peak shape and therefore identify more accurately where the simulated and experimental scans disagree. These data will assist in refining the mosaic block model.

The simple mosaic block model used here can be extended to include a distribution of block size, interfacial roughness, and point defects. These refinements will allow more accurate matching to the experimental data from all reflections. For the asymmetric reflections it will increase the intensity in the regions indicated by the dashed line in Fig. 7.1. The mosaic block model could also be extended by incorporating a more realistic (hexagonal) block shape, and including twist of the mosaic blocks, i.e., rotation of the block about the c -axis (see Sec. 1.2.4)). In order to incorporate twist into the model, experimental input is required from diffraction scans sensitive to twist. These are ϕ scans in asymmetric (or skew symmetric) diffraction geometry, ω scans in skew symmetric geometry (Heinke *et al.*, 1999), or grazing incidence in-plane X-ray diffraction (GIIXD) (Lafford *et al.*, 2003a). The GIIXD arrangement is shown in Fig. 7.2. This technique has the advantage that twist can be measured directly (unlike the ϕ or ω scans). Investigation of a hexagonal block shape would required reciprocal space mapping in $q_x - q_y$ space.

Increasing the number of parameters within the model requires that many reflections would need to be scanned to constrain the solution, thereby allowing a unique set of parameters to be obtained. This will make data analysis very time consuming, and a minimisation routine suitable for fitting several scans simultaneously will be required. In this context the convergence criteria needs to be considered carefully to ensure that it is sensitive to small, but important, diffraction features (such as thickness oscillations). The possibility of using a parallel computing environment would be desirable for multi-parameter fitting.

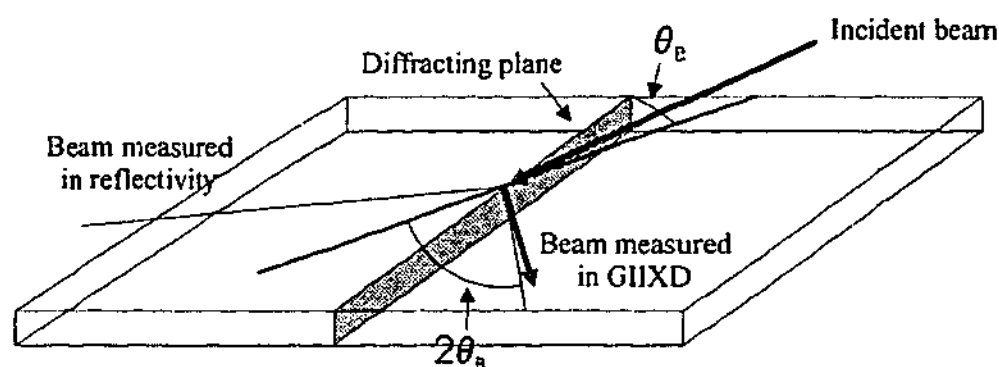


Figure 7.2: A schematic diagram of the grazing incidence in-plane X-ray diffraction (GIIXD) technique. The incident X-ray beam is diffracted from the which has its normal parallel to the sample surface. This allows a direct measure of twist mosaicity to be made (after Lafford *et al.*, 2003a).

Extensions to the mosaic block model described above would not assist in matching the peak shape for the $\text{In}_{0.42}\text{Ga}_{0.58}\text{N}$ layer. The diffraction profiles from the $\text{In}_{0.42}\text{Ga}_{0.58}\text{N}$ layer were significantly different from those with a lower InN content. This leads us to conjecture that there was segregation, or clustering, within this sample. Several cluster models for statistical diffraction theory have been presented in the literature (see e.g., Nesterets and Punegov (2000)). The diffracted amplitude from the clusters would be uncorrelated with the amplitude from the mosaic blocks, so the intensities from the two defect distributions can be summed. However, the crystal truncation rod (CTR) scan collected from the $\text{In}_{0.42}\text{Ga}_{0.58}\text{N}$ layer showed many peaks, suggesting some other ordered structure is present. This structure has not yet been identified. Transmission electron microscopy (TEM) would help elucidate the origin of the peaks in the CTR scan. TEM would also give a direct measurement of the mosaic block size and misorientation (although from a small volume of the crystal), which we could compare to X-ray diffraction results. Such a comparison would assist in validating the statistical diffraction theory as applied to Group III nitrides.

The IP method described in Chapter 5 for collecting two-dimensional reciprocal space maps can also be extended to collect three-dimensional (3D) maps from small volumes of reciprocal space. This would provide a simple technique for investigation of samples that are laterally inhomogeneous. Further work is required to determine the spatial resolution that can be achieved for a 3D map, and the validity of the interpolation schemes.

7.3 Summary

This thesis has investigated Group III nitrides using triple axis diffractometry and statistical diffraction theory. The defect structure of the Group III nitride samples was modelled as mosaic blocks as described in Sec. 2.9. The lateral and perpendicular size, and orientation of the blocks can be varied in order to fit the simulated peak profiles to the experimental data. A mosaic block model was shown to be adequate for fitting the experimental scans of symmetric reflections, reproducing the diffracted peak profiles accurately in most cases.

Using triple axis diffractometry and statistical diffraction theory we identified a structural difference between annealed 30 nm and 70 nm LT-AlN buffer layers, and provided an explanation of the higher crystalline quality for GaN grown on 30 nm buffers. We also demonstrated that the shape of the diffraction peak from the $\text{In}_{0.42}\text{Ga}_{0.58}\text{N}$ layer differs from that predicted by the mosaic block model, indicating the presence of another defect structure (likely to be clusters).

A rapid method for collecting reciprocal space maps using imaging plates was described in Chapter 5. This method is useful for determining peak positions, and measuring broad diffraction peaks. The method can also be extended to three dimensions, without an increase in data collection time.

In Chapter 6 we investigated the chemical ordering of an AlGaN layer. Both statistical diffraction theory and the Williamson-Hall method were used to analyse the experimental results. Both approaches pointed to the presence of anti-phase domains within the ordered structure; however, statistical diffraction theory also suggested that there are two lateral correlation lengths (lateral block sizes). After annealing the AlGaN showed significant chemical intermixing, which could only be described by the statistical diffraction theory.

In conclusion, statistical diffraction theory (SDT) is a flexible and powerful analytical technique. We have applied SDT to Group III nitrides – identifying important structure features in multilayer samples. Suggested extension to the modelling approach provide a framework for establishing SDT as a quantitative analytical technique for characterising Group III nitrides.

APPENDIX A

The Wave Equation in Polarizable Media

In order to describe the electromagnetic wave inside a crystal we require the wave equation formulated for a polarizable media. This treatment is given in many texts, such as Jackson (1975) and Pinsky (1978). We begin with the Maxwell equations (in Gaussian units)

$$\nabla \cdot \mathbf{E} = 4\pi\rho \quad (\text{A.1})$$

$$\nabla \cdot \mathbf{H} = 0 \quad (\text{A.2})$$

$$\nabla \times \mathbf{E} + \frac{1}{c} \frac{\partial \mathbf{H}}{\partial t} = 0 \quad (\text{A.3})$$

$$\nabla \times \mathbf{H} - \frac{1}{c} \frac{\partial \mathbf{E}}{\partial t} = \frac{4\pi\mathbf{j}}{c} \quad (\text{A.4})$$

where \mathbf{E} is the electric field vector, \mathbf{H} is the magnetic field vector, \mathbf{j} is the current density, c is the speed of light, and ρ is the charge density. The current density is written as

$$\mathbf{j} = \frac{\partial \mathbf{P}}{\partial t}, \quad (\text{A.5})$$

where \mathbf{P} is the polarisation.

Substituting $\mathbf{P} = \chi\mathbf{E}/4\pi$ and assuming a harmonic time dependence, $e^{i\omega t}$, we rewrite Eq. (A.5) as

$$\mathbf{j} = i\omega\mathbf{P} = i\omega \frac{\chi\mathbf{E}}{4\pi}. \quad (\text{A.6})$$

Taking the curl of Eq. (A.3) gives:

$$\nabla \times (\nabla \times \mathbf{E}) = \nabla \times \left(-\frac{1}{c} \frac{\partial \mathbf{H}}{\partial t} \right) = -\frac{1}{c} \frac{\partial}{\partial t} (\nabla \times \mathbf{H}). \quad (\text{A.7})$$

Substituting from Eq. (A.4) gives:

$$\nabla \times (\nabla \times \mathbf{E}) = -\frac{1}{c^2} \left[\frac{\partial}{\partial t} \left(\frac{\partial \mathbf{E}}{\partial t} + 4\pi \mathbf{j} \right) \right] \quad (\text{A.8})$$

$$= -\frac{1}{c^2} \left[\frac{\partial^2 \mathbf{E}}{\partial t^2} + \frac{\partial}{\partial t} (4\pi \mathbf{j}) \right] \quad (\text{A.9})$$

$$= -\frac{1}{c^2} \left[-\omega^2 \mathbf{E} + \frac{\partial}{\partial t} (i\omega \chi \mathbf{E}) \right] \quad (\text{A.10})$$

$$= -\frac{1}{c^2} [-\omega^2 \mathbf{E} - \omega^2 \chi \mathbf{E}] \quad (\text{A.11})$$

$$= \frac{\omega^2}{c^2} (\mathbf{E} + \chi(\mathbf{r}) \mathbf{E}) \quad (\text{A.12})$$

$$= k^2 (1 + \chi(\mathbf{r})) \mathbf{E}. \quad (\text{A.13})$$

Hence the wave equation is:

$$\nabla \times (\nabla \times \mathbf{E}) - k^2 (1 + \chi(\mathbf{r})) \mathbf{E} = 0 \quad (\text{A.14})$$

The wave equation is used in Sec. 2.4 to derive the fundamental equations of the dynamical theory of diffraction.

APPENDIX B

Conversion of Angular Co-ordinates to Reciprocal Space Vectors

Referring to Fig. 2.12(b) and using simple trigonometry we can resolve the q_z and q_x components relative to the reciprocal lattice point. Starting with q_z :

$$q_z = - [k \sin(\theta_2 + \omega') + k \sin(\theta_1 + \omega) - k \sin \theta_2 - k \sin \theta_1].$$

The q_z vector is defined as pointing into the crystal, hence the first negative sign. Using standard trigonometric identities, we write q_z as

$$q_z = -k \{ [\sin \theta_2 \cos \omega' + \cos \theta_2 \sin \omega'] + [\sin \theta_1 \cos \omega + \cos \theta_1 \sin \omega] - [\sin \theta_2 + \sin \theta_1] \}.$$

Making the assumption that ω and ϵ are small (the validity of this assumption depends on the size of the RSM), we set $\cos \omega \approx 1$ and $\sin \omega \approx \omega$, whence

$$q_z = -k \{ [\sin \theta_2 \cos \omega' + \cos \theta_2 \sin \omega'] + \omega \cos \theta_1 - \sin \theta_2 \}$$

Substituting $\omega' = \epsilon - \omega$ (Eq. (2.129)), and using appropriate trigonometric identities we obtain

$$q_z = -k \{ [\sin \theta_2 \{ \cos \epsilon \cos(-\omega) - \sin \epsilon \sin(-\omega) \} + \cos \theta_2 \{ \sin \epsilon \cos(-\omega) + \cos \epsilon \sin(-\omega) \}] + \omega \cos \theta_1 - \sin \theta_2 \}.$$

Substituting $\cos \epsilon \approx \cos \omega \approx 1$, $\sin \epsilon \approx \epsilon$, $\sin \omega \approx \omega$, and $\epsilon \omega \approx 0$:

$$q_z = -k [\epsilon \cos \theta_2 + \omega \{ \cos \theta_1 - \cos \theta_2 \}].$$

Finally, substituting $\theta_1 = \theta_B - \varphi$ and $\theta_2 = \theta_B + \varphi$ we arrive at Eq. (2.131)

$$q_z = -k [\epsilon \cos \theta_2 + 2\omega \sin \theta_B \sin \varphi].$$

Starting from

$$q_x = k \cos(\theta_2 + \omega') - k \cos(\theta_1 + \omega) - (k \cos \theta_2 - k \cos \theta_1)$$

and using similar arguments as above, Eq. (2.130) can also be derived, i.e.,

$$q_x = 2k\omega \sin \theta_B \cos \varphi - k\varepsilon \sin \theta_2.$$

References

- Afanas'ev, A. M. and Kohn, V. G. "Dynamical theory of X-ray diffraction in crystals with defects", *Acta Cryst.* **A27**, 421-430, 1971.
- Akasaki, I. "Nitride semiconductors - impact on the future world", *J. Crystal Growth* **237-239**, 905-911, 2002.
- Akasaki, I. and Amano, H. "Crystal growth and conductivity control of group III nitride semiconductors and their application to short wavelength light emitters", *Jpn. J. Appl. Phys.* **36**, 5393-5408, 1997.
- Akasaki, I., Amano, H., Koide, Y., Hiramatsu, K. and Sawaki, N. "Effects of AlN buffer layer on crystallographic structure and on electrical and optical properties of GaN and $\text{Ga}_{1-x}\text{Al}_x\text{N}$ ($0 < x \leq 0.4$) films grown on sapphire substrate by MOVPE", *J. Crystal Growth* **98**, 209-219, 1989.
- Alferov, Z. I. "Nobel lecture: The double heterostructure concept and its applications in physics, electronics, and technology", *Rev. Mod. Phys.* **73**, 767-782, 2001.
- Als-Nielsen, J. and McMorrow, D. *Elements of Modern X-ray Physics*, John Wiley & Sons, Ltd, Chichester, 2001.
- Amano, H. and Akasaki, I. X-ray diffraction characterisation of GaN-based materials: triple axis diffractometry, in J. H. Edgar, S. Strite, I. Akasaki, H. Amano and C. Wetzel, eds, "Properties, processing and applications of Gallium Nitride and Related Semiconductors", INSPEC, The Institution of Electrical Engineers, London, pp. 264-272, 1999.
- Amano, H., Kito, M., Hiramatsu, K. and Akasaki, I. "P-type conduction in Mg-doped GaN treated with low-energy electron beam irradiation (LEEBI)", *Jpn. J. Appl. Phys.* **28**, L2112-L2114, 1989.
- Amano, H., Sawaki, N., Akasaki, I. and Toyoda, Y. "Metalorganic vapor phase epitaxial growth of a high quality GaN film using an AlN buffer layer", *Appl. Phys. Lett.* **48**, 353-355, 1986.

- Ambacher, O. "Growth and applications of Group III-nitrides", *J. Phys. D: Appl. Phys.* **31**, 2653-2710, 1998.
- Angerer, H., Brunner, D., Freudenberg, F., Ambacher, O., Stutzmann, M., Höpler, R., Metzger, T., Born, E., Dollinger, G., Bergmaier, A., Karsch, S. and Körner, H.-J. "Determination of the Al mole fraction and the band gap bowing of epitaxial $\text{Al}_x\text{Ga}_{1-x}\text{N}$ films", *Appl. Phys. Lett.* **71**, 1504, 1997.
- Authier, A. Dynamical theory of x-ray diffraction - i. perfect crystals, in A. Authier, S. Lagomarsino and B. K. Tanner, eds, "X-Ray and Neutron Dynamical Diffraction: Theory and Applications", Plenum Press, New York, pp. 1-31, 1996a.
- Authier, A. Dynamical theory of x-ray diffraction - ii. deformed crystals, in A. Authier, S. Lagomarsino and B. K. Tanner, eds, "X-Ray and Neutron Dynamical Diffraction: Theory and Applications", Plenum Press, New York, pp. 43-62, 1996b.
- Authier, A. *Dynamical Theory of X-Ray Diffraction*, Oxford University Press, New York, 2001.
- Ayers, J. E. "The measurement of threading dislocation densities in semiconductor crystals by X-ray diffraction", *J. Crystal Growth* **135**, 71-74, 1994.
- Balzar, D. and Popović, S. "Reliability of the simplified integral-breadth methods in diffraction line-broadening analysis", *J. Appl. Cryst.* **29**, 16-23, 1996.
- Barnea, Z., Creagh, D. C., Davis, T. J., Garrett, R. F., Janky, S., Stevenson, A. W. and Wilkins, S. W. "The Australian diffractometer at the Photon Factory", *Rev. Sci. Instrum.* **63**, 1069, 1992.
- Bartels, W. J. "Characterization of thin layers on perfect crystals with a multipurpose high resolution x-ray diffractometer", *J. Vac. Sci. Technol.* **B1**, 338-345, 1983.
- Batterman, B. W. and Cole, H. "Dynamical diffraction of X-rays by perfect crystals", *Rev. Mod. Phys.* **36**, 681-717, 1964.
- Becker, P. and Al Haddad, M. "Diffraction by a randomly distorted crystal. I. The case of short-range order", *Acta Cryst.* **A46**, 123-129, 1990.
- Becker, P. and Al Haddad, M. "Diffraction by a randomly distorted crystal. II. General theory", *Acta Cryst.* **A48**, 121-134, 1992.

- Behr, D., Wagner, J., Ramakrishnan, A., Obloh, H. and Bachem, K.-H. "Evidence for compositional inhomogeneity in low In content InGaN obtained by resonant raman scattering", *Appl. Phys. Lett.* **73**, 241-243, 1998.
- Benamara, M., Kirste, L., Albrecht, M., Benz, K. W. and Strunk, H. P. "Pyramidal-plane ordering in AlGaIn alloys", *Appl. Phys. Lett.* **82**, 547-549, 2003.
- Boulle, A., Masson, O., Guinebretière, R., Lecomte, A. and Daurer, A. "A high-resolution X-ray diffractometer for the study of imperfect materials", *J. Appl. Cryst.* **35**, 606-614, 2002.
- Bragg, W. H. and Bragg, W. L. "The reflection of x-rays by crystals", *Proc. Roy. Soc. (London) A* **88**, 428-438, 1913a.
- Bragg, W. L. *Nature* **90**, 410, 1912.
- Bragg, W. L. *Proc. Cambridge Phil. Soc.* **17**, 43-57, 1913.
- Bragg, W. L. "The reflection of x-rays by crystals II", *Proc. Roy. Soc. (London) A* **89**, 248-277, 1913b.
- Brandt, O., Waltereit, P. and Ploog, K.H. "Determination of strain state and composition of highly mismatched group-III nitride heterostructures by x-ray diffraction", *J. Phys. D: Appl. Phys.* **35**, 577-585, 2002.
- Burm, J. General remarks on GaN-based transistors and potential for high temperature/power operation, in J. H. Edgar, S. Strite, I. Akasaki, H. Amano and C. Wetzel, eds, "Properties, processing and applications of Gallium Nitride and Related Semiconductors", INSPEC, The Institution of Electrical Engineers, London, pp. 569-571, 1999.
- Bushuev, V. A. "Influence of structure defects on the angular distribution of X-ray diffraction in crystals with a disturbed surface layer", *Sov. Phys. Solid State* **31**, 1877-1882, 1989a.
- Bushuev, V. A. "Statistical dynamical theory of X-ray-diffraction from nonperfect crystals with an account of the angular-distribution of intensities", *Kristallografiya* **34**, 279-287, 1989b.
- Butler, B. D., Haefner, D. R., Lee, P. L. and Welberry, T. R. "High-energy X-ray diffuse scattering using Weissenberg flat-cone geometry", *J. Appl. Cryst.* **33**, 1046-1050, 2000.

- Chatterjee, S. K. and Sen Gupta, S. P. "An integral breadth analysis for particle size and strain determinations in cold-worked FCC alloys", *J. Phys. D: Appl. Phys.* **5**, 609-612, 1972.
- Chierchia, R., Böttcher, T., Figge, S., Diesselberg, M., Heinke, H. and Hommel, D. "Mosaicity of GaN epitaxial layers: Simulation and experiment", *Phys. Rev. Lett.* **228**, 403-406, 2001.
- Cho, H. K., Lee, J. Y., Kim, K. S., Yang, G. M., Song, J. H. and Yu, P. Won "Effect of buffer layers and stacking faults on the reduction of threading dislocation density in GaN overlayers grown by metalorganic chemical vapor deposition", *J. Appl. Phys.* **89**, 2617-2621, 2001.
- Chuang, S. L. and Chang, C. S. "Effective-mass hamiltonian for strained wurtzite GaN and analytical solutions", *Appl. Phys. Lett.* **68**, 1657-1659, 1996a.
- Chuang, S. L. and Chang, C. S. "k-p method for strained wurtzite semiconductors", *Phys. Rev.* **B54**, 2491-2504, 1996b.
- Chukhovskii, F. N. and Guigay, J. P. "Towards a rigorous treatment of the wave-field propagation according to the statistical theory of dynamical diffraction", *J. Phys. D: Appl. Phys.* **26**, A53-A56, 1993.
- Creagh, D. C., Foran, G. J., Cookson, D. J., Garrett, R. F. and Johnson, R. "An eight-position capillary sample spinning stage for the diffractometer at BL20B at the Photon Factory", *J. Synchrotron Rad.* **5**, 823-825, 1998.
- Darwin, C. G. "The theory of X-ray reflexion", *Phil. Mag.* **27**, 315-333, 1914a.
- Darwin, C. G. "The theory of X-ray reflexion. part ii", *Phil. Mag.* **27**, 675-691, 1914b.
- Darwin, C. G. "The reflexion of X-rays from imperfect crystals", *Phil. Mag.* **43**, 800-829, 1922.
- Davis, T. J. "Imperfect crystals and dynamical X-ray diffraction in the complex reflectance plane", *Aust. J. Phys.* **44**, 693-704, 1991.
- Davis, T. J. "A stochastic model for X-ray diffraction from imperfect crystals", *Acta Cryst.* **A48**, 872-879, 1992.

- Davis, T. J. "The measurement of defect parameters in imperfect crystals using X-ray diffraction", *Acta Cryst.* **A49**, 755–762, 1993.
- Davis, T. J. "Dynamical X-ray diffraction from imperfect crystals: a solution based on the Fokker-Planck equation", *Acta Cryst.* **A50**, 224–231, 1994.
- Duke, Philip John *Synchrotron Radiation*, Oxford University Press, Oxford, 2000.
- DuMond, J. W. M. "Theory of the use of more than two successive X-ray crystal reflections to obtain increased resolving power", *Phys. Rev.* **52**, 872–883, 1937.
- Ebel, R., Fehrer, M., Figge, S., Einfeldt, S., Selke, H. and Hommel, D. "Buffer layers for the growth of gan on sapphire by molecular beam epitaxy", *J. Crystal Growth* **201/202**, 433–436, 1999.
- Einfeldt, S., Reitmeier, Z. J. and Davis, R. F. "Surface morphology and strain of gan layers grown using 6H-SiC(0001) substrates with different buffer layers", *J. Crystal Growth* **253**, 129–141, 2003.
- El-Masry, N. A., Piner, E. L., Liu, S. X. and Bedair, S. M. "Phase separation in InGaN grown by metalorganic chemical vapor deposition", *Appl. Phys. Lett.* **72**, 40–42, 1998.
- Emery, L. and Borland, M. "Top-up operation experience at the Advanced Photon Source", *Proc. IEEE Part. Accel. Conf.* **1**, 200–202, 1999.
- Ewald, P. P. "Zur Theorie der Interferenzen der Röntgenstrahlen in Kristallen", *Phys. Z.* **14**, 465–472, 1913.
- Ewald, P. P. "Zur Begründung der Kristallographie: Teil I: Theorie der dispersion", *Ann. Physik* **49**, 1–38, 1916a.
- Ewald, P. P. "Zur Begründung der Kristallographie: Teil II: Theorie der Reflexion und Brechung.", *Ann. Physik* **49**, 117–143, 1916b.
- Ewald, P. P. "Zur Begründung der Kristallographie: Teil III: Die Kristallographie der Röntgenstrahlen", *Ann. Physik* **54**, 519–597, 1917.
- Farrow, R. F. C. *Molecular Beam Epitaxy*, Noyes Publications, Park Ridge, 1995.
- Fewster, P. F. "X-ray diffraction from low-dimensional structures", *Semicond. Sci Technol.* **8**, 1915–1934, 1993.

- Fewster, P. F. "X-ray analysis of thin films and multilayers", *Rep. Prog. Phys.* **59**, 1339-1407, 1996.
- Fewster, P. F. "Reciprocal space mapping", *Crit. Rev. Solid State Mater. Sci.* **22**, 69-110, 1997.
- Fewster, P. F. "X-ray diffraction tools and methods for semiconductor analysis", *Inst. Phys. Conf. Ser.* **164**, 197-206, 1999.
- Fewster, P. F. *X-ray Scattering from Semiconductors*, Imperial College Press, London, 2003.
- Fewster, P. F., Holý, V. and Andrew, N. L. "Detailed structural analysis of semiconductors with X-ray scattering", *Mat. Sci. Semicon. Proc.* **4**, 475-481, 2001.
- Figge, S., Böttcher, T., Einfeldt, S. and Hommel, D. "In situ and ex situ evaluation of the film coalescence for GaN growth on GaN nucleation layers", *J. Crystal Growth* **221**, 262-266, 2000.
- Foran, G. J., Garrett, R. F., Gentle, I. R., Creagh, D. C., Peng, J. B. and Barnes, G. T. "Focusing monochromator and imaging-plate camera for grazing-incidence diffraction studies of thin films", *J. Synchrotron Rad.* **5**, 500-502, 1998.
- Garrett, R. F., Cookson, D. J., Foran, G. J., Sbine, T. M., Kennedy, B. J. and Wilkins, S. W. "Powder diffraction using imaging plates at the Australian National Beamline Facility at the Photon Factory", *Rev. Sci. Instrum.* **66**, 1351, 1995.
- Gay, P., Hirsch, P.B. and Kelly, A. "The estimation of dislocation densities in metals from X-ray data", *Acta Met.* **1**, 315-319, 1953.
- Gerhard, T., Albert, D. and Faschinger, W. "High-resolution X-ray diffraction study of degrading ZnSe-based laser diodes", *J. Crystal Growth* **214**, 1049, 2000.
- Gonsalves, M., Kim, W., Narayanan, V. and Mahajan, S. "Influence of AlN nucleation layer growth conditions on quality of GaN layers deposited on (0 0 0 1) sapphire", *J. Crystal Growth* **240**, 347-354, 2002.
- Greiner, W. and Reinhardt, J. *Quantum Electrodynamics*, Springer-Verlag, Berlin, 1994.

- Guigay, J. P. and Chukhovskii, F. N. "Reformulation of the dynamical theory of coherent wave propagation by randomly distorted crystals", *Acta Cryst.* **A48**, 819–826, 1992.
- Guigay, J. P. and Chukhovskii, F. N. "Reformulation of the statistical theory of dynamical diffraction in the case $E = 0$ ", *Acta Cryst.* **A51**, 288–294, 1995.
- Guinier, A. *X-ray diffraction in crystals, imperfect crystals, and amorphous bodies*, Dover, New York, 1994.
- Halder, N. C. and Wagner, C. N. J. "Separation of particle size and lattice strain in integral breadth measurements", *Acta Cryst.* **20**, 312–313, 1966.
- Halliwell, M. A. G. and Lyons, M. H. "The interpretation of X-ray rocking curves from III-V semiconductor device structures", *J. Crystal Growth* **68**, 523–531, 1984.
- Hanser, A. D. and Davis, R. F. Sic substrates for growth of GaN and related compounds, in J. H. Edgar, S. Strite, I. Akasaki, H. Amano and C. Wetzel, eds, "Properties, processing and applications of Gallium Nitride and Related Semiconductors", INSPEC, The Institution of Electrical Engineers, London, pp. 386–390, 1999.
- Härtwig, J. "Hierarchy of dynamical theories of X-ray diffraction for deformed and perfect crystals", *J. Phys. D: Appl. Phys.* **34**, 70–77, 2001.
- Heinke, H., Kirchner, V., Einfeldt, S. and Hommel, D. "Analysis of the defect structure of epitaxial GaN", *Phys. Stat. Sol.* **176**, 391, 1999.
- Herres, N., Kirste, L., Obloh, H., Köhler, K., Wagner, J. and Koidl, P. "X-ray determination of the composition of partially strained group-III nitride layers using the extended bond method", *Mat. Sci. Eng.* **B91-92**, 425–462, 2002.
- Hersee, S. D., Ramer, J. C. and Malloy, K. J. "The microstructure of metalorganic chemical vapor deposition GaN on sapphire", *MRS Bulletin* **22**, 45–51, 1997.
- Hiramatsu, K., Itoh, S., Amano, H. and Akasaki, I. "Growth mechanism of GaN grown on sapphire with AlN buffer layer by MOVPE", *J. Crystal Growth* **115**, 628–633, 1991.
- Ho, I. and Stringfellow, G. B. "Solid phase immiscibility in GaInN", *Appl. Phys. Lett.* **69**, 2701–2703, 1996.

- Holý, V., Kuběna, J., Abramof, E., Lischka, K., Pesek, A. and Koppensteiner, E. "X-ray double and triple crystal diffractometry of mosaic structure in heteroepitaxial layers", *J. Appl. Phys.* **74**, 1736-1743, 1993b.
- Holý, V., Kuběna, J., Abramof, E., Pesek, A. and Koppensteiner, E. "X-ray diffraction of small defects in layered systems", *J. Phys. D: Appl. Phys.* **26**, A146-A150, 1993a.
- Holý, V., Pietsch, U. and Baumbach, T. *High-Resolution X-Ray Scattering from Thin Films and Multilayers*, Springer-Verlag, Heidelberg, 1999.
- Holý, V., Wolf, K., Kastner, M., Stanzl, H. and Gebhardt, W. "X-ray triple-crystal diffractometry of defects in epitaxial layers", *J. Appl. Cryst.* **27**, 551-557, 1994.
- Hordon, M. J. and Averbach, B. L. "X-ray measurements of dislocation density in deformed copper and aluminium single crystals", *Acta Met.* **9**, 237-246, 1961.
- Hsieh, J. *Computed Tomography*, SPIE Press, Bellingham, 2003.
- Hsu, L. and Walukiewicz, W. "Effect of polarization fields on transport properties in AlGaIn/GaN heterostructures", *J. Appl. Phys.* **89**, 1783-1789, 2001.
- Iida, A. and Kohra, K. "Separate measurements of dynamical and kinematical X-ray diffractions from silicon crystals with a triple crystal diffractometer", *Phys. Stat. Sol. (a)* **51**, 533-542, 1979.
- Iliopoulos, E., Jr, K. F Ludwig, Moustakas, T. D. and Chu, S. N. G. "Chemical ordering in AlGaIn alloys grown by molecular beam epitaxy", *Appl. Phys. Lett.* **78**, 463-465, 2001.
- Ito, T., Ohtsuka, K., Kuwahara, K., Sumiya, M., Takano, Y. and Fuke, S. "Effect of AlN buffer layer deposition conditions on the properties of GaN layer", *J. Crystal Growth* **205**, 20-24, 1999.
- Itoh, N. and Rhee, J. C. "Study of cracking mechanism in GaN/ α -Al₂O₃ structure", *J. Appl. Phys.* **58**, 1828-1837, 1985.
- Jackson, J. D. *Classical Electrodynamics*, John Wiley & Sons, Inc., New York, 1975.
- Kandalam, A. K., Blanco, M. A. and Pandey, R. "Theoretical study of Al_nN_n, Ga_nN_n, and In_nN_n (n = 4, 5, 6) clusters", *J. Phys. Chem. B* **106**, 1945-1953, 2002.

- Kato, N. "Pendellösung fringes in distorted crystals I.", *J. Phys. Soc. Jpn.* **18**, 1785, 1963.
- Kato, N. "Pendellösung fringes in distorted crystals II. Application to two-beam cases", *J. Phys. Soc. Jpn.* **19**, 67-77, 1964a.
- Kato, N. "Pendellösung fringes in distorted crystals III. Application to homogeneously bent crystals", *J. Phys. Soc. Jpn.* **19**, 971-985, 1964b.
- Kato, N. "On extinction. I. General formulation", *Acta Cryst.* **A32**, 453-457, 1976.
- Kato, N. "On extinction. II. The theory of secondary extinction", *Acta Cryst.* **A32**, 458-466, 1976.
- Kato, N. "Statistical dynamical theory of crystal diffraction. I. general formulation", *Acta Cryst.* **A36**, 763-769, 1980.
- Kato, N. "Statistical dynamical theory of crystal diffraction II. intensity distribution and integrated intensity in the laue cases", *Acta Cryst.* **A36**, 770-778, 1980.
- Kato, N. "On secondary extinction", *Z. Naturforsch* **87**, 485-489, 1982.
- Kato, N. Statistical theory of dynamical diffraction in crystals, in A. Authier, S. Lagomarsino and B. K. Tanner, eds, "X-Ray and Neutron Dynamical Diffraction: Theory and Applications", Plenum Press, New York, pp. 111-135, 1996.
- Kim, C., Robinson, I. K., Myoung, J., Shim, K., Yoo, M-C. and Kim, K. "Critical thickness of GaN thin films on sapphire (0001)", *Appl. Phys. Lett.* **69**, 2358-2360, 1996.
- Kim, C., Robinson, I., Myoung, J., Shim, K. and Kim, K. "Buffer layer strain transfer in AlN/GaN near critical thickness", *J. Appl. Phys.* **85**, 4040-4044, 1999.
- Kinne, A., Thoms, M., Röss, H. R., Gerhard, T., Ehinger, M., Faschinger, W. and Landwehr, G. "Image plates as one-dimensional detectors in high-resolution X-ray diffraction", *J. Appl. Cryst.* **31**, 446, 1998.
- Kobayashi, Y., Akasaka, T. and Kobayashi, N. "Thermal stability of low-temperature GaN and AlN buffer layers during metalorganic vapor phase epitaxy monitored by *In Situ* shallow-angle reflectance using ultraviolet light", *Jpn. J. Appl. Phys.* **37**, L1208-L1210, 1998.

- Korakakis, D., Jr., K. F. Ludwig and Moustakas, T. D. "Long range order in $\text{Al}_x\text{Ga}_{1-x}$ films grown by molecular beam epitaxy", *Appl. Phys. Lett.* **71**, 72-74, 1997.
- Krost, A., Bläsing, J., Lünenbürger, M., Protzmann, H. and Heuken, M. "Evaluation of strain and in content in (InGaN/GaN) multiquantum wells by x-ray analysis", *Appl. Phys. Lett.* **75**, 689-691, 1999.
- Krukowski, S., Leszczynski, M. and Porowski, S. Thermal properties of the group III nitrides, in J. H. Edgar, S. Strite, I. Akasaki, H. Amano and C. Wetzel, eds, "Properties, processing and applications of Gallium Nitride and Related Semiconductors", INSPEC, The Institution of Electrical Engineers, London, pp. 21-28, 1999.
- Kulda, J. "Random elastic deformation (RED) - and alternative model for extinction treatment in real crystals", *Acta Cryst.* **A43**, 167-173, 1987.
- Kulda, J. "The RED extinction model. I. An upgraded formalism", *Acta Cryst.* **A44**, 283-285, 1988a.
- Kulda, J. "The RED extinction model. II. refinement of extinction and thermal vibration parameters for SrF_2 crystals", *Acta Cryst.* **A44**, 286-290, 1988b.
- Lafford, T. A., Tanner, B. K. and Parbrook, P. J. "Direct measurement of twist mosaic in GaN epitaxial films as a function of growth temperature", *J. Phys. D: Appl. Phys.* **36**, A245-A248, 2003a.
- Lasdon, L. S., D. Ware, A., Jain, A. and Ratner, M. W. "Design and testing of a generalized reduced gradient code for nonlinear optimization", *ACM Trans. Math. Softw.* **4**, 34-50, 1978.
- Laügt, M., Bellet-Amalric, E., Ruterana, P. and Omnès, F. "Ordering in undoped hexagonal $\text{Al}_x\text{Ga}_{1-x}\text{N}$ grown on sapphire (0001) with $0.09 < x < 0.247$ ", *Phys. Stat. Sol.* **236**, 729-739, 2003.
- Lester, S., Ponce, F., Craford, M. and Steigerwald, D. "High dislocation densities in high efficiency GaN-based light-emitting diodes", *Appl. Phys. Lett.* **66**, 1249-1251, 1995.
- Leszczynski, M. Common crystal structures of the group III nitrides, in J. H. Edgar, S. Strite, I. Akasaki, H. Amano and C. Wetzel, eds, "Properties, processing and applications of Gallium Nitride and Related Semiconductors", INSPEC, The Institution of Electrical Engineers, London, pp. 3-5, 1999.

- Leszczynski, M., Suski, T., Domagala, J. and Prystawko, P. Lattice parameters of the group III nitrides, *in* J. H. Edgar, S. Strite, I. Akasaki, H. Amano and C. Wetzel, eds, "Properties, processing and applications of Gallium Nitride and Related Semiconductors", INSPEC, The Institution of Electrical Engineers, London, pp. 6-10, 1999.
- Martin, R. W., Middleton, P. G., O'Donnell, K. P. and der Stricht, W. Van "Exciton localization and the Stokes' shift in InGaN epilayers", *Appl. Phys. Lett.* **74**, 263-265, 1999.
- Maruska, H. P. and Tietjen, J. J. "The preparation and properties of vapor-deposited single-crystal-line GaN", *Appl. Phys. Lett.* **15**, 327-329, 1969.
- Metzger, T., Höppler, R., Born, E., Ambacher, O., Stutzmann, M., Stömmer, R., Schuster, M., Göbel, H. and and, S. Christiansen "Defect structure of epitaxial GaN films determined by transmission electron microscopy and triple-axis X-ray diffractometry", *Phil. Mag.* **77**, 1013-1025, 1998.
- Morkoç, H. *Nitride Semiconductors and Devices*, Springer, Berlin, 1999.
- Morkoç, H. "III-Nitride semiconductor growth by MBE: Recent issues", *J. Mat. Sci.: Mat. Elec.* **12**, 677-695, 2001.
- Mudie, S., Pavlov, K., Morgan, M., Tabuchi, M., Takeda, Y. and Hester, J. "High-resolution X-ray diffractometry investigation of interface layers in GaN/AlN structures grown on sapphire substrates", *Surf. Rev. Lett.* **10**, 513, 2003.
- Mudie, S. T., Pavlov, K. M., Morgan, M. J., Hester, J. R., Tabuchi, M. and Takeda, Y. "Collection of reciprocal space maps using imaging plates at the Australian National Beamline Facility at the Photon Factory", *J. Synchrotron Rad.* **11**, 406-413, 2004.
- Mudie, S. T., Pavlov, K. M., Morgan, M. J., Takeda, Y., Tabuchi, M. and Hester, J.R. "Analysis of GaN/AlN buffer layers grown on sapphire substrates via statistical diffraction theory", *Proceedings of COMMAD 2002 Sydney*, 111-116, 2002.
- Nakamura, S. "InGaN-based blue light-emitting diodes and laser diodes", *J. Crystal Growth* **201/202**, 290-295, 1999.

- Nakamura, S., Muka, T. and Senoh, M. "Candela-class high-brightness InGaN/AlGaIn double-heterostructure blue-light-emitting diodes", *Appl. Phys. Lett.* **64**, 1687-1689, 1994.
- Nakamura, S., Pearton, S. and Fasol, G. *The Blue Laser Diode: The complete story. Second Edition.*, Springer, Berlin, 2000.
- Nesterets, Y. and Punegov, V. "The statistical kinematical theory of X-ray diffraction as applied to reciprocal-space mapping", *Acta Cryst.* **A56**, 540-548, 2000.
- Nistor, L., Bender, H., Vantomme, A., Wu, M. F., Landuyt, J. Van, O'Donnell, K. P., Martin, R., Jacobs, K. and Moerman, I. "Direct evidence of spontaneous quantum dot formation in a thick InGaIn epilayer", *Appl. Phys. Lett.* **77**, 507-509, 2000.
- Northrup, J. E. and Romano, L. T. Planar defects in GaIn: basal plane faults, prismatic faults, stacking mismatch boundaries and inversion domain boundaries, *in* J. H. Edgar, S. Strite, I. Akasaki, H. Amano and C. Wetzel, eds, "Properties, processing and applications of Gallium Nitride and Related Semiconductors", INSPEC, The Institution of Electrical Engineers, London, pp. 213-220, 1999a.
- Northrup, J. E., Romano, L. T. and Neugebauer, J. "Surface energetics, pit formation, and chemical ordering in InGaIn alloys", *Appl. Phys. Lett.* **74**, 2319-2321, 1999b.
- O'Donnell, K. P., Martin, R. W. and Middleton, P. G. "Origin of luminescence from InGaIn diodes", *Phys. Rev. Lett.* **82**, 237-240, 1999.
- O'Donnell, K. P., Mosselmans, J. F. W., Martin, R. W., Pereira, S. and White, M. E. "Structural analysis of InGaIn epilayers", *J. Phys.: Condens. Matter* **13**, 6977-6991, 2001.
- Osamura, K., Naka, S. and Murakami, Y. "Preparation and optical properties of Ga_xIn_xN thin films", *J. Appl. Phys.* **46**, 3432, 1975.
- Osborn, J. C. and Welberry, T. R. "A position-sensitive detector system for the measurement of diffuse X-ray scattering", *J. Appl. Cryst.* **23**, 476-484, 1990.
- Park, S. and Chuang, S. "Crystal-orientation effects on the piezoelectric field and electronic properties of strained wurtzite semiconductors", *Phys. Rev.* **B59**, 4725-4737, 1999.

- Pavlov, K. M. and Punegov, V. I. "Statistical dynamical theory of X-ray diffraction in the Bragg case: application to triple-crystal diffractometry", *Acta Cryst.* **A56**, 227-234, 2000.
- Pavlov, K. M., Punegov, V. I. and Faleev, N. N. "X-ray diffraction diagnostics of laser structures", *JETP* **80**, 1090-1097, 1995.
- Pavlov, K. M., Punegov, V. I., Nesterets, Ya. I., Davis, J. R. and Faleev, N. N. "Implementation of the statistical diffraction theory for triple-axis diffractometry of a mosaic block structure", *Unpublished*, 2004.
- Pavlov, K.M. and Punegov, V.I. "Models of spherically symmetric microdefects in the statistical dynamical theory of diffraction: II. correlation length", *Cryst. Rept.* **41**, 621-628, 1996.
- Pavlov, K.M. and Punegov, V.I. "Der Einfluss kugelymmetrischer Kristalldefekte auf die Winkelverteilung gebeugter Roentgenstrahlung", *Phys. Stat. Sol.* **199**, 5-14, 1997.
- Penning, P. and Polder, D. *Philips Res. Repts.* **16**, 419, 1961.
- Pereira, S., Correia, M. R., Pereira, E., O'Donnell, K. P., Martin, R. W., White, M. E., Alves, E., Sequeira, A. D. and Franco, N. "Splitting of X-ray diffraction and photoluminescence peaks in InGaN/GaN layers", *Mat. Sci. Eng.* **B93**, 163-167, 2002.
- Pinsker, Z. G. *Dynamical Scattering of X-Rays in Crystals*, Springer-Verlag, Berlin, 1978.
- Porowski, S. "Bulk and homoepitaxial GaN-growth and characterisation", *J. Crystal Growth* **189/190**, 153-158, 1998.
- Press, William H. *Numerical Recipes in C: the art of scientific computing*, Cambridge University Press, Cambridge, 1992.
- Prince, E. *International tables for crystallography, C.*, Kluwer Academic Publishers, Dordrecht, Holland, 1999.
- Punegov, V. I. "Statistical-dynamic theory of diffraction of x-rays by crystals with lattice parameters which continuously change along the thickness", *Sov. Phys. Crystallogr.* **35**, 336-340, 1990.

- Punegov, V. I. "Kinematic theory of diffraction on a imperfect epitaxial film with a constant strain gradient", *Sov. Phys. Tech. Phys.* **36**, 1369-1375, 1991.
- Punegov, V. I. "Dynamic theory of diffraction from an imperfect heterostructure", *Sov. Phys. Solid State* **33**, 136-140, 1991b.
- Punegov, V. I. "X-ray diffraction from multilayer structures with statistically distributed microdefects", *Phys. Stat. Sol.* **139**, 9-19, 1993.
- Punegov, V. I. "Dynamic X-ray diffraction in layered-inhomogeneous systems", *Tech. Phys. Lett.* **20**, 58-59, 1994.
- Punegov, V. I. and Vishnjakov, Y. V. "Dynamical theory of X-ray diffraction from damaged epitaxial layers with constant strain gradient", *J. Phys. D: Appl. Phys.* **28**, A184-A188, 1995.
- Punegov, V.I. and Pavlov, K.M. "Models of spherically symmetric microdefects in the statistical dynamical theory of diffraction: I. correlation function", *Cryst. Rept.* **41**, 575-584, 1996.
- Redwing, J. M., Tischler, M. A., Flynn, J. S., Elhamri, S., ahoujja, M., Newrock, R. S. and Mitchel, W. C. "Two dimensional electron gas properties of AlGa_N/Ga_N heterostructures grown on 6H-SiC and sapphire substrates", *Appl. Phys. Lett.* **69**, 963-965, 1996.
- Romano, L. T. Defects in GaN and related materials: partial dislocations, dislocation movement and cracks, in J. H. Edgar, S. Strite, I. Akasaki, H. Amano and C. Wetzel, eds, "Properties, processing and applications of Gallium Nitride and Related Semiconductors", INSPEC, The Institution of Electrical Engineers, London, pp. 221-225, 1999.
- Schoening, F. R. L. "Strain and particle size values from X-ray line breadths", *Acta Cryst.* **18**, 975-976, 1965.
- Schuster, M., Gervais, P. O., Jobst, B., Hösler, W., Averbek, R., Riechert, H., Iberl, A. and Stömmer, R. "Determination of the chemical composition of distorted InGa_N/Ga_N heterostructures from x-ray diffraction data", *J. Phys. D: Appl. Phys.* **32**, A56-A60, 1999.
- Silveira, E., Tabata, A., Leite, J. R., Trentin, R., Lemos, V., Frey, T., As, D. J., Schikora, D. and Lischka, K. "Evidence of phase separation in cubic In_xGa_{1-x}N

- epitaxial layers by resonant raman scattering", *Appl. Phys. Lett.* **75**, 3602-3604, 1999.
- Singh, R., Doppalapudi, D., Moustakas, T. D. and Romano, L. T. "Phase separation in InGaN thick films and formation of InGaN/GaN double heterostructures in the entire alloy composition", *Appl. Phys. Lett.* **70**, 1089-1091, 1997.
- Stringfellow, G. B. *Organometallic Vapor-Phase Epitaxy*, Academic Press, San Diego, 1999.
- Sumiya, M., Ogusu, N., Yotsuda, Y., Itoh, M., Fuke, S., Nakamura, T., Mochizuki, S., Sano, T., Kamiyama, S., Amano, H. and Akasaki, I. "Systematic analysis and control of low-temperature GaN buffer layers on sapphire substrates", *J. Appl. Phys.* **93**, 1311-1319, 2003.
- Tabuchi, M., Kyouzu, H., Takeda, Y., Yamaguchi, S., Amano, H. and Akasaki, I. "Atomic scale characterization of GaInN/GaN layers grown on sapphire substrates with low-temperature deposited AlN buffer layers", *J. Crystal Growth* **237-239**, 1133-1138, 2002.
- Takagi, S. "Dynamical theory of diffraction applicable to crystals with any kind of small distortion", *Acta Cryst.* **15**, 1311-1312, 1962.
- Takagi, S. "A dynamical theory of diffraction for a distorted crystal", *J. Phys. Soc. Jpn.* **26**, 1239-1253, 1969.
- Takeda, Y. and Tabuchi, M. Sapphire substrates for growth of GaN and related compounds, in J. H. Edgar, S. Strite, I. Akasaki, H. Amano and C. Wetzel, eds, "Properties, processing and applications of Gallium Nitride and Related Semiconductors", INSPEC, The Institution of Electrical Engineers, London, pp. 381-385, 1999.
- Takeda, Y. and Tabuchi, M. "X-ray CTR scattering and interference of atomic-scale characterization of semiconductor heterostructures", *J. Crystal Growth* **237-239**, 330-337, 2002.
- Takeda, Y., Tabuchi, M., Amano, H. and Akasaki, I. "Crystalline structure and the role of low-temperature-deposited AlN and GaN on sapphire revealed by X-ray CTR scattering and X-ray reflectivity measurements", *Surf. Rev. Lett.* **10**, 537-541, 2003.
- Taupin, D. "Théorie dynamique de la diffraction des rayons X par les cristaux déformés", *Bull. Soc. Franç. Minér. Crist.* **87**, 469-511, 1964.

- Thompson, A. G. "MOCVD technology for semiconductors", *Materials Letters* **30**, 255-263, 1997.
- Uren, M. J., Barnes, A. R., Martin, T., Balmer, R. S., Hilton, K. P., Hayes, D. G. and Kuball, M. "GaN devices for microwave applications", *10th IEEE International Symposium on Electron Devices for Microwave and Optoelectronic Applications* pp. 111-118, 2002.
- Van de Walle, C. G., Neugebauer, J. and Stampfl, C. Native point defects in GaN and related compounds. in J. H. Edgar, S. Strite, I. Akasaki, H. Amano and C. Wetzel, eds, "Properties, processing and applications of Gallium Nitride and Related Semiconductors", INSPEC, The Institution of Electrical Engineers, London, pp. 281-283, 1999.
- Vegard, L. "Ueber die Erklärung der Röntgenspektren und die Konstitution der Atome (definition of the rontgen spectra and the constitution of atoms)", *Phys. Z.* **22**, 271-274, 1921.
- Vickers, M. E., Kappers, M. J., Smeeton, T. M., Thrush, E. J., Barnard, J. S. and Humphreys, C. J. "Determination of the indium content and layer thicknesses in InGaN/GaN quantum wells by x-ray scattering", *J. Appl. Phys.* **94**, 1565-1574, 2003.
- von Laue, M. "Die dynamische theorie der Röntgenstrahlinterferenzen in neuer form", *Ergeb. Exakt. Naturw.* **10**, 133-158, 1931.
- von Laue, M., Fridrich, W. and Knipping, P. *Ann. Physik* **41**, 971, 1913.
- von Laue, M., Friedrich, W. and Knipping, P. Interferenz-erscheinungen bei röntgenstrahlen (interference features with x-ray), in "Sitzungsberichte Bayerische Akademie Wissenschaften Mathematisch-physikalische Klasse (Minutes of the Bavarian academy of sciences mathematical physics class)", pp. 303-322, 363-373, 1912.
- Warren, B. E. *X-ray Diffraction*, Addison-Wesley, Reading, 1969.
- Welberry, T. R., Goossens, D. J., Haefner, D. R., Lee, P. L. and Almer, J. "High-energy diffuse scattering on the 1-ID beamline at the Advanced Photon Source", *J. Synchrotron Rad.* **10**, 284-286, 2003.
- Wiedemann, H. *Synchrotron Radiation*, Springer-Verlag, Berlin, 2003.

- Williamson, G. K. and Hall, W. H. "X-ray line broadening from fcc aluminium and wolfram", *Acta Met.* **1**, 22-31, 1953.
- Wright, A. F., Leung, K. and van Schilfgaarde, M. "Effects of biaxial strain and chemical ordering on the band gap of InGaN", *Appl. Phys. Lett.* **78**, 189-191, 2001.
- Xing, H., Keller, S., Wu, Y-F., McCarthy, L., Smorchkova, I. P., Buttari, D., Coffie, R., Green, D. S., Parish, G., Heikman, S., Shen, L., Zhang, N., Xu, J. J., Keller, B. P., DenBaars, S. P. and Mishra, U. K. "Gallium nitride based transistors", *J. Phys.: Condens. Matter* **13**, 7139-7157, 2001.
- Yang, T.R., Dvoynenko, M.M., Cheng, Y.F. and Feng, Z.C. "Far-ir investigation of thin InGaN layers", *Physica B* **B324**, 268-278, 2002.
- Yoshida, S., Misawa, S. and Gonda, S. "Epitaxial growth of GaN/AlN heterostructures", *J. Vac. Sci. Technol.* **B1**, 250-253, 1983.
- Zachariasen, W. H. *Theory of X-Ray Diffraction in Crystal*, Dover Publications, New York, 1967.
- Zhang, J.C., Zhao, D.G., Wang, J.F., Wang, Y.T., Chen, J., Liu, J.P. and Yang, H. "The influence of AlN buffer layer thickness on the properties of GaN epilayer", *J. Crystal Growth* **268**, 24-29, 2004.
- Zielinska-Rohozinska, E., Gronkowski, J., Regulska, M., Majer, M. and Pakula, K. "X-ray diffraction study of composition inhomogeneities in $\text{Ga}_{1-x}\text{In}_x\text{N}$ thin layers", *Cryst. Res. Technol.* **36**, 903-910, 2001.

Supporting Publications

Mudie, S., Pavlov, K., Morgan, M., Tabuchi, M., Takeda, Y. and Hester, J. "High-resolution X-ray diffractometry investigation of interface layers in GaN/AlN structures grown on sapphire substrates", *Surf. Rev. Lett.* **10**, 513, 2003.

Mudie, S. T., Pavlov, K. M., Morgan, M. J., Hester, J. R., Tabuchi, M. and Takeda, Y. "Collection of reciprocal space maps using imaging plates at the Australian National Beamline Facility at the Photon Factory", *J. Synchrotron Rad.* **11**, 406-413, 2004.

Mudie, S. T., Pavlov, K. M., Morgan, M. J., Takeda, Y., Tabuchi, M. and Hester, J.R. "Analysis of GaN/AlN buffer layers grown on sapphire substrates via statistical diffraction theory", *Proceedings of COMMAD 2002 Sydney*, 111-116, 2002.

HIGH-RESOLUTION X-RAY DIFFRACTOMETRY INVESTIGATION OF INTERFACE LAYERS IN GaN/AlN STRUCTURES GROWN ON SAPPHIRE SUBSTRATES

STEPHEN MUDIE, KONSTANTIN PAVLOV and MICHAEL MORGAN
*School of Physics and Materials Engineering, Monash University,
Victoria 3800, Australia*

MAEAO TABUCHI and YOSHIKAZU TAKEDA
*Department of Materials Science and Engineering, Graduate School of Engineering,
Nagoya University, Nagoya 464-8603, Japan*

JAMES HESTER
*Australian Nuclear Science and Technology Organisation,
PMB 1, Menai NSW 2234, Australia*

GaN is an important wide band gap material with applications in short wavelength optoelectronic devices. The GaN layer is often grown on a sapphire substrate, with low-temperature-deposited AlN and thick GaN used as buffer layers. The growth regime consists of many steps, each of which contributes to the overall properties of the device. The aim of our high-resolution X-ray diffraction experiments, conducted at the Photon Factory (Tsukuba, Japan), was to investigate the structural quality of the AlN buffer layer, which affects the final properties of the device. Reciprocal space mapping was used to study samples (having various layer thicknesses) from each stage of the growth process. Analysis of the experimental data provides parameters such as mosaic block dimensions and orientation, lattice strain distribution, and layer thickness.

1. Introduction

Group III nitride semiconductors have attracted significant attention over the last several years, both for optoelectronics and transistor technologies. Optoelectronic devices utilizing this system cover almost all of the visible and near UV spectrum. Furthermore the strong bonding associated with nitrogen results in high chemical and thermal stability.¹ Development of commercial devices using this system has been hindered by the large lattice mismatch between the nitrides (in particular GaN) and common substrate materials (SiC or sapphire). This large mismatch results in defects within the GaN layer, with the formation of a dislocation net. The regions of the deformed crystal between the dislocation lines can be modeled as mosaic blocks. To overcome the lattice mismatch, a low-temperature(LT)-deposited AlN (buffer) layer can be inserted between the substrate (sapphire) and

the GaN layer.² This buffer layer enables the production of higher quality GaN by reducing the interfacial energy between GaN and the highly mismatched substrate lattice. To date most, if not all, investigations have only considered the effect of various buffer layers on the quality of the GaN layer, without analyzing the buffer layer itself. It is our objective to characterize each layer separately, and hence determine the effect of each layer on the crystalline quality of the optoelectronic active layer.

High-resolution X-ray diffraction (HRXRD) is frequently used to determine dislocation density and strain profiles of epitaxial layers.³⁻⁵ Unlike transmission electron microscopy, HRXRD is nondestructive and provides information on long-range ordering. However, HRXRD data can be difficult to evaluate. Various approaches have been used to analyze the experimental data⁶; these include measurement of

rocking curve line widths and shapes⁷⁻¹⁰ and reconstruction of complete rocking curves through numerical simulations.¹¹ Most simulations are based on the dynamical diffraction theory, developed by Takagi^{12,13} and Taupin,¹⁴ adapted to elucidating epitaxial layers.^{15,16}

One of the most informative HRXRD techniques is reciprocal space mapping (RSM).¹⁷ This provides information from a two-dimensional region of reciprocal space, and allows more accurate (less ambiguous) determination of physical properties. In order to achieve good resolution the detector must have a small angular acceptance; hence an analyzer crystal is used in the detection system in concert with a highly monochromatic incident X-ray beam.

In this paper we report synchrotron experiments on AlN/GaN multilayers (deposited on sapphire substrates). RSM and rocking curve data were analyzed following the approach described by Metzger *et al.*⁷ This method utilizes the broadening of the rocking curves ($\theta - 2\theta$ and ω scanning regimes) for the (0002), (0004) and (0006) symmetric reflections in order to determine mosaic block size and dislocation density. Measurements of this kind were initially performed by Gay *et al.*¹⁸ and Hordon and Averbach¹⁹ for metals, using a double crystal experimental scheme. Ayers⁸ adapted this method to semiconductors, with Metzger *et al.*⁷ utilizing it for triple crystal diffractometry.

In our work we apply triple-axis HRXRD to investigate the quality of a LT-AlN buffer layer at various stages of the growth process.

2. Experimental

2.1. Sample preparation

Samples were prepared using organometallic vapor phase epitaxy (OMVPE). All the samples were grown on sapphire (0001) substrates. Figure 1 shows a schematic of the growth process. The substrates were kept at 1150°C for 5 min in a H₂ environment to clean the surfaces. NH₃ flow was started when the substrate temperature was lower than 800°C. Growth was stopped at three stages during the growth process, and samples removed in order to take measurements. As shown in Fig. 1, the first stage was just after the LT-AlN buffer layer was deposited at 400°C (sample A). The second stage occurred after the sample was heated to 1100°C (sample B), and

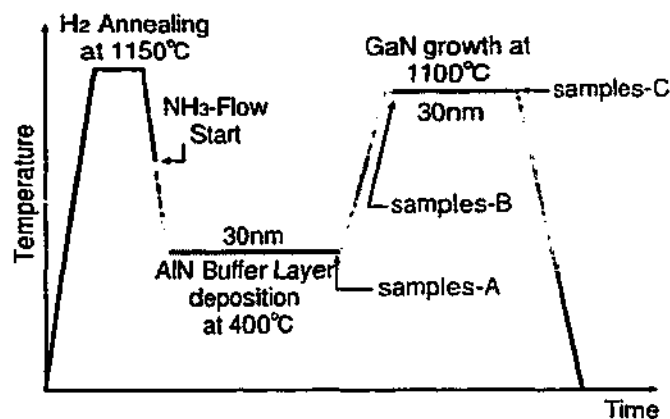


Fig. 1. Growth process for sample production. The arrows with sample numbers indicate the time at which the samples were removed from the growth chamber (after cooling). Note that three AlN buffer thicknesses were used: 10, 30 and 70 nm.

the third stage was after the growth of a 30-nm-thick GaN layer at the same temperature (sample C).

2.2. Characterization

X-ray measurements of all samples were performed with synchrotron radiation using Beamline 20B, at the Photon Factory in Japan. The experimental setup consisted of a two-axis Huber goniometer housed inside a large vacuum chamber. The double bounce Si(111) beamline monochromator produces a beam with a wavelength resolution of $\frac{\Delta\lambda}{\lambda} = 4 \times 10^{-4}$ and divergence of approximately 20 arcseconds (due to dispersion). Hence a second Si(220) quadruple bounce crystal was used as a monochromator to reduce the wavelength resolution to $\frac{\Delta\lambda}{\lambda} = 7 \times 10^{-5}$, which corresponds to a divergence of less than 7 arcseconds. The entrance slit to the diffractometer was set to 0.5×2 mm for the samples without GaN capping, which was increased to 1.0×2.5 mm for the samples with GaN capping, to improve counting statistics. The analyzer crystal was a double bounce Si(220) crystal; a Radicon high count rate scintillation counter was used to record the X-ray intensity. The whole arrangement is described by the following orientation (+, -, -, +, -, +, +, -, +). The Si(220) crystals were designed for Cu K α radiation; hence this energy was selected for the synchrotron experiments. The samples were mounted on a glass slide using glue. The slide was attached to an aluminum

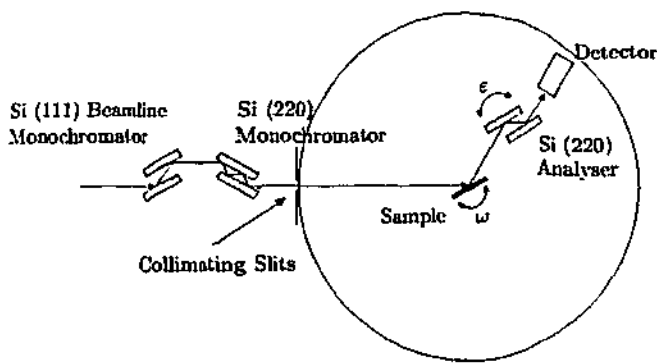


Fig. 2. Schematic representation of the experimental setup.

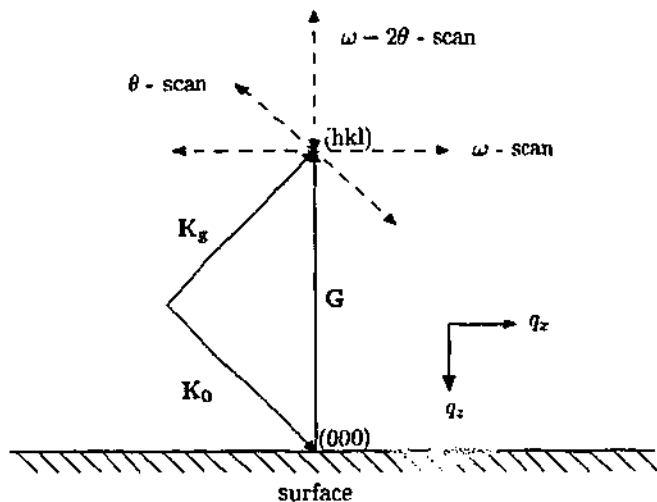


Fig. 3. Scan modes. Note that q_z is directed into the crystal.

post and mounted on the center stage of the goniometer. The setup is shown schematically in Fig. 2.

The goniometer was recalibrated for each sample using the strong sapphire (0006) peak as a reference. The diffractometer was evacuated before scanning to increase the signal-to-noise ratio. Scans were performed using the spec control software, and ranged in time from several minutes for one-dimensional ω and $\omega - 2\theta$ scans, to several hours for the two-dimensional RSM scans (depending upon the scan range). Each scan can be related to reciprocal space,^{17,20} as shown in Fig. 3, i.e.

$$\begin{aligned} q_x &= 2k \sin \theta_B \omega \cos \varphi - k\epsilon \sin \theta_2, \\ q_z &= -2k \sin \theta_B \omega \sin \varphi - k\epsilon \cos \theta_2, \end{aligned} \quad (1)$$

where ω is the rotation angle of the sample, ϵ is the rotation angle of the analyzer, φ is the asymmetry

angle of the sample, and θ_2 is the exit angle ($\theta_b + \varphi$) for the sample.

3. Results and Analysis

Three different buffer layer thicknesses were investigated: 10 nm, 30 nm and 70 nm. Three samples, type A, B and C (see Fig. 1), for each thickness were investigated, in order to explore the evolution of the layer properties during the growth process. It was determined that the 30 nm buffer layer produced the higher quality GaN top layer. Hence the analysis will concentrate on these three 30 nm samples. Table 1 summarizes the parameters determined from RSM experiments.

Sample A consisted of the 30 nm LT-deposited AlN layer on a sapphire substrate. The analysis (which utilized data from 0002 and 0004 reflections) shows that the layer had a dislocation density of $n_d = 4 - 8 \times 10^{11} \text{ cm}^{-2}$, which corresponds to a lateral mosaic block size of $L_x = 10-15 \text{ nm}$.

Sample B was identical to sample A, except that it was annealed at 1100°C , as shown in Fig. 1. The RSM about the AlN(0002) reciprocal lattice point indicates that two layers exist, as shown by the two peaks in Fig. 4. The first layer produces a narrow peak, indicating low mosaicity; it is also at the expected position for a relaxed AlN layer, which is indicative of minimal strain. This layer was found to be approximately 23 nm thick (based on thickness oscillations). It has a lateral mosaic block size of 84 nm, and an associated dislocation density of $1.4 \times 10^{10} \text{ cm}^{-2}$. The second layer produces a broad peak which indicates a larger mosaic spread, and hence higher dislocation density, $2.4 \times 10^{11} \text{ cm}^{-2}$; the corresponding lateral block size was 20 nm. This layer is greater than 9 nm thick. As AlN was the only deposited layer, it can be concluded that the annealing process has caused the AlN layer to split into two sublayers: a

Table 1. Summary of parameters.

	L_x (nm)	n_d (cm^{-2})
A	10-15	$4 - 8 \times 10^{11}$
B	1: top (23 nm)	1.4×10^{10}
	2: bottom (>9 nm)	2.4×10^{11}
C	1: top	$0.1 - 3 \times 10^{10}$
	2: bottom	$0.3 - 1 \times 10^{11}$

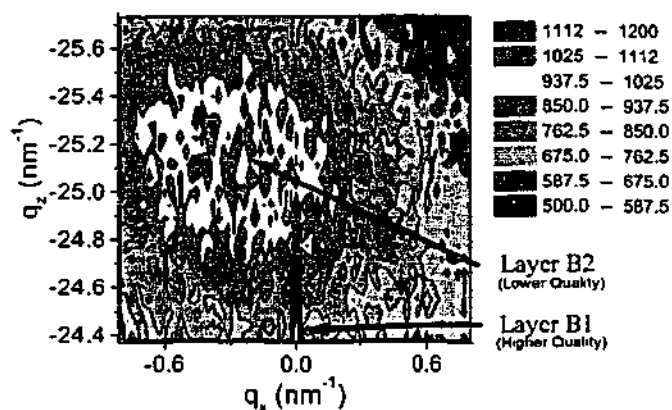


Fig. 4. RSM about the AlN(0002) reciprocal lattice point of sample B.

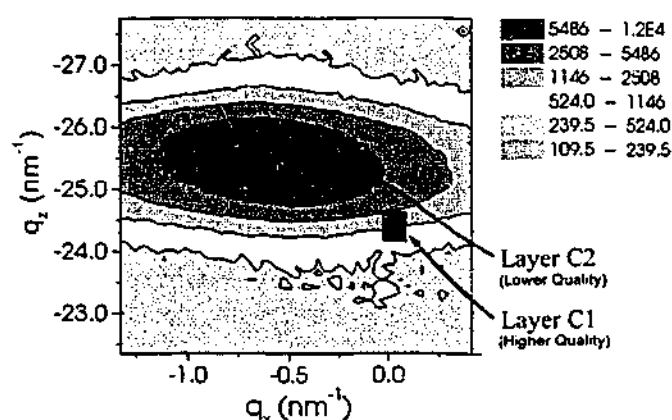


Fig. 5. RSM about the AlN(0002) reciprocal lattice point of sample C. The black square indicates the approximate position of the AlN peak, which was only observable in the more precise $\omega - 2\theta$ scan and ω scan.

thin low quality layer immediately on the substrate and a higher quality upper sublayer. We suggest that this process is important for producing a higher quality GaN layer. The bottom sublayer accommodates the lattice mismatch between the substrate and the AlN through a higher dislocation density, but the formation of the lower dislocation density AlN layer allows the production of quality GaN.

Sample C was the same as sample B, except that a 30 nm GaN layer was deposited on top at 1100°C, as illustrated in Fig. 1. The experimental data again shows two AlN sublayers of different dislocation densities, although the peak for the higher quality sublayer is absent from the RSM (see Fig. 5). This is in part due to masking from the lower quality sublayer and also to the necessarily coarse step size required to measure

the RSM in a reasonable time frame. However, the second AlN peak was evident in the $\theta - 2\theta$ scan (with $\Delta\omega = 2\omega - \varepsilon = 0$) and ω scan, with its position shown in Fig. 5 as a black square.

The higher quality sublayer has been reduced in thickness (with a subsequent increase in thickness of the lower quality sublayer); it has a lateral mosaic block size of 28–56 nm, and a dislocation density of $0.1 - 3 \times 10^{10} \text{ cm}^{-2}$. This is similar to sample B. The lower quality sublayer, however, improved compared to sample B, with lower dislocation density, $0.3 - 1 \times 10^{11} \text{ cm}^{-2}$, and larger lateral mosaic block size, 30–50 nm. A comparison between sample B and sample C shows that the low quality layer has an increased tilt, as shown by the peak moving further to the left in Fig. 5. This suggests that the dislocations have migrated from the volume to the mosaic block walls.²¹ This in turn decreases the volume dislocation density, as evident from Table 1.

These changes in quality can be attributed to two physical sources: increased time at high temperature while GaN is deposited (i.e. further annealing of AlN, allowing the migration of dislocations), and the presence of the GaN layer itself. An observable effect of GaN on AlN is the strain. The calculated unstrained position for the AlN peak is 18.002° . However, the low quality layer of sample B appears at a mean position of 18.5° , and for sample C at 18.75° . These correspond to compressive stresses of $\frac{\Delta d}{d} = -0.027$ and $\frac{\Delta d}{d} = -0.040$, respectively. For sample B the strain is due to the mismatch between the AlN and sapphire lattice constants. This mismatch causes a lateral tensile strain, and hence a compressive strain perpendicular to the surface. This strain may be reduced by the higher quality layer. The increase in the strain for sample C would, in part, be due to the presence of GaN,²² as it also has a larger lattice parameter than AlN.

The results for sample C with a 30 nm AlN layer can be compared to the result for the sample with a 70-nm-thick LT-AlN buffer and GaN capping, shown in Fig. 6. Here only a tilted AlN layer with a large gradient of deformation is visible, i.e. there are not two layers with different dislocation density.

4. Conclusion

HRXRD studies were carried out on a series of GaN/AlN heterostructures with different thicknesses of LT-AlN buffer layers. It is found that a 30 nm

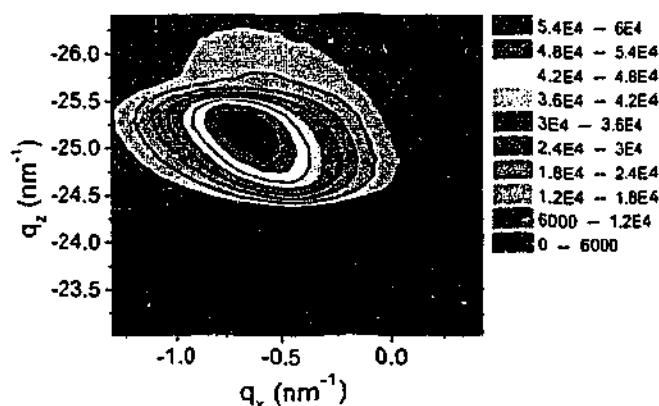


Fig. 6. RSM of sample with 70 nm AlN buffer layer.

AlN buffer layer increases the quality of the whole heterostructure. RSM shows that the 30 nm LT-AlN buffer layer segregates into two sublayers. We conjecture that the origin of the improvement in quality is due to the "localization" of dislocations in the lower part of the AlN buffer. It is also observed that a GaN layer changes the structure of the AlN buffer; in particular it reduces the thickness of the high quality upper buffer sublayer. Further synchrotron experiments and TEM studies are required to validate this conjecture for a larger range of growth parameters.

Acknowledgments

This work has performed at the Australian National Beamline Facility with support from the Australian Synchrotron Research Program, which is funded by the Commonwealth of Australia under the Major National Research Facilities Program. S. M. acknowledges the support of an Australian Postgraduate Award.

References

1. I. Akasaki and H. Amano, *Jpn. J. Appl. Phys.* **36**, 5393 (1997).

2. H. Amano, N. Sawaki, I. Akasaki and Y. Toyoda, *Appl. Phys. Lett.* **48**, 353 (1986).
3. V. Harutyunyan, A. Aivazyan, E. Weber, Y. Kim, Y. Park and S. Subramanya, *J. Phys.* **D34**, A35 (2001).
4. H. Heinke, V. Kirchner, H. Selke, R. Chierchia, R. Ebel, S. Einfeldt and D. Hommel, *J. Phys.* **D34**, A25 (2001).
5. V. Ratnikov, R. Kyutt, T. Shubina, T. Paskova and B. Monemar, *J. Phys.* **D34**, A30 (2001).
6. P. Fewster, *Semicond. Sci. Technol.* **8**, 1915 (1993).
7. T. Metzger, R. Höpler, E. Born, O. Ambacher, M. Stutzmann, R. Stömmner, M. Schuster, H. Göbel, S. Christiansen, M. Albrecht and H. Strunk, *Philos. Mag.* **A77**, 1013 (1998).
8. J. Ayers, *Journal of Crystal Growth* **135**, 71 (1994).
9. P. Healey, K. Bao, M. Gokhale, J. Ayers and F. Jain, *Acta Cryst.* **A51**, 498 (1995).
10. V. Srikant, J. Speck and D. Clarke, *J. Appl. Phys.* **82**, 4286 (1997).
11. E. Koppensteiner, A. Schuh, G. Bauer, V. Holý, G. Watson and E. Fitzgerald, *J. Appl. Phys.* **28**, A114 (1995).
12. S. Takagi, *Acta Crystallogr.* **15**, 1311 (1962).
13. S. Takagi, *J. Phys. Soc. Japan* **26**, 1239 (1969).
14. D. Taupin, *Bull. Soc. Fr. Minéral. Cristallogr.* **57**, 469 (1964).
15. O. Brandt, P. Waltereit and K. Ploog, *J. Phys.* **D35**, 577 (2002).
16. V. Holý, K. Wolf, M. Kastner, H. Stanzl and W. Gebhardt, *J. Appl. Cryst.* **27**, 551 (1994).
17. V. Holý, U. Pietsch and T. Baumbach, *High-Resolution X-Ray Scattering from Thin Films and Multilayers* (Springer-Verlag, 1999).
18. P. Gay, P. Hirsch and A. Kelly, *Acta Metallurgica* **1**, 315 (1953).
19. M. Hordon and B. Averbach, *Acta Metallurgica* **9**, 237 (1961).
20. Y. Nesterests and V. Punegov, *Acta Cryst. A* **56**, 540 (2000).
21. A. Kazimirov, N. Faleev, H. Temkin, M. Bedzyk, V. Dmitriev and Yu. Melnik, *J. Appl. Phys.* **89**, 6092 (2001).
22. C. Kim, I. Robinson, J. Myoung, K. Shim and K. Kim, *J. Appl. Phys.* **85**, 4040 (1999).

Collection of reciprocal space maps using imaging plates at the Australian National Beamline Facility at the Photon Factory

S. T. Mudie,^{a*} K. M. Pavlov,^a M. J. Morgan,^a
J. R. Hester,^b M. Tabuchi^c and Y. Takeda^c

^aSchool of Physics and Materials Engineering, Monash University, Victoria 3800, Australia, ^bAustralian Nuclear Science and Technology Organisation, PMB 1, Menai, NSW 2234, Australia, and ^cDepartment of Materials Science and Engineering, Graduate School of Engineering, Nagoya University, Nagoya 464-8603, Japan.
E-mail: stephen.mudie@spme.monash.edu.au

Weissenberg screens and a translating cassette have been employed to allow an imaging plate to collect 30 scans per readout. In this configuration the imaging plate functions as a curved one-dimensional position-sensitive detector and, by changing the sample angle for each of the scans, two-dimensional images were produced in reciprocal space. This method of data collection leads to a reduction in scan time compared with methods based on a scintillation detector, particularly for asymmetric reflections. The data-collection method was tested using InGaN/GaN/AlN multilayers on sapphire substrates, since these exhibit broad features in reciprocal space. The geometry of the scans in reciprocal space required the data to be interpolated onto a Cartesian grid. Several interpolation schemes were investigated, with the results compared with the reciprocal space maps collected using a triple-axis scheme with a point detector. The quality of the interpolated reciprocal space maps depends upon the size and shape of the feature in reciprocal space, the interpolation method used, and the step size of the sample rotation. The method can be extended to three dimensions without an increase in data-collection time.

Keywords: reciprocal space maps; high-resolution X-ray diffraction; triple-axis diffraction; imaging plates; position-sensitive detectors.

1. Introduction

Synchrotron radiation is used to non-destructively characterize semiconductor heterostructures that are an integral part of advanced technology. In particular, X-ray diffraction provides important information about the quality and structure of semiconductor materials, ranging from those composed of several layers with varying composition to very complex multilayer structures, such as quantum dots, wires and superstructures (Fewster, 1997). The advantage of using synchrotron radiation derives from its high flux. However, even with large flux, it can still take many hours to investigate the region about a single reciprocal lattice point (RLP) as the layers are often thin (nanometres to micrometres) and/or of low crystalline quality. Since synchrotron beam time is limited, it is desirable to find ways of decreasing the time required to collect reciprocal space maps (RSMs), particularly as semiconductor structures become more complex and require more detailed experimental data for full characterization. Experimentally, it is necessary to examine a large region of reciprocal space to determine Bragg peak positions and intensities. However, to elucidate fine structure in the diffracted intensity

requires that small regions of reciprocal space be mapped at high resolution about many RLPs.

Currently, point detectors (e.g. scintillation counters) and area detectors (CCDs, imaging plates and film) are used for diffraction experiments. When coupled with high-precision rotation stages and high-quality analyser crystals in the triple-axis diffractometry (TAD) scheme (Iida & Kohra, 1979; Fewster, 1997; Holý *et al.*, 1999), point detectors offer large dynamic range, ease of data extraction, flexibility and very high angular resolution (several arcseconds). However, data-collection rates are low because the sample and/or analyser/detector position needs to be changed for each datum point. Position-sensitive detector (PSD) schemes overcome this problem by sampling extended areas of reciprocal space simultaneously. Unfortunately these detectors have poorer spatial resolution, dynamic range and signal-to-noise ratio than point detectors. Further, the analyser crystal discriminates intensity based on angle, whereas a PSD cannot distinguish between beams striking the detector at the same position but from different angles (and hence from different parts of the sample).

Selection of the detector and the diffractometer arrangement depends on the sample type. Semiconductor heterostructures are often grown as layers on thick highly crystalline substrates, which requires Bragg diffraction geometry and a detector robust enough to handle high-intensity beams diffracted from the substrate or thick high-crystalline layers, while still being capable of measuring low-intensity diffraction from thin layers. Since the individual layers are often of high crystalline quality the diffraction distribution exhibits fine structure, which should be measured with a high angular resolution. Therefore RSMs of semiconductor heterostructures have been routinely acquired using TAD because of the resolution and dynamic range characteristics (Fewster, 1997; Holý *et al.*, 1999).

As mentioned above the TAD method is slow, hence PSDs have been used for the collection of RSMs that may be applicable to characterizing semiconductor heterostructures. Gerhard *et al.* (2000) utilized a method whereby a ZnSe-based laser diode structure is illuminated by a highly divergent X-ray beam (from a synchrotron microfocus beamline). The diffracted intensity pattern is recorded on an imaging plate (IP). The incident-beam divergence is equivalent to rocking the sample during exposure to plane-wave irradiation. This method is very fast and simple, although the spot size used is small (10 μm) to achieve the greatest incident wavevector range possible. A small spot size avoids the various wavevectors being separated spatially. Hence this method collects information from a very small region of the sample, which can be an advantage or disadvantage depending upon the sample and the information required. A disadvantage of collecting a range of incident wavevector angles simultaneously is the integration of diffuse intensity within reciprocal space. The integration length depends directly on the range of wavevectors utilized. Gerhard *et al.* (2000) used a small wavevector distribution range, and so avoided excessive integration. If wide scans are required then it is necessary to use point (or one-dimensional) detectors to avoid integration over a large region of reciprocal space. Since one-dimensional detectors have a finite size they will also integrate along one reciprocal space direction. However, the integration is not affected by the angular range of the scan. The range of the integration can be reduced by using suitable slits to decrease the angular acceptance of the detector perpendicular to the diffraction plane.

A number of authors (Kinne *et al.*, 1998; Butler *et al.*, 2000; Welberry *et al.*, 2003) have used IPs as one-dimensional detectors. Weissenberg slits have been employed to mask the IP, which is translated perpendicular to the plane of diffraction. Kinne *et al.*

(1998) and Butler *et al.* (2000) report the collection of RSM data acquired by translating the IP and rotating the sample simultaneously to fill the entire detector area. Welberry *et al.* (2003) use a similar procedure except that the IP is stationary while being exposed. They have collected up to 300 strips, each 0.5 mm wide, on one imaging plate. Of these authors only Kinne *et al.* (1998) studied epitaxial layers on substrates, the sample type in which we are interested, using an IP detector in a one-dimensional mode. Butler *et al.* (2000) and Welberry *et al.* (2003) studied small single crystals. These systems are simple to set up compared with TAD, use a widely available PSD (IPs), and have a reasonable resolution and dynamic range. The level of integration within reciprocal space is dependent upon the slit width and can be made quite small. Each of these methods require angular calibration of the image plates (Kinne *et al.*, 1998; Butler *et al.*, 2000; Welberry *et al.*, 2003). This was carried out using high-intensity well known reflections from the sample. Welberry *et al.* (2003) also required a calibration to account for the decay in the recorded intensity with time over the duration of the scan.

Osborn & Welberry (1990) and Boule *et al.* (2002) both describe curved one-dimensional position-sensitive wire (or blade) detectors, which allow many scans to be collected without the need to change film or imaging plate. Although these detector systems allow high resolution to be achieved, they are expensive and can be damaged by synchrotron beam intensities. This is particularly true for samples that exhibit strong substrate reflections. Hence, despite their advantages, these detectors are not suited to our experimental work, which uses synchrotron radiation to investigate epitaxial layers grown on substrates.

Owing to the advantages outlined above, we used IPs and Weissenberg slits to collect RSMs. Unlike Kinne *et al.* (1998) we performed our experiments at a synchrotron facility. In contrast to Kinne *et al.* (1998), Butler *et al.* (2000) and Welberry *et al.* (2003), we compare the results obtained with IPs to RSMs collected in a high-resolution (TAD) mode using a point detector, and outline the interpolation methods used. In brief, the organization of this paper is as follows. In §2 we outline the mathematical relationship between angular (real) space and reciprocal space, and detail the experiment where RSMs were collected using IPs. §3 presents the results from the experiment, with a discussion in §4.

2. Experiment

For clarity we begin by describing the geometry of the IP and TAD methods in detail. Fig. 1 shows the experimental arrangement used to collect RSMs in the TAD scheme. Figs. 2(a) and 2(b) show the detailed diffraction geometry for angular and reciprocal space. The angle designations are the same as those used by Nesterets & Punegov (2000), where ω and ω' are the angular deviations (from the appropriate Bragg conditions) of the incident and diffracted waves,

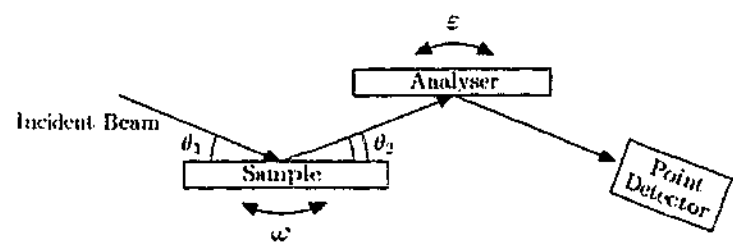


Figure 1 Geometry used in triple-axis diffractometry (TAD) to collect high-resolution RSMs. In a variant of the TAD scheme the detector is placed (with a narrow slit in front of it) perpendicular to the diffracted beam.

respectively, and ϵ is the angular deviation of the diffracted beam from the initial Bragg condition for the analyser. The angle between the surface of the sample and the diffraction planes (asymmetry angle) is specified by φ . The vectors k_0 and k_h are the incident and diffracted wavevectors, with magnitude $k = 2\pi/\lambda$; q_x and q_z are the reciprocal space vectors in the x and z directions, respectively, as shown in Fig. 2(b). The angles are related via the following equations,

$$\theta_1 \cong \theta_B - \varphi, \tag{1}$$

$$\theta_2 \cong \theta_B + \varphi, \tag{2}$$

$$\omega = (\epsilon/2) + \Delta\omega. \tag{3}$$

The definition of (3) is applied such that $\Delta\omega$ specifies the deviation from the θ - 2θ scan. The reciprocal space diagram in Fig. 2(b) can be produced from Fig. 2(a) by rotating the coordinate system until the sample surface is horizontal. This is equivalent to a rotation angle of $\omega + \theta_B - \varphi$. Hence the angle between the q_x axis and the direction to the detector slit position (or the middle of the angular window of the analyser crystal) is given by

$$\omega' + \theta_2 = 2\theta_B + \epsilon - (\omega + \theta_B - \varphi) \tag{4}$$

$$= \theta_2 + \epsilon - \omega, \tag{5}$$

and hence

$$\omega' = \epsilon - \omega. \tag{6}$$

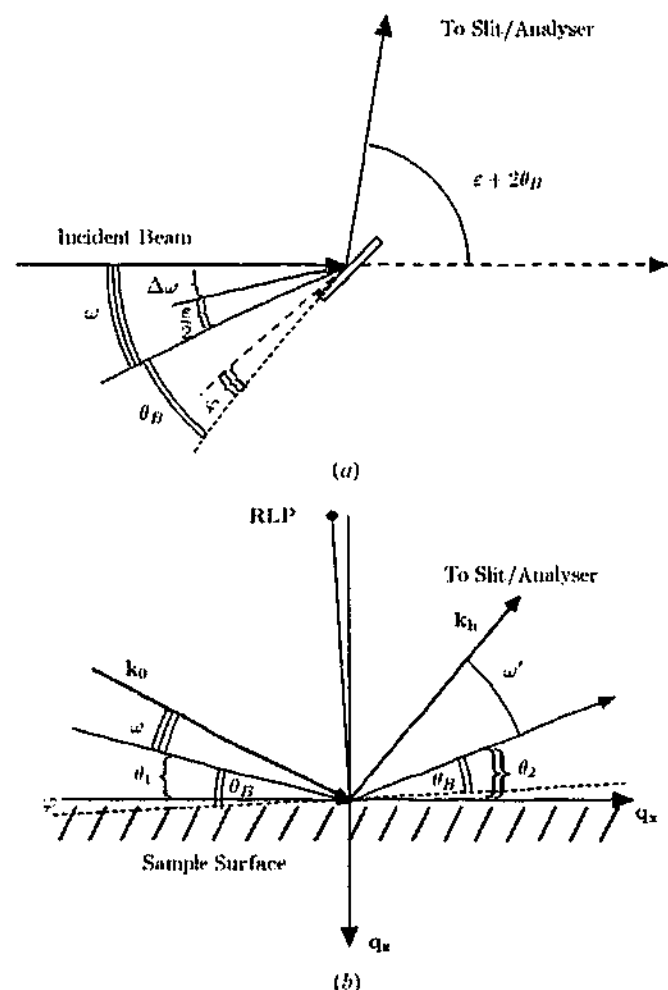


Figure 2 Angle definitions for scans in (a) angular space and (b) reciprocal space.

research papers

The following equations are used to convert from angular space to reciprocal space, assuming small deviations from the Bragg condition (Nesterets & Punegov, 2000),

$$q_x = 2k\Delta\omega \sin \theta_B \cos \varphi - k\varepsilon \cos \theta_B \sin \varphi, \quad (7)$$

$$q_z = -2k\Delta\omega \sin \theta_B \sin \varphi - k\varepsilon \cos \theta_B \cos \varphi. \quad (8)$$

For a symmetric reflection ($\varphi = 0$), q_x is parallel to the $\Delta\omega$ axis for small values of $\Delta\omega$, and q_z is antiparallel to the $\varepsilon/2$ axis (see Fig. 3b).

Replacing the analyser crystal and the point detector in Figs. 1 and 2 with a one-dimensional PSD, and keeping ω constant, the intensity is now recorded along a circular arc in reciprocal space as shown in Fig. 3(a). A curved two-dimensional map in reciprocal space is produced by collecting data from the PSD for several ω positions. If the small-angle approximation is valid then the map is not curved, and equation (3) can be rearranged to give

$$\Delta\omega = \omega - (\varepsilon/2). \quad (9)$$

For constant ω the coordinate along the PSD is linear in ε ; in $(\varepsilon/2)-\Delta\omega$ space the PSD produces scans at 45° to the $\varepsilon/2$ axis, with intercept ω (see Fig. 3b). No assumptions have been made about the size of ω or ε , hence the $(\varepsilon/2)-\Delta\omega$ representation is useful for avoiding otherwise curved scans in q_x-q_z space when the ω and ε ranges are large. It is particularly important for the interpolation described in §3.

Having described the geometry we now move to the particulars of the actual experiment. All experimental work was performed at the

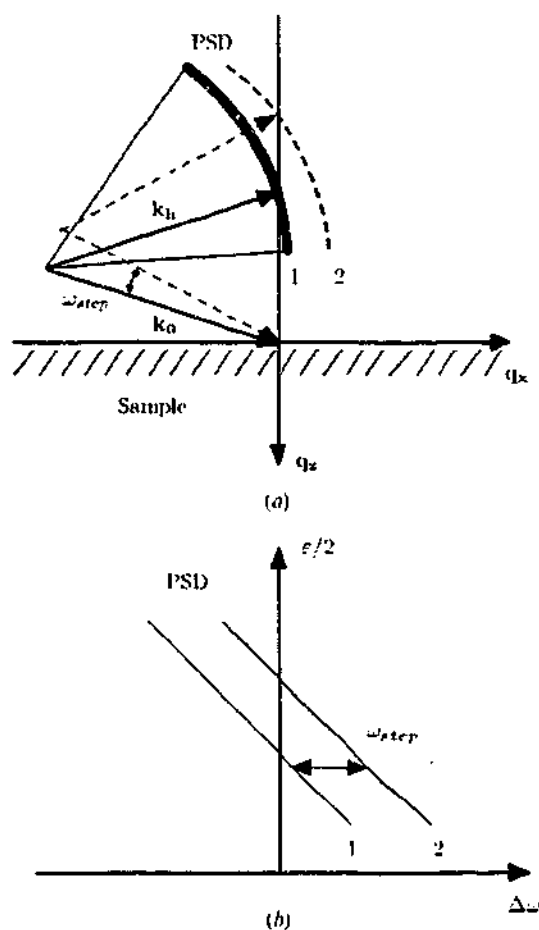


Figure 3 Symmetric reflection with a position-sensitive detector in (a) reciprocal space and (b) angular space. 1 and 2 indicate two different ω positions of the sample, and show how the position-sensitive detector covers reciprocal space to produce an RSM.

Australian National Beamline Facility (ANBF) on beamline 20B, at the Photon Factory, Tsukuba, Japan. The bending-magnet source delivers radiation from 4 keV to 25 keV ($\sim 3-0.05$ Å), with a Si(111) channel-cut monochromator selecting the desired energy. The monochromator can be de-tuned to reject higher harmonics.

The experimental hut contains a large diffractometer (Barnea *et al.*, 1992; Garrett *et al.*, 1995) which can be evacuated to 0.01 torr in about 20 min. It houses a Huber 410 goniometer (ω) and a Huber 420 rotation arm (2θ), which are mounted coaxially with the axis of rotation horizontal. The IP cassette is centred on the ω goniometer, with radius 0.573 m, and covers $\pm 160^\circ$ in 2θ . The capacity of the cassette is eight 400 mm \times 200 mm IPs, with the long side oriented along the circumference. Radioactive fiducial markers are installed in the cassette to provide an angular standard on the IP. Weissenberg screens can be installed so that only 4 mm of the plate is exposed at one time. The IP cassette can be translated perpendicular to the plane of diffraction (see Fig. 4) so that up to 30 exposures can be collected on one plate, with a 1.5 mm gap between each exposed strip. The rotation stages, IP cassette, slits and detectors are computer controlled.

The IPs were scanned using a Fuji Film BAS2000 system, which provides a dynamic range of 10^4 and an effective spatial resolution of 100 μm . This resolution equates to an angular resolution of 0.01° in 2θ . Software written in-house at the ANBF is available for angular calibration of the IP using the fiducial marks, plate-rotation correction and for extracting individual strips from the scan. A high-count-rate scintillation detector (Radicon) is used for double- and triple-axis diffractometry.

The samples investigated in this experiment were InGaN/GaN(2 μm)/AlN(30 nm) multilayers grown on sapphire substrates. The AlN and GaN layers serve as buffers between the optoelectronically active InGaN layer and the lattice mismatched sapphire substrate. Three InGaN compositions ($\text{In}_{0.3}\text{Ga}_{0.7}\text{N}$, $\text{In}_{0.05}\text{Ga}_{0.95}\text{N}$ and $\text{In}_{0.42}\text{Ga}_{0.58}\text{N}$) were used. The 5% In layer was 200 nm thick and the other two layers were 20 nm thick. We have studied these samples at the ANBF previously (Mudie *et al.*, 2002, 2003), using a scintillation detector for the collection of the RSMs in the TAD scheme. Although high-resolution RSMs were collected in these earlier experiments, data acquisition was time-consuming. We have therefore employed a low-resolution scheme using a PSD, which is less time-demanding than TAD. The low-resolution scheme can be used for our samples because they exhibit no fine structure in the RSMs.

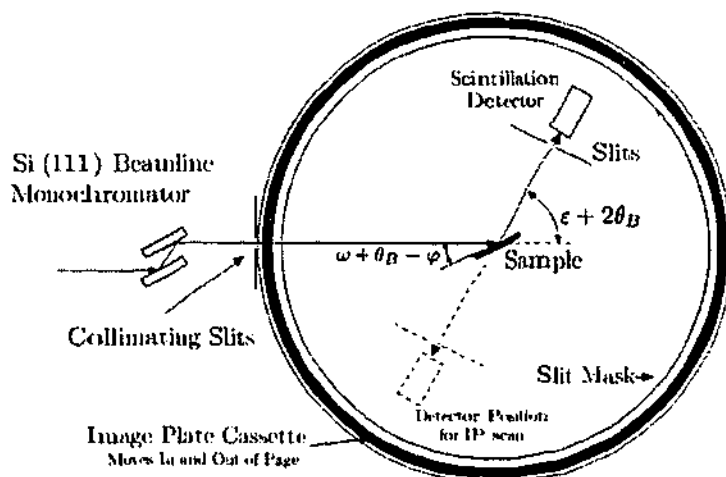


Figure 4 Diffractometer configuration (side view) showing the location of the IP cassette.

An incident wavelength of 1.54 Å was selected and the monochromator was de-tuned to reject higher-order harmonics. The diffractometer entrance slits were adjusted to 4 mm × 0.1 mm (width × height). This matched the beam to the width of the IP strips, and to the spatial resolution of the IP. The sample stage was mounted on the ω goniometer and the scintillation detector and slits were mounted on the 2θ arm. This configuration is shown schematically in Fig. 4.

The scintillation detector was used to align the sample and to collect an RSM using the TAD scheme (see Fig. 1 and caption); a 0.5 mm-wide slit was used in front of the detector. The TAD RSM was subsequently compared with RSMs collected using the IPs. The detector was rotated to the bottom of the diffractometer during IP collection, as indicated in Fig. 4, so as not to obscure the synchrotron beam. The diffractometer was evacuated for the collection of all RSMs to reduce air scatter.

The first strip on each IP was reserved for a crystal truncation rod (CTR) scan [see Takeda & Tabuchi (2002) and references therein]. The CTR scan was collected by rotating the sample over the angular region of interest, including the nearest substrate peak, pausing for 1 s at each ω position to expose the IP strip. The CTR was used to confirm the correct angular calibration of the plate. As only one IP was used to collect an RSM, the number of ω positions was restricted to 29, and the 2θ angular range to 40°. The 2θ angular range is superfluous, but was set by the IP size. To increase the number of ω positions the IP would need to have been changed every 29 scans. Although this is possible, it would require the diffractometer to be evacuated each time, significantly increasing the time required to collect the RSM.

A software script was written by the authors to control the ω stage, the IP cassette and the shutter during collection of RSMs. Initially the exposure time was varied to determine a suitable value for our samples. Using the highest sensitivity on the scanner, a time of 45 s per strip avoided overexposing the peak due to the thick 2 μ m GaN layer, while being long enough to collect peaks originating from the thin 20–200 nm InGaN layer.

3. Results

Fig. 5 shows a section of an 'as collected' IP for the $\text{In}_{0.3}\text{Ga}_{0.7}\text{N}/\text{GaN}/\text{AlN}$ sample about the GaN(0004) reflection. The strips are clearly identifiable near the peaks; however, within each strip the peak intensity is not centred. This was corrected for later by varying the off-plane angle of the sample. The strip on the far left is the CTR and the bright spot on the extreme right is a fiducial mark. The IP scans were converted into 30 one-dimensional scans using in-house software. The software calibrated the ε axis using the fiducial marks, then integrated in the ω direction across each scan to obtain the intensity.

The unprocessed data in Fig. 5 lie on a regular two-dimensional Cartesian grid in ω –($\varepsilon/2$) space. We can move to $\Delta\omega$ –($\varepsilon/2$) space (see Fig. 6) using equation (9) [and then to q_x – q_z space using equations (7) and (8)]; however, the grid formed is not regular along the $\Delta\omega$ axis. In order to plot the RSMs and extract profiles along various directions, the data must be interpolated onto a regular (Cartesian) grid. A number of interpolation schemes were implemented; however, the simplest is to interpolate in the $\Delta\omega$ direction. A cubic spline interpolation was used, as it was easy to implement and matches the data smoothly.

Fig. 6 shows the geometry of an entire scan after the unprocessed data (shown in Fig. 5) has been transformed to angular coordinates $\Delta\omega$ –($\varepsilon/2$). Within reciprocal space the scan would be an arc (see Fig. 3a), because the small-angle approximation breaks down owing to the large angular range (*i.e.* 20° in $\varepsilon/2$).

Fig. 7 shows a comparison of an RSM acquired with an IP and the TAD scheme. The scans are about the GaN(0004) peak and encompass the $\text{In}_{0.3}\text{Ga}_{0.7}\text{N}$ (0004) peak. The line profiles have been extracted from the RSM, not collected separately. The background has been subtracted and the scans normalized to the InGaN peak height. The error plot (Fig. 7b) is given by

$$\text{RSM}_{\text{Error}} = \log_{10}(\text{RSM}_{\text{IP}}/\text{RSM}_{\text{TAD}}). \quad (10)$$

An IP scan was also collected with half the step size in the ω direction (see Fig. 8). Only one IP was used, which covered half the area of the RSM presented in Fig. 7. This results in the truncation seen in Fig. 8(a). The data-collection time was identical to the lower-resolution scan shown in Fig. 7.

In Fig. 7 the step size in the $\Delta\omega$ direction (as determined by the interpolation of the IP RSM) was matched to that used for the TAD technique. The small-angle approximation [equations (7) and (8)] was

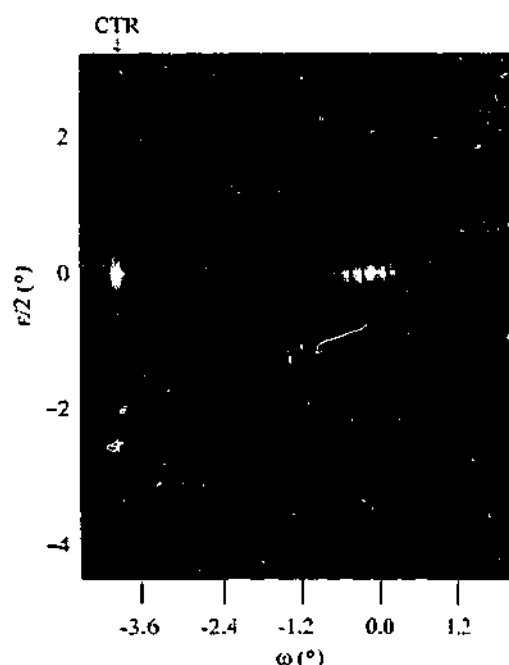


Figure 5 Section of an unprocessed imaging plate for the $\text{In}_{0.3}\text{Ga}_{0.7}\text{N}/\text{GaN}/\text{AlN}$ sample about the (0004) reflection.

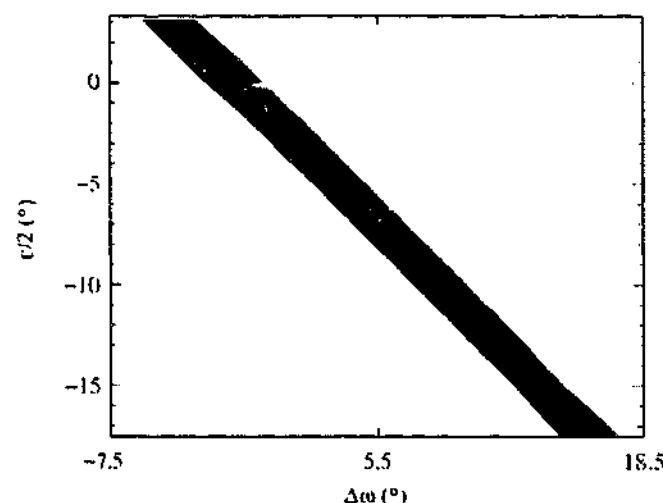


Figure 6 Entire RSM from a single imaging plate after cubic spline interpolation for the $\text{In}_{0.3}\text{Ga}_{0.7}\text{N}/\text{GaN}/\text{AlN}$ sample about the (0004) reflection.

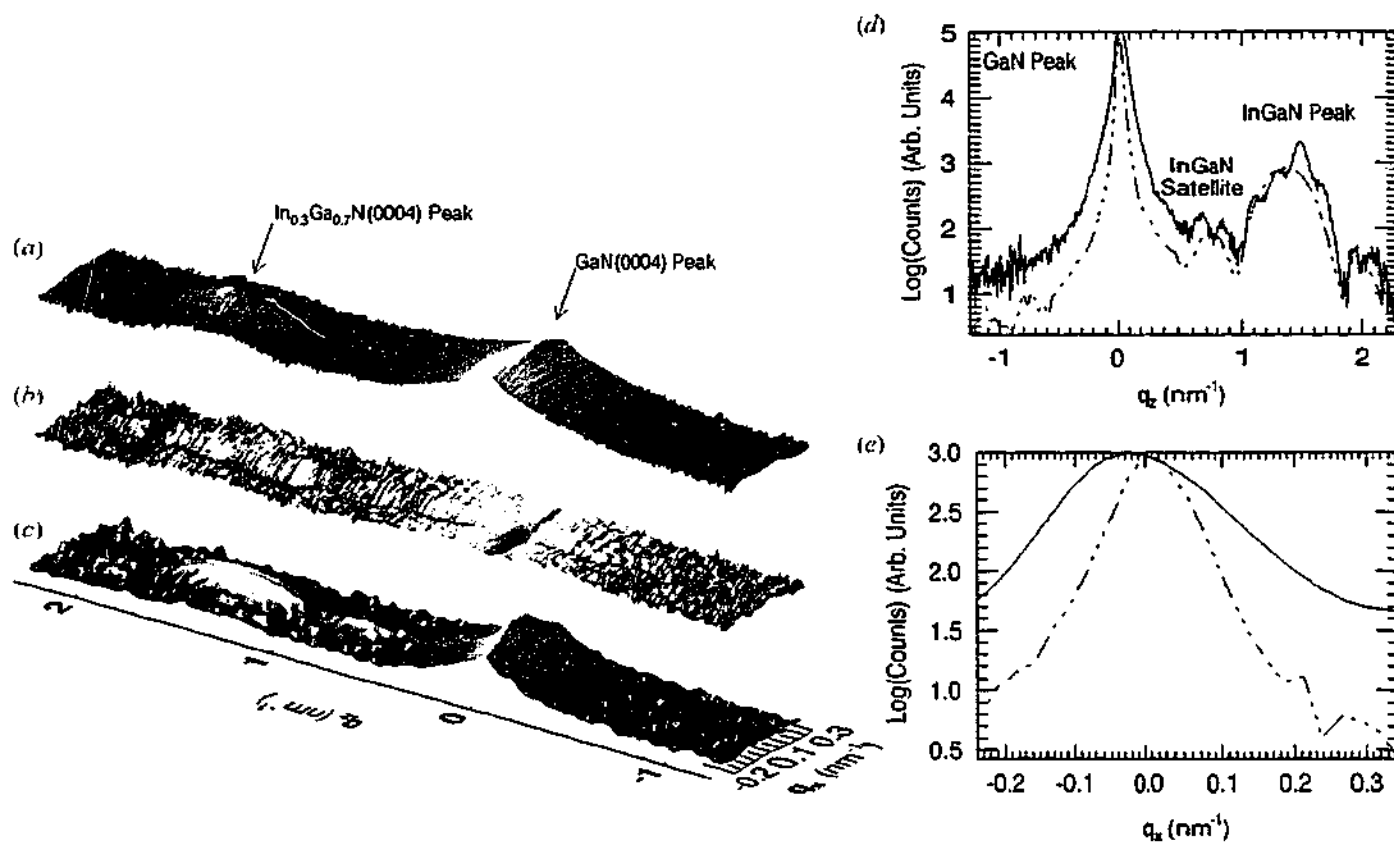


Figure 7
 Comparison of triple-axis RSM and interpolated IP data. (a) Interpolated IP RSM, (b) error plot, (c) triple-axis RSM, (d) ω - 2θ scan (extracted from RSM), and (e) ω scan (extracted from RSM). Note that a logarithmic vertical axis is used for each plot. Full line: IP method with interpolation. Dashed line: TAD technique.

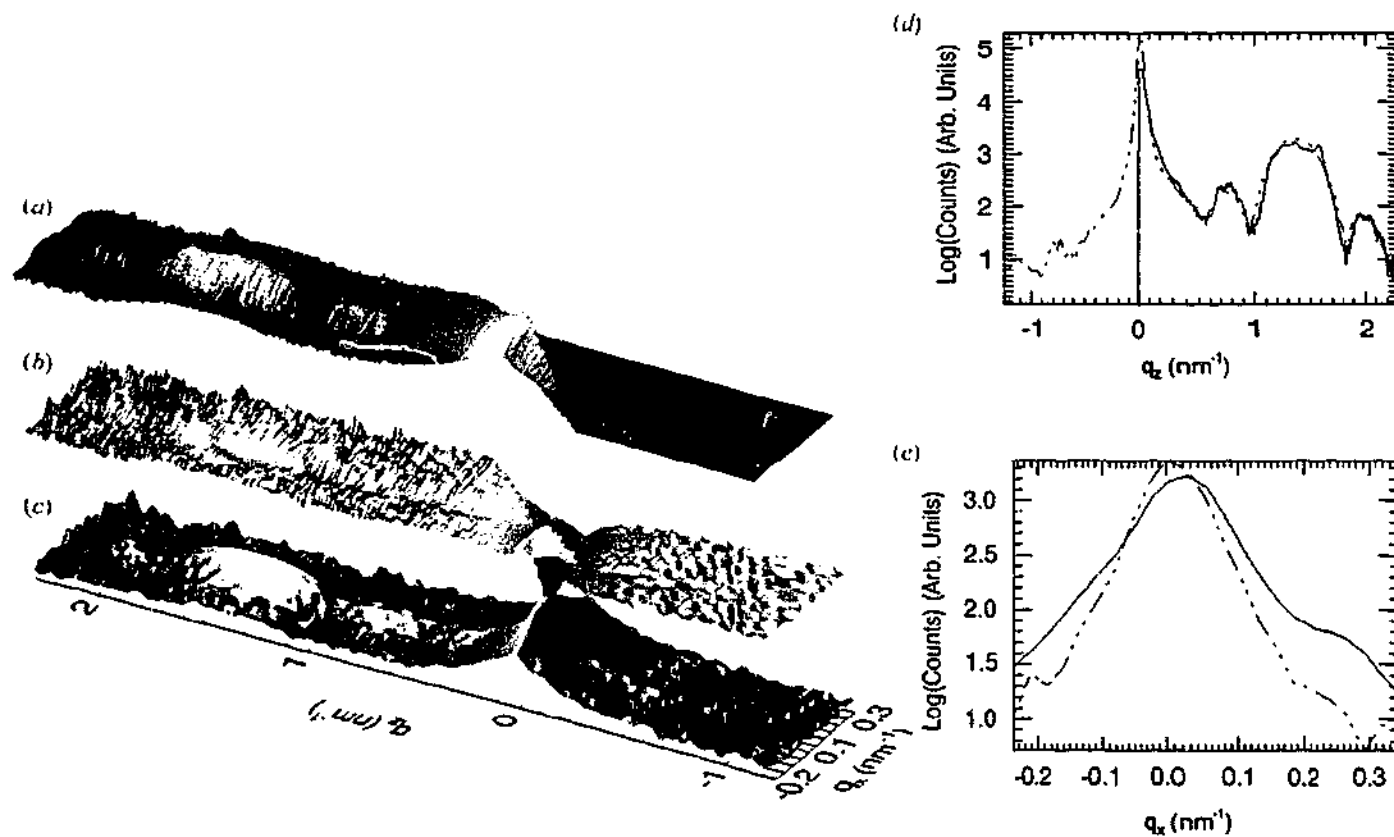


Figure 8
 Comparison of triple-axis RSM and interpolated high-resolution IP data. (a) Interpolated IP RSM, (b) error plot, (c) triple-axis RSM, (d) ω - 2θ scan (extracted from RSM), and (e) ω scan (extracted from RSM). Note that a logarithmic vertical axis is used for each plot. Full line: IP method with interpolation. Dashed line: TAD technique.

assumed in transforming from angular space [$\Delta\omega-(\epsilon/2)$] to reciprocal space to avoid further interpolation.

Fig. 9 shows two plots around the (11 $\bar{2}$ 4) reflection for different samples.

All interpolation and analysis was performed using software written in IDL 6.0 by the authors.

4. Discussion

The aim of this experiment was to utilize the IPs for collecting RSMs rapidly. Superficially the IP method appears attractive, since a scan can be acquired in approximately 45 min, which includes evacuation of the diffractometer chamber and readout of the IPs. A TAD scan, covering the same peak features, requires 3–4 h depending upon the region of interest and spatial resolution. However, before IPs are adopted for routine reciprocal space mapping, it is imperative to establish the suitability of the method for various scan types and to validate the accuracy of the RSM data obtained in the present experiments. These issues are addressed in the remainder of the paper.

Fig. 7 indicates that there are significant differences between the RSM data collected using the TAD method and the IP with interpolation. In particular, the peak is substantially widened in the ω direction (see Fig. 7e), and does not have the correct shape. The $\omega-2\theta$ scan, however, is more accurate, showing all features of the TAD RSM. This means that the IP method can be successfully used for producing $\omega-2\theta$ scans with an IP detector for Group III nitride multilayer samples. It is difficult to specify a resolution for the IP scans because the data are highly asymmetric. The spacing between collected lines (see Fig. 3b) in the $\Delta\omega$ direction (before interpolation), as determined by ω_{step} , is 0.18° for Fig. 7 and 0.09° for Fig. 8. However, along the lines (see Fig. 3b) the step size is up to 20 times smaller (i.e. 0.01°). Limiting ourselves to one IP has resulted in a low

spatial resolution compared with Kinne *et al.* (1998). The resolution could be increased, using only one IP, if the Weissberg screens are made narrower and the IP cassette step size is reduced.

Fig. 8 shows that reducing the ω step size by a factor of two significantly improves the result, in both the q_x and q_y directions. This suggests that, for our sample type, 58 scans are sufficient to cover the range of interest. This should be easy to obtain with some minor modification to the IP system, namely slit and step sizes. The majority of the scan collection time is spent evacuating the system and handling/scanning the IPs. Hence an increase in the number of strips on one plate will not significantly change the scan collection time. Note that information on the IP degrades with time, and can require a correction as explained by Welberry *et al.* (2003). However, as we collected a small number of scans, and hence achieved fast IP throughput, this problem was avoided.

In attempting to cover an extended range in reciprocal space by using a large ω_{step} (see Fig. 3d), the interpolation procedure introduces false peaks. These can be seen in the InGaN peak, and its satellite in the $\omega-2\theta$ scan (see Fig. 7d). Fig. 10 shows a schematic illustration of this phenomenon for a peak elongated along the q_x direction (e.g. the InGaN peak). In Fig. 10(a) the data points lying on

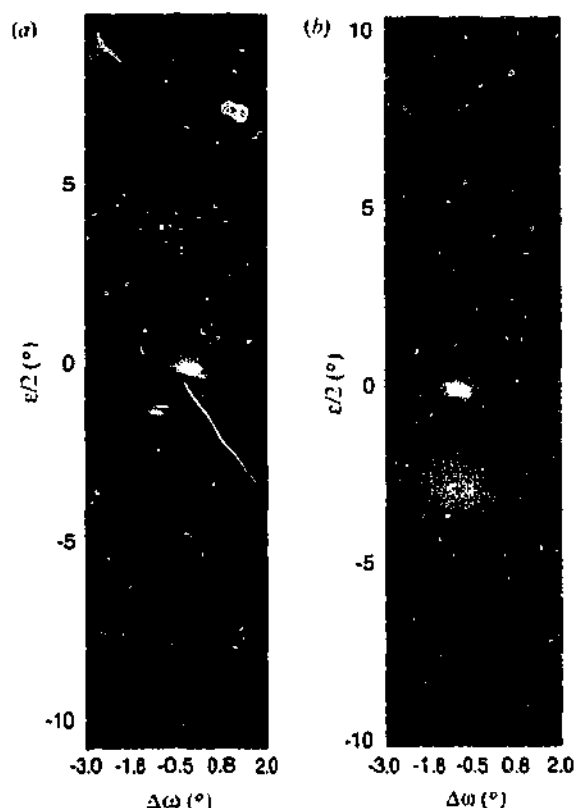


Figure 9
Plots of (11 $\bar{2}$ 4) reflections. Note that axes are in angular units.

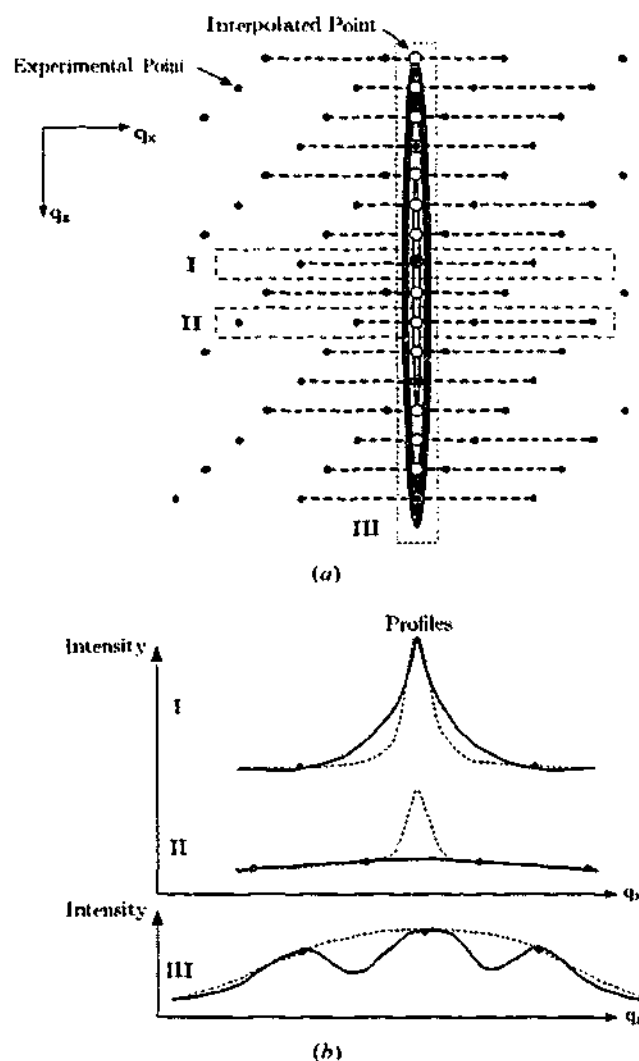


Figure 10
Schematic explaining the origin of peak splitting when ω_{step} is large. (a) Sketch of the RSM showing the position of the experimental (filled circles) and interpolated (open circles) points compared with the 'true' peak, and (b) profiles across the 'true' (dotted line) and interpolated (solid line) peaks, from regions I, II and III indicated in (a).

the peak are generated, *via* interpolation in the q_x direction, from widely spaced experimental points. In general, the experimental points straddle the peak position and hence give a result less than the true peak intensity. This situation is evident in region II in Fig. 10(a). A profile of this region is displayed in Fig. 10(b), which clearly indicates that the interpolated scan has a lower intensity than the true peak. Fig. 10(a) shows that the experimental points are arranged obliquely to the peak direction. Hence some experimental points lie closer to, or on, the peak leading to a more accurate peak intensity. This is the case for region I where an experimental point lies exactly on the peak. The resulting profile is shown in Fig. 10(b). Therefore a translation in the q_x direction produces a series of maxima as shown for region III. A similar problem arises for the GaN peak, which is elongated in the q_x direction, if interpolation is performed in the q_x direction. Therefore the result of interpolation depends on the geometry, and in particular the width of the peak being interpolated compared with the resolution (if a large ω_{step} is used).

Since no explicit smoothing has been applied (only that inherent in the interpolation scheme), further improvement may be possible through the application of suitable filtering; however, such a procedure would require careful justification.

The IP scans were collected in approximately one quarter of the time required for the TAD technique. Hence, subtracting every second row and column reduces the TAD RSM to one that would have been collected in approximately the same time as the IP scans. Fig. 11 compares the cross sections of the high- and low-resolution

TAD RSMs with the interpolated IP scans. The low-resolution TAD RSM was linearly interpolated onto the same grid size as the high-resolution RSM. Comparing the sparse TAD scan with the IP scan suggests that, for the region of interest, data of similar or better quality can be collected in a comparable time using the TAD method than with the IP method. The sparse TAD RSM is of a higher resolution than the IP RSM because the sample spacing is less asymmetric. However, the TAD method requires:

- (i) Greater time for set-up;
- (ii) *A priori* knowledge of the peak positions in reciprocal space. This is problematic for unknown samples, especially for asymmetric reflections (see Fig. 9) and requires long alignment times;
- (iii) More complicated instrumentation, such as a second axis of rotation for the detector/analyser.

The RSMs collected by the IP cover a much wider range than the specific region of interest shown in Fig. 7, although much of this extended region is featureless. However, there are specific cases where the large region can be useful. For example, Fig. 12 shows a scan where powder lines, possibly due to segregated In clusters, were observed across the entire RSM, simultaneously with the Bragg and diffuse peaks.

Fig. 9 shows two RSMs about (1124). RSMs of asymmetric reflections must cover wide regions of reciprocal space, because the peaks do not necessarily align with the q_x or q_y axes. Hence the ability of the IP scans to cover a large region of reciprocal space in a short period of time is very useful for scanning asymmetric reflections (even with low resolution). The range along the $\Delta\omega$ axis shown in Fig. 9 is more than seven times wider than that shown for the symmetric reflection in Fig. 7.

We have introduced integration in the q_x direction by summing across the strips. Summing in the q_x direction over a small range can also introduce errors if the peaks in that direction have different widths. It may be more valid to use the central line of pixels from the strip, and hence remove any integration; however, this would require that the scan be centred correctly on the strip. The TAD method also integrates in the q_x direction (Holý *et al.*, 1999). Kinne *et al.* (1998) fill an entire IP by scanning it past a narrow slit, thereby avoiding the need to integrate in the q_x direction. However, we observed that very bright features caused streaks on the IP in the $\Delta\omega$ direction, presumably because of saturation. Increasing the gap between strips reduces the intensity of the streaks at the adjacent strip position on the IP. No such gaps exist for the procedure adopted by Kinne *et al.* (1998), although the lower count rate of the laboratory X-ray source

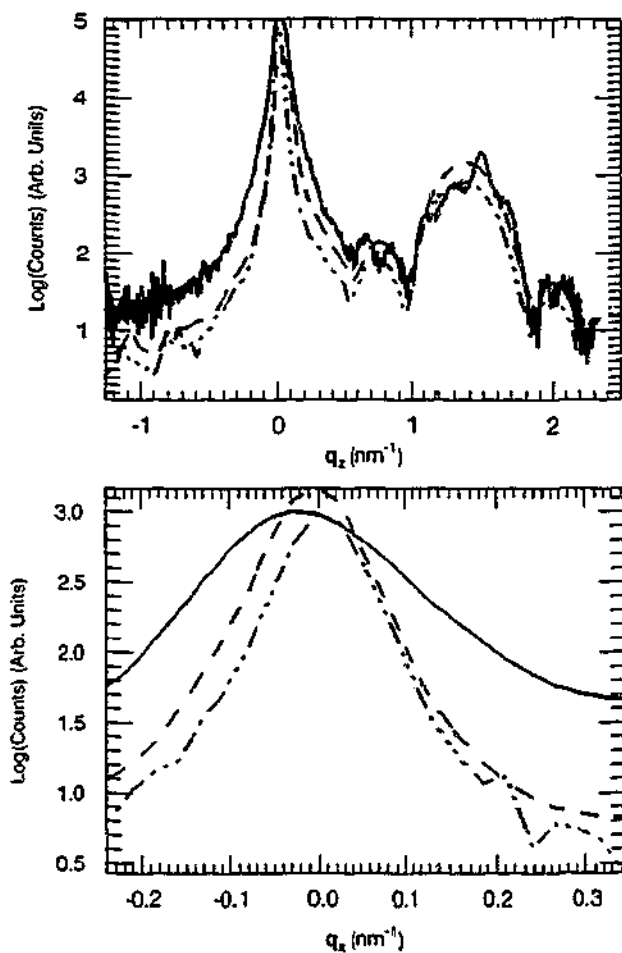


Figure 11 Comparison of RSMs obtained using an IP, TAD and the reduced TAD method. Full line: IP RSM. Dashed line: resized standard RSM. Dot-dashed line: full standard RSM.

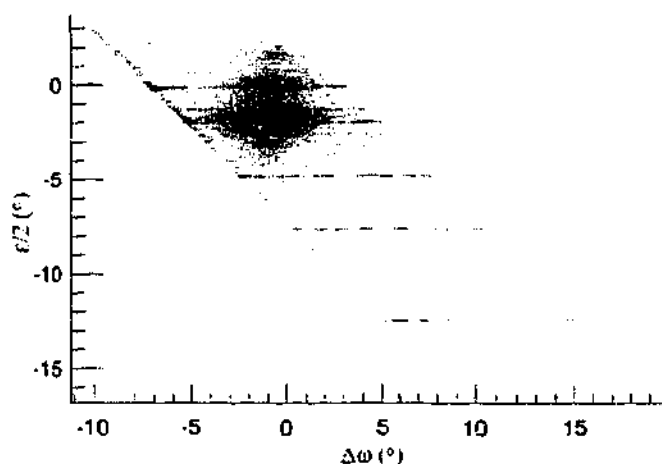


Figure 12 Powder lines collected across the whole imaging plate, possibly due to In segregation.

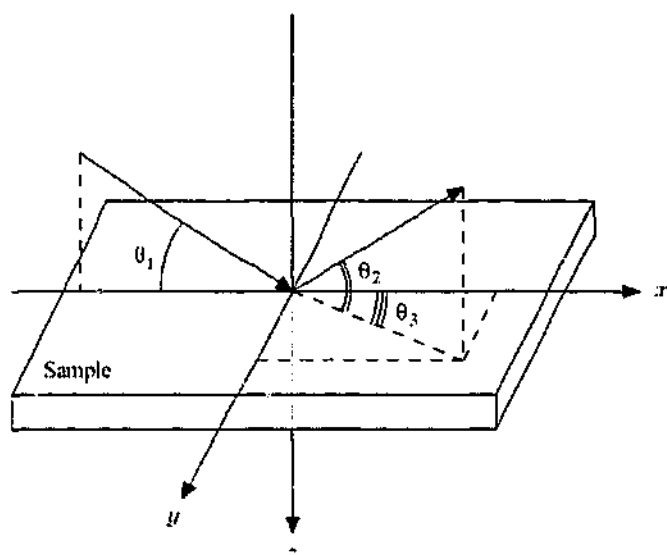


Figure 13
Angle designations for the three-dimensional diffraction geometry.

may have resulted in a less severe problem. The optimum detector for this collection regime would have digital on-line readout, such as that used by Boule *et al.* (2002), but be capable of handling synchrotron intensity, be vacuum stable, and have an appropriate dynamic range. Such detectors are not readily available.

Experimentally we integrate over a small range of reciprocal space, because of a number of instrumental effects (*e.g.* the slits are not infinitely narrow). If the Weissenberg slits were removed, the lateral direction would be available for detecting intensity. This direction corresponds to q_y , which for an incident plane wave is given by

$$q_y = k \cos \theta_2 \sin \theta_3, \quad (11)$$

where θ_2 and θ_3 are defined in Fig. 13. [Note that equations (7) and (8) are not valid in the three-dimensional case.] Gerhard *et al.* (2000) use this fact to collect their RSMs. Their results are similar to a CTR scan (see *e.g.* Takeda & Tabuchi, 2002) with no Weissenberg slits installed. Such a CTR is still integrated over the q_x range, determined by the ω limit selected, but now provides information from a two-dimensional region of reciprocal space. The CTR projects the three-dimensional RSM onto the q_y - q_z plane, *i.e.* perpendicular to the RSM. Hence, by collecting two-dimensional RSMs and two-dimensional CTRs, two perpendicular planes can be gathered without the need to rotate the sample about the q_z axis between the two scans. This ensures that the same region of the sample is investigated for both the q_y - q_z and q_x - q_z planes.

If only a small q_y range is required, and the incident beam has low angular divergence in both the q_x and q_z directions, then our technique can be used to produce a three-dimensional RSM. This is achieved by simply using the profile across the strips, instead of integrating. This cannot be easily achieved using other techniques, except for that of Welberry *et al.* (2003), although in this latter case it would have very limited range.

5. Conclusion

We have implemented a method for collecting reciprocal space maps using imaging plates at the Australian National Beamline Facility. The results indicate that for sparse data care must be taken when interpolating onto a regular grid. More specifically, peaks that are narrow in the q_z direction should be interpolated in the q_x direction, and *vice versa*, to avoid producing false peaks. For our sample type, and the range required, we found that as few as 58 strips can produce acceptable results. The IP method is very useful for scanning large areas when the peak position and shape are not known exactly, which occurs for asymmetric peaks; further, it does not require more sophisticated equipment, such as analyser crystals and 2θ arms. Significantly, sample features of interest may only be observed because of large angular range, such as powder peaks that suggests cluster segregation or polycrystalline regions.

This work was performed at the Australian National Beamline Facility with support from the Australian Synchrotron Research Program, which is funded by the Commonwealth of Australia under the Major National Research Facilities Program. The samples were prepared by Professors H. Amano and I. Akasaki at the Department of Materials Science and Engineering, Meijo University. The authors would like to thank Dr Imants Svalbe, Professor Rob Lewis, Dr Karen Siu and Professor Vasily Punegov for their valuable contributions. STM acknowledges the support of an Australian Post-graduate Award. KMP and MJM acknowledge the support of the Australian Research Council.

References

- Barnea, Z., Creagh, D. C., Davis, T. J., Garrett, R. F., Janky, S., Stevenson, A. W. & Wilkins, S. W. (1992). *Rev. Sci. Instrum.* **63**, 1069–1072.
- Boule, A., Masson, O., Guinebretière, R., Lecomte, A. & Dauger, A. (2002). *J. Appl. Cryst.* **35**, 606–614.
- Butler, B. D., Haeffner, D. R., Lee, P. L. & Welberry, T. R. (2000). *J. Appl. Cryst.* **33**, 1046–1050.
- Fewster, P. F. (1997). *Crit. Rev. Solid State Mater. Sci.* **22**, 69–110.
- Garrett, R. F., Cookson, D. J., Foran, G. J., Sabine, T. M., Kennedy, B. J. & Wilkins, S. W. (1995). *Rev. Sci. Instrum.* **66**, 1351–1353.
- Gerhard, T., Albert, D. & Faschinger, W. (2000). *J. Cryst. Growth*, **214**, 1049–1053.
- Holy, V., Pietsch, U. & Baumbach, T. (1999). *High-Resolution X-ray Scattering from Thin Films and Multilayers*. Heidelberg: Springer-Verlag.
- Iida, A. & Kohra, K. (1979). *Phys. Status Solidi*, **51**, 533–542.
- Kinne, A., Thoms, M., Röss, H. R., Gerhard, T., Ehinger, M., Faschinger, W. & Landwehr, G. (1998). *J. Appl. Cryst.* **31**, 446–452.
- Mudie, S., Pavlov, K., Morgan, M., Tabuchi, M., Takeda, Y. & Hester, J. (2003). *Surf. Rev. Lett.* **10**, 513–517.
- Mudie, S. T., Pavlov, K. M., Morgan, M. J., Takeda, Y., Tabuchi, M. & Hester, J. R. (2002). *Proceedings of the 2002 Conference on Optoelectronic and Microelectronic Materials and Devices (COMMAD 2002)*, Sydney, Australia, 11–13 December 2002, pp. 111–116. Piscataway, NJ: IEEE.
- Nesterets, Y. & Punegov, V. (2000). *Acta Cryst.* **A56**, 540–548.
- Osborn, J. C. & Welberry, T. R. (1990). *J. Appl. Cryst.* **23**, 476–484.
- Takeda, Y. & Tabuchi, M. (2002). *J. Cryst. Growth*, **237/239**, 330–337.
- Welberry, T. R., Goossens, D. J., Haeffner, D. R., Lee, P. L. & Almer, J. (2003). *J. Synchrotron Rad.* **10**, 284–286.

ANALYSIS OF GaN/AlN BUFFER LAYERS GROWN ON SAPPHIRE SUBSTRATES VIA STATISTICAL DIFFRACTION THEORY

S.T. Mudie¹, K.M. Pavlov¹, M.J. Morgan¹, Y. Takeda², M. Tabuchi², and J. Hester³

¹School of Physics and Materials Engineering
Monash University 3800, Australia

²Department of Materials Science and Engineering
Nagoya University, Nagoya, Japan

³Australian Nuclear Science and Technology Organisation
PMB 1, Menai, NSW 2234, Australia

Email: [REDACTED]

ABSTRACT

GaN layers are often grown on a sapphire substrate, with a low-temperature-deposited AlN layer and a thick GaN buffer layer. High-resolution X-ray diffraction experiments were conducted on BL20-B at the Photon Factory (Tsukuba, Japan), to investigate the structural quality of the AlN and GaN layers. Reciprocal Space Mapping was used to study samples at each stage of the growth process and for various layer thicknesses.

Two analysis techniques were compared. The first utilised broadening of reflections in reciprocal space, and the second was based on Statistical Diffraction Theory (SDT). Both techniques yield information about the mosaic blocks and layer thicknesses; however, simulations based on SDT give information on strain and tilt distribution within the AlN layer, evident in off centre, non-symmetric, peaks. This suggests a possible mechanism by which AlN buffer layers can be exploited to improve device characteristics. Our work also demonstrates the efficacy of SDT for the analysis of these structures.

1. INTRODUCTION

Group III nitride semiconductors are important for optoelectronic and transistor technologies. They cover almost all of the visible and near UV spectrum, and have good thermal stability [1]. Development of devices which utilise this semiconductor system has been hindered because a suitable substrate (with matched lattice parameters and thermal expansion) is not available. Incorrect matching of the substrate (e.g., sapphire) to the semiconductor results in the formation of a dislocation net. The regions of deformed crystal between the dislocation lines can be modelled as mosaic blocks. A successful technique to reduce the dislocation density is the inclusion of a low-temperature (LT) deposited AlN (buffer) layer between the substrate and the GaN active layer [2].

In a previous paper [3] we reported results of High Resolution X-Ray Diffraction (HRXRD) experiments to characterise AlN (buffer) layers of various thickness, including the subsequent GaN layers deposited on top. The analysis was performed following the approach used by Metzger *et al.* [4]. Here we present a more advanced analysis, which utilises Statistical Diffraction Theory (SDT), and compare our results to the previous analysis.

Reciprocal Space Maps (RSMs) contain a significant amount of information about the sample structure because they collect information from a two-dimensional region of reciprocal space. However, traditional analysis techniques discard some of this information by only utilising one-dimensional rocking curves, (see e.g., [3] and references therein). In order to maximise the information, a theory is required which treats both the coherent and the diffuse scattering. We have applied Kato's statistical theory [5, 6] to achieve this goal. This theory was developed to treat Triple-Crystal Diffractometry in both the dynamical [7] and kinematical [8] cases. A redevelopment and simplification of the dynamical case for multilayer systems is in preparation for publication [9], and has been previously used in the kinematical limit for the analysis of nitride samples [10]. Within this redevelopment the intensity registered by the detector is given as:

$$I^{det}(\mathbf{Q}) = \int dq_{hx} R(q_{hx}) [I_h^c(q_{hx}, Q_x, Q_z) + I_h^d(q_{hx}, Q_x, Q_z)] \quad (1)$$

where \mathbf{Q} is the scattering vector, R is the reflectivity of the analyser crystals, I_h^c and I_h^d are the coherent and

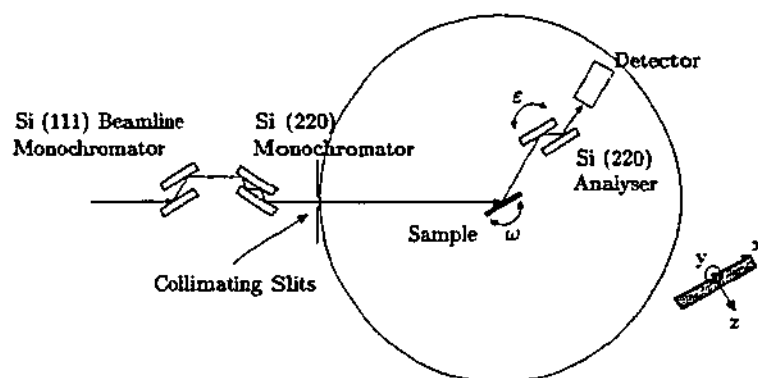


Figure 1: Triple crystal set-up.

diffuse intensities respectively, and q_{hr} describes the divergence of the diffracted beam.

Utilising the SDT, the epitaxial layer is modelled as an array of mosaic blocks. The traditional approach for diffraction by mosaic blocks can be found in Zachariasen's book [11]; however, the present approach must be formulated within the SDT framework in order to treat randomly distributed defects. Mosaic block models are reported in the literature for SDT, including work by Nesterests and Punegov [8], Holý *et al* [12], Bushuev [13, 14], and Kato [15]. Of these, Nesterests and Punegov's model [8] is the most general, since it considers rotation and size of the blocks; further it more accurately describes real epitaxial layers by assuming the blocks to be parallelepipeds (usually confirmed by TEM). Of the other models Holý *et al.* [12] assume the blocks to be spheres, and Kato [15] and Bushuev [13, 14] assume laterally infinite blocks, with rotation of the blocks only in one direction.

The work presented here utilises SDT in the kinematical limit with the model of Nesterests and Punegov [8] describing the mosaic blocks. Mosaic block dimensions and orientation, lattice strain and layer thickness can all be determined quantitatively. The kinematical limit is justified because the samples are thin and are of low-crystalline quality. Investigation of the low-temperature deposited AlN buffer layer is reported, and compared with previous analyses [3].

2. EXPERIMENTAL

2.1 Sample Preparation

The sample Preparation has been described elsewhere [3]. In brief, the samples were produced using organometallic vapour phase epitaxy (OMVPE) on (0001) sapphire substrates. Three sample types were produced, from different stages of the growth process:

- A: AlN buffer layer deposited at 400°C;
- B: AlN buffer deposited at 400°C and annealed at 1100°C;
- C: GaN layer (30nm) deposited at 1100°C on an annealed AlN buffer.

Three different buffer layer thicknesses were used; namely 10nm, 30nm and 70nm.

2.2 Characterisation

Triple Crystal Diffractometry (TCD) measurements were reported in an earlier paper [3]. The experiments were conducted at the Australian National Beamline Facility (ANBF), on beamline 20B at the Photon Factory, Japan. The set-up (see Fig. 1) utilised a Si(002) quad bounce crystal in addition to the regular beamline monochromator. This configuration reduced the incident beam divergence (≈ 7 arcseconds) and wavelength dispersion ($\Delta\lambda/\lambda = 7 \times 10^{-5}$). A Si(002) double bounce crystal was used for the analyser, which restricted the angular range registered by the detector. A Radicon high count rate scintillation detector was used to record the x-ray intensity. The analyser, detector and sample stage were mounted within a vacuum chamber to reduce air scatter.

3. RESULTS AND ANALYSIS

In what follows, *layer* refers to an entire epitaxial layer, whilst *sub-layer* refers to a stratum within a layer

Table 1: Parameters for the fitting routine .

			I						II	
			l (nm)	L_x (nm)	L_z	Δ (°)	$\Delta d_{\perp}/d$	Tilt (°)	l (nm)	L_z (nm)
70nm	A	AlN:1	22	30	4.2	6	-0.016	-0.9	40	40
		AlN:2	48	30	1.5	6	0.06	-0.9	30	30
	B	AlN:1	18.7	30	4.8	5	-0.027	-0.6	18.7	18.7
		AlN:2	51.3	30	1.0	5	0.06	-0.6	51.3	51.3
	C	AlN:1	-	100	-	2	See Figure 4		10	10
		AlN:2	-	100	-	2	See Figure 4		60	60
30nm	A	AlN:1	10	30	2.5	8	-0.013	-1	10	10
		AlN:2	20	30	1.5	8	0.02	-1	20	20
	B	AlN:Top	4	100	4	0.05	-0.008	0	4	4
		AlN:Middle	8.7	30	6.5	5	-0.032	-0.6	13	13
		AlN:Bottom	17.3	30	1.5	5	0.03	0	13	13
	C	AlN:Top	-	400	5	0.02	See Figure 4		-	-
		AlN:Bottom	-	10	5.5	2.3	See Figure 4		30	30

defined by specific physical properties (e.g., strain).

Complete analysis was performed for the 30nm and 70nm samples only. The 10nm samples did not provide enough intensity for acceptable RSM scans. The experimental data consisted of RSMs and one-dimensional scans about the AlN(0002), and in some cases AlN(0004), reciprocal lattice points. The analysis was performed using simulations written in the IDL programming language.

Two approaches were taken to fit the data. The first (I) was to assume that each sub-layer had a constant strain value, and allows L_z (mosaic block size in z direction) to take any value, equal to, or smaller than, the thickness of the sub-layer, in order to fit the peak width in the q_z direction. In the second approach (II) L_z was set to the thickness of the sub-layer (as is evident in TEM images for some systems) and a strain gradient was introduced within the thickness of the sub-layer.

Table 1 shows the results of the simulations. Note that l is the thickness of the layer, L_x is the lateral dimension of the mosaic blocks, Δ is the width of the orientation (Gaussian) spread of the blocks around the y -axis, and the tilt is the rotation of the entire sub-layer about the y -axis. The simulation parameters are identical for approaches I and II, except for l , L_z , and the strain (although the average strain is the same). In the alternative approach (II) l and L_z are also indicated in Table 1. Note that the thicknesses reported were not measured directly, because thickness oscillations were not observable. Hence layer thicknesses determined by the growth regime were assumed correct, with simulations providing the ratio of sub-layer thicknesses.

Two peaks near AlN(0002) were apparent for sample type A, for both thicknesses, and type B for the 70nm sample, suggesting that the AlN layer has segregated into two sub-layers. In the q_z direction one peak is much wider than the other, as indicated by the L_z values. The average strain indicates that the thin sub-layer is predominantly in compression and the other sub-layer in tension. A compressive stress would be due to a positive strain in the sub-layer parallel to the surface, with a concomitant negative strain in the perpendicular direction and vice versa. It has been reported [16] that the AlN epitaxial layer is rotated 30° with respect to the substrate. The alignment of the atomic sites produces a lateral compression (not tension as the lattice parameters would suggest), and hence tensile strain in the z direction. Therefore the lowest quality sub-layer (in tension) is likely in direct contact with the substrate. All peaks are broad in the q_x direction, which indicates either a large Δ , or a small L_x . Unfortunately the scans were noisy and not wide enough to determine the contribution from each parameter. Hence Table 1 only indicates the maximum Δ and minimum L_x . For the 70nm annealed sample, an acceptable RSM is available for fitting - not simply one-dimensional scans. Hence with additional work we could further constrain the parameters. This is a strength of this technique. However, for all three samples (i.e., 70nm A and B, and 30nm A) the mosaic blocks are small.

For the 30nm sample type B, three layers were observed. Two of the sub-layers have similar characteristics to those discussed above, i.e., exhibiting small mosaic blocks and large Δ . However, the third layer is significantly different, with a much larger block size and reduced Δ . It is also effectively unstrained with no tilt. As larger block sizes are synonymous with lower defect density, and because there is a small mis-orientation of the blocks,

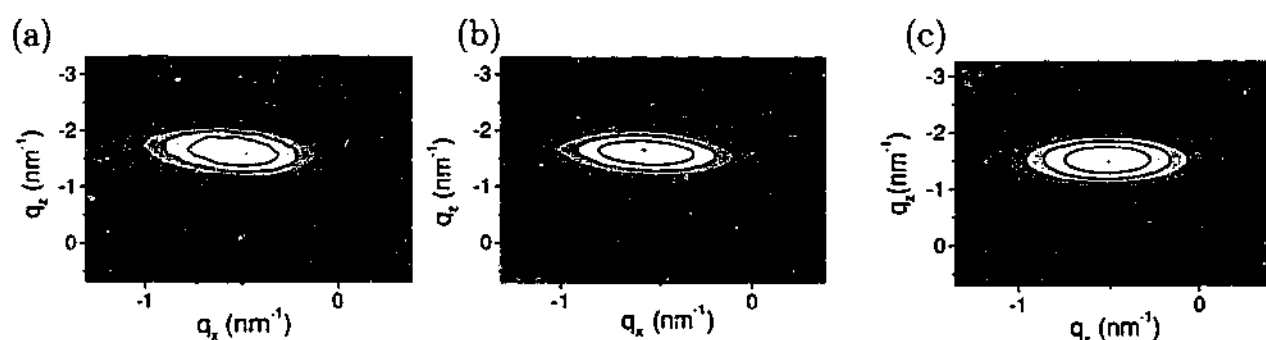


Figure 2: RSMs about the 30nm AlN(0002) reciprocal lattice point. (a) Experimental, (b) Simulation: strain gradient, and (c) Simulation: no strain gradient.

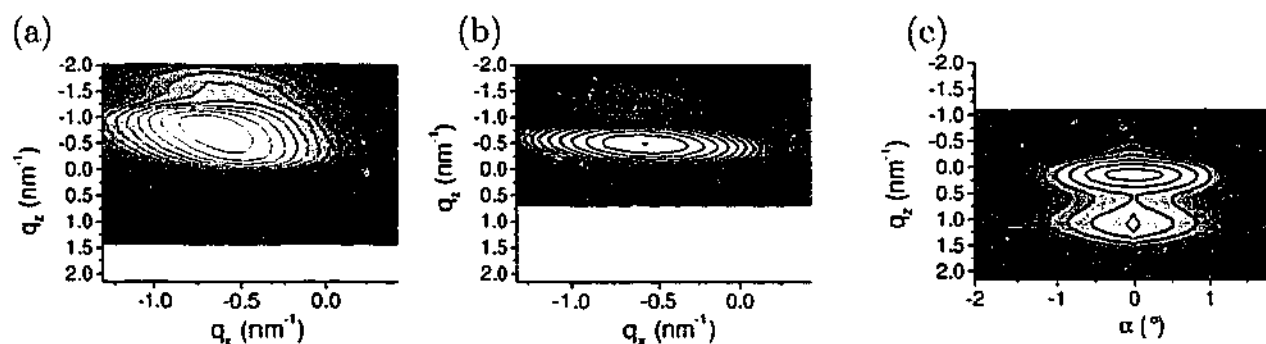


Figure 3: Scans (logarithmic scale) about the 70nm AlN(0002) reciprocal lattice point. (a) Experimental RSM layer, (b) Simulation of RSM, and (c) Experimental CTR.

we can describe this sub-layer as almost perfectly crystalline. The analysis did not indicate which layer was on top (a dynamical approach would be required), nevertheless it is indicative of a higher quality layer forming on top of the lower quality layer, as indicated in Table 1.

The samples of type C, i.e., capped with 30nm of GaN, were characterised on a subsequent visit to the Photon Factory, using a larger slit size. The increased incident intensity improved the counting statistics, and did not seem to diminish the angular resolution. Figures 2 and 3 show the experimental and simulated data for sample C. A strain gradient was necessary to fit the 70nm sample, hence only approach II was utilised; l and L_z is not reported for approach I in Table 1. A further extension to the model allowed the tilt to vary across the sub-layer so that the complex peak shape could be fitted correctly. The strain and tilt profiles are shown in Figure 4a. The oscillation in the tilt profile at zero thickness is due to experimental noise and the bump at about 60nm is due to the second layer.

Two broad AlN peaks were seen for the 70nm sample, showing a high level of strain. The GaN layer was also observed. It has not been analysed, but it is more narrow in the q_z direction than in q_x , suggesting minimal strain, but some degree of mosaicity. The GaN layer was not tilted.

A tilt gradient (and hence strain gradient) was required for the 30nm sample (type C) simulation so as to reconstruct the slight rotation of the peak in reciprocal space. If this rotation was ignored, the fit could have been made with one layer, by decreasing L_z as indicated in Table 1 and shown in Figure 2c.

The 30nm sample (type C) contains two AlN layers - a higher quality layer and a lower quality layer. The higher quality layer was not evident in the RSM, because the step size was too large to see the very narrow peak. The peak was observed in the θ - 2θ scan. This layer has an even larger lateral block size than the uncapped layer with a reduced Δ . It proved difficult to determine the relative thicknesses of these sub-layers (hence thicknesses for this sample are not reported in Table 1), because the higher quality layer seems too thin. This suggests that it may contain a high density of point defects. However, it appears that the lower quality layer is significantly thicker than the higher quality layer.

Previous results [17] indicate that, of the thicknesses investigated, a buffer layer of 30nm produces the best quality optoelectronic active layer. We conjecture that this is due to the high quality layer seen for the 30nm sample, produced during the annealing of the sample. The same conclusion was reached in our previous work; however, in that case only the dislocation density and the L_x size was explored, and only for the 30nm samples. For sample type B the previously determined L_x sizes were 84nm and 20nm, which compares well to the 100nm

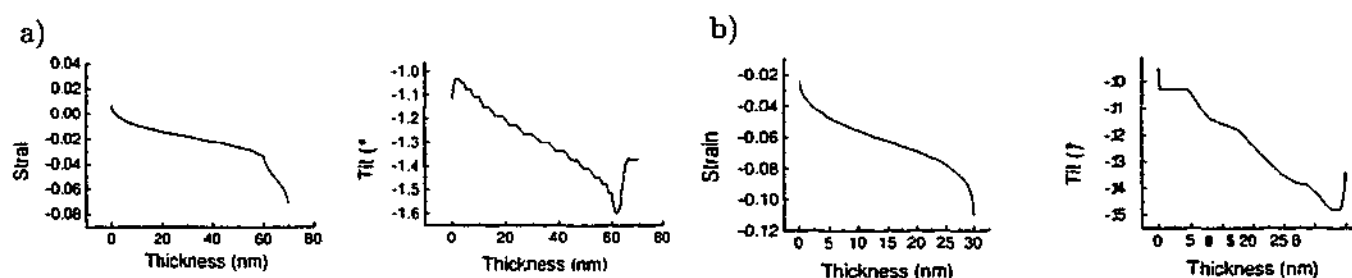


Figure 4: Distribution of strain (*left*) and tilt (*right*) for sample type C: (a) 70nm and (b) 30nm thick AlN layer.

and 30nm determined using SDT. The thickness values also compare favourably. However, for sample type A and C the L_z sizes are different by a factor of 3-10. This discrepancy may be due to the inadequacy of the data used (particularly sample type A), or problems with the previous model.

In addition to our RSM measurements, synchrotron Crystal Truncation Rod (CTR) data has been obtained [17]. Sapphire and GaN peak positions agree (e.g., GaN peak at $q_z = 1\text{nm}^{-1}$ in Figures 3a and c), however, discrepancies are seen for the position and width of the AlN peaks. As the AlN layer is of a low quality this discrepancy may be due to spatial inhomogeneity of the sample, with different regions sampled for the two experiments. However, in order to confirm this we compared the two-dimensional CTR data (see Figure 3c) to the RSMs. We emphasise that these are not equivalent scans. RSMs are sensitive to variations in q_x and CTR in q_y . Hence Figure 3a indicate a tilt of the entire layer about the y-axis (offset peak in RSM) but not the x-axis (on axis in CTR, Figure 3c). This assumes the samples had the same orientation for both experiments.

It is difficult to indicate the uncertainty for the parameters simulated in this work, because of their interdependence. This is particularly true for Δ and L_x , and also for L_z and the strain distribution. In the former case, analysis of a different set of data [10] showed that with a better signal-to-noise ratio, and a wider scan range in Q_x , the two parameters can be disentangled through their peak shape.

The problems in the present analysis highlight the difficulty in achieving high quality scans with very thin samples. We are attempting to fit many parameters, and hence a large amount of data is required to ensure that the solutions converge. However, RSMs about asymmetric reflections will give us information about the strain in the lateral direction and help constrain the other parameters, particularly L_z . Additionally CTR scans of different regions of the sample would determine the homogeneity of the material.

4. CONCLUSION

HRXRD studies were performed on AlN buffer layers deposited on sapphire substrates. RSM data was analysed using the Statistical Diffraction Theory in order to determine relevant physical parameters. It was shown that the buffer layers segregate into two sub-layers. For the 30nm sample it was found that one of these layers was of a higher crystalline quality. This layer would be capable of supporting a high quality optoelectronic active layer, effectively matching GaN semiconductor to the sapphire substrate. However, further synchrotron studies are required in order to make more specific recommendations on the optimum growth parameters.

ACKNOWLEDGMENTS

This work has performed at the Australian National Beamline Facility with support from the Australian Synchrotron Research Program, which is funded by the Commonwealth of Australia under the Major National Research Facilities Program. SM acknowledges the support of an Australian Postgraduate Award.

References

- [1] I. Akasaki and H. Amano, *Jpn. J. Appl. Phys.* **36**, 5393 (1997).
- [2] H. Amano, N. Sawaki, I. Akasaki and Y. Toyoda, *Appl. Phys. Lett.* **48**, 353 (1986).
- [3] S. Mudie, K. Pavlov, M. Morgan, Y. Takeda, M. Tabuchi, and J. Hester, *Surface Review and Letters* (in press).
- [4] T. Metzger, R. Höppler, E. Born, O. Ambacher, M. Stutzmann, R. Stömmer, M. Schuster, H. Göbel, S. Christiansen, M. Albrecht and H. Strunk, *Philosophical Magazine A* **77**, 1013 (1998).

- [5] N. Kato, *Acta Cryst.* **A36**, 736 (1980).
- [6] N. Kato, *Acta Cryst.* **A36**, 770 (1980).
- [7] K. Pavlov and V. Punegov, *Acta Crystallogr.* **A56**, 227 (2000).
- [8] Y. Nesterests and V. Punegov, *Acta Cryst.* **A56**, 540 (2000).
- [9] K. Pavlov, and V. Punegov, (2002) (in preparation).
- [10] L. Kirste, K. Pavlov, S. Mudie, V. Punegov and N. Herres XTOP-2002. 6th Biennial Conference on High Resolution X-Ray Diffraction and Imaging, 10-14th Sept. 2002, Grenoble, France. Presented as a poster P57. Collected Abstracts p. 137.
- [11] W. Zachariasen, *Theory of X-Ray Diffraction in Crystals*, Dover Publications, New York (1967).
- [12] V. Holý, J. Kubena, E. Abramof, K. Lischka, A. Pesek and E. Koppensteiner, *J. Phys. D: Appl. Phys.*, **74**, 1736 (1993).
- [13] V. Bushuev, *Sov. Phys. Solid State*, **31**, 1877 (1989a).
- [14] V. Bushuev, *Sov. Phys. Crystallogr.*, **34**, 163 (1989b).
- [15] N. Kato, *Z. Naturforsch.*, **37a**, 485 (1982).
- [16] Y. Takeda and M. Tabuchi, *Gallium Nitride and Related Semiconductors*, Ed. J.H. Edgar, S. Strite, I. Akasaki, H. Amano, and C. Wetzel, INSPEC, IEE, London, 381 (1999).
- [17] M. Tabuchi, H. Kyouzu, Y. Takeda, S. Yamaguchi, H. Amano, and I. Akasaki, *J. Cryst. Growth.*, **237-239**, 1133 (2002).